Aim and Scope

The objective of the *Journal of Residuals Science & Technology* (JRS&T) is to provide a forum for technical research on the management and disposal of residuals from pollution control activities. The Journal publishes papers that examine the characteristics, effects, and management principles of various residuals from such sources as wastewater treatment, water treatment, air pollution control, hazardous waste treatment, solid waste, industrial waste treatment, and other pollution control activities. Papers on health and the environmental effects of residuals production, management, and disposal are also welcome.

Editor-in-Chief

P. Brent Duncan
Department of Biology
University of North Texas
Denton, TX, USA
pduncan@unt.edu

Editorial Advisory Board

Muhammad Abu-Orf
AECOM, USA
mohammad.abu-orf@aecom.com

Steve Dentel
University of Delaware, USA
dentel@udel.edu

Richard Dick
Cornell University, USA
rid1@cornell.edu

Guor-Cheng Fang, Ph.D.
Hungkuang University, Taiwan
gcfang@sunrise.hk.edu.tw

Robert Hale
Virginia Iustitute of Marine Science, USA
hale@vims.edu

Paul F. Hudak
University of North Texas, USA
hudak@unt.edu

Blanca Jimenez Cisneros
Inst. de Ingenieria, UNAM, Mexico
bjc@mumas.iingen.unam.mx

Julia Kopp
Technische Universitat
Braunschweig, Germany
j.kopp@tu-bs.de

Uta Krogmann
RutgersUniversity, USA
krogmann@aesop.rutgers.edu

D. J. Lee
National Taiwan University, Taiwan
djlee@ntu.edu.tw

Giuseppe Mininni
Via Reno 1, Italy
mininni@irsa.rm.cnr.it

John Novak
Virginia Tech, USA
jtnov@vt.edu

Nagaharu Okuno
The University of Shiga Prefecture,
Japan
okuno@ses.usp.ac.jp

Jan Oleszkiewicz
University of Manitoba, Canada
oleszkie@ms.umanitoba.ca

Banu Örmeci
Carleton University, Canada
banu_ormeci@carleton.ca

Ian L. Pepper
University of Arizona, USA
ipepper@ag.arizona.edu

Ioana G. Petrisor
Co-Editor-in-Chief
Environmental Forensics Journal, USA
Environmental.Forensics@gmail.com

Bob Reimers
Tulane University, USA
rreimers@tulane.edu

Dilek Sanin
Middle East Technical University,
Turkey
dsanin@metu.edu.tr

Mike Switzenbaum
Professor Emeritus
Marquette University, USA
michael.switzenbaum@marquette.edu

Heidi Snyman
Golder Associates Africa (Pty) Ltd.,
South Africa
hsnyman@golder.co.za

Ludovico Spinosa
Consultant at Commissariat
for Env. Energ. in Region,
Puglia, Italy
ludovico.spinosa@fastwebnet.it

P. Aarne Vesilind
Bucknell University, USA
aarne.vesilind@gmail.com

Doug Williams
California Polytechnic State
University, USA
wmsengr@thegrid.net

JOURNAL OF RESIDUALS SCIENCE & TECHNOLOGY—Published quarterly—January, April, July and October by DEStech Publications, Inc., 439 North Duke Street, Lancaster, PA 17602.

Indexed by Chemical Abstracts Service. Indexed/abstracted in Science Citation Index Expanded. Abstracted in Current Contents/Engineering, Computing & Technology. Listed in ISI Master Journal.

Subscriptions: Annual $219 per year. Single copy price $60. Foreign subscriptions add $45 per year for postage.

(ISSN 1544-8053)

DEStech Publications, Inc.
439 North Duke Street, Lancaster, PA 17602-4967, U.S.A.

©Copyright by DEStech Publications, Inc. 2016—All Rights Reserved

CONTENTS

Research

Removal of Cadmium from Aqueous Solutions using Ceramsite Mainly Composed of Pb-Zn Tailings

SHUNCAI WANG, SHUANG LI, YUE ZHAO and ZHICHENG WEI
Key Laboratory of Integrated Regulation and Resource Development on Shallow Lake of Ministry of Education,
College of Environment, Hohai University, Nanjing 210098, China

ABSTRACT: This paper studied the feasibility of applying ceramsite that is mainly composed of Pb–Zn tailings for cadmium removal in a laboratory environment. The influences of dosage, contact time, pH and the adsorption isotherm were examined via batch experiments. Further, two models including Freundlich and Langmuir isotherms were used to fit the experimental data. Results show that the removal rate of cadmium increases from 25% to 98% when pH increases from 2 to 12. Due to high efficiency, this type of ceramsite shows great potential for application in cost-effective elimination of cadmium from industrial wastewater.

INTRODUCTION

HEAVY METALS, such as lead, zinc, cadmium, copper and nickel are toxic to human bodies and other living creatures if their concentrations exceed the acceptance limit [1]. Among these metals, cadmium is one of the most hazardous substances. Due to its difficulty in being detoxified, cadmium tends to be assimilated, gathered and stored by organisms. Eventually, it may accumulate in human bodies via the food chain, and induce cancer, hypertension, weight loss, bone lesions and Itai-Itai disease [2]. Cd^{2+} is a toxic heavy metal ion, typically found in industrial wastewater. In particular, Cd^{2+} often exists in wastewater generated during manufacturing of alloys, pigment, and plastic, as well as processes like electroplating, mining, smelting, metallurgy and refining [3]. To protect the health of humans and the environment, Cd^{2+} is expected to be eliminated from wastewater.

Adsorption is an economic, effective, and efficient method for wastewater purification [4]. During adsorption, the cost and effectiveness of the adsorbent used in adsorption often determines the quality of an adsorptive separation process. As a result, a variety of adsorbents have been studied and developed during the last decade, such as clay minerals [5], activated carbon [6], chitosan [7], natural inorganic minerals [8], zeolites [9], tailings [10], lignocelluloses [11] and functionalized polymers [12]. Nevertheless, the majority of these adsorbents are either ineffective because of less active surface sites and diffusion limitations, or show difficulties of separation from wastewater, production of another waste, and a high cost. This work is aimed at studying the feasibility of utilizing ceramsite mainly composed of Pb-Zn tailings to adsorb cadmium Cd^{2+} from wastewater. Specifically, small scale experiments were carried out to test the adsorption characteristics of ceramsite for application in cadmium Cd^{2+} elimination from wastewater. In addition, the influences of dosage, contact time, pH, and the adsorption isotherm were examined in batch experiments by using cadmium nitrate solutions.

MATERIALS AND METHODS

Preparation of Ceramsite

The precursor powders used in this study were lead–zinc flotation tailings provided by the Nanjing Pb-Zn flotation plant in China. The Pb-Zn flotation tailings with 5% moisture were baked at 378K. According to the experimental results, ceramsite is sintered from a mixture of tailings, clay and activated carbon (tailings: clay: activated carbon = 420:60:10). The weight percentage of calcium lignosulphonate solution (binder) is 10%. Ceramsite is fabricated using a granulating disc machine and baked at 1513K in a muffle furnace for 30 min. The particle diameter of the ceramsite is around 5–10 mm. Physical properties of ceramsite and

---

*Author to whom correspondence should be addressed.
E-Mail: wshcai@hhu.edu.cn; Tel.: +86-025-8378-7870; Fax: +86-025-8378-7870

1544-8053/16/02 S001-05

doi:10.12783/issn.1544-8053/13/4/S1

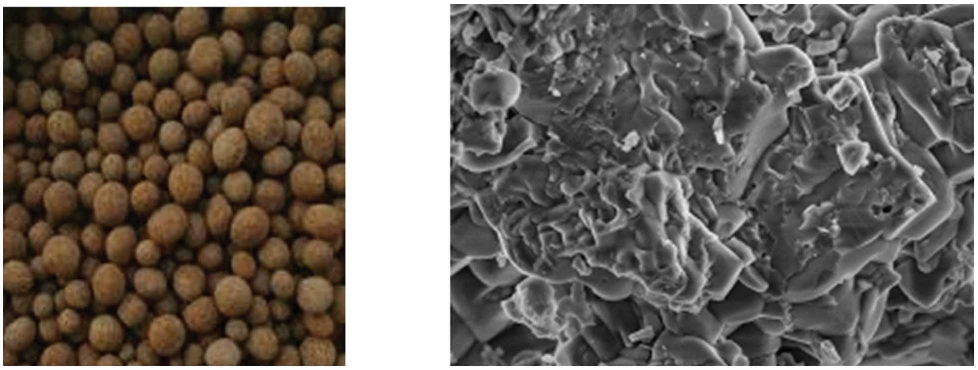

Figure 1. *Pictures of the ceramsite and SEM.*

its chemical composition are presented in Table 1 and Table 2. A picture of ceramsite and a SEM image of its surface are shown in Figure 1.

Preparation of Synthetic Solution

The cadmium nitrate solutions containing 4, 10, 16, 20 and 30 mg Cd/L were prepared by dissolving solid $Cd(NO_3)_2$ (analytical reagent grade) in distilled water.

Experimental Procedure

To examine cadmium adsorption, 1500 mg ceramsite was placed in a 150 mL conical flask and 100 mL cadmium nitrate solution with a known concentration was added. The conical flask was capped and placed on an orbital shaker and agitated at 180 rpm for 2 h to reach adsorption equilibrium at room temperature (20–25°C). The suspension was filtered using a 0.8 µm-lmpore glass fiber filter paper after the agitation was completed, then the filtrate was analyzed. Because the cadmium concentration in the filtrate decreased, the elimination of Cd^{2+} was realized.

Analytical Methods

An atomic absorption spectrophotometer (AAS, GGX-600) provided by Sea-ray Equipment was used to test the concentration of cadmium concentration. The scanning electron microscope (SEM, S-3400N) was used to test the chemical composition of the ceramsite.

Table 1. Physical properties of Ceramsite.

Physical Parameters	Apparent Density (g/cm^3)	Bulk Density (g/cm^3)	Specific Surface Area (m^2/g)	Porosity (%)
Values	2.51	0.81	0.0212	67.67

RESULTS AND DISCUSSION

Effect of Adsorbent Dosage

The effect of adsorbent dosage of ceramsite (0.2–4 g) on the adsorption of Cd^{2+} is presented in Figure 2. The experiments were conducted at a constant initial concentration of 10 mg/L, pH = 9, contact time of 120 min and room temperature (20–25°C).

According to Figure 2, the Cadmium elimination percentage first increases with the increase in the dosage of ceramsite and then gradually reaches a steady state. Therefore, the optimum dosage of ceramsite for the elimination of Cd^{2+} concentration of 10 mg/L was 1500 mg/150 mL.

Effect of Contact Time

The influence of contact time (10–240 min) on the adsorption of Cd^{2+} is illustrated in Figure 3. The study was conducted at a constant initial concentration of 10 mg/L, adsorbent dosage of 1500 mg/150 mL, pH = 9 and room temperature (20–25°C).

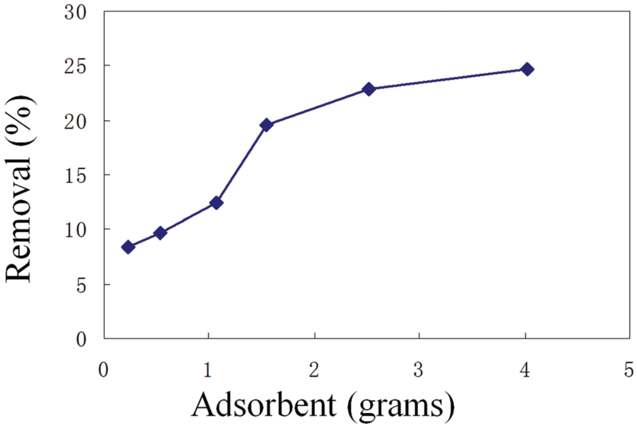

Figure 2. *Effect of adsorbent dosage.*

Table 2. Chemical Composition of Ceramsite (%w/w).

Chemical Composition	SiO_2	Al_2O_3	MgO	CaO	MnO	SO_3	Fe_2O_3	Loss on Ignition
Ceramsite	59.36	3.92	1.88	17.66	5.08	5.21	4.35	0.096

From Figure 3, it is clear that the Cadmium elimination percentage first increases rapidly at the initial stage and then was stabilized at a certain value. The adsorption elimination ratio approximately reached a maximum value at contact time of 120 min. That is, the optimum contact time for the elimination of Cd^{2+} concentration of 10 mg/L was 120 min.

Effect of pH

At the solid-liquid interface, one of the important parameters that influence the adsorption of ions is the pH of the solution. The pH effect on cadmium adsorption by ceramsite is shown in Figure 4. The study was conducted at a constant initial concentration of 10 mg cadmium/L, adsorbent dosage of 1500 mg/150 mL, contact time of 120 min and room temperature (20–25°C).

According to Figure 4, the Cadmium elimination percentage increases from 25% to 98% when the pH increases from 2 to 12. It was observed that the optimum pH for the elimination of Cd^{2+} with a concentration of 10 mg/L was 11. The reasons are proposed as follows:

1. When the pH of the solution is relatively low, the concentration of H^+ in the solution is relatively high, thus H^+ can compete with Cd^{2+} for adsorption sites, resulting in a lower Cd^{2+} removal rate.
2. When the pH of the solution increases, the OH^- concentration increases and the H^+ concentration decreases, which reduces the number of positively charged sites on the adsorbent surface and increases the number of negatively charged sites [14]. This phenomenon may be explained by the formation of OH^- complexes on the surface [15,16]. The OH^- complexes on the surface can adsorb more Cd^{2+} through surface complex reactions, resulting in sharply increased adsorption. This is because when the pH increases, OH^- is attracted to the metal ions (Al^{3+}, Mg^{2+}, Ca^{2+}, Mn^{2+} and Fe^{2+}) which locate at the surface of the ceramsite. At the same time, Cd^{2+} is converted to $Cd(OH)_x^n$ (x: 1–4), n: –2–1) (Figure 5) [13].

Cadmium Adsorption Isotherm

Figure 6 shows the experimental results regarding the cadmium adsorption isotherm. The typical L-curve isotherm can represent the experimental data. The capacity of cadmium adsorption increases when the cadmium equilibrium concentration increases. Further, the experimental data is compared to Freundlich and Langmuir isotherms.

Freundlich isotherm:

$$q = KC^{1/n} \tag{1}$$

Langmuir isotherm:

$$q = \frac{bq_m C}{1 + bC'} \tag{2}$$

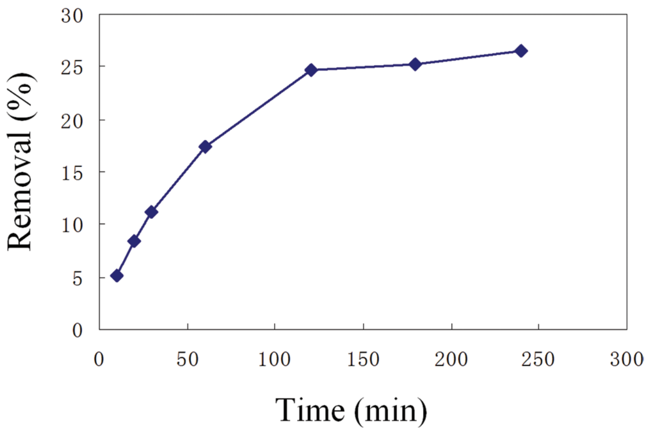

Figure 3. *Effect of contact time.*

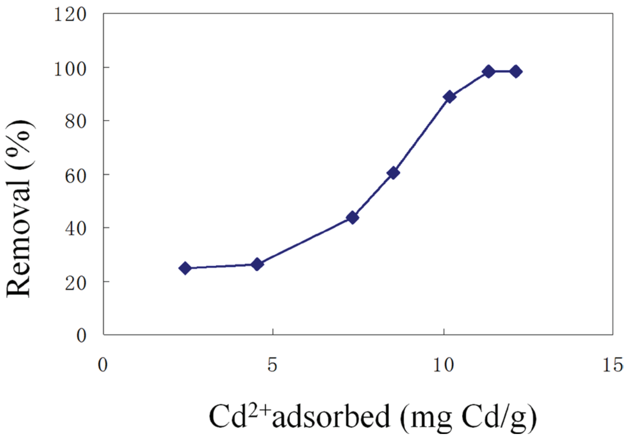

Figure 4. *Effect of pH.*

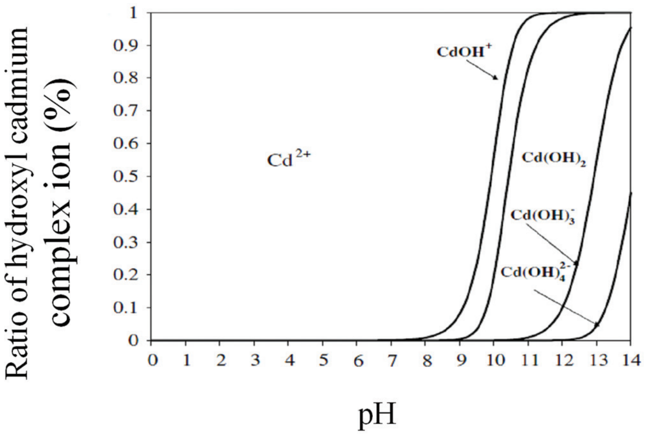

Figure 5. *Speciation diagram for cadmium as pH function 13].*

The adsorption amount at equilibrium (mg/g) is described by q, and the equilibrium concentration of the solution (mg/L) is described by C. The regression of the experimental data can determine different constants.

In this work, the experimental data of cadmium adsorption on the ceramsite are well fitted using Freundlich and Langmuir isotherm models, respectively (Figure 6). Table 3 shows the estimated model parameters with the correlation coefficient (R^2). Figure 6 illustrates the fitting curves of these two isotherms. It is shown that Freundlich and Langmuir isotherm models can well describe the experimental data of cadmium adsorption on the ceramsite.

CONCLUSIONS

Ceramsite is primarily composed of Pb-Zn tailings. The ability of the ceramsite to eliminate Cadmium from wastewater was evaluated through batch experiments. According to the experimental results, the conclusions are drawn as follows.

1. The cadmium adsorption increases from 25% to 98% when the pH value increases from 2 to 12.
2. The Freundlich and Langmuir isotherm models can well describe the experimental data of cadmium adsorption on the ceramsite.

Table 3. Estimated Isotherm Parameters for Cadmium Adsorption on the Ceramsite.

Langmuir Equation ($q = (q_m bc)/(1 + bc)$)			Freundlich Equation ($q = Kc^{1/n}$)		
q_m (mgCd/g)	b (L/mgCd)	R^2	K	$1/n$	R^2
0.9449	0.0281	0.9992	0.0305	0.816	0.9971

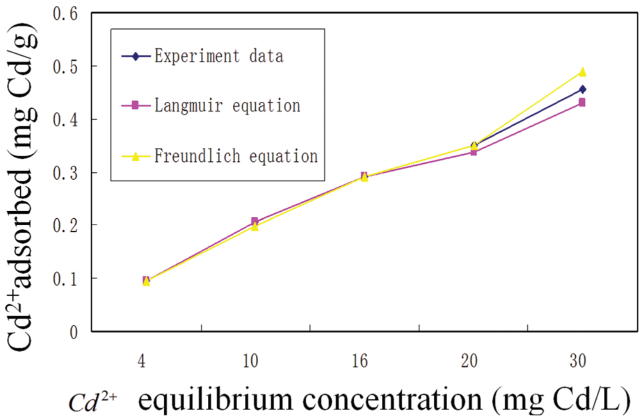

Figure 6. *Cadmium adsorption isotherm for the ceramsite at 25°C and pH 9.*

3. The ceramsite mainly composed of Pb-Zn tailings is a promising candidate to remove cadmium from industrial wastewater in a cost-effective way.

ACKNOWLEDGMENTS

The authors gratefully acknowledge the financial support of the Project Funded by the Priority Academic Program Development of Jiangsu Higher Education Institutions and Top-notch Academic Programs Project of Jiangsu Higher Education Institutions.

REFERENCES

1. Gupta, V.K., Nayak, A., "Cadmium removal and recovery from aqueous solutions by novel adsorbents prepared from orange peel and Fe_2O_3 nanoparticles", *Chemical Engineering Journal*, No. 180, 2012, pp. 81–90. http://dx.doi.org/10.1016/j.cej.2011.11.006
2. Godt, J. *et al.*, "The toxicity of cadmium and resulting hazards for human health", *Journal of Occupational Medicine and Toxicology*, No. 1, 2006, pp. 1–6. http://dx.doi.org/10.1186/1745-6673-1-1
3. Ding, Y., *et al.*, "Biosorption of aquatic cadmium(II) by unmodified rice straw, Bioresour", *Technol. No.* 114, 2012, pp. 20–25.
4. Gupta, V. K. *et al.*, "Low cost adsorbents: growing approach to wastewater treatment—A review", *Crit. Rev. Environ. Sci. Technol,* No. 39, 2009, pp. 783–842.
5. Hizal, J., Apak, R., "Modeling of cadmium (II) adsorption on kaolinite-based clays in the absence and presence of humic acid", *Appl. Clay Sci, No. 32*, 2006, pp. 232–244. http://dx.doi.org/10.1016/j.clay.2006.02.002
6. Venkatesan. G., Senthilnathan, U., Rajam, S., "Cadmium removal from aqueous solutions using hybrid eucalyptus wood based activated carbon: adsorption batch studies", *Clean Techn Environ Policy, No. 16*, 2014, pp. 195–200. http://dx.doi.org/10.1007/s10098-013-0628-0
7. Bamgbose, J. T., *et al.*, "Adsorption kinetics of cadmium and lead by chitosan", *Afr. J. Biotechnol*, No. 9, 2010, pp. 2560–2565.
8. Ju, S. H. *et al.*, "Removal of cadmium from aqueous solutions using red mud granulated with cement", *Trans. Nonferrous Met. Soc. China, No.* 22, 2012, pp. 3140–3146.
9. Fan, H. T., *et al.*, "Removal of cadmium (II) and lead (II) from aqueous solution using sulfur-functionalized silica prepared by hydrothermal-assisted grafting method", *Chemical Engineering Journal,* No. 198-199 2012, pp. 355–363. http://dx.doi.org/10.1016/j.cej.2012.05.109

10. Wang, S. C. *et al.*, “Adsorptive removal of phosphate from aqueous solutions using lead-zinc tailings”, *Water Science & Technology,* Vol. 67, No. 5, 2013, pp. 983–988. http://dx.doi.org/10.2166/wst.2013.649
11. Dubey, A., Mishra, A., Singhal, S., “Application of dried plant biomass as novel low-cost adsorbent for removal of cadmium from aqueous solution”, *Int. J. Environ. Sci. Technol,* No. 11, 2014, pp. 1043–1050.
12. Guo, H., *et al.*, “Removal of cadmium (II) from aqueous solutions by chemically modified maize straw”, *Carbohydrate Polymers, No. 115*, 2015, pp. 177–185. http://dx.doi.org/10.1016/j.carbpol.2014.08.041
13. Scorzelli, I. B., “Cadmium and Zinc removal by ionic flotation”, *Catholic University of Rio de Janeiro*, PUC-Rio, Brazil, 1999.
14. Frini-Srasra, N., Srasra, E., “Acid treatment of south Tunisian palygorskite: Removal of Cd(II) from aqueous and phosphoric acid solutions”, *Desalination,* Vol. 250, No. 1, 2010, pp. 26–34. http://dx.doi.org/10.1016/j.desal.2009.01.043
15. Selatnia, A. *et al.*, “Biosorption of Cd^{2+} from aqueous solution by a NaOH-treated bacterial dead Streptomyces rimosus biomass”, *Hydrometallurgy,* Vol. 75, No. 1–4, 2004, pp. 11–24. http://dx.doi.org/10.1016/j.hydromet.2004.06.005
16. Zouboulis, A. I., Loukidou, M. X., Matis, K. A., “Biosorption of toxic metals from aqueous solutions by bacteria strains isolated from metal-polluted soils”, *Process Biochemistry,* Vol. 39, No. 8, 2004, pp. 909–916. http://dx.doi.org/10.1016/S0032-9592(03)00200-0

Progress on Dust Removal, Denitrification and Desulfurization Technology in Coal-fired Industrial Boiler

B.Y. SUN, X.H. YANG*, M.S. LI and F.F. WU
[1]*School of Environment, Beijing Normal University, 100875, China*

ABSTRACT: Pollutants discharge from coal combustion is one of the main causes of smog and haze. Many countries focus on research and development of clean combustion, waste heat utilization and removal of pollutants (e.g. Dust, NO_x and SO_x) and other key technology and equipment considering the whole process of coal-fired industrial boiler emissions and energy efficiency. In this paper, we make a comparative analysis of domestic and foreign coal-fired industrial boilers ultra-low emissions technology, and points out the research breakthroughs and achievements our country may get in the future.

INTRODUCTION

THE coal output amount was 8.165 billion tons all over the world in 2014, accounting for 30% of the world energy amount. Dust, NO_x and SO_x emissions from coal-burning were 159, 60 and 196 million tons respectively, which was the main source of air pollution. In London, for example, in the 1950s, air dust, NO_x and SO_x and other concentrations of 4.46 mg/m^3, 3.20 mg/m^3 and 3.83 mg/m^3, as the world famous "smog city", posed a serious crisis on people's health [1]. Thus, the world attached great importance to coal energy production process and equipment research and development of ultra-low emission technology, focusing on research and development of efficient and clean burning of coal, dust removal, desulfurization and denitrification and other key technologies, which had made significant technological progress. Through the use of advanced technology and equipment, the London air dust, NO_x and SO_x and other concentrations decreased year by year, which was 0.10 mg/m^3, 0.04 mg/m^3 and 0.005 mg/m^3 respectively in 2014. The "smog city" hat had been removed, which had become an international financial and livable metropolis [2]. Our coal-fired industrial boilers were about 47 million units, which accounted for 600 MW coal-fired industrial boilers amount to 90%. China's coal-fired industrial boilers in coal consumption was about 10 million tons, accounting for about 25% of the country's total coal consumption. Due to clean combustion, flue gas waste heat recovery and dust removal, SCR, desulfurization and other related technology was relatively backward, high concentrations of pollutants soot emission of coal-fired industrial boilers, SO_2, NO_x and other emissions accounted for approximately 44.8%, 36.7% and 45.6% of the country's total emissions. Pollutants discharge from coal combustion is one of the main reasons of smog and haze [3].

DUST REMOVAL

In the dust removal field, the foreigners focused on the electrostatic precipitator, bag filter and electric dust bags and other technical equipment. Germany electrostatic dust removal technology can reduce coal-fired boiler flue dust concentration to 20 mg/m^3 or less, and achieve 5 mg/m^3 or less discharged through the subsequent bag filter. Japan's low-low temperature (below the dew point) and the moving electrode ESP combination of technology, the efficiency of coal-fired boiler dust removal is more than 99%, but there were lots of shortcomings such as high cost, corrosion and so on American Electric Power Research Institute developed the electrical dust bags and patented technology, the integrated use of electrostatic precipitators and fabric filters principle, can effectively remove PM2.5 [4]. Our use of electrostatic dust, dust bag, and bag dust electric technology will reduce the dust concentration in the flue gas to 10~50 mg/m^3. By increasing the elec-

---

*Author to whom correspondence should be addressed.
E-mail: xiaohuayang@bnu.edu.cn

1544-8053/16/02 S007-04

doi:10.12783/issn.1544-8053/13/4/S2

tric field intensity, high frequency power supply, the fixed electrode to measure the movable electrode so as to improve the collection efficiency of electrostatic precipitators, developed a low-temperature low-ESP, dual zone electrostatic precipitator and other new filter. Baghouse dust concentration may be greater than 30 mg/m^3 of dust further removed, will reduce the export of dust concentration to 10~30 mg/m^3. Winterthur Inner Mongolia Power Plant 200 MW Unit 2 using baghouse units put into operation in 2001, and the dust emission concentration is less than 50 mg/m^3. To further enhance the effect of dust, China began to develop "before after power bag" bag dust electric technology, developed electric hybrid dust collector bags, successfully applied in Fujian Huadian Zhangping Thermal Power Co., Ltd., export dust concentration of about 20 mg/m^3 [5].

DENITRIFICATION

In denitrification field, the traditional presence of alkaline denitration emissions of large quantities of solid waste, and the liquid waste is difficult to disposal, selective catalytic reduction (Selective Catalytic Reduction, SCR) DeNO$_x$ technology has become a hot topic, because there was no solid waste and liquid discharge end, and high NOx removal efficiency, low cost. Nippon Shokubai Kasei Co., Ltd., Babcock-Hitachi Corporation, Cambridge University, University of Michigan, and the Japanese National Institute for Materials chemistry invest a lot of manpower and resources to the development of SCR technology and equipment, focus on the new NH$_3$-NO$_x$ catalyst, denitration mechanism, spent catalyst and regeneration, to achieve a coal-fired industrial boilers NOx emission concentration of 30~100 mg/m^3. Low-cost, high efficiency, high anti-toxic and renewable low-temperature SCR catalysts are the focus of research and the development trend of SCR technology [6]. China mainly uses SCR and SNCR technology, but the core technology and products mainly rely on imports. Domestic research work mainly focused on the development of the catalyst, the catalyst component focuses on the active component and new carriers and so on. State Power Institute of Science and Technology has developed a Mn-Ce-M Preparation/TiO$_2$ catalyst by optimizing nitric acid titanium Ti (NO$_3$)$_4$ as TiO$_2$ precursor synthesis parameters, significantly improved the anti-catalyst SO$_2$/H$_2$O poisoning performance. Beijing University of Technology developed a low-temperature SCR catalyst complex kind of V$_2$O$_5$, Bi$_2$O$_3$, MoO$_3$ and BaO mixture of active substances with good low-temperature catalytic and anti-drug performance [7].

DESULFURIZATION

In the desulfurization, we developed three categories including wet, dry and semi-dry. Semi-dry has become one of the major desulfurization technology in the future because of low cost, high desulfurization efficiency, operability, which adapted to a wide range of advantages. Finnish company IVO and Tampelle jointly developed Furnace Sorbent Injection humidifier activation method, combined with dust bag allows total desulfurization efficiency of 60–80%. ABB developed a NID (New Integrated Desulphurization) semidry desulfurization process for the low-sulfur coal desulfurization efficiency over 80%. B & W has developed a low-cost semi-dry desulfurization process, based on the amount of feedback regulation absorbent chimney outlet sulfur content, to achieve the SO$_x$ emission concentration 30~60 mg/m^3. The new intelligent and efficient desulfurization tower, desulfurization ash comprehensive utilization technology and equipment, has become the hot spot in the field of research [8]. Mainly domestic terminal desulfurization includes wet, dry and semi-dry method. Wet desulfurization has higher one-time investment, high costs of equipment operation, a large quantity of wastewater [9]. Dry desulphurization has no wastewater discharge, but sorbent utilization and desulfurization efficiency is not high. Semi-dry desulfurization combines the advantages of wet and dry, and no wastewater, desulfurization efficiency approaching wet, high efficiency desulfurization agent. Commonly used semi-dry desulfurization spray drying desulfurization technology and circulating fluidized bed desulfurization technology. Wherein the circulating fluidized bed desulfurization technology is particularly suitable for circulating fluidized bed coal-fired industrial boilers. Huadian Fujian Zhangping Thermal Power Co., Ltd. using the furnace desulfurization of flue gas SO$_2$ will be reduced to 100 mg/m^3 or less. Sinosteel Tiancheng Environmental Protection Technology Co., Ltd. has developed a sintering nose desulfurization dust removal device integration, reducing investment in fixed assets. Coal Institute of Science and Technology Co., Ltd. has developed a semi-dry purification technology, which make full use of favorable conditions for low-temperature coal combustion, fly ash as a desulfurization agent active calcium, reducing the cost of desulfurization, SO$_2$ concentration was reduced to 100 mg/m^3 or less [10].

CONCLUSION

In summary, the research on foreign coal-fired industrial boiler emissions technology started early, forming a comprehensive standard abatement technology patented front-end control of pollutants and the end of treatment (Table 1). The goal of front control was to improve coal combustion efficiency, thus to reduce pollutant emissions per unit of energy. The goal of end of treatment was to improve dust, NO_x and SO_x removal efficiency and reduce costs, thus to reduce emissions. Therefore we should be conducted in-depth research in this area, such as the new cold catalyst technology, Integrated Electrical bag dust technology.

Table 1. The Main Foreign Coal-fired Industrial Boiler Technology Patents and Standards.

Patent No. / Standard	Patentee	Field and Scope	Patent Expiration Date	Remark
US2003/0019356A1, US2007/0014706A1	Tesa Aktiengesellschaft	Circulating fluidized bed combustion technology and equipment clean; flue gas treatment effect reached: smoke less than 5 mg/Nm^3, SO_2 less than 15 mg/Nm^3	30 January 2023	Patent
EP2444142A2	Babcock & Wilcox Power Generation Group	A variety of air pollutants emission control and protection methods SCR catalyst to extend the catalyst life cycle	25 April 2032	Patent
WO2010/114873A2	BASF Catalysts LLC	Emission control system and NH_3-SCR catalyst, the catalyst is a zeolite-type copper-based catalyst, the temperature can be adapted to 150~180°C, the denitration rate of 90%.	7 October 2030	Patent
WO2015/128663A1, WO2015/145178A2	Johnson Matthey	NH_3-SCR catalyst and its preparation and use of low temperature, a temperature of 250°C	3 September 2035	Patent
KR20120012934(A)	Korea South Power Co Ltd	Semi-dry desulfurization equipment and the corresponding new CFB boiler	13 February 2032	Patent
JP2008264656(A)	Japanese precision detector Corporation	Desulfurization method and apparatus; reaction speed, time is short, compact device	2 November 2028	Patent
JP5212239(A), JP5309229(A)	Mitsubishi Heavy Industries Ltd	Desulfurization method and apparatus; lime powder as desulfurizer, desulfurization rate of about 80%, the desulfurization process temperature dropped 50 ~ 60°C.	24 August 2013	Patent
WO2007/020205A1	Solvay Chemicals, Inc.	Desulfurization technology and equipment to detect the concentration of SO_2 in the flue gas desulfurizer to adjust the amount of investment, the flue gas temperature of 320~480°C.	22 February 2027	Patent
JP2000288423(A)	Ishikawajima Harima Heavy Ind.	Operation and electrostatic precipitator boiler flue gas treatment apparatus; a greater flue gas capacity, the electrode voltage can be adjusted according to the boiler load.	17 October 2020	Patent
JP5337315(A), JP5337314(A), JP9206532(A)	Nippon Steel Corporation	Bag filter method and apparatus; relates baghouse dust collector filter cloth easy replacement and fast fault diagnosis technology.	12 August 2017	Patent
US2015/0135949A1	Mitsubishi Heavy Industries Ltd	Wet ESP desulphurization methods and equipment; have a high space charge relaxation effect, thereby enhancing the effect of dust.	21 May 2035	Patent
Directive 2010/75/ EU of the European Parliament and of the Council	The European Parliament and the Council of the European Union	SO_2: < 200 mg/Nm^3, NO_x: < 200 mg/Nm^3, Dust: < 20 mg/Nm^3	24 November 2010	Patent
Integrated Pollution Prevention and Control Reference Document on Best Available Techniques for Large Combustion Plants	The European Parliament and the Council of the European Union	Efficiency cogeneration 75~90%; SO_2: < 20~150 mg/Nm^3; NO_x: < 90~150 mg/Nm^3; Dust: < 5~10 mg/Nm^3	July 2006	Document

REFERENCES

1. UN Population Division, World Population Prospects: The 2012 Revision, New York, United States (2013).
2. BP P.L.C., BP Statistical Review of World Energy, London, United Kingdom (2014).
3. Energy Information Administration, International Energy Outlook, Washington, D.C., United States (2013).
4. Mitchell, B.R., International Historical Statistics 1750–2005, Palgrave Macmillan, New York, United States (2007).
5. ICIS ATEC 4th Update, Vergiate, Italy (2014).
6. International Energy Agency, Energy Balances of Non-OECD Countries, Paris, France (2014).
7. International Energy Agency, World Energy Outlook, Paris, France (2014).
8. World Bank, Global Purchasing Power Parities and Real Expenditures, Washington D.C., United States (2014).
9. Energy Information Administration, Short-Term Energy Outlook, Washington, D.C., United States (2014).
10. Yang X.H., He J., Di C.L., Li J.Q., Vulnerability of assessing water resources based on the improved set pair analysis, *Thermal Science,* Vol. 18, No. 5, 2014, pp. 1531–1535. http://dx.doi.org/10.2298/TSCI1405531Y

Improvement of Traditional Mining Tailings Storage Facilities

SHUNCAI WANG*, YUE ZHAO, SHUANG LI and ZHICHENG WEI
Key Laboratory of Integrated Regulation and Resource Development on Shallow Lake of Ministry of Education,
College of Environment, Hohai University, Nanjing 210098, China

ABSTRACT: Traditional mining tailings storage facilities may generate calamities and contaminants that cause the infiltration of tailings dam and even lead to dam failures. In view of this, new tailings storage facilities are designed in this paper by combining traditional tailings storage facilities with barrier systems including a vertical drainage system, a compound liner system, a fluid collection system and a caps system. With the vertical drainage system, water in contact with tailings can be transported into the fluid collection system. With the compound liner system, fluid can find a waterproof environment, which prevents the contamination of the environment such as surface water, groundwater, soil and food chain. With the fluid collection system, water in contact with tailings and fluid can be collected and removed to wastewater treatment plants, thus avoiding dam failure and AMD generation caused by the reaction of iron sulphides with water and oxygen.

1. INTRODUCTION

MINERAL resources are the basis for human survival and development, and play an important role in industrial economies. Since the Stone Age, humans have mined about 1.15×10^{10} tons of heavy metals (lead, zinc, copper, chromium, cadmium and cobalt). Nowadays, 5~7 billion tons of mining tailings have been produced per year worldwide [1]. These mining tailings would occupy an area of 52 km^2 with hundreds of meters in height approximately [2]. However, it is noticed that mining and ore dressing wastes can result in damages to ecosystem and threats to human health [3]. Mineral extraction generates a lot of tailings and hazards that can cause serious environmental pollution. Besides, it also brings many other problems such as occupation of land, waste of resources and so on.

2. IMPROVEMENT OF TRADITIONAL MINE TAILINGS STORAGE FACILITIES

Wet mining tailings deposition nearby mining sites is the most economic and commonly used technique. The wet mining tailings deposition can be designed based on the downstream or upstream dam construction method by placing a dam across the valley at the head of drainage. The downstream and upstream dam construction methods are the so-called traditional mining tailings storage facilities.

2.1. Calamities of Traditional Mine Tailings Storage Facilities

In the downstream and upstream dam construction methods, the tailings slurry containing 35–40% solids is discharged by either point or line. The discharge line or point is moved regularly and gravimetrical separation of tailings grain size occurs. The tailings of coarse grain size deposit nearby the tailings discharge line or point, while those of fine grain size deposit far away the tailings discharge line or point. With the movement of tailings discharge line or point, inhomogeneous horizontal and vertical layers of fine sand with clay and silt make the deposition hydrological conditions of the tailings very complicated. Usually, the inhomogeneous horizontal layers have a significant effect on the permeability and behavior of the water in contact with tailings, which can be represented by the permeability coefficients. The permeability coefficients should be tested via permeability experiments by using the tailings sample of on-site storage [4]. Due to the complicated tailings deposition, traditional mining tailings storage facilities may release contaminant that can cause infiltration of the tailings dam and even a rupture accident. With the unparalleled mining and the acceleration of mineral processing over the past

---

*Author to whom correspondence should be addressed.
E-mail: wshcai@hhu.edu.cn; Tel.: +86-025-8378-7870; Fax: +86-025-8378-7870

1544-8053/16/02 S011-04

doi:10.12783/issn.1544-8053/13/4/S3

decades, the disposal methods of tailings, as well as the irreversible effects of contaminant release, tailings dam seepage and dam wall failure, have attracted extensive attention all over the world. In the future, more extreme weather events related with global climatic change and lower grade ores may increase the possibility of the risks of contaminant release, tailings dam seepage and dam wall failure [5]. It is the largest problem that the high potential energy in traditional mining tailings storage facilities and the seismic activity can threaten the stability of tailings dam construction. As a matter of fact, due to the natural disasters and/or extreme weather events, several dam failures and catastrophes of tailings release have occurred over the past years. According to the United Nations Environment Program (UNEP) and International Commission on Large Dams (ICOLD) [6,7], the main reasons for these failures and events are the inadequate regulation of water balance and tailings deposition homogeneousness, the absence of advanced tailings dam construction methods and the lack of safe operations. In October 2010, substantial widespread farmland and water were polluted by an unparalleled disastrous release of ~0.7 million m^3 of red slurry in Ajka, Hungary [8]. On 5th November 2015, more than 30 million m^3 of water and mining wastes were released by the tailings dam of the Samarco Mine in Minas Gerais, Brazil [9].

2.2. Pollution of Traditional Mine Tailings Storage Facilities

In recent years, the geochemical instability of waste rocks and tailings has been concerned worldwide. Among these wastes, there is a significant amount of sulphide minerals (such as iron sulphide). When iron sulphides react with water and oxygen, an acidic leachates known as acid mine drainages (AMD) can be generated. AMD contains high concentrations of and toxic metal ions (such as Fe^{2+}, Fe^{3+}, Pb^{2+}, Zn^{2+}, Cd^{2+} and Cu^{2+}), which can pollute the environment, such as groundwater, surface water, soil and food [10]. Toxic metal ions can exist in natural ecosystems for a long period and accumulate in the biological chain, thus causing chronic or acute diseases to humans [11]. Toxic metals can disrupt the metabolic functions of organs or glands such as the brain, heart, liver, bone and kidneys by accumulation in these organs or glands, or hinder their biological functions by absorbing, displacing or interfering with nutritional minerals [12]. The generation of AMD is a series of complicated chemical and biological reactions and mineral dissolution processes [13]. The mechanism of the generation of AMD is as follows [14]:

1. When iron sulphides contact with water and oxygen, the iron sulphides can react with water and oxygen by the following redox reaction: $FeS_2 + 7/2O_2 + H_2O \rightarrow Fe^{2+} + 2SO_4^{2-} + 2H^+$.
2. Under the conditions of enough oxygen and suitable pH, microorganism can oxidize Fe^{2+} to Fe^{3+} by $Fe^{2+} + 1/4O_2 + H^+ \rightarrow Fe^{3+} + 1/2H_2O$, $Fe^{3+} + 3H_2O \rightarrow Fe(OH)_{3\,solid} + 3H^+$, or $FeS_2 + 14Fe^{3+} + 8H_2O \rightarrow 15Fe^{2+} + 2SO_4^{2-} + 16H^+$.
3. When H^+ ions are generated, toxic metal ions in the tailings should be dissolved and AMD comes into being [15].

2.3. Improvement of Traditional Mining Tailings Storage Facilities

Traditional mining tailings storage facilities have faced an enormous challenge to the treatment and disposal of tailings and require a multidisciplinary research, because the tailings can pollute environment by AMD and lead to tailings dam failures due to leakage, instability, liquefaction, and poor design [16,7]. Since the 1960s, 77 mining tailings dams have collapsed worldwide mainly because of the geotechnical instability, and caused at least 471 deaths as well as environmental destruction and serious economic impacts [17]. Nevertheless, traditional mining tailings storage facilities are still the most economic and commonly used tailings treatment and disposal technique. In this case, how to eliminate or reduce the risks associated with conventional valley dam impoundments seems more practical than abandoning these facilities. More opportunities of reducing or eliminating the risks can be obtained in the design phase of mining technique [18]. According to the sustainable development concept, the treatment and disposal of mining and mineral processing waste must be inert, stable, controllable, improvable and suitable to local characteristics [19]. Following this principle, traditional tailings storage facilities are designed with barrier systems including a vertical drainage system, a compound liner system, a fluid collection system and a caps system. The compound liner system [20] (see Figure 1) consists of a compacted clay layer, a geomembrane layer, a gravel layer, fluid collection pipes and a filter soil layer. The compacted clay layer locates at the bottom in contact with the soil, the geomembrane layer locates over the compacted clay layer, the gravel layer locates over the

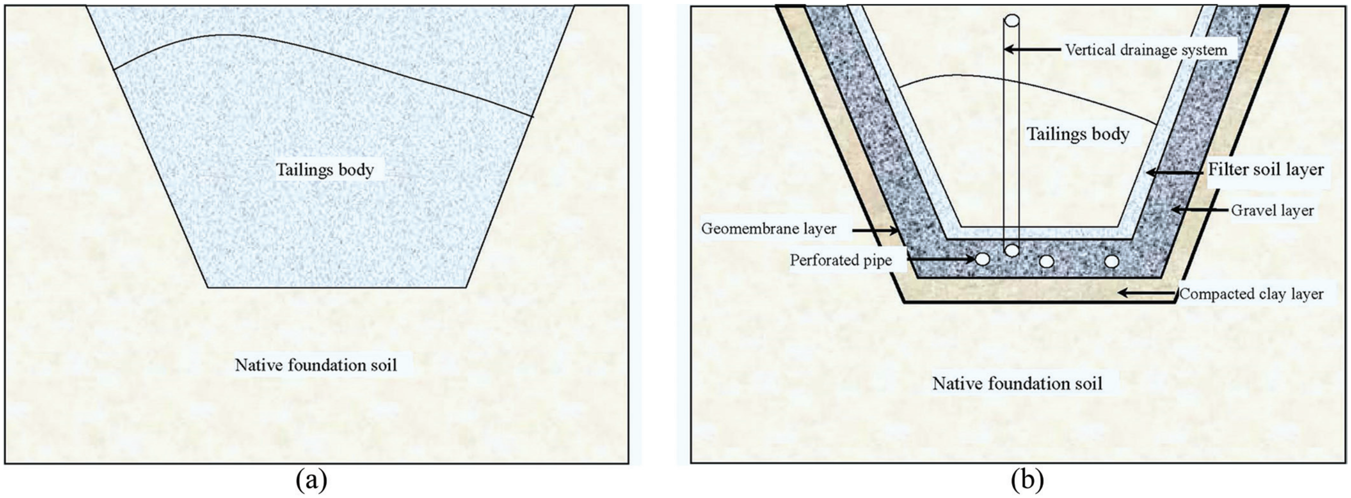

(a) (b)

Figure 1. *Schematic diagram to the structure of tailings storage facilities: (a) tradition;and (b) new.*

geomembrane layer, and perforated pipes for collecting fluid are deployed in the gravel layer. In order to avoid the moving fine tailings particles blocking the holes in the perforated pipes, the filter soil layer locates over the gravel layer. With the compound liner system, the fluid would encounter a waterproof medium, thus avoiding contaminating the environment (such as groundwater, surface water and soil) [20]. The fluid collection system can control the water balance in the tailings storage facilities to avoid dam failures, and prevent the reaction of iron sulphides with water and oxygen to produce AMD. In order to reduce or eliminate the rainwater and contact water, two control systems are employed: Figure 1(a) rain water collection and diversion system, in which ditches are employed to collect and divert the rainwater runoff on the surface around the tailings body to the fluid collection system; and Figure 1(b) contact water vertical drainage system, in which perforated pipes are put vertically in the tailings body in the design phase. The vertical drainage system is a traditional ground improvement method to speed up the consolidation process and therefore increase the shear strength of fine-grained materials [1]. This system can be used to reduce the increase of pore water pressure and is most beneficial towards the storage centre beyond the ‘zone of influence’ of the deliquoring bores. Meanwhile, it also works as the quick response to any incremental loading with each pour, and serves to improve the effectiveness of the deliquoring bores (and vice versa), since it helps provide an additional flow path for liquor in tailings to find a sand zone where it can thereafter be drawn off by the deliquoring bores. The design of the vertical drainage system requires the prediction of the dissipation rate of excess pore water pressures using radial seepage in the vertical drains, as well as the evaluation of the vertical drainage contribution [18]. The fluid collection system consists of ponds or sumps, pipelines and pumps. In order to keep water balance of the tailings body, the collected water in the sumps or ponds is pumped to water treatment plants periodically. The caps system is used to avoid dust pollution during operation or closure, and multifarious cover materials can prevent surface runoff erosion and dust pollution and generate growth media for future reclamation [6].

CONCLUSIONS

Traditional mine tailings storage facilities may generate calamities and contaminant released due to tailings discharge, tailings dam seepage and dam wall failures. In this paper, traditional tailings storage facilities are combined with barrier systems including a compound liner system, a vertical drainage system, a fluid collection system and a caps system, and this improvement design can effectively eliminate the calamities and environmental pollution caused by mining tailings.

ACKNOWLEDGMENTS

The authors gratefully acknowledge the financial support of the Project Funded by the Priority Academic Program Development of Jiangsu Higher Education Institutions and Top-notch Academic Programs Project of Jiangsu Higher Education Institutions.

REFERENCES

1. Mudd, G., Boger, D. V., “The ever growing case for paste and thickened tailings—towards more sustainable mine waste management”, *Aust. Inst. Min. Metall. Bull*, No. 2, 2013, pp. 56–59.
2. Smuda, J., *et al.*, “Element cycling during the transition from alkaline to acidic environment in an active porphyry copper tailings impoundment, Chuquicamata, Chile”, *J. Geochem. Explor*, No. 140, 2014, pp. 23–40.
3. Palmer, M. A. *et al.*, “Mountaintop mining consequences”, *Science*, No. 327, 2010, pp. 148–149. http://dx.doi.org/10.1126/science.1180543
4. Dold, B., “Basic concepts in environmental geochemistry of sulfidic mine”, In: Er Kumar ES (ed) *Waste management*, InTech, Rijeka, 2010, pp 173–198. http://dx.doi.org/10.5772/8458
5. Edraki, M. *et al.*, “Designing mine tailings for better environmental, social and economic outcomes: A review of alternative approaches”, *J. Clean. Prod*, No. 84, 2014, pp.411–-420. http://dx.doi.org/10.1016/j.jclepro.2014.04.079
6. Fourie, A., “Preventing catastrophic failures and mitigating environmental impacts of tailings storage facilities”. *Proced. Earth. Planet. Sci*, No. 1, 2009, pp. 1067–1071.
7. Kossoff, D. *et al.*, “Mine tailings dams: Characteristics, failure, environmental impacts, and remediation”, *Applied Geochemistry*, No. 51, 2014, pp. 229–245. http://dx.doi.org/10.1016/j.apgeochem.2014.09.010
8. Klebercz, O. *et al.*, “Ecotoxicity of fluvial sediments downstream of the Ajka red mud spill, Hungary”, *J. Environ. Monit*, No. 14, 2012, pp. 2063–2071. http://dx.doi.org/10.1039/c2em30155e
9. Beatrice, L., “Mining dam failure: Business as usual?”, *The Extractive Industries and Society*, No. 3, 2016, pp. 651–-652. http://dx.doi.org/10.1016/j.exis.2016.03.010
10. Cruz, L. S. *et al.*, “Chemical characteristics of acid mine drainage from an As-W mineralized zone in western Spain”, *Procedia Earth and Planetary Science*, No. 7, 2013, pp. 284–287. http://dx.doi.org/10.1016/j.proeps.2013.03.199
11. Akpor, O. B., Muchie, M., “Remediation of heavy metals in drinking water and wastewater treatment systems: Processes and applications”, *Int. J. Phys. Sci*, Vol. 5, No. 12, 2010, pp. 1807–1817.
12. Singh, R., *et al.*, “Heavy metals and living systems: An overview”, *Ind. J. Pharmacol*, Vol. 43, No. 3, 2011, pp. 246–253. http://dx.doi.org/10.4103/0253-7613.81505
13. Akcil, A., Koldas, S., “Acid Mine Drainage (AMD): causes, treatment and case studies”, *J. Clean. Prod*, No. 14, 2006, pp. 1139–1145. http://dx.doi.org/10.1016/j.jclepro.2004.09.006
14. Geoffrey, S. S., Sehliselo., N. “Acid mine drainage: Challenges and opportunities”. *Journal of Environmental Chemical Engineering*, No. 2, 2014, pp. 1785–1803. http://dx.doi.org/10.1016/j.jece.2014.07.021
15. Dold, B., “Evolution of Acid Mine Drainage Formation in Sulphidic Mine Tailings”, *Minerals*, Vol. 4, No. 3, 2014, pp. 621–641. http://dx.doi.org/10.3390/min4030621
16. Rico, M. *et al.*, “Reported tailings dam failures: A review of the European incidents in the worldwide context”. *Journal of Hazardous Materials*, Vol. 152, No. 2, 2008, pp. 846–852. http://dx.doi.org/10.1016/j.jhazmat.2007.07.050
17. WISE, “World Information Service on Energy, Chronology of major tailings dam failures”. Available online at:www.wise-uranium.org/mdaf.html, accessed 6 March 2007.
18. McLellan, B. C. *et al.*, “Incorporating sustainable development in the design of mineral processing operations e review and analysis of current approaches”, *J. Clean. Prod*, No.17, 2009, pp. 1414–1425.
19. Franks, D. M. *et al.*, “Sustainable development principles for the disposal of mining and mineral processing wastes”, Resource. Policy, No. 36, 2011, pp. 114–-122.
20. Bouazza, A. Van Impe, W. F., “Liner design for waste disposal sites”, Environmental Geology, Vol. 35, No. 1, 1998, pp. 41–54. http://dx.doi.org/10.1007/s002540050291

Treatment of Lakeside Domestic Wastewater by an Artificial Horizontal Undercurrent Wetland

JIA-XING GUO, XIAO-ZHEN LIU* and YUE LIANG
School of Resources, Environmental & Chemical Engineering, Nanchang University, Nanchang 330031;
Key Laboratory of Poyang Lake environment and resource utilization, Ministry of Education,
Nanchang University, Nanchang 330047, Peoples Republic of China

ABSTRACT: More than 50% of pollutants found in lake waters in China are derived from rural non-point pollution sources, resulting from untreated domestic wastewater released in rivers that feed into the lakes. There is a need of cost-effective means to treat wastewater locally. To this aim, an undercurrent artificial wetland pilot system was constructed to treat domestic wastewaters of the Wucheng lakeside area. Performance of the planted wetland was assessed by measuring removal rates of chemical oxygen demand (COD), the ammonia fraction of nitrogen (NH_3-N), total nitrogen (TN) and total phosphorus (TP). Water samples were taken before, during and after treatment, over a period of 7 months covering autumn through early spring. The levels of dissolved oxygen (DO) were also determined. The results showed temporal variations in pollutant concentrations in the wastewater before treatment (except for COD) with higher levels in autumn. The average removal efficiencies of the determined pollutants by the artificial wetland were 42.86% for COD, 29.46% for NH_3-N, 31.35% for TN and 21.75% for TP. Removal rates of these pollutants were subject to minor seasonal variation. Along the 20 m horizontal water flow studied, the removal rates were highest in the first section. A horizontal undercurrent artificial wetland is simple to construct, easy to manage, and with low running costs it can treat waters effectively and efficiently. To ensure efficient water purification and reach optimal water quality, the hydraulic load and DO levels should be carefully managed.

1. INTRODUCTION

WATER pollution of surface waters such as rivers and lakes remains a considerable problem in China. The Chinese Environmental Bulletin (Edition 2014) summarized data that suggested 3.28% of national surface waters was mildly polluted, 21.31% suffered from moderate eutrophication, 59.02% was found to be highly polluted with nutritional compounds and 3.28% represented oligotrophic lake waters. Studies have shown that more than 50% of pollutants found in lake water are derived from rural non-point pollution sources, mainly from upstream areas that feed into the lakes [1], and these mostly represent domestic wastewater. The composition and concentration of wastewater is subject to variation depending on location and time [2–4], related to differences in the residents' life style and the diversity and complexity of local economic conditions. Due to restricted availability of the sewage network, a considerable fraction of domestic wastewater from populations residing on lake- and riversides is not targeted to urban wastewater treatment plants, but instead is released untreated in lakes and rivers. A technology that could be implemented at low cost, with low energy consumption and ease of management should be adopted to treat such wastewater on a regional and local level.

Constructed wetlands (CWs) are engineered water treatment systems that rely on indigenous microorganisms, various substrates and plants for their purifying activity. They are typically covered by plants such as canna, vetiver grass, calamus, water hyacinth, and planktonic algae [5–7]. CWs are often used for treatment of wastewater (municipal, agricultural and industrial wastewaters, landfill leachate and stormwater runoff), a world-wide practice that makes use of the complex ecological interactions of microorganisms, substrates, plants and the percolating water [8–11]. CWs have also been used in communities to treat wastewater prior to sustainable reuse in arid countries [12].

---

*Author to whom correspondence should be addressed.
E-mail: liuxiaozhen@ncu.edu.cn, Tel: 008679188304087 or 008613576933362

1544-8053/16/02 S015-08

doi:10.12783/issn.1544-8053/13/4/S4

The relationship between water quality parameters and planktonic communities in CWs has been the subject of various studies [6,10]. Since their operation is influenced by temperature, the effect of heat preservation measures was studied in cold areas [13]. Mangrove CWs generally reach higher removal percentages of biological nutrients as well as toxic pollutants (heavy metals, polyaromatic hydrocarbons and phenol) than non-mangrove CWs [14]. CWs designed with algae can increase dissolved oxygen (DO) levels in the water body by stimulating photosynthesis; this significantly improves removal of total nitrogen (TN) and total phosphorus (TP) [6]. Both the diversity of specific biological communities and the nature of plants are crucial for the activity and efficiency of CWs. For instance, it has been shown that the removal efficiency of various parameters of CWs based on umbrella sedge was higher than those depending on vetiver grass; this study investigated vertical flow CWs under various hydraulic loading rates [15]. Other studies presented a risk assessment of heavy metals removal [16] or hydraulic conductivity in a given CW [17].

Constructed wetlands thus provide a cost-effective means to treat water pollution locally, as they are simple to manage at relatively low cost [18]. They have proven to be quite effective and efficient, both in terms of economic efficiency and environmental effectiveness, especially for treatment of wastewater in rural areas [19–20]. In order to test if this solution may also suit the demands for treating lakeside wastewater, a horizontal undercurrent artificial wetland was constructed in the town of Wu-Cheng, of Jiu-Jiang City. The site was used to determine the most important water quality parameters over a period of seven months, and to evaluate its processing efficiency over time. To this extent, the following parameters were measured: oxygen demand (COD), ammonia-nitrogen (NH_3-N), total nitrogen (TN), total phosphorus (TP) and dissolved oxygen (DO).

2. MATERIALS AND METHODS

2.1. Experimental Design

A horizontal undercurrent artificial wetland was constructed, located in the Wu-Cheng Town of Jiu-Jiang City, People's Republic of China. The CW is situated near Poyang lake (Figure 1), which is fed by two rivers: Gan River and Xiu River. In the current situation, domestic wastewater from Wu-cheng town is led into Poyang lake directly, without treatment. The wetland was built in a plot covering 60 m^2 flat grass land

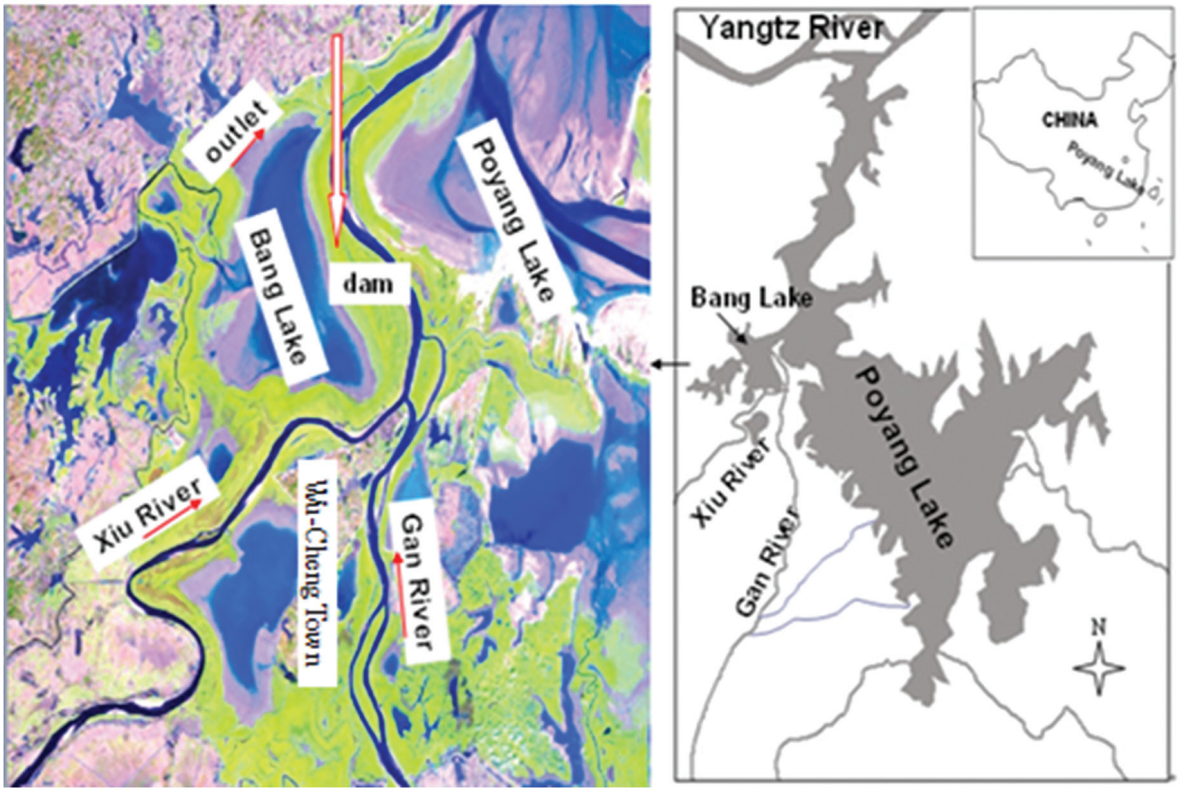

Figure 1. *Location of the constructed wetlands in Wu-cheng town near Poyang lake.*

Figure 2. *Plan of the artificial wetland design.*

directly upstream of a dam, with the purpose to test its effectiveness in wastewater treatment. The width of the water flow was 0.5 m with an effective depth of 0.6 m, while the total effective length was 20.0 m. The bottom of the wetland was covered by two layers of water-impermeable material (Polyvinylchloride, PVC). The sand that was used as a substrate formed a layer with a height of 0.4 m. The artificial wetland was planted with canna (*Canna indica* L.) and stock (*Matthiola incana*) with a plant density of 9 plants/m^2. The wetland and its sampling points are schematically shown in Figure 2. From entry to exit, 7 sampling spots were located, separated by 2.5 m.

The artificial wetland was built in May 2014, with an hourly hydraulic load varying from 0.10 m^3 to 0.13 m^3 per square meter. Monthly samples were taken from September 2014 onwards, i.e. the first sample was taken when the wetland had been in operation for 3 months, and sampling continued for seven months. The exact sampling times were (in 2014) 15 September, 18 October, 14 November, and 14 December and (in 2015) 17 January and 14 March. On each sampling day, three samples were taken (one in the morning, one at noon and one in the evening) using a 100 ml injection syringe with infusion tube. The collecting volume was 500 ml for each sample taken.

During each sampling day, water was sampled at inlet and at outlet, and five parameters of water quality were determined: COD, NH_3-N, TN, TP, and DO for all samples except one (the noon sample of October 2014 could not be analysed due to a pipe burst). Any decrease in parameter concentration at outlet was taken to reflect removal of the pollutant by the wetland system.

2.2. Analytical Methods Applied

All detection methods are described in *Water and Waste Water Detection Method, Fourth edition* [21]. The DO was detected by use of a Multi-340i online monitoring instrument. COD was detected by the rapid microwave potassium dichromate method. Nessler's reagent visible spectrophotometry was used to detect the NH_3-N. TN was detected by the potassium persulfate digestion method and recorded by ultraviolet spectrophotometry, and TP was detected by the molybdate visible spectrophotometry method. For these assays, either a 722 G type visible spectrophotometer, a WTW CR3200 microwave digestion apparatus or a UV-2100 type of ultraviolet-visible spectrophotometer was used.

2.3. Data Analysis and Presentation

Statistical analysis of the data was performed using SPSS19.0 software. The concentrations of COD, DO, TN, TP and NH_3-N of samples from different collecting timepoints were averaged and then compared, and removal rates were calculated. The figures presented were drawn using Origin 9.0.

3. RESULTS AND DISCUSSION

3.1. Wastewater Characteristics

The water quality parameters for the wastewater used in this study are shown in Table 1. The water was derived from the domestic wastewater of the Wu-Cheng Town without any processing. Seasonal variation was apparent in the concentration of most pollutants: the concentrations of all contaminants other than COD were higher in autumn than in winter and early spring.

3.2. Analysis of Operation Effect of the Artificial Wetland

During operation, the COD concentration varied between 150.00 and 416.66 mg/L, whereby levels at

Table 1. The Quality of Input Wastewater (mg/L).

	COD	NH_3-N	TN	TP	DO
Maximum	416.66	148.23	161.47	24.30	1.17
Minimum	150.00	18.17	32.98	4.17	0.73
Mean	255.07	55.75	89.47	10.05	1.07
SD	76.20	32.39	40.38	4.99	0.13

input were usually higher in the morning and evening compared to samples drawn at noon [Figure 3(a)]. The average removal rates of COD slightly differed according to the time of day (on average 41.21% at morning, 43.66% at noon and 43.72% at night), however, these differences were not significant ($P > 0.05$). The average removal efficiency of COD was 48.52% in September, with slightly different efficiencies in the other months (42.13% in October, followed by 51.42%, 34.50%, 38.58% and 41.54% in the subsequent months) but again these differences over time were not significant ($P > 0.05$).

The concentration of NH_3-N was highly variable at input [Figure 3(b)], and its average removal efficiency varied during the day from 39.52% in the morning decreasing to 27.27% at noon and increasing again to 39.52% at night; these differences were significant ($P < 0.05$). A linear relationship was observed between the values of NH_3-N at input and the concentrations of NH_3-N at outlet, which could be expressed as $Y = 0.6111X + 4.9567$, $R^2 = 0.9276$, $P < 0.05$. Although the average removal efficiency varied slightly over the sampled months (36.59%, 27.29%, 25.17%, 27.29%, 26.70% and 35.30%, respectively), these differences were not significant ($P > 0.05$).

The removal efficiency of TN is shown in Figure 3(c). The average removal efficiency of TN was 43.97%, 20.04%, 26.33%, 20.04%, 38.82% and 34.32% for the six months that were sampled, but this variation over time was not significant ($P > 0.05$). Average removal rates were 36.42%, 30.66% and 26.96% respectively during the different times of day, again without a statistical significance ($P > 0.05$). The average concentration of TN in the water leaving the constructed wetland was 57.59 mg/L.

Finally, Figure 3(d) shows the levels of TP concentration, which were highest at inlet for the samples taken in September and October, after which the levels remained below 15 mg/L. The monthly average removal efficiency of TP were 28.98%, 20.48%, 19.35%,

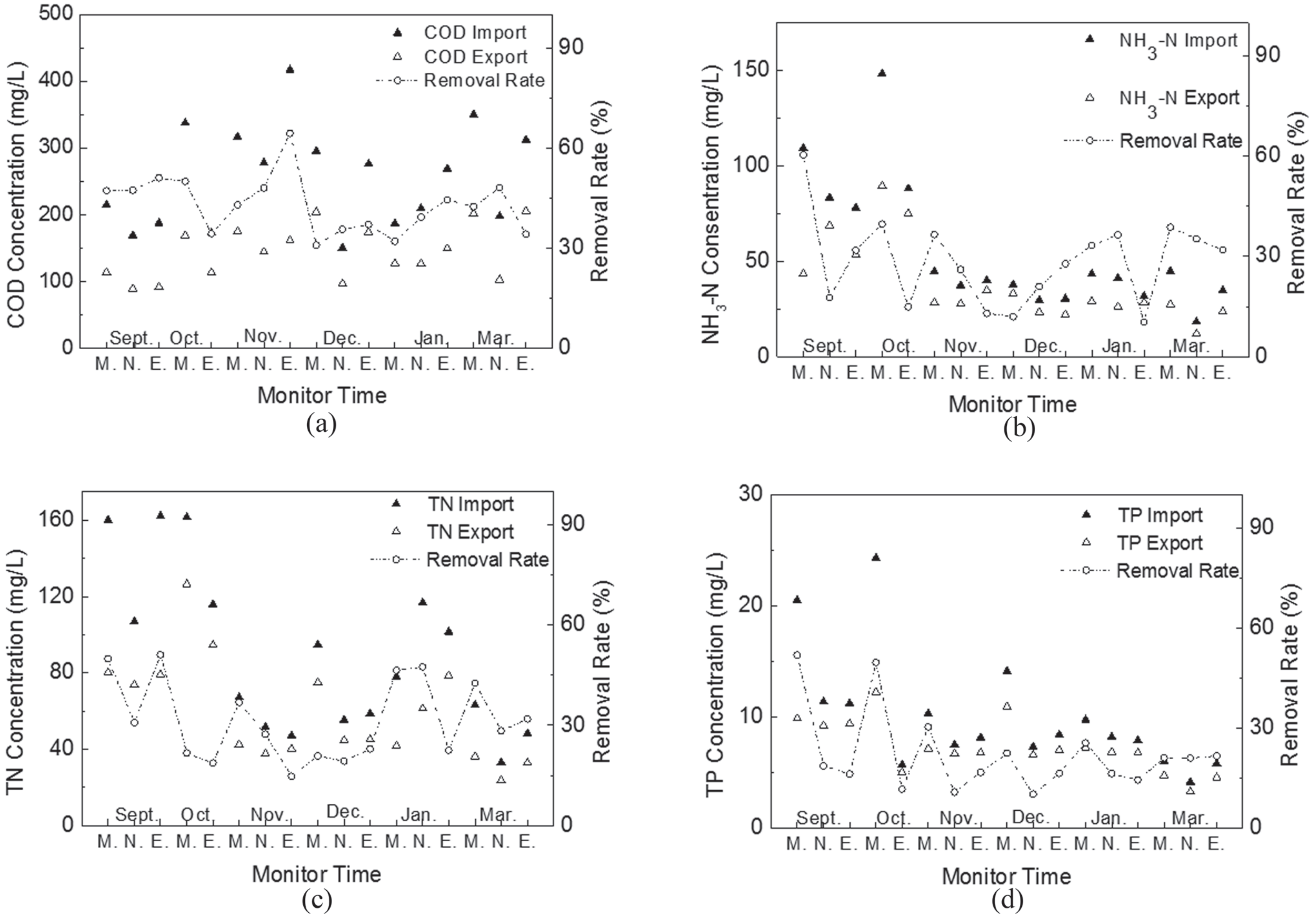

Figure 3. *Analytical data of water sampled over seven months, with monthly samples taken in the morning (M), at noon (N) and in the evening (E) on each sampling day. Shown are levels for (a) COD; (b) NH_3-N; (c) TN; and (d) TP. In each panel, closed triangles represent the levels of inlet water and open triangles the levels of outlet water, whereas open circles record the removal rate corresponding to the scale on the right.*

20.48%, 18.84% and 21.31%, without a significant difference ($P > 0.05$). The average removal efficiency during the day was highest in the morning (33.52%) and remained constant at noon and during the evening (15.48% and 16.26%, respectively). The difference of noon and evening samples compared to the morning samples was significant ($P < 0.05$).

The overall average removal efficiencies of the determined parameters were 42.86% for COD, 29.46% for NH_3-N, 31.35% for TN and 21.75% for TP. Thus, removal was most efficient for total nitrogen and chemical oxygen demand, and least efficient for total phosphorus.

3.3. Evolution of Pollution Concentration Along the Wetland

The efficiency of pollutant removal was also determined along the flow within the wetland. Three sampling points were located between the inlet and the ditch, and three downstream of the ditch (Figure 2). Together with the water at inlet, in the ditch and at outlet, 9 locations were sampled. The average values of DO for these locations are shown in Figure 4. The decrease in DO was rapid for the first 10 m but continued to decrease for the total length of the wetland (20 m). The water sampled from the ditch had a higher DO content due to air exposure.

The average concentrations and accumulative removal rates of the various pollutants were also determined along the flow of the wetland, summarized in Figure 5. Figure 5(a) shows that the accumulative removal rate of COD continued to increase along the length of the wetland; removal was most efficient at sampling point 1, where the removed COD comprised 50% of the total removal rate. This was interpreted to be the result of higher DO concentrations at point 1, since rhizosphere bacteria that are mostly responsible for the degradation and transformation of COD in artificial wetlands require a higher DO [22]. Moreover, higher COD levels support higher microbial growth, which would apply to the situation in the first sample point of the wetland, where the formation of biofilms in the rhizosphere is expected to be more abundant. Their matrix would prevent insoluble materials from being absorbed by plants, while organic material would be rapidly degraded by fast-growing bacteria [23], resulting in high removal rates for COD. Further downstream, the DO was reduced (Figure 4), resulting in improved growth conditions for heterotrophic anaerobic bacteria which could now outcompete aerobic species. This resulted in fewer bacterial biofilms, and the degradation of organic matter decreased, resulting in COD removal rates reaching a plateau.

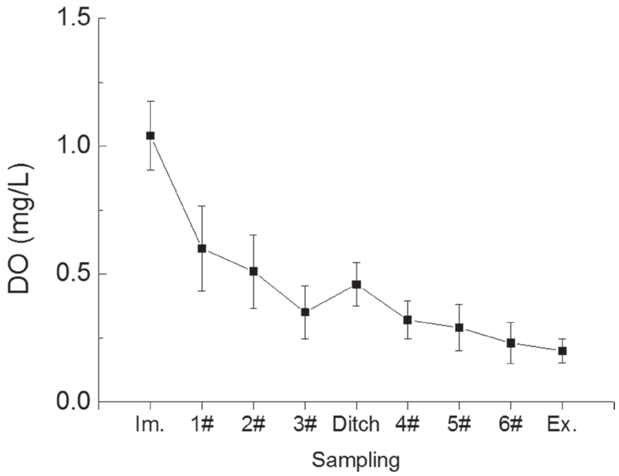

Figure 4. *The change of DO along the wetland.*

The accumulative removal rate of NH_3-N was most significant in the first half of the wetland, reaching a plateau in the second half [Figure 5(b)]. Thick plant roots secrete extracellular polymeric substances which formed an impermeable layer where biofilms and total suspended particulate matter would be abundant [24–26]. All of these are beneficial for wastewater treatment. Bacterial nitrification by biofilms is mainly responsible for removal of ammonia nitrogen, with a minor contribution by plants and soil via absorption [24–25]. DO is an important factor for nitrification. Between the inlet and the third sampling point, the relatively high levels of DO could maintain efficient NH_3-N nitrification, while growth of heterotrophic bacteria was restricted [27]. Instead, autotrophic nitrifying bacteria would dominate here, resulting in high levels of nitrification. Once the DO in the water was consumed, the oxygen produced by plant roots could no longer compensate for the anoxic environment inside the wetland, and under these conditions only limited NH_3-N was removed by the action of heterotrophic bacteria via anaerobic ammonia oxidation reaction [28]. In a few samples NH_3-N seemed to slightly rise; the overall concentration was the result of a balance between plant uptake and deposit as well as microbial activity, and when this balance was disturbed, NH_3-N precipitated, resulting in a slight rise in concentration.

The trends along the CW measured for TN were similar to those determined for NH_3-N [Figure 5(c)]. In the first part of the wetland (from entry to sample point 3) TN removal was relatively efficient (reaching to 29.70%), after which it plateaued. The removal of

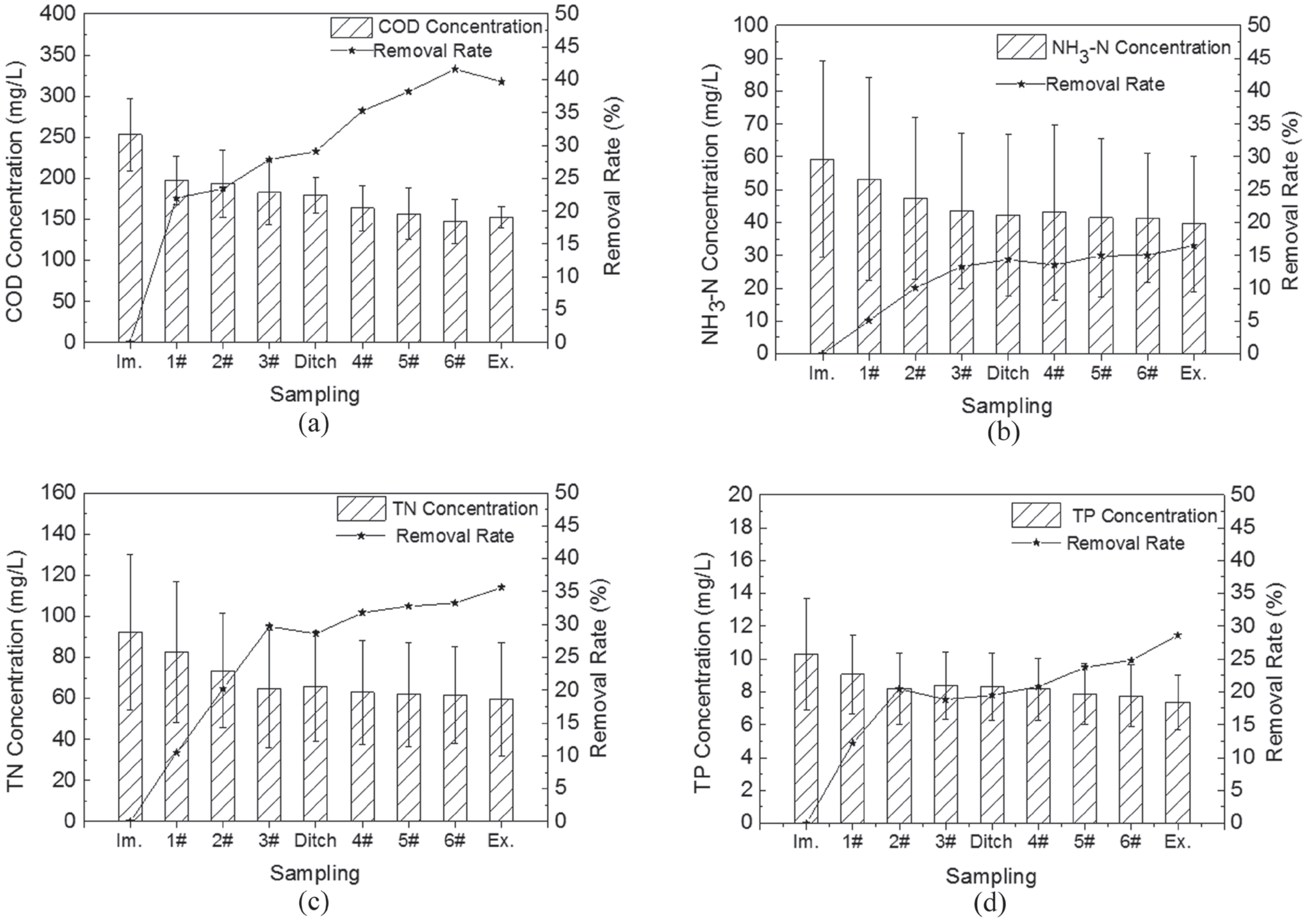

Figure 5. Average concentration and accumulative removal rate of pollutants along the wetland. Shown are average data for (a) COD; (b) NH_3-N; (c) TN; and (d) TP.

TN in wetlands is a complex process, including nitrogen absorption by the organic matrix and by plants, together with ion exchange and nitrogen fixation as well as chemical and biological nitrification and denitrification [29]. The main fraction of nitrogen is removed by the bacterial processes of nitrification and denitrification. Nitrifying bacteria are aerobic and require sufficient levels of DO to act as the final electron acceptor during the process of oxidating NH_3 to NO_3. Denitrifying bacteria use oxygen or NO_3 as the final electron acceptor, to produce N_2 gas which is released into the atmosphere.

In the vicinity of aquatic plant roots an oxygen-rich environment would be created, where NH_3 is converted to NO_3, while at a distance from the roots an anaerobic or anoxic environment would exist, which could support removal of N by strictly anaerobe heterotrophic denitrifying bacteria. In contrast, nitrifying non-heterotrophic bacteria depend on an organic carbon source. In the direction of the water flow the number of denitrifying bacteria would decrease due to the degradation of organic matter, resulting in a gradually less efficient decrease of TN due to the decreasing denitrification rate along the flow.

The decrease of TP concentration and its accumulative removal rate is shown in Figure 5(d). From the inlet to the second sampling point the removal rate of TP was fast, after which it slowed down. TP is mainly removed by the adsorption of the intercept matrix [30], by plant absorption and by bacterial consumption. Since the growth of microbes was highest near the water entry, more phosphorus was required here, resulting in high removal rates of TP. Further downstream a balance between absorption, decomposition and dissolution was reached.

4. CONCLUSIONS

A horizontal undercurrent artificial wetland was studied to treat wastewater at the lakeside of Poyang Lake. The average removal was highly efficient for COD, with an accumulative removal rate of 42.86%, followed by the removal of ammonia-nitrogen and total nitrogen (29.46%, and 31.35% accumulative removal rate, respectively), while the least efficient removal was obtained for total phosphorus (21.75%). Water quality improved considerably as a result of passage through the wetland, with total nitrogen levels decreasing from 89.47 mg/L on average at inlet to 57.59 mg/L after treatment. Likewise, TP levels decreased from 10.05 mg/L to 7.83 mg/L. The efficiency of water treatment was subject to seasonal variation. The removal rates of TN and NH_3-N varied, but by and large they followed the same trends. It was shown that there was a linear relationship for NH_3-N between the removal rate and pollutant concentration at input ($P < 0.05$).

Considerable variation in the COD concentration of the untreated wastewater was observed, with a peak in winter but no clear seasonable trend. In contrast, the other pollutants in the untreated wastewater (NH_3-N, TN and TP) reached higher concentrations in autumn than in winter. The obtained removal efficiencies of COD and TP were higher in autumn than in winter, while no seasonable patterns were observed for removal of TN and NH_3-N. From the data presented here we conclude that the horizontal undercurrent of this artificial wetland can efficiently contribute to wastewater purification by removal of pollutants, whereby the hydraulic load and a sufficient DO should be guaranteed to obtain optimal water quality.

5. ACKNOWLEDGMENTS

This study work was kindly sponsored by grants provided by the National Natural Science Foundation of China (No. 41563001), Jiangxi Provincial Department of Science and Technology (20123BBG70192, 20151BBE50047, 20161ACG70011) and Key Laboratory of Poyang Lake Environment and Resource Utilization, Ministry of Education, Nanchang University (13006462) as well as Special funds for the graduate student innovation project in 2014 in Jiangxi province, P.R. China (YC2014-S011).

6. REFERENCES

1. Duan Y.H., Zhang N.M., Analysis on current status of rural area non-point pollution in dianchi lake basin, *Environment Protection*, Vol. 31, No. 7, 2003, pp. 28–30.
2. Zhang K.S., Zhou Q.X., Sun T.H., Advances in treatment technology of urban domestic wastewater, *World sic-tech R & D*, Vol. 24, No. 5, 2003, pp. 5–10.
3. Li W.S., Wang H.Y., Pan S.J., Present status on decentralized domestic sewage in rural areas of china and its treatment technology, *Tianjin Agricultural Sciences*, Vol. 14, No. 6, 2008, pp. 75–77.
4. Zhang Z.S., Yang Y.F., Xu G.D., Chen J.H., Research progress on technology for decentralized treatment of rural domestic sewage, *Pollution Control Technology*, Vol. 21, No. 6, 2008, pp. 65–67.
5. Yan Y.J., Xu J.C., Improving Winter Performance of Constructed Wetlands for Wastewater Treatment in Northern China: A Review, *Wetlands*, Vol. 34, No. 2, 2014, pp. 243–253. http://dx.doi.org/10.1007/s13157-013-0444-7
6. Zhao Z.M., Song X.S., Wang Y.H., Wang D., Wang S., Effects of algal ponds on vertical flow constructed wetlands under different sewage application techniques, *Ecological Engineering*, Vol. 93, 2016, pp. 120–128. http://dx.doi.org/10.1016/j.ecoleng.2016.05.033
7. Aiello J. R., Bagarello V., Barbagallo S., Lovino M., Marzo A., Evaluation of clogging in full-scale subsurface flow constructed wetlands, *Ecological Engineering*, Vol. 95, 2016, pp. 505–513. http://dx.doi.org/10.1016/j.ecoleng.2016.06.113
8. Birch G.F., Matthai C., Fazeli M.S., Suh J.Y., Efficiency of a constructed wetland in removing contaminants from stormwater, *Wetlands*, Vol. 24, No. 2, 2004, pp. 459–466. http://dx.doi.org/10.1672/0277-5212(2004)024[0459:EOACWI]2.0.CO;2
9. Cuil L., Ouyang Y., Lou Q., Yang F., Chen Y., Removal of nutrients from wastewater with Canna indica L. under different vertical-flow constructed wetland conditions, *Ecological Engineering*, Vol. 36, No. 8, 2010, pp. 1083–1088. http://dx.doi.org/10.1016/j.ecoleng.2010.04.026
10. Chen P.Y., Lee P.F., Ko C.J., Ko C.H., Chou T.C., Associations between water quality parameters and planktonic communities in three constructed wetlands, Taipei, *Wetlands*,Vol. 31, No. 6, 2011, pp. 1–8. http://dx.doi.org/10.1007/s13157-011-0236-x
11. Vymazal J., Constructed wetlands for treatment of industrial wastewaters: A review, *Ecol. Eng.*, Vol. 73, 2014, pp. 724–751. http://dx.doi.org/10.1016/j.ecoleng.2014.09.034
12. Elzein Z., Abdou A., ABD EIGawad I., Constructed wetlands as a sustainable wastewater treatment method in communities, *Procedia Environmental Sciences*, Vol. 34, 2016, pp. 605–617. http://dx.doi.org/10.1016/j.proenv.2016.04.053
13. Li Y., Zhang Y., Zhang X., Heat preservation of subsurface flow constructed wetland in cold area in winter and its operation effect, *Procedia Environmental Sciences*, Vol. 10, No. 1, 2011, pp. 2182–2188. http://dx.doi.org/10.1016/j.proenv.2011.09.342
14. Jonathan Y.S.L., Cai Q.H., Nora F.Y. T., Comparing subsurface flow constructed wetlands with mangrove plants and freshwater wetland plants for removing nutrients and toxic pollutants, *Ecological Engineering*, Vol. 95, 2016, pp. 129–137. http://dx.doi.org/10.1016/j.ecoleng.2016.06.016
15. Kantawanichkul S., Sattayapanich S., Van D. F., Treatment of domestic wastewater by vertical flow constructed wetland planted with umbrella sedge and Vetiver grass, *Water Sci Technol*, Vol. 68, No. 6, 2013, pp. 1345–51. http://dx.doi.org/10.2166/wst.2013.379
16. Paramasivam K., Ramasamy V., Suresh G., Impact of sediment characteristics on the heavy metal concentration and their ecological risk level of surface sediments of Vaigai river,Tamilnadu, India, *Spectrochimica Acta Part A: Molecular and Biomolecular Spectroscopy*, Vol. 137, 2015, pp. 397–407. http://dx.doi.org/10.1016/j.saa.2014.08.056
17. Wang, Y., Song, X., Liao, W., Niu R., Wang W., Impacts of inlet–outlet conflguration, flow rate and firate size on hydraulic behavior of quasi-2-dimensional horizontal constructed wetland: NaCl and dye tracer test, *Ecol. Eng.*,Vol. 69, No. 4, 2014, pp. 177–185. http://dx.doi.org/10.1016/j.ecoleng.2014.03.071
18. Kivaisi A.K., The potential for constructed wetlands for wastewater treatment and reuse in developing countries: A review, *Ecological Engineering*, Vol.16, No. 4, 2001, pp. 545–560. http://dx.doi.org/10.1016/S0925-8574(00)00113-0
19. Lu S.B., Zhang X.L., Wang J.H., Pei L., Impacts of different media on constructed wetlands for rural household sewage treatment, *Journal of Cleaner Production*, Vol. 127, 2016, pp. 325–330. http://dx.doi.org/10.1016/j.jclepro.2016.03.166
20. Saeed T., Sun G., A review on nitrogen and organics removal mechanisms in subsurface flow constructed wetlands: Dependency on environmental parameters, operating conditions and supporting media, *Journal of Environmental Management*, Vol. 112, No. 24, 2011, pp. 429–448.

21. The State Environmental Protection Administration, Water and wastewater monitoring analysis method, Fourth Edition, *China Environmental Science Press*, Beijing, China, 2002, pp. 200–284.
22. Yang L., Guo X.S., Zhou Y., A study on the effect of along purification in hybrid flow constructed wetlands under different residence time, *Acta Agriculturae Universitatis Jiangxiensis*, Vol. 35, No. 6, 2013, pp. 1341–1346.
23. Paing J., Voisin J., Vertical flow constructed wetlands for municipal wastewater and septage treatment in French rural area, *Water Science and Technology*, Vol. 51, No. 9, 2005, pp. 145–155.
24. Huang J., Wang S.H., Yan L., Liu Y., Wang F., Intensity of nitrification and denitrification in subsurface flow constructed wetlands, *Environmental Science*, Vol. 28, No. 9, 2007, pp. 1965–1969.
25. Christors S.A., Vassilions A.T., Effect of temperature, HRT, vegetation and porous media on removal efficiency of pilot-scale horizontal subsurface flow constructed wetlands, *Ecological Engineering*, Vol. 29, No. 2, 2007, pp. 173–191. http://dx.doi.org/10.1016/j.ecoleng.2006.06.013
26. Hua G.F., Zhao Z.W., Kong J., Guo R., Effects of plant roots on the hydraulic performance during the clogging process in mesocosm vertical flow constructed wetlands, *Environmental Science and Pollution Research*, Vol. 21, No. 22, 2014, pp. 13017–13026. http://dx.doi.org/10.1007/s11356-014-3249-1
27. Su D.L., Wang J.L., Liu K.W., Kinetic performance of oil-field produced water treatment by biological aerated filter, *Chinese Journal of Chemical Engineering*, 2007, 15(4): 591–594. http://dx.doi.org/10.1016/S1004-9541(07)60129-3
28. Shen J.Q., Fan W.P., Wu S.M., Wang J.Y., Li S., Removal of NH_3-N by microbe without organic carbon source under oxygen limited condition, *Microbiology China*, Vol. 33, No. 1, 2006, pp. 94–96.
29. Jin W.H., Fu R.B., Gu G.W., Plant growth characteristics and nutrient uptake from eutrophic water in constructed wetlands, *Research of Environmental Sciences*, Vol. 20, No. 3, 2007, pp. 75–80.
30. Yan Z.S., Wang S.H., An exploratory discussion of substrates for phosphorus removal potential for constructed wetland, *Ecology and Environment*, Vol. 16, No. 2, 2007, pp. 661–666.

Nitrogen and Biomass Recovery from Low Carbon to Nitrogen Ratio Wastewater by Combing Air Stripping and Microalgae Cultivation

SHANSHAN MA[1], HAIFENG LU[1,*], YUANHUI ZHANG[2,*], BAOMING LI[1], TAILI DONG[3] and DONGMING ZHANG[3]
[1]*College of Water Resource and Civil Engineering, China Agriculture University, Beijing 100083, China*
[2]*Agricultural Engineering Sciences, University of Illinois at Urbana-Champaign, 332N AESB, MC-644 1304 W, Pennsylvania Avenue, Urbana IL 61801, USA*
[3]*Minhe Animal Husbandry Incorporated Company, Penglai 265607, China*

ABSTRACT: An air stripping-microalgae cultivation system was proposed to recover nitrogen and produce biomass from biogas fertilizer production wastewater. Air stripping was firstly used for reducing the nitrogen to low levels. Then microalgae were used for absorbing the residual nitrogen. Results showed that the nitrogen removal reached 95.0%, with a microalgae productivity and biomass yield of 0.21 (g/L/d) and 4.29 (g-biomass/g-nitrogen), respectively. For the system, 87.7% of the total nitrogen was recycled, from which 83.9% came from air stripping and 3.8% from microalgae absorption. This system enables carbon-emission reduction, wastewater treatment and the promotion of nitrogen recovery.

1. INTRODUCTION

POULTRY litter digested effluent is one type of nutrient-rich wastewater [1]. It contains a high concentration of nitrogen, phosphorus, trace elements, ammonia acid, organic acid, humic acid and auxin [2], which can be processed for use in foliar fertilizer, animal feed and culture solution [3]. The use of membrane technology as a potential method for condensing anaerobic-digested streams to produce foliar fertilizer has been recently developed [4]. However, the effluent generated from membrane-condensing processing, called biogas fertilizer production wastewater (BFPW), still contains a relatively high concentration of nutrients. After filtration, the total organic carbon (TOC) of the effluent is relatively low (600–650 mg/L), whereas its ammonium (NH_4^+) concentration (2200–3000 mg/L) and pH value (8.4-8.5) are very high [5]. This effluent is a special type of high ammonia/nitrogen-containing and low carbon to nitrogen ratio (C/N) wastewater which is difficult to dispose using traditional biotechnology methods [5]. If not properly disposed, this effluent will lead to nitrogen resource loss and environmental pollution.

Microalgae is a type of eukaryotic micro-organism that has been attracting significant worldwide attention for wastewater treatment, as it has the ability to capture CO_2 and meanwhile absorb nitrogen and phosphorus from wastewater through various metabolic pathways. Since the 1950s, researchers have studied the use of microalgae to treat anaerobic-digested effluents such as swine effluent, dairy effluent and poultry litter digested effluent both to recover their nutrients and to generate useful biomass [6]. However, the initial total nitrogen (TN) and total phosphorus (TP) of anaerobic-digested effluent were approximately 802–3213 (mg/L) and 50–987 (mg/L), respectively [6], which exceeds the nutrient demand for microalgae growth. Especially for ammonium nitrogen; the tolerance concentration of ammonium for different algae species varies from 450 (mg/L) to 18000 (mg/L) [7]. Excess ammonium has a repressive effect on microalgae [7]. Thus, the nutrients concentration must be controlled at a proper level for microalgae growth. Common methods used for ammonia nitrogen removal include physiochemical processes such as dilution [8], air stripping [9], struvite precipitation [10] and chlorination, membrane filtration [11,12] along with biological methods such as nitrification and denitrification [13]. Air stripping has successfully been used to remove nitrogen from various wastewaters, such as dairy manure [9] and landfill lechate [10]. Air stripping of the anaerobic-digested stream in a biogas

---

*Authors to whom correspondence should be addressed.
E-mail: hfcauedu@163.com (H. Lu); yzhang1@illinois.edu (Y. Zhang)
Full mailing address: Qinghuadonglu No.17, 67#, Haidian District, Beijing, China
Phone: +86 10 62737329; Fax: +86 10 62736904

1544-8053/16/02 S023-09

doi:10.12783/issn.1544-8053/13/4/S5

plant is more feasible than other technologies for nitrogen removal because of its low economic investment, the availability of heat from biogas utilization, and the basic pH of an anaerobic-digested stream [9,14].

Therefore, in this work, a system combining air stripping and microalgae cultivation was proposed to realize nitrogen resource recovery, wastewater purification and microalgae biomass production from the low C/N BFPW. First, nitrogen in BFPW was reduced by air stripping to proper levels. Then microalgae were used for absorbing the residual-nitrogen and producing biomass. During the above processing, the wastewater treatment efficiency, nitrogen resource recovery efficiency, biomass production and nitrogen footprint of the system were all evaluated.

2. MATERIAL AND METHODS

2.1. The Characteristics of Wastewater

The BFPW was provided by Minhe Animal Husbandry Incorporated Company, where ultra-and nanofiltration membranes were used for the production of water soluble foliar fertilizer. The characteristics of the BFPW were as follows: chemical oxygen demand (COD) was 1800–3000 (mg/L), total organic carbon (TOC, mg/L) was 500–1000 (mg/L), TN was 2500–3500 (mg/L), ammonia nitrogen (NH_3-N) was 2000–3000 (mg/L), TP was below 30 (mg/L), potassium was 1341 (mg/L), colour was 5.0, turbidity was 0.30, pH was 8.3–8.5. The C/N ranges from 1:7 to 1:2.5, which represents a low C/N wastewater.

2.2. Microalgae Strain

The microalgae was *Chlorella vulgaris* 1067 (FACHB-1067). It was obtained from the Chinese Academy of Science's Institute of Hydrobiology (Wuhan, China). It was cultivated in a standard BG-11 medium [5]. A previous literature review showed that *Chlorella* sp. is highly resistant to inhibitors in wastewaters [15]. Therefore, *Chlorella vulgaris* 1067 was chosen as the test strain. The enrichment cultivation of the *Chlorella vulgaris* 1067 was carried out in 500 (mL) flasks. All of the flasks were placed in a light incubator with a light intensity of 200 (μmol/(photons·m·s)). The incubator was maintained at 26°C with a daily lighting schedule of 12 h on:off. No CO_2 was supplied during the cultivation. The carbon source came from sodium bicarbonate in the BG-11 medium. All of the *Chlorella vulgaris* 1067 used in the experiments was in the logarithmic growth phase (approximately 4–6 days after the starting day).

2.3. Experiment Setup and Procedures

2.3.1. The Feasibility Study of using BFPW to Cultivate Microalgae

The BFPW was diluted to four NH_3-N concentration levels. There was a BG-11 medium run as well, which was made using BG-11 medium. The experiments were carried out in 1000 (ml) batch reactors (flasks). The inoculum size varied from 0.07 to 0.10 (g/L). The cultivation conditions were the same as pure cultivation (Section 2.2).

2.3.2. The Experimental Setup and Procedures of the Combination System

The experimental setup is primarily composed of five parts (Figure 1): the main reactor (1000 mL), the absorption system (1000 mL), the pure cultivation system (1000 mL), the air stripping system, and the CO_2 supplementation system. The ammonia nitrogen stripping, pH regulation and microalgae cultivation by BFPW were carried out in the main reactor. The absorption system was used for the absorption of the ammonia nitrogen that was stripped from the main reactor. The pure cultivation system was used for the pure cultivation of microalgae. The air stripping system was used for nitrogen stripping. The combination of an air stripping system and a CO_2 supplementation system was used to carry out both pH regulation and microalgae cultivation. The operation steps and the experimental procedures of each step are shown as follows.

The first step was air stripping for ammonia nitrogen removal and adsorption. For air stripping, 600 (mL) BFPW was poured into the main reactor. Air was blown through the air stripping system into the main reactor. The ammonia nitrogen was blown out and flowed into the absorption system. When the ammonia nitrogen concentration decreased to a suitable level (below 600 mg/L), the air stripping was stopped. Moreover, the stripped ammonia nitrogen was absorbed by 1 (mol/L) H_2SO_4 in the adsorption system.

The second step was pH regulation using CO_2. This step was carried out in the main reactor. Following ammonia nitrogen stripping, the air stripping system and the CO_2 supplementation system were simultaneously opened to form the mixed gas that ultimately contained 4% CO_2. Next, the 4% CO_2 mixed gas was blown into

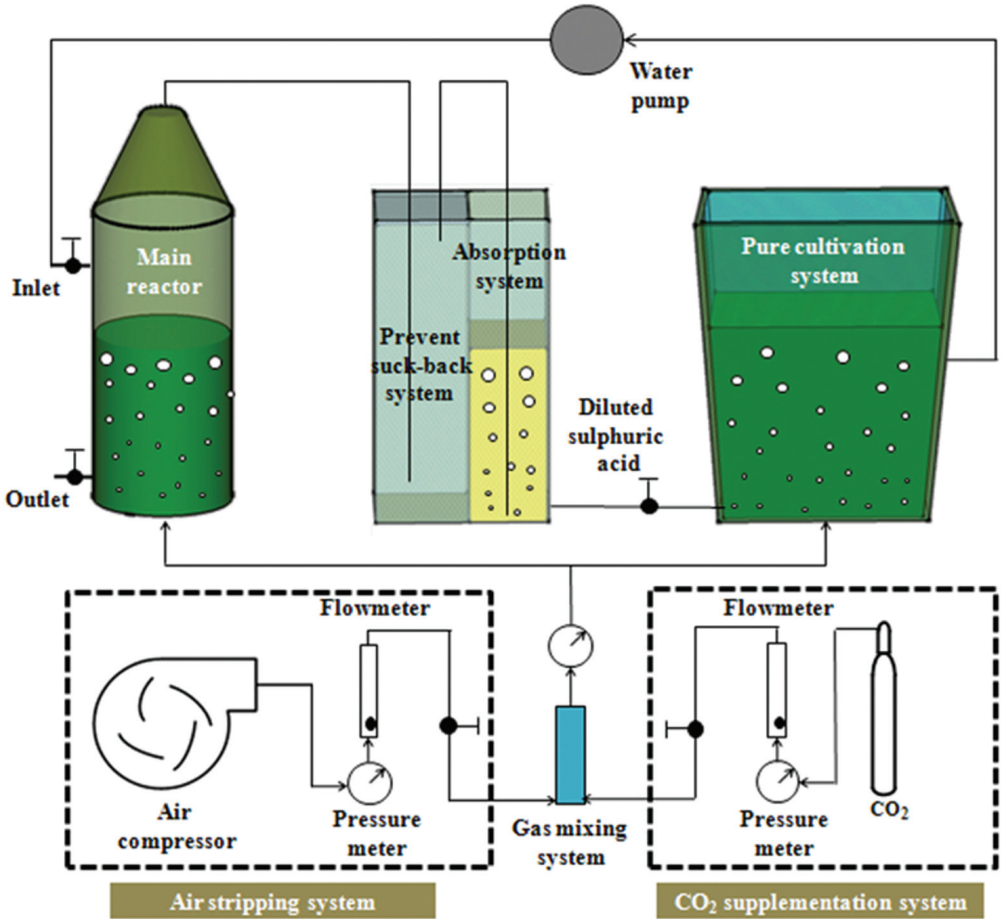

Figure 1. *The combined system of air stripping-microalgae cultivation used for the BFPW treatment, biomass production and nitrogen recovery.*

the main reactor to regulate the pH to 7.2 for 30 (min) with a flow rate of 1.0 (L/min).

The third step was microalgae cultivation. This step can be divided into two parts, each of which was carried out in different reactors. The first part involved microalgae cultivation in the BFPW (in the main reactor). When the pH regulation step finished, microalgae were inoculated into the main reactor and cultivated with a continuous supplementation of the mixture gas (4% CO_2). The light and temperature conditions were the same as the pure cultivation system (Section 2.2). The microalgae and the BFPW were collected from the main reactor for biomass and water analysis every two days.

The second part involved the pure cultivation of microalgae (in the pure microalgae cultivation reactor). The ammonia nitrogen was absorbed by 1.0 (mol/L) H_2SO_4 to form the $(NH_4)_2SO_4$ solution in the absorption system. Next, the $(NH_4)_2SO_4$ solution was used for *Chlorella vulgaris* 1067 cultivation in the pure cultivation system.

2.4. Analysis Methods

The fate of nitrogen can be analysed and described as Figure 2.

The calculation of each part of the nitrogen can be seen as follows:

A = TN in the BFPW before air stripping (mg/L) × the total volume of the BFPW before air stripping (L) (1)

$B = B_1 + B_2$ (2)

B_1 = TN in the $(NH_4)_2SO_4$ solution (mg/L) × the $(NH_4)_2SO_4$ solution volume (L) (3)

C = TN in the BFPW after the air stripping step is finished (mg/L) × the total volume of the BFPW after air stripping step is finished (L) (4)

C_1 = Nitrate (NO_3^--N) in the BFPW after air stripping step is finished (mg/L) × the total volume of the BFPW after the air stripping step is finished (L) (5)

C_2 = NH_3-N in the BFPW after the air stripping step is finished (mg/L) × the total volume of the BFPW after the air stripping step is finished (L) (6)

C_3 = dry cell weight of *Chlorella vulgaris* 1067 at the end of the cultivation process (mg/L, 10 d) × the total volume of the BFPW after the air stripping step is finished (L) × N element content in the harvest *Chlorella vulgaris* 1067 at the 10th day (%) – dry cell weight of *Chlorella vulgaris* 1067 at the beginning of the cultivation process (mg/L, 0 d) × the volume of the BFPW after *Chlorella vulgaris* 1067 cultivation finished (L) × N element content in the inoculated *Chlorella vulgaris* 1067 (%) (7)

C_4 = TN in the BFPW after microalgae cultivation is finished (mg/L) × the volume of the BFPW after *Chlorella vulgaris* 1067 cultivation is finished (L) (8)

COD, TN, TP, NH_3-N, NO_3^--N, NO_2^--N, colour and turbidity were tested using the standard methods for water and wastewater examination [16]. Dry cell weight was measured according to Lee and Shen [17]. Representative aliquots of algal cultures were taken and the cells were separated using a 0.22 (μm) membrane. The filter membranes were then pre-weighed. The cells were normally washed with diluted medium or buffer several times, followed by rinsing with distilled water. The drying temperature was 100°C. After the filter membrane cooled in a desiccator at room temperature for about 15–30 (min), the dried sample was weighed immediately once taken out of the desiccator. TOC was analyzed using a Torch Combustion TOC analyzer (TOC-VCPN, Shimadzu Co., Tokyo, Japan). The pH was measured with a previously calibrated pH meter (FE20, Mettler Toledo Co., Inc., Germany). The potassium was measured with a Perkin Elmer Optima 5300 DV ICP (Perkin Elmer Inc., America).

The nitrogen and carbon of the dry cell biomass were measured through elemental analysis (LECO CHNS-932 with oxygen furnace VTF 900, LECO Corporation, St. Joseph, MI, USA). Samples were placed in the oven's capsules for combustion at 950°C using pure oxygen as the combustion gas and pure helium as the carrier gas. Carbon was determined through infrared absorption, and nitrogen was measured as N_2 using a thermal-conductivity detection system [18].

All of the measurements were carried out three times and all of the results were reported as the average values. The data was statistically analysed using one-way ANOVA (SPSS 17.0) based on the bottles as replicates ($n = 3$). After checking the data for homoscedasticity and normal distribution of the variances, the Duncan test was used for multiple average comparisons and to detect any differences between pairs of variables at a significance level of $p < 0.05$.

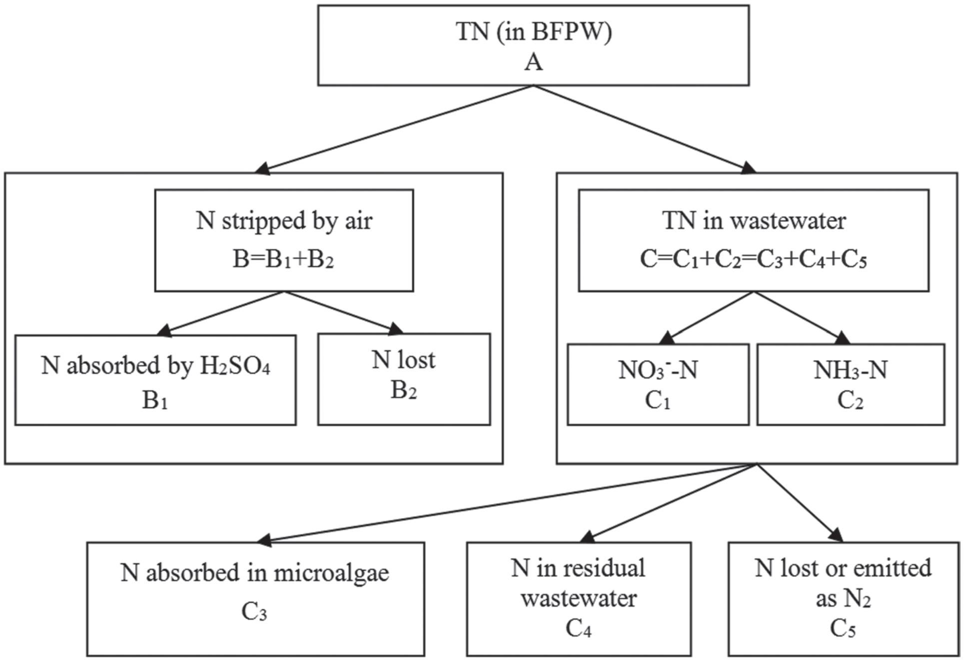

Figure 2. *The nitrogen footprint in the air stripping-microalgae cultivation system.*

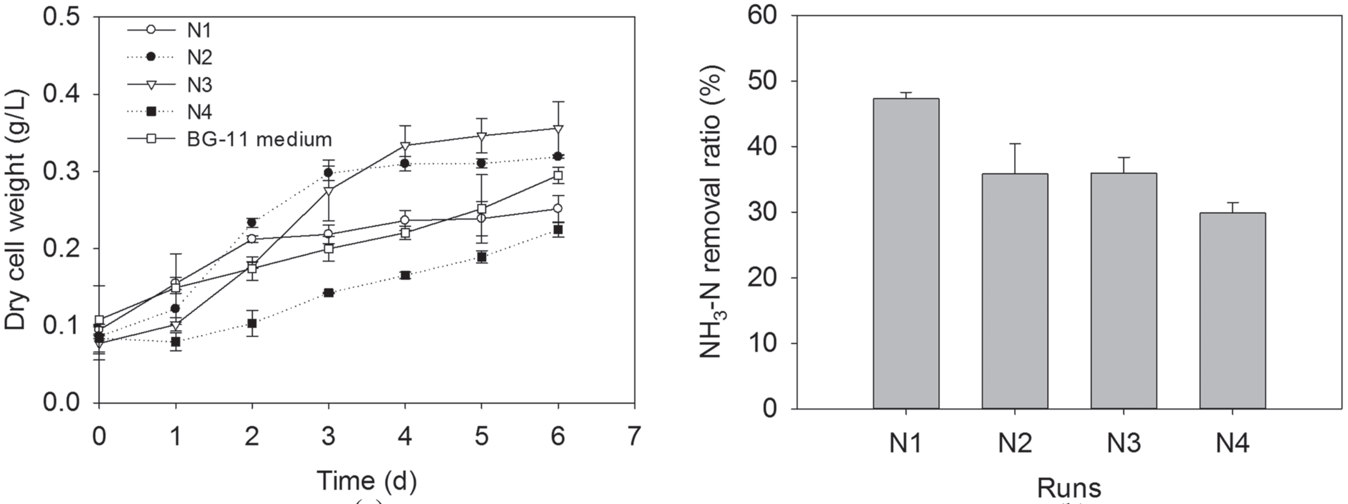

(a) (b)

Figure 3. *(a) Dry cell weight, and (b) NH_3-N removal ratiochanges at different dilution times with the initial NH_3-N concentration for N1, N2, N3, N4 of 84.1, 280.4, 560.7, 1120 mg/L, respectively; inoculum size was from 0.07 to 0.10 (g/L) dry cell weight, 200 (μmol/(photons·m·s)), 26°C, no CO_2 was supplemented.*

3. RESULTS AND DISCUSSION

3.1. Appropriate Ammonia Nitrogen Concentration for *Chlorella vulgaris* 1067 Growth in BFPW

High ammonia nitrogen is toxic to microalgae [19], therefore, the proper nitrogen concentration for *Chlorella vulgaris* 1067 growth was firstly investigated. In practical pure cultivation of microalgae, BG-11 medium is often used as a supplementation. Therefore, biomass production from the BFPW and regular pure cultivation were compared. *Chlorella vulgaris* 1067 could grow in all diluted BFPW runs (Figure 3). The suitable ammonia nitrogen concentration of the BFPW for *Chlorella vulgaris* 1067 growth was from 200 to 600 (mg/L). The final dry cell weights of N2 and N3 were all higher than that of the BG-11 medium run. The highest dry cell weight appeared in the N3 run with 0.38 (g/L) at 6 d. The final dry cell weights of N1 and N4 runs were both lower than that of the BG-11 medium run.

The BG-11 medium run showed a very different performance compared to the other BFPW runs. The logarithmic growth phase appeared from the beginning of the test to the end. The initial nitrogen concentration in the BG-11 medium run was 363.2 (mg/L), which was higher than the N2 run (280.4 mg/L) and lower than the N3 run (560.7 mg/L). However, the biomass was lower than both the N2 and N3 runs at the end of the test. They are three main reasons for the above phenomenon. The carbon limitation might be one reason. In the BG-11 medium, the carbon source was Na_2CO_3 with the concentration of 2.26 (mg/L). In N2 and N3 run, the TOC concentration was 118.2 and 230.9 (mg/L), respectively, which provided more carbon sources for *Chlorella vulgaris* 1067. The different metabolic mode might be another reason. In the BG-11 medium run, the carbon source was CO_3^{2-}. *Chlorella vulgaris* 1067 carried out in autophotosynthetic mode [17]. While in BFPW runs, organic and inorganic carbon both existed, *Chlorella vulgaris* 1067 was carried out in mixotrophic mode [17]. For *Chlorella vulgaris*, the maximum specific growth rate of mixotrophic growth was higher than that of the photosynthetic and heterotrophic growth [17]. In addition, the initial phosphorus concentration in N1 was very low, just 1.0 (mg/L), which might lead to the phosphorus limitation for microalgae growth compared to the BG-11 medium run.

The NH_3-N removal ratio was also measured to investigate the nitrogen recovery from the BFPW. The highest NH_3-N removal ratio appeared in the N1 run (47.3%); ultimately, the NH_3-N concentration was 44.3 (mg/L). In other words, the utilization efficiency of microalgae with respect to nitrogen was very low. That might have been caused by the low C/N ratio. The ratio of carbon, nitrogen and phosphorous was very important for microalgae growth and nutrients uptake. For this, the Redfield ratio of 106C: 16N: 1P is widely used, as a point of departure, to quantify possible nutrient limitations [17]. In the BFPW, the C/N ratio was 0.3, which showed the severe deficiency of the carbon source. Hence, a supplemental carbon source might promote biomass production and nitrogen utilization.

Therefore, as the above results, the nitrogen concentration must be cut down firstly. Then the carbon source must be supplemented and the pH value must be reduced to realize the promotion of biomass production and nitrogen recovery.

3.2. Air Stripping for Ammonia Removal

Air stripping is always used for treating wastewater which contains a high concentration of ammonia (> 500 mg/L). Previous works showed that the pH value, temperature, flow rate and flow time influenced the nitrogen removal in air stripping [15,20]. In this work, the initial pH was 8.3–8.5, which can be regulated to 9.0 or 10.5 by NaOH and HCl; however, because of the very high initial potassium concentration in the wastewater, the addition of NaOH would lead to the microalgae experiencing salinity stress. Therefore, in this work, air stripping without pH correction was performed. Figure 4 showed that the NH_3-N concentration decreased with time in all three flow rate runs. There was no substantial difference between the 6.0 (L/min) run and the 8.0 (L/min) run with respect to NH_3-N concentration changes. To save energy, 6.0 (L/min) was the optimal choice. Without pH regulation, the NH_3-N concentration degraded below 500 (mg/L) after 3.5 hours of air stripping.

However, the pH value in the BFPW decreased to 7.8 when the air stripping finished, which was still not suitable for microalgae growth. Accordingly, the pH value had to be regulated to a more suitable level for microalgae cultivation.

3.3. CO_2 Supplementation for Biomass Production and Nitrogen Recovery

After air stripping, the NH_3-N concentration in the BFPW ranged from 470 to 490 (mg/L), and the pH value was 7.8. Firstly, the pH value was regulated by CO_2. With the supplementation of the mixture gas that contained 4% CO_2, the pH in the BFPW dropped to 7.2 after 30 (min). Secondly, different flow rate runs of the mixture gas with 4% CO_2 for *Chlorella vulgaris* 1067 cultivation was carried out to investigate the dry cell weight and the NH_3-N concentration changes.

Figure 5 showed that the dry cell weight and NH_3-N removal ratio increased with time. In addition, a high flow rate led to rapid biomass accumulation and NH_3-N degradation. The highest biomass, daily productivity, specific growth rate and biomass yield all occurred in the 1.0 (L/min) run with the values of 2.38 (g/L), 0.2113 (g/L/d), 0.2203 (d^{-1}), 4.287 (g-biomass/g-nitrogen), respectively. Except for the 0.2 (L/min) run, the final NH_3-N concentration in all of the other runs met the discharge standard of pollutants for livestock and poultry breeding (< 80 mg/L) [21].

The optimal flow rate ranged from 0.6 to 1.0 (L/min). For the 0.6, 0.8 and 1.0 (L/min) runs, after 3 days, *Chlorella vulgaris* 1067 entered the logarithmic growth and lasted to the end. In 0.6, 0.8 and 1.0 (L/min) runs, after 10 days' treatment, the final NH_3-N removal ratio of all samples was above 95%.

It can be seen from the above results that the daily productivity and NH_3-N removal ratio were approximately 3-fold or 2-fold times of that without CO_2 supplementation (Figure 3). Especially, the elements analysis also showed that a higher CO_2 supplementation quantity led to a higher carbon and nitrogen content in the microalgae. With different flow rates of mixture gases, the carbon and nitrogen elements in *Chlorella vulgaris* 1067 were all promoted 1.8 to 2.0-fold, and 1.6 to 1.8-fold, respectively. Researchers have found that there are some relationships between the carbon and nitrogen metabolism [22]. Carbon's metabolism produces ATP, which affects the assimilation of nitrogen. Flynn [22] had found that the adjustment of algae to nitrogen stress can be realized through changing the proportions of the key metabolites of carbon and nitrogen. It has been supposed that there are two key metabolites: α-ketoglutaric acid and glutamic acid. When the α-ketoglutaric acid/glutamic acid ratio decreased, the intensity of nitrogen transportation, nitrogen metabolism and the nitrogen cycle were enhanced. Thus, CO_2 supplementation will also increase the inorganic carbon in the BFPW, which will promote nitrogen re-

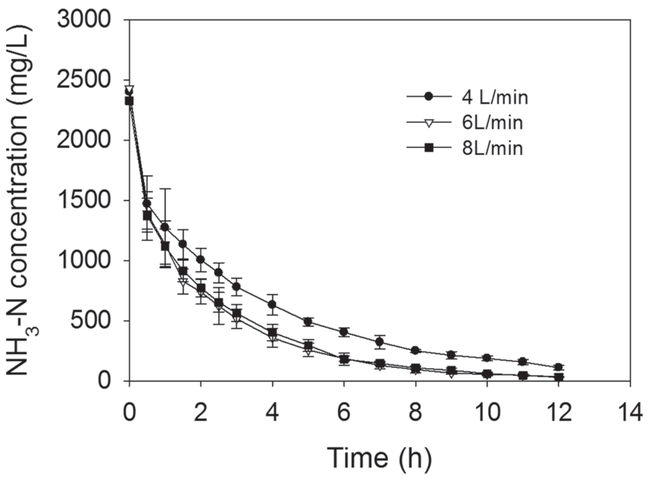

Figure 4. *NH_3-N concentration changes with different inflow rates, pH at 8.5.*

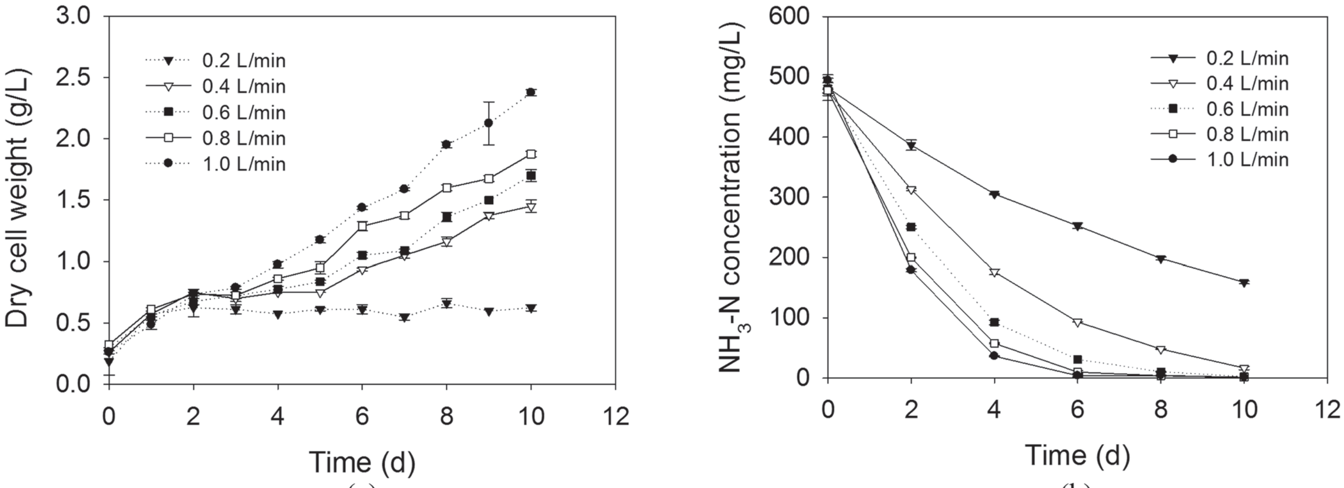

(a) (b)

Figure 5. *Using the residual BFPW to cultivate Chlorella vulgaris 1067, 25°C; inoculum size was from 0.2 to 0.3 (g/L). (a) Dry cell weight changes with different flow rate; and (b) NH_3-N changes with time in different flow rate runs.*

covery by microalgae through the metabolic pathway of autophotography.

Compared to Singh's and Bhatnagar's work [1, 23], the biomass daily productivity in this study is higher, and the tolerance of *Chlorella* sp. to wastewater was promoted approximately 16.8-fold. This might be caused by the higher light intensity, lower colour and turbidity, and extra carbon source supplementation in this work, which enhanced the mixotrophic metabolism of microalgae [17]. In Liang's work, the highest biomass was obtained as 0.7 (g/L/d) [24], which was approximately 3.5-fold times the value presented in this work. The supplementation of glucose as a carbon source and the continuous cultivation mode in Liang's work might be the main reason that leads to the high biomass production. Therefore, in order to promote biomass productivity from BFPW, the CO_2 supplementation quantity, the carbon source addition and cultivation mode need to be investigated in the future.

3.4. Nitrogen Footprint of the Whole System

In the BFPW, nitrogen was recovered from the combined system through two pathways: air stripping and microalgae absorption. In order to investigate the efficiency of nitrogen resource recovery from the combined system, the nitrogen footprint was studied. Figure 6 showed that most of the nitrogen was absorbed by H_2SO_4 (83.9%) and then formed $(NH_4)_2SO_4$. 3.8% of the nitrogen was synthesized into microalgae cells. It could be confirmed that the nitrogen disused from the combined system took 3.3%, which came from two parts. One part was the nitrogen that was lost during the air stripping or H_2SO_4 adsorption processing (2.4%) and other part was the nitrogen that stayed in the residual wastewater (after microalgae cultivation processing finished, 0.9%). In addition, the specific fate of the 9.0% nitrogen in the whole system cannot be confirmed. It might be lost or completely transformed into N_2, or both exist. During microalgae cultivation

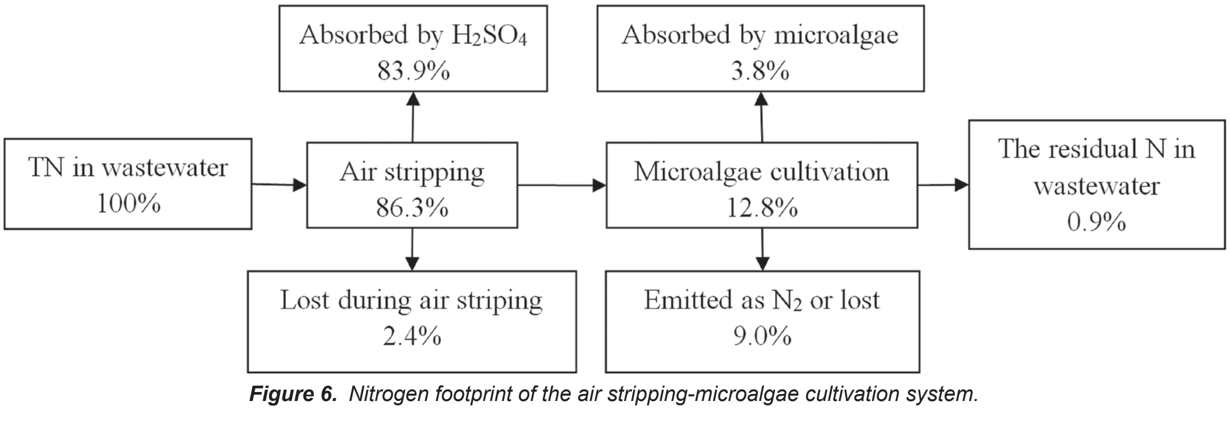

Figure 6. *Nitrogen footprint of the air stripping-microalgae cultivation system.*

with CO_2 supplementation, the CO_2 flow might strip some of the ammonia from the wastewater. Meanwhile, *Chlorella vulgaris* 1067 utilized nitrogen during the cultivation processing, in which some of the nitrogen was assimilated as the cell components, and the other might be totally oxidized into N_2 that was then released into the atmosphere [25]. However, this hypothesis needs to be further investigated. If 9.0% of nitrogen was totally lost because of the stripping effect, the nitrogen resource recovery efficiency from the combined system would reach up to 87.7%. If this part was totally transformed into N_2 by *Chlorella vulgaris* 1067, then the harmless efficiency of the nitrogen to the environment of this system would reach up to 96.7%.

In addition, the nitrogen recovered by air stripping can be used for ammonium fertilizer production and pure microalgae cultivation, thus realizing the generation of multi-utilization by-products. For the purification of the initial fertilizer production wastewater, the collected microalgae can be used as chicken feed and raw materials for biocrude oil production. However, there are some points of caution that need to be considered with regard to the collected microalgae. For example, after being collected after membrane filtration, the ash content of the collected microalgae reached up to 23.1%, which lead to low oil production and a low heating value of biocrude oil. Therefore, pre-treatment methods that can remove ash from the biomass is very important.

4. CONCLUSIONS

A combined air stripping and microalgae cultivation system was used to treat BFPW and recover nitrogen. The final effluent of the system met the discharge standard of pollutants for livestock and poultry breeding, with a microalgae daily productivity and biomass yield of 0.2113 (g/L/d) and 4.287 (g-biomass/g-nitrogen) respectively. The nitrogen resource recovery efficiency reached up to 87.7% and the harmless efficiency of nitrogen to the environment reached up to 96.7%. The nitrogen recovered by air stripping can be used for ammonium fertilizer production and pure microalgae cultivation, thus ensuring multi-utilization of the process by-products. The collected microalgae can be used as chicken feed and raw materials for biocrude oil production as well. In future, for the biogas products from biogas engineering, if the CO_2 that was purified from the biogas can be used in microalgae cultivation, the enabling carbon-emission reduction and nitrogen recovery promotion could be realized.

5. ACKNOWLEDGEMENTS

The authors thank the National Natural Science Foundation of China (51576206 and 51308535) and Minhe Animal Husbandry Incorporated Company for their financial support. Thank Jamison Watsons from the University of Illinois at Urbana-Champaign for revising the language.

6. REFERENCES

1. Singh, M., Reynolds, D. L., Das, K. C., "Microalgal system for treatment of effluent from poultry litter Aanaerobic digestion", *Bioresour. Technol.*, Vol. 102, No. 23, 2011, pp. 10841–10848. http://dx.doi.org/10.1016/j.biortech.2011.09.037
2. Wang, L., Li, Y. C., Chen, P., Min, M., Chen, Y. F., Zhu, J., Ruan, R., "An aerobic digested dairy manure as a nutrient supplement for cultivation of oil-rich green microalgae *Chlorella* sp.", *Bioresour. Technol.*, Vol. 101, No. 8, 2010, pp. 2623–2628. http://dx.doi.org/10.1016/j.biortech.2009.10.062
3. Lens, P., Hamelers, B., Hoitink, H., Bidlingmaier, W. 2004. *Resource Recovery and Reuse in Organic Solid Waste Management*, London: IWA Publishing.
4. Konieczny, K., Kwiecińska, A., Gworek, B., "The recovery of water from slurry produced in high density livestock farming with the use of membrane processes", *Sep. Sci. Technol.*, Vol. 80, No. 3, 2011, pp. 490–498. http://dx.doi.org/10.1016/j.seppur.2011.06.002
5. Zhang, T. T., Lu, H. F., Dong, T. L., Niu, X. C., Li, B. M., Zhang, D. M., Zhang, Y. H., "A strain of *Chlorella* sp. was used for chicken manure fermentation broth treatment and bio-crude oil feedstock production", *Adv. Mater. Res.*, Vol. 955-959, 2014, pp. 2714–2720. http://dx.doi.org/10.4028/www.scientific.net/amr.955-959.2714
6. Cai, T., Park, S. Y., Li, Y. B., "Nutrient recovery from wastewater streams by microalgae: status and prospects", *Renew. Sust. Energ. Rev.*, Vol. 19, 2013, pp. 360–369. http://dx.doi.org/10.1016/j.rser.2012.11.030
7. Zhang, L., Lu, H. F., Zhang, Y. H., Li, B. M., Liu, Z. D., Duan, N., "Nutrient recovery and biomass production by cultivating *Chlorella vulgaris* 1067 from four types of post-hydrothermal liquefaction wastewater", *J Appl Phycol*, Vol. 28, No. 2, 2016, pp. 1031–1039. http://dx.doi.org/10.1007/s10811-015-0640-3
8. Zhou, W. G., Chen, P. C., Min, M., Ma, X. C., Wang, J. H., Griffith, R., Hussain, F., Peng, P., Xie, Q. L., Li, Y., Shi, J., Meng, J. Z., Ruan, R., "Environment-enhancing algal biofuel production using wastewaters", *Renew. Sust. Energ. Rev.*, Vol. 36, 2014, pp. 256–269. http://dx.doi.org/10.1016/j.rser.2014.04.073
9. Jiang, A., Zhang, T. X., Zhao, Q. B., Li, X. J., Chen, S. L., Frear, C. S., "Evaluation of an integrated ammonia stripping, recovery, and biogas scrubbing system for use with anaerobically digested dairy manure", *Biosyst. Eng.*, Vol. 119, 2014, pp. 117–126. http://dx.doi.org/10.1016/j.biosystemseng.2013.10.008
10. Huang, H., Huang H., Xiao, D., Zhang Q. R., Ding L., "Removal of ammonia from landfill leachate by struvite precipitation with the use of low-cost phosphate and magnesium sources", *J. Environ. Manage.*, Vol. 145, No. 1, 2014, pp. 191–198. http://dx.doi.org/10.1016/j.jenvman.2014.06.021
11. Bonisławska, M., Nędzarek, A., Drost, A., Rybczyk, A., Tórz A., "The application of ceramic membranes for treating effluent water from closed-circuit fish farming", *Arch. Environ. Prot.*, Vol. 42, No. 2, 2016, pp. 59–66. http://dx.doi.org/10.1515/aep-2016-0012
12. Nędzarek, A., Drost, A., Harasimiuk, F., Tórz, A., Bonisławska, M., "Application of ceramic membranes for microalgal biomass accumulation and recovery of the permeate to be reused in algae cultivation", *Photochem. Photobiol. B.*, Vol. 153, 2015, pp. 367–372. http://dx.doi.org/10.1016/j.jphotobiol.2015.09.009

13. Grady Jr, C. P., Daigger, G.T., Lim, H.C. 1999. *Biological Wastewater Treatment*, second ed., New York: Marcel Dekker, Inc.
14. Ippersiel, D., Mondor, M., Lamarche, F., Tremblay, F., Dubreuil, J., Masse, L., "Nitrogen potential recovery and concentration of ammonia from swine manure using electrodialysis coupled with air stripping", *J. Environ. Manage.*, Vol. 95, Supplement, 2012, pp. S165–S169. http://dx.doi.org/10.1016/j.jenvman.2011.05.026
15. Guštin, S., Marinšek-Logar, R., "Effect of pH, temperature and air flow rate on the continous ammonia stripping of the anaerobic digestion effluent", *Process Saf. Environ. Prot.*, Vol. 89, No. 1, 2011, pp. 61–66. http://dx.doi.org/10.1016/j.psep.2010.11.001
16. APHA, AWWA, WEF. 2005. *Standard methods for the examination of water and wastewater*, 21st ed., Washington DC: American Public Health Association, American Water Works Association and Water Environment Federation.
17. Richmond, A. 2004. *Handbook of Microalgal Culture: Biotechnology and Applied Phycology*, Iowa: Blackwell Publishing Co.
18. Li, H., Liu, Z. D., Zhang, Y. H., Li, B. M., Lu, H. F., Duan, N., Liu, M. S., Zhu, Z. B., Si, B. C., "Conversion efficiency and oil quality of low-lipid high-protein and high-lipid low-protein microalgae via hydrothermal liquefaction", *Bioresour. Technol.*, Vol. 154, 2014, pp. 322–329. http://dx.doi.org/10.1016/j.biortech.2013.12.074
19. Chen, G. Y., Zhao, L., Qi, Y., "Enhancing the productivity of microalgae cultivated in wastewater toward biofuel production: A critical review", *Appl. Energ.*, Vol. 137, No. 1, 2015, pp. 282–291. http://dx.doi.org/10.1016/j.apenergy.2014.10.032
20. Zhang, L., Lee, Y. W., Jahng, D., "Ammonia stripping for enhanced biomethanization of piggery wastewater", *J. Hazard. Mater.*, Vol. 199-200, 2012, pp. 36–42. http://dx.doi.org/10.1016/j.jhazmat.2011.10.049
21. *Discharge standard of pollutants for livestock and poultry breeding*, GB 18596-2001 2003-01-01. 2001. Beijing: The Ministration of Environmental Protection of People's Republic of China.
22. Flynn, K. J., "Algal carbon-nitrogen metabolism: A biochemical basis for modeling the interactions between nitrate and ammonium up take", *J. Plankton Res.*, Vol. 13, No. 2, 1991, pp. 373–387. http://dx.doi.org/10.1093/plankt/13.2.373
23. Bhatnagar, A., Chinnasamy, S., Singh, M., Das, K. C., "Renewable biomass production by mixotrophic algae in the presenceof various carbon sources and wastewaters", *Appl. Energ.*, Vol. 88, No. 10, 2011, pp. 3425–3431. http://dx.doi.org/10.1016/j.apenergy.2010.12.064
24. Liang, G. B., Mo, Y. W., Zhou, Q. F., "Optimization of digested chicken manure filtrate supplementation for lipid overproduction in heterotrophic culture *Chlorella* protothecoides", *Fuel*, Vol. 108, 2013, pp. 159–165. http://dx.doi.org/10.1016/j.fuel.2013.02.003
25. Madigan, M. T., Martinko, J. M., Parker, J. 2002. *Brock Biology of Microorganisms*, New York: Prentice Hall, Inc.

Study of Consolidation Technology for Municipal Solid Waste and Its Safety Assessment

JIAYING SUN[1,*] and NAN LI[2]
[1]*Professor, Ningbo Institute of Technology, Zhejiang University, Ningbo, China*
[2]*Post Graduate Student, Department of Civil Engineering, Shanghai University, Shanghai, China*

ABSTRACT: We studied the stale municipal waste consolidation effect and safety of a new curing technology in this paper. Research results demonstrate that the consolidation technology can generate a municipal solid waste (MSW) product with a 28 day strength of more than 38 MPa, and superior performance in terms of durability, such as frost resistance, water resistance, dry-wet circulation resistance and sulfate resistance. The heavy metal concentrations in the leachate satisfy the Identification Standard for Hazardous Wastes of China, indicating that the heavy metals are effectively cured and stably bound.

1. INTRODUCTION

As the volume of MSW increases at the rate of 8–10 % every year, the pressure to deal with this waste also increases. At present, the technology for domestic waste disposal includes landfill, incineration, composting, recycling of resources, and so on [1,2]. Decades of practice of waste disposal shows that there is no one processing technique for municipal waste that is efficient and pollution-free. Each technique suffers from drawbacks, such as landfill produces biogas, leachate and mosquitoes, incineration produces dioxin and furan and other harmful substances [3,4]. At present, the utilization ratio of waste as a type of resource is not high no matter in China or the rest of the world [5]. We removed stale waste held in a landfill for more than 3 years, and added a consolidation agent to render the toxic and harmful substances in stale garbage, especially heavy metal ions, bound and stable, and thereby decreased potential secondary pollution to the environment. The consolidation of municipal waste to a specific strength can render it usable for road construction. The study uses a new curing method to solidify MSW, and assesses the consolidation effect and the safety of the technology.This MSW disposal method can reduce environmental pollution to a minimum degree, and does not produce harmful substances, meanwhile makes the product get effective usage. Comparing with other methods with MSW disposal, solidification of MSW has obvious advantages.

2. EXPERIMENTAL METHOD

2.1. Raw Materials

1. *Slag*: The Baotian New Building Material Co. Ltd production of blast furnace slag powder, with a specific surface area of 460 m^2/kg, and chemical composition as shown in Table 1.
2. *Steel slag*: The Baotian New Building Material Co. Ltd production of steel slag powder, with a specific surface area is 500 m^2/kg, and chemical composition as shown in Table 1.
3. *Municipal waste*: Stale municipal waste (more than 3 years old).
4. *Curing agent*: Dispensed by the research team.

2.2. Experimental Method

In the raw materials, mineral and steel slag mix together fellow the ratio 1:1, the percentage of curing agent is 10%, 20% and 30% respective, after mixing mineral slag, steel slag and curing agent together, add the same amount mass MSW. Put the mixed product into the module, then tamp and cure. The testing procedure follows the standard GB/T17671-1999.

---

*Author to whom correspondence should be addressed.
E-mail: jakys@163.com

1544-8053/16/02 S033-05

doi:10.12783/issn.1544-8053/13/4/S6

Table 1. Chemical Composition of Slag Powder and Steel Slag Powder (in wt%).

Sample	SiO_2	Al_2O_3	Fe_2O_3	CaO	MgO	SO_3	Loss
Slag	33.2	13.4	0.1	41.0	6.7	1.1	1.88
Steel slag	17.4	5.1	23.0	43.1	7.0	0.8	0.99

The mechanical properties of the consolidated product of the MSW were tested using the standard GB/T17671-1999 method (i.e., the cement mortar strength test method). The test to determine the dry-wet circulation resistance was carried out using specimens soaked in water for 4 days, and dried for 5 hours in 80 ± 5°C, and then soaked in water for 5 hours per cycle. The water resistance test was carried out using specimens soaked in water for 30 days in order to test their quality and strength.

The frost resistance test was carried out using the GBJ82-85 standard. The specimens were soaked in water for 4 days, and then, while in a dry saturated surface condition, the specimens were placed in a refrigerator at –20~ –17°C for 4 hours, and then removed and placed in water at 10~20°C for 4 hours per cycle. The sulfate resistance test was carried out using the GBJ82-85 standard.

The high temperature resistance was tested by determining the strength ratio between the strength of specimens at 80°C for 29 days and then at room temperature for 24 hours, and that of specimens kept under standard conditions. The leaching toxicity of heavy metals in the consolidated product was tested using the national standard HJ557-2010 (i.e., solid waste leaching toxicity and leaching method—level oscillation method) [6], and also by reference to the leached amount of heavy metals using the US EPA SW-846 (TCLP) (i.e., toxicity characteristic leaching method) [7]. Mechanism analysis of heavy metal stability using the sequential extraction procedure (SEP), and adding soluble water based on Tessier method [8]. Take 1 gram sample, following the process noted in Table 5, by improving the effective of the extraction agent to the specificity and selectivity of heavy metals during experiment, extracting heavy metal element from sample one by one.

3. RESULTS AND DISCUSSION

3.1. Study of Consolidation Effect on Municipal Waste

The consolidation product of the MSW is composed of slag, steel slag, curing agent, and a certain amount of stale municipal waste, under the conditions of 20 ± 3°C for 7 days, and also for 28 days. The effect of different dosages of curing agent was tested, and the compressive strength of the corresponding specimens were measured and are shown in Table 2.

Table 2. Strength of Consolidated MSW Product.

Number	Dosage of Curing Agent (%)	Compressive Strength 7 d	Compressive Strength 28 d
1#	10	9.8	16.2
2#	20	18.4	29.2
3#	30	24.7	38.4

The compressive strength of the solidified product improves with increasing amounts of curing agent from the experimental data. When the amount of curing agent reached 30%, the 7 day strength of the consolidated product reached 24.7 MPa, while the 28 day strength reached up to 38.4 MPa. At the same time, it can be observed that the early strength of the solidified product increases with increasing amounts of curing agent.

3.2. Strength Development Law of MSW Consolidated Product

It can be see that the consolidated MSW product has high compressive strength. However, in order to understand the long-term strength development of this MSW product, we have to measure the strength over a longer time frame. Figure 1 shows the development of strength of the consolidated MSW product.

The results in Figure 1 show that the consolidated MSW product not only has a high early strength, but also has long term potential strength development, with the strength reaching up to 49 MPa after 120 days, with no indication of any loss of strength.

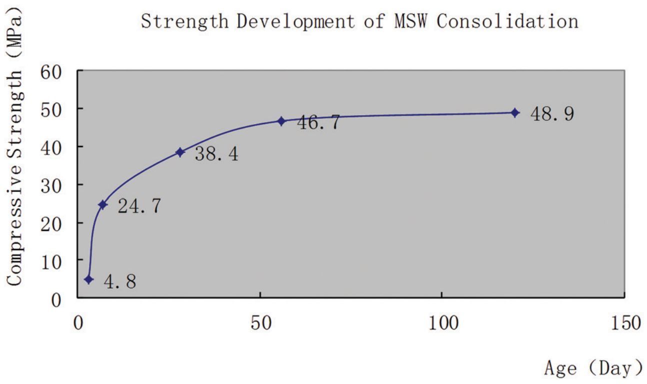

Figure 1. Strength development during consolidation of the MSW.

Table 3. Durability of Consolidated MSW Product.

Durability Project	Durability Index		
	Curing Agent 10%	Curing Agent 20%	Curing Agent 30%
High temperature resistance (80°C for 7 days)	1.05	1.06	1.08
Water resistance (under water for 30 days)	0.97	1.04	1.09
Dry-wet circulation resistance (30 times)	0.90	1.00	1.03
Freezing and thawing circulation resistance (100 times)	0.73	0.81	0.86
Sulfate resistance (5% Na_2SO_4 for 30 days)	1.01	1.06	1.10
Chloride resistance (5% NaCl for 30 days)	0.84	0.89	0.92

3.3. Durability of MSW Consolidated Product

The durability of the consolidated MSW product is shown in Table 3, where the values represent the ratio of the strengths relative to the 7 day strengths given in Table 2. It can be seen that after 30 cycles of the dry-wet circulation, strength loss decreases with increasing amounts of the curing agent.

In the tests, the consolidated MSW product can meet the technical requirements of road engineering applications in high temperature and wet environments. In addition, the experimental results also show that after 100 freezing and thawing circulation cycles, the loss of strength of the consolidated MSW product is 2~14%, but that the freezing and thawing circulation resistance improves with increasing amounts of curing agent. The consolidated MSW product basically meets the engineering requirements for frost resistance, when the amount of curing agent added is above 20%.

The sulfate resistance of the consolidated MSW product is an important aspect of its durability. Groundwater and some soils often contain a significant concentration of SO_4^{2-}, such that the consolidated product can frequently be subjected to sulfate attack. Sulfate attack is a complex physical and chemical process that the consolidated MSW product preferably resists. Pores and micro cracks in the product exert a significant influence on its sulfate resistance.

The results of sulfate resistance and chloride resistance tests show that the strength of the consolidated MSW product increased by 1~10% after immersion in 5% Na_2SO_4 solution for 30 days. This indicates that the consolidated MSW product has a superior resistance to sulfate attack. The loss of strength of the consolidated product is less than 16% after immersion in 5% NaCl solution for 30 days, while the resistance to chloride clearly increases with increasing dosage of curing agent.

3.4. Study of Leaching Toxicity of the Consolidated MSW Product

From the above experimental results, we determined that consolidated MSW product scored high in terms of physical properties and durability. In order to getting to know the safety of the material, a leaching toxicity study was carried out. Table 4 compares the heavy metal leaching of the consolidated MSW product after 56 days with that of two standards.

Table 4 shows that the amount of heavy metals determined by the horizontal oscillation test method was less than the emissions thresholds or limit values of the National Solid Waste Discharge Standard and the National Waste Water Discharge Standard, and that the consolidated MSW product maximum leaching of heavy metals over 56 days, tested using the US EPA (TCLP) rotationally oscillating method, was also less than the emissions thresholds of the above two stan-

Table 4. Leaching Toxicity of Six Heavy Metals from Consolidated MSW Product After 56 Days (in mg/l).

Type	Pb	Zn	Cd	Cr	Cu	Ni
National solid waste discharge standard	3	50	0.3	10	50	10
National waste water discharge standard	1.0	5.0	0.1	1.5	2.0	1.0
56 days leaching of heavy metals from consolidated MSW product	0.06	0.01	0.02	0.02	1.60	None
56 days maximum leaching from consolidated product	0.38	0.19	0.06	0.02	0.08	None
Dry waste leaching toxicity without consolidation	22.79	86.42	2.04	7.09	7.21	1.49
Percentage of heavy metal in product bound by curing agent (%)	98.33	99.78	97.06	99.72	98.89	100

Table 5. Results of SEP Experiment (in wt%).

	Water-soluble	Calcium Ion Exchange State	Acid Soluble State	Organic Bound State	Amorphous Iron Oxide State	Crystal Iron Oxide State	Residue State
Pb	1.56	2.01	10.99	1.67	15.89	54.77	16.60
Zn	1.00	1.23	2.89	1.89	38.81	42.79	11.24
Cr	3.70	2.96	5.11	11.49	28.61	7.89	42.09
Cd	8.10	5.98	25.89	6.23	18.89	15.99	20.07

dards. At the same time, it can be seen that the leaching toxicity of heavy metals from the MSW before consolidation greatly exceeds the threshold values for Pb, Zn and Cd of the National Solid Waste Discharge Standard, and all the threshold values of the National Waste Water Discharge Standard. Consolidation using the curing agent binds the heavy metal ions in a stable form, and the method is effective in binding up to 98.33% of the Pb, 99.78% of the Zn, 97.06% of the Cd, 99.72% of the Cr, 98.89% of the Cu, and 100% Ni.

3.5. Mechanism Analysis of Heavy Metal Stability of MSW Consolidated Product

In order to determine the long-term stability of the heavy metals in the consolidated products,sequential extraction procedure (SEP) was used. Table 5 gives the results of SEP experiment.

According to the data, the acid-soluble Pb accounts for 10.99% of the Pb, and this is the fraction of the heavy metal in carbonate and hydroxide, and is easily separated under acidic conditions. However, an acid-soluble fraction of Pb that is under 12% of total Pb would not violate the national emissions standard. Amorphous iron oxide accounts for 15.89%, and crystalline iron oxide accounts for 54.77% of the Pb represent that the Pb is hardly leachable. Greater than 60% of heavy metals in the consolidated MSW product occurs in the form of organic-bound, amorphous iron oxide, crystalline iron oxide and residual, which are stable mineral forms under natural environmental conditions, from which the three heavy metal ions cannot be readily leached or separated-out. Therefore, the consolidated MSW product, which was generated from stale municipal waste, can be safely used in standard construction.

3.6. Example Project

The design thickness of the bearing stratum for the reconstruction of the Shanxi North Road, Shanghai City is 35 cm. The original design plan was to use lime-fly ash bound macadam, but this was changed to the consolidated product from stale waste. Notably, there were double paving layers required, and the construction temperature was 30°C. The details of the deflection values after 3 days maintenance are shown in Table 6.

Based on the experimental data, the deflection value of the road that was paved using the consolidated MSW product after 3 days maintenance was 0.47 mm. This value satisfies the technical requirement for the road, which is under 2mm. At the same time, the deflection value of the road paved by lime-fly ash bound macadam was 2.17mm, which increased to 0.51mm after 10 days maintenance. Therefore, the consolidated product derived from stale waste satisfied the technical requirements 7 days sooner than lime-fly ash bound macadam.

4. CONCLUSIONS

1. By using the consolidation method on stale waste, the strength of the consolidated MSW product reached above 38 MPa after 28 days, without any observable degeneration over the longer time frame.The stable compressive strength providing a basis and a guarantee for the MSW consolidated product to be used as the load-carrying part in road foundation construction.
2. During tests of its durability, the consolidated MSW product scored high in freezing resistance, waterproof, dry-wet cycle resistance, corrosion resistance by sulfate, and other measures of durability.With the high durability, the consolidated

Table 6. Results of Paving Experiment.

	Deflection Value of Measuring Point (mm)			
Material Name	A1	A2	A3	A4
Consolidated MSW product	0.513	0.455	0.411	0.501
Ordinary two ash crushed stone	2.566	1.786	—	—

products can be used as the material of subgrade bearing layer, when facing all kinds of environment, frost melting, water and all kinds of chemical erosion conditions to ensure the stability of road safety.

3. Heavy metal ions derived from stale waste were bound into the consolidated MSW product using a curing agent. Using this consolidation method, up to 98.33% of the Pb, 99.78% of the Zn, 97.06% of the Cd, 99.72% of the Cr, 98.89% of the Cu and 100% of the Ni from the MSW can be stably bound. These six toxic heavy metals are thus firmly fixed in the consolidated MSW product, allowing the product to be safely used in an industrial area.

ACKNOWLEDGMENTS

I deeply appreciate the help of my students Nan Li, Wang Zhixin and Qiao Yan in conducting experiments and editing the manuscript. I would also like to express my gratitude to all those who talked things over, read, wrote, offered comments, allowed me to quote their remarks and assisted in the proofreading. The study was supported by the Shanghai science and technology development Seed fund No. 0323H1362.

REFERENCE

1. Qian Xu. Research of waste incineration bottom slag property and model test of embankment. *Hubei University of Technology*, 2014.
2. Yan Shao. Mechanism study of slag cementing material curing MSW[D]. *Wuhan University*, 2014.
3. Ying Yao and Jiafu Tang. Significance and Countermeasures of Waste Reduction and Resource Utilization. *Forum*, 2003, pp. 25–27.
4. Jiafu Tang and Hongfa Ma. Discussion on the Utilization of Municipal Solid Waste Resources. *J. Research on Renewable Resources*, No. 4, 2000, pp. 31–33.
5. Hui Liu, Jinghua Meng, and Xuefeng Shi.Technology summary of heavy metals stabilization of living garbage incineration fly ash. *J. Environmental Science and Management*, Vol. 41, No. 5, 2016.
6. HJ557-2010. *Toxic leaching method for leaching of solid waste: horizontal oscillation method*. 2010, pp. 225–227.
7. Kosson D.S, Vardersloot H.A, Homes T, et al. A. Leaching Properties of Untreated Residues Tested in the USEPA Program for Evaluation of Treatment and Utilization Technologies of Municipal Waste Combustor Residues. Gouumans JJJM, Vandersloot H.A, and Aalbers ThG. Waste Materials in Construcation. *C. The Netherland: Elsevier science BV*, 1991, pp. 119–134.
8. Tessier A, Campbell P. G. C., and Bission M. Sequential extraction procedure for the speciation of particulate trace metals. *J. Analytical Chemisty*, Vol. 51, No.7, 1979, pp. 844–850. http://dx.doi.org/10.1021/ac50043a017

Thermo-gravimetric Study of Coal Mine Rejects Pyrolysis with Methane Present in the Gas Environment

MING-CHU RAN[1,*] and LIN YANG[1,2]
[1]College of Power engineering, Chongqing University, Chongqing, 400030, China
[2]College of Computer Science and Information Engineering, Chongqing Technology and Business University, Chongqing, 400067, China

ABSTRACT: How to utilize the coal mine rejects and the coal bed gas (a mainly ingredient is methane) highly efficiently is becoming a hot issue. The pyrolysis of the coal mine rejects with different methane concentration was carried out by thermo-gravimetric method. The results show that the temperature zone of stimulative coal mine rejects pyrolysis reaction with some methane ingredients is existed. The stimulative coal mine rejects pyrolysis effects are more obviously with increasing the methane concentration. At the same time, the Stimulative coal mine rejects Crossover Temperature (SCT) and the Initial Carbon Appearance Temperature (ICAT) are occurred because of the together action of the crack of C-H of CH_4 in high temperature zone and coal mine rejects pyrolysis. The equation of SCT and ICAT can be expressed as a different equation of second order.

1. INTRODUCTION

COAL mine rejects is comprise of combustible carbonaceous rocks associated with coal in its formation process, with its organic matter sharing similar chemical composition and structure as coal, though with inherently high ash contents (> 50%), low volatile matter (< 20%) and fixed carbon contents (< 30%), and it is the largest emissions of industrial solid waste at present.

Coal mine rejects is difficult to combustion because of its low volatile, high ash content, low calorific value, and these characters limit the large-scale use of coal mine rejects in the world. Mixing the coal mine rejects with low calorific value gas can improve its combustion efficiency [1–3]. One of an important low calorific value gas is the mine gas which is produced while coal being exploited. The combustion and pyrolysis reaction will take place at a same time in furnace for a mixed fuel such as coal mine rejects with coal mine gas. During this process, the low calorific value gas (such as coal mine gas) has an important influence on the coal mine rejects pyrolysis characteristics, and coal mine rejects pyrolysis with reasonable ingredients can improve the combustion efficiency.

The studies about the characteristics of the low calorific value fuels such as coal mine rejects concentrated pyrolysis with carrier nitrogen and combustion [1–7], and about coal mine rejects pyrolysis with carrier methane ingredient have rarely been reported. Currently, researches focused on the pyrolysis characters of high-carbon and high volatile coal with different ingredients, such as pyrolysis characteristics of coal with hydrogen or inert gas [8–11]. Luo *et al.* [12] carried out pyrolysis experiment of coal and natural gas in fixed bed at atmospheric pressure. Jing *et al.* [13] researched the mechanism of nitrogen N metastasis during coal pyrolysis in a fixed bed reactor used temperature-programmed method for three different carbon content of coal samples with argon, methane, 15% water vapor, and hydrogenation. The weight loss characters of Longkou lignite was studied with thermo-gravimetric analysis in methane by Gao *et al.* [14]. Also, Wang *et al.* [15] studied the changes of the thermal analysis of chlorine in coal with different ingredients (inert gas, oxidizing gas, a mixture of steam among them) and at different heated time (0~45 min), *meanwhile*, pyrolysis temperature and different ratios of water vapor on the precipitation of chlorine separating out from coal [16]. Liao *et al.* [17] used lignite of Yunnan in 10g fixed-bed reactor, respectively, pyrolyzed with hydrogen, nitrogen, syngas and coke oven gas under total pressure (3 MPa) and hydrogen partial pressure (3 MPa). Li *et al.* [18], respectively, with different H_2, CH_4, CO and other gases consisting of pyrolysis atmo-

---

*Author to whom correspondence should be addressed.
E-mail: 18996085138@189.cn

1544-8053/16/02 S039-09

doi:10.12783/issn.1544-8053/13/4/S7

sphere, investigated the variation of the yield of Pioneer lignite pyrolysis products using a 10g fixed-bed reactor.

Also, there are some literatures about investigating pyrolysis characteristics for low-rank coal. The co-pyrolysis characteristics of low-rank coal were studied in the presence of Fe_2O_3/CaO catalyst in different proportions by Cheng *et al.* [19]. Zhao *et al.* [20] investigated the effects of two kinds of iron ore on the pyrolysis characteristics of a low-rank bituminous coal from Hami, China, and the pyrolysis and its products distribution were studied using thermo-gravimetric method and a fixed bed reactor. Li *et al.* [21] had finished to study pyrolysis and catalytic upgrading of low-rank coal using a NiO/MgO–Al_2O_3 catalyst. Zhang *et al.* [22] investigated the structural changes in nascent chars during the gasification of two low-rank coals in CO_2 at 1000°C and 1200°C. Inhibitory effect of coal direct liquefaction residue on lignite pulverization during co-pyrolysis had been studied by Qu *et al.* [23]. Lv *et al.* [24] investigated properties of direct coal liquefaction residue water slurry and the effect of treatment by low temperature pyrolysis. Thermal behavior and kinetics of bio-ferment residue/coal blends during co-pyrolysis had been finished by Du *et al.* [25].

Above all, Even if there are many literatures about investigating pyrolysis performance for coal with mixed carrier multi-ingredients, low-rank coal and gasification or liquefaction residue, there are few studies on the characters and mechanism of coal mine rejects pyrolysis with different ingredients have not fully understood, which blocks the further application and development of the coal mine rejects energy technology.

Therefore, to study the pyrolysis characteristics of high-ash and low fixed carbon coal mine rejects with different methane concentrations is necessary. It will lay a foundation for the low concentration of methane gas for gas (methane concentration < 50%) with the use of coal mine rejects combustion technology development, and provide the technical support for the rational use of the coal mining process generated a large number of associated products (methane gas and coal gangue). The results have much more economic and social benefits for using methane gas and coal mine rejects resources and reducing environmental pollution.

2. EXPERIMENT METHOD

Netzsch STA409PC comprehensive thermal analyzer (TGA) was adopted in the experiment. Coal mine rejects in the study were collected from Guizhou LiuPanShui, Chongqing YongChuan, Yunnan Shizong, Shanxi SiHe coalmine in China. The samples are respectively defined as LPS, YC, SZ, SH. To keep aeration-drying the samples in 50°C environment about 1~2 hours is necessary for reducing the influences of water in samples on the experimental results. The samples were crashed and their powders (0.0745 mm ~ 0.180 mm) were collected, then stored them in the sealed sample bags, and put the bags in the drying oven to use.

3. EXPERIMENTAL SAMPLES AND ITEMS

The method (Chinese GB/T 212-2008) of proximate analysis of coal was applied in the experiment to determine the content of various components of the samples (be shown in Table 1). The starting and the ending of the temperature in pyrolysis experiment was 100°C and 1000°C, and CH_4 carrier gas for 80 ml/min. When the experiment was started, the carrier under a certain pressure (0.1 Mpa) was put into the TGA, and the air was chased away from heating area, and then weighed the samples after airflow stable. Then, heated it timely, and input the carrier gas sequentially. The TGA automatically recorded the weight changes during the experiments. This paper investigates the influence of CH_4 on coal mine rejects pyrolysis with different CH_4

Table 1. Proximate Analysis of Coal Mine Rejects with Chinese GB/T212-2008(%).

Coal Mine Rejects	M_{ad}/%	V_{ad}/%	A_{ad}/%	FC_{ad}/%
	1.75	12.92	56.02	29.31
LPS	2.01	13.26	55.82	28.91
	1.66	13.29	55.62	29.43
Average	1.80	13.16	55.82	29.22
	2.17	12.26	66.40	19.17
YC	2.45	12.71	66.30	18.54
	2.03	12.48	65.94	19.55
Average	2.21	12.48	66.21	19.10
	2.57	12.23	75.39	9.81
SZ	2.76	12.27	75.16	9.81
	2.47	12.23	75.38	9.92
Average	2.60	12.24	75.31	9.85
	1.38	9.75	82.48	6.39
SH	1.76	9.81	82.69	5.74
	1.65	9.47	82.44	6.44
Average	1.60	9.67	82.54	6.19

Table 2. Experimental Items.

Number	Heating Rate (°C/min)	Particle Size (micron)	Pressure (Mpa)	Carrier Gas Composition
1	15	200	0.1	0% CH_4 + 100% N_2
2	15	200	0.1	10% CH_4 + 90% N_2
3	15	200	0.1	30% CH_4 + 70% N_2
4	15	200	0.1	60% CH_4 + 40% N_2
5	15	200	0.1	100% CH_4 + 0% N_2

concentrations. The ratio of volume of A (CH_4) and B (nitrogen N_2) are 1:9; 3:7; 6:4; 0:10, which means the concentration of CH_4 are 10%, 30%, 60% and 100% of the carrier gas. Experimental items are shown in Table 2.

4. PYROLYSIS EXPERIMENTAL RESULTS AND ANALYSIS

CH_4 is a non-polar molecule, and its structure is regular tetrahedron. Carbon atoms are located in the center of the tetrahedron, four hydrogen atoms are located in the four vertices of the tetrahedron (bond angle is 109°28′). The numerous bond energy of C-H is 413 kJ/mol, so the chemical properties are particular stable. The α-Al_2O_3 crucible is applied in this study. Therefore, before the pyrolysis experiment of coal mine rejects with methane ingredient, the blank experiment should be done with methane ingredient.

The blank experiment results show that there is no active component on the Al_2O_3 carrier under 1000°C, and few of the CH_4 can be pyrolyzed only. With the temperature increasing, there is no carbon separated out and no H_2 sent out, and TG value changes little. At the terminal temperature 1000°C, TG value from the beginning of 0 increases to 0.0011 mg. This is agree with the conclusion of reference [26] , which reported that only above 1000°C, the methane on the oxides such as Al_2O_3 can be obviously pyrolyzed.

Figure 1 show the TG and DTG characteristics of four kinds of coal mine rejects pyrolysis: (a) LPS; (b) YC; (c) SZ; and (d) SH; with different concentration of methane ingredient. The TG variation trend curves are similar for different coal mine rejects with N_2 and different concentrations of CH_4 ingredient in Figure 1. At a low temperature zone (below 895°C for LPS, 820° for YC, 795°C for SZ, 790°C for SH), CH_4 makes the weight loss change obviously during pyrolysis of coal mine rejects, this is to say that CH_4 makes a stimulative action for coal mine rejects pyrolysis. Also, at this temperature zone, more CH_4 concentration is, the stimulative action is more obviously on coal mine rejects pyrolysis, and it is changed with the species of the coal mine rejects.

The experimental results (Figure 1) also show that CH_4 takes part in the pyrolytic reaction during the coal mine rejects pyrolysis process. In the whole pyrolysis process, semi-finished coke is occurred and will react with CH_4, and sample weight loss is increased. Specially, the methane ingredient has a good promoting effect for coal mine rejects pyrolysis while the heated temperature is reached 200°C. Below a certain temperature (895°C for LPS, 820°C for YC, 795°C for SZ and 790°C for SH), TG with CH_4 mixed ingredient is always less than with N_2 ingredient, and the normalized sample weight is lighter than that of with N_2 ingredient, which means that the weight loss value is bigger than with N_2 ingredient. During the coal mine rejects pyrolysis process, its productions mainly are CO_2, CO, CH_4, H_2 and hydrocarbons, and the presence of CH_4 promotes the pyrolysis effects with coal mine rejects. In high-temperature region (higher than 895°C for LPS, 820°C for YC, 795°C for SZ and 790°C for SH), the weight loss is decreased during coal mine rejects pyrolysis with increasing CH_4 ingredient, which is caused by the CH_4 cracking and carbon separating out.

At the temperature (895°C for LPS, 820°C for YC, 795°C for SZ and 790°C for SH), the normalized sample weight has began to crossover change from lighter to heavier with comparing in pure N_2 ingredient, and form this temperature, the weight loss value is smaller than that of with pure N_2 ingredient. Also, when the CH_4 ingredient concentration becomes higher, the TG will be increasing.

However, CH_4 separating out carbon begins at the temperature with the TG curve just appears rising, or the weight loss rate decreasing value of coal mine rejects pyrolysis with CH_4 ingredient is bigger than that of pure N_2 ingredient in DTG. At crossover temperature (895°C for LPS, 820°C for YC, 795°C for SZ and 790°C for SH), the normalized sample weight with the two kinds of ingredient (CH_4 and N_2) is the same value, which is resulted from the combined action between separating out carbon and pyrolysis reaction.

Coal mine rejects respectively pyrolysis with CH_4 and N_2 ingredient and the weight loss difference of the two characteristics curve show that: CH_4 begins to separate out carbon at a certain temperature (650°C for LPS, 575°C for YC, 560°C for SZ and 660°C for SH) during coal mine rejects pyrolysis. From the blank curve of CH_4, CH_4 does not pyrolyze before these tem-

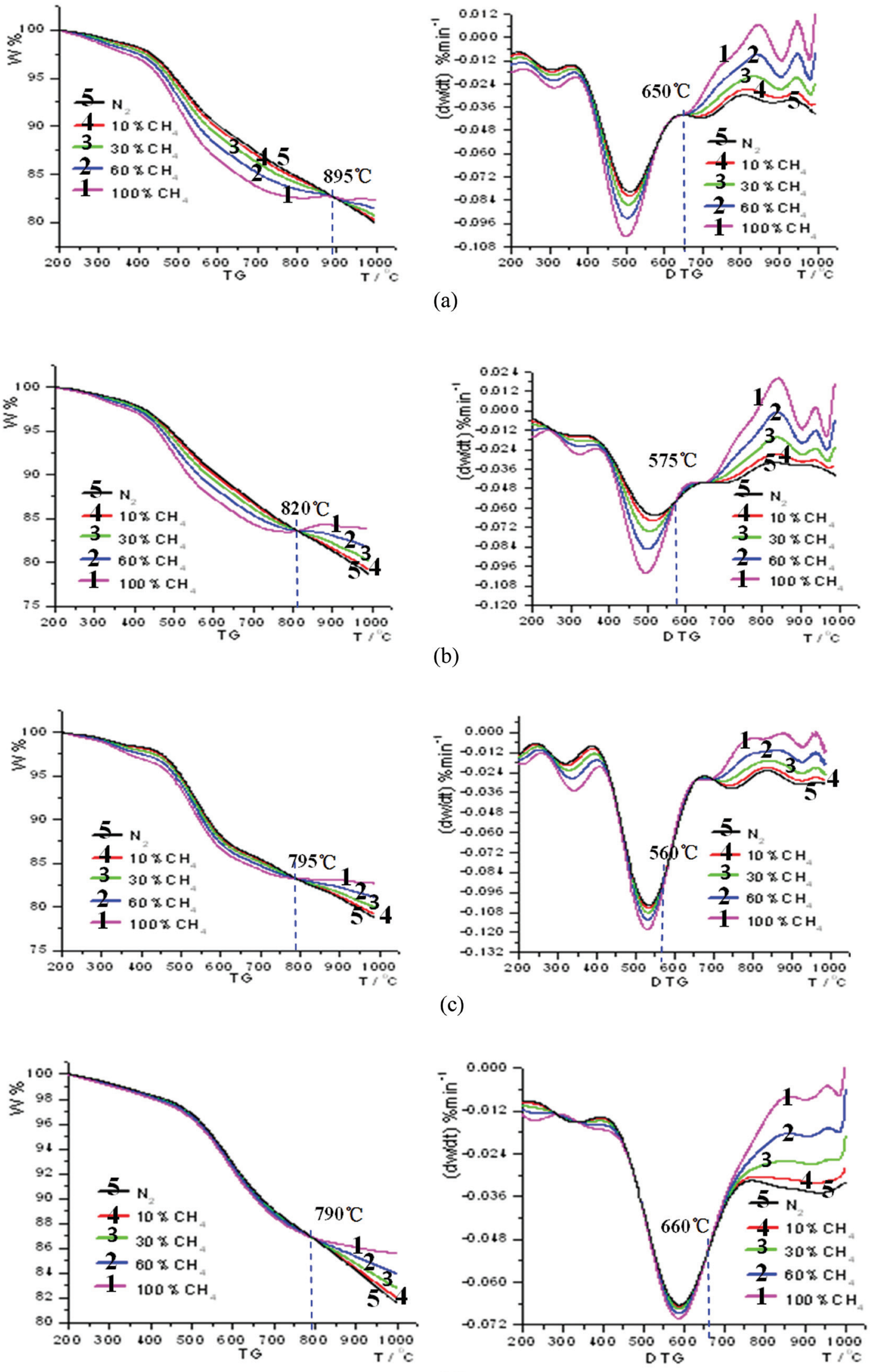

(a)

(b)

(c)

(d)

Figure 1. *TG and DTG of different coal mine rejects pyrolysis at different CH_4 concentration. (a) LBS coal mine rejects; (b) YC coal mine rejects; (c) SZ LBS coal mine rejects; and (d) SH LBS coal mine rejects.*

peratures without coal mine rejects, which means that the presence of the coal mine rejects promote the methane pyrolysis. Egiebor *et al.* [27] considered that the coal can do activate to CH_4, which makes CH_4 pyrolyse into methyl and dimethyl at a low temperature, and provides active hydrogen radical. The view agrees with the results of the experiment. The coal mine rejects begins to pyrolyse and also to produce the active radical at 200°C, and CH_4 begins to pyrolyse with the effect of the active radical fragment between 200°C to the separating out carbon temperature (650°C for LPS, 575°C for YC, 560°C for SZ and 660°C for SH). Meanwhile, the process will release the active methyl and the dimethyl active fragment, which will promote the coal mine rejects pyrolysis reaction in return. Because there is a carbon in coal mine rejects and methane, both of them can produce much C_2H_4 while coal mine rejects pyrolyse with CH_4. On the other hand, there are some chemical reactions for C_2H_4 with the organic matter of coal mine rejects, which make the amount of weight loss increase. Therefore, the TG curves of coal mine rejects with CH_4 ingredient are sharply changed than that of with N_2 ingredient during 200°C to the separating out carbon temperature (650°C for LPS, 575°C for YC, 560°C for SZ and 660°C for SH). Higher than the separating out carbon temperature, the degree of the CH_4 pyrolysis becomes deeper and carbon separates out much more. As a result, the TG curve starts to rise, and the weight loss begins to decrease. This is said that the radical fragment produced by coal mine rejects pyrolysis can promote CH_4 pyrolysis reaction, and the radical fragment produced by CH_4 pyrolysis will also promote the coal mine rejects pyrolysis reaction in return.

The DTG curve in Figure 1 shows that the pyrolysis rate with CH_4 ingredient is obviously higher than that of with N_2 ingredient while coal mine rejects being a low temperature zone (below 650°C for LPS, 575°C for YC, 560°C for SZ and 660°C for SH). However, the shapes of DTG curves are similar. At a higher temperature (650°C for LPS, 575°C for YC, 560°C for SZ and 660°C for SH), there is a significant pyrolysis rate reduce trend. That is to say, increasing turn towards the positive direction is occurred, and DTG increases with temperature increasing. The reason is that CH_4 beginning to split decomposition at separating out carbon temperature, the surface of coal mine rejects is covered with carbon by separated out from CH_4. Therefore, it displays as a decrease of weight loss rate. When the concentration of CH_4 is 100% and the temperature is 895°C for LPS, 820°C for YC, 795°C for SZ and 790°C for SH, the change rate has become a positive value, which fully proves the influence of carbon separating out from CH_4. The different coal mine rejects DTG curves show that CH_4 of different concentration separates out different content of carbon. While lower than the concentration of 10% CH_4, carbon by separated out is little, which has little effects on the weight loss rate. At the same time, there is a trend of downward increase at the end of DTG curve, which can be regarded as caused by H_2 from CH_4 pyrolysis reacts with minerals in coal mine rejects.

Table 3 shows the pyrolysis characteristics parameters of coal mine rejects with different concentrations of CH_4 (Where, T_s is the initial temperature of separating out volatiles, $T_{\max}$ is the temperature at $(dw/dt)_{\max}$, $\Delta T_{1/2}$ is the half peak width temperature at $(dw/dt)/(dw/dt)_{\max} = 1/2$, T_f is the final pyrolysis temperature and $T_f = 2T_{\max} - T_s$, D is the index of separating out volatiles, and $D = (dw/dt)_{\max}/(T_{\max} \cdot T_s \cdot \Delta T_{1/2})$.

From the Table 3, while the coal mine rejects pyrolyse with CH_4, the initial temperature T_s, the peak temperature $T_{\max}$, and the half peak width temperature $\Delta T_{1/2}$ are decreased with the concentration of CH_4 increasing. These means that CH_4 stimulate the coal mine rejects pyrolysis, and the stimulative coal mine rejects pyrolysis effects are more obviously with increasing the methane concentration, also the corresponding peak value is bigger, and the reaction is more violent.

Table 3 also shows: the peak temperature of LPS coal mine rejects pyrolysis changes considerably with the change of methane concentration, and the *D*-value of peak temperatures between CH_4 and N_2 ingredient is 24°C, when both concentrations of them are 100%. The *D*-value of YC coal mine rejects is 13°C, and the *D*-value of the other kinds of coal mine rejects is only a few Celsius degrees, which is mainly caused by the different fixed carbon content in coal mine rejects. The pyrolysis peak temperature changes with the concentration of CH_4, and the changes become bigger while the content of fixed carbon is greater in coal mine rejects. Although CH_4 has a promoting effect on the coal mine rejects pyrolysis reaction, the data in table 3 show that the thermo-weight loss decrease with increasing the concentration of CH_4. Obviously, the weight loss is not the coal mine rejects' own weight loss, and it includes the separating carbon adhering to the surface of sample, which increases the weight of the sample. That is to say, coal mine rejects has a promoting effect on the reaction of CH_4 to separating out carbon, and the carbon content increases with the concentration of

Table 3. Pyrolysis Characteristics Parameters of Coal Mine Rejects with Different Concentration.

Sample	CH_4 (%)	T_s (°C)	T_{max} (°C)	T_f (°C)	$\Delta T_{1/2}$ (°C)	$(dw/dt)_{max}$(% min^{-1})	$D \times 10^{-9}$	Final Wt. Loss (%)
YC	N_2	294	510	726	220	0.08	2.41	20.16
	10	292	508	724	200	0.08	2.76	19.92
	30	288	505	722	185	0.09	3.21	19.43
	60	283	502	721	174	0.09	3.77	18.70
	100	279	497	715	162	0.10	4.57	17.73
LPS	N_2	295	519	743	399	0.07	1.06	21.66
	10	293	512	731	357	0.07	1.26	21.12
	30	288	506	724	295	0.07	1.74	20.05
	60	283	502	721	245	0.09	2.45	18.43
	100	280	495	710	161	0.10	4.49	16.28
SZ	N_2	300	532	764	154	0.10	4.22	21.58
	10	297	532	767	155	0.10	4.23	21.15
	30	295	531	767	146	0.11	4.73	20.27
	60	290	530	770	144	0.11	5.01	18.96
	100	285	528	771	138	0.12	5.69	17.20
SH	N_2	285	588	891	247	0.07	1.60	18.46
	10	283	587	891	239	0.07	1.68	18.06
	30	281	585	889	232	0.07	1.78	17.25
	60	278	586	894	225	0.07	1.88	16.05
	100	275	585	895	217	0.07	2.02	14.44

CH_4 increasing. There is a tight relationship between the influence of CH_4 to coal mine rejects pyrolysis and the internal structure of coal, the varieties and contents of minerals, and the extent of reaction among carbon, H_2 separating out from CH_4 and minerals.

5. SCT AND ICAT OF THE PROMOTING EFFECTS OF COAL MINE REJECTS PYROLYSIS WITH CH_4

In order to detailedly state the promoting or inhibiting pyrolysis reaction effects on coal mine rejects with CH_4, there is a define for the variable $\Delta W_{CH_4} = \Delta W_{N_2} - \Delta W_{CH_4}$.

ΔW_{CH_4} is the *D*-value (Table 3) between the weight loss percentages of coal mine rejects pyrolysis reaction with CH_4 and with N_2, W_{N_2} is normalized sample weight with N_2 ingredient, W_{CH_4} is normalized sample weight with mixed CH_4 ingredient at the same temperature. Obviously, ΔW_{CH_4} states the degree of suppressive ($\Delta W_{CH_4} < 0$) or stimulative ($\Delta W_{CH_4} > 0$) coal mine rejects pyrolysis with CH_4.

Figure 2 show the relationship of ΔW_{CH_4} and *T* with different concentration of CH_4 and different kinds of coal mine rejects. The pyrolysis influences of CH_4 to coal mine rejects have an enough differences with different kinds of coal mine rejects. Nevertheless, both of them appear promoting effects while lower their Initial Carbon Appearance Temperature (ICAT, to define it as t_c). This is to say, while $\Delta W_{CH_4} > 0$, the promoting effects are more obvious with increasing the temperature. However, while ΔW_{CH_4} increases to a certain value, ΔW_{CH_4} appears a little subdued segment and then falls back slowly. As a result, there is a Stimulative coal mine rejects Crossover Temperature (SCT, to define it as t_{cr}) with CH_4, because there may be dissociation of CH_4 with miner in the rejects above t_{cr}. Also, the t_{cr} is mainly influenced by carbon content in the sample, so the t_{cr} is nearly constant at different CH_4 consternation for the same sample. The simulative effect changes little with the concentration of CH_4 changes when the temperatures lower than t_{cr} (all are promoting effects on coal mine rejects pyrolysis reaction). Therefore, it is decided to take the peak value of ΔW_{CH_4} as tcr value while the concentration of CH_4 is 100%. The value of ΔW_{CH_4} falls back, which is caused by CH_4 pyrolyzing, and carbon separating out at high temperature. The temperature when ΔW_{CH_4} starts to fall back is tcr, and the carbon begins to separating out from CH_4. The tcr and tc values of all kinds of coal mine rejects pyrolysis with 100% concentration of CH_4 are as shown in Table 4.

Figure 2 also show that the influences of CH_4 to coal mine rejects pyrolysis is different according to the concentration of CH_4. The volatile production by coal mine rejects pyrolysis also includes CH_4, which have an influence on the concentration of carrier gas. The quantity of sample in the experiment is small, so the production is little, which has little influence on the situation when the concentration of carrier gas. However, at a low concentration, the influence is more obvious than at higher concentration. When coal mine rejects pyrolysis with N_2, there is a little CH_4 produced by coal mine rejects itself pyrolysis. When the concentration of CH_4 is low, there is little difference between property of coal mine rejects pyrolysis with N_2 and with CH_4. The curves of ΔW_{CH_4} are almost straight lines, and the values fluctuate around zero. As shown in Figure 2, with increasing the concentration of CH_4, the affection created by CH_4 become dominant, which has a deep influence on the coal pyrolysis process.

Table 4. The SCT and ICAT (t_{cr}/t_c) of Coal Mine Rejects Pyrolysis at CH_4 Environment.

Coal Rejects	**LPS**	**YC**	**SZ**	**SH**
t_{cr} (°C)	895	820	795	790
t_c (°C)	650	575	560	660

Tables 4 and 1 show that the Stimulative coal mine rejects Crossover Temperature (SCT) t_{cr} and Initial Carbon Appearance Temperature (ICAT) t_c have a certain relationship to the carbon content in coal mine rejects, which can be also seen from Figure 3. Figure 3(a) shows the variation between the t_{cr} and the car-

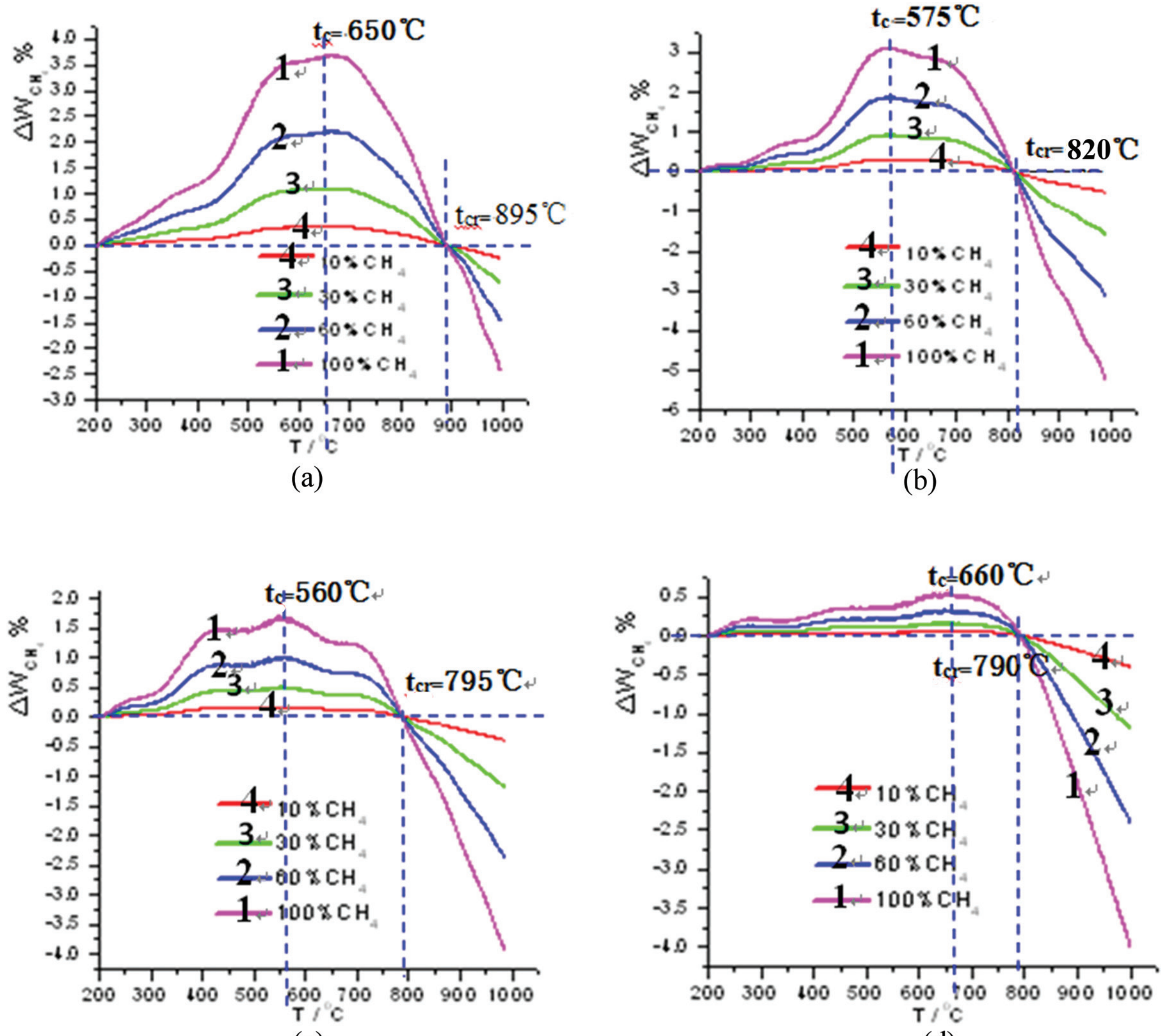

(a) (b)

(c) (d)

Figure 2. *Variation of ΔW_{CH4} with pyrolysis temperature for coal mine rejects. (a) LBS coal mine rejects; (b) YC coal mine rejects; (c) SZ LBS coal mine rejects; and (d) SH LBS coal mine rejects.*

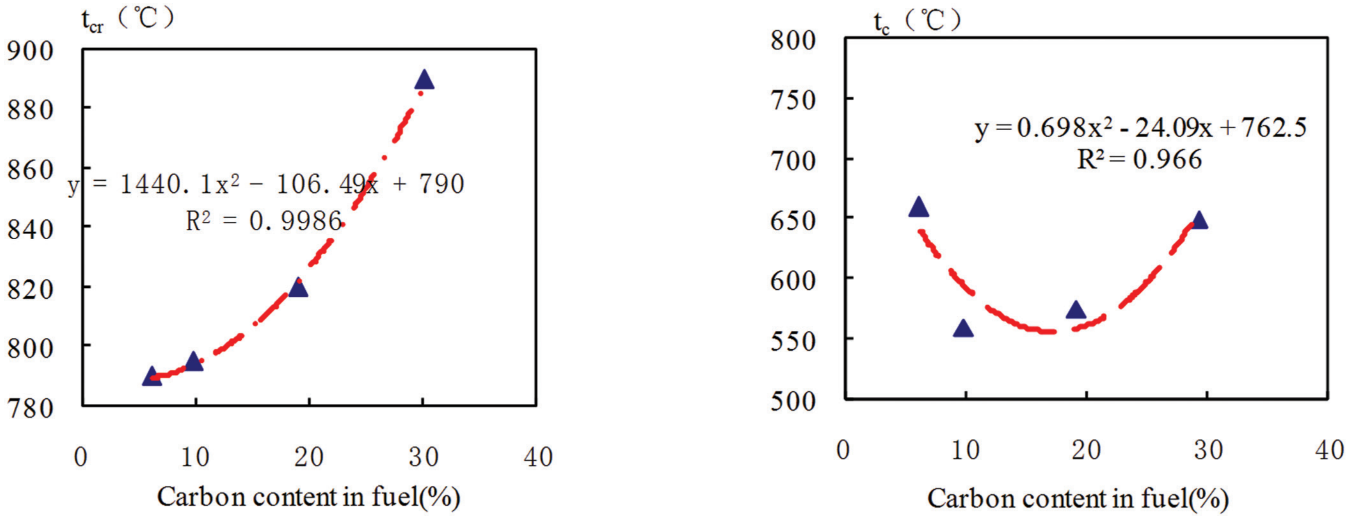

(a) (b)

Figure 3. *Variation of t_{cr} and t_c with carbon content in fuel.*

bon content in coal mine rejects. It can be found that the relationship between t_{cr} and the carbon content in coal mine rejects can be described as a parabolic equation. According to the results of the coal mine rejects pyrolysis experiment, the expression is $t_{cr} = 1440.1C^2 - 106.49C + 790$. Figure 3(b) shows that the variation between t_c and the carbon content in coal mine rejects can also be described as a parabolic equation, which is $t_c = 0.698C^2 - 24.09C + 762.5$.

6. CONCLUSIONS

The pyrolysis performance of four different kinds of coal mine rejects with different methane ingredient has been carried out by thermo-gravimetric method. The conclusions are listed as following.

1. The temperature zone of stimulative coal mine rejects pyrolysis with some CH_4 ingredients is always existed. The promoting effects on coal mine rejects pyrolysis reaction are more obviously with increasing the methane ingredient concentration.
2. The influence of different concentration of CH_4 on the coal mine rejects pyrolysis is taken place in subsections, and different influence effects are existed in different temperature section. ΔW can be used to determine the conversion percentage of coal mine rejects pyrolysis with different concentrations of CH_4 ingredients (ΔW is the D-value between the weight loss percentage of coal mine rejects pyrolysis with N_2 ingredient and with CH_4 ingredients, and $\Delta W = \Delta W_{N_2} - \Delta W_{CH_4}$).
3. There are SCT and ICAT because of the together action of the crack of CH_4 in high temperature zone and coal mine rejects pyrolysis. Below SCT, CH_4 has a promoting effect on the coal mine rejects pyrolysis. At the same time, below ICAT, there is no carbon being separated out for CH_4. The relationship between carbon content in coal mine rejects and SCT & ICAT can be described as parabolic equations.
4. There are obvious pyrolysis reaction differences at different CH_4 concentration ingredients for coal mine rejects. Also, more CH_4 concentration is, more deeply promoting effects on the coal mine rejects pyrolysis is.

7. ACKNOWLEDGEMENTS

The authors gratefully acknowledge the financial support from the key natural science foundation of Chongqing Municipal Government (cstc2013jjB90003).

8. REFERENCES

1. Ran, J.Y.; Niu, B.; Zhang, L.; Pu, G.; Tang, Q., Study on General Combustion Performance and Kinetic Characteristics of Combustion of Coal Residue, *Proceedings Of The CSEE*, Vol. 26, No. 15, 2006, pp: 58–62.
2. Li, S.Q.; The Characteristics and Kinetic Mechanisms of Coal Residue Pyrolysis in the different Atmosphere, Degree Thesis of Master of Chongqing University, 2008, pp: 3–50.
3. Yang, L.; Ran, J.Y.; Zhang, L., Mechanism and Kinetics of Pyrolysis of Coal With High Ash and Low Fixed Carbon Contents, *J. of Energy Resources Tech., Trans. of the ASME*, Vol. 133, No. 3, 2011, pp: 701–708.
4. Ran, J.Y.; Hu, J.H.; Wang, Y.M.; Zhang, L., Effects Of Compounds

With Metal Elemen and Pressure on the Combustion Characteristics of Mixed Industrial Sludge, *Acta Scientiae Circumstantiae*, Vol. 28, No. 1, 2008, pp: 108–113.

5. Ran, J.Y.; Niu, B.; Zhang, L., Thermogravmi Etric Study on Pyrolysis Performance and Mechan Ism of Coal Residue, *J. of Chin. Coal Society*, Vol. 31, No. 5, 2006, pp: 640–643.
6. Zhou, J.; Yang, Z.; Liu, X.F.; Wu, L.; Tian, Y.H.; Zhao, X.C., Study On Microwave Co-Pyrolysis Of Low Rank Coal And Circulating Coal Gas, *Spectroscopy and Spectral Analysis*, Vol. 36, No. 2, 2016, pp: 459–465.
7. Xu,Y.; Zhang, Y.F.; Zhang, G.J.; Guo, Y.F.; Zhang, J.; Li, G.Q., Pyrolysis Characteristics and Kinetics of Two Chinese Low-Rank Coals, *Journal of Thermal Analysis and Calorimetry*, Vol. 122, No. 2, 2015, pp: 975–984. http://dx.doi.org/10.1007/s10973-015-4801-z
8. Liu, S.; Xia, H.; Liu, Q.; Zhang, M., The Impact of Coal Sample Characteristics on Microwave Pyrolysis, Energy Sources, Part A: Recovery, *Utilization and Environmental Effects*, Vol. 37, No. 17, 2015, pp: 1829–1835. http://dx.doi.org/10.1080/15567036.2014.925988
9. Luo, K.; Zhang, C.; Zhu, S.H.; Bai, Y.H.; Li, F., Tar Formation During Coal Pyrolysis Under N_2 and CO_2 atmospheres at Elevated Pressures, *Journal of Analytical and Applied Pyrolysis*, Vol. 118, No. 3, 2016, pp: 130–135. http://dx.doi.org/10.1016/j.jaap.2016.01.009
10. Yuan, Q.; Ge, X.; Zhou, S., Fractal and Pyrolysis Characteristics of Ultra-Fine Pulverized Coal Particles, Energy Sources, Part A: Recovery, *Utilization And Environmental Effects*, Vol. 37, No. 14, 2015, pp: 1568–1574. http://dx.doi.org/10.1080/15567036.2011.629282
11. Du, R.L.; Wu, K.; Xu, D.A.; Chao, C.Y.; Zhang, L.; Du, X.D.; A Modified Arrhenius Equation to Predict the Reaction Rate Constant of Anyuan Pulverized-Coal Pyrolysis at Different Heating Rates, *Fuel Processing Technology*, Vol. 148, No. 1, 2016, pp: 295–301. http://dx.doi.org/10.1016/j.fuproc.2016.03.011
12. Luo, M.; Zhang, J.M.; Gao, M.S., Research on Co-Pyrolysis Behavior of Coal and Natural Gas, *Coal Science and Tech.*, Vol. 34, No. 5, 2006, pp: 56–60.
13. Jing, X.X.; Chang, L.P.; Xie K.C., Effect Of Reaction Gas on NH_3 Released During Coal Pyrolysis, *Coal Conversion*, Vol. 28, No. 1, 2005, pp: 14–16.
14. Gao, M.S.; Zhang J.M.; Luo, M., Study of Weight Loss Characters and Promoting Function to Sulfur Release During Lignite Pyrolysis in Methane, *Coal Conversion*, Vol. 28, No. 4, 2005, pp: 7–10.
15. Gao, M.S.; Zhang J.M.; Luo, M., Research Progress of Coal Pyrolysis Desulfurization in Reductive Atmospher, *Clean Coal Tech.* Vol.11, No.1, pp: 34–38.
16. Wang, J.P.; Zhang, D.X.; Gao, J.S., Pyrolysis Removal Of Chlorine In Coal Under Different Gas Atmospheres, *Coal Conversion,* Vol. 26, No. 2, 2003, pp: 29–32.
17. Liao, H.Q.; Sun, C.G.; Li, B.Q., Coal Pyrolysis Under Hydrogen Rich Gases, *J. of Fuel Chem. and Tech*. Vol. 26, No. 2, 1998, pp: 14–18.
18. Cheng, Xiaohan, He, Xuanming; Chen, Cheng; Yi, Shuang, Influence of Fe_2O_3/CaO Catalysts on the Pyrolysis Products of Low-Rank Coal, *Energy Technology*, Vol. 3, No. 10, 2015, pp: 1068–1071. http://dx.doi.org/10.1002/ente.201500152
19. Zhao, H.Y.; Li, Y.H.; Song, Q.; Lv, J.X.; Shu,Y.F.; Liang, X.X.; Shu, X.Q., Effects of Iron Ores on the Pyrolysis Characteristics of a Low-Rank Bituminous Coal, *Energy and Fuels*, Vol. 30, No. 5, pp: 3831–3839. http://dx.doi.org/10.1021/acs.energyfuels.6b00061
20. Li, Y., Amin, M.N.; Lu, X.M.; Li, C.; Ren, F.Q.; Zhang, S.J., Pyrolysis and Catalytic Upgrading of Low-Rank Coal Using a Nio/Mgo–Al_2O_3 catalyst, *Chemical Engineering Science*, Vol. 155, No. 11, 2016, pp: 194–200. http://dx.doi.org/10.1016/j.ces.2016.08.003
21. Zhang, L.; Kajitani, S.; Umemoto, S.; Wang, S.; Quyn, D.; Song, Y.; Li, T.T.; Zhang, S.; Dong, L.; Li, C.Z., Changes In Nascent Char Structure During the Gasification of Low-Rank Coals in CO_2, *Fuel*, Vol. 158, No. 6, 2015, pp: 711–718. http://dx.doi.org/10.1016/j.fuel.2015.06.014
22. Qu, Y.; Chu, M.; Shen, G.D.; Yuan, Y.; Zhang, Y., Inhibitory Effect of Coal Direct Liquefaction Residue on Lignite Pulverization During Co-Pyrolysis, *Fuel Processing Technology*, Vol. 147, No. 8, 2015, pp: 57–63.
23. Lv, D.M.; Bai, Z.Q.; Wei Y.C.; Bai, J.; Kong, L.X.; Guo, Z.X.; Li, X.; Xu, J.L.; Li, W., Properties Of Direct Coal Liquefaction Residue Water Slurry: Effect of Treatment by Low Temperature Pyrolysis, *Fuel*, Vol. 179, No. 9, 2016, pp:135–140. http://dx.doi.org/10.1016/j.fuel.2016.03.081
24. Du, Y.Y.; Jiang, X.G.; Lv, G.J.; Ma, X.J.; Jin, Y.Q.; Wang, F.; Chi, Y.; Yan, J.H., Thermal Behavior and Kinetics of Bio-Ferment Residue/Coal Blends During Co-Pyrolysis, *Energy Conversion and Management*, Vol. 88, No. 12, 2014, pp: 459–463. http://dx.doi.org/10.1016/j.enconman.2014.08.068
25. Qiu, F.L.; Fu,X.Y.; Lin, S.H., Study on Steam Reforming of Natural Gas at High Temperatures, *J. of Fuel Chem. and Tech*. Vol. 11, No. 1, 1983, pp: 10–14.
26. Egiebor, N. O.; Gray, M. R., Evidence for Methane Reactivity during Coal Pyrolysis and Liquefaction, *Fuel*, Vol. 69, No. 10, 1990, pp: 1276–1282. http://dx.doi.org/10.1016/0016-2361(90)90289-3

Role of Sorbent Surface Functionalities, Partition and Microporosity in 2, 2′, 4, 4′-Tetrabromodiphenyl Ether Sorption onto Biochars in a Single-Solute System

YULIN YAN[1], JIAJI SUN[1], FANGFANG SU[1], WEIFANG MA[1,*], XIAOXIU LUN[1] and HAO GUO2
[1]*College of Environmental Science and Engineering, Beijing Forestry University, Beijing 100083, China*
[2]*Beijing Association of Sustainable Development, Beijing 100084, China*

ABSTRACT: A study was conducted to investigate the sorption behavior and mechanisms of 2, 2′, 4, 4′-tetrabromodiphenyl ether (BDE-47) onto a series of corn straw biochars pyrolysed at 300, 500 and 700°C (BC300, BC500 and BC700). The micropore volume of BC700 was 34 times higher than BC300 and BC500, which indicates that the biochar developed more high energy pore-filling adsorption sites and the carbonization was accelerated as pyrolytic temperatures increased,. The kinetics results showed that the fast sorption rate constants ranged from 4.01 h^{-1} to 6.62 h^{-1} while the slow sorption rate constants ranged from 0.18 h^{-1} to 0.40 h^{-1}. The fast sorption was attributed to the partitioning. The adsorption isotherm parameters indicate that the sorption mechanisms were different among the different biochars. For BC300, partitioning was the main adsorption mechanism while for BC500, the pore-filling adsorption dominated the sorption progress at low concentration, while partitioning dominated at high concentration. The pore-filling adsorption dominated the entire sorption progress for BC700.

1. INTRODUCTION

KNOWN as PBDEs, polybrominated diphenyl ethers are commonly added to industrial production, including electronic appliances, textile, furniture, and building materials, due to their excellent fire-retarding performance and low cost [1]. Due to their high bioaccumulation effect and endocrine disturbance characteristics, tetra-, penta-, hexa-, and hepta-BDE had been included in Article 3 and Annex A of the Stockholm convention in May 2009 [2,3]. 2, 2′, 4,4′-tetrabromo diphenyl ether (BDE-47), which is the congeners of PBDEs, is frequently detected in various environmental compartments. As a result of increasing environmental pollution and concerns of human health, it has drawn much attention [4].

Recently, PBDEs have been detected in various environmental compartments—not only industrial areas, i.e., e-waste dismantling sites [5], municipal solid waste incinerator [6] but also non-industrial areas. i.e., Taihu Lake [7], European background soils [8], and the Yangtze River Delta. Among various environmental media, soil is the most important for PBDEs, which is significant for the bioavailability, biodegradability and accumulation. Moreover, PBDEs of comparatively high concentrations have been examined in soil samples; thereby, it is urgent to find a possible soil amendment and a potential low-cost adsorbent to control their further transport. Currently, some studies have shown that at contaminated sites biochar (BC) can be utilized as a measure of remediation to isolate pollutant and control contaminants migration in the soil, increasing soil pH (in acidic soils) and CEC, as well as enhance recycling of agricultural and forestry wastes. As a type of carbon-rich material with porosity [9], BC is combusted under low oxygen conditions and produced from biological remains, such as crop remains, timber and livestock waste. Simultaneously, several previous studies have shown that its physicochemical properties and pollutant retention ability can be affected by the source of material and productive process [10,11,12,13]. Besides, some present reports have observed the removal studies of Cd and explosive compounds by buffalo-weed biochar-alginate bead [14] and influential factors of sorption utilizing rice husk biochar [15].

As a key procedure, adsorption controlled the devel-

---

*Author to whom correspondence should be addressed.
E-mail address: mpeggy@163.com; Tel.: +86-10-62799780; Fax:+ 86-10-62336615; Complete postal address: College of Environmental Science and Engineering, Beijing Forestry University, Qinghua East Road 35, Haidian District, Beijing 100083, China

1544-8053/16/02 S049-11

doi:10.12783/issn.1544-8053/13/4/S8

opment of hydrophobic organic compounds (HOCs) [9,16,17]. As one kind of HOCs, PBDEs have been mainly adsorbed by soils and sediments [18], however, these natural adsorbents were limited to utilize due to their low removal efficiency of PBDEs. Biochars showed a high affinity and high sorption capacity for HOCs and heavy metals, therefore, it can be a cost-effective and eco-friendly adsorbent [14,15]. Due to different adsorption mechanisms could impact the re-emission and bioavailability of sorbed contaminants after biochar amendments, hence, the mechanisms involved are important for post-remediation risk assessment and management [18]. Many studies have been conducted to research the sorption mechanism of hydrophobic organic compounds on biochar. Some researchers believe that surface adsorption or/and pore-filling is significant for HOCs sorption [18,19,20]. At the same time, other research has indicated that sorption mechanisms vary significantly for biochar obtained at different pyrolytic temperatures. As pyrolysis temperature increases, the sorption mechanisms change from partitioning dominated to adsorption controlled [21]. However, few works have attempted to clarify the contribution of linear and nonlinear sorption to heterogeneous sorption development under specific conditions. Meanwhile, the sorption kinetics of HOCs on biochar, which is beneficial for understanding the adsorption progress, has rarely been reported. The lack of research has made it difficult to analyze sorption mechanisms clearly and accurately as well as execute related risk assessments efficiently.

In this study, corn straw was chosen as the raw material to produce biochar due to its rich output in China, which is more than 0.2 billion tons per year [9]. Because tetra- BDE (BDE-47) is frequently detected in various environmental compartments, it was selected as a model PBDE for exploring the interaction with the obtained biochars. Batch sorption experiments were adopted to study the sorption behaviors of 3 biochars which were prepared at three pyrolysis temperatures (300°C, 500°C, 700°C) for 3 hr on BDE-47. The goal of the research was to (1) through specific surface area (SSA), C/H ratio, O/N ratio and aromaticity, discuss the properties of biochar influenced by pyrolysis temperatures, and the adsorption mechanism of BDE-47 on biochar, and (2) for biochars at different pyrolysis temperatures, combine the study of kinetics and isothermal sorption to illuminate the contribution of linear and nonlinear sorption under different contaminant concentrations. To explore sorption mechanism, the Freundlich isotherm model and Polanyi-Dubinin-Manes model (PDM) were used to fit pore-filling adsorption. Based on this analysis, a dual-mode model based on adsorption (Freundlich model) and partitioning was adopted to quantitatively assess the contribution of adsorption and partitioning on the whole sorption progress. This study will provide useful information for understanding PBDE (BDE-47) sorption mechanisms on biochars and will be valuable in developing a low-cost and excellent biochar material for soil amendment to reduce BDE-47 pollution in the environment.

2. MATERIALS AND METHODS

2.1. Reagents

Standards of 2, 2, 4, 4-tetrabromodiphenyl ether (BDE-47) with a purity > 99.5% were purchased from AccuStandard Co. (USA). The log*Kow* of BDE-47 is 6.39 and the solubility (S_w) is 94.7 μg/L [22]. Methanol was used to prepare a stock standard solution of BDE-47. Methanol and hexane both of HPLC-grade were acquired from J. T. Baker (USA). The whole other chemical reagents ($CaCl_2$, NaN_3) were obtained from Chengdu Best Reagent Co., Ltd, China of analytical grade.

2.2. Preparation of Biochars

In this study, corn straw derived from farmlands of the Daxing district in Beijing was chosen as a biochar material. Once its biomass was obtained, it was air-dried and then crushed into small pieces. The corn straw powder was pyrolyzed in a crucible with a porcelain lid under O_2-limited conditions at 300°C, 500°C, and 700°C for 3hr and named BC300, BC500, BC700, respectively, and then passed through a No. 80 mesh (0.180 mm pore size) and stored in dark brown glass bottles at room temperature.

2.3. Characterization of Biochar

A series of analysis were conducted to evaluate the structure and properties of BC materials, including the specific surface areas (SSA), micropore volume, elemental composition (CHO), infrared spectra and the solid-state ^{13}C NMR spectra (NMR). The Autosorb-iQ-C (Quantachrome, Boynton Beach, FL, USA) was utilized to determine the specific surface areas (SSA) and micropore volume by using Brunauer, Emmett and Teller (BET) methods and Horvath-Kawazoe (HK) methods, respectively. The Hitachi S-3400N scanning electron microscopy was used for taking images of the biochars. Elemental composition (CHO) was determined by dry combustion using an EA 3000 CHNS/O Analyzer (Euro Vector, Italy). A spectrometer of Nicolet 6700 Fourier transform infrared (FT-IR) from Thermo Fisher Scientific Company of USA was used to detect functional groups. With a resolution of 4 cm^{-1}, the spectrum region ranged from 4000 to 400 cm^{-1}, and for each spectrum the whole scans collected were 32. A Bruker Avance III 600 NMR spectrometer from Bruker Biospin Ag of Switzerland was used to analyze the solid ^{13}C NMR operated at 150 MHz. With a double-resonance probe head, the whole tests employed 4-mm sample rotors by the spinning speeds up to 5.0 kHz. Three parameters, O/C ratio, SSA, and (C_δ108–162/ C_δ0–108)(based on ^{13}CNMR spectra), were taken to indicate the surface functionalities, microporosity and aromaticity of the BC materials.

2.4. Kinetics and Adsorption Isotherm Experiments

The kinetics and adsorption isotherm experiments were conducted using a batch equilibration. For fear of evaporation loss, brown glass vials sealed with screw caps were used to perform experiments. The ratio of BC sorbent (BC300, BC500, or BC700) to background solution mixture was 1:40 (w/v) for the kinetics and adsorption isotherm experiments, thus making the quantification of PBDE accurate. The background solution included 200 mg/L NaN_3 to inhibit activities of microorganisms and 0.01 mol/L $CaCl_2$ to sustain a fairly steady ionic strength in ultra-pure water.

According to the former w/v ratios of 1 mg: 40 mL, through adding BDE-47 solution to vials, the investigation of adsorption kinetics was performed with an initial concentration of 50 μg/L of BDE-47. Obvious equilibrium for BDE-47 was achieved within 2 days indicated by preliminary experiments. Thereby, at 180 r/min and 25 ± 1°C in the dark, multiple specimens in the same mixture were shaken for 10 min, 20 min, 30 min, 1 h, 2 h, 4 h, 6 h, 8 h, 12 h, 16 h, 24 h, 36 h or 48 h. Samples were prepared in triplicate at each treatment time, and once the reaction time was reached, the glass vials were left standing for 4h. Then, the supernatants were extracted and detected the BDE-47 through a gas chromatography-mass spectrometry (GC-MS).

In the adsorption isotherm experiment, the preparation of BDE-47 aqueous solutions was through utilizing the background solution to dilute the stock solution in triplicate, and concentrations varied from 5 μg/L to 50 μg/ L. Because the obvious equilibrium for BDE-47 was achieved within 2 days indicated by preliminary kinetics experiments, the samples were shaken at 180 r/min at 25°C in the dark for 2 days. Then, the following steps were followed according to the kinetics experiments.

2.5. Chemical Analysis

The quantitative analysis of BDE-47 was accomplished through a gas chromatography (Agilent 7890, Santa Clara, CA) combined with a mass spectrometry (Agilent 5975, Santa Clara, CA). At a flow rate of 1.0 mL min^{-1}, a DB-5 MS capillary column (J&W Scientific) (30 m × 0.25 mm × 0.1 um) was applied to separate in constant flow mode. Initially, the oven temperature lasted for 1 min at 140°C, later at the rate of 15°C /min the temperature grew to 170°C and sustained for 1 min, then at the rate of 8°C /min the temperature grew to 240°C for 1 min. When operated in electron impact ionization (EI) mode, the MS detector was persisted at 280°C. And the temperature of quadrupole and ionic source were at 150°C and 250°C, respectively. Besides, the energy of electron was 70 eV, and the ultimate quantification was determined by the selective ion mode [12,23].

2.6. Data Analysis

The BDE-47 sorption kinetics was described by the two-compartment first-order kinetic model, and the formula is as follows [Equation (1)]:

$$\frac{q_t}{q_e} = f_1(1-e^{-k_1 t}) + f_2(1-e^{-k_2 t}) \qquad (1)$$

As PBDEs absorbed on the absorbent matrix, q_t (mg/kg) represents the reaction concentration, q_e (mg/kg) is the equilibrium concentration, and $t(h)$ is the reaction time. Moreover, $k_1(h^{-1})$ shows the fast sorption rate constants, and the slow sorption rate constants is expressed by $k_2(h^{-1})$. In [Equation (1)], for f_1 and f_2, on behalf of the parts of the fast and slow compartments, respectively, $f_1 + f_2 = 1$ [24,25].

Freundlich isotherm model is an empirical equation, which assumes heterogeneous sorptive energies on the sorbent. The Freundlich isotherm model [Equation (2)] is as below:

$$q_{f_{oc}} = K_{f_{oc}} C_e^N \qquad (2)$$

In adsorbent matrix C_e (μg L^{-1}) represents the aqueous phase equilibrium concentration and q_{foc} (mg kg^{-1}) is the concentration on the sorbent matrix, the Freundlich affinity coefficient is expressed by K_{foc} [(mg kg^{-1})/(μg L^{-1})^N], and the linearity parameter of isotherm is showed by N, which indicates site energy heterogeneity. When C_e = 0.01 S_w (solubility), 0.05 S_w, 0.1 S_w, the single-point distribution coefficient (K_d) could be figured out from the K_{foc}.

The relationship between K_d and $1/T$ at various temperatures was represented based on the Gibbs equation [Equation (3)]:

$$\ln K_d = \frac{\Delta G}{RT} \tag{3}$$

Current researches have shown that the description models of the organics adsorption to BC materials could be reached on the basis of the Polanyi adsorption theory [26,27]. In the Polanyi equation [Equation (4)], solute adsorption is considered to condense in pores of the sorbent. The condensate is believed to be similar to its unconfined, pure organic liquid [27].

$$q_e = \rho_{sorbate} q_{\max} \exp\left\{-z\left[\frac{RT}{n}\ln\left(\frac{S_w}{C_e}\right)\right]^d\right\} \tag{4}$$

where q_e (μg kg^{-1}) is the adsorbed volume capacity, ρ_{sorbate} (g mL^{-1}) is the density of adsorbate, $q_{\max}$ (10^{-3} mL g^{-1}) is the maximum adsorbed volume capacity, S_W (μg L^{-1}) is the aqueous solubility, C_e (μg L^{-1}) is the aqueous concentration, R is the gas constant [J (mol K)$^{-1}$], and T is the Kelvin temperature (K). Z and d were model parameters. As for weakly polar adsorbates adsorbed on biochar surfaces, the normalizing factor n was effectively equivalent to:

$$n = V_s = \frac{(MW \times 10^{-6})}{\rho_{sorbate}} \tag{5}$$

where V_s(10^{-3} mL mol^{-1}) is the molar volume of adsorbates, and MW(10^{-3} mL mol^{-1}) is the molecular mass of adsorbates [18].

Biochar materials worked as heterogeneous sorbents. They mainly comprise soft carbon and hard carbon, and HOCs sorption on the two parts was considered as partitioning and adsorption, respectively. Thus, the BDE-47 sorption on biochars was believed to be a superposition of partitioning and an adsorption process. The respective contributions of nonlinear adsorption and partitioning to the BDE-47 sorption were calculated using the dual-mode model (DMM) [Equation (6)]. The formula is as follows:

$$q_e = q_{ad} + q_P = K_f C_e^N + K_d C_e \tag{6}$$

where q_{ad} (mg kg^{-1}) and q_p (mg kg^{-1}) are the adsorption and partition fractions, respectively, K_f (mg kg^{-1})/(μg L^{-1})^N represents the adsorption capacity, N and K_d (L g^{-1}) are the isotherm linearity parameter and partitioning coefficient, respectively.

3. RESULTS AND DISCUSSION

3.1. Characterization of Sorbents

For biochar samples (BC300, BC500, and BC700), the elemental ratio (H/C, O/C), SSA, average pore diameter, micropore volume and aromaticity are shown in Table 1. For the resulting biochar, although the raw materials were the same, the increase in pyrolytic temperature greatly impacted their physical properties.

As shown in Table 1, when the temperature increased from 300–700°C, significantly decline was occurred in O/C and H/C, according to the order: 0.27 > 0.15 > 0.13 and 0.71 > 0.50 > 0.21 for BC300, BC500 and BC700, respectively. As a token of aromatization and polarity, the H/C and O/C ratio of BC700 were 3.38 and 2.08 times bigger than that of BC300, which indicated that with an increase in pyrolysis temperature, the carbon alkanes may be cracking. An aromatic structure gradually formed in the biochars, and the process of organic matter condensation and aromatization accelerated, which is consistent with most of the previous studies on carbon materials [28].

The SSA and micropore volume followed the order:

Table 1. Physicochemical Properties of Three Biochar Samples.

Samples	C%	H%	O%	H/C	O/C	SSA (m^2/g)	Pore Volume (10^{-3} cm^3/g)	Pore Size (nm)	Micropore Volume (10^{-3} cm^3/g)	Aromaticity
BC300	62.82	3.69	22.17	0.71	0.27	9.98	18	2.20	6	1.62
BC500	69.76	2.92	13.54	0.50	0.15	10.25	16	2.19	6	1.95
BC700	63.33	1.11	11.64	0.21	0.13	312.62	271	1.67	204	—

BC300 ≤ BC500 < BC700. A large SSA was observed in BC700 (312.62 m^2/g) followed by BC500 (10.29 m^2/g) and BC300 (9.97 m^2/g). The Horvath-Kawazoe (HK) micropore volumes of BC300, BC500 and BC700 were 0.006, 0.006 and 0.204 cm^3/g, respectively. The micropore volume accounted for 33.3%, 37.5% and 75.3% of the total pore volume for BC300, BC500 and BC700, respectively. These results indicated that some mesopores were developed in BC300 and BC500, while for the micropores for BC700, mainly because of the biochar materials, with increasing pyrolysis temperature, the internal porous structures developed and microporous structure increased. Furthermore, the SEM micrographs (Figure 1) show that the pore structure and surface morphology among these biochars were different.

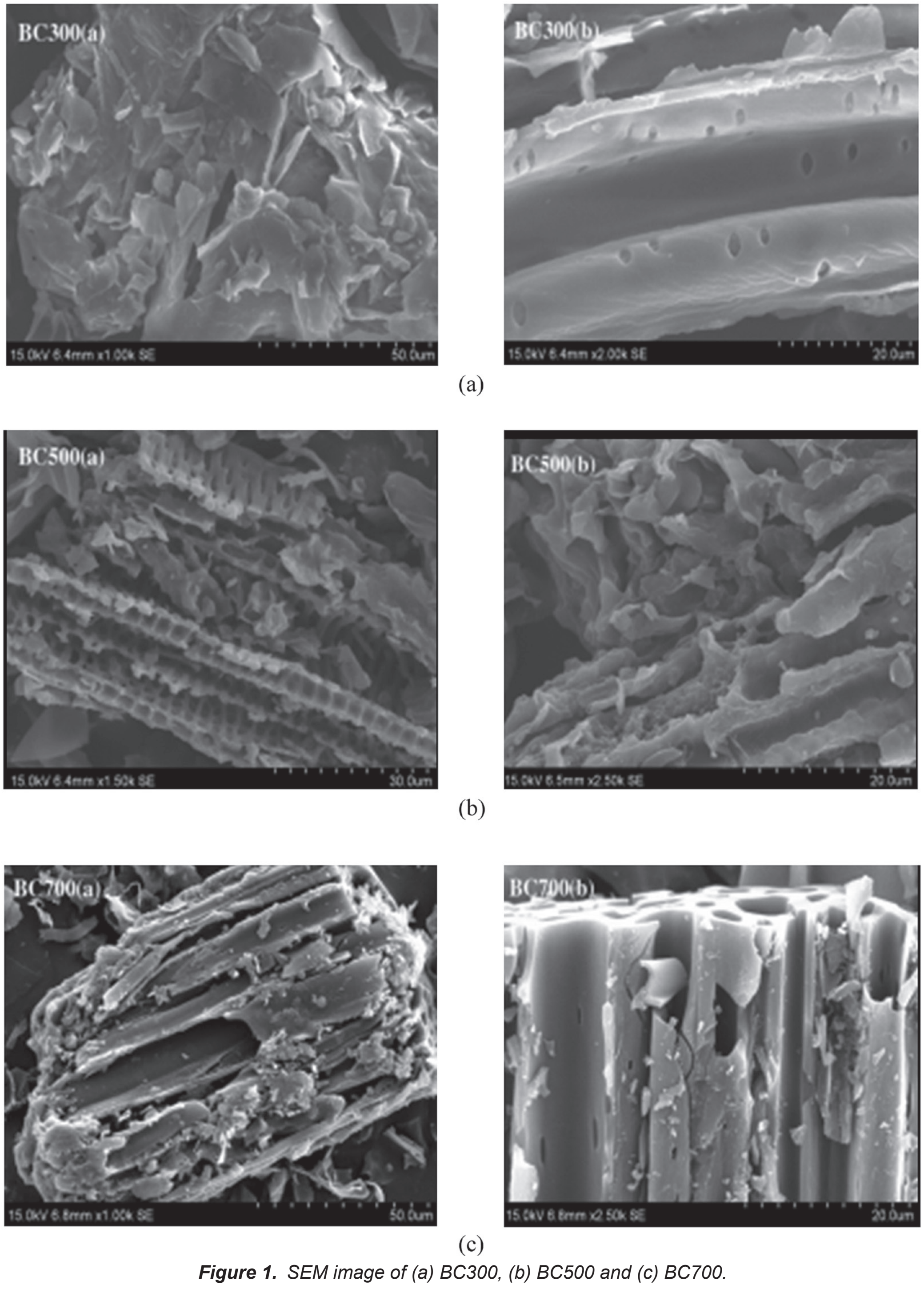

Figure 1. *SEM image of (a) BC300, (b) BC500 and (c) BC700.*

The FT-IR spectra (Figure 2) indicate the presence of various functional groups in the BC. The presence of aromatic C=O (1705 cm^{-1}) stretching with a more powerful absorption band, aromatic C=C stretching (1616 cm^{-1}), and aromatic C–H stretching (750–870 cm^{-1}) were more obvious in BC500 and BC700 as compared to BC300. Almost a homologous infrared spectrum in addition to a dramatical decline of O–H stretching (3200–3600 cm^{-1}) and methyl C–H stretching (2929 cm^{-1}) in the absorption band was shown by BC700 but not by BC500 indicating that higher pyrolysis temperature was favorable for condensation. Several obvious changes occurred in the spectrum after the sorption of BDE-47. Some peaks shifted in the biochars after BDE-47 sorption: BC300 (3574–3563 cm^{-1}), BC500 (3605–3569 cm^{-1}), and BC700 (3602–3571 cm^{-1} and 1504–1535 cm^{-1}). Besides, some new peaks at 1500 cm^{-1} were observed in BC500 and BC700, and this phenomenon could also explain the adsorption mechanism of biochars [29].

In ^{13}C NMR spectra (Figure 3), aliphatic carbon (0–108 ppm) and aromatic carbon (108–162 ppm) were 35.90% and 56.8% for BC300 and 30.87% and 60.27% for BC500. This results showed that for biochar, the main carbon construction is aromatic carbon. The aromaticity increased from BC300 (1.62) to BC500 (1.95), which indicated that when the temperature increased, the carbonization of samples was accelerated, and this conclusion is consistent with the elements analysis and the FT-IR spectra analysis.

3.2. Adsorption Kinetics and the Contribution of Fast Adsorption

According to the two-compartment first-order model of the adsorption kinetics, the fitting results of BDE-47 on the biochar samples are depicted in Figure 4, which was quite suitable for all the adsorption kinetics. For three biochar samples, the fast rate constants (k_1) changed from 4.01 h^{-1} to 6.62 h^{-1} and slow sorption rate constants (k_2) varied from 0.18 h^{-1} to 0.40 h^{-1}. Simultaneously, the fast rate constants (k_1) were 15–35 times greater than the slow rate constants (k_2), indicating that fast sorption played a predominant role during the sorption process.

The fast compartment fraction (f_1) for BC300, BC500 and BC700 were 0.773, 0.728 and 0.526, respectively. Compared with BC300 and BC500, BC700 exerted a lower contribution to the whole amount of sorption. Fast compartment is influenced by the hydrophobicity of the biochars, and it is likely to be controlled by the amorphous organic carbon of biochars [18] while slow adsorption is controlled by condensed organic carbon of biochars. With increasing pyrolysis temperature, the degree of alkanes condensation and the content of the condensed organic carbon increased because BC700 lost its hydrophobicity, therefore, slow adsorption process is more obvious in BC with higher amount of internal pores. Based on Figure 4, the fast compartment dominated the sorption process at the beginning, however, as the contact time increased, the portion of the slow compartment controlled the sorption until the sorption process reached an equilibrium.

Previous studies have demonstrated that for the adsorption of phenanthrene and PBDEs, the fast compartment mainly makes a contribution to the initial linear sorption and slow compartment follows the nonlinear

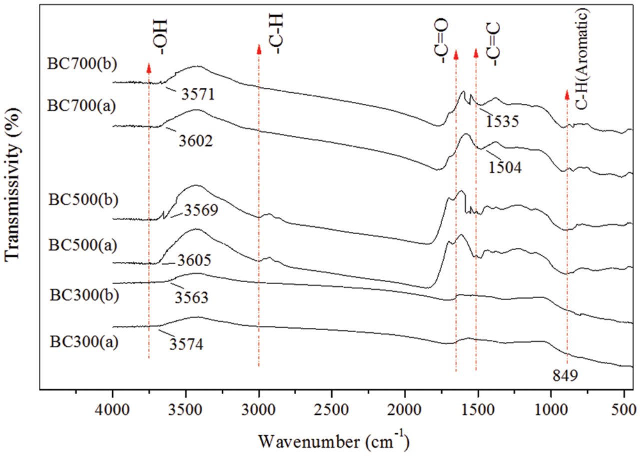

Figure 2. The FT-IR spectra of (a) biochar before BDE-47 sorption and (b) after sorption.

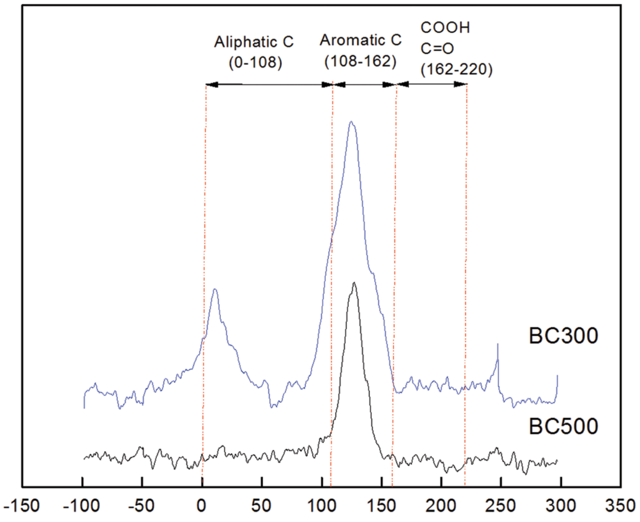

Figure 3. ^{13}C NMR spectra of biochar samples; in ^{13}C NMR spectra, due to their low H content, BC700 could not acquire NMR spectra.

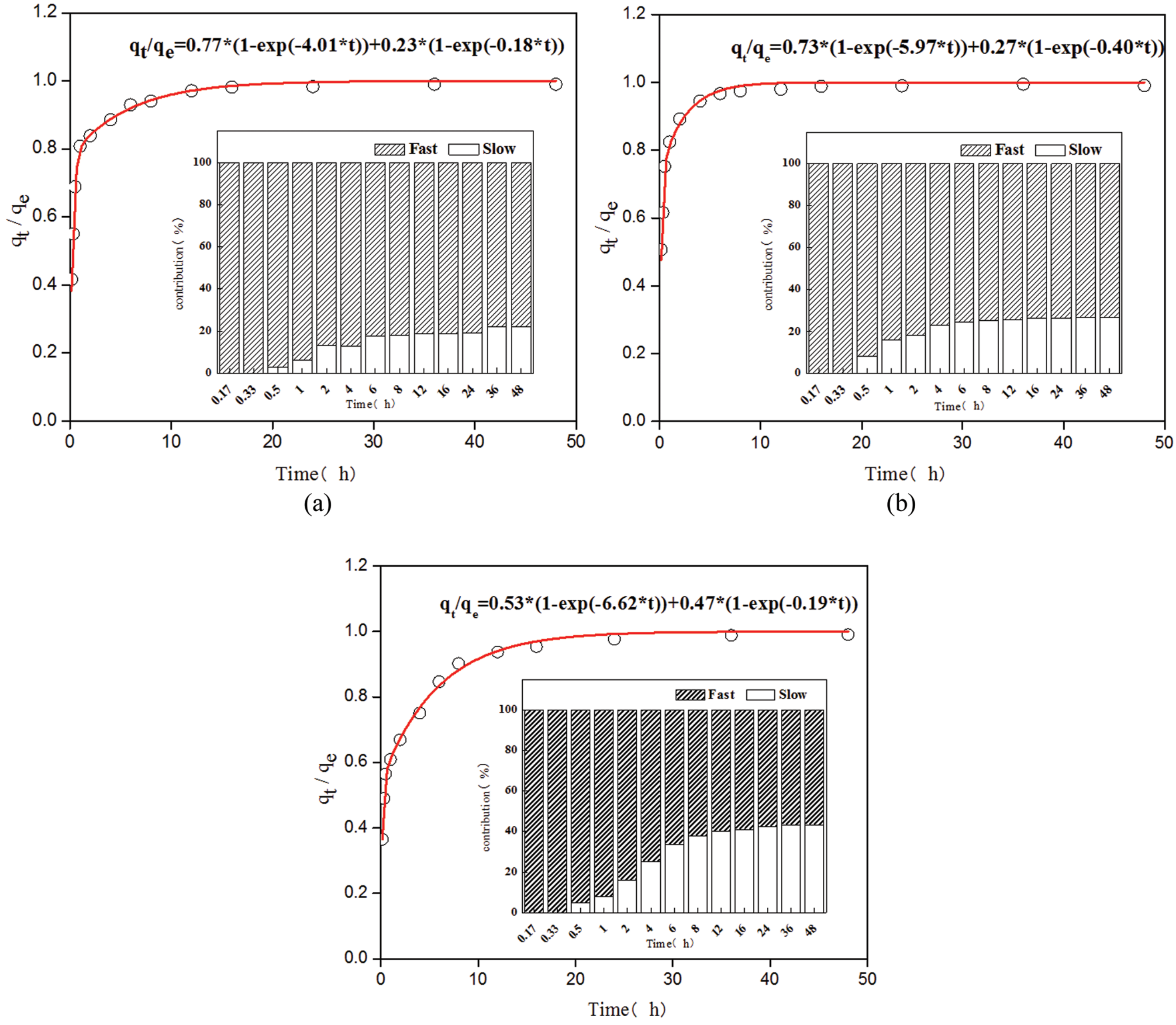

(a) (b) (c)

Figure 4. *Adsorption kinetics of BDE-47 by different biochar samples using a two-compartment first-order model. (a) BC300; (b) BC500; and (c) BC700.*

sorption [30]. In this study, connected to behaviors of the sorption isothermal of BDE-47 in 3.4, the fast sorption compartments contributed mainly to partitioning on biochars. BC300 had the biggest compartment fraction due to its high partitioning contribution to the sorption progress; meanwhile, the fast compartment fraction of BC500 and BC700 decreased, indicating that the main adsorption mechanism had changed.

3.3. Application of Freundlich Isotherm and Polanyi-based Model

As illustrated in Figure 5(a), combined with the data acquired from the adsorption isotherms, the Freundlich model fitted fairly appropriate of the biochar samples. The fitting parameters were presented in Table 2. The OC–normalized sorption capacity K_{foc} ranged from 227.84 to 1558.21 (mg/kg)/(μg/L)^N for all samples, which indicated that under different pyrolysis temperatures, the biochar samples had significant differences on nonlinear adsorption ability. The degree of nonlinearity, N, followed the order: BC300 (0.93) > BC500 (0.62) > BC700 (0.52), which indicated that with increasing pyrolysis temperature, the nonlinearity of adsorption was enhanced. The BDE-47 molecule is a strong π-electron-acceptor because of its high electron

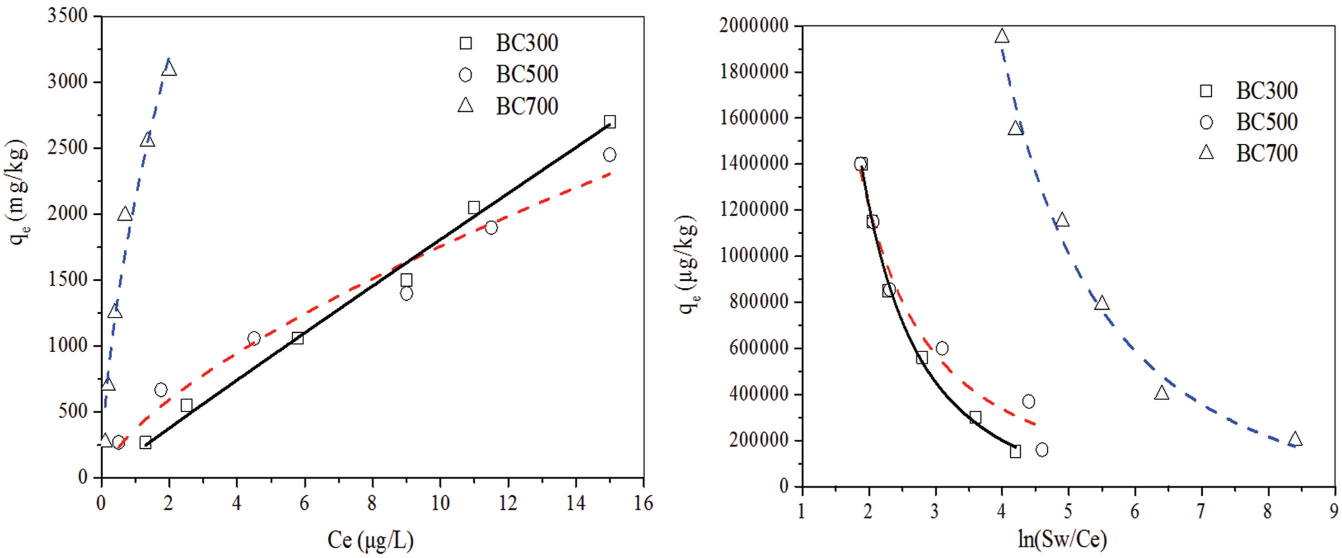

(a) (b)

Figure 5. *Freundlich isotherm (a) and Polanyi model (b) for biochar samples.*

withdrawing ability for Br groups and the ether [18]. With increasing pyrolysis temperature, the carbon content increased and the biochar became a strong π-donor [17]; therefore, π-π interactions between high-temperature biochars and BDE-47 molecule would become stronger, possibly dominating surface adsorption. Because biochar is a porous material, with increasing pyrolytic temperature, more high-energy micropores formed, providing more high–energy, pore-filling adsorption sites.

Moreover, the adsorption ability of biochars was dependent on the concentrations of BDE-47 in the aqueous phase, so three C_e levels ($C_e = 0.01\ S_w$, $C_e = 0.05\ S_w$, $C_e = 0.1\ S_w$) were chosen to calculate the single-point sorption coefficients K_{oc}. As shown in Table 2, at $C_e = 0.01\ S_w$, the K_{oc} values followed the order of BC700 > BC500 > BC300, while at $C_e = 0.1\ S_w$, the order became BC700 > BC300 >BC500, which showed that several adsorption mechanisms participated in the whole adsorption process. As the concentration varied, the involved adsorption mechanism changed.

The ΔG values calculated using the Gibbs equation are presented in Table 3. The ΔG value was between -2.66 kJ mol^{-1} and -9.66 kJ mol^{-1} which demonstrate that sorption of BDE-47 onto the surface of biochars was a spontaneous process, mainly due to physical adsorption. The absolute values followed the order of BC700 > BC500 > BC300, and the results indicate that the sorption process was more favorable in BC700 which has less polar functional groups and more hydrophobic.

In the case of the biochar samples, the Polanyi-Manes isotherm fitting results and parameters were shown in Figure 5(b) and Table 4, respectively. In this study, the Polanyi-based model fitted the result well.

For BC300 and BC500, $q_{\max}$ ($10.65 \times 10^{-3} - 34.7 \times 10^{-3}$ ml/g) exceeded the values of their micropore volume (6×10^{-3} ml/g), which implied adsorption not only in microporous regions but also in macroporous regions and surface regions. For BC700, $q_{\max}$ (42.19×10^{-3} ml/g) was smaller than the value of micropore volume (42.19×10^{-3} ml/g), which indicated that pore-filling adsorption dominated the BC700 sorption process. For BC300 and BC500, comparing adsorption capacity at different concentration ranges with their micropore volume, we found: at low and medium concentration ($C_e/S_w = 0.01$ and $C_e/S_w = 0.05$), the single point adsorption capacity (q') obtained as $q_e/\rho_{sorbate}$,

Table 2. The Fitting Parameters of Freundlich Isotherm for Biochar Samples.

				K_{oc}		
Sample	K_{foc}	**N**	R^2	$C_e/S_w = 0.01$	$C_e/S_w = 0.05$	$C_e/S_w = 0.1$
BC300	227.84	0.93	0.992	228.74	203.7	193.79
BC500	440.16	0.62	0.993	449.36	243.77	187.33
BC700	1558.2	0.52	0.961	1280	591	423

Table 3. Gibbs Free Energy Parameters (ΔG) of BDE-47 on biochars.

ΔG (kJ mol^{-1})	BC300	BC500	BC700
BDE-47	–2.26	–2.31	–9.66

Table 4. FittingParameters of Polanyi Based Model for Biochar Samples.

					q' (10^{-3} mL/g)		
Sample	q_{max} (10^{-3} mL/g)	**Z**	**d**	R^2	$C_e/S_w = 0.01$	$C_e/S_w = 0.05$	$C_e/S_w = 0.1$
BC300	10.65	2146.55	0.89	0.98	0.13	0.97	5.69
BC500	34.7	400.49	0.47	0.96	0.26	1.01	6.3
BC700	42.19	2445	0.80	0.99	1.36	5.88	19.85

was smaller than the micropore volume, while at high concentration ($C_e/S_w = 0.1$), the single point adsorption capacity (q') is close to or greater than the micropore volume. This indicated that the micropores could not provide more adsorption sites. Micropore filling adsorption became weak, and surface adsorption dominated at high concentrations.

3.4. Application of Dual Mode Model (DMM)

With increasing pyrolytic temperature, nonpolar surfaces and internal porous microstructures developed, leading to the change in adsorption mechanism. Thus, to discuss the contribution of partitioning and nonlinear adsorption over the whole concentration range, the combined sorption model [Equation (6)] was chosen to fit the experimental data.

As represented in Figure 6, for three type biochars, when pyrolytic temperature increased, the sorption mechanisms varied distinctly. The fitted model parameters were summarized in Table 5.

For BC300, a high partitioning contribution was observed, and it increased from 65% to 89%, while the adsorption contribution declined from 35% to 11%. This indicated that both partitioning and nonlinear adsorption were involved in the adsorption process, but when the concentration increased, partitioning became stronger. For BC500, the contribution of partitioning and adsorption varied with the change in concentration. At low concentration, nonlinear adsorption was significantly higher than the partitioning process, while when the concentration increased, a high partitioning contribution was observed. For BC700, the partitioning contribution increased from 3% to 28%, and the nonlinear adsorption contribution declined from 97% to 72%. This indicates that partitioning and nonlinear

Table 5. Fitting Parameters of DMM for Biochar Samples.

	Partitioning Fraction			Nonlinear Adsorption Fraction		
Sample	K_d (mg/kg)	C_0 (μg/L)	**Percentage (%)**	K_f (mg/kg)	C_0 (μg/L)	**Percentage (%)**
BC300	86.49	5.00	65	38.04	5.00	35
		10.00	67		10.00	33
		20.00	84		20.00	16
		30.00	90		30.00	16
		40.00	84		40.00	16
		50.00	89		50.00	11
BC500	67.81	5.00	17	217.82	5.00	83
		10.00	23		10.00	77
		20.00	48		20.00	52
		30.00	68		30.00	32
		40.00	65		40.00	35
		50.00	71		50.00	29
BC700	318.47	5.00	3	1032.85	5.00	97
		10.00	13		10.00	88
		20.00	15		20.00	85
		30.00	18		30.00	82
		40.00	28		40.00	72
		50.00	28		50.00	72

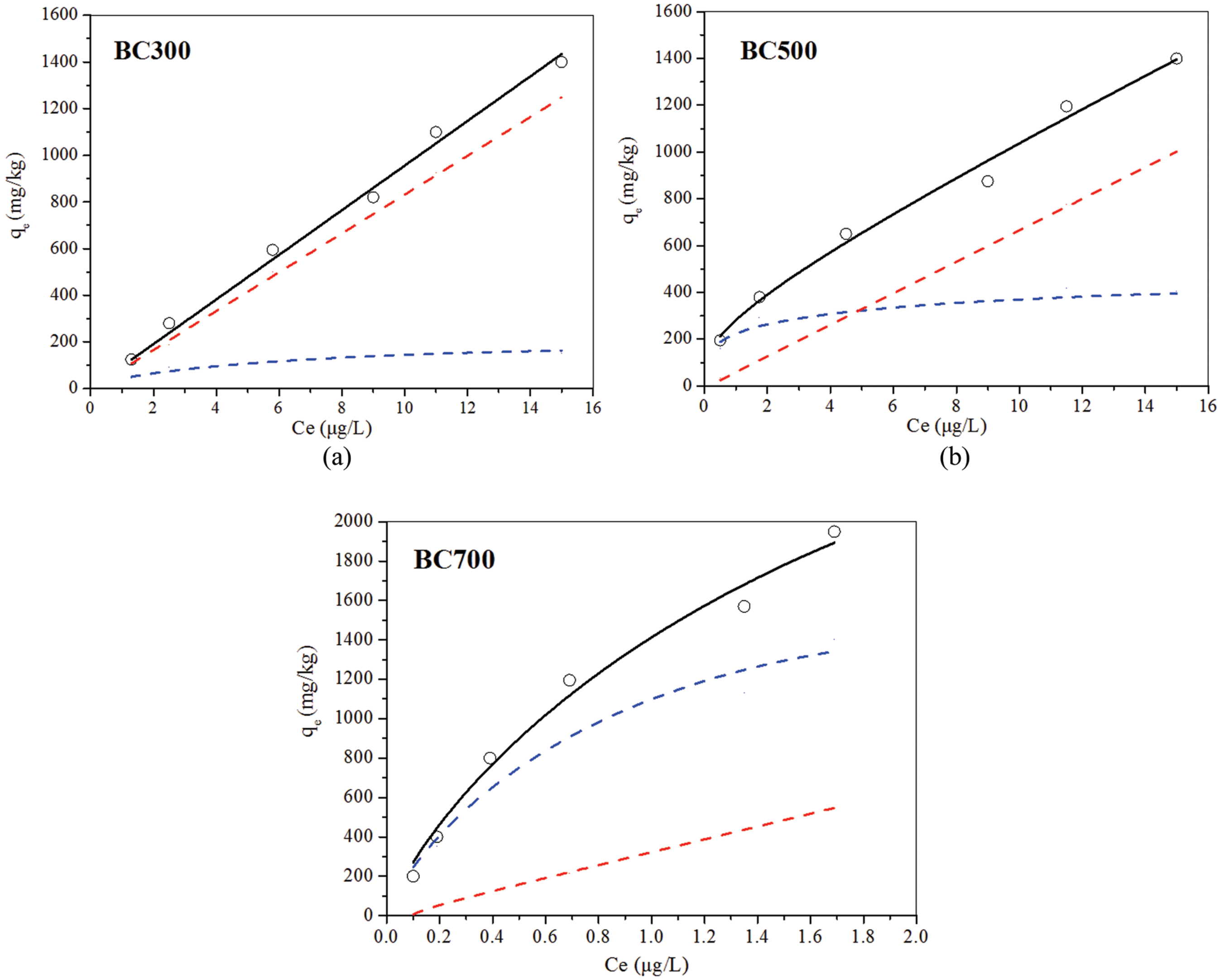

(a) (b)

Figure 6. The fitting results of the dual-mode model for BDE-47. The solid line (—) represent the combined isotherm; the dashed line (– – –) represents the partitioning part; and the dotted line (– – –) represents the adsorption part.

sorption were included in the sorption process, but nonlinear sorption dominated the sorption process.

Combining the fitting results of DMM with the fitting results of the Polanyi-based model in Section 3.3 [Figure 5(b) and Table 4], for BC300 and BC500, both partitioning and micropore filling were involved in the adsorption process at low concentration, but when the concentration increased, partitioning dominated the sorption process. For BC700, partitioning and micropore filling adsorption were involved in the adsorption process, but the micropore-filling made a great contribution to the sorption process.

4. CONCLUSIONS

In this study, the comparison of biochar properties demonstrated thatthe process of organic matter condensation and aromatization accelerates with increases in pyrolytic temperature. The sorption kinetics showed that fast sorption dominated the sorption process, and the fast compartments contributed mainly to the initial linear sorption and the slow sorption compartments followed nonlinear sorption. The sorption isotherm experiment showed the following: (1) for BC300, partitioning dominated the whole sorption process; (2) for BC500, in the lower concentration range, micropore filling was the main adsorption mechanism, but when the concentration increased, partitioning dominated the sorption process; and (3) in the adsorption process for BC700, partitioning and micropore-filling sorption were included, but micropore-filling sorption dominated the sorption process. This research can provide a meaningful information to understanding PBDE (BDE-47) sorption mechanisms on biochars and the information is valuable in developing a biochar as a low-cost adsorbent material in soil remediation to reduce the risk of the BDE-47 migration in the environment.

5. ACKNOWLEDGMENTS

The authors gratefully acknowledge financial support from National Natural Science Foundation of China (51678052) and the Beijing Natural Science Foundation (8132040).

6. REFERENCES

1. Alaee M., Arias P., Sjodin A. and Bergman A., An overview of commercially used brominated flame retardants, their applications, their use patterns in different countries/regions and possible modes of release, *Environment International*, Vol. 29, No. 6, 2003, pp. 683–689.
2. Vonderheide A. P., Mueller K. E., Meija J. and Welsh G. L., Polybrominated diphenyl ethers: Causes for concern and knowledge gaps regarding environmental distribution, fate and toxicity, *Science of the Total Environment*, Vol. 400, No. 1–3, 2008, pp. 425–436.
3. McDonald T. A., A perspective on the potential health risks of PBDEs, *Chemosphere*, Vol. 46, No. 5, 2002, pp. 745–755.
4. Cai Z. W. and Jiang G. B., Determination of polybrominated diphenyl ethers in soil from e-waste recycling site, *Talanta*, Vol. 70, No. 1, 2006, pp. 88–90.
5. Wang H. M., Zhang Y., Liu Q., Wang F. F., Nie J. and Qian Y., Examining the relationship between brominated flame retardants (BFR) exposure and changes of thyroid hormone levels around e-waste dismantling sites. *International Journal of Hygiene Environment Health*, Vol. 213, No. 5, 2010, pp. 369–380.
6. Wang M. S., Chen S. J., Huang K. L., Lai Y. C., Chang-Chien G. P., Tsai J. H., Lin W. Y., Chang K. C. and Lee J. T., Determination of levels of persistent organic pollutants (PCDD/Fs, PBDD/Fs, PBDEs, PCBs, and PBBs) in atmosphere near a municipal solid waste incinerator. *Chemosphere*, Vol. 80, No. 10, 2010, pp. 1220–1226.
7. Qiu X. H., Zhu T. and Hu J. X., Polybrominated diphenyl ethers (PBDEs) and other flame retardants in the atmosphere and water from Taihu Lake, East China. *Chemosphere*, Vol. 80, No. 10, 2010, pp. 1207–1212.
8. Hassanin A., Breivik K., Meijer S. N., Steinnes E., Thomas G. O. and Jones K. C., PBDEs in European background soils: Levels and Factors Controlling Their Distribution. *Environmental Science & Technology*, Vol. 38, No. 3, 2004, pp. 738–745.
9. Zhao X. C., Ouyang W., Hao F. H., Lin C. Y., Wang F. L., Han S. and Geng X. J., Properties comparison of biochars from corn straw with different pretreatment and sorption behaviour of atrazine. *Bioresource Technology*, Vol. 147, 2013, pp. 338–344.
10. Beesley L., Moreno-Jimenez E., Gomez-Eyles J. L., Harris E., Robinson B. and Sizmur T., A review of biochars' potential role in the remediation, revegetation and restoration of contaminated soils. *Environment Pollution*, Vol. 159, No. 12, 2011, pp. 3269–3282.
11. Demiral I. and Ayan E. A., Pyrolysis of grape bagasse: Effect of pyrolysis conditions on the product yields and characterization of the liquid product. *Bioresource Technology*, Vol. 102, No. 4, 2011, pp. 3946–3951.
12. Jia F. and Gan J., Comparing black carbon types in sequestering polybrominated diphenyl ethers (PBDEs) in sediments. *Environment Pollution*, Vol. 184, 2014, pp. 131–137.
13. Zou J. L., Dai Y., Wang X., Ren Z. Y., Tian C. G., Pan K., Li S., Abuobeidand M. and Fu H. G., Structure and adsorption properties of sewage sludge-derived carbon with removal of inorganic impurities and high porosity. *Bioresource Technology*, Vol. 142, 2013, pp. 209–217.
14. Roh H., Yu M-R., Yakkala K., Koduru J. R., Yang J-K. and Chang Y-Y. (2015). Removal studies of Cd(II) and explosive compounds using buffalo weed biochar-alginate beads. *Journal of Industrial and Engineering Chemistry*, Vol. 26, 2015, pp. 226–233.
15. Lingamdinne L. P., Roh H., Choi Y-L., Koduru J. R., Yang J-K. and Chang Y-Y., Influencing factors on sorption of TNT and RDX using rice husk biochar. *Journal of Industrial and Engineering Chemistry*, Vol. 32, 2015, pp. 178–186.
16. Mohan D., Sarswat A., Ok Y. S. and Pittman Jr. C. U., Organic and inorganic contaminants removal from water with biochar, a renewable, low cost and sustainable adsorbent—A critical review. *Bioresource Technology*, Vol. 160, 2014, pp. 191–202.
17. Zheng H., Wang Z. Y., Zhao J., Herbert S. and Xing B. S., Sorption of antibiotic sulfamethoxazole varies with biochars produced at different temperatures. *Environment Pollution*, Vol. 181, 2013, pp. 60–67.
18. Xin J., Liu R. L., Fan H. B., Wang M. L., Li M. and Liu X., Role of sorbent surface functionalities and microporosity in 2, 2′, 4, 4′-tetrabromodiphenyl ether sorption onto biochars. *Journal of Environmental Sciences*, Vol. 25, No. 7, 2013, pp. 1368–1378.
19. Ji L. L., Chen W., Duan L. and Zhu D. Q., Mechanisms for strong adsorption of tetracycline to carbon nanotubes: A comparative study using activated carbon and graphite as adsorbents. *Environmental Science and Technology*, Vol. 43, No. 7, 2009, pp. 2322–2327.
20. Zhu D. Q., Kwon S. and Pignatello J. J., Adsorption of single-ring organic compounds to wood charcoals prepared under different thermochemical conditions. *Environmental Science and Technology*, Vol. 39, 2005, pp. 3990–3998.
21. Chen B., Zhou D. and Zhu L., Transitional adsorption and partition of nonpolar and polar aromatic contaminants by biochars of pine needles with different pyrolytic temperatures. *Environmental Science and Technology*, Vol. 42, 2008, pp. 5137–5143.
22. Wania F. and Dugani C. B., Assessing the long-range transport potential of polybrominated diphenyl ethers: A Comparison of Four Multimedia models. *Environmental Toxicology Chemistry*, Vol. 22, No. 6, 2003, pp. 1252–1261.
23. Xin J., Liu X. and Jiang L., BDE-47 sorption and desorption to soil matrix in single- and binary-solute systems. *Chemosphere*, Vol. 87, 2012, pp. 477–482.
24. Liu W. X., Li W. B., Hu J., Ling X., Xing B. S., Chen J. L. and Tao S., Sorption kinetic characteristics of polybrominated diphenyl ethers on natural soils. *Environmental Pollution*, Vol. 158, No. 9, 2010, pp. 2815–2820.
25. Li J. Z., Fu J., Xiang X., Wu M. M. and Liu X., Kinetics, equilibrium, and mechanisms of sorption and desorption of 17 alpha-ethinyl estradiol estradiol in two natural soils and their organic fractions. *Science of the Total Environment*, Vol. 452, 2013, pp. 404–410.
26. Kleineidam S., Schuth C. and Grathwohl P., Solubility-Normalized Combined Adsorption-Partitioning Sorption Isotherms for Organic Pollutants. *Environmental Science and Technology*, Vol. 36, No. 21, 2002, pp. 4689–4697.
27. Sander M. and Pignatello J. J., Characterization of Charcoal Adsorption Sites for Aromatic Compounds: Insights Drawn from Single-Solute and Bi-Solute Competitive Experiments. *Environmental Science and Technology*, Vol. 39, 2005, pp. 1606–1615.
28. Zhao L., Zheng W. and Cao X. D., Distribution and evolution of organic matter phases during biochar formation and their importance in carbon loss and pore structure. *Chemical Engineering Journal*, Vol. 250, 2014, pp. 240–247.
29. Lingamdinne L. P., Chang Y-Y., Yang J-K., Singh J., Choi E-H., Shiratani M., Koduru J. R. and Attri P., Biogenic reductive preparation of magnetic inverse spinel iron oxide nanoparticles for the adsorption removal of heavy metals. *Chemical Engineering Journal*, Vol. 307, 2017, pp. 74–84.
30. Johnson M. D., Ii T. M. K. and Weber W. J. Jr., A distributed reactivity model for sorption by soils and sediments. 14. Characterization and modeling of phenanthrene desorption rates. Environmental Science and Technology, Vol. 35, 2001, pp. 1688–1695.

Effects of Composted Sewage Sludge on Soil Properties and Vegetable Quality from Abandoned Quarries

WEIFANG MA[1,*], JIAJI SUN[1], GUO HAO[2], XIAOXIU LUN[1] and FARIDULLAH[3]
[1]*College of Environmental Science and Engineering, Beijing Forestry University, Beijing100083, China*
[2]*Beijing Association of Sustainable Development, Beijing100084, China*
[3]*Department of Environmental Sciences, COMSATS Institute of Information Technology, Abbottabad 22060, Pakistan*

ABSTRACT: The effects of composted sewage sludge on soil properties and vegetable quality were investigated in a field experiment for two years. The soil was amended with 3, 15 or 30 t/ha of compost. The results indicated that the vegetable net production increased with the amendment dosage of 3 and 15 t/ha, while the net production decreased in the application amount of 30 t/ha. However, the Vitamin C (Vc) content of the three vegetables was reverse. The heavy metals concentrations in vegetables and soils could meet the national food and soil environmental quality standards of China (II). The accumulation concentrations of Cd, As and Hg in the three vegetables increased with the increasing amendment dosage, while the concentrations of Cr and Pb changed significantly with different types of vegetable. Heavy metal accumulation ability was in the order of celery > lettuce > cabbage, except for Cr. The accumulation of different heavy metals in soil was related to the migration characteristic of heavy metals, plant absorption capacities and the amendment dosage. The concentration of polycyclic aromatic hydrocarbons (PAHs) and polychlorinated biphenyls (PCBs) in the soils increased with addition of 15 t/ha and 30 t/ha, while the change was not statistically significant between the amendment of 3 t/ha and the control. The concentration of PCBs and PAHs in vegetables was positively correlated with compost addition amounts. The dissipation rate of PCBs and PAHs followed the principle of first-order kinetics, and vegetables could improve the dissipation rate. Therefore, the application of compost as soil amendment to abandoned quarries is a feasible strategy for sludge disposal because appropriate amount of compost could enhance the soil fertility, while the long-term application should be considered seriously.

1. INTRODUCTION

THOUSANDS of tons of compost are used to improve the soil nutrient content annually in China. The Urban sewage water treatment plant can produce 13.2 million tons of sludge with 80% moisture content per year in China [1]. This amount may exceed 60 million tons in 2020. This increase has posed problems with sewage sludge utilization and disposal, which is more prominent in big cities. Beijing produced 1.46 million tons of sludge with 80% moisture content per year, the amount will reach 1.83million tons in 2020 [2,3]. Composted sewage sludge used in agriculture got a wide range of applications, and is an economic and effective method [4]. In the European, the amount of application of dry sludge in land was about 4 million tons every year. The sewage sludge production in 2020 will be 13 million tons, and 44% of this total amount is expected to be recycled in land [5]. Abandoned quarries in Beijing are often suffered from severe soil erosion and degradation of soil nutrients, adversely affecting soil physical and chemical properties, reducing income of farmers and increasing risks of erosion and desertification. Sewage composted sludge amendment is a cost effective waste disposal approach and a potential method to improve fertility for plant growth. Sewage sludge contained many valuable components such as organic compound and N, P, K which are essential nutrients for plants [6]. In the meanwhile, the application of compost to soil as amendment can prevent soil and water loss, increase the presence of beneficial soil organisms, reduce the application amount of fertilizers and pesticides, improve biological and physical properties of soil, and reduce organic wastes from landfills [7].

---

*Author to whom correspondence should be addressed.
Address: College of Environmental Science and Engineering,
Beijing Forestry University, Beijing 100083, China. Phone: 2176938427
E-mail: mpeggy@163.com

1544-8053/16/02 S061-11

doi:10.12783/issn.1544-8053/13/4/S9

Although the application of mature compost at reasonable amount improves vegetable growth because sewage sludge contains nutrients such as organic matter, phosphorus and nitrogen [8,9]. On the other hand, it also contains a variety of toxic compounds including heavy metals, polychlorinated biphenyls (PCB), persistent organic pollutants (POPs), polycyclic aromatic hydrocarbons (PAHs), and other microbial pollutants, which would be pose a potential risk to human health in the use of agriculture [10,11].

There are about 50650 hectares abandoned mines in China [12]. Only in Beijing, there are approximately 90000 hectares of degraded limestone quarries and sandy soil, which can potentially use 2 million and 330 thousand tons of sludge with 80% moisture content every year. This method may be a new strategy to improve soil fertility and sludge disposal. Reclamation of limestone quarries soil and sandy soil using compost had been wildly used in barren soil of mountains. The composted sewage sludge is very popular due to its improvement on crop yields. Tiana (2012) reported that the compost increased the growth of cucumber, and the trace elements concentration in vegetables and soil water did not exceeded the national standard that would prevent compost as a soil amendment [13]. Almendro (2013) reported that Ni showed a high migration characteristic to soil and groundwater after sewage sludge being applied [14]. Zhou *et al.* (2010) reported that the compost added into soil increased plant growth, while heavy metals accumulation in watercress demonstrated that the contents of Cd, Ni, Cu, Zn, Pb and Cr in the crop were lower than the standard limitation of Chinese criteria for vegetables [15]. PCBs and PAHs are semi-volatile substances with low solubility in water and can bio-accumulate in food chain because they could absorb strongly onto organic matrices of sediment and soil [11,16]. This toxicity issue of compost-amended mining residues soil is comparatively few and is rarely noticed in the practice. Further, Chinese national control standards for pollutants in sludge from agricultural use on such topic might limit the application of sludge compost in agriculture [17]. Further investigations are requested to improve the information of the amendment of compost in farmland before making a final decision.

In this study, a field experiment was designed to research the influence of compos application on vegetable characteristics, soil properties and concentrations of heavy metals, PCBs and PAHs in vegetables and soils. This would provide a basic knowledge on further application of sewage sludge compost as soil conditioner.

2. MATERIALS AND METHODS

2.1. Material Characteristics

The compost was produced using the aerobic windrow composting process in Panggezhuang sludge composting plant in China. The original sludge gathered from a gravity primary thickener sludge and then a mechanical belt thickener sludge in Gaobeidian municipal wastewater treatment plant (WWTP) which are mainly composed of aerobic grit chamber, primary settling tank, anaerobic tank, anoxic tank, aerobic tank and secondary settling tank. The mixture of 50% sludge (with 80% moisture content), 10% percentage of composted product, and 40% sawdust was used in this study which was generated in 25 d of aerobic compost. The characteristics of the compost are presented in Table 1. The analytical characteristics of the soil from the Mentougou district are presented in Table 2. The soil texture is sandy loam.

2.2. Experimental Procedure

The experiment was conducted in the Mentougou Area of Beijing over two seasons from May to July within two years. According to the fresh weight, the amendment ratios of compost to soil were 0, 3, 15 and 30 t / ha each year from the perspective of soil nutrients supplement. And then the soil was mixed with different

Table 1. Characteristics of the Composted Sewage Sludge.

Moisture (%)	pH	Organic Carbon (g/kg)	TN[a] (g/kg)	TP[b] (g/kg)	TK[c] (g/kg)	PAHs[d] (μg/kg)	Pb (mg/kg)	Cd (mg/kg)	Cr (mg/kg)	As (mg/kg)	Hg (mg/kg)	PCBs[e] (μg/kg)
32 ± 3.2	8.7 ± 0.3	337.4 ± 3.6	36.7 ± 2.2	59.6 ± 3.5	12.6 ± 2.6	442.7 ± 21.4	29.8 ± 2.8	0.9 ± 0.2	43.2 ± 4.3	17.0 ± 2.9	5.6 ± 0.9	35 ± 6.5

[a] Total nitrogen.
[b] Total phosphorus.
[c] Total potassium.
[d] Polycyclic aromatic hydrocarbons.
[e] Polychlorinated biphenyls.

Table 2. Analytical Characteristics of Soils (0~20 cm) Units: mg/kg.

Organic Carbon	TN	AP[a]	AK[b]	PAHs	As	Pb	Cd	Cr	Hg	pH
26.2 ± 3.2	0.65 ± 0.2	226.1 ± 9.7	151.5 ± 6.8	0.112 ± 0.07	3.51 ± 0.9	14.8 ± 2.1	0.35 ± 0.1	51.2 ± 4.1	0.88 ± 0.2	8.3 ± 0.3

[a] Available Phosphorus.
[b] Available Potassium.

dosages of compost with cultivator. Celery (*Ventura*), Cabbage (*Po Gan II*) and Lettuce (*Emperor*) which are widely planted in north China as common vegetables, were selected for experiments. Each treatment was 1 ha with 5 replicates. The vegetables were harvested after 70 days. The artificial planted and control soils were destructively sampled at the end of cultivation. Five replicates of each treatment in twelve treatments were obtained in a randomized manner. 500 g soils were freeze-dried, ground into 0.5 mm pieces, bagged, and then stored at –18°C for use.

All the vegetables were carefully separated from the soil in a completely randomized manner. All samples were rinsed with water to remove attached soil, and purified with deionized water. The vegetables were freeze-dried, cut into 0.5 mm pieces and stored at –18°C.

2.3. Analytical Methods

Soil and compost samples were first digested with $HClO_4$ and *aqua regia* (Chen *et al.*, 2007), and then the concentrations of the five heavy metals (Cd, As, Pb, Cr, and Hg) were measured by ICP with a ICP-MS (X Series, Thermo). The vegetable samples were first dried at 105°C, and then digested with *aqua regia*. Soil and compost samples were analyzed by the method of soil chemical analysis [18]. The pH value was measured in a 1:2.5 (w/v) $CaCl_2$ solution with a WTW-82362 pH meter (WTW, Germany). The analysis of potassium, nitrogen, and phosphorus were performed with the method proposed by Lu [19]. Total organic carbon (TOC) was detected by a solid total organic carbon analyzer (SCSH, TOC-VCPH, Japan).

The samples were extracted and purified by EPA 3546 (2007) and some improvements were made [20,21]. PCBs and PAHs in vegetables and soils were extracted using a series of microwave extraction methods and cleaned with a silica gel cartridge. Quantitative analysis of PAHs in plant and soil extracts was done by GC-MS (Agilent 6890-5973, USA). Contents were analyzed for 16 PAHs in all samples. They were benzo[*ghi*]perylene(Bpe), acenaphthylene (Any), naphthalene (Nap), phenanthrene (Phe), fluorene (Fle), dibenz[*ah*]anthracene (Daa), chrysene (Chr), anthracene (Ant), fluoranthene (Fla), benzo[*k*]pyrene(Bap), benzo[*a*]fluoranthene (Bkf), indeno[*123cd*]pyrene (I1p), benzo[*k*]fluoranthene (Bbf), benz[*a*]anthracene (Baa), acenaphthene (Ane), and pyrene (Pyr).

Samples for PCBs determination were extracted with n-hexane/actone (V/V 1:1) by Soxhlet extraction and purified with sulfuric and a Florisil solid phase extraction column (SPE, 1 g/6 ml) and concentrated by N_2 blowing. The analysis was carried out by using GC-MS (Agilent 6890-5973, USA). Concentrations of 16 PCBs were determined in all samples. They were PCB189, PCB180, PCB169, PCBS167, PCBS156, PCB153, PCB138, PCB126, PCB123, PCB118, PCB114, PCB105, PCB101, PCB77, PCB52, and PCB28.

The results expressed with mean values and their standard deviations for five replicates. The variance among different treatments and correlation coefficient (*r*) were evaluated with the analysis of variance (ANOVA) and Pearson correlation analysis. The statistical analysis was done by Statistical Package for Social Science (SPSS) (version 17.0).

3. RESULTS AND DISCUSSION

3.1. Effect of Compost on the Accumulation of Heavy Metal in Soil

The field experiment was carried out for two seasons, the vegetables were harvested 2 times. The heavy metals in the different vegetable soils for all treatments are shown in Figure 1. Significant differences ($P < 0.10$) of heavy metals content between planted and non-planted control soils were observed in the addition amount of 30 t/ha. The contents of Cd and Cr in different vegetable soil and for different treatment increased significantly with the increasing of the amount of compost, especially suitable for Cd in the soil growth with lettuce, while the results were different for Pb and As. The concentration of Hg was lower than 0.5 mg/kg in all treatment soils with different vegetables because the content of Hg in compost is relatively low which has evaporation characteristic. The heavy metal contents in all five soil samples are lower than the national standard of soil environmental quality in China (GB15618–1995) [22] after two seasons of amendment.

Cd content in soils amended with 30 t/ha compost increased significantly by 46.7%, 52.9% and 41.6% compared to those controlled soil planted with lettuce, cabbage and celery, respectively [Figure 1(a)]. This result was consistent with the cumulative amount of heavy metals in vegetables. The uptake amount of Cd in three vegetable was in the order of celery > lettuce > cabbage [Figure 1(b)]. According to the total balance, the residue of Cd in soil planted with celery was the minimum because the yield and the unit accumulation were the highest for celery. The residual content of Cr in soil increased significantly with composted sludge amendment amount, especially for lettuce and celery soils. Because Cr is a type of heavy metal which is toxic to plants, therefore, the accumulation amount of Cr in lettuce and celery was beyond the detection limit and only the lettuce accumulated a certain amount of Cr. Some studies reported that the performance of bioavailability of Cr in the soil will be low if DTPA-extractable Cr was below 2 mg/kg in the sludge samples [23,24].

The concentration of Pb did not statistically significantly increase with the amount of compost increased [Figure 1(c)] because whose plant absorbability and transfer ability are lower than the other four heavy metals [3]. The accumulation concentration in the soils planted with vegetables was in the order of lettuce > celery > cabbage. The content of Pb in the soil planting lettuce increased from 3% to 12% compared to the control. For Pb, the concentrations were observed to gradually accumulate in the soil without much absorption and migration. The results on Pb did not consistent with the bioavailability or the transfer ability from the results of Fuentes (2006) [25].

The accumulation amounts of As in the soil planted with vegetables were in the order of celery > cabbage > lettuce [Figure 1(d)]. The content of As did not change statistically significantly in the soil planted with celery in all treatments. The concentration of As increased 3.57%, 22.26%, and 25.4% for lettuce soil and 5.50%, 21.10%, and 24.77% for cabbage soil with compost amendment of 3 t/ha, 15 t/ha, 30 t/ha, respectively. The result has indicated that the accumulation of different heavy metals in soil was associated with the characteristics of heavy metal species and plant absorption capacities. The accumulation trend are comparable with previously published values.

Therefore, the long-term of compost would pose a potential risk to both soil and food safety.

3.2. Effect of Compost on Soil pH

The change of pH in different soils was not statistically significant using different amount of composted sludge compared to the unamendment control soil (Figure 2). The control soil with high initial pH value (8.3) was more strongly buffered than that with low pH, while the acidic soil was found the change of pH in soil amendment with sewage sludge [26,27]. The pH of the soil planted with different vegetables also were slightly different, which might be related to plant root exudates.

3.3. PAHs and PCBs Concentration in Soil and Attenuation Effect

Addition of 15 t/ha and 30 t/ha compost led to the increase of the PAHs concentration in soil samples, while PAHs content decreased under the addition of 3 t/ha compost [Figure 3(a)]. The highest PAHs concentration appeared in the soil with the addition of 30 t/ha compost, while the change was not statistically significant among different treatment. The vegetables biomass increased with the application of 3 t/ha composted sludge which led to the high removal efficiency of PAHs. The analysis conducted after 2 seasons of vegetables growth showed the reductions of PAHs concentration by 34.1% in the control soil, and 38.8%, 40.5%, and 41.3% in 3 t/ha, 15 t/ha, and 30 t/ha compost addition, respectively. The PAHs concentration did not have statistically differences in the same treatment for soils planted with different vegetables. This showed that the degradation of PAHs in soils did not have significant correlation with the amount of PAHs accumulated in plants. The large leaf area of lettuce and celery might affect the volatilization of PAHs because gaseous deposition was the the main approach to the accumulation of PAHs in vegetables [28].

In all soil samples, increasing the amount of sludge compost resulted in the increase of PCBs concentration [Figure 3(b)]. The smallest PCBs concentration was noted in the control soil and the highest was noted in soil amended with the highest compost dose. The results demonstrated an increase in PCBs accumulation with increasing amendment of compost, which was similar with PAHs accumulation. Nevertheless, no statistically significant difference was noted in the same treatment soil planted with different vegetables.

Figure 4(a) shows the fitting curve of PAHs dissipation rate constants in control soil and soil planted with vegetables. The average concentration of PAHs

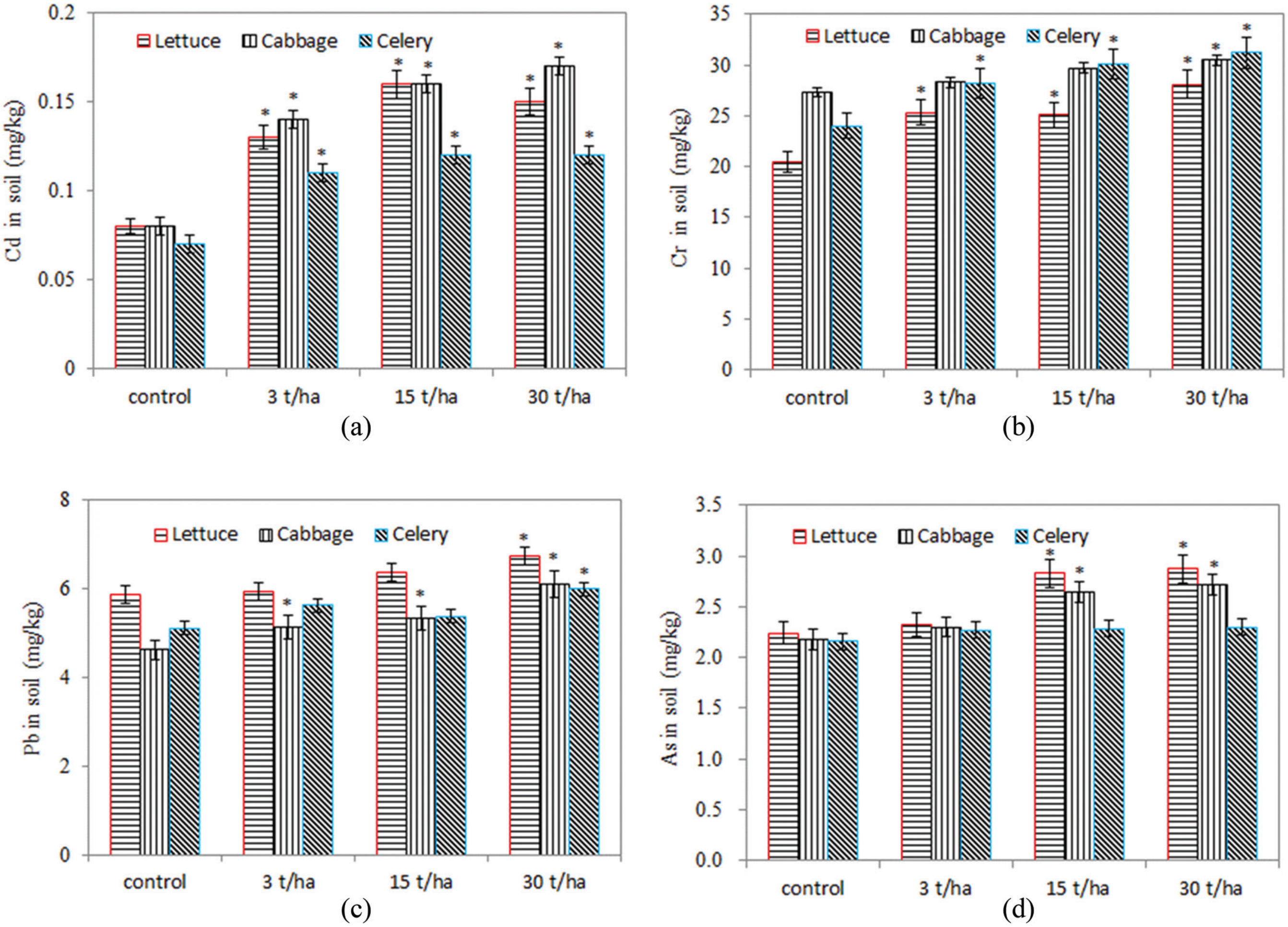

***Figure 1.** Effect of composted on the accumulations of heavy metals in soil. Error bars represent the standard deviation of three samples. *P < 0.10, significant differences between amendment and control.*

at different time is expressed by C_i, and the original concentration in soil is C_0. The PAHs decay rate constants were 0.0052 d^{-1} in control soil and 0.0057 d^{-1} in soil planted with vegetables, respectively, which were calculated by fitting curves according to the content versus time. The results showed that the dissipation of PAHs followed the principle of first-order kinetics. The concentration at different time can be calculated according to the following formulas for different treatment.

$$C_{ic} = C_0 e^{-0.0052ti+4.8441}, \quad C_{iV} = C_0 e^{-0.0057hi+4.767} \qquad (1)$$

t_i = time, d
C_0 = the concentration of PAHs at the beginning $t_0 = 0$
C_{ic} = the concentration of PAHs in control soil at different time t_i
C_{iV} = the concentration of PAHs in soil with composted sludge at different time t_i

The curves were well fitted to both control soil and soil planted with vegetables [Figure 3(a)]. The concentration of PAHs in soil planted with vegetables fell a

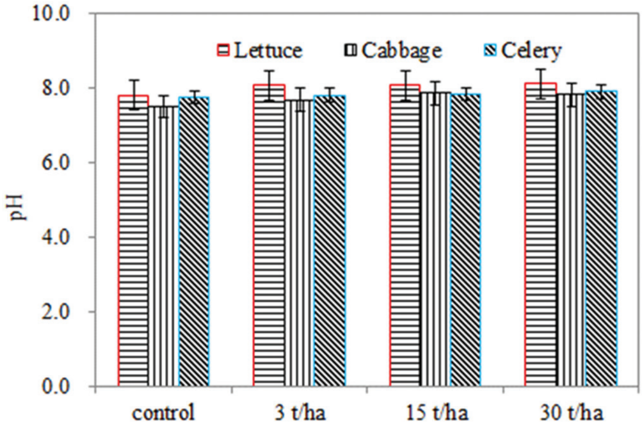

***Figure 2.** Effect of composted on soil pH. Error bars represent the standard deviation of three samples. *P < 0.10, significant differences between amendment and control.*

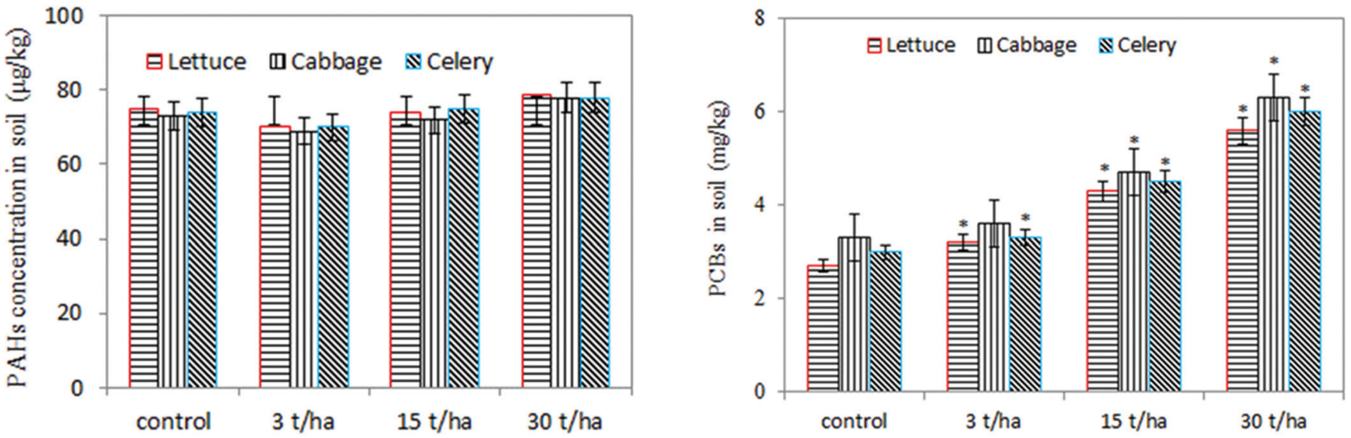

(a) (b)

Figure 3. *PAHs and PCBs concentration in soil. Error bars represent the standard deviation of three samples. *P < 0.10, significant differences between amendment and control.*

little bit faster than the control, in which the degradation came from the combined effect of microorganism and plant.

The PCBs decay rate constants were 0.0002 d^{-1} in control soil and 0.001 d^{-1} in soil planted with vegetables, respectively, which also followed the principle of first-order kinetics [Figure 4(b)]. But the decay rate constant of PCBs was smaller than PAHs because PCBs was harder refractory than PAHs. The half-life of PCBs in soils was more than 6 months, while the half-life of most PAHs was between 2–200 d [29,30]. The concentration of PCBs at different time can be calculated according to the following formulas for different treatment.

$$C_{ic} = C_0 e^{-0.0002ti+1.8395}, \quad C_{iV} = C_0 e^{-0.001hi+1.8442} \tag{2}$$

3.4. Effect of Compost on the Biomass Production of Three Vegetables

The three vegetables net production increased with an amendment dosage of 3 and 15 t/ha of composted sewage sludge, while the net production increasing percentage varied with different types of vegetables. Because proper addition dosage could improve organic matter and mineral nutrients for plants, such as phosphorus, potassium and nitrogen, while avoids introducing too many harmful substances [31]. With the increasing addition of composted sludge, the weight per plant increased obviously in different treatment for cabbage and celery (Figure 5). The weight per plant for lettuce increased under the application of 3 t/ha and 15 t/ha, while it decreased under the addition of 30 t/ha, because excessive heavy metals, PAHs and PCBs might be absorbed by plants with big leaves from soil and accumulated in plant tissues in the soils amendment with 30 t/ha composted sludge. Significant differences ($P < 0.10$) of the weight per strain between control and 15 t/ha amendment were observed, while no statistically significant change between control and 3 t/ha amendment. The maximum biomass of single lettuce increased by 15.1 g (12.6%) compared with control when the compost application amount was 15 t/ha, while the increase was only 8.8 g (8.0%) under the application of 30 t/ha. This indicated that excess compost inhibited the growth of lettuce. The weight increasing rate of unit cabbage and celery became slower with the increase addition amount. Therefore, the optimal dosage of the composted sewage sludge was 15 t/ha from the perspective of production. Through the method of saving compost, the amount of 15 t/ha can provide adequate nutrients for the vegetables by saving compost [32].

3.5. Effect of Compost on the Quality of Three Vegetables

The content of vitamin C (Vc) in vegetables is one of the main index to evaluate the quality of agricultural products [33]. The results showed that the change of Vc content in the three vegetables was not statistically significant with the different application dosage of compost (Figure 6). The content of Vc in lettuce and celery increased with 3 t/ha compost ($P < 0.05$), while the content of Vc in lettuce decreased with 30 t/ha compost. The change of Vc content of cabbage was not statistically significant. The Vc content decreased with the increasing addition of compost, es-

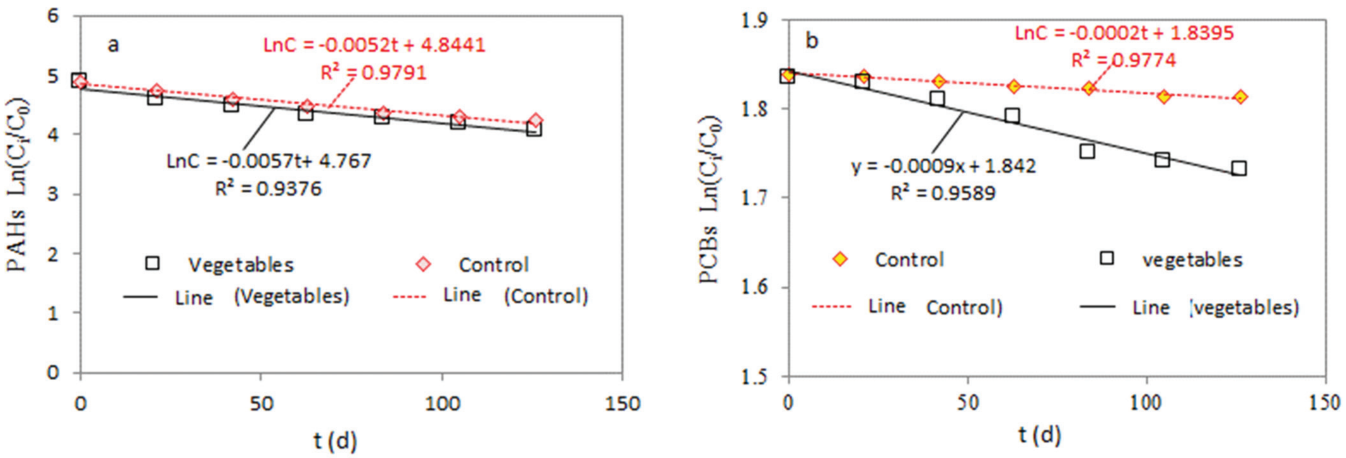

(a) (b)

Figure 4. *Fitting curve of PAHs and PCBs attenuation rate constants.*

pecially for lettuce. When the application rates were 30 t/ha, the Vc content of lettuce was lower than the control. This indicated that cabbage and celery were better resistance than lettuce and they were the high quality kinds of vegetables because in protecting cells against oxidative damage and free radicals Vc plays a key role. The major water-soluble antioxidant in vegetable cells was directly related to the content of Vc, therefore, the Vc content of lettuce was lower than the other vegetables because its high accumulation of PAHs and PCBs. Similar ranges of Vc content were reported in previous research [34]. Some studies have found an increase of the Vc concentration in different plants amended with organic wastes, suggesting that composted waste causes the changes of Vc content that favor the accumulation of antioxidants [35]. Herein, the optimal amendment amount of compost to abandoned quarries in this study was between 3 to 15 t/ha.

3.6. Effect of Compost on the Accumulations of Heavy Metals in Vegetables

Heavy metals accumulations in vegetables have been studied widely [36]. The results showed that the content of heavy metals increased significantly in the three vegetables with the increasing amount of composted sludge (Figure 7). However, the accumulation ability of heavy metals varies for different vegetable species and heavy metals characteristics because the ability of absorption and accumulation of heavy metals in different vegetable varieties was varied widely, even among cultivars and varieties within the same species. The contents of As, Cd and Hg in all the three vegetables increased with an increase dosage of compost, while the contents of Cr and Pb changed statistically

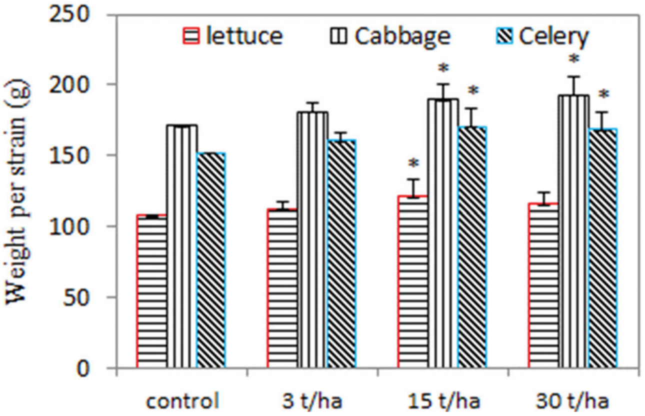

Figure 5. *Effect of compost on the biomass production of three vegetables. Error bars represent the standard deviation of three samples. *P < 0.10, significant differences between amendment and control.*

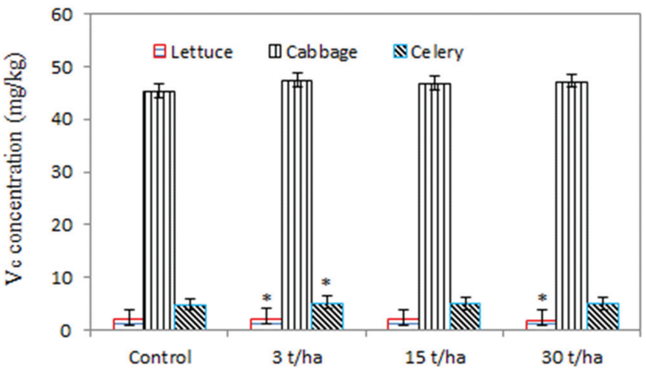

Figure 6. *Effect of compost on the vitamin C content of three vegetables. Error bars represent the standard deviation of three samples. *P < 0.10, significant differences between amendment and control.*

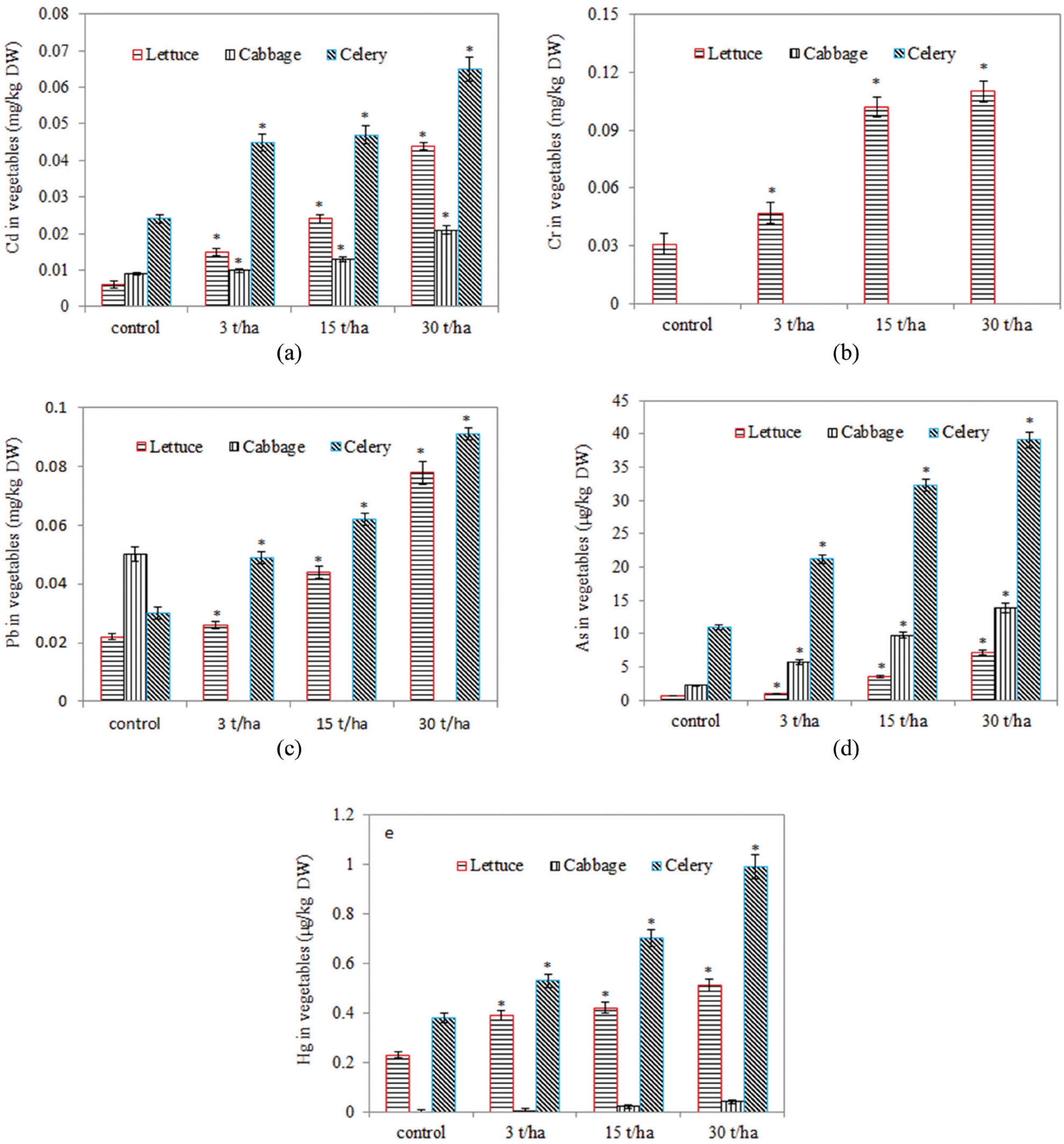

(a) (b) (c) (d) (e)

*Figure 7. Effect of compost on the accumulation of heavy metals in three vegetables. Error bars represent the standard deviation of three samples. *P < 0.10, significant differences between amendment and control.*

significantly with different type of vegetables [Figure 7(b) and 7(c)]. As a whole, heavy metal accumulation ability was in the order of celery > lettuce > cabbage, except for Cr. In China, the maximum allowable concentrations of As, Cd, Hg and Pb in vegetables were 0.7, 0.2, 0.02 and 0.2 mg/kg, respectively [37]. Our mean exposure data of the five heavy metals concentration in vegetables was lower than the maximum allowable values.

Cd is a non-essential trace element for vegetables, which has stronger transfer ability [36]. The content of Cd was not very low in three vegetables [Figure 7(a)] although the concentration in soil and compost were very low because Cd could be easily absorbed by roots and transported to shoots where it is unevenly distributed in plant [38]. The accumulation content of Cd in three vegetables increased with the addition amount of compost because the ability of vegetables with large leaves have high ability to uptake, transport and accumulate heavy metals [39].

Cr is a kind of heavily toxic heavy metal with strong biotoxicity and bioactivity. The accumulation of Cr in lettuce increased with increasing dosage, while the content of Cr in celery and cabbage could not be detected in all treatments [Figure 7(b)]. The result indicated that lettuce had the accumulation capacity for Cr, because the larger leaf area of lettuce had the function of absorption, transportation and vacuolar storage which might keep its high accumulation [40]. Five heavy metals have accumulated in lettuce which showed that lettuce has no selective absorption of heavy metals [41].

For Pb, whose plant absorbability and transfer ability are lower than As and Hg [3], the accumulation concentration was found to be lower than other heavy metals of As and Hg, especially for cabbage [Figure 7(c)]. There was a positive correlation for As between the amendment amount of the compost that accumulated in the plant and the concentration of As in soil [Figure 6(d)]. In general, compared to the non-leafy plants, leafy vegetables accumulated more As in their edible parts which has been observed. The maximum accumulation capacity of As was celery, and then was cabbage which was comparable with previously published values [42]. The accumulation of Hg in the three vegetables were not high due to the high volatility and bio-toxicity, which indicated that the a balance of the role of function of restrain, dilution and absorption [Figure 7(e)].

The results revealed that a certain amount of heavy metals accumulated in leafy vegetables grown in the improved soil with compost might pose potential health risk due to long-term eating.

3.7. Effect of Compost on the Accumulation of PCBs and PAHs in Vegetables

Addition of 15 t/ha and 30 t/ha compost led to an increase of PCBs concentrations in the three vegetables, while the PAHs concentrations in cabbage had not statistically difference between the control and the addition of 3 t/ha (Figure 8). The smallest PCBs concentration was noted in cabbage, while the maximum was lettuce, which was associated with vegetable species. The adsorption or absorption of PCBs into roots of the plant and their subsequent translocation into the other parts of the plant structure, atmospheric deposition were the main mechanisms of plants accumulation of PCBs [43]. The volatilization from soil and atmospheric deposition were the main entry routes for PCBs and PAHs accumulation in plant foliage, which might be due to the fact that lettuce has the largest area of leaves and more vacuole. The accumulation of PCBs was the highest in lettuce which was consistent with previous study [44].

Notably, the target value for PCBs and PAHs was below than 10 μg/kg and 50 μg/kg in the Netherlands. Total PAHs in vegetable samples were below than 50 μg/kg except for lettuce with compost addition of 30 t/ha. Total PAHs in vegetable samples were significantly correlated with compost addition amount. The PAHs concentrations in the three vegetables increased with the increasing addition of compost. The accumulation

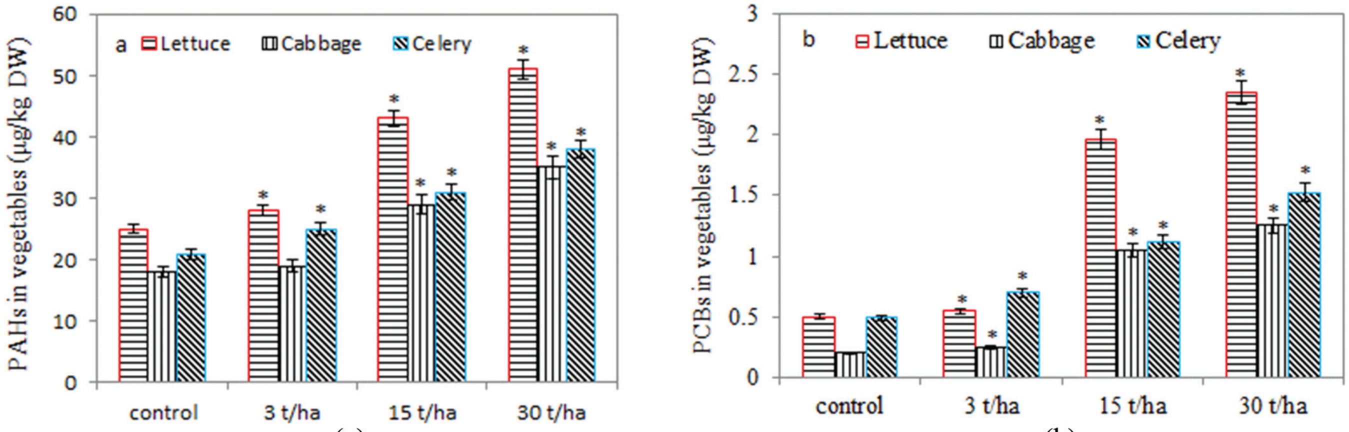

(a) (b)

Figure 8. *Effect of compost on the accumulation of PCBs (a) and PAHs (b) in three vegetables. Error bars represent the standard deviation of three samples. *P < 0.10, significant differences between amendment and control.*

amount of PAHs was in the order of lettuce > celery > cabbage, which might be directly related to leaves surface area and rhizosphere structure. The result showed that PAHs accumulation in vegetables mainly comes from volatilization from soil and dry wet deposition, rather than through root absorption or other ways. Tao *et al.* (2004) reported that the large leaf areas were the direct cause for lettuce to accumulate a large number of PAHs [45]. Therefore, the optimum addition amount of compost to abandoned quarries was 3 t/ha in this case.

Figure 8. Effect of compost on the accumulation of PCBs (a) and PAHs (b) in three vegetables. Error bars represent the standard deviation of three samples. $*P < 0.10$, significant differences between amendment and control.

4. CONCLUSIONS

The application of appropriate amount of composted sewage sludge in abandoned quarries should be between 3 to 15 t/ha from the point view of food safety and soil environment properties because this application amount could improve vegetable production and Vc content. Thus, excessive amendment of sludge compost might be detrimental to soil and plants. The concentrations of heavy metals, PCBs and PAHs in soils and vegetable were positively correlated with amendment amount of composted sludge. The accumulations of different heavy metals in soil and vegetables were related to the characteristic of heavy metals, vegetables absorption capacities and the amendment dosage. The PCBs and PAHs dissipation rate constants were 0.0002 d^{-1} and 0.001 d^{-1}, 0.0052 d^{-1} and 0.0057 d^{-1} in unamend control soil without plant, soil amendment with 30 t/ha compost and planted with vegetables, respectively, which followed the principle of first-order kinetics. Therefore the long-term application of excessive amount composted sludge might be detrimental because it increase heavy metals, PAHs and PCBs concentration due to the low degradation rate. In order to fully use in large scale field conditions, more in-depth studies should be carried out based on continuous large-scale field experiments to avoid the secondary environmental pollution during the process.

5. ACKNOWLEDGEMENTS

The authors gratefully acknowledge financial support from the Beijing Forestry University Young Scientist Fund (BLX2011021) and the National Natural Science Foundation of China (51678052).

6. REFERENCES

1. Wang S.P., Liu X.A., Zheng Q., Yang Z.L., Zhang R.X. and Yin B.H., Characteristic and feasibility study of sewage for landscaping application in XI'AN, China, *Environmental engineering and management journal*, Vol. 12, No. 7, 2013, pp. 1515–1520.
2. Xing Y.J., Ma W.F., Chen G.W., Guo H., and Han D.M., Study on Present Disposal Status and Ecological Use of Sewage Sludge in Beijing, *China Water and Wastewater*. Vol. 28, No. 4, 2012, pp. 31–34.
3. Ma W.F., Liu F., Cheng X., Jing Y., Nie C. and Zhang P.Y., Environmental evaluation of the application of composted sewage sludge to landscaping as soil amendments: a field experiment on the grassland soils in Beijing, *Desalination and Water Treatment*, Vol. 54, No. 4–5, 2015, pp. 1118–1126. http://dx.doi.org/10.1080/19443994.2014.916629
4. Singh R.P. and Agrawal M., Effects of sewage sludge amendment on heavy metal accumulation and consequent responses of Beta vulgaris plants, *Chemosphere*, Vol. 67, No. 11, 2007, pp. 2229–2240. http://dx.doi.org/10.1016/j.chemosphere.2006.12.019
5. European Commission 2008, 2010. Environmental, economic and social impacts of the use of sewage sludge on land. In: Final Report Part I: Overview Report. *Resources, Conservation and Recycling*, Vol. 54, pp. 1109–1116.
6. Song U. and Lee E.J., Environmental and economical assessment of sewage sludge composted application on soil and plants in a landfill. *Resources, Conservation and Recycling*, Vol. 54, No.12, 2010, pp. 1109–1116. http://dx.doi.org/10.1016/j.resconrec.2010.03.005
7. Almendro-Candel M.B., Navarro-Pedre-o J., Jordán M.M., Gómez I. and Meléndez-Pastor I, Use of municipal solid waste composted to reclaim limestone quarries mine spoils as soil amendments: Effects on Cd and Ni. *Journal of Geochemical Exploration*, Vol. 144, 2014, pp. 363–366. http://dx.doi.org/10.1016/j.gexplo.2013.11.002
8. US EPA, 1998. A Citizen's Guide to Phytoremediation. EPA 542-F-98-011. Washington, DC.
9. Andres P., Mateos E., Tarrason D., Cabrera C. and Figuerola B., Effects of digested, composted, and thermally dried sewage sludge on soil microbiota and mesofauna, *Applied Soil Ecology*, Vol. 48, No. 2, 2011, pp. 236–242. http://dx.doi.org/10.1016/j.apsoil.2011.03.001
10. Zhang, Y., Zhu, Y.-G., Houot, S., Qiao, M., Nunan, N. and Garnier, P., Remediation of polycyclic aromatic hydrocarbon (PAH) contaminated soil through composting with fresh organic wastes, *Environmental Science and Pollution Research*, Vol. 18, No. 9, 2011, pp. 1574–1584. http://dx.doi.org/10.1007/s11356-011-0521-5
11. Feng L.J., Zhang L.Q. and Feng L., Dissipation of polycyclic aromatic hydrocarbons in soil amended with sewage sludge composted, *International Biodeterioration & Biodegradation*. Vol. 95, 2014, pp. 200–207. http://dx.doi.org/10.1016/j.ibiod.2014.04.012
12. Wang p., Abandoned mine covers about 45% of the mine development area, *China Land and Resources*. Vol. 23, No. 5, 2015, 21–24.
13. Tiana Y.Q., Chen L.M., Gao L.H., Jr F. C. M., Keener H. M.,Klingman M. and Dick W. A., Composting of waste paint sludge containing melamine resin and the composted's effect on vegetable growth and soil water quality, *Journal of Hazardous Materials*, Vol. 243, 2012, pp. 28–36. http://dx.doi.org/10.1016/j.jhazmat.2012.09.013
14. Almendro-Candel M.B., Navarro-Pedre-o J., Jordán M.M., Gómez I., Meléndez-Pastor I., Use of municipal solid waste composted to reclaim lime stone quarries mine spoils as soil amendments: Effects on Cd and Ni, *Journal of Geochemical Exploration*, Vol. 144, 2014, pp. 363–366. http://dx.doi.org/10.1016/j.gexplo.2013.11.002
15. Zhou S.Q., Lu W.D. and Zhou X., Effects of heavy metals on planting watercress in kailyard soil amended by adding composted of sewage sludge, *Process Safety and Environmental Protection*. Vol. 88, No. 4, 2010, pp. 263–268. http://dx.doi.org/10.1016/j.psep.2010.03.005
16. Melissa L., Åslund W., Zeeb B.A., Rutter A. and Reimer K.J., In situ phytoextraction of polychlorinated biphenyl-(PCB) contaminated soil, *Science of The Total Environment,* Vol. 374, No. 1, 2007, pp. 1–12. http://dx.doi.org/10.1016/j.scitotenv.2006.11.052
17. Control standards for pollutants in sludges from agricultural use, GB 4284-84, China.

18. Lu R., 1999. Soil and Agriculture Chemistry Analysis. *Agriculture Science Technology Press*. Beijing, China.
19. Sempere A., Oliver J. and Ramos C., Simple determination of nitrate in soils by second-derivative spectroscopy, *European Journal of Soil Science*, Vol. 44, No. 4, 1993, pp. 633–639. http://dx.doi.org/10.1111/j.1365-2389.1993.tb02328.x
20. Nabulo G., Black C.R. and Young S.D., Trace metal uptake by tropical vegetables grown on soil amended with urban sewage sludge, *Environmental Pollution*, Vol. 159, No. 2, 2011, pp. 368–376. http://dx.doi.org/10.1016/j.envpol.2010.11.007
21. EPA Method 3546. Microwave extraction.
22. Environmental quality standard for soils, China. GB15618-1995.
23. Wong J.W.C., Li K., Fang M. and Su D.C., Toxicity evaluation of sewage sludges in Hong Kong, *Environment international*, Vol. 27, No. 5, 2001, pp. 373–380. http://dx.doi.org/10.1016/S0160-4120(01)00088-5
24. Unver I., Madenoglu S., Dilsiz A. and Namli A., Influence of rainfall and temperature on DTPA extractable nickel content of serpentine soils in Turkey, *Geoderma*, Vol. 202–203, 2013, pp. 202–211.
25. Fuentes A., Llorens M., Saez J., Aguilar M. I., Marin A. B. P., Ortuno J. F. and Meseguer V.F., Ecotoxicity, phytotoxicity and extractability of heavy metals from different stabilized sewage sludges, *Environmental Pollution*, Vol. 143, No. 2, 2006, pp. 355–360. http://dx.doi.org/10.1016/j.envpol.2005.11.035
26. Latare A.M., Kumar O., Singh S.K. and Gupta A., Direct and residual effect of sewage sludge on yield, heavy metalscontent and soil fertility under rice–wheat system, *Ecological Engineering*, Vol. 69, 2014, pp. 17–24. http://dx.doi.org/10.1016/j.ecoleng.2014.03.066
27. Mylavarapu R.S. and Zinati G.M., Improvement of soil properties using composted for optimum parsley production in sandy soils, *Scientia Horticulturae*, Vol. 120, No. 3, 2009, pp. 426–430. http://dx.doi.org/10.1016/j.scienta.2008.11.038
28. Meudec A., Dussauze J.,Deslandes E. and Poupart N., Evidencen for bioaccumulation of PAHs within internal shoot tissues by a halophytic plant artificially exposed to petroleum polluted sediments. *Chemosphere*, Vol. 65, No. 3, 2006, pp. 474–481. http://dx.doi.org/10.1016/j.chemosphere.2006.01.058
29. Song S.J., Song M.Y., Zeng L.Z., Wang T.H, Liu R.Z., and Jiang G.B., Occurrence and profiles of bisphenol analogues in municipal sewage sludge in China, *Environmental. Pollution*, Vol. 186, 2014, pp. 14–19. http://dx.doi.org/10.1016/j.envpol.2013.11.023
30. Wyrwicka A., Steffani S. and Urbaniak M., The effect of PCBs-contaminated sewage sludge and sediment on metabolism of cucumber plants (*Cucumis sativus* L.), *Ecohydrology & Hydrobiology*, Vol. 14, No. 1, 2014, pp.75–82. http://dx.doi.org/10.1016/j.ecohyd.2014.01.003
31. Chen L., Tubail K., Kost D. and Dick W.A., Effects of gypsum enhanced composteds on yields and mineral compositions of broccoli and tall fescue, *Journal of Plant Nutrition*, Vol. 33, 2010, pp. 1040–1055. http://dx.doi.org/10.1080/01904161003728701
32. Rato Nunes J., Cabral F. and Lopez-Pineiro A., Short-term effects on soil properties and wheat production from secondary paper sludge application on two Mediterranean agricultural soils, *Environmental Pollution*, Vol. 99. No. 11, 2008, 4935–4942. http://dx.doi.org/10.1016/j.biortech.2007.09.016
33. He P. P., Lu X. Z. and Wang G.Y., Effects of Se and Zn supplementation on the antagonism against Pb and Cd in vegetables, *Environment International*, Vol. 30, No. 2, 2004, pp. 167–172. http://dx.doi.org/10.1016/S0160-4120(03)00167-3
34. Pascual I., Azcona, I. A., Aguirreolea J., Morales F., Corpas F.J., Palma J.M., Rellan-Alvarez R. and Sanchez-Diaz M., Growth, Yield, and Fruit Quality of Pepper Plants Amended with Two Sanitized Sewage Sludges, *Journal of Agricultural Food Chemistry*, Vol. 58, No. 11, 2010, pp. 6951–6959. http://dx.doi.org/10.1021/jf100282f
35. Wunderlich, S. M.; Feldman, C.; Kane, S. and Hazhin, T., Nutritional quality of organic, conventional, and seasonally grown broccoli using vitamin C as a marker, *International Journal Food Science Nutrition*, Vol. 59, No. 1, 2008, pp. 34–45. http://dx.doi.org/10.1080/09637480701453637
36. Chang C. Y., Yu H. Y., Chen J. J., Li F. B., Zhang H. H. and Liu C. P., Accumulation of heavy metals in leaf vegetables from agricultural soils and associated potential health risks in the Pearl River Delta, South China, *Environmental Monitoring and Assessment*, Vol. 186, No. 3, 2014, pp. 1547–1560. http://dx.doi.org/10.1007/s10661-013-3472-0
37. China National Food Safety Standard of Contaminants in Foods Limited, GB 2762-2012, 2012.
38. Mamun S.A., Chanson G., Benyas M.E., Aktar M., Lehto N., McDowell R., Cavanagh J., Liv Kellermann L., Clucas L. and Robinson B., Municipal composts reduce the transfer of Cd from soil to vegetables, *Environmental Pollution*, Vol. 213, 2016, pp. 8–15. http://dx.doi.org/10.1016/j.envpol.2016.01.072
39. Zou H., Yang W.T., Zhou X., Liu L., Gu J.F., Wang W.L., Zou J.L., Tian T., Peng P.Q. and Bo-Han Liao B.H., Accumulation of Heavy Metals in Vegetable Species Planted in Contaminated Soils and the Health Risk Assessment, *International Journal of Environmental Research and Public Health*, Vol. 13, No. 289, 2016, doi:10.3390/ijerph13030289. http://dx.doi.org/10.3390/ijerph13030289
40. Zhu H., Pan X.D., Wu P.G., Han J.L. and Chen Q., Heavy metals in vegetables and the health risk to population in Zhejiang, China, *Food Control*, Vol. 36, No. 1, 2014, pp. 248–252. http://dx.doi.org/10.1016/j.foodcont.2013.08.036
41. Li H. T. and Zhao K., Effect of Sludge Composted on Lettuce and Heavy Metal Morphology, *Agricultural Science & Technology and Equipment*, Vol. 24, No. 6, 2011, pp. 9–11. In Chinese.
42. Ramirez-Andreotta M. D., Brusseau M. L., Artiola J. F. and Maier R. M., A greenhouse and field-based study to determine the accumulation of arsenic incommon homegrown vegetables grown in mining-affected soils, *Science of the Total Environment,* Vol. 443, 2013, pp. 299–306. http://dx.doi.org/10.1016/j.scitotenv.2012.10.095
43. Zeng L., Li N., Shao D., Kang Y., Zhang Q., Lu P., Li L., Luo J. and Guo X., Concentrations, sources, and risk assessment of polychlorinated biphenyls in vegetables near a waste-incinerator site, South China, *Archives of Environmental Contamination and Toxicology*, Vol. 67, No. 1, 2014, pp. 78–86. http://dx.doi.org/10.1007/s00244-014-0045-3
44. Lovett A. A., Foxall C. D., Creaser C. S. and Chewe D., PCB and PCDD/DF congeners in locally grown fruit vegetable samples in Wales and England, *Chemosphere*, Vol. 34, No. S-1, 1997, pp. 1421–1436. http://dx.doi.org/10.1016/S0045-6535(97)00439-6
45. Tao S., Cui Y.H., Xu F.L., Li B.G., Cao J., Liu W.X., Schmitt G. and Wang X.J., Polycyclic aromatic hydrocarbons (PAHs) in agricultural soil and vegetables from Tianjin, *The Science of the Total Environment,* Vol. 320, No. 1, 2004, pp. 11–24. http://dx.doi.org/10.1016/S0048-9697(03)00453-4

Study on Release Mechanism and Control Technology of Hydrogen Sulfide Gas in Coal Mine

YULIANG WU[1,2,3], JIANJUN LIU[1,3,*] and KAIXIANG FAN[1,4]
[1]State Key Laboratory of Oil and Gas Reservoir Geology and Exploitation, Southwest Petroleum University, Chengdu 610500, China
[2]Technology Center, Sichuan Coal Industry Group Limited Liability Company, Chengdu 610091, China
[3]School of Geoscience and Technology, Southwest Petroleum University, Chengdu 610500, China
[4]School of Civil Engineering and Technology, Southwest Petroleum University, Chengdu 610500, China

ABSTRACT: In the process of high sulfur coal mining, with coal gas outburst, a large amount of highly toxic flammable hydrogen sulfide (H_2S) gas is produced which threats miner's health and pollutes the environment seriously. It is shown that adding an oxidizing agent in alkaline absorption liquid can obviously increase the removal rate of H_2S in mine air in the experiment results, and there's no the hydrogen sulfide gas evolution after oscillation of the absorbing tail liquid, the removal efficiency is very remarkable. It is also shown that surfactant can reduce the surface tension of the absorption liquid in the research, accelerate the process of mass transfer between gas-liquid two phases, and improve the absorption efficiency.

1. INTRODUCTION

In the process of high sulfur coal mining, with coal gas outburst, a large amount of highly toxic flammable hydrogen sulfide (H_2S) gas is produced. H_2S is an irritant and corrosive gas. According to statistics, the incidence of H_2S poisoning ranks No. 4, and the death toll ranks No. 2 in China. Meanwhile, H_2S corrosion of metallic materials will endanger the safety of the device [1,2].

In the year of 2015, Y. Chen studied the pollution characteristics of coal mining in the Kaili region. At the same year, Mengmeng Wu studied the microwave effects on the structure of CeO_2-doped zinc oxide sorbents for H_2S removal, in the year of 2013, Yajuan Wei studied the effect of H_2S concentration in gasified gas on the microstructure, and Lixia Ling studied Theoretical prediction of simultaneous removal efficiency of ZnO for H_2S and Hg^0 in coal gas. The removal methods of H_2S include physical method, chemical method, biological method and other methods. The physical methods include physical solvent process, activated carbon method, molecular sieve method, membrane separation, microwave method and irradiation decomposition method. The chemical methods include Claus sulfur recovery process, liquid phase catalytic oxidation, Iron, manganese, zinc compound desulfurization method and chemical absorption method. Although there are many methods to removal the H_2S, but because of the limited condition of coal mine, currently, the main prevention measures at home and abroad is to increase the amount of wind and spray alkaline solution. These two methods are generally used for low concentrations of H_2S governance; few literatures reported the treatment of H_2S outburst [3–5].There some other experiments of pollutant disposal in coal mine [6].

2. METHOD

Schematic diagram and photos of the experimental apparatus are shown in Figure 1 and Figure 2.

Controlling the concentration of hydrogen sulfide gas in the reactor: the test was carried out in a fume hood, the hydrogen sulfide gas is adjusted by the pressure reducing valve ① and the flow meter ② and flows into organic glass reactor, and then flows into water. The concentration of hydrogen sulfide is controlled by the flow rate and time. The initial concentration of hydrogen is 1000 ppm in the reactor, but the volume of the reactor is relatively small, the hydrogen sulfide gas is of high-purity, it is difficult to control the concentration of hydrogen sulfide in the container, which often exceeds the standard of 1000 ppm. So the method is taken that the high concentration of hydrogen sulfide is

---

*Author to whom correspondence should be addressed.
Email: liujj0906@sina.com

1544-8053/16/02 S073-11

doi:10.12783/issn.1544-8053/13/4/S10

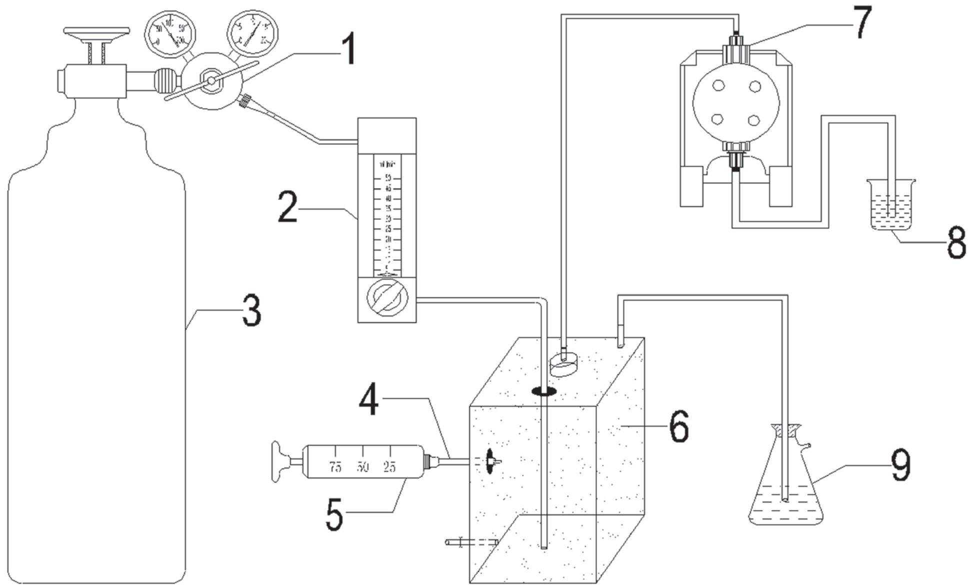

Figure 1. Schematic diagram of the experimental apparatus. (1. Relief valve, 2. Flow meter, 3. Hydrogen sulfide gas cylinders, 4. H_2S detector tube, 5. Gas sampler, 6. Reactor, 7. Dosing pump, 8. Absorption liquid, 9. Absorption bottle of tail gas).

injected in the reactor in the test, ensuring the error is plus or minus ≤ 10%.

Chemicals absorption test: a certain volume and concentration of the absorbing liquid is pressed by the dosing pump ⑦ through the fine atomizing nozzle to form mist into the reactor ⑥, and react with hydrogen sulfide gas completely. The residual concentrations of hydrogen sulfide is detected immediately after the dosing, then the absorbing liquid in the reactor is vibrated at speed of 100 times/min for 1min, and the concentration of hydrogen sulfide in the reactor is detected again after the end of the vibration.

Since the concentration of hydrogen sulfide in the reactor is high and unstable, it can cause the hydrogen sulfide poisoning of detector for easily over-range, so the gas samplers ⑤ and hydrogen sulfide detection tube are used currently in the concentration detection of hydrogen sulfide, as is shown in Figure 3. (The gas sampling tubes is made by the manufacturer named Draeger).

Detection methods: after cutting off both sides of the test tube, one side is inserted in the air inlet of the sampler, the other side is inserted inside the reactor, then the handle ⑤ of the sampler is pulled slowly to the second gear (100 mL), the time of air inletting is 2 min, when the color change of the indicator terminates in the detector tube, the data can be read from the scale on the brown pillar.

Figure 2. Photos of the experimental apparatus.

Figure 3. *Manual gas sampling and test tube.*

Table 1. Experimental Reagents.

Formula	Purity	Use
H_2S	99.99%	reaction gas
$FeCl_3$	AR	Catalytic oxidizer
NaClO	AR	Catalytic oxidizer
H_2O_2	30%, GR	Catalytic oxidizer
Fe_2SO_4	AR	Catalytic oxidizer
NaOH	AR	modifier
$NaHCO_3$	AR	absorbent
$NH_3 \cdot H_2O$	GR	ph regulator
NH_4Cl	AR	ph regulator
$C_{10}H_{14}N_2O_8Na_2 \cdot 2H_2O$	AR	complexant
$C_{18}H_{29}NaO_3S$	AR	activator
$C_6H_{18}N_4$	AR	absorbent
$C_6H_{15}NO_3$	AR	absorbent
$HO(CH_2)_2NH(CH_2)_2OH$	AR	absorbent
$H_2NCH_2CH_2OH$	AR	absorbent
$C_6H_{15}NO_2$	AR	absorbent

The initial removal rate, removal rate after oscillation and removal efficiency are used to evaluate H_2S removal effect. The initial removal rate ψ of H_2S can be written as:

$$\psi = \frac{\theta_0 - \theta_1}{\theta_0} \tag{1}$$

Where, θ_0 is the initial concentration of hydrogen sulfide gas in reactor, ppm θ_1 is the concentration of hydrogen sulfide gas after the end of dosing, ppm. The larger ψ value indicates that the effect of pesticides on the absorption of hydrogen sulfide gas is better.

Removal rate after oscillation η is

$$\eta = \frac{\theta_0 - \theta_s}{\theta_0} \tag{2}$$

Where, θ_s is the concentration of hydrogen sulfide gas after oscillation, ppm.

Removal efficiency of hydrogen sulfide gas can be calculated by the following formula:

$$\omega = \frac{\left[\dfrac{\theta_0 - \theta_t}{\theta_0}\right]}{t} \tag{3}$$

Where, θ_t is the remaining concentration of hydrogen sulfide in reactor after Dosing time t.

The main experimental reagents are listed in Table 1.

Taking into account the coal mine particular work environment, it is not convenience to use large machinery and equipment, and therefore a physical method to be used to remove hydrogen sulfide is restricted. Since hydrogen sulfide is an acid gas, having a higher solubility in alkaline solution, so the alkali is used as an absorption agent of hydrogen sulfide gas. Because corrosion of the equipment by amine is serious, so this article uses sodium carbonate solution and the amine solution as the preferred absorption alkali. With sodium carbonate solution, for example, hydrogen sulfide absorption reaction is as follows [7]:

$$Na_2CO_3 + H_2S \rightarrow NaHS + NaHCO_3 \tag{4}$$

HS^- is unstable and under the influence of the external environment it will be converted into hydrogen sulfide again and release into the air, especially in the case of mine water inrush, the absorption liquid is infinitely diluted by water which lead to chemical reaction, Equation (4), moving to the reverse reaction. Therefore, single-use alkali cannot achieve the effect of rapid treatment, an agent must be added to oxidize HS^- to elemental sulfur or sulfur-containing compounds with higher valence before it flows into the mine water. Its mechanism of action could be interpreted as two functions, the one is promotion, that is to promote the reaction of absorption of hydrogen sulfide in alkali to the positive direction, increasing the absorption efficiency; the other is oxidation, that is HS^- oxidation, to prevent the release of hydrogen sulfide from the absorption tail liquid in the effect of water dilution and disturbing, and the hydrogen sulfide in the air can be completely removed.

In addition, the polarization of the hydrogen sulfide was 3.64 × 10^{-30} m^3, the greater the polarizability is, the greater the molecular deformation is, under the same conditions, the greater the deformation of the molecules are adsorbed more easily. Based on the density and pore structure of coal analysis, it is shown that coal has the nature of gas adsorption and molecular sieves. Thus, the hydrogen sulfide is mainly under the state of adsorption in coal, which falling behind the process of production, loading and transportation, and releasing with the coal crushing and flipping repeatedly, the hydrogen sulfide will stop soon when the coal becomes loose at rest.

After years of development of Amine Method on desulfurization in industrial areas, the adopted solvents are: monoethanolamine (MEA), diethanolamine (DEA) and so on. Taking diethanolamine absorbing hydrogen sulfide as an example, the absorption reaction can be represented as follows:

$$R_2R'\mathrm{N} + \mathrm{H_2S} \leftrightarrow R_2R'\mathrm{NH}^+ + \mathrm{HS}^- \qquad (5)$$

As it can be seen from the reaction formula, the principle of alcohol amine solution of hydrogen sulfide absorption is similar to sodium carbonate, which is the use of alkali to convert it to hydrogen sulfide absorption HS^-. The commonly used monoethanolamine, diethanolamine, triethanolamine are selected as absorbent in test, and the effect of absorption of hydrogen sulfide is compared, the best absorption effect of alcohol amine solution is selected, and the character is changed by adding the activator and oxidant [8–14].

3. RESULTS

3.1. Hydrogen Sulfide Gas Absorption Effect of Sodium Carbonate Solution

Sodium hydrogen sulfide has a certain absorption effect; the solution will generate HS^- and HCO_3^- after absorption of hydrogen sulfide. Although the sodium carbonate solution can preferably absorb hydrogen sulfide, the carbon dioxide in coal generally has a higher absorption than hydrogen sulfide in the absorption liquid, the reaction is as follows:

$$\mathrm{Na_2CO_3 + H_2O + CO_2 \leftrightarrow 2NaHCO_3} \qquad (6)$$

Sodium bicarbonate can absorb hydrogen sulfide, the reaction is as follows:

$$\mathrm{NaHCO_3 + H_2S \leftrightarrow NaHS + H_2O + CO_2} \qquad (7)$$

By formulating different concentrations of sodium carbonate and sodium bicarbonate solution in 50 mL, the initial concentration of hydrogen sulfide is about 1000 ppm, the dosing time is 75s, and the concentration of hydrogen sulfide is detected in the reactor immediately after the end of dosing, the results is shown in Figure 4.

As it can be seen from Figure 4, when the is 0.5%, the removal rate of hydrogen sulfide is near 100%, then with the concentration of sodium increased, the removal rate of hydrogen sulfide stabilized. The optimal absorption concentration of sodium bicarbonate for the removal of hydrogen sulfide is 4%, the removal rate is 77.88%, when the amount of sodium bicarbonate is over 4%, the removal rate of hydrogen sulfide declines and sodium bicarbonate absorption efficiency of hydrogen sulfide can be seen far less sodium.

By formulating different concentrations of sodium carbonate solution in 50 mL for hydrogen sulfide absorption test, the initial concentration of hydrogen sulfide is about 1000 ppm, the dosing time is 72s, the concentration of hydrogen sulfide is detected immediately after the end of dosing in the reactor, then the absorbing liquid in reactor is vibrated for 100 times/min, and the concentration of hydrogen sulfide is detected in the end of vibration, the test results is shown in Figure 5.

It is shown in the results that with the increase of the concentration of sodium carbonate, the absorption liq-

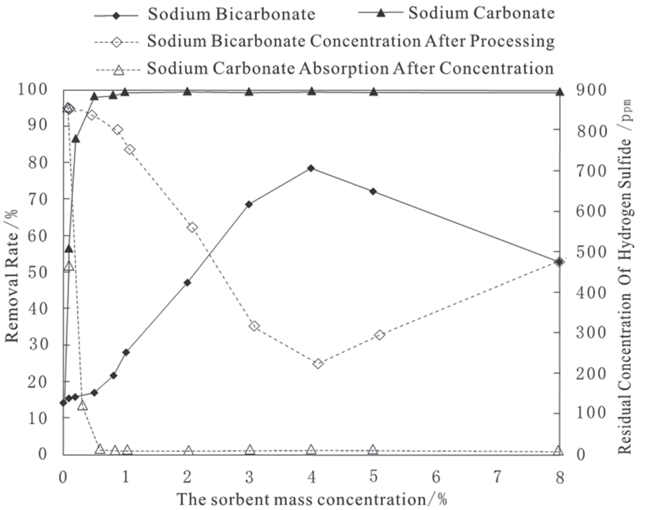

Figure 4. Comparison Chart of sodium carbonate and sodium bicarbonate for hydrogen sulfide absorption effect.

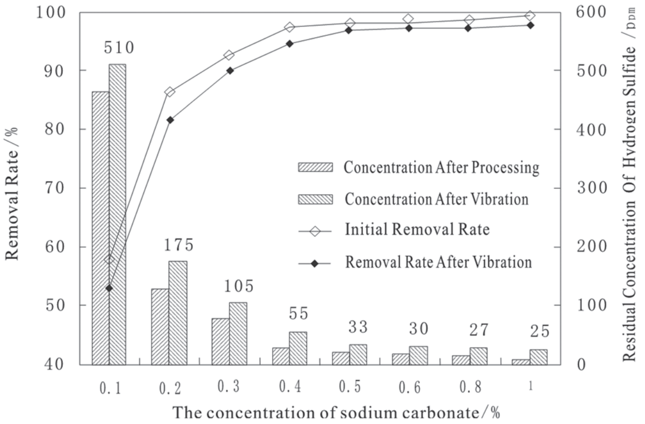

Figure 5. *Absorption effect of different concentrations of sodium carbonate solution of hydrogen sulfide.*

uid removal rate of hydrogen sulfide is also increasing. As it can be seen from Figure 5, when the concentration of sodium carbonate solution is 1%, the concentration of hydrogen sulfide decreases from 1100 ppm to 10ppm, the removal rate is 99.27%. Since the disturbance and dilution of coal mine water, the tail liquid of absorption will re-release the hydrogen sulfide gas, therefore, it cannot completely remove the hydrogen sulfide gas undermine with the single use of sodium carbonate as an absorbing liquid.

3.1.1. Influence of Oxidizer to Sodium Carbonate Solution for the Absorption of Hydrogen Sulfide

The method refers to the liquid phase catalytic oxidation method in industrial exhaust gas desulfurization process, it is an improvement of alkali absorption method. By adding one or more catalytic oxidizer sodium carbonate solution to improve absorption of the hydrogen sulfide, this catalyst can oxidize HS^- generated by the absorption of hydrogen sulfide in the alkali to elemental sulfur and sulfides, preventing the hydrogen sulfide regeneration, and promoting the transfer to the positive direction of alkali absorption balance, raising the alkali absorption efficiency. Taking into account that the drug cannot be recovered and no secondary pollution requirements, test selected oxidant (NT), sodium hypochlorite and chelated iron (III) as the catalytic oxidant.

3.1.1.1. Influence of Chelated Iron (III) on the H_2S Absorption Effect of Sodium Carbonate

Chelated iron (III) desulfurization technology is based on ferric ion oxidation of wet oxidation, but ferric ions in an alkaline solution is easy to produce iron hydroxide precipitate, thus the disodium EDTA is used as a complexing agent and complexed with ferric chloride to produce a trivalent iron. As is shown in Figure 6, EDTA iron sodium is a pale yellow powder soil, stable, soluble in water, with oxidizing of trivalent iron ions.

Chelated iron (III) produced has strong oxidation resistance of Fe^{3+},and it is soluble in alkaline solution, as shown in Figure 6 (right), the right side of the test tube is a yellow solution formed by the chelated iron added into the sodium hydroxide solution, and the left side of the test tube is a red-brown precipitate generated by the Fe^{3+} added into the sodium hydroxide solution.

Different concentrations of chelated iron (III) are added in sodium carbonate of 0.2% in 50 mL, and the hydrogen sulfide gas absorption is tested, the initial concentration of hydrogen sulfide is about 1000 ppm, the dosing time is 72s, the concentration of hydrogen sulfide is detected immediately after the end of dosing in the reactor, then the absorption of liquid in the reactor is vibrated at the speed of 100 times/min for 1min,

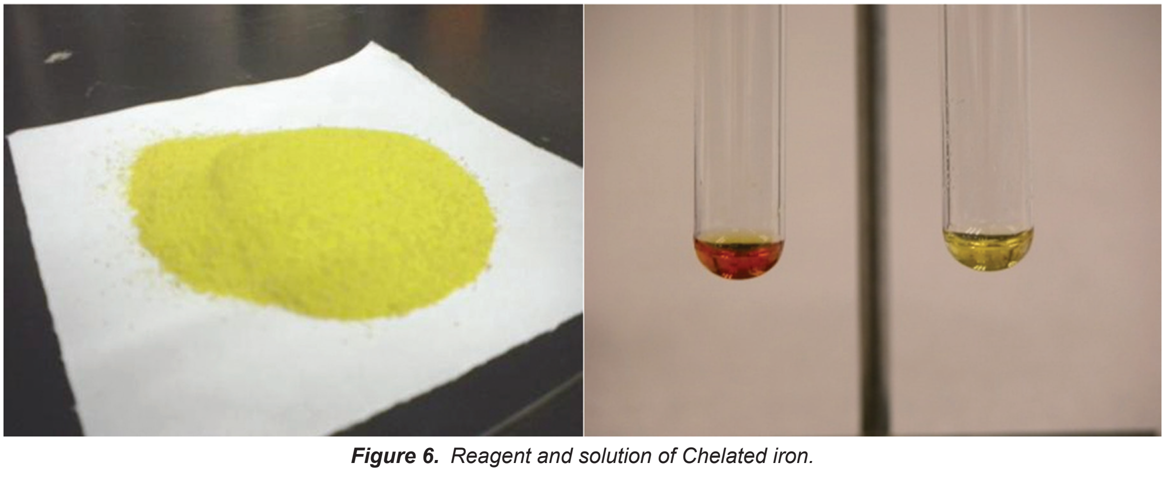

Figure 6. *Reagent and solution of Chelated iron.*

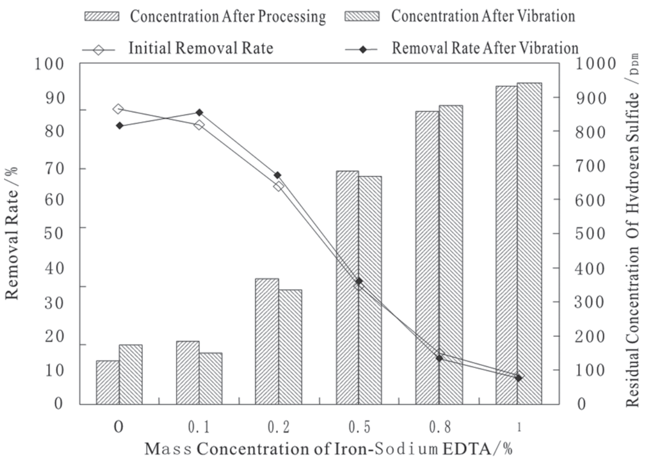

Figure 7. *Influence of sodium iron EDTA concentration on the H_2S absorption effect of sodium carbonate.*

and the concentration of hydrogen sulfide is detected once again in the reactor, the test results is shown in Figure 7.

It is shown in Figure 7 that with the increase of concentration of sodium iron EDTA, the removal efficiency of hydrogen sulfide in absorption liquid decreases, which is for that the sodium iron EDTA is a weak base salt (the pH is 3.5 to 5.5 when the solution is 1%), Therefore, sodium iron EDTA was added such that the alkaline absorbent solution decreases, leading to the solubility of hydrogen sulfide gas in the solution is decreased, so does the absorption efficiency.

In summary, the EDTA iron sodium has the advantage of non-toxic, but its aqueous solution is acidic, and the oxidation resistance is general. In the process of production, there may have precipitation produced by Fe^{3+} that are not complexed, which results in the Mist effect, limiting its industrial application.

3.1.1.2. Influence of Sodium Hypochlorite on the H_2S Absorption Effect of Sodium Carbonate

Sodium hypochlorite is a commonly used disinfectant in water treatment industry; it can be hydrolyzed to produce an aqueous solution of strong oxidizing hypochlorous acid, accomplishing the purpose of oxidation. Different concentrations of sodium hypochlorite are added in sodium carbonate solution of 0.1% in 50 mL for absorption test of hydrogen sulfide gas, the initial concentration of hydrogen sulfide is about 1000 ppm, the dosing time are 75s, the concentration of hydrogen sulfide is detected in the reactor immediately after the end of dosing, then the absorbing liquid in the reactor is vibrated at speed of 100 times/min for 1min, and the concentration of hydrogen sulfide in the reactor is detected again after the end of the vibration and the concentration of hydrogen sulfide is detected in air, the test results are shown in Figure 8.

From Figure 8, it is shown that with the increase of concentration of sodium hypochlorite, the removal rate of the solution to the absorption of hydrogen sulfide gradually increased, indicating that the sodium hypochlorite solution can promote the absorption of hydrogen sulfide in sodium carbonate, and particularly obvious for high concentration of sodium hypochlorite. The data is shown that when the concentration of sodium hypochlorite solution is 3%, the initial removal rate of hydrogen sulfide in absorption solution is 96.2%. In addition, it can also be seen from the figure, when the concentration of sodium hypochlorite is greater than 0.5%, the removal rate after vibration begins to be higher than the initial removal rate, there's no release of hydrogen sulfide after vibration for a period of time, and the concentration decreased, which indicated that the hydrogen sulfide can be thoroughly remove when the sodium hypochlorite is added in the absorbing liquid.

Although the sodium hypochlorite has the promotion of absorption of hydrogen sulfide in sodium carbonate, the promoting effect of low concentrations of sodium hypochlorite is not obvious, so a higher concentration of sodium hypochlorite is necessary. It is found in the test that when the concentration of sodium hypochlorite is over 2%, there's a pungent taste in the absorption liquid, and the sodium hypochlorite has an effect of sensitization, which the releasing free chlorine may cause poisoning, and the thermal decomposition will produce toxic and corrosive fumes, which has a strong corrosion and human harm.

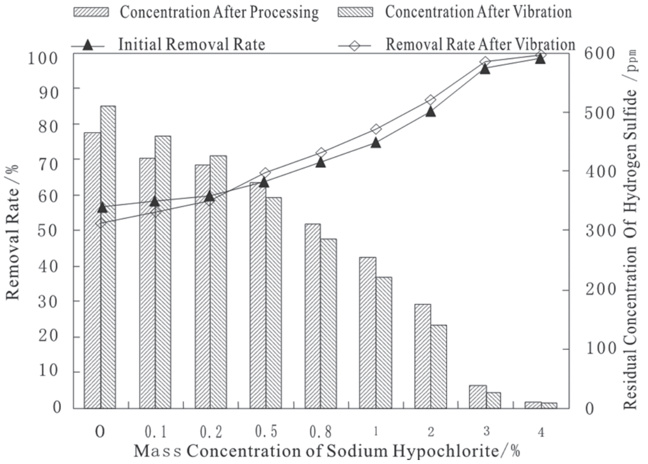

Figure 8. *Influence of sodium hypochlorite concentration on the H_2S absorption effect of sodium carbonate.*

3.1.1.3. Influence of Oxidizer on the H_2S Absorption Effect of Sodium Carbonate

NT is an oxidant, white crystalline powder, soluble in water, commonly used for topical disinfectant. Different concentrations of NT are added in the sodium carbonate solution of 0.1% in 50 mL for the test of hydrogen sulfide absorption. The initial concentration of hydrogen sulfide in the reactor is about 1000 ppm, the dosing time are 75s, the concentrations of hydrogen sulfide are detected immediately in the reactor after the end of dosing, then the absorbing liquid in the reactor is vibrated at speed of 100 times/min for 1min, and the concentration of hydrogen sulfide in the reactor is detected again after the end of the vibration, the test results are shown in Figure 9.

During the experiment, it is found that the absorption tail liquid is colorless and transparent when not add NT, the absorption tail liquid is yellow-green, slightly turbid when the concentration of NT is 0.3%, the absorption tail liquid pale-yellow when the concentration of NT is 0.5% (0.8%) at first, and white precipitate formed after standing for 30 minutes , as is shown in Figure 10.

Figure 9 shows that NT plays an obvious role in promoting sodium carbonate solution to absorb hydrogen sulfide, the concentration of hydrogen sulfide decreases from 1090 ppm to 0 ppm when the concentration of NT is 0.8%, the removal rate is 100%, and when concentration of NT ≥ 0.2%, the removal rate after vibration is greater than the initial removal rate, the absorption effect is thorougher, which is due to that the NT aqueous solution is slightly alkaline, and it is an extremely mild oxidizing agent in neutral or alkaline medium, and strong oxidizing substance generates when reacts with water, the effect is of moderate persistence, without any side effects, which is an ideal oxidizer.

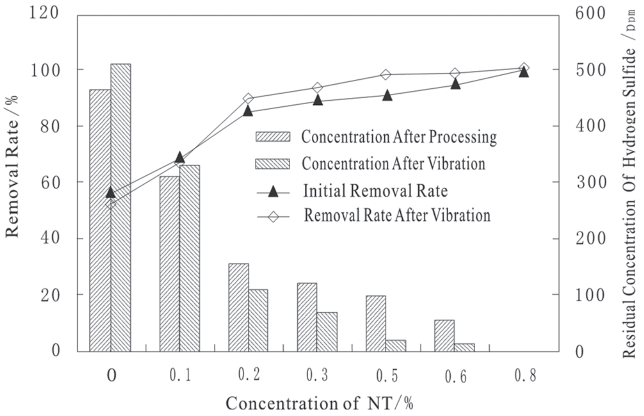

Figure 9. Influence of oxidizer concentration on the H_2S absorption effect of sodium carbonate.

Figure 10. Tail liquid generated by sodium carbonate solution containing 0.8% NT with absorption of hydrogen sulfide.

In order to determine the optimal ratio of the chemical agents, the hydrogen sulfide absorption is tested by formulating different concentrations of mixing solution in 30mL, the ratio of concentrations are selected: ① 0.1% sodium carbonate + 0.5% NT, ② 0.2% sodium carbonate +0.4 % NT, ③ 0.3% sodium carbonate + 0.3% NT, ④ 0.4% sodium carbonate + 0.2% NT, the initial concentration of hydrogen sulfide in the reactor is about 1000ppm, the dosing time are 75s, the absorption test results are shown in Figure 11.

As it can be seen from the initial removal Figure

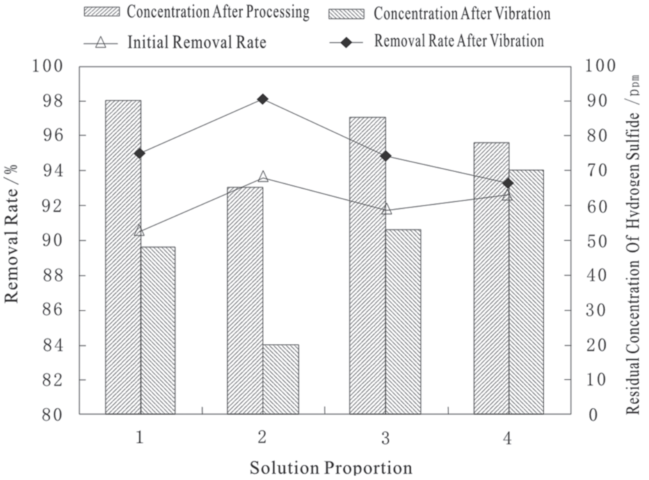

Figure 11. Influence of chemical agents ratio on mixing absorbing liquid for hydrogen sulfide removal.

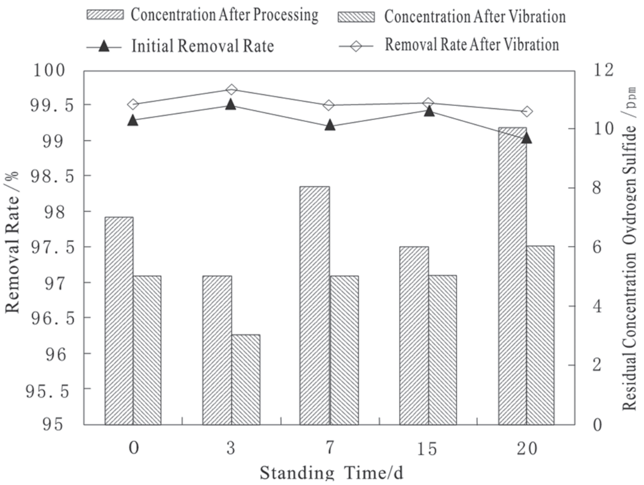

Figure 12. *Influence of standing time on the effect of removing hydrogen sulfide of mixing absorbing liquid.*

11, the order of absorption effect in descending is: ② > ④ > ③ > ①, it can be seen from the curve of removal rate after vibration, the order of absorption effect in descending is: ② > ① > ③ > ④, the content of sodium carbonate is relatively lower in the ratio of ①, and the alkaline solution is weaker than the other, so the initial removal rate is the lowest; the content of sodium carbonate is relatively lower in the ratio of ④, the removal rate after vibration is lower than the increase of initial removal rate, and the ratio of ②, that is the absorb liquid of 0.2% sodium carbonate + 0.4% NT formulated to hydrogen sulfide, has the best absorption.

In order to investigate the stability of the oxidant NT and simulate the environmental conditions under coal mine, the solution is formulated in a series of 0.2% sodium carbonate and 0.4% NT in 50 mL in test, which are standing for 0d, 3d , 5d, 10d, 20d in the normal conditions with room temperature, light and closed. The initial concentration of hydrogen sulfide in the reactor is about 1000ppm, the dosing time are 72s, and then the initial removal rate of hydrogen sulfide gas and the removal rate after vibration are tested, the results are shown in Figure 12.

It is shown in Figure 12 that with the increase of standing time, there is only slight variations between 99.02% ~ 99.50% of the removal rate on the absorption of hydrogen sulfide, without decreasing trend, indicating that NT is a relatively stable oxidant, and the solution is placed under natural light conditions for 20 days, there's no oxidation efficiency decrease, which is due to that the oxidant NT's hydrolysis in neutral and alkaline media is very slow, and no hydrolysis of NT itself does not have strong oxidizing, therefore under the same storage conditions, NT aqueous solution is more stable than sodium hypochlorite solution, which is long enough to effectively conducive to field applications.

Therefore, compared to chelated iron (III), sodium hypochlorite, NT has characteristics of good effect of removal and high oxidation stability as the catalytic oxidant, which is of non-toxic, and can meet the safety requirements in direct contact with the human body. The mixed absorption liquid compounded in 0.2% sodium carbonate + 0.4% NT has the best absorption of hydrogen sulfide, the solution of 50 mL can completely remove the hydrogen sulfide gas of 1500 ppm or less in the reactor (volume of 8L), and the removal rate is 100%.

3.1.2. Influence of Surfactant to Sodium Carbonate Solution for the Absorption of Hydrogen Sulfide

Different concentrations of Dodecyl benzene sulfonic acid sodium are added in sodium carbonate in 50 mL 0.1% solution as surfactant in the test, testing the influence of hydrogen sulfide absorption by alkali liquid when added in surfactant, the concentration of hydrogen sulfide in the reactor is about 1000 ppm, the dosing time are 75s, the initial removal rate and the removal rate after vibration of hydrogen sulfide gas are tested, the results are shown in Figure 13.

It is shown in Figure 13 that with the increase of the concentration of sodium dodecyl benzene sulfonate solution, the removal rate of hydrogen sulfide gradually increased. When the concentration of the surfactants increases to 0.3%, the increase trend of the removal rate curve gradually stabilized, when the concentration increases to 1%, the initial removal rate is 97.76%, the removal rate after vibration is 92.35%, which can be seen that the sodium dodecyl benzene sulfonate plays

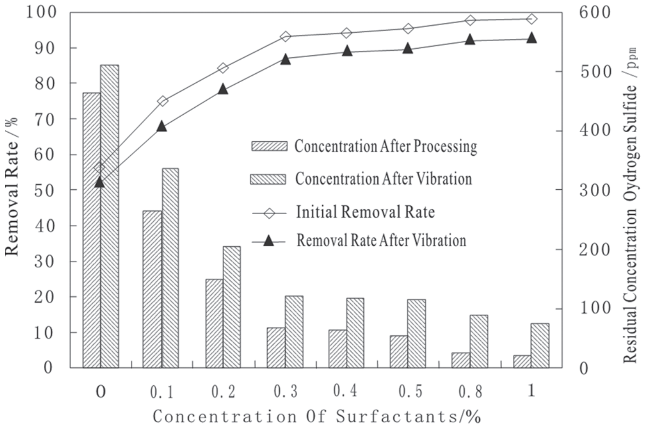

Figure 13. *Influence of different concentrations of surfactants to sodium carbonate solution for the absorption of hydrogen sulfide.*

a certain role in promoting the absorption of hydrogen sulfide in sodium carbonate solution, it is because that the sodium dodecyl benzene sulfonate solution reduces the surface tension of liquid absorption, accelerating the process of mass transfer between two phase of liquid-gas, enhancing the contact between the molecule of alkali liquid and the hydrogen sulfide gas, so the effect of absorption is improved. However, the hydrogen sulfide gas cannot be completely removed in the alkali liquid when added in sodium dodecyl benzene sulfonate solution, it can be seen in the figure above that removal rate after vibration is lower than the initial removal rate, indicating that the hydrogen sulfide will release after the vibration of absorption tail liquid.

3.2. Alcohol Amine Solution Test for Absorption of Hydrogen Sulfide Gas

Amine is an compound generated by the ammonia molecules hydrogen substituted by hydrocarbon, which is alkaline. According to the number of hydrogen substituted, the sequences are primary amines (RNH_2), secondary amines (R_2NH), tertiary amine (R_3N). The method of amine removing hydrogen sulfide has a certain effect on engineering applications, and the commonly used amines agents are monoethanolamine (MEA), diethanolamine (DEA) and so on. Therefore, compared with sodium carbonate solution, alcohol amine solution has a selective absorption of hydrogen sulfide, which is applicable to the conditions with high content of carbon dioxide.

3.2.1. Absorption Tests of Different Types of Alcohol Amine Solution for Hydrogen Sulfide

The monoethanolamine, diethanolamine, triethanolamine, triethylenetetramine are used as absorbent in the test, different concentrations of solution are made up to test the effect of absorption of hydrogen sulfide, the initial concentration of hydrogen sulfide in the reactor is about 1000ppm, the dosing time are 75s, the concentration of hydrogen sulfide in the reactor is detected immediately after the end of dosing, the results are shown in Figure 14.

It is can be seen from Figure 14 that in the same condition of certain amount, the effect of alcohol amine reagents on the absorption of hydrogen sulfide decreases as monoethanolamine > triethylenetetramine > diethanolamine > triethanolamine, the monoethanolamine has the best effect on absorption of hydrogen sulfide, the removal rate is 85.44% of hydrogen sulfide when the concentration of monoethanolamine is at low (0.1%). Monoethanolamine is a clear, colorless or pale yellow liquid medium viscosity, and is a primary amine, with a slight ammonia smell, easy to absorb moisture, and is instable when meet light, with weak irritant, the aqueous solution of 0.1 mol/L pH is 12.1.

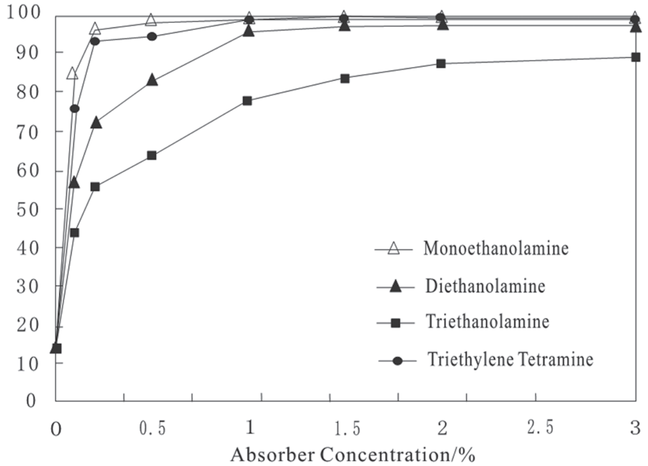

Figure 14. *Absorption effect of hydrogen sulfide of different types of alcohol amine solution.*

3.2.2. Effect of Oxidants on Alcohol Amine Solution to Absorb Hydrogen Sulfide

The effect of hydrogen sulfide absorption in different concentrations of monoethanolamine solution is tested, that is the absorption test, the initial concentration of hydrogen sulfide in the reactor is about 1000 ppm, the dosing time are 75s, the concentration of hydrogen sulfide are detected immediately after the end of dosing, then the absorbing liquid in the reactor is vibrated at speed of 100 times/min for 1min, and the concentration of hydrogen sulfide in the reactor is detected again after the end of the vibration, the test results are shown in Figure 15.

From Figure 15, we can know that with the increasing of the concentration of monoethanolamine, the removal rate of hydrogen sulfide in absorbing liquid gradually increased, when the concentration of monoethanolamine is 1%, the initial removal rate of hydrogen sulfide is 99.55%, the removal rate after vibration is 98.18%, and the removal rate after vibration is always lower than the initial removal rate. The absorption principle of Monoethanolamine solution to hydrogen sulfide is similar to sodium carbonate, which all convert hydrogen sulfide to HS^- by its alkaline, likewise, monoethanolamine absorption of hydrogen sulfide is not complete, the hydrogen sulfide will release from

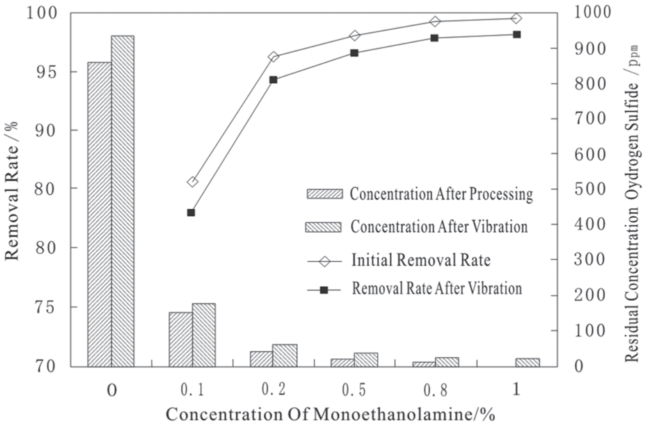

Figure 15. *Effect of hydrogen sulfide absorption of different concentrations of monoethanolamine.*

the absorbent tail liquid, resulting in the content of hydrogen sulfide rise in the air, therefore it is necessary to add oxidizing agent in the amine solution to achieve the purposes of hydrogen sulfide removal completely.

Taking into account the above-mentioned problem, different concentrations of oxidizer (NT) are added in monoethanolamine solution of 0.1% in 50 mL to test the hydrogen sulfide absorption. The initial concentration of hydrogen sulfide is about 1000 ppm, the dosing time are 73s, the concentration of hydrogen sulfide in the reactor is detected immediately after the end of dosing, then the absorbing liquid in the reactor is vibrated at speed of 100 times/min for 1 min, and the concentration of hydrogen sulfide in the reactor is detected again after the end of the vibration, the test results are shown in Figure 16.

As it can be seen from Figure 16, with the increasing of the concentration of NT the removal efficiency of hydrogen sulfide in the absorbing liquid gradually increased, when the concentration of NT is 0.8%, the initial removal rate is 99.52%, the removal rate after vibration is 100%, indicating that NT plays a significant role in promoting the absorption of hydrogen sulfide in the monoethanolamine solution. The removal efficiency of hydrogen sulfide in the mixed absorbing liquid is thorough, when the concentration of NT is 0.2%, the removal rate after vibration is higher than the initial removal rate, the initial removal rate is 88.57%, the removal rate after vibration is 90.00%, and there's no release of hydrogen sulfide after vibration of absorbing tail liquid for a period of time, while the concentration of hydrogen sulfide has decreased. There some theoretical research and numerical simulation on mechanics of flow and heat transport through porous media which has some reference value on the issue [15–17].

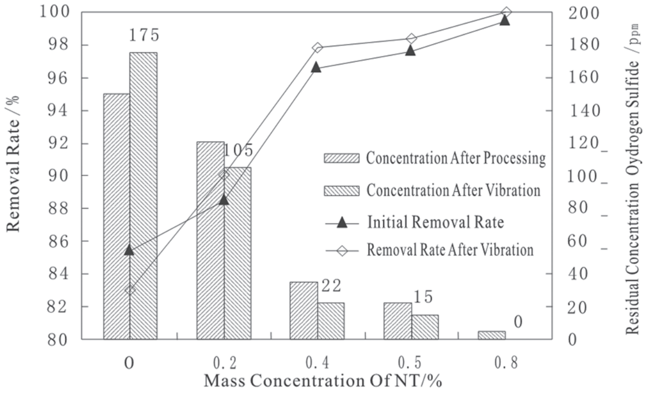

Figure 16. *Effects of different concentrations of monoethanolamine NT on the absorption of hydrogen sulfide.*

CONCLUSIONS

In order to solve the technical problems of hydrogen sulfide outburst in high sulfur coal mine, this paper chose sodium carbonate as an absorbing liquid. The results showed that: with the increasing of the concentration of sodium carbonate, the removal rate of hydrogen sulfide in the absorption liquid is also increasing, although the effect of hydrogen sulfide absorption in high concentration of sodium carbonate solution is better, the hydrogen sulfide gas will release again after vibration of the absorbing tail liquid, resulting in the absorption not complete, so it is not ideal to take the alkali as a single use for hydrogen sulfide absorption,

For the problem that the hydrogen sulfide cannot be completely removed in the single use of sodium carbonate solution, the catalytic oxidizers [complexing iron (III), sodium hypochlorite, NT] are added in alkali in the test. The results showed that compared to other oxidants, NT has the best hydrogen sulfide removal efficiency, with non-toxic, high stability, the mixed absorbing liquid has the best absorption efficiency to hydrogen sulfide in the ratio of 0.2% sodium carbonate + 0.4% NT, the initial removal rate of hydrogen sulfide in the reactor is 99.31% when the solution is 50 mL, the removal rate is 99.50% after vibration, and there's no decrease of the removal rate in the conditions of natural light and closure for 20 days.

In order to remove the hydrogen sulfide gas occurrence in the coal effectively, the dodecyl benzenesulfonate is added in the alkali in the test, the results shows that it has promotion for the sodium carbonate solution to absorb hydrogen sulfide, it has certain feasibility for the surfactant to remove the hydrogen sulfide gas occurrence in the coal, but the character of the surfactant and the effect of the hydrogen sulfide removal need to be tested to be confirmed.

The common used monoethanolamine, diethanolamine, triethanolamine, triethylenetetramine are selected as an absorbent absorption in the test, the results show that compared to other types of amine, monoethanolamine has the best effect on the absorption of hydrogen sulfide, when the concentration is 1%, the initial removal rate is 99.55%, the removal rate after vibration is 98.18%, monoethanolamine can be applied in the high content of CO_2 instead of sodium carbonate as alkali. Because the monoethanolamine cannot absorb hydrogen sulfide completely, the oxidant NT is added in amine solution, when the concentration of monoethanolamine is 0.1%, the concentration of NT is 0.8%, the initial removal rate of hydrogen sulfide in absorption liquid is 99.52%, the removal rate after vibration is 100%, which can achieve the purpose of hydrogen sulfide remove completely.

ACKNOWLEDGEMENTS

This work is financially supported by Natural Science Foundation of China (Grant No.51174170).

REFERENCES

1. Jin Shuqing, Ding Yongming, Yan Aihua, Zhang Qinqin, Li Qian, Zhao Fei. H_2S Management in 15# coal seam of Fenghuangshan Coal Mines. *Procedia Engineering, 26*(2011):1490–1494. http://dx.doi.org/10.1016/j.proeng.2011.11.2329
2. Mingju Liu, Qigen Deng, Fajun Zhao, Yanwei Liu. Origin of hydrogen sulfide in coal seams in China. *Safety Science, 50* (2012) 668–673. http://dx.doi.org/10.1016/j.ssci.2011.08.054
3. Liu Jianjun, Song Rui, Cui Mengmeng. Improvement of predictions of petrophysical transport behavior using three-dimensional finite volume element model with micro-CT images. *Journal of Hydrodynamics*. 2015, 27(2):234–241. http://dx.doi.org/10.1016/S1001-6058(15)60477-2
4. Meijun Wang, Yongfeng Hu, Jiancheng Wang, Liping Chang, Hui Wang. Transformation of sulfur during pyrolysis of inertinite-rich coals and correlation with their characteristics. *Journal of Analytical and Applied Pyrolysis*, 104(2013):585–592. http://dx.doi.org/10.1016/j.jaap.2013.05.010
5. Niu Wen-qiang, Li Xiao-bin. Analysis on prevention technology of hydrogen sulfide gas in fully mechanized mining face. *Shanxi Coal*, 2015, (2):119–121.
6. Zhang Yongcheng, Wang Honghui, Li Yingxiang, Zhao Haiping, Chi Xiaobiao. Generation Mechanism and Corrosion for Hydrogen Sulfide in Oil Field of 3rd Oil Plant in Qinghai Oilfield. *Journal of Southwest Petroleum University (Science and Technology Edition)*, 2011, 33(1):151–155.
7. Lin Hai, Wei Wei, Wang Ya-nan, Yu Yu-jiang. Study on the rapid removal of H_2S in underground coal mines. *Journal of China Coal Society*, 2012, 37(12):2065–2069.
8. Pei Guihong, Yu Feng, Liu Jianjun. Feasibility Study of Individual Treatments of Desizing Wastewater. *Journal of Residuals Science & Technology*. 2015, 12(S1):S85–S91. DOI:10.12783/issn.1544-8053/12/S1/13. http://dx.doi.org/10.12783/issn.1544-8053/12/S1/13
9. Liang Mingchao, Wei Junhong, Han Hongmei, Fu Chengguo, Liu Jianjun. A Comprehensive Model for Capillary Pressure Difference across a Drop/Bubble Flowing Through a Constructed Capillary. *Surface Review and Letters*, 2015, 22(6), AR1550077 DOI: 10.1142/S0218625X15500778. http://dx.doi.org/10.1142/S0218625X15500778
10. Zhao Huijun, Liu Kai, Li Huiling. The Experimental Study on the Biological Method applied to removing Hydrogen Sulfide. *Journal of Southwest Petroleum University (Science and Technology Edition)*, 2010, 32(1):125–129.
11. Jun Xiong, Xiaolan Huang, Hongling Ma. Gas leakage mechanism in bedded salt rock storage cavern considering damaged interface. *Petroleum*, 2015, 1(4):366–372. http://dx.doi.org/10.1016/j.petlm.2015.10.008
12. Zengli Du, Jianjun Liu, Wenge Liu and Chunhong Li. Frequency-space domain acoustic wave simulation with the BiCGstab (*l*) iterative method. *Journal of Geophysics and Engineering, 13*(2016): 70–77. http://dx.doi.org/10.1088/1742-2132/13/1/70
13. Lei Zhang, Yi He, Yanqiu Zhou, Ranran Yang, Qiangbin Yang, Dayong Qing, Qianhe Niu. A novel imidazoline derivative as corrosion inhibitor for P110 carbon steel in hydrochloric acid environment. *Petroleum*, 2015, 1(3): 237–243. http://dx.doi.org/10.1016/j.petlm.2015.10.007
14. Zeng Dezhi, Shang Jianfeng, Long Decai, *et al.* The Research on Corrosion in High-Sulfur Gas Purification Plants. *Journal of Southwest Petroleum University: Science & Technology Edition*, 2014, 36(6):135–142.
15. Haijun Lu, Jianjun Liu, Yuan Li, Yiqie Dong. Heat transport and water permeability during cracking of the landfill compacted clay cover. *Journal of Chemistry*, 2015, Vol. 2015, ID: 685871 (SCI: 000362769400001). DOI: 10.1155/2015/685871. http://dx.doi.org/10.1155/2015/685871
16. Gou Feifei, Liu Jianjun, Liu Weidong. Numerical Simulation of Chemical Transferring Using Finite Difference Method. *Journal of Southwest Petroleum University (Natural Science Edition)*, 2015, 37(6):112–118. DOI: 10.11885/j.issn.1674-5086.2015.03.04.09
17. Chen Zhanqing, Yu Bangyong. Research Progress of Seepage Mechanics in Rock Mass Affected by Mining. *Journal of Southwest Petroleum University: Science & Technology Edition*, 2015, 37(3):69–76. DOI: 10.11885/j.issn.1674-5086.2015.03.05.06

Optimization of Hexavalent Chromium Removal from Wastewater by Ferrite Precipitation

GUIHONG PEI[1], ZHENGYANG WEI[1,*], HUAFENG FU[2], JIANJUN LIU[3] and FENG YU[1]

[1]*School of Civil Engineering and Architecture, Southwest Petroleum University, Chengdu, 610500, China*

[2]*School of Chemistry and Chemical Engineering, XuChang University, XuChang, 461000, China*

[3]*School of Geoscience and Technology, Southwest Petroleum University, Chengdu, 610500, China*

ABSTRACT: Removal of hexavalent chromium ions (Cr^{6+}) from wastewater produced by surface treatment of aluminum was performed by ferrite precipitation. By varying the reactant concentrations and reaction conditions the optimal conditions were established for chromium removal. The following variables were tested: concentration of ferric salt ($FeSO_4 \cdot 7H_2O$), the pH during oxidation-reduction, the pH during co-precipitation, the reaction temperature and the incubation time. The results indicate that chromium removal is optimal when ferric salt is added in excess to chromium at a ratio of 14 to 1 (above the theoretical optimum), the redox reaction is performed at pH 4, precipitation is performed at pH 9, the reaction temperature is set at 75°C and the reaction duration is 20 min. Under these conditions, a removal rate of 99.97% could be obtained, resulting in a residual concentration of 0.29 mg/L hexavalent chromium from with initial concentrations of 1539 mg/L. Wastewater thus treated fulfilled the maximum allowed standard of 0.5 mg/L.

1. INTRODUCTION

With increasing industrial development, the quantitative demand of aluminum has steadily increased. Due to its chemical properties, aluminum is an attractive metal, but it has a relatively low corrosion resistance, so that aluminum surfaces require chemical treatments that have led to serious environmental consequences. In order to improve the corrosion resistance of aluminum and prolong its lifetime, aluminum surfaces are typically undergoing treatments of degreasing, alkaline etching, pickling, and anodic oxidation, alone or in combination.

Degreasing is the rust preventing mechanical removal of lubricating oil or grease from an aluminum surface, to ensure that corrosion can occur uniformly. The chemicals typically used for degreasing include acid solvents and surfactants, which result in large amounts of strongly acidic wastewater. Degreasing is typically followed by alkaline etching performed to remove contaminants and the natural oxide film from the surface of aluminum. Pickling on the other hand, removes residual black spots from aluminum surfaces, giving aluminum surfaces shiny appearance. Anodic oxidation is a chemical oxidation/reduction process, so that an artificial oxide film forms on the surface during electrolysis. Typical solvents used in anodic oxidation processes include NaF, $K_3Fe(CN)_6$ and CrO_3 (hexavalent chromium). Anodic oxidation produces large amounts of wastewater containing highly-toxic pollutants like chromium and fluorine in high concentrations.

The wastewater produced during aluminum surface treatment contains problematic environmental contaminants, including chromium, phosphorus, fluorine and sulfate radicals. Because of the complex composition, high concentration, high chromaticity, high toxicity and low biodegradability, disposing with these pollutants directly will cause severe environmental harm. In this paper, experiments were presented to remove highly-toxic hexavalent chromium from such wastewater by ferrite.

When chromium enters the aquatic environment via wastewater aquatic plants and animals suffer, reducing the self purifying capacity of natural surface water. Chromium exists in the valence states of three and six. Trivalent chromium can form $Cr(OH)_3$, which makes water turbid, while hexavalent chromium on the other hand turns water into brownish yellow. The toxicity of the latter is hundreds of times than that of trivalent chromium. Hexavalent chromium mainly presents as CrO_2^{2-} and $Cr_2O_7^{2-}$ [1]. It is a known genotoxic carcinogen that increases the risk of lung cancer upon inhalation; furthermore it causes serious damage to soils,

---

*Author to whom correspondence should be addressed.
Email: 1213792405@qq.com

1544-8053/16/02 S085-07

doi:10.12783/issn.1544-8053/13/4/S11

water and living organisms [1]. Upon reaching toxic concentrations in the human body exposure results in nosebleed, RTI, skin ulcers and eventually cancer [2,3]. The maximum allowed concentration of hexavalent chromium in discharged industrial wastewater is 0.5 mg/L, while that of total chromium is 1.5 mg/L [1]. According to WHO, the concentration of chromium ions in drinking water should not surpass 2 μmol/L [4].

In order to prevent environmental damage, it is necessary to prevent or remove hexavalent chromium ions from wastewater. The main technologies of dealing with the problem are chemical reduction [5,6], adsorption [7,8], electrolysis [9,10], and ion exchange [11,12]. Chemical reduction is adding a the reducing agent to the wastewater, to reduce hexavalent chromium to less toxic $Cr(OH)_3$, with reducing agents such as $FeSO_4$, $Na_2S_2O_3$ and $NaHSO_3$, but this is not practical at high concentrations, as the limit of total chromium disposition would be violated. Adsorption is adding an adsorbent for instance fly ash and activated carbon to wastewater, to mechanically remove hexavalent chromium. The electrolytic method uses iron as anode, to produce Fe^{2+} under electrolysis conditions while hexavalent chromium is reduced to $Cr(OH)_3$. Lastly, ion exchange removes hexavalent chromium by the effect of an ion exchanger. These treatments can be effective, but the cost is too high and sometimes procedures.is complicated.

This work concentrates on improvement of the ferrite method based on chromium removal by ferrite production and precipitation in an aqueous environment [13], by addition of iron ions [14,15,16]. Ferric salt (ferric sulfate, $FeSO_4 \cdot 7H_2O$), is added to the wastewater, so that hexavalent chromium reacts with the metal ions, generating a stable sediment that can be removed by filtration. Further developments of the principle resulted in the ultrasonic—ferrite method [17], electrolytic—ferrite method [18], GT-ferrite method [18] and other variants. Their advantages are easy, handling, requiring simple equipment only, a high removal rate, low costs and no secondary pollution [18].

The work is built on data by Chengbao Wu and colleagues, who removed Cr^{6+} from wastewater by the use of ferrite method [19]. The factors that influence efficiency of the process were studied, such as the required concentration of ferric salt, pH, reaction time and reaction temperature. The results showed that with a ratio of Fe^{2+} in excess to $Cr_2O_7^{2-}$ of 28:1 to 31:1, the reaction time was 10 to 15 min. The optimal conditions of removal Cr^{6+} are in pH range of 1–6 and 8–10 during oxidation-reduction, and during co-precipitation at reaction temperature range from 65–75°C, respectively. Here it is described how these parameters could be refined for removal of hexavalent chromium from wastewater produced by surface treatment of aluminum. The reaction conditions and reagent concentrations were optimized so as to enhance efficiency, and provide a theoretical basis for effective treatment of chromium-containing wastewater.

Table 1. Main Reagents.

Name of Reagents	Purity	Manufacturers
$FeSO_4 \cdot 7H_2O$	AR	Sinopharm Chemical Reagent Co., Ltd
$NH_3 \cdot H_2O$	AR	Tianjin Fuchen Chemical Reagents Factory
H_2SO_4	AR	Kaifeng Kaihua Co., Ltd Reagents Factory
$C_{13}H_{14}N_4O$	AR	Sinopharm Chemical Reagent Co., Ltd

Table 2. Main Facilities.

Name of Facilities	Type	Manufacturers
Ultraviolet-visible Spectrophotometer	UV-2550	Shimadzu Instrument Suzhou Co., Ltd
pH meter	PHS-3C	Shanghai INESA Scientific Instrument Co., Ltd.
Mixing water bath pot	HCJ-2C	Changzhou Baixiang Experimental Instrument Factory

MATERIALS AND METHODS

Experimental Reagents

Experimental Reagents are listed in Table 1.

Experimental Facilities

Experimental Facilities are listed in Table 2

Water Sample

The water samples are wastewater of aluminum surface treatment (chromium-containing wastewater), of which the main characters are seen in Table 3. *C* stands for concentration, the unit is mg/L.

Table 3. Main Characters of Water Sample.

pH	$C(Cr^{6+})$(mg/L)	Chromaticity
4	1539	2000

Experiment Procedures

After addition of $FeSO_4 \cdot 7H_2O$ to the wastewater, an oxidation-reduction (redox) reaction takes place in acidic conditions between Fe^{2+} and Cr^{6+}, transforming Cr^{6+} into Cr^{3+}, and Fe^{2+} into Fe^{3+}. When the pH of the solution increased, Fe^{3+}, Cr^{3+} and Fe^{2+} will co-precipitate into ferrite. The process is summarized as follows (adopted after [15]):

$$Cr_2O_7^{2-} + 6Fe^{2+} + 14H^{+} \rightarrow 2Cr^{3+} + 6Fe^{3+} + 7H_2O \quad (1)$$

$$Cr^{3+} + 3OH^{-} \rightarrow Cr(OH)_3 \quad (2)$$

$$Fe^{2+} + 2OH^{-} \rightarrow Fe(OH)_2 \quad (3)$$

$$Fe^{3+} + 3OH^{-} \rightarrow Fe(OH)_3 \quad (4)$$

$$Fe(OH)_3 \rightarrow FeOOH + H_2O \quad (5)$$

$$Fe(OH)_2 + FeOOH \rightarrow FeOOH \cdot Fe(OH)_2 \quad (6)$$

$$FeOOH + FeOOH \cdot Fe(OH)_2 \rightarrow FeO \cdot Fe_2O_3 + 2H_2O \quad (7)$$

$$Fe^{2+} + 2Cr^{3+} + 8OH^{-} \rightarrow FeO \cdot Cr_2O_3 + 4H_2O \quad (8)$$

$$3Fe^{2+} + 6Fe^{3+} + 24OH^{-} \rightarrow 3FeO \cdot Fe_2O_3 + 12H_2O \quad (9)$$

The method was performed as follows: 50 mL of a water sample was adjusted to acidic pH using H_2SO_4, after which excess $FeSO_4 \cdot 7H_2O$ was added and stirred for 4 min.The second, $NH_3 \cdot H_2O$ was used to increase the pH for the co-precipitation reaction. Acidic pH, alkaline pH and stirring time were varied. The incubation was performed at various temperatures by means of a water bath pot under continuous stirring. Then incubation the solution was filtered, and the concentration of the any residual hexavalent chromium in the eluent was determined by diphenylcarbazide spectrophotometry [20–22]. In an acid environment a reaction takes place between Cr^{6+} and diphenylcarbazide ($C_{13}H_{14}N_4O$) to generate a purplish red complex with a maximum absorption wavelength at 540 nm [23]. By means of a standard curve, the concentration of hexavalent chromium was determined for which a Type UV-2559 ultraviolet spectrophotometer of Shimadzu Instrument Suzhou Co., Ltd was used. All experiments were performed in triplicate.

RESULTS AND DISCUSSION

The Influence of $FeSO_4 \cdot 7H_2O$ Concentration on Removal Efficiency of Hexavalent Chromium

Based on reaction Equations (1), (8) and (9), the amount of $FeSO_4 \cdot 7H_2O$ (producing Fe^{2+}) was varied with a known, fixed amount of $Cr_2O_7^{2-}$ present in the used waste water.

$$n(Cr_2O_7^{2-}) = \frac{1}{2} n(Cr^{6+}) = \frac{1}{2} \frac{1539 \times 10^{-3} \times 50 \times 10^{-3}}{52} = 7.399 \times 10^{-4}\,\text{mol} \quad (10)$$

By variation of the ratio of Fe^{2+} and $Cr_2O_7^{2-}$, the effect on the residual concentration of hexavalent chromium was established (Figure 1). In this and all other experiments the initial concentration of Cr^{6+} was 1539 mg/L (0.74 mmol/L). The other parameters of this experiment were as follows: pH during redox step X, pH during precipitation Y, reaction temperature Z. The left axis in Figure 1 belongs to the blue curve, giving the concentration of residual Cr^{6+}, while the axis on the right represents the removal rate R, in % (red curve).

$$R = \frac{1539 - C(Cr^{6+})}{1539} \quad (11)$$

From Figure 1 it is concluded that the concentration of ferric salt needs to be at least 32 g/L, corresponding to a molar ratio of Fe^{2+} to $Cr_2O_7^{2-}$ of 8:1, in order to produce a removal rate of 99.93%, resulting in 1.14 mg/L residual Cr^{6+}. This is still beyond the maximally acceptable concentration of 0.5 mg/L for industrial wastewater discharge. Increasing the ratio to 14:1, the removal rate is increased to 99.98%, with residual $Cr^{6+} \leq 0.26$ mg/L, meeting the required standard. It is concluded that the amount of $FeSO_4 \cdot 7H_2O$ should be in excess to the theoretical value, and further experiments were conducted with a ratio of 14:1 for Fe^{2+} to $Cr_2O_7^{2-}$, corresponding to 56 g/L $FeSO_4 \cdot 7H_2O$ in Figure 1.

The Influence of pH on the Removal Efficiency of Hexavalent Chromium

The redox reaction [Equation (1)], only takes place under acidic conditions. The pH was varied between 1 and 6 and the effect on residual concentration of hexavalent chromium and removal rates was established (Figure 2). The other parameters of this experi-

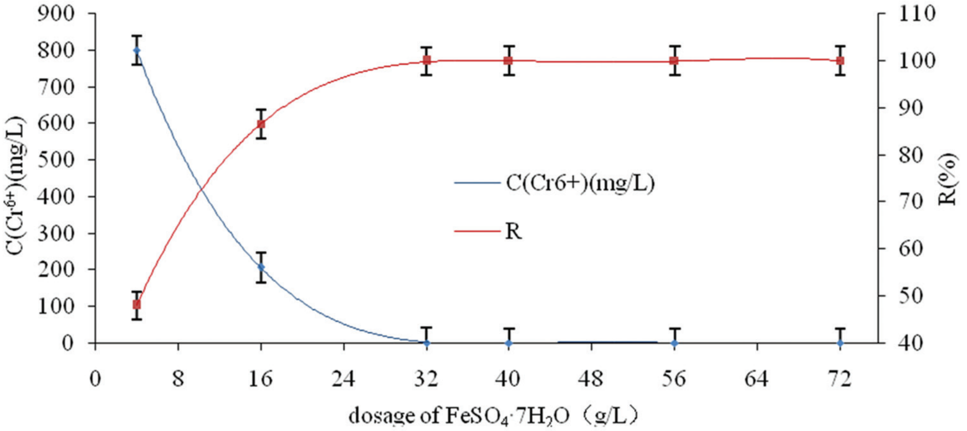

Figure 1. *Relation between amount of $FeSO_4{\cdot}7H_2O$ and residual concentration of hexavalent chromium as well as the removal rate.*

ment were as follows: Ratio of ferric salt to chromium 14:1, pH during precipitation *Y*, reaction temperature *Z*.

As can be seen, the system was permissive of pH variation during the redox reaction, as long as the pH remained at or below 4. At pH = 4, *R* = 99.97%, resulting in a residual Cr^{6+} concentration of 0.48 mg/L, just below the acceptable maximum. At higher pH values during the redox reaction the removal rate was insufficient. Based on these results, the optimal pH of the water sample during the oxidation-reduction step was set at pH 4.

The co-precipitation step [Equations (8) and (9)] requires an alkaline pH. To prevent the oxidation of Fe^{2+}, the pH of the solution needs to be increased (for which NH_3 was used), but since $Cr(OH)_3$ is amphoteric, excessive OH^- will cause $Cr(OH)_3$ to dissolve again, so the pH should not be increased too high [24].The pH value was varied between 6 and 11 to measure its effect (Figure 3).The other parameters of this experiment were as follows: Ratio of ferric salt to chromium was 14:1, pH during redox step was 4, and reaction temperature was *Z*.

As expected, a pH optimum was found with suboptimal performance for pH values above or below this. The optimum was identified at pH = 9, where *R* = 99.98% resulting in a residual Cr^{6+} concentration of 0.24 mg/L. A higher or lower pH resulted in substandard removal of hexavalent chromium.

The Effect of Reaction Temperature on the Removal Efficiency of Chromium Ions

Experiments were performed under optimal ferric

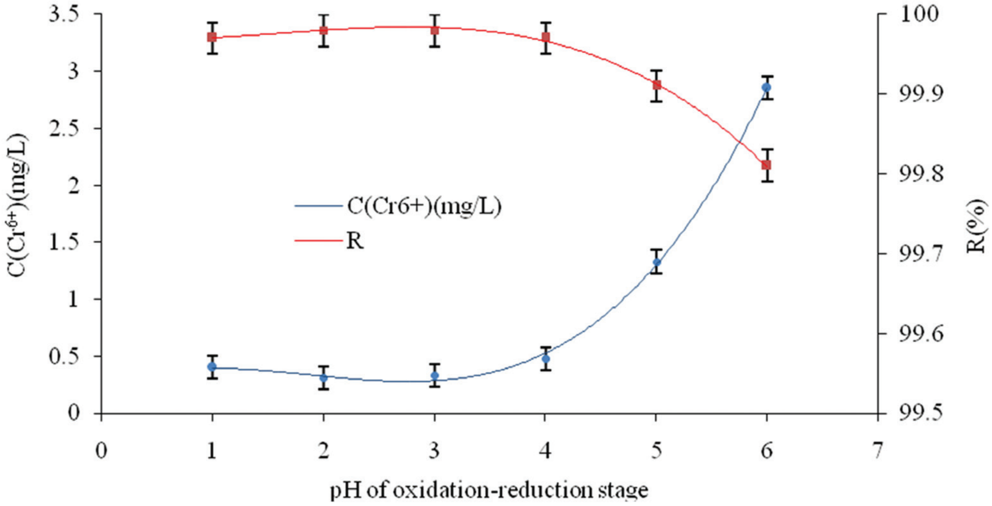

Figure 2. *Relation curve between pH and the residual concentration of hexavalent chromium as well as removal rate during oxidation-reduction stage.*

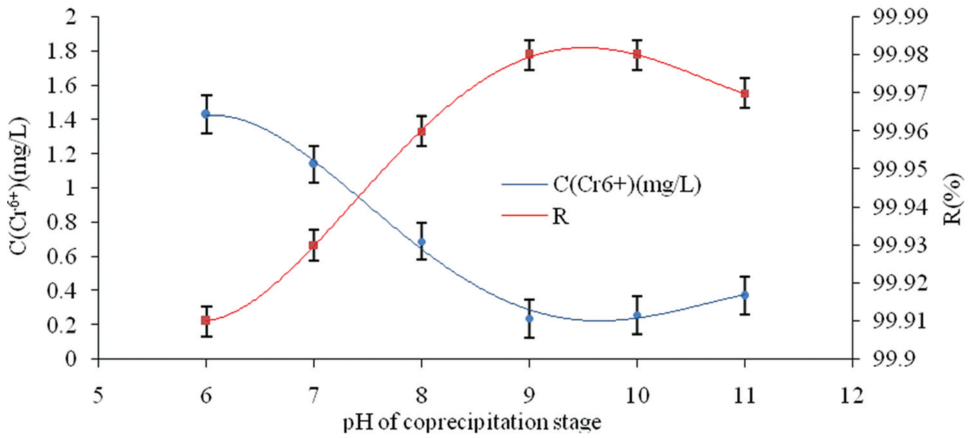

Figure 3. Relation curve between pH and the residual concentration of hexavalent chromium as well as removal rate during co-precipitation stage.

salt concentration and optimal pH conditions while the temperature was varied between 45 and 95°C. It has been described that with increasing temperature, the reaction probability is increased [25], but at high temperatures excessive Fe^{2+} will be transformed to Fe^{3+}, leading to insufficient precipitation of ferrite. Indeed, a temperature optimum of 75°C was observed, as shown in Figure 4. At this temperature, a removal rate of R = 99.97% was obtained.

The Effect of Stirring Time on the Removal Efficiency of Chromium Ions

The last variable that was tested, under conditions resembling the optimum for all other variables, was the stirring time, which was varied from 5 to 30 min. Figure 5 shows that after 25 min the removal rate levels off. However, with longer reaction times, energy consumption increases, so for efficiency reasons the reaction time of 20 min was chosen sufficient, as it removed 99.98% of hexavalent chromium, resulting in waste water with 0.29 mg/L residual concentration.

Treatment Effect verified by Appearance and Color

The original water sample used in the experiments was strongly colored as a result of high hexavalent chromium concentrations [Figure 6(a)]. Dilutions of 2,000 times were required to eliminate the color (data not shown).The middle panel of Figure 6 shows the water after processing but before filtering, while the filter step has reduced the color by a factor of 200 [Figure 6(c)]: a dilution of 10 times made the effluent water appear colorless.

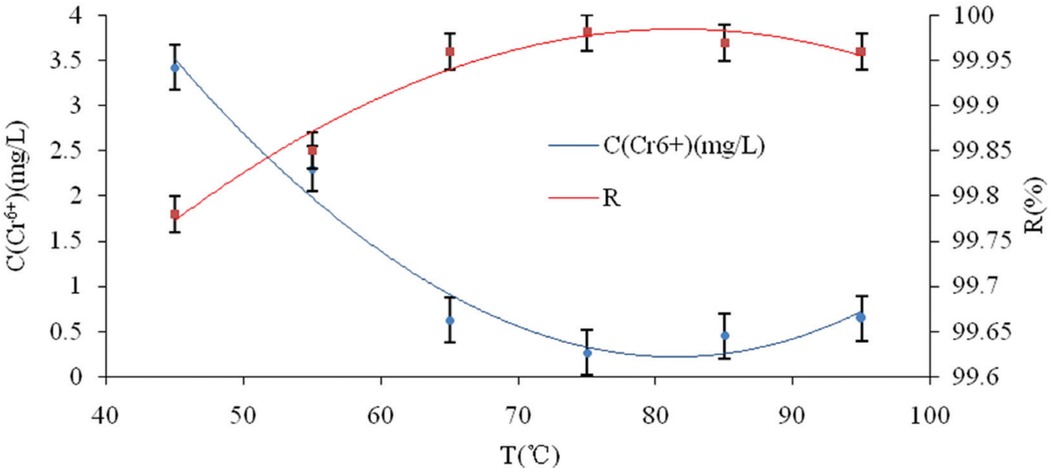

Figure 4. Relation curve between temperature and residual concentration of hexavalent chromium as well as removal rate.

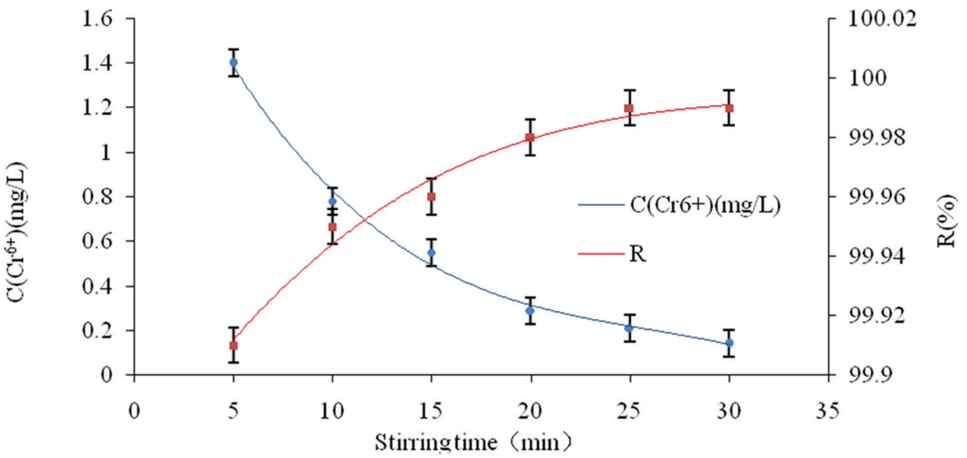

Figure 5. *Relation curve between stirring time and residual concentration of hexavalent chromium as well as removal rate.*

CONCLUSIONS

Hexavalent chromium was effectively removed from aluminum surface treatment wastewater by means of ferrite precipitation and the optimal reaction conditions were established. Starting with water contaminated with 1539 mg/L, the residual concentration of chromium ions after treatment was reduced to 0.29 mg/L, which is lower than the required discharge standard. The results reported here may guide the development of treating wastewater of aluminum surface treatment on an industrial scale.

REFERENCES

1. Yan Xu, Li Yafeng, “Treatment methods of chromic wastewater”, *Liaoning Chemical Industry*, Vol. 39, No. 2, 2010, pp. 143–146.
2. Babel, S., Kurniawan T. A., “Cr(VI) removal from synthetic wastewater using coconut shell charcoal and commercial activated carbon modified with oxidizing agents and/or chitosan”, *Chemosphere*, Vol. 54, 2004, pp. 951–967. http://dx.doi.org/10.1016/j.chemosphere.2003.10.001
3. Goswami, S., Ghosh, U. C., “Studies on adscription behavior on Cr(VI) onto synthetic hydrous stannic oxide”, *Water SA*, Vol. 31, 2005, pp. 597–602.
4. Costa M., “Potential hazards of hexavalent chromate in our drinking water”, *Toxicol Appl Pharmacol*, Vol. 188, 2003, pp. 1–5. http://dx.doi.org/10.1016/S0041-008X(03)00011-5
5. Qiu Mingliang, Luo Dan, Ding Xiaojing, *et al.*, “Cost comparison of chemical precipitation method for treating chromium-containing waste water”, *Environmental Protection and Circular Economy*, No. 3, 2012, pp. 61–62.
6. JAE Gon Kim, “Reduction of hexavalent chromium by pyrite-rich landsite in different anionic solutions”, *Environmental Geology*, Vol. 42, No. 6, 2002, pp. 642–648. http://dx.doi.org/10.1007/s00254-002-0567-2
7. Jiang Lingyan, Shao Shuai, Zheng Bingguo, “Adsorption effect comparison of several adsorbents for chromium-containing wastewater”, *New Chemical Materials*, Vol. 41, No. 8, 2013, pp. 164–166.
8. B. Qi, Y. Wang, L.-L. Lou, *et al.*, “Solvent-free aerobic oxidation of benzyl alcohol over palladium catalysts supported on MnOx prepared using an adsorption method”, *Reaction Kinetics, Mechanisms and Catalysis*, Vol. 108, No. 2, 2013, pp. 519–529. http://dx.doi.org/10.1007/s11144-012-0529-y
9. Zhou Jie, Chen Heyi, Wei Jun, *et al.*, “Experimental study on chromium-containing wastewater by iron-carbon microelectrolysis”, *Electroplating and Finishing*, Vol. 32, No. 6, 2013, pp. 43–45.
10. Manoiu, Vasile-Sorin, “Obtaining nanoparticles by electrolytic method”, *UPB Scientific Bulletin, Series B: Chemistry and Materials Science*, Vol. 72, No. 1, 2010, pp. 157–166.
11. Fan Li, Zhang Jianqiang, Cheng Xin, *et al.*, “Progress of treatment of

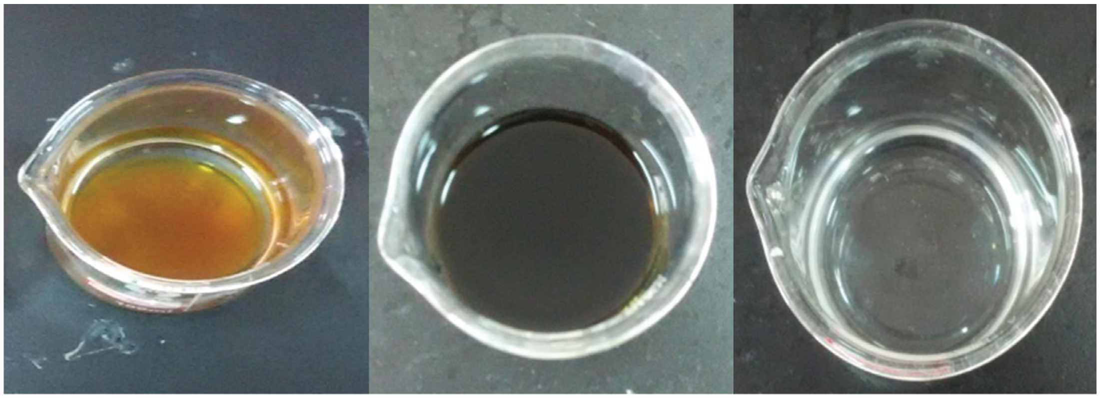
(a) (b) (c)

Figure 6. *(a) Original water sample, (b) processed water sample, (c) filter liquor.*

wastewater containing chromium by ion-exchange method and adsorption method", *Technology of Water Treatment*, Vol. 35, No. 1, 2009, pp. 30–33.

12. M. Vithal, S. Rama Krishna, G. Ravi, "Synthesis of Cu^{2+} and Ag^{+} doped $Na_2Ti_3O_7$ by a facile ion-exchange method as visible-light-driven photocatalysts", *Ceramics International*, Vol. 39, No. 7, 2013, pp. 8429–8439. http://dx.doi.org/10.1016/j.ceramint.2013.04.025
13. Mansour, S.F, "Structural and magnetic investigations of sub-nano Mn-Mg ferrite prepared by wet method" *Journal of Magnetism and Magnetic Materials*, Vol. 323, No. 13, 2011, pp. 1735–1740. http://dx.doi.org/10.1016/j.jmmm.2010.09.012
14. Guo Yanni, Fang Zengkun, Hu Jiehua, *et al.*, "Research development of treating wastewater containing heavy metals by chemical precipitation process", *Industrial Water Treatment*, Vol. 31, No. 12, 2011, pp. 9–12.
15. Lu Jiongyuan, Wang Sanfan, "Treatment of wastewater containing chromium by ferrite process", *Journal of Lanzhou Jiaotong University*, Vol. 28, No. 3, 2009, pp. 155–158.
16. Yi Liu, Shicheng Wei, Haoliang Tian, "Characterization of soft magnetic spinel ferrite coating prepared by plasma spray", *Surface and Coatings Technology*, Vol. 258, 2014, pp. 189–199. http://dx.doi.org/10.1016/j.surfcoat.2014.09.029
17. Shen Yongjun, Ding Jiandong, Zhu Peng, *et al.*, "A research on treatment of chromium containing wastewater with Ultrasonic-Ferrite method", *Electroplating and Pollution Control*, Vol. 34, No. 1, 2014, pp. 42–45.
18. Peng Weihua, Gui Herong, "Application status of ferrite process in treating industrial effluents of heavy metals in China", *Technology of Water Treatment*, Vol. 36, No. 5, 2010, pp. 22–27.
19. Chengbao Wu, Xiaofang Hu, Weiyin Luo, *et al.*, "Introduction about treating electroplating wastewater containing chromium by ferrite method", *Electroplating and Finishing*, Vol. 25, No. 5, 2006, pp. 51–55.
20. Pan Zhongcheng, Lai Na, "Research progress on application of dipehenylcarbohydrazide spectrophotometer", *Yunnan Chemical Technology*, Vol. 41, No. 1, 2014, pp. 34–37.
21. Liu Na, Yu Wenfang, Qu Jing, "Determination of chromium (VI) in drinking water by diphenylcarbazide spectrophotometry", *Environmental Science Survey*, Vol. 33, No. 1, 2014, pp. 96–98.
22. Wang Haiyun, Li Minrui, Liao Tao, *et al.*, "Influence of pH value on the determination of hexavalent chromium by diphenylcarbazide spectrophotometry", *Journal of Yangtze River Scientific Research Institute*, Vol. 29, No. 9, 2012, pp. 22–26.
23. Maurizio Pettine, Silvio Capri, "Removal of humic matter interference in the determination of Cr(VI) in soil extracts by the diphenylcarbazide method", *Analytica Chimica Acta*, Vol. 540, No. 2, 2005, pp. 239–246. http://dx.doi.org/10.1016/j.aca.2005.03.041
24. Hu Guorong, Wang Qinmeng, Peng Zhongdong, *et al.*, "Research on preparation of chromium hydroxide from high-carbon ferrochrome", *Inorganic Chemicals Industry*, Vol. 42, No. 11, 2010, pp. 30–32.
25. Liu Hongyu, "Analyze the influence of concentration and temperature and catalyst on the reaction rate", *Modern Business Trade Industry*, No. 21, 2010, pp. 377–378.

Phosphorus Speciation and Distribution in Sediments and the Relationship with Total Phosphorus in the Overlying Water

XIAOHUI LU, MENGEN SONG, PEIFANG WANG*, XIAO QIAO and RUI CHEN
School of Earth Science and Engineering, Ministry of Education Key Laboratory of Integrated Regulation and Resource Development on Shallow Lakes, Hohai University, Nanjing, Jiangshu, China

ABSTRACT: To study phosphorus (P) speciation and distribution in lake water and sediments, and the relationship with total P (TP) in the overlying water, the concentration of different forms of P in lake water and sediments was determined. Samples were collected from Xuanwu and Dong Lakes. The results indicated that the concentration of P in sediments was largely influenced by human processes, vegetation, hydraulic conditions, and geographic settings. The inorganic P (IP) content was much higher than the organic P (OP) content, while NaOH-extractable P (NaOH-P) was the main inorganic P fraction, accounting for 40–50% of IP. The HCl-extractable P (HCl-P: calcium (Ca) bound P) content was low but stable, because Ca bound P was not easily adsorbed. The TP content of lake water and sediments were positively correlated, as was NaOH-P and apatite P (AP), while there was no obvious correlation between the TP content of lake water and OP and HCl-P. This suggests that labile P accounted for most of the exchange capacity of P at the water-sediment interface. The results indicated that the content of P in lake-bottom sediments was closely related to the concentration in lake water, providing a theoretical basis for the treatment of eutrophic water bodies with regard to the internal P loading.

INTRODUCTION

EUTROPHICATION, leading to the explosive growth of algae, is a serious environmental problem around the world. The main causes of eutrophication are an oversupply of nutrients, together with environmental and biological factors. The input of excess nutrients to a water body is the root cause of eutrophication [1,2,4].

P is the most common limiting nutrient of blue-green algae blooms in lake water. Studies of the biogeochemical cycling of P in lakes have identified the processes involved in lake eutrophication, and have revealed the importance of blue-green algae blooms [5]. Nutrients entering a water body are ultimately retained in the sediment. Sediments can participate in exchange processes, and the P content can be bioavailable depending on its chemical form. The deposition of P in the lake under certain conditions may be an important source of nutrients [6], and therefore the relationship between the P content of sediments and lake water is very important [20].

In recent years, with the development of the Chinese economy, lake sediments have suffered varying degrees of pollution. Under certain environmental conditions, sediments can release nutrients (such as N and P) into the water body by diffusion, convection, and sediment resuspension processes, and therefore the degree of lake eutrophication and sediment nutrient release is closely linked [7]. However, the amount of P released from sediments to the overlying water depends on the content of the available P fractions rather than its total concentration in sediments. More useful information for predicting the potential ecological hazard of P could be provided by investigating the available fraction of P rather than the total P concentration in lake sediments [3]. Studies have shown that under controlled conditions, both endogenous and exogenous processes can gradually release P from sediments into the overlying water, where they can lead to lake eutrophication [8].

MATERIALS AND METHODS

Site Description

P was the focus of the research. Mature current ex-

---

*Author to whom correspondence should be addressed.
Email: pfwang2005@hhu.edu.cn; phone: 025-83787930

1544-8053/16/02 S093-07

doi:10.12783/issn.1544-8053/13/4/S12

perimental methods were employed, with sampling at different locations in Xuanwu and Dong Lakes, to investigate the different chemical forms of P.

Xuanwu Lake is located in Nanjing City, whichis a typical shallow lake (average depth of 1.3–1.4 m), with a surface area of about 3.7 km^2. Lake sediments are mainly a mixture of silt and clay, with a strong adhesive force [3]. In the late 1980s, the water in Xuanwu Lake experienced regular eutrophication. In July 2005 there was a blue-green algae bloom in Xuanwu Lake, leaving behind an unpleasant smell after later dying that had a serious adverse impact on the urban environment of Nanjing [4].

Dong Lake is the largest lake on the Jiangning Campus of Hohai University. All of the lake water is derived from a campus rainwater collection system. Dong Lake has a surface area of 12,000 m^2, with an average depth of about 3 m. The total capacity of the lake is 36,000 m^3, and the water is used for both irrigation and as a fire water supply, with an annual capacity of about 100,000 m^3.

Sample Collection

From July 9 to 11, 2015, a investigation team from the Institute of Hohai University in Nanjing conducted a field investigation and collected samples from Dong and Xuanwu Lakes. Sediment cores were taken from one (D) and four (X1, X2, X3, and X4) locations in Dong Lake and Xuanwu Lake, respectively, using cylindrical Plexiglas tubes. The vertical sampling depth was 16 cm. At each sampling location three parallel samples were collected and immediately packed into sealed bags and stored in a cool place. Overlying water samples were also collected from the surface of the water in 500 ml polyethylene bottles. Three parallel samples were collected from each sampling location. The conditions on the ground at each sampling site are given in Table 1. Each of the Xuanwu Lake sampling sites was identified using the global satellite positioning system (GPS), with the relative positions shown in Figure 1.

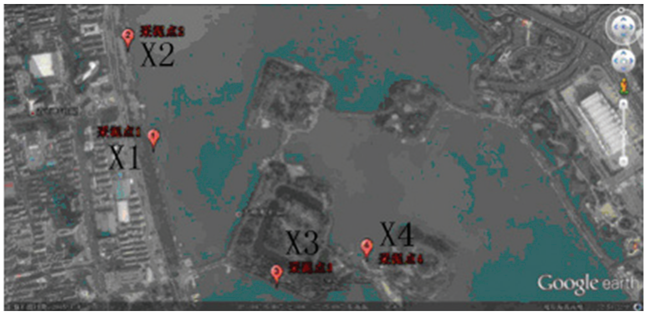

__Figure 1.__ Location of sampling sites in Xuanwu Lake.

Analytical Method

The total phosphorus (TP) concentration in water samples was determined by ammonium molybdate spectrophotometry. Sediment in unfiltered water samples was dissolved using potassium sulfate (or a nitric and perchloric acid combination) as the oxidant, and then ammonium molybdate spectrophotometry was used for the determination of TP. Total phosphorus includes dissolved P, organic P (OP), and inorganic P (IP). This standard method is applicable to surface water, sewage, and industrial waste water. TP and various other forms of P (IP, OP, NaOH-extractable P (NaOH-P), and HCl-extractable P (HCl-P: calcium (Ca) bound phosphorus)) were measured in lake bed sediments. At each individual site, samples from the same column of lake bed sediments were mixed, placed in an aluminum (Al) box, and then heated in an oven for 2 hours and at 105°C. The standards, measurements, and testing (SMT) protocol (European Commission) sequential extraction method [25] was then used to obtain five P fractions: (1) bound to Al, iron (Fe), and manganese (Mn) oxyhydrates; (2) apatite phosphorus (AP), bound to Ca; (3) IP; (4) OP; and (5) TP.

Phosphate in pore-water and in the extract of each fraction was determined by UV-Vis spectrophotometry, using the molybdenum blue method [10]. Results were obtained as the average values of triplicate determinations. All the reagents used were of analytical-reagent grade. All solutions were prepared using

__Table 1.__ __Field Description of Dong Lake and Xuanwu Lake Sampling Locations.__

Station	Name	Latitude	Longitude	Land Cover	Sewage Outfall
D	Dong Lake	N31°55′2″	E118°47′10″	Yes	Yes
X1	No. 1 in Xuanwu Lake	N32°4′40″	E118°46′56″	No	No
X2	No. 2 in Xuanwu Lake	N32°4′55″	E118°46′54″	Yes	Yes
X3	No. 3 in Xuanwu Lake	N32°4′18″	E118°47′14″	No	No
X4	No. 4 in Xuanwu Lake	N32°4′20″	E118°47′30″	No	No

de-ionized water (>18 MΩ), and all glassware and plastic ware were cleaned and rinsed three times with de-ionized water, after being soaked in 0.3% HCl overnight. A quality control procedure was applied throughout the different stages of sample preparation and analysis.

RESULTS AND DISCUSSION

Distribution of TP in Xuanwu Lakes and Dong Lakes

In Xuanwu Lake, the TP concentration in lake water ranged from 0.10 to 0.24 mg/L, with the minimum concentration occurring at site X1, and the maximum concentration occurring at site X3. The location of site X2 was close to a sewage outfall and therefore received more pollutants than the other three sampling locations, but the total P concentration in the water sampled from this location was only slightly higher (0.13 mg/L) than the lowest value at site X1. There were more aquatic plants at site X2, which inhibited the TP concentration. The morphological structure of the submerged plant communities, as well as the functional characteristics of the community and net metabolic balance of the lake, played an important role in controlling the P concentration. For example, some growth stages of *Vallisneria spiralis* can absorb high levels of P. The settlement of P from sediments in the water can play a positive role in promoting vegetation growth [9].

In Dong Lake, the TP concentration in lake water was 0.04 mg/L, which was lower than at all of the Xuanwu Lake sampling locations. Dong Lake's catchment is mainly rain water, with little domestic sewage discharged into the lake, resulting in a low TP concentration.

Distribution of P in the Sediments of Xuanwu and Dong Lakes Total Phosphorus (TP)

The TP concentration in the sediment of Dong Lake was 53.6 mg/L, while in Xuanwu Lake the TP concentration in sediment ranged between 107–810 mg/L. The TP concentration in Xuanwu Lake sediment was higher than in the sediment of Dong Lake. The highest concentration of TP was found at site X3 in Xuanwu Lake, with the lowest concentration at site X2. The second sampling location was shallow and close to a sewage outfall, but was accordingly rich in aquatic plants, resulting in a lower overall TP concentration in the sediment. The N and P in the sediment is released under biological and chemical action. Therefore, plant growth can effectively reduce the TP concentration in sediments [10]. The highest TP concentration in the sediment was found at site X3, where the water was deeper, Overall, the water was relatively clear and there was no sewage outfall in the vicinity. Because there was less vegetation in this location, a historically high P concentration was inferred due to minor plant utilization.

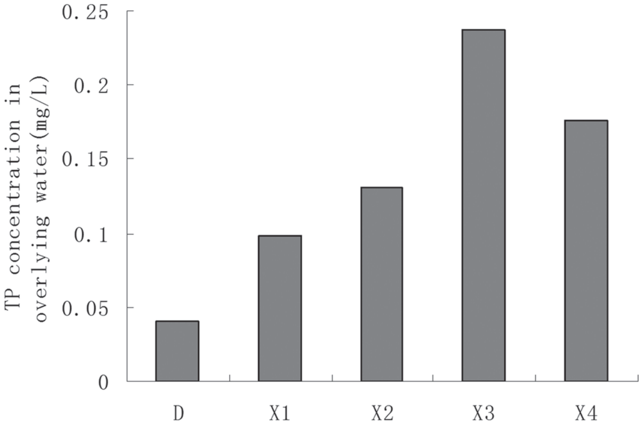

Figure 2. *Total phosphorus (TP) concentration in the overlying water at each sampling site.*

Dong Lake is an artificial lake, with a small surface area and a hydraulic connection to its source water that is less frequent water exchange than at Xuanwu Lake, but the TP concentration in the sediment of Dong Lake was lower than in the sediment of Xuanwu Lake, which TP concentration in the sediment of Dong Lake was 53.63 mg/kg and of Xuanwu Lake was 408.74 mg/kg in average. This was likely to be due to Dong Lake having fewer aquatic plants. The distribution of vegetation in Xuanwu Lake was not uniform, which may be related to industrial water inputs as well as pollution from domestic sewage.

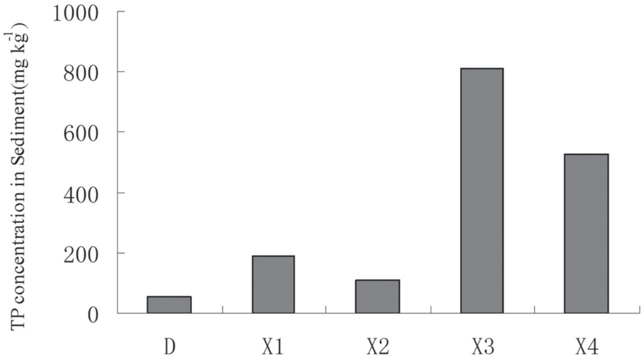

Figure 3. *Total phosphorus (TP) concentration in the sediments from each sampling site.*

Apatite Phosphorus (AP)

The overall distribution of AP was positively correlated with the TP concentration, and increased with increasing TP content (except at site X4). The highest AP concentration was 12.4 mg/L at site X3, and the lowest was 0.81 mg/L at site X2. At Dong Lake the concentration was 0.36 mg/L.AP is an active form of P. The term mainly refers to oxides in the sediment, hydroxides, and P adsorbed on the surface sites of clay minerals, all of which have a large impact on the nutritional status of a body of water. AP is also associated with the sedimentary environment [11]. At both sites D and X2 there were large amounts of aquatic plants, and the TP content was low. The AP was therefore also low. At X4, although there was a higher TP concentration, the AP concentration was low. It was speculated that historically there was an abundance of plants at this site, but due to the development of the cruise ship industry the environmental conditions have changed.

Organic Phosphorus (OP)

It can be seen from Figure 5 that the average OP concentration in Xuanwu Lake was almost twice as high as that in Dong Lake.The clay sediment of Xuanwu Lake had a larger specific surface area than the sediment of Dong Lake, enabling it to more easily adsorb organic substances. Clay colloids protect organic matter from decomposition by micro-organisms, thereby protecting against the microbial decomposition and mineralization of OP. The OP concentration was positively correlated with the sediment clay content. It has been observed elsewhere that plants can grow in relatively dry sediments, containing large amounts of phosphate solubilizing bacteria [12].

There was a large amount of aquatic vegetation at site X2 in Xuanwu Lake. The effects of organic acids secreted by plant roots can enhance their biological effectiveness [13,14], and enhance soil microbial activity, increasing the decomposition of OP and so decreasing OP concentrations. It has been reported that sediments with a large amount of adsorbed P and a high total organic carbon (TOC) content have a strong positive correlation with the Fe^{3+} concentration [6]. Site X4 in Xuanwu Lake was located near Xuanwu Lake Park, which is a small dock for cruise ships. The Fe concentration in the vicinity of X4 was increased due to human factors [6]. The oxidation reaction that formed Fe^{3+} resulted in the OP concentration at X4 being higher than at the other sites.

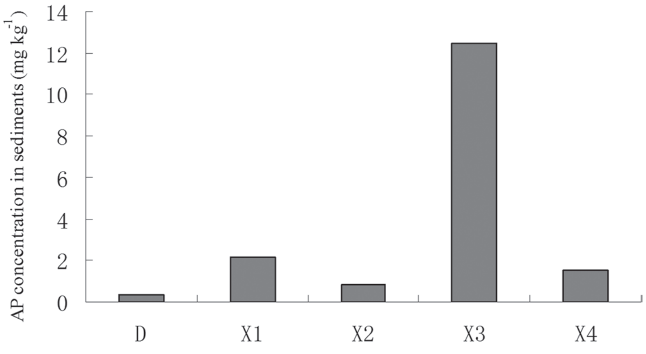

Figure 4. Apatite phosphorus (AP) concentration in sediments from each sampling site.

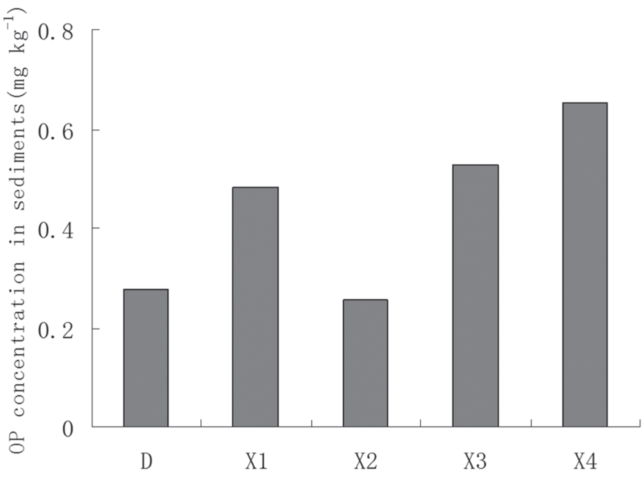

Figure 5. Organic phosphorus (OP) concentration in sediments at each sampling site.

HCl-extractable P (HCl-P)

The HCl-P concentration accounted for only a small proportion of the TP, because it is not easy to release the P bound to Ca [8,9]. There was little difference in the HCl-P concentration between Dong Lake and Xuanwu Lake, and it was much smaller than the OP concentration, indicating that the Ca-P binding was relatively stable in the sediments. It is therefore more difficult for HCl-P to be absorbed and utilized by plants from the sediments than other P fractions [15,16]. Xuanwu Lake is a flowing water lake, whereas Dong Lake is a stagnant water lake. Therefore, the P bound to Ca does not easily drain with water [17], and therefore the Dong Lake HCl-P content was only slightly higher than that of Xuanwu Lake. At the same time, OP and HCl-P could be combined [18], and studies have shown that the rotting of submerged wetland plants can promote soil HCl-P deposition [19]. From a comparison of Figs. 5 and 6, a very strong positive correlation between the

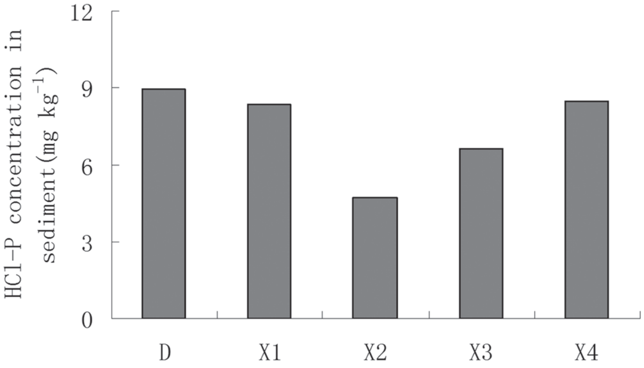

Figure 6. HCl-extractable phosphorus (HCl-P) concentration in sediments at each sampling site.

HCl-P and OP concentrations can be seen at sites X2 and X4.

Analysis of the P Concentration in Lake Bed Sediments and the Overlying Water

The phosphorus concentration was compared in different environmental media.

The Concentration of TP in Sediments and the Overlying Water

In Figure 7 it can be seen that there was a positive correlation between the TP concentration in the sediment and the overlying water at the five sample sites. The higher the TP concentration in the sediments, the higher the TP concentration in the overlying water. Site X2 was located close to a sewage outfall. It received more P, but was rich in vegetation, which enabled the TPconcentration of the overlying water to be effectively conyrolled and also considerably reduced the P concentration in the sediment. This shows that vegetation has a signification effect on TP concentrations in water and sediment. At the same time, under the influence of an external source, the release of the internal P loading in sediment is one of the reasons for the increase in the P concentration in water.

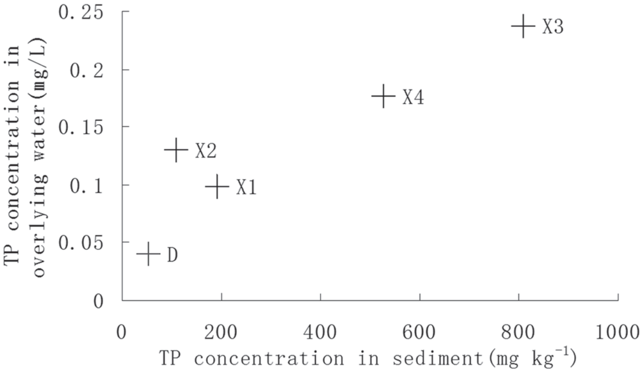

Figure 7. Total phosphorous (TP) concentration in sediments and overlying water at each sampling site.

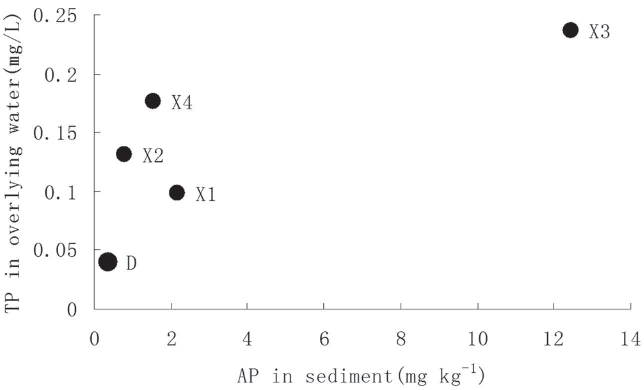

Figure 8. Relationship between the apatite phosphorus (AP) concentration in sediments and the total phosphorus (TP) concentration in overlying water at each sampling site.

Correlation between TP in the Overlying Water and AP in the Sediment

As it can be seen in Figure 8, there was a significant positive correlation between the AP concentration in sediments and the TP concentration in the overlying water.The adsorption desorption equilibrium between water and surface sediments in shallow lakes has a large influence on the P concentration in water [20]. The AP concentration was highest at site X3 where there was no growth of aquatic plants, and this site also had the highest TP concentration in the overlying water column. Both sites D and X2 contained aquatic plants, and the AP concentration was low. At site X2, the main source of P in the overlying water was drainage frome the sewage outfall. Site X4 contained no aquatic plants and had a low AP concentration, indicating that the source of TP in water was likely to be from the water pollution.

Correlation between TP in the Overlying Water and Sediment OP

Particulate OP is potential converted to inorganic salts by bacterial action in pores containing water, and can then enter the water body by molecular diffusion, bioturbation, bubbles, and hydrodynamic disturbances [20]. Plants can absorb and utilize OP [12]. OP can be released to the water body after biochemical degradation, which is a slow process and requires a suitable pH, temperature, and other conditions. There was little

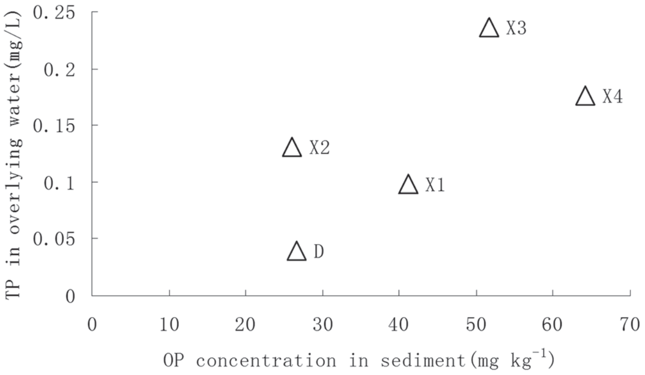

Figure 9. Relationship between the organic phosphorus concentration (OP) concentration in sediments and the total phosphorus (TP) concentration in overlying water at each sampling site.

OP transformation at the lake sediment water interface, and therefore the relationship between the OP concentration in sediments and the TP concentration in overlying water had a weak correlation (see Figure 9).

Correlation between TP in the Overlying Water and Sediment HCl-P

The HCl-P (i.e., Ca bound P) is a significant part of the TP in the sediment and is difficult to dissolve.It had less influence on the P concentration in the interstitial water and the overlying water [23]. Figure 10 shows the distribution of HCl-P in sediment and the distribution of TP in overlying water.

Correlation between TP in Overlying Water and Sediment NaOH-P

The NaOH-P (i.e., metal oxide bound P) was the main form of P in the sediments and was mainly a combination of Al and Fe oxides. Phosphorus in a form that can be used by biological organisms plays an important role in the release of P from sediments. It has a close relationship with the TP concentration in the overlying water. There was a positive correlation between the TP concentration in the overlying water and sediment NaOH-P, with the TP concentration in water increasing as the NaOH-P concentration increased in sediment .

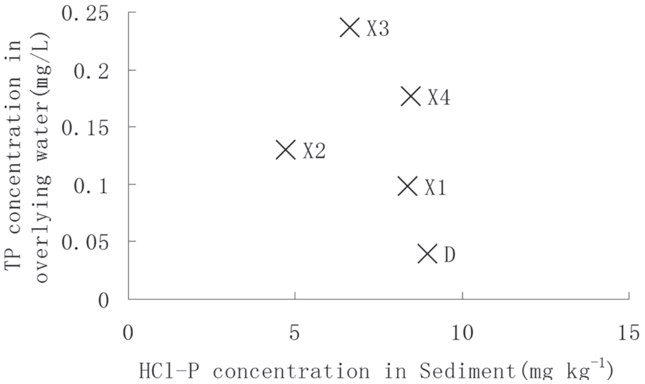

Figure 10. The relationships between the HCL-extractable phosphorus (HCl-P) concentration in sediments and the total phosphorus (TP) concentration in the overlying water at each sampling site.

The Relationship between the P Fractions in Sediments and P in Pore-Water

The relationship among the P fractions and the P concentration in pore-water was investigated by a correlation analysis. The correlation coefficients obtained are shown in Table 2.

The pore-water played an important role in the exchange and cycling of matter between the overlying water column and the sediments. The P concentrations in pore-water were significantly positively correlated with the AP, OP, and TP concentrations in overlying water, with correlation coefficients (r^2) of 0.85, 0.80, and 0.93, respectively, and were significantly negatively correlated with the HCl-P concentration ($r^2 = -0.06$, $p < 0.01$).

It is evident from the data in Table 2 that the AP and TP concentrations in the overlying water and OP concentrations of the sediments strongly influenced the distribution of the different P fractions and the TP concentration in sediments. The TP concentration in the overlaying water was significantly positively correlated to the OP concentrations in sediment profiles. These results suggest that TP concentrations in the overlying water would strongly influence the distribution of P fractions in lake sediments, and thus influence the behavior of P in the lake system.

CONCLUSION

From the above analysis of samples from Dong Lake and Xuanwu Lakes, it was clear that the P concentra-

Table 2. Correlation Coefficients Among the P Concentrations in Each Fraction. P Concentrations (n = 56).

	TP in Sediment	TP in Overlying Water	AP	OP	HCl-P
TP in sediment	1				
TP in overlying water	0.93	1			
AP	0.85	0.78	1		
OP	0.80	0.71	0.41	1	
HCl-P	–0.06	–0.40	–0.23	0.29	1

tions in lake sediments and water were related. There were larger concentrations of TP, IP, OP, and NaOH-P in Xuanwu Lake compared with that in Dong Lake, but there was a similar AP concentration in both lakes. In addition to the physical environment of the lakes, vegetation, hydraulic conditions, and human factors also affected the P concentration. The fixing of different forms of P by vegetation root systems was significantly different. The adsorption and utilization of AP was stronger than for the other forms of P. Hydraulic conditions and human sewage inputs caused significant changes in lake P concentrations. There were no significant correlations among sediment OP and HCl-P concentrations and the TP concentrations in the overlying water, but there were significant positive correlations among TP, AP, and NaOH-P concentrations in the sediment. The active P was more easily released from the sediment toverly water, and was the main P fraction resulting from the sediment to water P exchang process. It appears that endogenous and exogenous processes jointly controlled the P concentration in the lake. Exogenous processes were the primary source of P, and are a major cause of the eutrophication of water bodies, but the endogenous variables cannot be ignored. Through exogenous processes P accumulates in the sediments, which then become an internal source of P. In addition to controlling exogenous pollution, as an internal treatment, the reduction of P releases from sediment to water by enhancing the adsorption of P is an effective means to control the eutrophication of water bodies.

ACKNOWLEDGEMENTS

The study was financially supported by the Open Research Fund Program of the Ministry of Education Key Laboratory of Integrated Regulation and Resource Development on Shallow Lakes, Open Research Fund Program of Key laboratory of agricultural water resources, Chinese academy of sciences, “The National Natural Science Funds” [grant number 41202172], China Postdoctoral Science Foundation funded project, and the Fundamental Research Funds for the Central Universities.

REFERENCES

1. Xu, Cx, Yuan, J. (2011): Phosphorus speciation of the sediments and analysis methods for sequential extraction. *Rock and Mineral Analysis. 30* (6): 785–794 (in Chinese).
2. Ma Ting, Zhao Dayong. (2011): Nanjing and other major lakes in surface sediments Ecological Risk Assessment of Heavy Metal Pollution. *Ecology and Rural Environment. 27* (6): 37–42.
3. Wang Yuwen, Li Jianhong, Wu Min. (2007): Nanjing Xuanwu Lake and other water bloom of Microcystis species composition. *Environmental Science. 28* (10): 21, 872–876.
4. Ruttenberg K C. (1992): Development of aseqential extraction method for different forms of phosphorus in rnarine sediments. *Limnol & Oceanogr, 37* (7): 1460–1482. http://dx.doi.org/10.4319/lo.1992.37.7.1460
5. Gong Chunsheng, Yao Qi, Fang Chenxin, Dong Haoping , Zheng Chaohai & BAO Xianming. (2006): Release fluxes estimate of phosphorus in a urban shallow lake: Lake Xuanwu, Nanjing. *Journal of Lake Sciences.18* (2): 179–183. http://dx.doi.org/10.18307/2006.0212
6. JunHu, Qiangshen, Yongding Liu, Jiantong Liu. (2007): Mobility of different phosphorus pools in the sediment of lake Dianchi during Cyanobacterial blooms. *Environmental Monitor Assess. 132*:141–153. http://dx.doi.org/10.1007/s10661-006-9509-x
7. Heidenreich, M., & Kleeberg.A.(2003): Phosphorus-binding in iron-rich sediments of a shallow reservoir.Spatial characterization based on sonar data. *Hydrobiologia, 506*, 147–153. http://dx.doi.org/10.1023/B:HYDR.0000008621.44435.23
8. Y, Li, J.Q, Zhang, M. (2002): Temporal and spatial variations in kineticsof alkaline phosphatase in sediments of a shallow Chinese eutrophic lake (lake Donghu).*Water Research. 36*. 2084–2090.
9. Kalbacher T, Delfs J-O, Shao H *et al.* (2012): The IWAS-ToolBox: software coupling for an integrated water resources management. *Environ Earth Sci 65*(5):1367–1380. http://dx.doi.org/10.1007/s12665-011-1270-y
10. Chen Y, Chen S, Yu S *et al.* (2014): Distribution and speciation of phosphorus in sediments of Dongping Lake, North China. *Environ Earth Sci 72*(8):3173–3182. http://dx.doi.org/10.1007/s12665-014-3223-8
11. Linqist B A, Ruark M D, Hill J E. (2011): Soil order and management practices control soil phosphorus fractions in managed wetland ecosystems. *Nutrient Cycling in Agroecosystems. 90*(1): 51–62. http://dx.doi.org/10.1007/s10705-010-9411-3
12. Hou D, He J, Lu C et al. (2014): Spatial variations and distributions of phosphorus and nitrogen in bottom sediments from a typical north-temperate lake China. *Environ Earth Sci 71*(7):3063–3079. http://dx.doi.org/10.1007/s12665-013-2683-6
13. Chen M, Chen F, Yu Y, Ji J, Kong F. (2008): Genetic diversity of eukaryotic microorganisms in Lake Taihu, a large shallow subtropical lake in China. *Microb Ecol 56*:572–583. http://dx.doi.org/10.1007/s00248-008-9377-8
14. Gachter R, Muller B. (2003): Why the phosphorus retention of lakes does not necessarily depend on the oxygen supply to the sediment surface. *Limnol Oceanogr 48*:929–933. http://dx.doi.org/10.4319/lo.2003.48.2.0929
15. Patricia Pardo, Gemma Rauret. (2004): Shortened screening method for phosphorus fractionation in sediments: A complementary approach to the standards, measurements and testing harmonized protocol. *Analytica Chimica Acta. 508*, 201–205. http://dx.doi.org/10.1016/j.aca.2003.11.005
16. Zhu Guangwei, QIN Boqiang, Zhang Lu. (2006): Yangtze River lake sediments in the form of phosphorus and algae can utilize the amount of Science in China: *Series D Earth Sciences.* Vol. 49. Supp.128–137.
17. Eiler A, Olsson JA, Bertilsson S. (2006): Diurnal variations in the auto- and heterotrophic activity of cyanobacterial phycospheres (Gloeotrichia echinulata) and the identity of attached bacteria. *Freshw Biol 51*:298–311. http://dx.doi.org/10.1111/j.1365-2427.2005.01493.x
18. Liu S J, Li J, Yang Y K, et al. (2016): Influence of environmental factors on the phosphorus adsorption of lanthanum-modified bentonite in eutrophic water and sediment. *Environ Sci Pollut Res. 23*(3): 2487–2494. http://dx.doi.org/10.1007/s11356-015-5453-z
19. F. Wu, H. Qing, G. Wan. (2001): Regeneration of N, P, and Si near the sediment/water interface of lakes from south¬western China plateau. *Water Research, 35* (5), 1334–1341. http://dx.doi.org/10.1016/S0043-1354(00)00380-8

Process Research on Advanced Treatment of Yeast Wastewater Through Enhanced Catalytic Ozonation

XIANGLONG JING* and ZIFU LI
School of Civil & Environmental, 1214 University of Science & Technology Beijing, 100083 Beijing, P.R. China

ABSTRACT: After the secondary treatment of yeast wastewater, the chemical oxygen demand(COD) usually remains very high (approximately 800–1500mg/L) in this effluent, which contains various degradation-resistant substances. Because of the presence of bicarbonate ions, which are the inhibitor of ·OH free radical chain reaction, the direct ozonation of a secondary effluent treatment is limited. In this study, the addition of calcium hydroxide as a pretreatment not only eliminates adverse effects of bicarbonate ions on chain reaction of hydroxyl free radical's generation, but also enhances the indirect ozonation by increasing the pH value up to 11. At the same time, heterogeneous catalytic ozonation treatment is also conducted on the secondary effluent of yeast wastewater by the use of manganese sand (containing manganese dioxide as an effective constituent).The COD of the raw water is reduced to 389 mg/L from 853 mg/L, and the total removal rate reaches 54%. Process analysis is conducted on the pH value, Oxidation-Reduction Potential (ORP) value, and the concentration of dissolved ozone through an online monitoring system. A control method is also proposed to strengthen the catalytic ozonation technology by combining the ozone consumption and COD removal variation.

1. INTRODUCTION

YEAST industry is a new industry in China, with broad prospects for development. At the same time, yeast industry greatly reduces sugar molasses pollution, and the government vigorously supports the growth of yeast enterprises. China's current yeast has been produced by more than 10 enterprises, with an annual volume of about 129 thousand tons (dry yeast). Various volumes of wastewater from production processes are different among enterprises, and the amount of water is in the range of 80–130 m^3 wastewater for each ton of yeast-production. At present, most of Chinese enterprises wastewater treatment processes are planned by Purac and other well-known international water treatment design and construction companies. But the treated sewage cannot be discharged directly to rivers or lakes. The sewage treatment is a continuous process, where the waste water is discharged into the centralized sewage treatment plant as well as the urban domestic sewage treatment plant.

Yeast wastewater has high pollutant concentration, high colors, high amounts of degradation-resistant substances, and high salt content, among others [1]. The main yeast wastewater treatment technology includes the combined biological treatments of anaerobic and aerobic treatments, and the advanced treatment technology of chemical precipitation [2,3]. The COD of the effluent in the biological treatment step is relatively high, (i.e. 800–1500 mg/L) [4,5]. Chemical coagulation process uses the iron salts, but the dosage of ferric salts has two problems: first, the operation cost of iron processing is too high; second, it causes serious corrosion on the storage tank and pipeline. Taking a yeast production enterprise as an example, the operating cost of the whole wastewater treatment process was 30.6 Yuan for each ton of wastewater, and the final effluent quality was COD 600~700 mg/L. At the biological treatment stage wastewater treatment costs average about 5 Yuan per ton, and chemical processing part costs for 25.6 Yuan per ton. (the cost of chemicals is 15.3 Yuan, the sludge treatment costs 6.6 Yuan, wear and tear equipment costs 3.7 Yuan). Economic pressure on corporate environmental protection, and in general, the amount of iron deficiency cause, the effluent COD to reach above 700 mg/L.

Extensive studies have been conducted on ozone, which is used as a strong oxidant in the field of wastewater treatment [6], including the removal of colors [7,8], improvement on biodegradability [9–10], disinfection [11,12], removal of particular pollutants

---

*Author to whom correspondence should be addressed.
E-mail: jasonepoch@163.com; Tel: 0086 18811732010; Fax: 0086 010-62334378

1544-8053/16/02 S101-09

doi:10.12783/issn.1544-8053/13/4/S13

[13–15], and catalytic ozonation [16–18]. However, investigations on this complex system are rare because the oxidation process of the ozone is complex. Many intermediate products also exist, and the influence of the substances in water(such as accelerant and inhibitor) on the reaction cannot be controlled easily. Both the investment cost and operating cost of ozone equipment in practical application are extremely high. The water quality of real production wastewater is highly complex, and the efficient use of ozone is difficult. Therefore, the application of ozone is rare in the field of wastewater treatment in practical application.

In this study, a real yeast wastewater is used as a treatment object. Adding Calcium hydroxide as a pretreatment is used to remove bicarbonate ions in wastewater, thereby eliminating its disadvantageous effect on indirect ozone oxidation, enabling the pH value to be within the alkaline range at the same time, strengthening the treatment effect of catalytic ozonation. Heterogeneous catalytic ozonation technology is applied to the complex system to remove COD. The reaction processes of direct ozone oxidation and enhanced catalytic ozonation are also studied by comparing the online monitoring process parameters. A basis for ozone oxidation process control in the complex system is provided while studying COD removal and ozone consumption through advanced treatment on real wastewater using ozone catalytic oxidation technology.

2. EXPERIMENT PART

2.1. Introduction to Experimental Apparatuses

In the experiment, yeast wastewater is treated by using apparatuses (Figure 1). The contact oxidation tower used is a bubbling type reactor that is 150 cm in height, has an internal diameter of 5 cm, has an effective volume of 2 L, and is made of organic glass. Three electrodes are installed in a constant current device, i.e., a pH value electrode, a liquid-phase ozone concentration electrode and an oxidation-reduction potential electrode. These three electrodes correspond to the three parameters for monitoring the operation parameters in the ozone contact oxidation tower.

The online monitoring system mainly comprises the following parameters and devices: a gas-phase ozone concentration meter with a measurement range of 0–200 mg/L; a liquid-phase ozone concentration meter with a measurement range of 0 (model pH7685); pH measurement range of 0–14.00; ORP measurement range of –1000 mV to +1000 mV; a constant current device for pH, ORP, and liquid-phase ozone simultaneously; a data collection module with a model of FS-1208 and a software kit of TraceDAQ.

2.2. Experimental Water Quality and Material

The water used for the experiment is taken from the

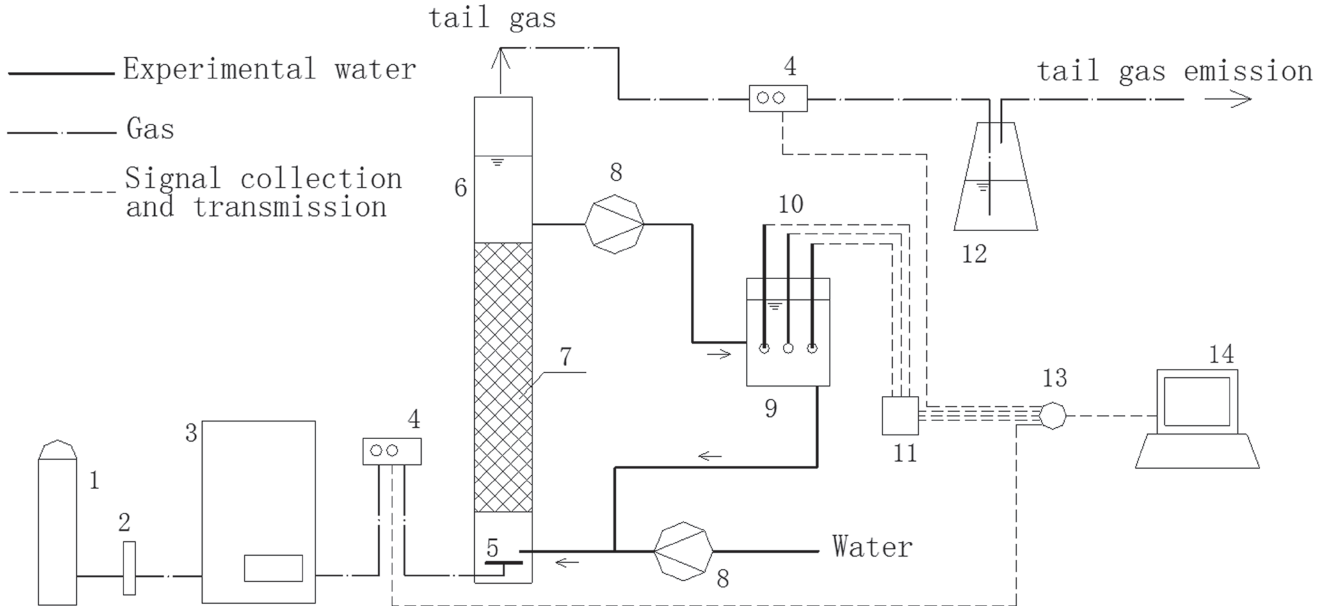

Figure 1. Experimental apparatuses for ozonation and online monitoring system. 1. Oxygen bottle; 2. Gas flow meter; 3. Ozone generator; 4. Gas-phase ozone concentration meter (in&out); 5. Micro porous aerator; 6. Ozone contact oxidation tower; 7. Manganese sand; 8. Feed/circulating pump; 9. Constant current device; 10. pH value, ORP value and liquid-phase ozone sensor; 11. pH value, ORP value and liquid-phase ozone transmitter; 12. KI tail gas absorption bottle; 13. Data collection module; 14. Computer.

Table 1. Composition of Raw Wastewater.

No.	Item	Result	Unit
1	COD	853	mg/L
2	BOD_5	46	mg/L
3	Bicarbonate	187	mg/L
4	Carbonate	< 0.1	mg/L
5	TDS	14300	mg/L
6	pH	8.1	–

effluent of a secondary sedimentation tank at a waste water treatment plant (Hebei Mali Food Co., Ltd.), and the water quality indexes are shown in the following table in detail.

Manganese sand is used as a catalyst. The effective constituent of this catalyst is manganese dioxide. The content of manganese sand is more than 35%, and its density is 2.8 g/cm^3. Calcium hydroxide is used as a pretreating agent. This pretreating agent is of analytical purity. COD determination is conducted by using the HACH fast method (HACH reagent HR1500) in cooperation with a spectrophotometer DR6000.

2.3. Experimental Method

Direct ozone oxidation and ozone catalytic oxidation are both conducted intermittently in the batch reactor. The raw water enters the ozone contact oxidation tower through the water pump. The ozone used in the experiment takes oxygen as a gas source. The oxygen enters the ozone generator to generate ozone. Then, the ozone enters from the micro porous aeration plate at the bottom of the ozone contact oxidation tower. At the upper part of the ozone contact oxidation tower, the tail gas is collected and then discharged into the tail gas absorption bottle containing a potassium iodide solution.

The catalyst used in the experimental process of catalytic ozonation is manganese sand; the effective constituent is manganese dioxide. Manganese sand is placed in the reactor and participates in the reaction in the form of a fixed bed. The system consists of an ozone contact oxidation tower and a loop circuit to form a continuous bubbling column reactor. In the reaction process, a water sample is pumped from the upper part of the contact tower to the constant current device. Thereafter, the water sample is returned to the bottom of the contact tower by backflow to achieve a uniformly mixed state of liquid in the contact tower. This is a continuous cycle and the quality of water sample is almost the same, whether in the contact tower or in the constant current device.

Bicarbonate ions are removed by adding calcium hydroxide. The pretreatment process of calcium hydroxide dosage is conducted in the beaker. The reaction between calcium hydroxide and bicarbonate ions in the solution is shown in the following Equation (1).

$$Ca(OH)_2 + HCO_3^- \rightarrow CaCO_3 \downarrow + H_2O + OH^- \quad (1)$$

The concentration of the bicarbonate ions in raw water is 187 mg/L and is calculated accordingly (227 mg/L of calcium hydroxide is added). A total of 400 mg calcium hydroxide is added to remove the bicarbonate ions in water. After the calcium hydroxide is added, a precipitation appears in the solution. After the precipitation caused by calcium hydroxide, the COD in the supernatant is 792 mg/L, and the pH value is 11.35.

The oxygen flow is kept constant in the experimental process. The ozone generator has an ozone output of 60–80 mg/L and a reaction time of 30 minutes. The amount of ozone entering or exiting from the ozone contact oxidation tower can be monitored by a gas flow meter and a gas-phase ozone concentration meter. This amount can also be obtained via calculations. The total amount of ozone added into the ozone contact oxidation tower increases with time extension.

In the reaction process, the inlet flow (mixed gas, with main components of oxygen and ozone) is stably controlled at 1 L/min and the volume of the liquid that participates in the reaction is constant at 1L. The concentrations of gas-phase ozone and liquid-phase ozone entering or exiting from the reactor are determined by online monitoring meters. Because the concentration of dissolved ozone is very low, the instantaneous variation of dissolved ozone could be negligible. The instantaneous ozone consumption is obtained by the following Equation (2).

$$C = \frac{(C_{G_1} - C_{G_2}) \times Q_G}{v_L} \quad (2)$$

where

C = instantaneous ozone consumption (mg/(L·min))
C_{G_1} = value of ozone concentration at a gas inlet end (mg/L)
C_{G_2} = value of ozone concentration at a gas outlet end (mg/L)
Q_G = gas flow (L/min)

3. RESULT AND DISCUSSION

This study aims to distinguish the process of the advanced treatment of yeast wastewater by strengthening catalytic ozonation. Thus the direct ozone oxidation is selected as a contrast experiment to compare the variations of process parameters, such as pH values, ORP values, and liquid-phase ozone concentration values; the situations in COD removal; the situations in effective utilization of ozone at the two experimental processes.

3.1. The Effect of Pretreatment

The experimental wastewater contains bicarbonate ions, which are an inhibitor of indirect ozone reaction. The indirect reaction involves hydroxyl radicals, which are highly unstable and undergo an immediate reaction with another molecule, in order to obtain the missing electron. In losing an electron, the molecule itself becomes a radical, which will react further, continuing the chain reaction. But bicarbonate radical is a kind of secondary free radical. These free radicals can terminate the chain reaction, inhibit the decomposition of ozone. This reaction is shown in the following Equation (3).

$$OH^{\bullet} + HCO_3^- \rightarrow OH^- + HCO_3^{\bullet} \qquad (3)$$

At the same time, the pH value can also be adjusted to the alkaline range by adding calcium hydroxide. Improving pH values is a method to enhance the effect of ozonation, and the dissociation degree of pollutants in water is improved [19]. To sum up, the pretreatment has two effects: One is the adverse effect of shielding bicarbonate on indirect oxidation, the other is to improve the decomposition of ozone, promoting indirect oxidation.

3.2. Changes of pH Value in the Reaction Process

The activity of ozone reacting with some inorganic substances and dissociative organic substances varies significantly with the variation of pH [19]. The ozonation rate is related to both direct and indirect reaction with the increasing pH value. On one hand, hydroxide ions can catalyze the decomposition of ozone, which is beneficial to indirect reaction. On the other hand, a high pH value can promote the dissociation of pollutants; thus, the direct reaction of ozone becomes a key factor in removing pollutants [20,21]. In the complex system, the influence of a pH value is highly complex.

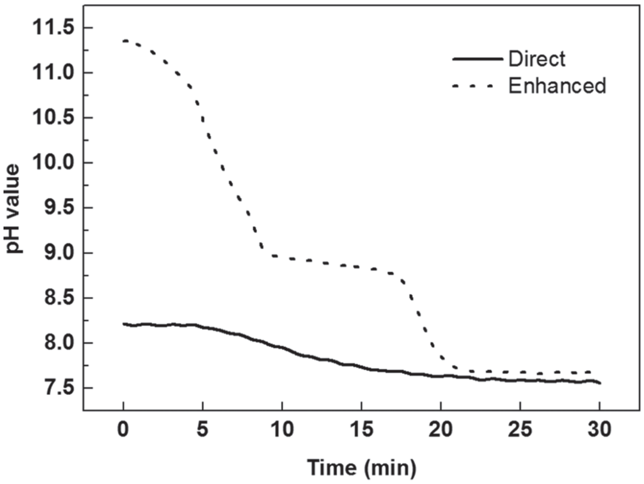

Figure 2. *pH value curve diagram.*

The pH value of the raw water is 8.1. The pH value in the process of direct ozone oxidation is slightly decreased, and the pH value is decreased to 7.8 when the reaction is stopped. The reduction of the pH value within a small range indicates that the reaction of hydroxide ions catalyzing the decomposition of ozone is conducted in water simultaneously. The ozone dissolved in the wastewater reacts with the pollutants mainly through the direct reaction due to the scavenging action of bicarbonate ions [see Equation (3)]. In the process of strengthening catalytic ozonation via calcium hydroxide to conduct pretreatment, the pH value has a large variation range and is decreased from the initial value of 11.35 to a final value of 7.64. After adding the calcium hydroxide, the concentration of the hydroxide ions in the solution during the strengthening process is increased, whereas the bicarbonate ions are converted into the calcium bicarbonate. In alkaline solution, the reaction is generated during the process of adding ozone, as shown in the following Equation (4).

$$O_3 + OH^- \rightarrow O_2^{\circ -} + HO_2^{\circ} \qquad (4)$$

This process shows a chain reaction of ozone decomposition production and hydroxyl free radical generation. The hydroxide ions in water are consumed continually with the reaction, and the pH value of the solution is rapidly reduced. The solution is within the neutral range after the concentration of the hydroxide ions is decreased. Therefore the decomposition reaction of ozone is weakened.

3.3. Changes of ORP Value in the Reaction Process

Every substance in water has oxidation-reduction properties. However, the mutual influence between these different substances forms the macroscopic oxidation-reduction properties. The organic pollutants in water, which can be oxidized with an oxidizer, have reducibility. The higher the concentration of the organic pollutants is, the smaller the value of the oxidation-reduction potential in water is. By contrast, the increase of the concentration of oxidizers, such as dissolved oxygen and dissolved ozone, etc. may cause the oxidation-reduction potential in water to increase. In the field of wastewater treatment, the oxidation-reduction potential is generally used to measure the anaerobic environment and oxygen deficient environment of microorganisms. The oxidation-reduction potential is used to study an advanced oxidation process with Fenton, however, this method is rarely used to study ozonation in the field of wastewater treatment.

The initial ORP value of the raw water is –257 mV. The ORP value is slowly increased with the addition of ozone, and the ORP value is –168 mV until the reaction is finished. The higher the concentration of the pollutants in the raw water is, the higher the concentration of the substances having reducibility is. The reaction of the ozone in the wastewater is mainly a direct reaction. The concentration of the pollutants is gradually decreased with the reaction, and the oxidation-reduction potential is increased to a small extent.

In the process of strengthening catalytic ozonation, the ORP value generates a large fluctuation. After being decreased from 110 mV to 30 mV at the early stage of the reaction, the ORP value is slowly increased to 106 mV. Then, the ORP is suddenly increased to 900 mV and stabilized to 919 mV. This process matches the research process of Chiang *et al.* [24]. In the process of strengthening catalytic ozonation, the direct reaction between the ozone and pollutants, the catalytic reaction between the ozone and the catalyst, and the decomposition reaction between the ozone and the hydroxyl ions exist in the wastewater. The concentration of pollutants, which can conduct the direct reaction with the ozone, is decreased with the consumption of the hydroxyl ions, and the reaction is gradually transitioned to a slow reaction stage from a fast reaction stage. Dissolved ozone appears in the solution. At this moment, the ORP value of the system is the comprehensive reflection of the liquid-phase ozone [25]; the hydroxyl free radicals and pollutants are in a reduction state in water. The ORP value obviously increases at the later stage because of the existence of the liquid-phase ozone.

3.4. Changes of Dissolved Ozone Value in the Reaction Process

The composition of wastewater in the process of ozonation is changed, and its reactivity with ozone is also changed. The process of waste waste ozonation can be divided into two phases. The first phase is at the beginning of the ozonation of efficient stage, whereas the second phase is at the inefficient ozonation rate of declining stage. The presence of ozone solubility in water is an important indication to distinguish the two phases [19,21,26].

In the process of directly adding ozone into the yeast wastewater, the liquid-phase ozone concentra-

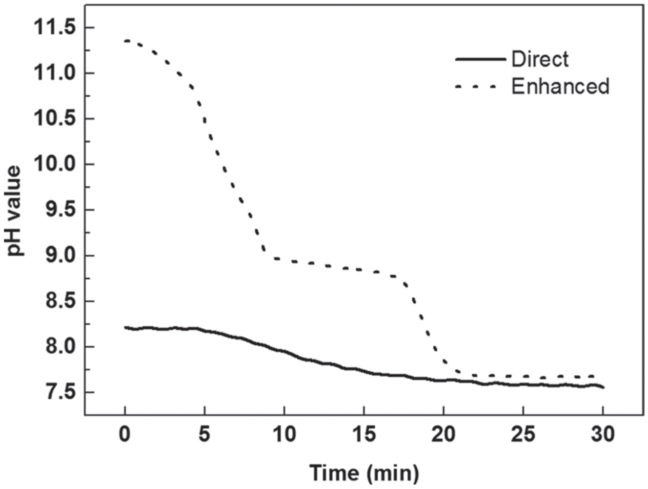

Figure 3. *ORP value curve diagram.*

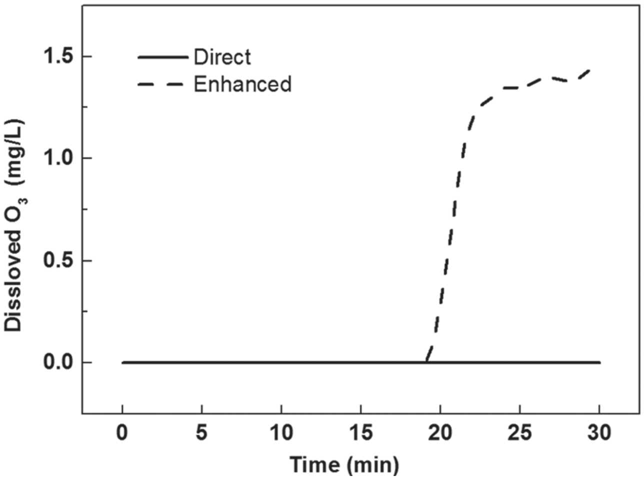

Figure 4. *Liquid-phase ozone concentration curve diagram.*

tion is always zero. The system is also the fast reaction system of the ozone; the substances can react immediately with the ozone existing in water. Finally, the ozone dissolved in water is rapidly decomposed. No liquid-phase ozone is monitored within the time period of reaction.

In the process of strengthening catalytic ozonation, the dissolved ozone appears in the system when the reaction is conducted in 20 minutes. The concentration is also rapidly increased to 1.4 mg/L, and is then kept stable. The appearance of the dissolved ozone in the solution indicates that the reaction between the ozone and the pollutants is transitioned from the fast reaction to the slow reaction. The bicarbonate ions are removed in the system, thereby eliminating the capturing effect on the hydroxyl free radicals. Substances containing free radicals, which are generated through catalysis, rapidly react with pollutants in water, thereby rapidly consuming the pollutants that can conduct direct reaction with the ozone via the ozone and the nonselective hydroxyl free radicals. Thus, the substances that can conduct the fast reaction with the ozone are consumed. At this moment, the system is transitioned from the fast reaction system to the slow reaction system, and the dissolved ozone appears.

3.5. Changes of Ozone Consumption in the Reaction Process

The ozone consumption curve reflects the consumption of ozone through the system in the reaction process. Although the ozone inflow can be stably controlled, the reduction of the concentration of pollutants in water results in the occurrence of the overflow and dissolution of ozone in the reaction process. The ozone consumption can be accurately calculated with the online monitoring system, thereby making an assessment basis for the utilization effect of the ozone.

In the process of direct ozone oxidation, ozone consumption via wastewater is rapidly increased to 58 mg/L. Then, it is slowly reduced to 47 mg/L and is kept stable. In the process of enhanced catalytic ozonation, ozone consumption via wastewater is rapidly increased to 78 mg/L from the beginning of reaction. Then, ozone consumption is slowly reduced to 39 mg/L and is kept stable. The common point of the two processes is that after reaching the maximum value, the ozone consumption is gradually decreased. But in the first 20 minutes of the reaction, the ozone consumption in the enhanced catalytic ozonation process was higher than that of the direct ozonation process. And after 20 minutes, the ozone consumption of the catalytic ozonation process was lower than that of the direct ozonation process.

The direct ozonation reaction mainly includes fast reaction between ozone and pollutants in water. The amount of ozone consumed by the wastewater is gradually decreased with the reaction, which is caused by the gradual decrease of the pollutant concentration. The analysis conducted on the dissolved ozone indicates that the early stage of the process of strengthening catalytic ozonation includes the decomposition reaction of ozone and the direct reaction of ozone. The later stage mainly includes indirect reaction. The ozone consumption indicates that at the early stage of reaction, the amount of ozone consumed by wastewater is obviously increased because of the presence of catalyst and hydroxide ions. At the later stage of reaction, the ozone consumption is less than that in the direct ozonation process, thus indicating that the content of substances capable of consuming ozone in wastewater

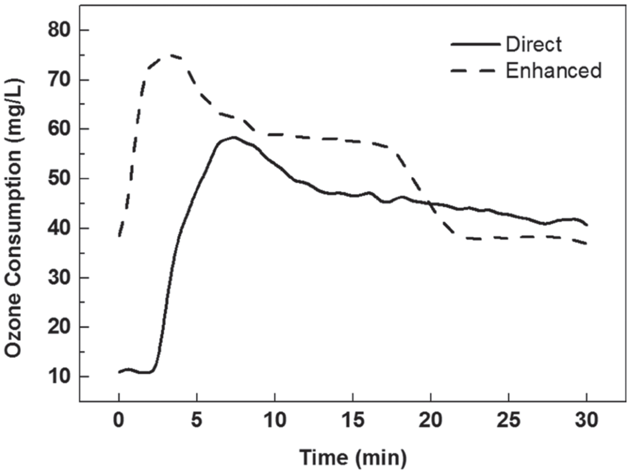

Figure 5. *Ozone consumption curve diagram.*

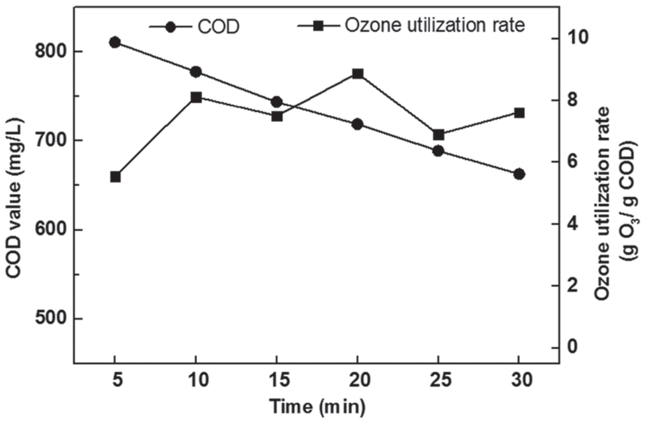

Figure 6. *Curve diagram of ozone utilization effect and COD degradation in direct ozonation process.*

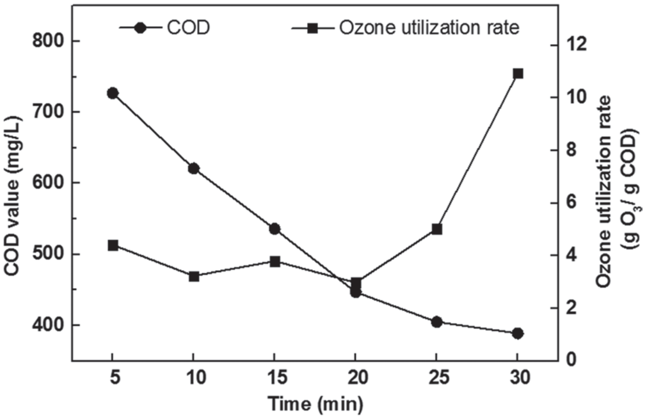

Figure 7. Curve diagram of ozone utilization effect and COD degradation in process of enhanced catalytic ozonation.

is decreased at the later stage of reaction. At the same time, given the transition to a slow reaction stage, the ozone in the system is mainly consumed by catalyst decomposition because a catalyst exists in this process. The ozone consumption is also less than that in the direct oxidation process.

The above figure shows a diagram of COD variation in wastewater and stage ozone consumption in a process of direct ozone oxidation. COD is gradually decreased to 663 mg/L from 853 mg/L, and the total removal rate is 22%. The integral calculation is conducted by taking every 5 minutes as a time unit in the reaction process in obtaining the ozone consumption within the time unit to measure the effective utilization rate of ozone for COD removal at each stage. The effective utilization rate of directly oxidized ozone is not high, which is 5.5 gO_3/g COD at the initial stage of reaction, and a maximum value of 8.8 gO_3/g COD is reached in the reaction process. The effective COD removal through the ozone in the reaction process is not ideal, and this process has no constant COD removal efficiency.

COD in the process of enhanced catalytic ozonation is reduced to 389 mg/L from 792 mg/L, and the removal rate reaches 47%. The ozone utilization rate is relatively stable at the early stage of reaction. It is also decreased to approximately 2.9 gO_3/gCOD from the initial 4.4 gO_3/gCOD, changing in a small range. The ozone utilization rate is also increased to 10.9 gO_3/gCOD at the last 5 minutes. At the first 25 minutes during reaction, the efficiency of COD removal through ozone is the highest. The ozone is decomposed, when the system enters the slow reaction stage because of the catalytic action. However, this process does not directly result in COD removal.

3.6. Study on Control Process

The study on the control process of ozone oxidation reaction in the complex system aims to use ozone effectively in providing a reliable control method for the application of the enhanced catalytic ozonation technology to the advanced treatment of yeast wastewater. The enhanced catalytic ozonation obtains a relatively good treatment effect in the advanced treatment of yeast wastewater. The variation of each process parameter in the reaction process is consistent with the reaction of ozone in water, and the measured values of each parameter at different stages are shown in the following table in detail:

According to the characteristics of different ozone reaction stages, which are obtained by judging the appearance of the dissolved ozone, the pH value is decreased at the fast reaction stage. The ORP value is also increased from a low value; the ozone consumption of wastewater is large; the removal effect of COD is obvious; COD is reduced to 405 mg/L from 792 mg/L (during the first 25 minutes of reaction); and the average utilization rate of ozone is 4.0 $gCOD/gO_3$. At the slow reaction stage, the pH value is stabilized at approximately 7.6; the ORP value is kept at a high level; the ozone consumption of the system is low, which is approximately 37.5 mg/L; and the removal effect of COD is poor, which is only 3.7%.

The process of the advanced treatment of yeast wastewater by strengthening catalytic ozonation indicates that both the pH and the ORP values generate large fluctuations in the reaction process, which can indicate the variation of the wastewater state with the reaction. The appearance of the dissolved ozone indicates that the reaction type of the ozone is converted by stages. Adding the ozone before the dissolved ozone appears is efficient for COD removal in water. However, continuing to add the ozone after the stable state is maintained following the appearance of the dissolved ozone is uneconomical. Therefore, a monitoring system for the pH value, ORP value, and dissolved ozone shall be established in actual production, to guide an effective use of ozone.

4. CONCLUSION

The effective advanced treatment can be conducted on the effluent of the secondary settling tank for yeast wastewater through enhanced catalytic ozonation technology. Bicarbonate ions in raw water can be removed through calcium hydroxide to conduct pretreatment, thereby eliminating the inhibition effect of these ions on indirect ozone oxidation, while adjusting the pH value of the solution to the alkaline range, and strengthening the indirect oxidation function of ozone oxidation. The COD of the effluent is reduced to 389 mg/L from 853 mg/L with manganese sand as a catalyst to conduct a catalytic ozonation reaction and with the calcium hydroxide added for pretreatment; the total removal rate reaches 54%. This technology can reach the COD requirement in the discharge standard of water pollutants for yeast industry (Chinese standard GB25462-2010).

The experimental design of the on-line monitoring system can accurately calculate each moment of the consumption of ozone. The enhanced catalytic ozonation reaction can be divided into two stages by comparing this reaction with COD removal and the consumption of ozone. In this reaction, the average utilization rate of ozone at the high-efficiency stage is 3.8 gO_3/gCOD, and the removal rate of COD is 48% during the first 25 minutes of reaction. The average utilization rate of ozone at the low-efficiency stage is 10.9 gO_3/gCOD, and the removal rate of COD is only 4.0%.

The state variation of the solution during the reaction can be reflected by the pH value and the ORP value. The different stages of the enhanced catalytic ozonation reaction process can be obviously distinguished by the concentration of dissolved ozone. The reaction process can be effectively monitored with the online monitoring system. Considering of the point of view of economy, adding ozone can be stopped when the reaction enters the slow reaction stage, thereby providing a control method reference for the application of the enhanced catalytic ozonation technology in the advanced treatment of yeast wastewater.

5. REFERENCE

1. Pirsaheb, M., Rostamifar, M., Mansouri, A.M., Zinatizadeh, A.A.L. and Sharafi, K. “Performance of an anaerobic baffled reactor (ABR) treating high strength baker's yeast manufacturing wastewater”, *Journal of the Taiwan Institute of Chemical Engineers*, Vol.47, 2015, pp. 137–148. http://dx.doi.org/10.1016/j.jtice.2014.09.029
2. Gengec, E., “Color removal from anaerobic/aerobic treatment effluent of bakery yeast wastewater by polyaniline/beidellite composite materials”, *Journal of Environmental Chemical Engineering*, Vol. 3, No. 4, 2015, pp. 2484–2491. http://dx.doi.org/10.1016/j.jece.2015.09.009
3. Zhou, Y., Z. Liang and Y. Wang, “Decolorization and COD removal of secondary yeast wastewater effluents by coagulation using aluminum sulfate”, *Desalination*, Vol. 225, No .1–3, 2008, pp. 301–311.
4. Gengec, E., M. Kobya, E. Demirbas, A. Akyol and K. Oktor, “Optimization of baker’s yeast wastewater using response surface methodology by electro coagulation”, *Desalination*, Vol.2, No. 3, 2012, pp. 200–209. http://dx.doi.org/10.1016/j.desal.2011.11.023
5. Kalyuzhnyi, S., Gladchenko, M., Starostina, E., Shcherbakov, S. and Versprille, A., “Combined biological and physico-chemical treatment of baker's yeast wastewater”, *Water Sci Technol*, Vol. 52, No. 1–2, 2005, pp. 175–81.
6. Suty, H., De Traversay, C. and Cost, M., “Applications of advanced oxidation processes: present and future”, *Water Sci Technol*, Vol. 4, No. 49, 2004, pp. 227–33. http://dx.doi.org/10.1002/chin.200443274
7. Turhan, K., Durukan, I., Ozturkcan, S A., and Turgut, Z., “Decolorization of textile basic dye in aqueous solution by ozone”, *Dyes and Pigments*, Vol. 92, No. 3, 2012, pp. 897–901. http://dx.doi.org/10.1016/j.dyepig.2011.07.012
8. Gao, M., Zeng, Z., Sun, B., Zou, H., Chen, J. and Shao, L., “Ozonation of azo dye Acid Red 14 in a microporous tube-in-tube microchannel reactor: Decolorization and mechanism”, *Chemosphere*, Vol. 89, No. 2, 2012, pp. 190–197. http://dx.doi.org/10.1016/j.chemosphere.2012.05.083
9. Do Ruel, S., Germirli-Babuna, F., Kabda L, I.K., Insel, G.L. and Orhon, D., “Effect of stream segregation on ozonation for the removal of significant COD fractions from textile wastewater”, *Journal of Chemical Technology & Biotechnology*, Vol. 78, No. 1, 2003, pp. 6–14. http://dx.doi.org/10.1002/jctb.713
10. Dai, L., Jing, X. and Song, Y., “Evaluation of change in the biodegradability of yeast wastewater after ozonation by the method of respiration rate”, *Industrial Water treatment*, Vol. 34, No. 6, 2014, pp. 46–48, 49.
11. Oh, J., Salcedo, D E., Medriano, C A. and Kim, S., “Comparison of different disinfection processes in the effective removal of antibiotic-resistant bacteria and genes”, *J Environ Sci* (China), Vol. 26, No. 6, 2014, pp. 1238–42. http://dx.doi.org/10.1016/S1001-0742(13)60594-X
12. Oh, K.S., Poh, P E., Chong, M N., Gouwanda, D., Lam, W H. and Chee, C Y., “Optimizing the in-line ozone injection and delivery strategy in a multistage pilot-scale greywater treatment system: System validation and cost-benefit analysis”, *Journal of Environmental Chemical Engineering*, Vol. 3, No. 2, 2015, pp. 1146–1151. http://dx.doi.org/10.1016/j.jece.2015.04.022
13. Martins, R.C., Ramos, C.M. and Quinta-Ferreira, R.M., “Low-Cost Catalysts To Enhance Ozone Action on the Depuration of Olive Mill Wastewaters”, *Industrial & Engineering Chemistry Research*, Vol. 53, No. 40, 2014, pp. 15357–15368. http://dx.doi.org/10.1021/ie501187e
14. Nie, Y., Xing, S., Hu, C. and Qu, J., “Efficient Removal of Toxic Pollutants Over Fe–Co/ZrO_2 Bimetallic Catalyst with Ozone”, *Catalysis Letters*, Vol. 142, No. 8, 2012, pp. 1026–1032. http://dx.doi.org/10.1007/s10562-012-0849-6
15. Mudliar, R., Umare, S S., Ramteke, D S. and Wate, S R., “Energy efficient—Advanced oxidation process for treatment of cyanide containing automobile industry wastewater”, *Journal of Hazardous Materials*, Vol. 164, No. 2–3, 2009, pp. 1474–1479. http://dx.doi.org/10.1016/j.jhazmat.2008.09.118
16. Fu, P., Feng, J., Yang, T. and Yang, H., “Comparison of alkyl xanthates degradation in aqueous solution by the O_3 and UV/O_3 processes: Efficiency, mineralization and ozone utilization”, Vol. 81, *Minerals Engineering*, 2015, pp. 128–134. http://dx.doi.org/10.1016/j.mineng.2015.08.001
17. Chen, C., Yoza, B., Chen, H., Li, Q. and Guo, S., “Manganese Sand Ore Is an Economical and Effective Catalyst for Ozonation of Organic Contaminants in Petrochemical Wastewater”, Vol. 226, No. 6, *Water, Air, & Soil Pollution*, 2015. http://dx.doi.org/10.1007/s11270-015-2446-y
18. Yoon, Y., Hwang, Y., Kwon, M., Jung, Y., Hwang, T. and Kang, J., “Application of O_3 and O_3/H_2O_2 as post-treatment processes for color removal in swine wastewater from a membrane filtration system”, *Journal of Industrial and Engineering Chemistry*, Vol. 20, No. 5, 2014, pp. 2801–2805. http://dx.doi.org/10.1016/j.jiec.2013.11.010
19. Gottschalk, C., Libra, J.A. and Saupe, A., 2004, *Ozonation of Water and Waste Water*. Wiley-VCH.
20. Zhuang, H., Han, H., Hou, B., Jia, S. and Zhao, Q., “Heterogeneous catalytic ozonation of biologically pretreated Lurgi coal gasification wastewater using sewage sludge based activated carbon supported manganese and ferric oxides as catalysts.” Vol. 166 *Bioresource Technology*, 2014, pp. 178–186. http://dx.doi.org/10.1016/j.biortech.2014.05.056
21. Von Sonntag, C. and von Guten, U., 2012, *Chemistry of Ozone in Water and Wastewater Treatment: From Basic Principles to Applications*. IWA Publishing.

22. Wu, H. and Wang, S., "Impacts of operating parameters on oxidation-reduction potential and pretreatment efficacy in the pretreatment of printing and dyeing wastewater by Fenton process", Vol. 243, *Journal of Hazardous Materials*, 2012, pp. 86–94. http://dx.doi.org/10.1016/j.jhazmat.2012.10.030
23. Yu, R., Chen, H., Cheng, W., Lin, Y. and Huang, C., "Monitoring of ORP, pH and DO in heterogeneous Fenton oxidation using nZVI as a catalyst for the treatment of azo-dye textile wastewater", Vol. 45, No. 3, *Journal of the Taiwan Institute of Chemical Engineers*, 2014, pp. 947–954.
24. Chiang, Y., Liang, Y., Chang, C. and Chao, A., "Differentiating ozone direct and indirect reactions on decomposition of humic substances", Vol. 65, No. 11, *Chemosphere*, 2006, pp. 2395–2400. http://dx.doi.org/10.1016/j.chemosphere.2006.04.080
25. Buchan, Kevin A H., Martin-Robichaud, Debbie J., and Benfey, Tillmann J., "Measurement of dissolved ozone in sea water: A comparison of methods", Vol. 33, No. 3, *Aquacultural Engineering*, 2005, pp. 225–231.
26. Beltran, F.J., 2007, *Ozone Reaction Kinetics for Water and Wastewater System*. Lewis Publishers.

Decontamination Features and Mechanism Research of Copolymerization Dissolved Air Flotation Process

YONG LEI WANG[1,2,*], BAOZHEN LIU[1,2], KEFENG ZHANG[1,2], HONGBO WANG[1,2], MEI LI[1,2],
RUIBAO JIA[3] AND WUCHANG SONG[3]

[1]*College of Environmental and Municipal Engineering, Shandong Jianzhu University, 250101, Jinan, China*
[2]*Co-Innovation Center of Green Building, 250101, Jinan, China*
[3]*Shandong Province City Water Supply and Drainage Water Quality Monitoring Center, 250021, Jinan, China*

ABSTRACT: In the traditional dissolved air flotation (DAF), micro bubbles generally cannot mesh and adhere to particles efficiently, and the adhesion between microbubbles and particles is not stable, either. In this paper, a self-developed copolymerization dissolved air flotation (Co-DAF) system was proposed to strengthen the copolymerization of condensation reaction during the adhesion of bubbles and flocs, by grading the refluxed dissolved air water, which could significantly enhance the adhesion efficiency and the stability of the bubble-flocs. On this basis, raw water of low turbidity, high algae and high organic contents from the Yellow River reservoir was used as the water supply to verify the effectiveness of the proposed system. The results showed that the average removal rate of turbidity was 95.2%, among, which 93.6% of the particles larger than 2 μm were removed effectively. Meanwhile, the removal rates of COD_{Mn}, UV254, DOC, SUVA and ammonia nitrogen were 43.2%, 48.5%, 38.2%, 20.5 and 77.3%, respectively, and those of organics with molecular weight between 3000–10000 Da and more than 3000 Da were 30.6% and 85%, respectively. However, for those organics with molecular weight less than 1000 Da, only a removal rate of 10% was achieved. During the test, DBPFP could be well controlled by the Co-DAF process, and the removal rates of $CHCl_3$, $CHClBr_2$, $CHCl_2Br$ and $CHBr_3$ were 22.9%, 21.9%, 16.0% and 18.2%, respectively. It was deduced that the mechanisms of removing pollutants by the Co-DAF process mainly included the collision and adhesion effects between micro bubbles-floc particles, the copolymerization between microbubble-flocs and particles, and the adsorption bridging effects among bubble-flocs, microbubbles and particles.

INTRODUCTION

WATER pollution caused by eutrophication is a critical environment problem for the contemporary society. In recent years, the lake algae blooms and reproduction events have occurred frequently around the world and exerted serious influences on the quality of urban water supply, which require the public to pay more attention to the deterioration of water supply and the increase of organic components. On the other hand, traditional water purification process is confronting huge challenges [1]. For example, reservoir storage is usually used as the method of regulating water supply in response to the interruption of the Yellow River, but this kind of water generally has low temperature, low turbidity, high algae concentration and high degree of organic pollution. At low temperatures, the number of particles in the raw water is small during low turbidity period [2]. In terms of composition, the particles are mainly thin and homogeneous colloidal particles with high zeta negative potential and low efficiency of collision [3–4]. What's more, the density of flocs formed after adding flocculants is too small to be precipitated effectively [5]. Therefore, it is difficult to treat the raw water of Yellow River reservoir by traditional sedimentation methods. Flotation is an efficient and rapid solid-liquid separation technology used in the treatment of water supply [6–7], which is especially suitable for disposing the northern micro-polluted raw water with low temperature, low turbidity and high algae content [8–12]. For the reservoir water with a turbidity lower than 100 NTU, the dissolved air flotation (DAF) is a universally applicable technology, and has been widely used in many countries [13–14]. Wang and Liu compared the effect of the DAF with that of the sedimentation process on treating the raw water with a turbidity between 5–15 NTU in the pilot-plant in Tian-

---

*Author to whom correspondence should be addressed.
E-mail: jasonepoch@163.com; Tel: 0086 18811732010; Fax: 0086 010-62334378

1544-8053/16/02 S111-08

doi:10.12783/issn.1544-8053/13/4/S14

jin Area, where the raw water quality was identified as low-turbidity and seasonal algae-rich [10–11], and the treatment results of the DAF were desirable. However, in the traditional DAF, the dissolved air water only reflows once. In other words, the dissolved air water reflows in the DAF tank after the raw water is fully coagulated, so that those microbubbles are not involved in the particle coagulation process. Furthermore, the microbubbles may collide and conglutinate with destabilized particles, which is equivalent to a secondary flocculation of microbubbles and flocs. Consequently, the flocculation process is longer, and the copolymerization of microbubbles and flocs cannot be exerted during the water purification process. That is to say, the adhesion of microbubbles and flocs is inefficiency, and the effective utilization rate of microbubbles is low. In fact, the actual consumption of the dissolved air water is very high, which is far more than the theoretical consumption calculated by the concentration of solid particles in water [15]. Therefore, the traditional DAF can be optimized in many aspects, such as the structure of contact room, the water flow characteristics, the foam state and other aspects of adhesion. In order to solve numerous problems of the traditional DAF technology, e.g., the low adhesion efficiency of particles, the undesirable trapping effects, the unstable adhesion of foam and so on [16–17], a new copolymerization dissolved air flotation (Co-DAF) process was developed in this paper. The Co-DAF process was based on the characteristics of Jinan Yellow River reservoir water supply, such as low turbidity and high organic matter, and added the refluxed water separately to enhance the flotation copolymerization adhesion. Subsequently, the operation characteristics of the Co-DAF process and the copolymerization mechanisms of microbubbles were analyzed. Finally, some technical support was provided for the popularization and application of the Co-DAF process.

APPARATUS AND METHODOLOGY

Apparatus and Methodology

Figure 1 shows the schematic of the experimental apparatus. The apparatus consists of a coagulation system, a dissolved air system and an outgassing system. Coagulation and flotation reactions are carried out in a reaction cell with an effective volume of 8 L. The dissolved air water intakes and sample connections are placed in the bottom section of the reaction cell. The stirring speed and time are controlled by a stirring motor with adjustable speed (60KTYZ) in the coagulation-mixing system. A TS type release is used in the outgassing system. In addition, to ensure the dissolved air water can stably flow into the process during the test, a diverter valve is equipped in water outlet end.

The typical test procedures can be depicted as follows. Firstly, flocculants are added into the injected raw water, and then the mixture is rapidly agitated for 90 s. Afterwards, the mixture is stirred for 2 min with one-grade rotate speed, and the dissolved air water is refluxed. Subsequently, the residual mixture is stirred for 4 min with two-grade rotate speed to form copolymer bubble flocs through the copolymerization of microbubbles with flocs, after which the dissolved air water is refluxed again. Finally, after standing for a cer-

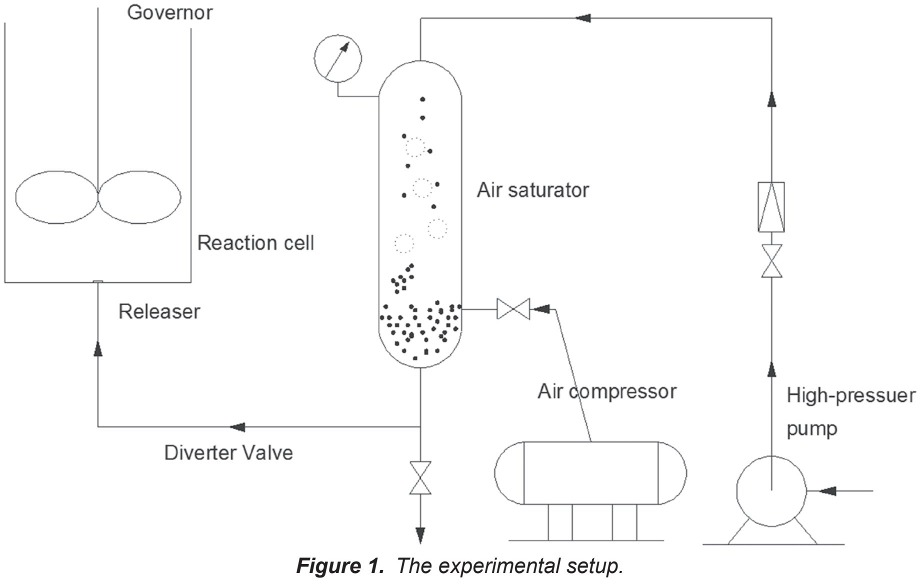

Figure 1. *The experimental setup.*

Table 1. Raw Water Quality.

Parameter	Value	Parameter	Value
pH	8.08~8.24	COD_{Mn} (mg/L)	5.65~7.26
Turbidity (NTU)	13.3~20.2	UV_{254} (cm^{-1})	0.145~0.152
DOC (mg/L)	6.95~7.78	NH_3-N (mg/L)	0.352~0.458
Particulate matter (CNT/mL)	85058~96736	SUVA	0.018~0.021

tain time, water samples are taken from the bottom of the tank to determine water quality indicators.

The main process parameters are as follows. The dosage of the coagulant, polyaluminium ferric chloride (PAFC), is 5 mg/L (calculated as Al3+). The pressure of the dissolved air is 0.38 MPa. The total reflux rate of the dissolved air water is 12%, and the first reflux accounts for 1/3. The stirring velocity gradient of one-grade rotate speed is 63 $^{-1}$, and the copolymerization turbulence intensity is 10 s^{-1}.

Raw Water Quality

Raw water was derived from the Queshan Yellow River Reservoir in Jinan. The test was conducted from October to December, and the raw water temperature varied between 5.0- 22.0 ?. Table 1 provides the main indicators for the raw water quality.

Test Items and Methods

According to the *Water and Wastewater Monitoring and Analysis Method (Fourth Edition)*, pH value was determined by the PHS-3D pH tester; turbidity was measured using the TSZ-400A scattering turbidimeter; CODMn was determined by the acidic potassium permanganate method; UV254 was measured by the TU-1810 UV-vis spectrophotometer; DOC was determined by the SHIMADZU TOC-VCPH-CPN; determination of ammonia Nitrogen Uncertainty by Nessler's Reagent Photometer; the particulate count was determined by the particle counter of GREAN IBR Versa Count. In addition, the specific detection methods are shown in Table 2.

RESULTS

Removal Characteristics

Turbidity Removal

As an alternative parameter of particulate matter and pathogenic microorganisms, turbidity can generally indicate the total removal of the particulate matter and pathogenic microorganisms. Figure 2 shows the turbidity removal in the Co-DAF process. As can be seen, when the raw water turbidity is in the range of 13.3–20.2 NTU, the effluent turbidity of the Co-DAF process keeps stable between 0.565–1.08 NTU, with an average removal rate of 95.2%. After separate injection of microbubbles, the removal of turbidity can be effectively enhanced. In fact, the coagulation process of Co-DAF is a micro-flocculation process, and the size of the produced flocs is relatively small. Meanwhile, the dissolved air water is refluxed in different grades, and the microbubbles can directly participate in the flocculation process, thus promoting the copolymerization of microbubbles and flocs. As a result, the collision and adhesion efficiency of bubbles and flocs can be significantly improved, thus enhancing the stability of the bubble-flocs. In addition, the produced scum is not easy to sink, which strengthens the effect of air flotation.

Wang studied the treatment of high algae-laden raw water with a turbidity of 5.62–5.74 NTU by the coagulation/flotation process, and the removal rate of turbidity was reported as only 90.1% [18]. Liu treated the micro-polluted raw water using the enhanced coagulation DAF, and the removal rate of turbidity was found to be 80–90%, with a low turbidity of 4–6 NTU. Therefore, it can be deduced that the Co-DAF process, which has a remarkable water purification effect, is superior to the traditional DAF [12]. Since the dissolved air wa-

Table 2. Test Items and Methods.

Parameter	Methods	Parameter	Methods
pH	Glass electrode method	Turbidity	TSZ-400A scattered light turbidimeter
UV_{254}	Spectrophotometry	CODMn	Acidic potassium permanganate method
DOC	TOC-VCPH-CPN	Organic molecular weight distribution	Membrane filtration, TOC analyzer
Particulate matter	Particle counter	NH_3-N	Nessler's reagent colorimetric method

The organic molecular weight distribution can be measured as follows. Firstly, water sample flowed successively through the ultrafiltration membrane with a molecular weight distribution of 100 kDa, 50 kDa, 30 kDa, 10 kDa, 5 kDa and 1 kDa. Thus, water samples of different molecular weight distributions were obtained. Finally, the TOC value can be measured by the SHIMADZU TOC-VCPH-CPN total organic carbon analyzer.

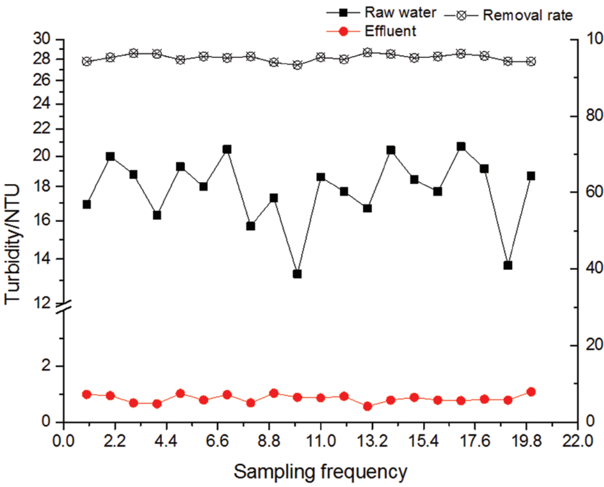

Figure 2. *Turbidity removal in the Co-DAF process.*

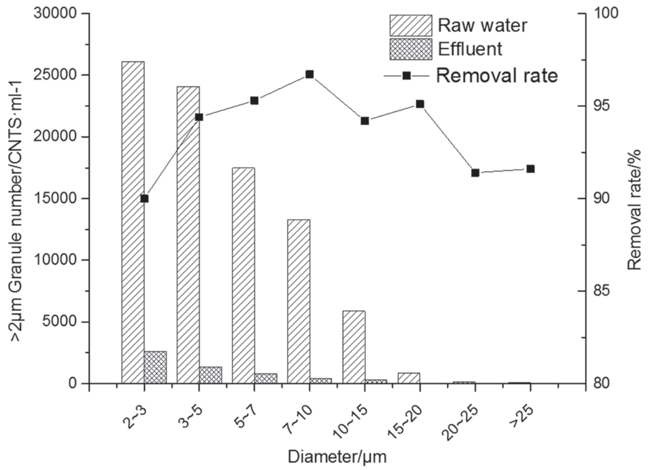

Figure 3. *Particulate matter removal in the Co-DAF process.*

ter is refluxed separately in the Co-DAF process, colloidal particles can be retained in the initial setting time during the first reflux. Destabilized colloidal particles can provide bubbles for the dissolved air water to form "nuclear" sites, which are conducive to the formation of microbubbles. In the meantime, microbubbles and destabilized particles may copolymerize and grow up together. Thus, bubble-flocs can be formed through bubbles wrapping flocs, which are easier to be floated and then removed.

Particulate Matter Removal

Particle detection is the main method for detecting and controlling particulate materials, which can effectively reflect the size of particles larger than 1 μm, thus covering the shortage of turbidity detection. Figure 3 shows the removal characteristics of particulate matter in the Co-DAF process. As can be seen, the Co-DAF process is very efficient in removing particles larger than 2 μm. The particulate matter decreases from 87942 to 5597 CNTS/mL, and the removal rate is as high as 93.6%. Herein, the removal rate of the particles with the size lager than 2 μm is between 90–96.7%, which indicates the good removal effect of the Co-DAF process on the particles larger than 2 μm. Figure 4 reflects the distribution of the particles greater than 2 μm in the effluent. It can be seen that the number of particles with different diameters decreases with the increase of particle diameter. In particular, the particles of 2–5 μm account for 75% of the total, and those of 2–10 μm accounts for more than 90%. That is to say, the Co-DAF process has a satisfactory performance in the removal of the particles between 2–10 μm.

Organics and NH_3-N Removal

Organic matter and ammonia are the major oxide consumable pollutants in water. Organic matter is the main source that causes water to produce odor and chroma, while ammonia is the nutrient in water that can lead to eutrophication phenomenon. As shown in Table 3, NH_3-N content in the raw water is 0.458 $mg \cdot L^{-1}$ (less than 0.5 $mg \cdot L^{-1}$), and the raw water quality is in the range of the standard of *Environmental Quality Standards for Surface Water* (II TP, GB 3838-2002) [19]. The Co-DAF process is very efficient in the removal of NH_3-N, and the average removal rate can be up to 77.3%. Meanwhile, the COD_{Mn} and DOC can also be removed by the Co-DAF process, and the average removal rates reach to 43% and 38.2%, respectively. Similarly, the process also has a good removal effect

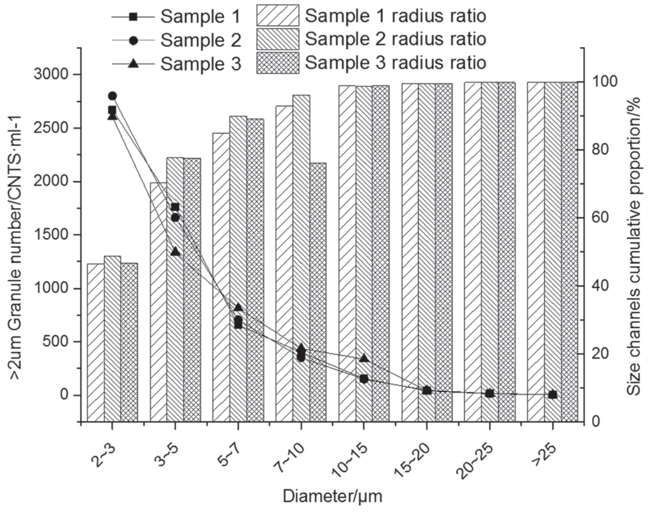

Figure 4. *Effluent particle distribution.*

Table 3. Organics and NH_3-N Removal Rules.

	Detection Index							
Water Samples	**NH_3-H**	**COD_{MN}**	**DOC**	**>30000**	**10000–30000**	**3000–1000**	**1000–3000**	**<1000**
Units	$mg·L^{–1}$	$mg·L^{–1}$	$mg·L^{–1}$	$mg·L^{–1}$	$mg·L^{–1}$	$mg·L^{–1}$	$mg·L^{–1}$	$mg·L^{–1}$
Raw water	0.458	6.48	7.78	1.2	1.05	3.69	0.99	0.85
Effluent	0.104	3.69	4.8	0.159	0.568	2.56	0.752	0.765
Removal rate, %	77	43	38.2	87.1	45.9	30.6	24	10

on organic matter, especially for the organics with molecular weight greater than 3000 Da. By monitoring the content of organics with different molecular weights, the removal rate can reach to 85%. It is noticed that the capacity of the Co-DAF removing organics decreases with the decrease of organic molecular weight. The removal rate of organic matter with molecular weight between 3000–10000 Da can reach to 30.6%, whereas that of organic matter with molecular weight less than 10000 Da is only 10%. In this study, the removal rate of organic matter with molecular weight larger than 3000 Da is approximately 35% in the Co-DAF process; in addition, the organic compounds with molecular weight less than 1000 Da can be removed by subsequent processes such as biofilter and active carbon adsorption. Recent studies found that the removal effect of biofilter on the DOC with molecular weight less than 3000 Da was significant, and that the removal rates of organic compounds with molecular weight less than 500 Da and between 500–1000 Da were 54.9% and 36.1% respectively [20]. Besides, the ability of activated carbon to absorb organic compounds with molecular weight between 500–3000 Da was strong. According to Lu's research, the removal rate of 500–1000 Da was 86.7%, and that of 1000–3000 Da was approximately 70% [21].

Disinfection By-products Formation Potential (DBPFP) Removal

Disinfectants such as chlorines and chlorine dioxides can form disinfection by-products (DBPs), and react with the non-active microbial pathogens such as trihalomethanes (THMs) and haloacetic acids (HAAs) when added to drinking water. Natural organic matter (NOM) and disinfectant reaction are the major factors in the production of DBPs. Therefore, the key to control DBPs is to reduce the NOM in water, especially the DBP precursors and the dissolved organic matter (DOC). Investigating the removal effect of the Co-DAF process on DBP precursors, DOC, UV_{254}, SUVA and DBP were selected as alternative parameters of DBPFP, and the test results before and after the Co-DAF process are shown in Table 4. As can be seen, the removal efficiency on DOC, UV_{254} and SUVA follows the order of UV > DOC > SUVA, and the removal rates are 48.5%, 36.2% and 20.5%, respectively. Meanwhile, the Co-DAF process has a good inhibitory effect on the removal rate of DBPs, and the removal rates of $CHCl_3$, $CHClBr_2$, $CHCl_2Br$ and $CHBr_3$ are 22.9%, 21.9%, 16% and 18.2%, respectively. Comparing these different alternative parameters of DBPFP, it can be concluded that SUVA index is the most relevant parameter to DBPs, since SUVA can reflect the humification degree of organic matter, the relative content of aromatic organics or unsaturated double bond organics, and the degree of aromatic structure, whereas UV_{254} mainly characterizes the content of aromatic compounds in DOC or organics with conjugated double bonds.

Mechanism Analysis

Copolymerization of microbubbles refers to that the microbubbles directly participate in the floccula-

Table 3. DBPFP Removal of the Co-DAF Process.

	Detection Index						
Water Samples	**DOC**	**UV_{254}**	**SUVA**	**$CHCl_3$**	**$CHClBr_2$**	**$CHCl_2Br$**	**$CHBr_3$**
Units	$mg·L^{–1}$	$cm^{–1}$	—	$mg·L^{–1}$	$mg·L^{–1}$	$mg·L^{–1}$	$mg·L^{–1}$
Raw water	7.06	0.152	0.022	0.035	0.032	0.025	0.011
Effluent	4.36	0.077	0.017	0.027	0.025	0.021	0.009
Removal rate, %	38.2	48.5	20.5	22.9	21.9	16.0	18.2

tion process and meanwhile copolymerize with flocs to grow up gradually. The micro-flocs serve as the nuclei during the generation process of bubbles, and finally form flocs-microbubble particles. This can significantly improve the collision and adhesion efficiency of bubbles and flocs, and meanwhile enhances the stability of the bubble-flocs.

Bubble-flocs Observation

In order to observe the adhesion state of microbubbles and floc particles during the flotation process in the Co-DAF, the clarifying mechanism of flotation water was analyzed from the microscopic perspective. During the test, water samples at every reaction stage were observed by the microscope, and the results are shown in Figure 5.

As can be seen, particles in raw water are in suspension state or colloidal state before coagulation [Figure 5(A)]. Under the effects of Brownian motion and charge repulsion, particles acquire a “gathering stability” in the water, so that they do not agglomerate with each other. In the initial setting process, charge neutralization between the coagulants charged particles and the negatively charged colloidal particles occurs, and the colloidal particles begin to gather. Here, the major coagulation mechanisms are charge neutralization and adsorption bridging action, whereas the net rooling-sweeping action between particles is weak. As shown in Figure 5(B), there are almost no linear or mesh flocs in the initial flocculation water. During the primary reflux process of dissolved air water, the destabilized particles can provide bubbles for the reflux water to form “nucleation” sites; in addition, the floc particles and microbubbles are both hydrophobic, with a large specific surface and excess free surface energy. Hence, the collision efficiency of flocs and microbubbles can be increased by stirring in low G values. As a result, the copolymers of microbubbles and flocs grow up gradually, and form abundant bubble-flocs, as shown in Figure 5(C). After the secondary reflux of dissolved air water, microbubbles and flocs are flocculated once again. Under the action of in-phase flocculation, microbubbles, particles and flocs collide with each other, and the bubble-flocs grow bigger and bigger under the combined effects of charge neutralization, adsorption bridging and net rooling-sweeping. As shown in Figure 5(D), bubble-flocs are mostly network-like bubble-floc colloidal particles at this stage.

Mechanism of Particle Removal

Water turbidity is mainly produced by the suspended particulate matter and colloids, which are mainly composed of the suspended inorganic and organic matter, soil particles, microbial particles and other suspended particles. Water purification mechanism of the traditional DAF is mainly the collision and adhesion of raw water to the injected microbubbles during coagulation pretreatment, which can form coarse flocks through coagulant charge neutralization and destabilization, adsorption bridging or flocculation with particulate matter. Then the coarse flocks are separated and removed by flotation. The Co-DAF is different from the traditional DAF. Firstly, the crucial differences lie in the dissolved gas and the graded water reflux, which can shorten the primary flocculation time and promote microbubbles to directly participate in the coagulation process. Then, with the complete combination of microbubbles and large floc grains, copolymerized floc bubbles are generated in the middle of floc grains, as shown in Figure 5(D). Hence, the cohesion of bubbles in the Co-DAF process can develop thoroughly. On the other hand, the bubbles can firmly adhere to floc grains, so that the flocculated particles with air are stable enough to keep floating in the flotation progress. During the copolymerization process of the Co-DAF, the dissolved air water is injected after initial coagulation,

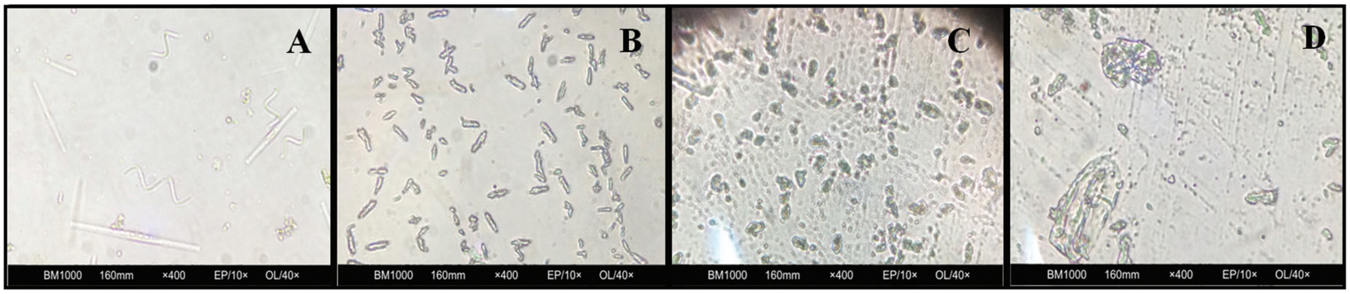

Figure 5. *Observation of flocs at different reaction stages under the microscope: A. Particles in raw water; B. Particles in initial flocculation water; C. Adhesion morphology of microbubbles and floc after the first injection of dissolved air water; D. Morphology of bubble-flocs after the secondary injection of dissolved air water.*

and the main coagulation mechanisms are destabilization and electrical neutralization, rather than adsorption bridging and sweep flocculation. During the first recycle of dissolved air water, the primary mechanism of microbubbles adhering to particles is the collision and adhesion between microbubbles and flocs. After the secondary injection of dissolved air water, the main clarification mechanisms include the collision and adhesion between microbubbles and flocs, the adsorption bridging and the sweep flocculation of bubble-flocs and floc-microbubble-particles.

Removal Mechanism of Organics and Ammonia Nitrogen

Our experimental results show that the Co-DAF process has a good effect on the removal of organics, and the removal rate is about 35%, which conforms to the organic matter removal rate of 30–40% in the conventional treatment method. In the Co-DAF process, the removal of organics mainly depends on the pre-processing during the coagulation stage, and the main mechanisms include: (1) the charge neutralization, destabilization and cohesion of positively charged metal ions and colloidal organic matter; (2) metal ions and soluble organic molecules forming insoluble complex precipitation and destabilization; (3) synergistic floation effect by surface adsorbing heterogeneous structure molecules.

Figure 6 shows the distribution of organic matter before and after the Co-DAF process. As can be seen, before the Co-DAF process, the organic molecular weight of the Yellow River reservoir raw water mainly distribute in the range of 3000–10000 Da (about 50%), and the organic matter with molecular weight above 3000 Da accounts for about 70% of the total. After the Co-DAF process, the removal rate of organic compounds with molecular weight above 3000 Da can reach to 85%, but that of organic compounds with organic molecular weight less than 1000 Da is below 10%. That is to say, there is basically no removal of small organic molecules; the effluent water even shows an increasing number of small organic molecules compared with raw water. It is found that the removal mechanism of different forms of organic matter is different. Organic matter with molecular weight above 1000 Da mainly exists in the colloidal form, and its major removal mechanisms are (1) and (3). These organics have strong hydrophilicity, and only a small portion of them can be removed based on the mechanisms of (2) and (3). With the increase of molecular weight, the hydrophobility of organic matter becomes stronger, so that it can be adsorbed on the surface of alumen ustum more easily, thus achieving a higher removal rate. The organics with molecular weight between 3000–10000 Da exist in the solution state or colloidal form, and the removal mechanisms involve the combined effects of destabilization cohesion, aggregation precipitation and surface adsorption, which can completely remove these organics. The mechanism of removing NH_3-N in the traditional DAF depends mainly on the biosorption of nitrifying bacteria, which can oxidize ammonia to nitrite and then to nitrate. This process needs enough dissolved oxygen (DO) and a better environment for the biofilm growth. However, the reaction time in the contract zone of the traditional DAF is so short that there are no biofilm conditions. In contrast, the removal of NH_3-N by the Co-DAF depends mainly on the cohesion effect. The NH_3-N, adhered and wrapped by colloidal particles, can be destabilized, condensed and polymerized during the coagulation stage, and then adsorbed on the surface of alumen ustum. Finally, it can be removed by the adhesion of microbubbles through the floating process.

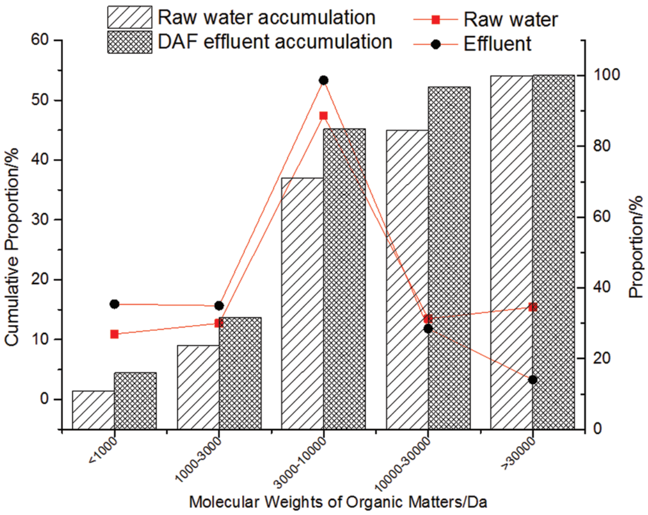

Figure 6. *Distribution of organic matter before and after the Co-DAF process.*

CONCLUSIONS

1. The Co-DAF process is particularly effective in the removal of turbidity and particles when the turbidity of raw water is between 13.3–20.2 NTU. The average removal efficiency of turbidity is 95.2%, and the average removal rate of particles with size greater than 2 μm is 93.6%.

2. The Co-DAF process has a good removal effect on organic compounds and NH_3-N, and meanwhile has a good inhibitory effect on DBPFP. The average removal rates of COD_{Mn}, UV_{254}, DOC, SUVA and NH_3-N are 43.2%, 48.5%, 38.2%, 20.5% and 77.3% respectively, and the removal rates of $CHCl_3$, $CHClBr_2$, $CHCl_2Br$ and $CHBr_3$ are 22.9%, 21.9%, 16% and 18.2% respectively. It is noticed that the removal rate of organic compounds with molecular weight above 3000 Da can reach to 85%, but only 10% of organic compounds with molecular weight less than 1000 Da is removed during the Co-DAF process.
3. In the first reflux process of dissolved air water, the main adhesion mechanism of the flotation is the adhesion, collision and copolymerization between microbubbles and floc particles; during the secondary reflux, the main adhesion mechanisms include the collision adhesion between the microbubbles and floc particles, the adsorption bridging and the sweep flocculation of flocs-microbubbles-particles. These adhesion mechanisms of the Co-DAF process are different from those of the traditional DAF.

ACKNOWLEDGEMENTS

This work was financially supported by the Natural Science Foundation of Shandong Province ZR2016EEM32, Ministry of Housing and Urban-Rural Development Technology Projects (2014-K5-026), Shandong Province Science and Technology Development Projects (2014GSF120003) Shandong Province Key Development Projects (2015GSF117003), the Doctoral Fund of Shan-dong Jianzhu University in 2015(XNBS1511), the Universities Innovation Programmer of Jinan City (201303076) and the Natural Science Foundation of Shandong Province (ZR2014EEM009).

REFERENCES

1. Qu, J. H., “Thought on the main problems of drinking water quality in the future of China,” *J. Water & Wastewater Engineering*, Vol. 34, No. 4, pp. 1–3.
2. Song, W. C., Chen, J. Q., Shi, R. Q., *et al.*, “Full-Scale Test And Study On Enhanced Coagulation For Water Plants With Conventional Process During The Period of Low temperature and Low turbidity”, *J. Technology of Water Treatment*, Vol. 41, No. 06, 2015, pp. 71–74.
3. Edzwald, J. K., “Coagulation in drinking water treatment: Particles, organics and coagulants”, *J. Water Science and Technology*, Vol. 27, No. 11, 1993, pp. 21–35.
4. Matilainen, A., “Vepsäläinen, M., Sillanpää, M., Natural organic matter removal by coaglation during drinking water treatment: A review”, *J. Advances in Colloid and Interface Science*, Vol. 159, No. 2, 2010, pp.189–197. http://dx.doi.org/10.1016/j.cis.2010.06.007
5. Edzwald, J. K., “Dissolved air flotation and me”, *J. Water Research*, Vol. 44, No. 7, 2010, pp. 2077–2106. http://dx.doi.org/10.1016/j.watres.2009.12.040
6. Edzwald, J., Haarhoff, J. 2011. *Dissolved air flotation for water clarification*, McGraw Hill Professional.
7. Lundgren, H., “Theory and practice of dissolved-air flotation”, *J. Journal Filtration and Separation*, Vol. 13, No. 1, 1976, pp. 24–28.
8. Zou, J., Zhu, J. T., Pan, C., *et al.*, “Comparative Study of Dissolved Air Flotation and Sedimentation Process for Treating Reservoir Water with Low Temperature, Low Turbidity and High Natural Organic Matter”, *J. Applied Mechanics and Materials*, Vol. 71, 2011, pp. 2767–2771. http://dx.doi.org/10.4028/www.scientific.net/AMM.71-78.2767
9. Wang, Y., Li, J., Zhang, K., *et al.*, “Experimental research on treating reservoir water contaminated by algae using GAC-sand dual media filter flofilter”, *J. CIESC Journal*, Vol. 65, No. 6, 2014, pp. 2335–2343.
10. Liu, S.-P. 2007. *Pilot Study on Micro-polluted Raw Water Treatment by Enhanced Coagulation-DAF process*, Tianjin:Nankai University.
11. Wu, Y.-B., Wang, Q.-S., Wang, Y.-H., *et al.*, “Optimization of Parameters in Coagulation/Flotation Process for Algae Removal”, *J. China Water & Wastewater*, Vol. 24, No. 3, 2008, pp. 5-99.
12. Liu, S. P., Pilot Study on Micro-polluted Raw Water Treatment by Enhanced Coagulation-DAF process, doctor`s degree thesis, PA: Nankai University.
13. Martinez, F. M., Cabrales, N. J. M., Rincon, J. A. D., Process to reduce the chemical oxygen demand, total organic carbon, and total solids in vinasse by electro-flotation/oxidation: U.S. Patent 8,425,755, 2013-4-23.
14. Hu, H., Li, G., Liu, J., *et al.*, “Experimental Study on Improving Recovery of Copper from a Copper Ore by Carrier Flotation”, *J. Mining Research and Development*, Vol. 1, 2013, pp. 009.
15. Firouzi, M., Nguyen, A. V., Hashemabadi, S. H., “The effect of microhydrodynamics on bubble- particle collision interaction”, *J. Minerals Engineering*, Vol. 24, No. 9, 2011, pp. 973–986. http://dx.doi.org/10.1016/j.mineng.2011.04.005
16. Guo, J., Wang, Y., Li, D., *et al.*, “Counterflow co-flocculation flotation for water purification”, *J. Journal of Environmental Science and Health, Part A*, Vol.38, No. 5, 2003, pp. 923–934. http://dx.doi.org/10.1081/ESE-120018601
17. Eades, A., Brignall, W. J., “Counter-current dissolved air flotation/filtration”, *J. Water Science and Technology*, Vol. 31, No. 3, 1995, pp. 173–178. http://dx.doi.org/10.1016/0273-1223(95)00215-9
18. Wu, Y. b., Wang, Q. S., Wang, Y. H., *et al.*, “Optimization of Parameters in Coagulation/Flotation Process for Algae Removal”, *J. China Water & Wastewater*, Vol. 24, No. 3, 2008, pp. 95–99.
19. “Environmental quality standards for surface water”, *J. China Environmental Protection Industry*, No. 6, 2002, pp. 8–9.
20. Ling, J. Q., Ling L. Z., Wang Z. S., “Removal of Different Molecular Weights Organics from A Surface Water by Bio-filter and Conventional Treatment”, *J. Chongqing Environmental Science*, Vol. 25, No. 12, 2003, pp. 46–47.
21. Luo, X. H., Cao, L. L., Wang, Z. S., “Study on the removal of different molecular-weight organics by water purification process”, *J. China Environmental Science*, Vol. 18, No. 4, 1998, pp. 341–344.

The Effects of Indoor Activities on Pollution Characteristics of Air Particles in an Office Environment

GUOZHONG ZHENG*, ZHENGZHENG ZHAO, ZHIHAO LI and YUEFEN GAO
North China Electric Power University, Mailbox 62, 619 Yonghua North Street, Baoding 071003, China

ABSTRACT: This article compares the effects of different indoor activities on pollution characteristics of air particles in an office. Some indoor activities, such as smoking, mopping floor, wiping table, sweeping floor, walking and air humidification, were studied. The dynamical changes of the mass concentration and the particle number concentration over time were analyzed. The concept of area is introduced to rank the health hazards. The results indicate that the effects of the humidification on the indoor particulate matter are the most significant, then the sweeping floor, smoking, mopping floor, and the walking and wiping table are the least. For indoor particulate matter, the guideline value system for PM1.0 and the exposure time can be set as 1 hour.

INTRODUCTION

In modern society, people spend most time in the room [1]. Indoor air quality directly influences peoples' health. Indoor air particle pollution mainly refers to the particle with size less than 10 μm, in which particulate matter 2.5 (PM2.5) can absorb a variety of toxic substances and lead to a variety of human diseases.

Particulate, a carrier of various substances, can be suspended in the air for a long time [2]. The aerodynamic diameter is used to indicate the particle size of the particulate matter. According to the aerodynamic diameter, the particulate matter (PM) can be categorized into: total suspended particles (aerodynamic diameter < 100 μm), inhalable coarse particles (diameter < 10 μm, namely PM10.0), fine particles (diameter < 2.5 μm, namely PM2.5) and ultrafine particles (diameter < 1.0 μm, namely PM1.0).

Related researches indicated that long-term or short-term exposure to the polluted air both would cause the morbidity and mortality to rise [2–4]. Mar *et al.* [5] indicated that number of first aid in asthma of children was closely affected by the pollution level of ultrafine particles in Seattle city. Pope *et al.* [6] found that PM2.5 can induce the incidence and morbidity of respiratory diseases and cardiovascular system, and lead to arrhythmia, heart failure, ischemic heart disease. In addition to above harm, air pollution can also affect the cardiopulmonary and reproductive system and even lead to cancer [7]. It can be seen that the indoor particulate matter has a serious impact on human health, especially fine particles.

Many scientists investigated the effects of indoor pollution sources on indoor environment, such as smoking [8–11], vacuuming [12–14], and cleaning [15–16]. Smoking is one of the indoor pollution sources and greatly affects peoples' health [8–11]. However studies on the cleaning, walking and air humidification are limited. In addition, systematic studies on the effects of the indoor activities on pollution characteristics are rare. In this paper, the pollution characteristics and dynamic changes of indoor particulate matter in each indoor activity are studied. It is conducive to find out the main factors of indoor pollution and put forward specific means for improving the indoor air quality. It can also give important reference for the revision of the indoor air quality standard.

EXPERIMENT AND METHODS

Experiment Site

The experimental subject is an office on the third floor in a university office building (100m away from the street in urban areas). The office area is about 38 m^2 (7.6 m × 5.1 m). There are four windows and a door (Figure 1). The size of the door is 0.9 m × 2.0 m, and the size of the window is 1.2 × 0.87 m. The floor is composed of ordinary cement mortar. One wooden

---

*Author to whom correspondence should be addressed.

1544-8053/16/02 S119-10

doi:10.12783/issn.1544-8053/13/4/S15

table and sixteen chairs are arranged in the room. During the experiment, to avoid the influence of people walking, there were only two experiment personnel sitting in the room. And the experiment personnel wore a mask and were required to avoid walking in the room. The door and windows were all closed. The office was cleaned for one time every two days.

Experiment Instruments

The mass concentrations of PM1.0, PM2.5 and PM10.0 were measured by TSI DUSTTRAK 8520, its measurement range is 0.001~100 mg/m^3 and its measurement accuracy is ± 0.001 mg/m^3. The number concentrations of the indoor particles were measured by TSI AEROTRAK 8220, its measurement range is 0.3–10 µm, and its measurement accuracy is ± 5%.

Experimental Scheme

According to the indoor activities, the conditions contains: smoking, mopping floor, wiping table, sweeping floor, walking, purified water humidification (PWH), tap water humidification (TWH) and cool boiled water humidification (CBWH).

The central point was set as the sample point to measure the mass concentration and particle number concentration [17]. And the height of the sample point was 0.8 m.

In the smoking condition, the cigarette position in the room is shown in Figure 1. To reduce indoor personnel activities, the spontaneous burning of the cigarette was adopted to replace the smoking of the people. The cigarette was firstly fixed on a bracket (a water bottle), then it was lighted. The cigarette burnt from the 0th minute to the 12th minute.

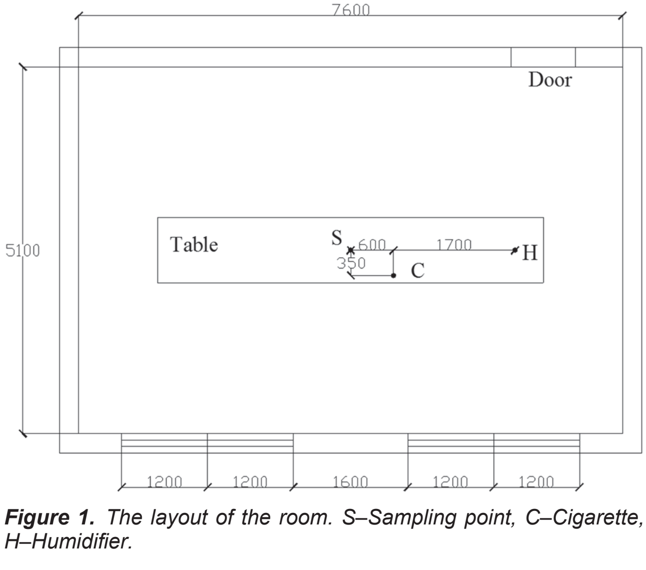

Figure 1. The layout of the room. S–Sampling point, C–Cigarette, H–Humidifier.

The conditions of mopping floor, wiping table, sweeping floor and walking lasted for 10 minutes (from the 0th minute to the 10th minute). The floor was mopped by a wet swab, the table was wiped by a wet cloth, and the floor was swept by a broom.

In the walking conditions, two people continuously walked in the office for 10 minutes at the speed of 1.4 m/s.

In the humidification conditions, the conditions of PWH, TWH and CBWH lasted for 2 hours continuously. The humidifier was ordinary ultrasonic humidifier. The humidifier was placed on the table and 2.3 meters away from the sampling point. In the experiment, the humidifier was working in the maximum humidification speed.

For every condition, the mass concentrations and the particle number concentrations were measured each 5 minutes from the 0th minute to the 120th minute.

RESULTS

The Effects of Smoking on Indoor Particulate Matter

The mass concentrations of the indoor particulate matter with different sizes in smoking condition are shown in Figure 2. For PM1.0, when smoking starts, the mass concentration of PM1.0 increases rapidly. The cigarette burns out at the 12th minute. The mass concentration of PM1.0 reaches the maximum value in the 25th minute. The maximum value is 191 µg/m^3, which shows an increase of 131 µg/m^3 over the initial value. Then it gradually decreases and reaches 131 µg/m^3 in the 120th minute, which is 101 µg/m^3 more than the initial value. For PM1.0–2.5, the mass concentration fluctuates in a small range. Its maximum value is 18 µg/m^3, which shows an increase of 13 µg/m^3 over the initial value. For PM 2.5–10.0, similar with those of PM1.0–2.5, its mass concentration also fluctuates in a small range. Compared with the mass concentration of PM1.0, the mass concentration of PM1.0–2.5 and PM2.5–10.0 shows no significant change in smoking condition. At the 0th minute, the ratios of PM1.0, PM1.0–2.5 and PM2.5–10.0 are 56.6%, 9.4% and 34.0%, at the 25th minute, the ratios are 87.6%, 4.8%, 7.6%, while at the 120th minute, the ratios are 92.9%, 2.8%, 4.3%. The cigarette burns out at the 12th minute. The mass concentration of PM1.0 reaches the maximum value in the 25th minute. The reason is that, be-

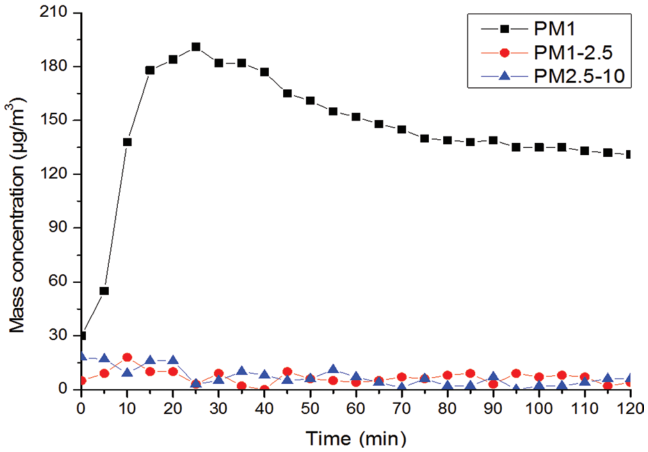

Figure 2. *The mass concentration in smoking condition.*

cause of the flowing law, the smoke first rises and then sinks and finally spreads to the whole room.

The particle number concentrations of the indoor particulate matter with different sizes in smoking condition are shown in Figure 3. For PM0.3–1.0, when the cigarette is lit, the particle number increases rapidly as the burning of the cigarette. When the cigarette burns out, the particle number still increases, reaches the maximum value at 20th minute and then gradually decreases. The maximum particle number concentration is 1.3 × 10^8 particles/m^3, while the initial value and the final value are 4.5×10^7 and 8.3 × 10^7 particles/m^3. For PM1.0-2.5 and PM2.5-10.0, the particle number concentrations are far less than those of PM0.3–1.0. And the particle number concentrations of PM1.0–2.5 and PM2.5–10.0 fluctuate in a certain range between 0th minute and 120th minute. It can be concluded that, smoking shows significant influence on particle number concentrations of PM0.3–1.0, while it shows no significant influence on the particle number concentrations of PM1.0–2.5 and PM 2.5–10.0.

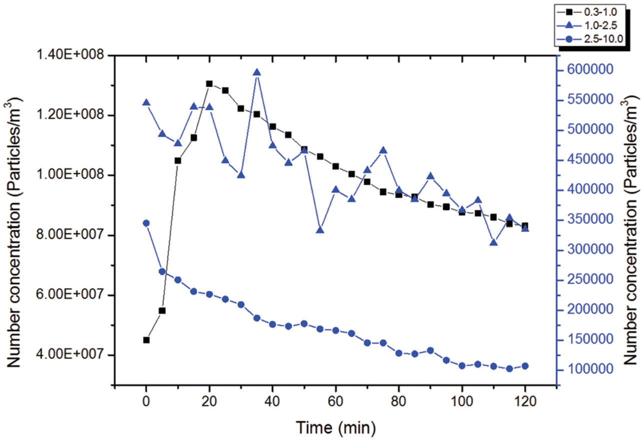

Figure 3. *The particle number concentration in smoking condition.*

From the mass concentration and the particle number concentration of the indoor particulate matter in smoking condition, it can be concluded that, smoking mainly influences the particulate matter less than 1.0 μm, and it shows no significant influence on larger particles. Thus, the particles emitted from the burning of the cigarette are smaller than 1.0 μm. When people smokes in a room, particulate matters less than 1.0 μm are the main part of the indoor air. In addition, the concentrations of the particulate matters less than 1.0 μm are still at high level at two hours after smoking. Therefore, smoking in a room directly threatens people's health and a cigarette's effects last for long duration.

The Effects of Cleaning on Indoor Particulate Matter

The Effects of Sweeping Floor on Indoor Particulate Matter

The mass concentrations of the indoor particulate matter with different sizes in sweeping floor condition are shown in Figure 4. The mass concentrations all increase as the floor is swept. All of them reach the maximum at the 15th minute, namely 5 minutes after the end of the sweeping. And the increment of PM2.5–10.0 is the largest (599 μg/m^3), then the PM1.0–2.5 (140 μg/m^3), and the increment of PM1.0 is the smallest (29 μg/m^3). Thereafter, the mass concentration of PM2.5–10.0 drops quickly in the 15th minute to 40th minute, then it gradually decreases. And at the 120th minute, the final value is only 13 μg/m^3 larger than the initial value, which is very close to the initial value. The mass concentrations of PM1.0 and PM1.0–2.5 decrease quickly in the 15th minute to 25th minute, then they gradually

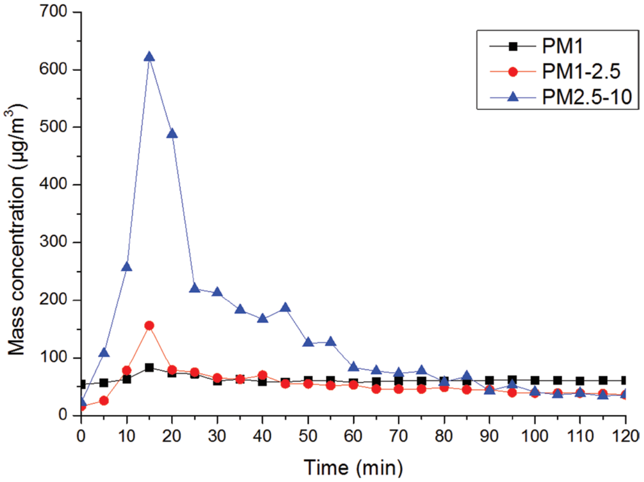

Figure 4. *The mass concentration in sweeping floor condition.*

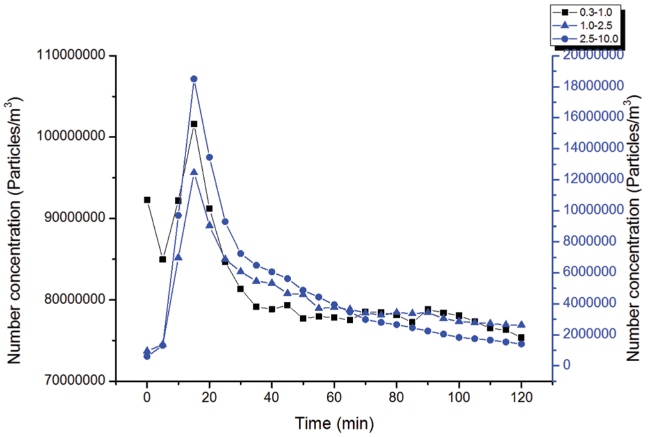

Figure 5. *The particle number concentration in sweeping floor condition.*

decrease. At the 120th minute, the final values are only 7 and 20 μg/m^3 larger than the initial values. It indicates that, at 110 minutes after the sweeping, the mass concentrations of the indoor particulate matter are still a little higher than the initial values. Sweeping floor will greatly influence the indoor particle mass concentration.

The particle number concentrations of the indoor particulate matter with different sizes in sweeping floor condition are shown in Figure 5. The particle number concentrations all increase as the floor is swept. Similar with the mass concentration, they reach the maximum at the 15th minute. And the increments of PM0.3–1.0, PM1.0–2.5 and PM2.5–10.0 are 1.0 × 10^7, 1.2 × 10^7 and 1.8 × 10^7 particles/m^3. Thereafter, they gradually decrease. At the 120th minute, the final values are 7.5 × 10^7, 2.6 × 10^6 and 1.4 × 10^6 particles/m^3. It indicates that, sweeping floor will greatly affect the particle number concentration of the indoor particulate matter.

From Figure 4 and Figure 5, it can be concluded that, the effects of the sweeping floor on indoor particulate matter last for long duration. When cleaners sweep the floor, they need to wear masks, and other personal protection measures are also recommended. In addition, it needs time for the indoor particulate matter to recover to their initial concentration levels. After finishing the sweeping, people should not immediately enter the room.

The Effects of Mopping Floor on Indoor Particulate Matter

The mass concentrations of the indoor particulate matter with different sizes in mopping floor condition are shown in Figure 6. For PM1.0, when the floor is mopped, the mass concentration begins to increase, and reaches the maximum value at 5th minute. When it reaches the maximum value, the increment is 25 μg/m^3. Then it gradually decreases and finally stabilizes. At 120th minute, the final mass concentration is 71 μg/m^3, which is lower than the initial value (93 μg/m^3). It indicates that, after mopping the floor, some of the particulate matter will be attached to floor. For PM1.0–2.5 and PM2.5–10.0, the change trends of the mass concentration are similar with that of the PM1.0. However, when they reach the maximum values, the increments of PM1.0–2.5 and PM2.5–10.0 are 73 and 97 μg/m^3, which are far larger than that of PM1.0. At 120th minute, the final mass concentrations are 15 and 11 μg/m^3, which are very close to the initial values. Thus, it can be concluded that, mopping floor will greatly increase the mass concentration of the inhalable coarse particles at its beginning. And mopping floor causes larger effects on PM1.0–2.5 and PM2.5–10.0. As the cleaners stay in this indoor environment for a long time each day, they should wear a mask to keep away the health risk of the indoor particulate matter.

The particle number concentrations of the indoor particulate matter with different sizes in mopping floor condition are shown in Figure 7. For PM0.3–1.0, PM1.0–2.5 and PM2.5–10.0, their particle number concentrations reach the maximum at the 5th minute. And the increments of PM0.3–1.0, PM1.0–2.5 and PM2.5–10.0 are 3.1 × 10^7, 4.9 × 10^6 and 4.4 × 10^6 particles/m^3. Thereafter, they gradually decrease. At the 120th minute, the final values are 8.6 × 10^7, 1.2 × 10^6 and 4.9 × 10^5 particles/m^3. It indicates that, mopping floor mainly affect the particle number concentration of PM0.3–1.0.

From Figure 6 and Figure 7, it can be concluded

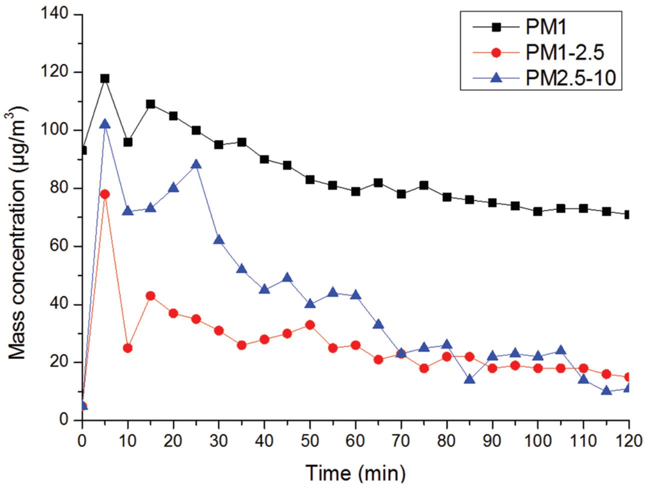

Figure 6. *The mass concentration in mopping floor condition.*

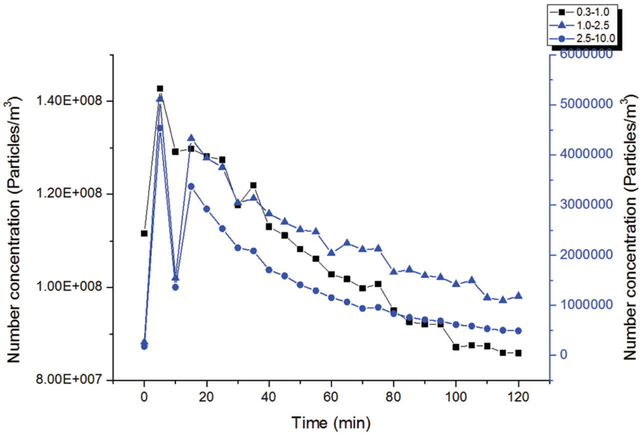

Figure 7. The particle number concentration in mopping floor condition.

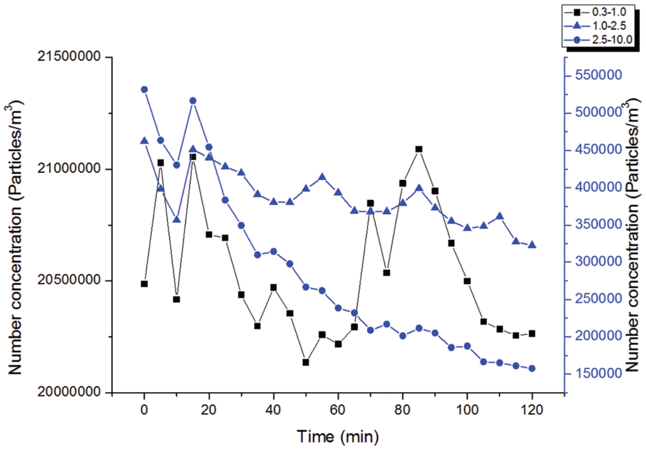

Figure 9. The particle number concentration in wiping table condition.

that, mopping floor will increase the concentration of indoor particulate matter.

The Effects of Wiping Table on Indoor Particulate Matter

The mass concentrations of the indoor particulate matter with different sizes in wiping table condition are shown in Figure 8. For PM1.0, when the table is wiping, there is a small increase in the mass concentration. At 120th minute, the final value is 10 μg/m^3 larger than the initial value. For PM1.0–2.5 and PM2.5–10.0, there is a small fluctuation. It indicates that, wiping table do not significantly affect the mass concentration of the indoor inhalable coarse particles.

The particle number concentrations of the indoor particulate matter with different sizes in wiping table condition are shown in Figure 9. The particle number concentration of PM0.3–1.0, PM1.0–2.5 and PM2.5–10.0 are stable, and there are no significant changes. It indicates that, wiping table do not significantly affect the particle number concentrations of indoor inhalable coarse particles.

Based on Figure 8 and Figure 9, it can be concluded that, wiping table do not significantly affect the concentration of indoor inhalable coarse particles.

The Effects of Walking on Indoor Particulate Matter

The mass concentrations of the indoor particulate matter with different sizes in walking condition are shown in Figure 10. For PM1.0 and PM1.0–2.5, at the 15th minute, the increments are only 9 and 12 μg/m^3, and the corresponding increase rates are 37.5% and 150%. Then their mass concentrations gradually decrease. For PM2.5–10.0, the mass concentration increase quickly in the first 15 minutes. At the 15th minute, the increment is 51 μg/m^3, and its corresponding

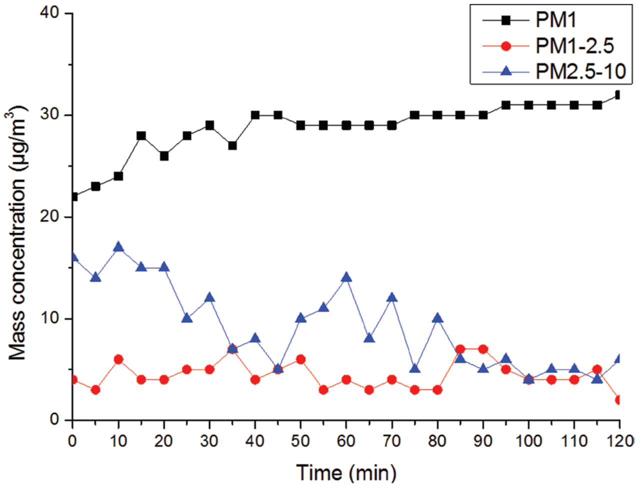

Figure 8. The mass concentration in wiping table condition.

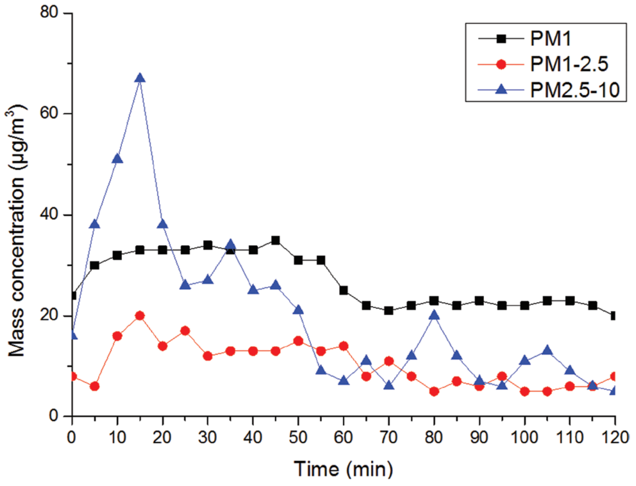

Figure 10. The mass concentration in walking condition.

increase rate is 318.8%. Then it gradually declines. It indicates that, walking will greatly affect the indoor particle mass concentrations.

The particle number concentrations of the indoor particulate matter with different sizes in walking condition are shown in Figure 11. The particle number concentrations all increase in the first 15 minutes and then gradually decrease. At the 15th minute, the increments of PM0.3–1.0, PM1.0–2.5 and PM2.5–10.0 are 0.5×10^7, 1.4×10^6 and 1.3×10^6 particles/m^3, and the corresponding increase rates are 24.5%, 260.2% and 209.5%. At the 120th minute, their particle number concentrations are 1.9×10^7, 6.4×10^5 and 2.4×10^5 particles/m^3, which are very close to the initial values. It indicates that, walking will affect the particle number concentrations of the indoor particulate matter.

From Figure 10 and Figure 11, it can be concluded that, walking will results in the rise of the particles in the floor. Thus the concentration of the indoor particulate matter is affected.

The Effects of Air Humidification on Indoor Particulate Matter

The Effects of TWH on Indoor Particulate Matter

The mass concentrations of the indoor particulate matter with different sizes in TWH condition are shown in Figure 12. For PM1.0, because of humidification, the mass concentration continues to rise. At the 10th minute, it increases from 47 μg/m^3 to 213 μg/m^3. And at the 120th minute, the mass concentration increases by 670 μg/m^3. For PM1.0–2.5 and PM2.5–10.0, there are fluctuations in a certain range. It indicates that, humidification by tap water greatly affect the mass concentration of PM1.0.

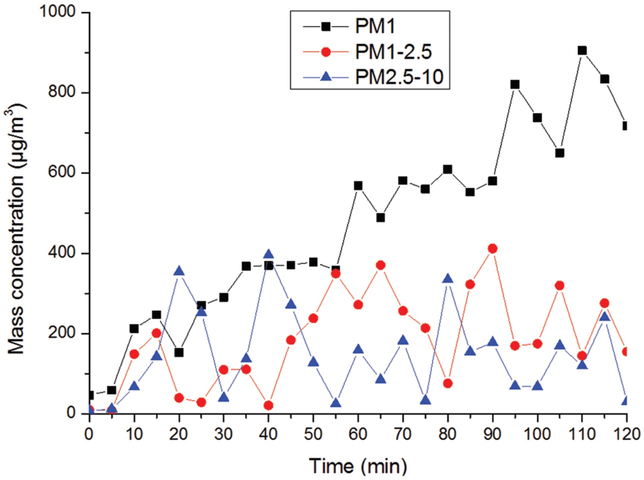

Figure 12. *The mass concentration in TWH condition.*

The particle number concentrations of the indoor particulate matter with different sizes in TWH condition are shown in Figure 13. For PM0.3–1.0, there is a rapid increase in the first 10 minutes, and then gradual increase continues. At the 10th minute and the 120th minute, the particle number concentration is 1.5×10^9 and 1.9×10^9 particles/m^3, individually. For PM1.0–2.5, there is a very few increase, while for PM 2.5–10.0, the values are stable. It indicates that, humidification by tap water mainly affect the particle number concentration of PM0.3–1.0.

From Figure 12 and Figure 13, it can be concluded that, humidification by tap water mainly affect the concentration of PM1.0. The reason is that, there are calcium ion and magnesium ion in the tap water, and the calcium ion and magnesium ion are emitted by humidification, thus calcium carbonate and magnesium carbonate enter into the air. Therefore, the particles in the air increase.

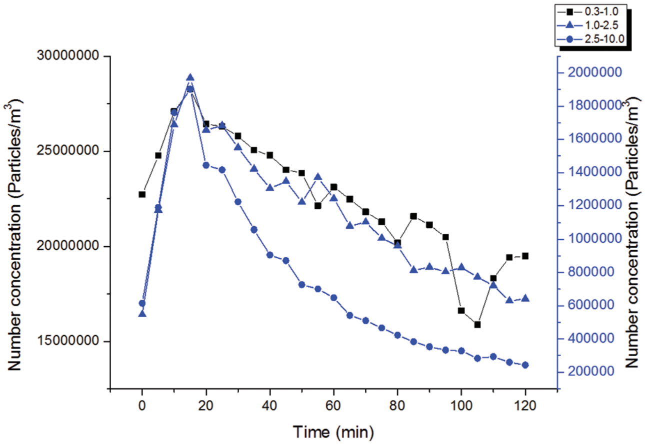

Figure 11. *The particle number concentration in walking condition.*

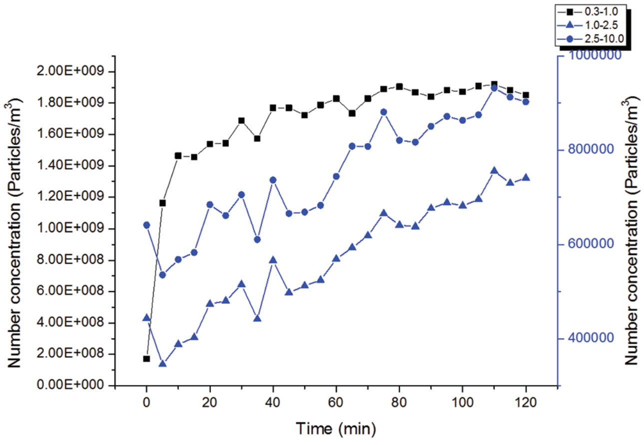

Figure 13. *The particle number concentration in TWH condition.*

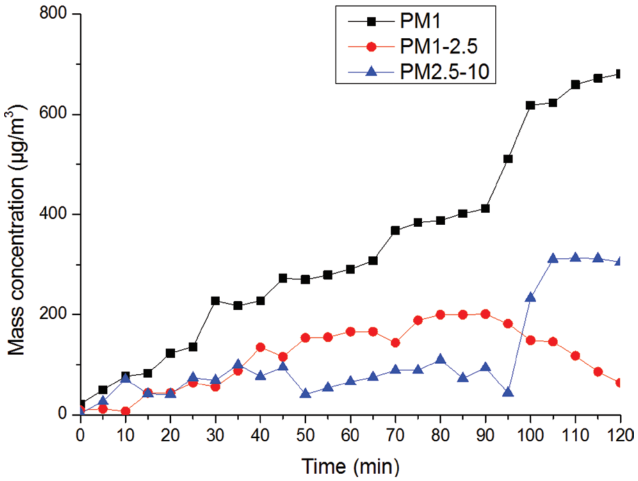

Figure 14. *The mass concentration in CBWH condition.*

The Effects of CBWH on Indoor Particulate Matter

The mass concentrations of the indoor particulate matter with different sizes in CBWH condition are shown in Figure 14. As shown in the figure, the change trends are similar with those of the TWH. For PM1.0, the increase speed and the increment in the CBWH condition are smaller than those in the TWH condition. For PM1.0–2.5 and PM2.5–10.0, the fluctuation ranges in the CBWH are smaller than those in the TWH condition.

The particle number concentrations of the indoor particulate matter with different sizes in CBWH condition are shown in Figure 15. As shown in the figure, the change trends are similar with those of the TWH. For PM0.3–1.0, at the 10th minute and the 120th minute, the particle number concentrations are 7.6 × 10^8 and 1.1 × 10^9 particles/m^3, individually.

From Figures 12–15, it can be concluded that, humidification by cool boiled water mainly affect the concentration of PM1.0. And the increase speed and the increment in the CBWH condition are smaller than those in the TWH condition. The reason is that, the calcium carbonate and magnesium carbonate are formed as scale on the kettle, thus the calcium ion and magnesium ion in the cool boiled water are fewer than those in the tap water.

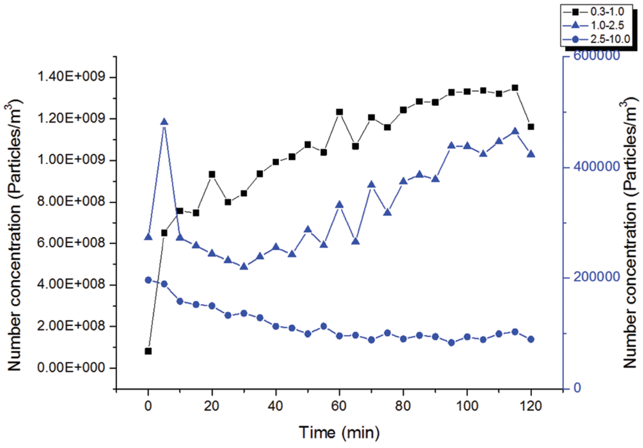

Figure 15. *The particle number concentration in CBWH condition.*

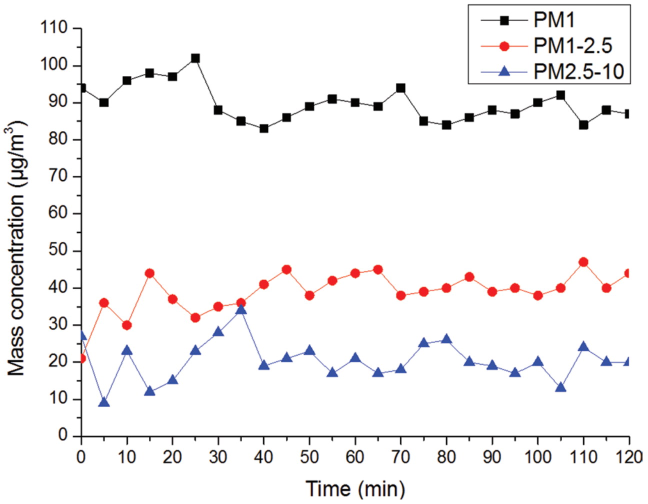

Figure 16. *The mass concentration in PWH condition.*

The Effects of PWH on Indoor Particulate Matter

The mass concentrations of the indoor particulate matter with different sizes in PWH condition are shown in Figure 16. It indicates that, the mass concentrations all fluctuate in a small range.

The particle number concentrations of the indoor particulate matter with different sizes in PWH condition are shown in Figure 17. As shown in the figure, for PM0.3–1.0, there is small fluctuation, and for PM1.0–2.5 and PM2.5–10.0, the values are stable.

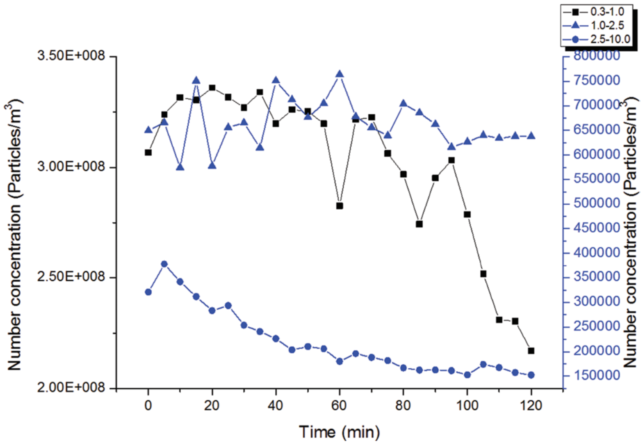

Figure 17. *The particle number concentration in PWH condition.*

From Figure 16 and Figure 17, it can be concluded that, humidification by purified water do not affect the concentration of the indoor particulate matter. The reason is that, the calcium ion and magnesium ion are removed in the purified water. Therefore, in order to prevent increase of indoor particulate matter by humidification, the water should be purified.

DISCUSSION

The Hazard Effects of Indoor Pollution Sources

Hazards of particulate matter to human body are mainly related to the particle size, particle composition, particle concentration, and body's exposure time [18].

The particle size determines its hazard effects on human. Particles larger than 10 µm will be blocked by the nose in vitro, and their harm to human health is small. Particles in 2.5–10 µm can enter the respiratory passage, and then they are deposited in the throat and other respiratory system [19]. Some of them can be excreted through the sputum, thus their harm to human health is relatively small [20]. The fine particles in 1.0–2.5 µm can enter the bronchus and other lower respiratory system, the fine particle in 0.1–1.0 µm can enter the lungs, and the ultrafine particles can penetrate the alveolar, and then enter the various parts of the body through the blood circulation, finally cause greater harm to human health [21,22]. Relevant researches shows that fine particulate matter PM2.5 can induce respiratory, cardiovascular, heart, lung and reproductive system diseases, damage the DNA structure, and leads to cancer [23,24].

Different kinds of particles cause different hazards on human health. Particulate matter is mainly divided into biological particles, mineral particles and combustion particles [25]. Biological particles mainly refer to animal dander, hair and microorganisms. The microorganisms (bacteria and fungi) can cause a decline in human immune function and allergic asthma, which can lead to certain respiratory diseases [26]. Indoor mineral particles mainly come from indoor decoration and outdoor industrial and agricultural production, transportation and other human activities. The mineral particles are often attached by a variety of metal elements.

The combustion particles mainly include particles caused by heating, cooking, burning garbage, boiler combustion and smoking. Attached by a large number of toxic and harmful substances, the combustion particles are harmful to human health. Smoking not only increases the incidence of asthma and the incidence of the disease, but also extends the duration of the symptoms and weakens the lung function [27].

As illustrated above, to rank the hazards of the indoor generated sources, the particle size, particle composition, particle concentration, and body's exposure time should be comprehensive considered.

However, as the detailed particle composition of each indoor activity is not studied in this paper, the particle composition of the particles is not considered. Therefore, the particle size, the particle concentration and the exposure time are only considered. The concept of area is introduced to rank the health hazards. According to Figures 2, 4, 6, 8, 10, 12, 14 and 16, the enclosed area by the curves of the mass concentration and the horizontal ordinate (time) is adopted to reflect the hazard effects. The enclosed area can be calculated as follows.

$$A = \frac{(C_{t_2} + C_{t_1})}{2} \times (t_2 - t_1) + \frac{(C_{t_3} + C_{t_2})}{2} \times (t_3 - t_2) + \cdots + \frac{(C_{t_i} + C_{t_{i-1}})}{2} \times (t_i - t_{i-1}) \tag{1}$$

where A is the enclosed area of the curve (particle size); C_{t_i} is the concentration at the time t_i; t_i is the ith measure time in min($i = 0, 1, 2 \ldots, 25$ in these experiments).

The enclosed area of the PM1.0, PM1.0–2.5 and PM2.5–10.0 associated with each indoor activities are shown in Table 1.

As shown in Table 1, only consider the particle size, particle concentration and exposure time, the hazard effects of the humidification are the most significant, then the sweeping floor, smoking, mopping floor, and the walking and wiping table are the least.

For smoking, mopping floor, wiping table, walking and humidification conditions, their hazard effects

Table 1. The Rank of the Hazard Effects.

Source	Area			Sum	Rank
	PM1.0	PM1.0–2.5	PM2.5–10.0		
Smoking	17.5975	0.8075	0.805	19.21	4
Mopping floor	10.275	3.2	4.97	18.445	5
Sweeping floor	7.4525	6.625	17.0425	31.12	3
Wiping table	3.46	0.54	1.095	5.095	7
Walking	3.25	1.245	2.4625	6.9575	6
TWH	56.75	22.6775	8.2025	87.63	1
CBWH	39.7625	14.2925	13.27	67.325	2
PWH	10.7625	4.7075	2.4375	17.9075	4

of PM1.0 are the most significant. For sweeping floor condition, the effect of PM2.5–10.0 is the largest.

For hazard effect of PM1.0, it is mainly affected by TWH, CBWH, PWH and smoking conditions. For hazard effect of PM1.0–2.5, it is mainly affected by TWH, CBWH and sweeping floor. For hazard effect of PM2.5–10.0, it is mainly affected by sweeping floor, CBWH and TWH.

The results of this paper verify the previous finding that smoking is an important source of indoor fine particles [28,29].

Results from the present study are basically consistent with the finding demonstrating that PM2.5–10 was greatly influenced by the occupants and cleaning activities [30].

The Guideline Values for the Indoor Particles

The World Health Organization (WHO) gives the 24-hour guideline value as 25 μm/m^3 for PM2.5 [31], the U.S. Environmental Protection Agency (USEPA) proposes the 24-hour standard value as 35 μm/m^3 for PM2.5 ambient air [32]. And the Canadian Environmental Health Directorate recommends 100 μm/m^3 as acceptable short-term (1-hour) exposure for the indoor exposure guidelines [33]. China issued a 24-hour guideline value as 35 μm/m^3 (or 75 μm/m^3) for PM2.5 in ambient air in 2012 [34]. However, for the particulate matter in indoor environment, there is only guideline value (150 μg/m^3 for 8-hour exposure) for indoor PM10.0, and the guideline value of indoor PM2.5 has not yet been issued. The chemical composition and substance of the indoor generated particles are widely different from local outdoor particles. Thus their health effects are significant different. Therefore, there is an urgent need to issue the guideline values of the fine particles in indoor environment in China. Some advices for the guideline values are as follows.

(1) As ultrafine particles (PM1.0) cause greater harm to human health, and indoor activities (smoking, cleaning, walking and humidification) increase the concentration of PM1.0, the guideline value for PM1.0 can be added. Thus, for indoor particulate matter, the guideline value system for PM10.0, PM2.5 and PM1.0 can be established.

(2) For second-hand smokers and cleaners, although their exposure time in the polluted environment are not as long as 8h or 24h, there are high concentration of fine and ultrafine particles, thus the exposure time can be set as 1 hour.

Limitation of the Study

This paper only considers the particle size, the particle concentration and the exposure time to rank the hazard effects. Chemical composition analysis can be adopted to analyze the particle composition in further study.

SUMMARY

This paper studied the influences of different indoor activities on particle characteristics in an office. The mass concentration and number concentration of PM1.0, PM1.0–2.5 and PM2.5–10.0 in each indoor activity were measured. The concept of area is introduced to rank the health hazards of the indoor activities on human health. The conclusions are shown as follows.

(1) The effects of the humidification on the indoor particulate matter are the most significant, then the sweeping floor, smoking, mopping floor, and the walking and wiping table are the least.

(2) For smoking, mopping floor, wiping table, walking and humidification conditions, their hazard effects on PM1.0 are the most significant. For sweeping floor condition, the hazard effect of PM2.5–10.0 is the largest.

(3) For hazard effect of PM1.0, it is mainly affected by TWH, CBWH, PWH and smoking conditions. For hazard effect of PM1.0–2.5, it is mainly affected by TWH, CBWH and sweeping floor. For hazard effect of PM2.5–10.0, it is mainly affected by sweeping floor, CBWH and TWH.

(4) The guideline value for PM1.0 can be added. Thus, the guideline value system for PM10.0, PM2.5 and PM1.0 can be established for indoor particulate matter.

(5) For guideline values of indoor particulate matter, the exposure time can be set as 1 hour.

ACKNOWLEDGMENTS

This study has been supported by National Natural Science Foundation of China (Grant No. 51408220).

REFERENCE

1. Klepeis, N. E., W. C. Nelson, W. R. Ott, J. P. Robinson, A. M. Tsang, and P. Switzer. 2001. “The National Human Activity Pattern Survey (NHAPS): A Resource for Assessing Exposure to Environmental Pol-

lutants," *Journal of Exposure Analysis and Environmental Epidemiology, 11*(3): 231–252. https://doi.org/10.1038/sj.jea.7500165

2. Brook, R. D., S. Rajagopalan, and C. A. Pope. 2010. "Particulate Matter Air Pollution and Cardiovascular Disease: An Update to the Scientific Statement from the American Heart Association," *Circulation, 121*(21): 2331–2378. https://doi.org/10.1161/CIR.0b013e3181dbece1
3. Dockery, D.W. 2009. "Health Effects of Particulate Air Pollution," *Annals of Epidemiology, 19* (4): 257–263. https://doi.org/10.1016/j.annepidem.2009.01.018
4. Kan, H., S. J. London, G. Chen, Y. Zhang, G. Song, N. Zhao, L. Jiang, and B. Chen. 2008. "Season, Sex, Age, and Education as Modifiers of the Effects of Outdoor Air Pollution on Daily Mortality in Shanghai, China: The Public Health and Air Pollution in Asia (PAPA) Study," *Environmental Health Perspectives, 116*(9): 1183-1188. https://doi.org/10.1289/ehp.10851
5. Mar T. F., G.A. Norris, J.Q. Koenig, and T. V. Larson. 2000. "Associations between Air Pollution and Mortality in Phoenix," *Environmental Health Perspectives, 108*(2): 347-353. https://doi.org/10.1289/ehp.00108347
6. Pope, C.A., R.T. Burnett, G.D. Thurston, M. J. Thun, E. E. Calle, D. Krewski, and J. J.Godleski. 2004. "Cardiovascular Mortality and Long-term Exposure to Particulate Air Pollution: Epidemiological Evidence of General Pathophysiological Pathways of Disease," *Circulation, 1*(8): 2654–2670.
7. Susanne, S., R. Stefan, E. Clive, S. Sean, M. T. Marsailidh, F. B. Christine, R. L. Sarah, R. H. Mathew, H. David, L. Chun, and W. Hao. 2015. "Personal Exposure Monitoring of PM2.5 in Indoor and Outdoor Microenvironments," *Science of the Total Environment, 508*(5): 383–394.
8. Lai, H.K., M. Kendall, H. Ferrier,I. Lindup, S. Alm, O. Haenninen, O. Hänninend, M. Jantunend, P. Mathyse, R. Colvilea, M.R. Ashmoref, P. Cullinang, and M.J. Nieuwenhuijsen. 2004. "Personal Exposures and Microenvironment Concentrations of PM2.5, VOC, NO_2 and CO in Oxford, UK," *Atmospheric Environment, 38*(37): 6399–6410. https://doi.org/10.1016/j.atmosenv.2004.07.013
9. Simoni, M., A. Scognamiglio, L. Carrozzi, S. Baldacci, A. Angino, F. Pistelli, F. Di Pede, and G. Viegi. 2004. "Indoor Exposures and Acute Respiratory Effects in Two General Population Samples from a Rural and an Urban Area in Italy," *Journal of Exposure Analysis and Environmental Epidemiology, 14*: S144–152. https://doi.org/10.1038/sj.jea.7500368
10. Acevedo-Bolton, V., W.R. Ott, K.C. Cheng, R.T. Jiang, N.E. Klepeis, and L.M. Hildemann. 2014. "Controlled Experiments Measuring Personal Exposure to PM2.5 in Close Proximity to Cigarette Smoking," *Indoor Air, 24*(2): 199–212. https://doi.org/10.1111/ina.12057
11. Thatcher, T.L., and D. W. Layton. 1995. "Deposition, Resuspension, and Penetration of Particles within a Residence," *Atmospheric Environment, 29*(13): 1487–1497. https://doi.org/10.1016/1352-2310(95)00016-R
12. Lee, J.Y., S. G. Lim, K. Y. Lee, X. B. Guo, R. Kamath, H. Yamato, A. L. Abas, S. Nandasena, A. A. Nafees, and N. Sathiakumar. 2010. "Secondhand Smoke Exposures in Indoor Public Places in Seven Asian countries," *International Journal of Hygiene and Environmental Health, 213*(5): 348–351. https://doi.org/10.1016/j.ijheh.2010.05.007
13. Gehin, E., O. Ramalho, and S. Kirchner. 2008. "Size distribution and emission rate measurement of fine and ultrafine particle from indoor human activities," *Atmospheric Environment, 42*(35): 8341–8352. https://doi.org/10.1016/j.atmosenv.2008.07.021
14. Glytsos, T., J. Ondracek, L. Dzumbova, I. Kopanakis, and M. Lazaridis. 2010. "Characterization of Particulate Matter Concentrations during Controlled Indoor Activities," *Atmospheric Environment, 44*(12): 1539–1549. https://doi.org/10.1016/j.atmosenv.2010.01.009
15. Cheng, H., M. Hu, L.W. Zhang, and L. Wan. 2009. "PM2.5 Concentrations in Indoor and Outdoor Air and Their Relationship in the Fall of Beijing," *Journal of Environment and Health, 26*(9): 787–789.
16. Gui, F., Q. W. Ye, Y. P. Zhou, and H. Q. Huang. 2013. "Influence of Sweeping on the Concentration of Particulate Matter in the Indoor Air," *Journal of Anhui University of Technology (Natural Science), 30*(3): 250–254.
17. Indoor air quality standard, GB/T18883-2002(in Chinese).
18. Zhao, Z. Z. 2016. Study on the Pollution Characteristics and Dynamic Changes of Particulate Matter in an Office Environment. Baoding: North China Electric Power University.
19. Yang, H. B., X. D. Zou, H. Y. Wang, and Y. C. Liu. 2012. "Study Progress on PM2.5 in Atmospheric Environment," *Journal of Meteorology and Environment, 28*(3): 77–82.
20. Zhu, Z. Y., B. Li, Q. Y. Zhao, S. J. Xia, and L. Li. 2013. "A Review and Outlook of the Research and Pollution Control on PM2.5 in Domestic and Overseas," *Environmental Science and Technology, 26*(1): 70–74.
21. Beckett K. P., S. P. Freer, and G Taylor. 2000. "The Capture of Particulate Pollution by Rrees at Five Contrasting Urban Sites," *Arboricultural Journal, 24*(3): 209–230. https://doi.org/10.1080/03071375.2000.9747273
22. Cai, G. 2012. "Method for Determination of PM2.5 in Ambient Air," *Gansu Science and Technology, 28*(12): 45–46.
23. Susanne, S., R. Stefan, C. E. Sabel, S. Semple, M. M. Twigg, C. F. Braban, S. R. Lesson, M. R. Heal, D. Harrison, C. Lin, and H. Wu. 2015. "Personal Exposure Monitoring of PM2.5 in Indoor and Outdoor Microenvironments," *Science of the Total Environment*, 2015, 508: 383–394. https://doi.org/10.1016/j.scitotenv.2014.12.003
24. Almaskut, A., P. J. Farrell, and D. Krewski. 2012. "Statistical Methods for Estimating the Environmental Burden of Disease in Canada, with Applications to Mortality from Fine Particulate Matter," *Environmetrics, 23*(4): 329–344. https://doi.org/10.1002/env.2148
25. Zong, Q. S. 2012. Study on the Distribution and Deposition of Indoor Particulate Matter. Ma'anshan: Anhui University of Technology.
26. Qin, X. G. 1997. "The Living Environment with Dust Mite Allergic Asthma," *Foreign Medical Sciences (Hygiene Fascicule)*, *24*(5): 286–289.
27. Repace, J.L., 2007. "Exposure to Secondhand Smoke," In: Ott, W., Steinemann, A., Wallace, L. (Eds.), Exposure Analysis. CRC Press, Boca Raton, FL.
28. Wallace, L. 1996. "Indoor Particles: a Review," *Journal of the Air & Waste Management Association, 46*(2): 98–126. https://doi.org/10.1080/10473289.1996.10467451
29. Heroux, M.E., N. Clark, K. Van Ryswyk, R. Mallik, N. L. Gilbert, I. Harrison, K. Rispler, D. Wang, A. Anastassopoulos, M. Guay, M. MacNeill, and A. J. Wheeler. 2013. "Predictors of Indoor Air Concentrations in Smoking and Non-smoking Residences," *International Journal of Environmental Research & Public Health, 7*(8):3080–3099. https://doi.org/10.3390/ijerph7083080
30. Urso, P., A. Cattaneo, G. Garramone, C. Peruzzo, D. M. Cavallo, and P. Carrer. 2015. "Identification of Particulate Matter Determinants in Residential Homes," *Building and Environment, 86*: 61–69. https://doi.org/10.1016/j.buildenv.2014.12.019
31. WHO. 2006. WHO Air Quality Guidelines for Particulate Matter, Ozone, Nitrogen Dioxide and Sulfur Dioxide. Global Update 2005. World Health Organization, Geneva, Switzerland.
32. USEPA. 2006. National Ambient Air Quality Standards for Particulate Matter. Final Rule, Federal Register. US Environmental Protection Agency.
33. Health-Canada. 1987. Exposure Guidelines for Residential Indoor Air Quality. Health Canada, Environmental Health Directorate, Ottawa, Ontario.
34. Ambient air quality standards, GB3095-2012. (in Chinese)

Mechanical Behaviors of High Performance Concrete Beams Prestressed with CFRP Strands

W. C. XUE*, X. H. WANG, X. HU and R. G. ZHENG
Department of Structural Engineering, College of Civil Engineering, Tongji University, Shanghai 200092, China

ABSTRACT: The merits of high performance concrete (HPC) and fiber reinforced polymer (FRP) could be combined for using in the concrete structures to improve the structural mechanical behavior. Six beams cast with HPC and prestressed with Carbon FRP (CFRP) strands were tested and discussed in this paper. Test variables included partial prestressing ratio (PPR) of CFRP strands and material of reinforcements (steel and Glass FRP). Test results indicated that all the beams failed in two modes, i.e., compression failure mode and tension failure mode. The ultimate deflection of all the beams reached 1/70-1/41 of the spans and the ductility coefficients of the steel reinforced beams were higher than 3.5 (except the one with the highest steel reinforcement ratio), indicating good deformability and ductility. An increase in partial prestressing ratio (PPR) had a positive effect on ductility. The ductility of Glass FRP reinforced beam was much lower than that of steel reinforced beams while the deformability was quite similar.

INTRODUCTION

STEEL tendons corrosion in prestressed concrete structures is potentially dangerous due to the relatively small cross sections of members and high tensile stress of tendons and thus corrosion damaged tendons can result in sudden and catastrophic failure. Thus the construction industry is in urgent need for alternative materials to steel tendons which do not corrode.

Researchers are currently exploring the use of fiber reinforced plastic (FRP) tendons as a promising solution for the corrosion problem of steel tendons. Among available FRPs, carbon fiber reinforced polymer's (CFRP) combination of high tensile strength, high chemical resistance, low relaxation and high fatigue strength makes it particularly attractive for prestressing application. At present, two types of CFRP are commercially available including rigid rods and flexible cables. CFRP rods have been used as prestressing reinforcements in concrete beams for years. However, CFRP cables, which can be coiled and are ease to handle, are gaining popularity in prestressed applications recently. In case of flexure of concrete beams prestressed with bonded CFRP tendons, the high strength characteristics of CFRP tendons could perhaps be effectively used in combination with high performance concrete (HPC). The advantages of HPC not only include its high compressive strength but also low permeability, good durability and volume stability [1]. The author's previous research [2] which showed that the high strength CFRP strands had good bond performance with HPC provided essential support needed for CFRP strands were used in HPC beams.

Investigation of concrete beams prestressed with FRP tendons first started in German in 1974 [3]. After that, extensive research was carried out on flexural behaviors of concrete beams prestressed with FRP tendons. Tests on seven post-tensioned concrete beams prestressed with CFRP tendons and three counterpart beams prestressed with steel tendons were carried out by Mutsuyoshi *et al.* [4]. Results indicated that two modes of flexural failure were observed: (1) rupture of prestressing reinforcement; and (2) crushing of concrete in compression. Other researchers' studies showed that when the specimens were failed due to rupture of FRP tendons, elastic strain energy was released and was partly absorbed by the concrete, thus causing extensive cracking and spalling [5,6,7]. When failure of a prestressed beam was caused by crushing of concrete, cracking was less extensive as compared with those beams that failed by rupture of tendons. Some researchers reported that failure by crushing of

---

*Author to whom correspondence should be addressed.
E-mail: E-mail: xuewc@tongji.edu.cn; Tel: +086-21-65981216;
Fax: +086-21-65981216

1544-8053/16/02 S129-06

doi:10.12783/issn.1544-8053/13/4/S16

Table 1. Details of Specimens.

Specimens	B1	B2	B3	B4	B5	B6
Tendons	1Ø12.5CFRP	1Ø12.5CFRP	1Ø12.5CFRP	1Ø12.5CFRP	2Ø12.5CFRP	2Ø12.5CFRP
PPR	0.7	0.5	0.5	0.5	0.5	0.7
Jacking stresses (σ_{con})	0.55 f_{ptk}	0.55 f_{ptk}	0.55 f_{ptk}	0.65 f_{ptk}	0.55 f_{ptk}	0.55 f_{ptk}
Bottom longitudinal reinforcements (A_b)	2Ø10	2Ø16	2Ø19 (GFRP)	2Ø16	2Ø22	2Ø14
Top longitudinal reinforcements (A_t)	2ϕ8 (Steel bars) for all specimens					

Note: f_{ptk} represents the ultimate tensile strength of CFRP tendons.

concrete in beams prestressed with CFRP strands resulted in increased ductility in comparison with those by rupture of CFRP strands [8]. This behavior was attributed to somewhat plasticity of concrete developed in compression which helped to dissipate energy. Some researchers found that deflection of beams prestressed with CFRP tendons was equivalent to that of reference beams prestressed by steel strands provided that the failure was controlled by the crushing of concrete in the compression zone while if the failure was governed by rupture of the CFRP bars, the deflection at failure was considerably smaller. The number of cracks in beams prestressed by CFRP was less than that of the beams with steel due to the lower flexural bond strength of the CFRP bars [9]. This behavior was also observed by Motavalli *et al.* [10].

Generally, despite some previous studies with regard to bonded CFRP prestressed concrete beams have been carried out as mentioned above, however, current studies are mainly focused on normal concrete beams, hardly has there been any conducted to investigate HPC beams prestressed with bonded CFRP strands. In view of this, the present study aims at investigating the static behaviors of six HPC beams prestressed with high strength bonded CFRP strands under monotonic loading.

EXPERIMENTAL PROGRAM

A total of six HPC beam specimens (denoted as B1 to B6, correspondingly) were cast and tested. The main experimental parameters included partial prestressing ratio (PPR) and material of reinforcements. Details of the beams are given in Table 1 and Figure 1. All specimens were designed with C50 HPC. Content of cement, grinded blast furnace slags, water, middle grit, gravels, superplasticizer and fibers in HPC were 260 kg, 260 kg, 188 kg, 864 kg, 1024 kg, 2.6–7.8 kg, 1.8 kg per m^3, respectively. The added grinded blast furnace slags in concrete with fineness of 5 × 10^3 cm^2/g were used to replace part of cement for strengthening the activity of admixtures. The adding of polypropylene fibers (15 mm in length) with 2.3% volume fraction of cement was an attempt to increase the anti-dry-shrinkage cracking property of cement mortar in hardening stage and fire-resistance capacity of concrete. Mechanical properties for reinforcements are listed in Table 2. The mechanical properties measured for the concrete used were: cube and cylinder compressive strength of 57.7 and 45.0 MPa, respectively; a splitting tensile strength of 4.5 MPa; and an modulus of elasticity of 3.37 × 10^4 MPa.

Note that the high strength CFRP strands used in

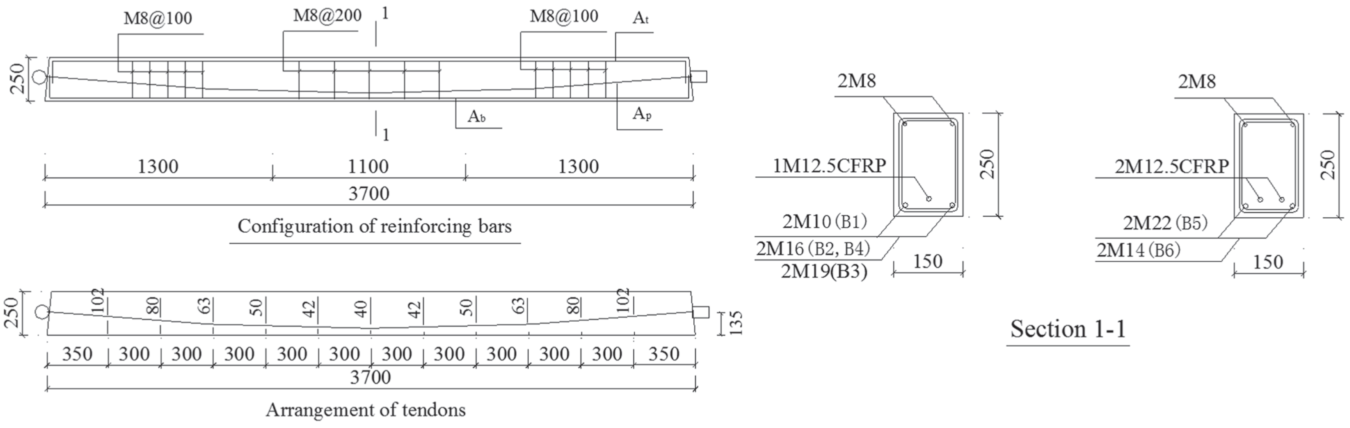

Figure 1. *Details of specimens (mm).*

Table 2. Mechanical Properties of Reinforcements.

	Conventional Reinforcements					FRP Bars/Tendons	
Mechanical Properties	**M8**	**M10**	**M14**	**M16**	**M22**	**M19GFRP**	**M12.5CFRP**
Yielding strength f_y (MPa)	418.0	318.0	341.0	321.0	324.5	—	—
Ultimate strength f_u (MPa)	541.0	471.0	513.0	498.0	481.0	698.5	2400
Modulus of elasticity E_s (MPa)	1.81×10^5	1.68×10^5	1.81×10^5	1.71×10^5	1.82×10^5	4.15×10^4	1.43×10^5
Elongation ratio	24.5%	20.0%	23.0 %	20.0%	23.0%	6.0%	1.5%

this test are carbon fiber composite cables (CFCC) produced by Tokyo Rope Mfg. Co. Ltd, Japan with measured ultimate strength of 2400 MPa and guaranteed tensile strength of 1868 MPa [11]. The individual wires of CFCC are manufactured by a roving prepreg process using polyacrylonitrile type carbon fibers. The prepreg is twisted to create a fiber core and then wrapped by synthetic yarns. The purpose of the yarn is to protect the fiber from ultraviolet radiation, mechanical abrasion, and improve the bond properties of the wires to concrete. The high strength CFRP strands are made up of seven wires that are twisted to allow better stress distribution through the cross section. Resin-sleeve anchorage system was used for CFCC. The inside surface of the sleeve is deformed to improve the load transfer. The GFRP bars used in the tests were provided by Aslan Company. All the beams were simply supported and tested under four-point monotonic static loads. The loading rate was about 5 kN/min before the beam yielding and about 1.5 mm/min after the beam yielding. Deflection, strains of prestressed strands and nonprestressed bars were measured in the test.

TEST RESULTS AND DISCUSSIONS

Failure Modes

The failure modes of the six beams were divided into two types, i.e., compression failure and tension failure. For specimens B2, B3, B5 and B6, the failure was initiated due to crushing of concrete before rupture of the tendons (compression failure). In contrast, for specimens B1 and B4, the failure was initiated by rupture of tendons prior to crushing of concrete (tension failure). Figure 2 depicts the two failure modes.

Load-deflection Relationship

The measured load-deflection curves of the six specimens is given in Figure 3. The characteristic loads of the specimens are listed in Table 3. Note that traditional definition of yielding was invalid for B3 because GFRP bars had no yielding point. Considering this, nominal yielding, which was determined according to the criteria for equivalent elasto-plastic energy absorption [12], was adopted. The followings could be obtained from the figure and table:

1. Except for B3, three significant points refer to cracking load, yielding load and ultimate load, which corresponded to first cracking of the beams, yielding of the beams and maximum load, respectively, could be observed in the curves. However, B3 showed a different flexural behavior that no yielding point was observed after cracking. It behaved linearly up to cracking and linearly after cracking with reduced stiffness up to failure. This different behavior was due to the unique characteristics of GFRP bars, which responded linearly up to failure under tension.
2. Before concrete cracking, all of the beams had a similar slope in the load versus deflection curves. However, initiation of cracking resulted in a more drastic reduction in the stiffness of B1 and B3 than in other specimens. This was because B1 contained the lowest amount of nonprestressed tensile reinforcements and the significantly lower modulus of elasticity of GFRP bars in B3.
3. For the specimens with identical prestressed strands, decreasing the PPR by increasing the amount of nonprestressed steel bars caused an


(a) (b)

Figure 2. *Typical failure modes of the specimens. (a) Compression failure and (b) Tension failure.*

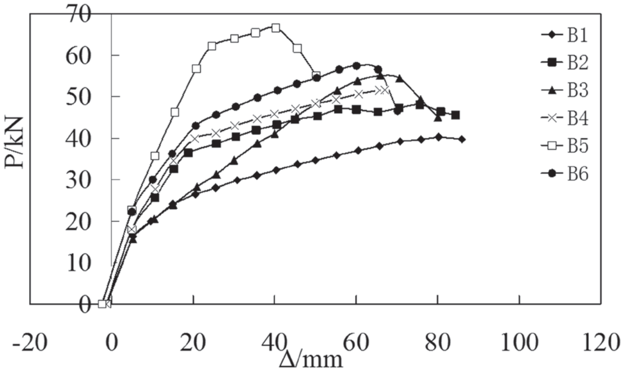

Figure 3. *Load-deflection curves.*

increase in the load-carrying capacity because the additional steel bars provided a significant contribution to resist loads.

4. Cracking loads of B2 and B3 were almost the same, which indicated that the type of nonprestressing reinforcement did not result in obvious influence on cracking loads of specimens. However, the ultimate load of B3 was 14.2% higher. The reason was that GFRP bars had significantly higher ultimate strength than steel bars.

Table 3. Characteristic Loads of Specimens.

Specimens	B1	B2	B3	B4	B5	B6
Cracking load P_{cr} (kN)	12.2	12.2	12.1	12.5	18.2	18.4
Yielding load P_y (kN)	25.1	37.2	32.1	38.2	60.8	41.4
Ultimate load P_u (kN)	40.3	48.5	55.4	51.7	66.9	58.3
P_y/P_{cr}	2.06	3.05	2.65	3.06	3.34	2.25
P_u/P_y	1.61	1.32	1.72	1.37	1.11	1.41

Verification of Plane Section Assumption

Whether the assumption of plane section remaining plane is fulfilled, is one of the most important standards to evaluate the integrity of a section. Figure 4 displays the evolution of the strain distributions over the mid-span section of the typical specimens under different load levels. As can be seen, the strain distributions were basically linear in compression zones and plane section assumption remained valid.

Displacement Ductility and Deformation Capacity

Ductility coefficients (μ) of the beams are defined as

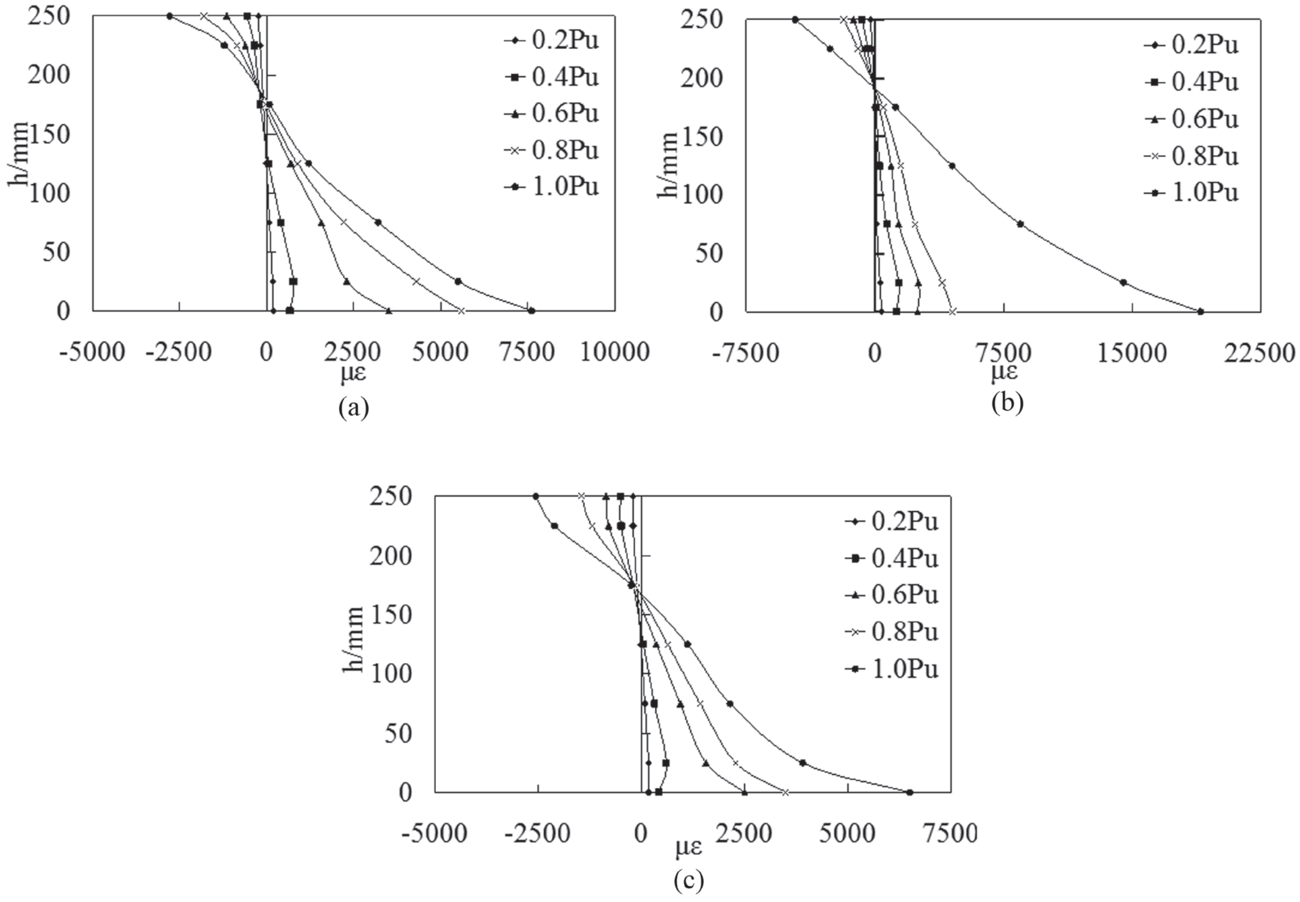

(a) (b) (c)

Figure 4. *Strain distributions of mid-span sections. (a) B1, (b) B3 and (c) B4.*

$\mu = \Delta y/\Delta u$, where Δu is the maximum displacement of the load-deflection curves without descending part or the displacement corresponding to 85% of the maximum load in descending part; and Δy is the yielding displacement corresponding to yielding of tensile steel bars for the five specimens reinforced with steel bars. Note that the nominal yielding displacement defined in Section 3.2 was adopted for B3 due to the linear elastic stress-strain relationship of GFRP bars. Comparisons of ductility and deformation capacity of the specimens are summarized in Table 4. Seen from the table:

1. For all specimens, the actual deflection level at ultimate reached 1/70-1/41 of the beam span. Thus all beams deflected sufficiently to give physical warning before failure.
2. The displacement ductility coefficients of the specimens reinforced with steel bars were ranged from 3.57 to 5.27 except for B5 which exhibited the lowest ductility coefficient of 2.13 because of a relatively higher tensile reinforcement ratio. As expected, B3 performed a relatively low ductility coefficient attributed to the linear elastic stress-strain relationship of GFRP bars.
3. For the specimens containing identical prestressing reinforcements, it could be found that an increase in PPR had a positive effect on displacement ductility by comparing the ductility coefficients of B1 with B2 and B5 with B6. The reason was that the specimens with higher PPR were reinforced with lower amount of steel bars and yielded under relatively lower displacements.

CONCLUSIONS

Six CFRP prestressed HPC beams with different design parameters including PPR and material of non-prestressed reinforcements were tested. The following conclusions could be stated:

1. The flexural behavior of the five specimens reinforced with steel bars were similar to each other and the specimens experienced three stages including initial cracking stage, yielding stage, and ultimate stage during the loading process. Specimen B3 reinforced with GFRP bars exhibited marked differences. There was no obvious yielding stage observed in specimen B3 due to the linear elastic stress-strain relationship of GFRP bars.
2. Failure modes for all specimens were dominated by flexural effects and could be divided into compression failure and tension failure according to different reinforcement ratios.
3. The actual deflection level of the six specimens reached 1/70-1/41 of the beam span at ultimate which showed that these specimens had relatively high deformability.
4. The ductility coefficients of the five specimens reinforced with non-prestressing steel bars were higher than 3.5 except for the one with the highest steel reinforcement ratio. While the specimen reinforced with GFRP performed a relatively low displacement coefficient because of the linear elastic stress-strain relationship up to failure of GFRP bars.
5. For the specimens with identical prestressed strands, decreasing of PPR would cause an increase in yield as well as ultimate loads while resulting in a negative effect on displacement ductility. However, cracking loads were less sensitive to the influence of PPR.

ACKNOWLEDGEMENTS

The authors gratefully acknowledge the financial support of the National Program on Key Basic Research Project (2012CB026200) and the Fund of Western Communications Construction Scientific and Technological Project by the Ministry of Communications of the P. R. China (200631882244).

Table 4. Characteristic Displacements and Ductility Coefficients of Specimens.

Specimens		B1	B2	B3	B4	B5	B6
Cracking	Δ_{cr} (mm)	2.55	2.52	2.92	2.39	3.23	3.12
	Δ_{cr}/L	1/1373	1/1389	1/1198	1/1464	1/1083	1/1122
Yielding	Δ_y (mm)	16.1	18.8	28.0	19.0	23.3	17.8
	Δ_y/L	1/217	1/184	1125	1/184	1/150	1/185
Ultimate	Δ_u (mm)	85.0	84.4	77.5	67.9	49.6	69.2
	Δ_u/L	1/41	1/41	1/45	1/52	1/70	1/50
Ductility coefficient	μ	5.27	4.49	2.76	3.57	2.13	3.87

REFERENCES

1. L. Biolzi, S. Cattaneo, and F. Mola, “Bending-shear response of self-consolidating and high-performance reinforced concrete beams”, *Engineering Structures*, V. 59, No. 2, 2014, pp. 399–410. https://doi.org/10.1016/j.engstruct.2013.10.043
2. W. C. Xue, X. H. Wang, and S. L. Zhang, “Bond Properties of High-Strength Carbon Fiber-Reinforced Polymer Strands”, *ACI Structural Journal*, V. 105, No. 1, 2008, pp. 303–311.
3. G. Rehm, and L. Franke, “Kunstharzgebundene glasfaserstäbe als bewehrung im betonbau”, *Die Bautechnik*, 1979, pp. 115–120.
4. H. Mutsuyoshi, K. Veharak, and A. Machida, “Mechanical properties and design methods of concrete beams reinforced with CFRP”, *Transactions of the JCI*, V. 12, No. 4 1990, pp. 231–238.
5. C. Lee, S. Shin, S. Lee, “Modelling of load-deflection of concrete beams internally prestressed with unbonded CFRP tendons”, *Magazine of Concrete Research*, V. 67, No. 13, 2015, pp. 730–756. https://doi.org/10.1680/macr.14.00367
6. N. F. Grace, E. Jensen, V. Matsagar, *et al.*, “Performance of AASHTO Beam Bridge Prestressed with CFRP Tendons”, *Journal of Bridge Engineering*, V. 18, No. 2, 2013, pp. 110–121. https://doi.org/10.1061/(ASCE)BE.1943-5592.0000339
7. B. W. Jo, G. H. Tae, and B. Y. Kwon, “Ductility evaluation of prestressed concrete beams with CFRP tendons”, *Journal of Reinforced Plastics and Composites*, V. 23, No. 8, 2004, pp. 843–859. https://doi.org/10.1177/0731684404033492
8. N. F. Grace, and G. Abdel-Sayed, “Ductility of Prestressed Bridges Using CFRP Strands”, *Concrete International*, V. 20, No. 6, 1998, pp. 25–30.
9. T. J. Lou, S. M. R. Lopes, A. V. Lopes, “A comparative study of continuous beams prestressed with bonded FRP and steel tendons”, *Composite Structures*, V. 124, No. 6, 2015, pp. 100–110. https://doi.org/10.1016/j.compstruct.2015.01.009
10. M. Motavalli, C. Czaderski, K. Pfyl-Lang, “Prestressed CFRP for Strengthening of Reinforced Concrete Structures, Recent Developments at Empa, Switzerland”, *Journal of Composites for Construction*, V. 15, No. 2, 2011, pp. 194–205. https://doi.org/10.1061/(ASCE)CC.1943-5614.0000125
11. Tokyo Rope Mfg. Co. Ltd., “Technical Data on CFCC, Product Manual”, 1993.
12. R. Park, “Evaluation of ductility of structures and structural assemblages from laboratory testing”, *New Zealand National Society for Earthquake Engineering*, V. 22, No. 3 1989, pp. 155–166.

Microstructure and Mechanical Properties of NiCr Alloy Coatings with Lanthanum Oxide Formed by Furnace Fused Processing

BUNV LIANG[1], ZHENYU ZHANG[1,*] and HONGJIAN GUO[2]
[1]*Material Engineering Department, Lanzhou Institute of Technology, Lanzhou, Gansu 730050, China*
[2]*State Key Laboratory of Solid Lubrication, Lanzhou Institute of Chemical Physics,*
Chinese Academy of Sciences, Lanzhou, 730050, China

ABSTRACT: NiCr coatings with different contents of La_2O_3 were produced on carbon steel by flame spray and then furnace fused processing. A field emission gun scanning electron microscope (FEGSEM), energy dispersive X-ray (EDX) microanalysis and X-ray diffraction analysis (XRD) were employed to observe the microstructure characteristics of the coatings. The effect of La_2O_3 on microstructure and mechanical properties of coatings was investigated. The result shows that the addition of La_2O_3 would refine and purify the microstructure of the coatings, when the addition of La_2O_3 is about 0.8 wt.%, the coatings obtain the highest hardness.

1. INTRODUCTION

FAILURE and damage of the components usually originate from the surface. Especially some critical mechanical parts cease to be useful just due to the damage on the surface by wear, corrosion and oxidation [1–2]. Therefore, surface modification techniques are necessary to repair the components and increase the service life of the machine components. A lot of technique are used to repair the damaged surface of machine parts, flame spray is one of commonly and widely applied technique. The advantages of flame spray is economical and versatility [3–7]. However, it has some drawbacks such as high porosity, inter-layer oxides and poor adherence [8]. This limitation would be overcome by furnace fused processing. In this technique, furnace fusing can reduce the porosity and forms metallurgical bonds between the coatings and the substrate [9]. So in the present work, experimental research on the microstructure, mechanical properties of NiCr alloy with lanthanum oxide is explored so as to expand the field of application of rare earth.

2. EXPERIMENTAL DETAILS

Carbon steel (1045) was used as a substrate material for flame spray and furnace fusing. Commercial NiCr alloy powders (State Key Laboratory of New Nonferrous Metal Materials, China) was used as coating material. The particles of NiCr alloy powders were less than 110 μm in size and were spherical in shape. The chemical composition of the powder is C 0.6~0.8, B 3.0~4.0, Si 4.0~5.0, Cr 14.0~16.0, Fe ≤ 5.0 wt.%, and the remainder is Ni. In order to improve the microstructure and properties of the coatings, 0.4 wt.%, 0.8 wt.% and 1.2 wt.% of La_2O_3 (having a purity of over 99%) was added being to the NiCr alloy powder. NiCr alloy powders and La_2O_3 are mixed up with ethanol in a carnelian bowl and well stirred for 30 min, and dried before spraying.

Carbon steel substrate was cleaned and grit blasted with Al_2O_3 grade 24 before spraying. The flame spraying coatings were obtained using an oxy-acetylene SPH-7/h gun (China). The tests were carried out with different parameters to obtain lower porosity and higher quality of coatings, and the best spray parameters were as follow: oxygen pressure: 400 kPa, acetylene pressure: 55 kPa, acetylene flow rate: 0.85 m^3/h, oxygen flow rate: 1.2 m^3/h, average impact velocity: 40 m/s, spray distance: 180 mm. After spraying, the coated material was heated and fused in a VF-79J furnace operating under argon to avoid the coating oxidation.

The analysis specimens were cut along the vertical direction of spraying, polished with fine diamond paste and etched in mixture composed of 10 ml HNO_3 and 30 ml HCl. Microstructure characterization of the coating

---

*Author to whom correspondence should be addressed.

1544-8053/16/02 S135-05

doi:10.12783/issn.1544-8053/13/4/S17

was observed using a JSM-5600LV scanning electron microscope, a field emission gun scanning electron microscope equipped with EDS. The phase structure of the coatings was determined by an X'Pert PRO X-ray diffraction (XRD). An MH-5-VM tester with a load of 4.9 N measured the microhardness along the depth in cross-section.

Bond strength experiments were performed using a WEW-50A (China) tensile tester according to the national standard GB/T228-1987 of the People's Republic of China. This test involves spraying and fusing two carbon steel bars in accordance with the process stated above.

3. RESULTS AND DISCUSSION

3.1. Microstructure Characterization of Coatings

Figure 1 presents the microstructure of the coatings with 0 wt.%, 0.4 wt.%, 0.8 wt.% and 1.2 wt.% of La_2O_3. It can be seen that the microstructure of the coatings with La_2O_3 is finer than that of without La_2O_3. When the content of La_2O_3 is approximately 0.8 wt.%, the refine effect is best as shown in Figure 1(c). However, the grain size of the coating became larger when the addition of La_2O_3 increased to 1.2 wt.% as shown in Figure 1(d). Thus microstructure characterization suggests that there exists an optimum addition of La_2O_3 (0.8 wt.% La_2O_3) for the best grain refinement. The effect of the addition of La_2O_3 attribute to the special chemical properties of rare earth element Lanthanum. On the one hand, Lanthanum is a chemically active element, it can form stable high melting point compounds while reacting with O, S, and N, etc. During furnace fusing processing, these high melting point compounds will float and be removed as molten slag, therefore, the microstructure of the coating with Lanthanum oxide becomes finer and purified with the

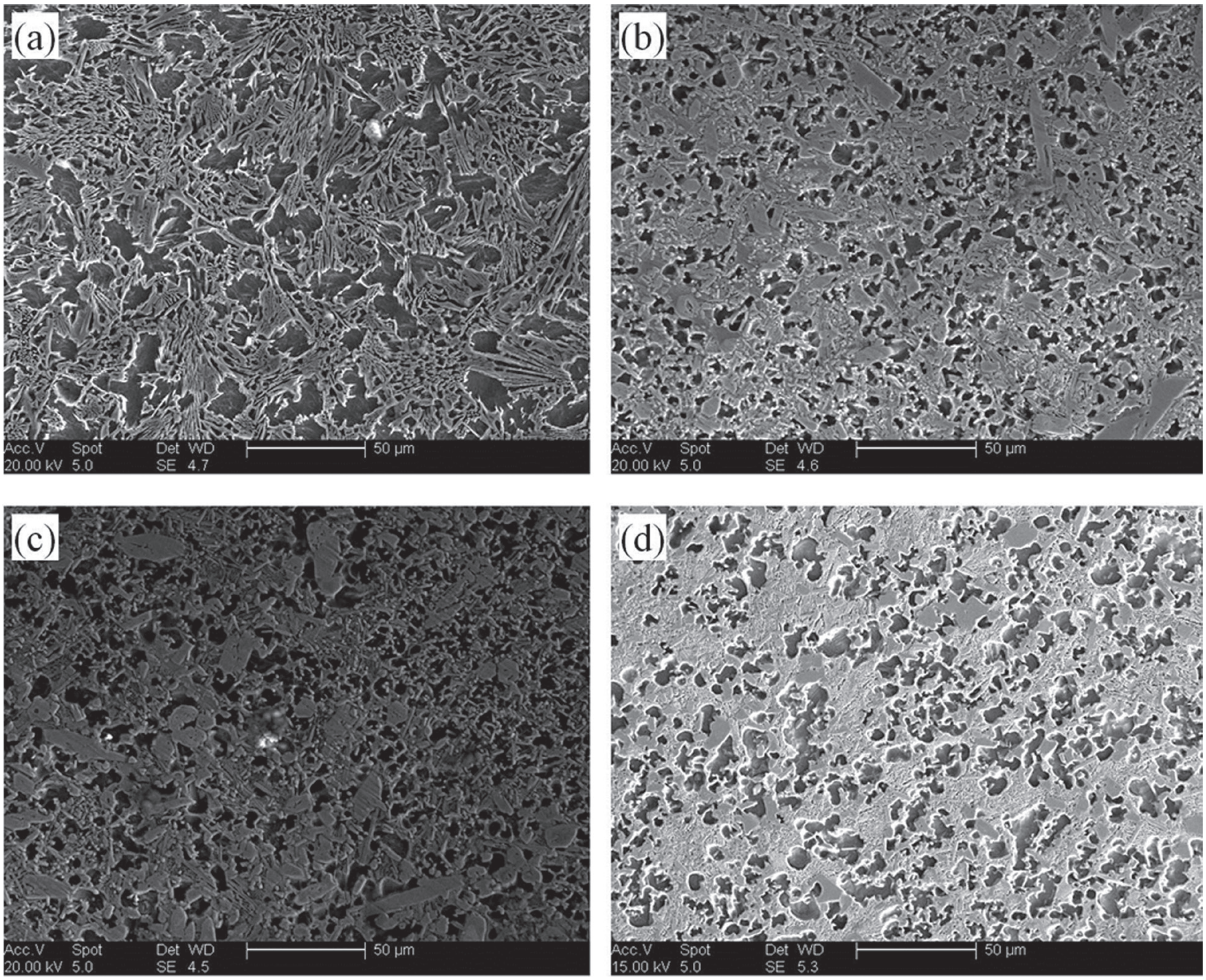

Figure 1. *Microstructure of the NiCr alloy coatings with La_2O_3, the contents of the La_2O_3 are: (a) 0, (b) 0.4, (c) 0.8 and (d) 1.2 wt.%.*

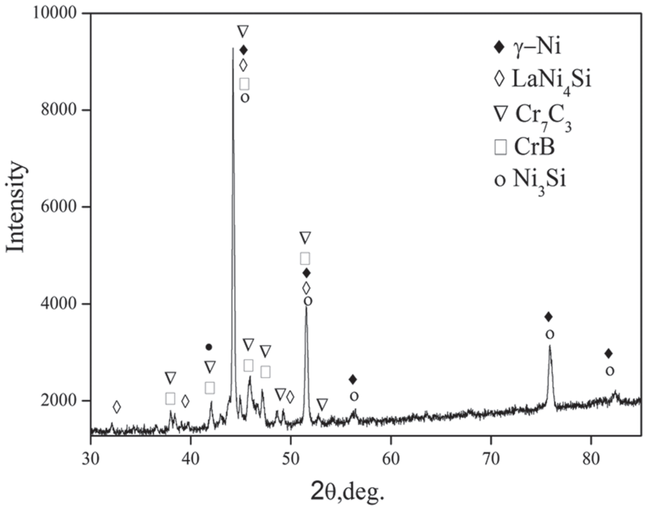

Figure 2. *XRD spectra of the NiCr alloy coating with optimum addition of 0.8 wt.% La$_2$O$_3$.*

inclusion number decreasing. On the other hand, due to rather large atomic radius, Lanthanum in the grain leads to distortion of lattice, which push Lanthanum over the grain boundary [10–12], so Lanthanum is rich over the grain boundary, the enrichment of Lanthanum on the grain boundary can cause a dragging effect on the growth of grain. As a result, the growth of grain will be prevented and the microstructure is further refined. Furthermore, the melting point of Lanthanum oxide is high (2315°C) [12], so Lanthanum oxide can act as heterogeneous nucleating sites for grains during solidification, and the number of grain is increased, the more grains, the finer the grain size [12].

The various phases such as γ-Ni, Cr_7C_3, CrB, Ni_3Si and $LaNi_4Si$ were identified by XRD analysis of the coating with suitable addition of Lanthanum oxide as shown in Figure 2. A new phase existence of $LaNi_4Si$ can be confirmed in the coating with the addition of 0.8 wt.% Lanthanum oxide. Figure 3 shows the elemental distribution of the coating with 0.8 wt.% Lanthanum oxide. The distribution curves are rising or falling indicates the different contents of Ni, Fe, Cr, and Si in various phases. It reveals that the elements Ni and Si are rich in area A (matrix phase of γ-Ni/ Ni_3Si), the elements Cr is rich in area B and area C (hard phases of CrB and Cr_7C_3), the elements Ni and Si are rich in area D (eutectic phase of γ-Ni +Ni_3Si).

3.2. Bond Strength and Interface Characteristics of the Coatings

Figure 4 presents the bond strength of coating/substrate and the results of tensile strength test. It shows that the bond strength of the coating/substrate with 0.8 wt.% Lanthanum oxide is higher than that of other coatings. Since the NiCr coating has different physical and mechanical properties from the addition of Lanthanum oxide, the microstructure of the coating is quite different because of adding Lanthanum oxide. It is also reported previously that the addition of rare earth can promote the diffusion at the interface, and make the microstructure finer and purified [13–14]. Moreover, Lanthanum can react with O, S and N during furnace fusing process, result in decreasing of the inclusion content by deoxidation and desulfuration, which is beneficial for the improvement of the bond strength. Cross-sectional

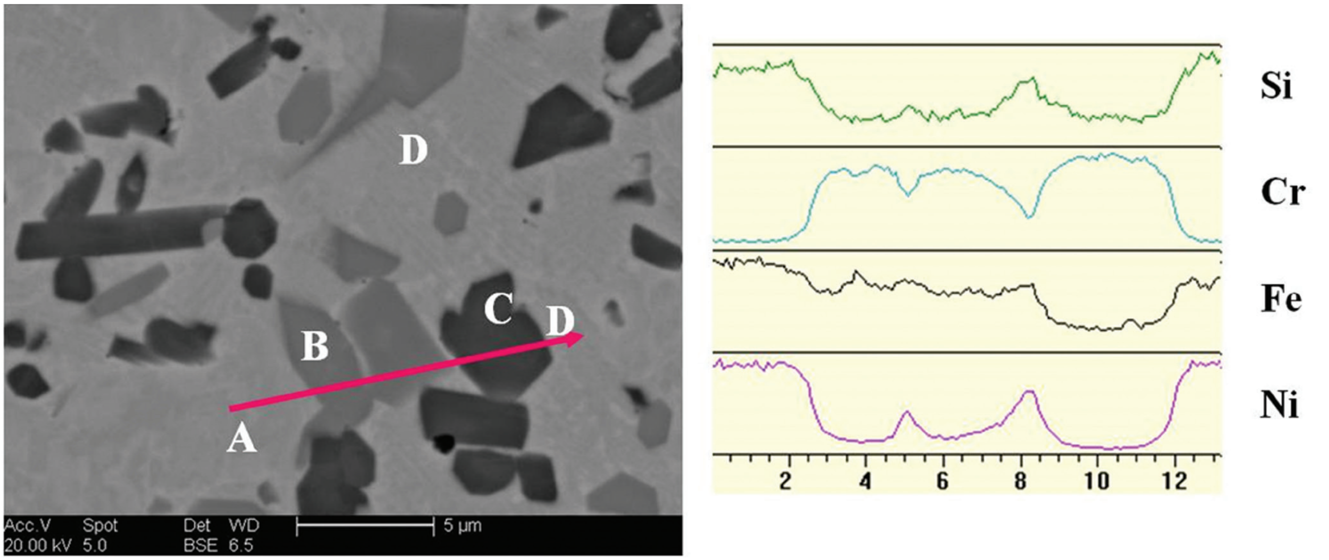

Figure 3. *Back scattered electron images of NiCri alloy with La$_2$O$_3$ and elements line distribution of Ni, Cr, Fe and Si.*

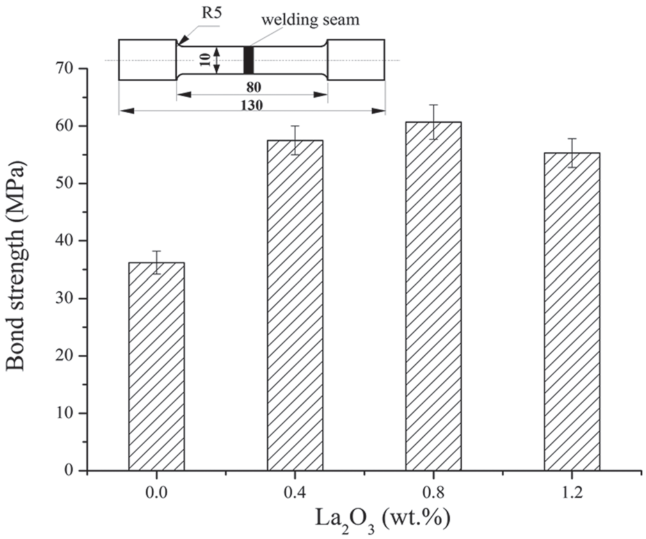

Figure 4. *Bond strength of the coatings with different addition of La_2O_3.*

micrographs of the interface are shown in Figure 5. An interfacial bonding zone and the X-ray elemental maps of Ni, Fe and Cr can be seen in Figure 5. As can be observed, the coating area is rich with Cr and Ni which is main elements of the powder, the substrate area is rich with Fe of carbon steel substrate. It appeared that Ni, Fe and Cr diffused in the interface, which indicates that the bond between the coating and the substrate belongs to metallurgical bond. During fusing the coatings are heated to a point between the solidus and liquids, and the diffusion processes take place. Unmelted particles, voids and porosity are greatly reduced through fusing. A good metallurgical bond exists between the coating and the substrate [13–14]. As stated above, the effects of Lanthanum oxide and the furnace fuse process lead to improvement of the bond strength.

3.3. Microshardness Distribution

Figure 6 shows the hardness distribution of the flame spraying and furnace fusing coatings. It can be seen that three distinct regions are distinguished in the hardness profile, corresponding to coating, interface and substrate, respectively. The addition of La_2O_3 can increase the microhardness of the coatings. The results present an optimum effect on the hardness in the addition of Lanthanum oxide. The difference of the coatings could be due to refinement of the grain size with Lanthanum oxide. In this experiment, the microhardness value of the coating with 0.8 wt.% Lanthanum oxide is higher than that of coatings with 0 wt.%, 0.4 wt.% and 1.2 wt.% Lanthanum oxide.

4. CONCLUSIONS

The flame sprayed NiCr alloy coatings with various amount of Lanthanum oxide were fused in a furnace. The optimum amount of Lanthanum oxide was found to be more beneficial for microstructure, bond strength,

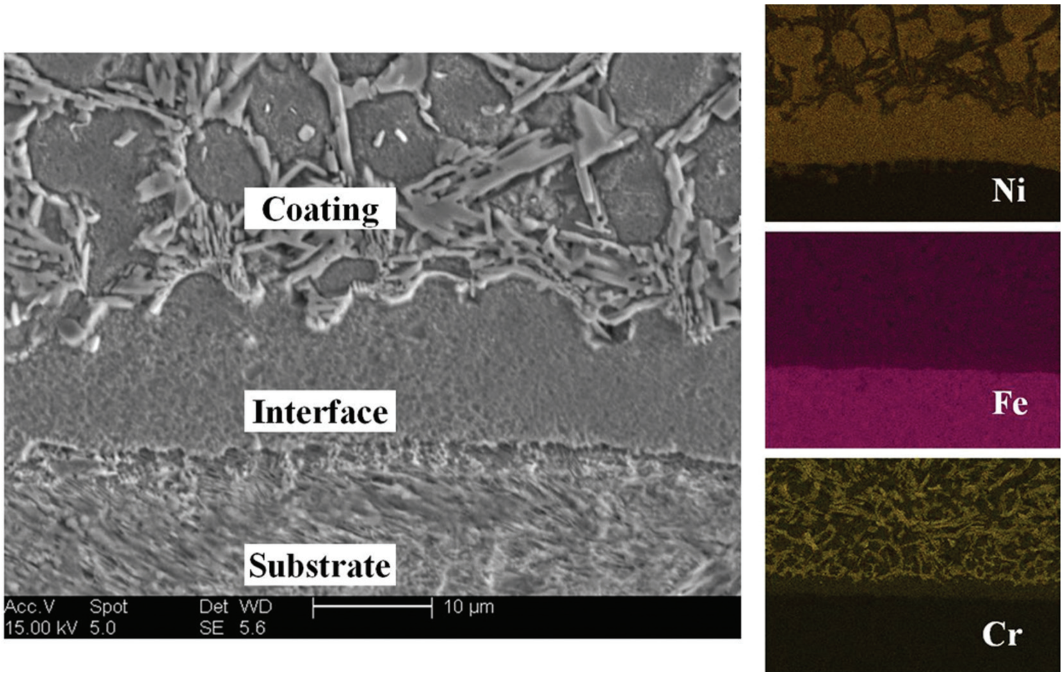

Figure 5. *Interface microstructure of coatings with La_2O_3 and elements distribution of Ni, Fe and Cr.*

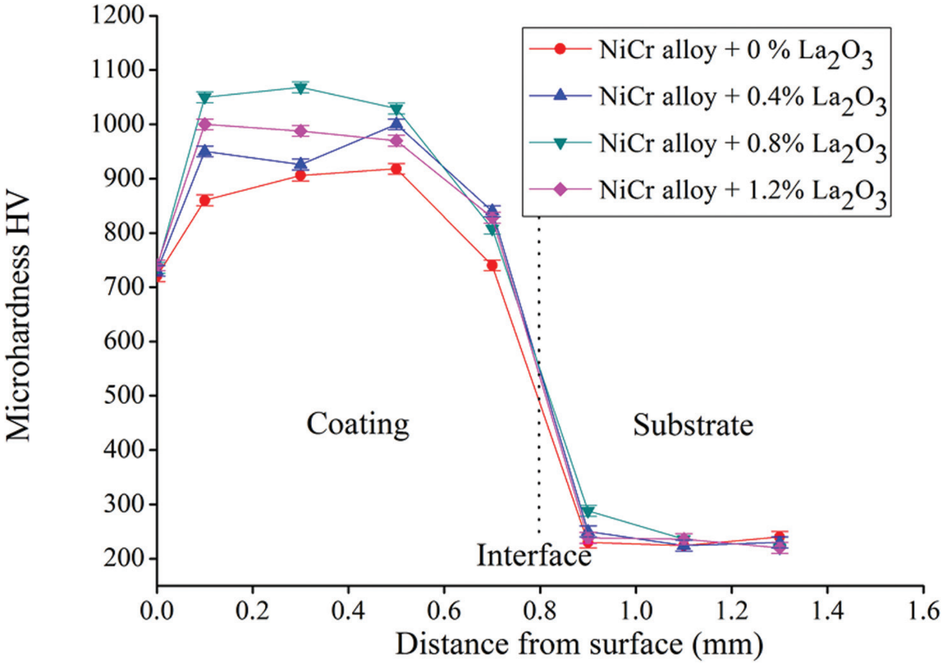

Figure 6. *Microhardness values on the sectioned surface different coatings vary with depth normal to the top surface.*

hardness and abrasive wear resistance. The following conclusions may be drawn:

1. The furnace fuse process produces a metallurgical bond between the coating and the substrate. The addition of Lanthanum oxide increases the mechanical properties of the coatings.
2. An optimum amount of Lanthanum oxide refine and purify the microstructure of the furnace fused coatings, but when the content of Lanthanum oxide is more or less, the effect is not good.

5. ACKNOWLEDGEMENTS

This study was financially supported by the National Natural Science Foundation of China (No. 51361020 and 51365024).

6. REFERENCES

1. Wu Yuping, Lin Pinghua, Chu Chenglin, *et al.* Cavitation erosion characteristics of a Fe-Cr-Si-B-Mn coating fabricated by high velocity oxy-fuel(HVOF) thermal spray. *Materials letters*, Vol. 61, 2007, pp. 1867–1872. https://doi.org/10.1016/j.matlet.2006.07.147
2. L. Prchlik, S. Sampath. Effect of the microstructure of thermally sprayed coatings on friction and wear response under lubricated and dry sliding conditions. *Wear*, Vol 262, 2007, pp. 11–13. https://doi.org/10.1016/j.wear.2006.03.042
3. B.Vamsi Krishna, V.N. Misra, P.S.Mukherjee, *et al.* Microstructure and properties of flame sprayed tungsten carbide coatings. *Int. J. Refract. Met. Hard Mater*, Vol 20, 2002, pp. 355–374. https://doi.org/10.1016/S0263-4368(02)00073-2
4. L. Lin, K. Han. Optimization of surface properties by flame spray coating and boriding. *Surf. Coat. Technol.*, Vol 106, 1998, pp. 100–105. https://doi.org/10.1016/S0257-8972(98)00501-5
5. Šárka Houdková, Eva Smazalová, Marek Vostřák, *et al.* Properties of NiCrBSi coating, as sprayed and remelted by different technologies. *Surf. Coat. Technol.*, Vol 253, 2014, pp. 14–26. https://doi.org/10.1016/j.surfcoat.2014.05.009
6. Susumu Uozato, Kazuhiro Nakata, Masao Ushio. Evaluation of ferrus powder thermal spray coatings on diesel engine cylinder bores. *Surf. Coat. Technol.*, Vol 200, 2005, pp. 2580–2586. https://doi.org/10.1016/j.surfcoat.2005.05.042
7. L. Lin, K. Han. Optimization of surface properties by flame spray coating and boriding. *Surf. Coat. Technol.*, Vol 106, 1998, pp. 100–105. https://doi.org/10.1016/S0257-8972(98)00501-5
8. R. Gonzalez, M.A. Garcia, I. Penuelas, *et al.* Microstructural study of NiCrBSi coatings obtained by different processes. *Wear*, Vol 263, 2007, pp. 619–624. https://doi.org/10.1016/j.wear.2007.01.094
9. Qiang Li, Dawei Zhang, Tingquan Lei, *et al.* Comparison of laser-clad and furnace-melted Ni-based alloy microstructures. *Surf. Coat. Technol.*, Vol 137, 2001, pp. 69–72. https://doi.org/10.1016/S0257-8972(00)00732-5
10. Limin Zhang, Dongbai Sun, Hongying Yu. Characteristics of plasma cladding Fe-based alloy coatings with rare earth metal elements. *Mater. Sci. Eng.*, A, Vol 452–453, 2007, pp. 619–624. https://doi.org/10.1016/j.msea.2006.10.142
11. S.P.Sharma, D.K.Dwivedi, P.K.Jain. Effect of La_2O_3 addition on the microstructure, hardness and abrasive wear behavior of flame sprayed Ni based coatings. *Wear*, Vol 467, 2009, pp. 853–859. https://doi.org/10.1016/j.wear.2008.12.029
12. Xiubo Liu, Rongli Yu. Effect of La_2O_3 addition on microstructure and wear properties of laser clad $\gamma/Cr_7C_3/TiC$ composite coatings on TiAl intermatallic alloy. Mater. Chem. Phys., Vol 101, 2007, pp. 448–454. https://doi.org/10.1016/j.matchemphys.2006.08.013
13. Hyung-Jun Kim, Soon-Young Hwang, Chang-Hee Lee. Assessment of wear performance of flame sprayed and fused Ni-based coatings. *Surf. Coat. Technol.*, Vol 172, 2003, pp. 262–269. https://doi.org/10.1016/S0257-8972(03)00348-7
14. Zhenyu Zhang, Bunv Liang, Hongjian Guo, Interface Microstructure and Tribological Properties of Flame Spraying NiCr/La_2O_3 Coatings, *J. Therm spray techn*, Vol 23, No.8, 2014, pp. 1404–1412.

Bearing Capacity Calculation and Fiber-reinforced Polymer Repair of Corroded Beam-slabs in a Wharf

Y. F. XIE*, Y. FAN and J. Y. WANG

Department of Transportation, Southeast University, Nanjing, 210096, China

ABSTRACT: Corrosion of steel reinforcement bars is a common problem for high-pile wharf in service, with the aim of solving this problem, a method to calculate the actual bearing capacity of corroded beam-slabs is proposed, in which the rate of loss of area and the reduction in strength of steel bars due to corrosion are considered. Taking Zhanjiang Port as an example, the actual bearing capacity of corroded beam slabs is calculated and is compared with that found under normal service conditions. For repair of corroded beam-slabs, a method in which fiber-reinforced polymer (FRP) bars partly replace the steel bars is proposed, and the basic assumptions and method of calculation for this mixed-reinforcement components are discussed.

1. INTRODUCTION

WHARF structures are exposed to a damp environment for long periods of time, especially in high-pile wharfs with open-type substructures, where beams and slabs are in direct contact with air and water. Even in the absence of external loading, because of the porosity of concrete, this corrosive medium can penetrate through the pores, thereby coming into contact with steel reinforcement bars and causing rusting. This corrosion will result in a decrease in the area of the steel, and thus to a deterioration in interfacial bonding between steel and concrete. The consequent reduction in the reinforcement capacity of the steel will have deleterious effects on the safety and durability of the whole structure, finally leading to decreased bearing capacity and even damage.

Most high-pile wharfs have been in service for decades, with consequent widespread corrosion of beam-slabs, some of which is severe and has serious ramifications for the shipping industry [1]. Therefore, it is an important task to evaluate the actual bearing capacity of damaged wharfs and devise an appropriate plan for their maintenance.

Fiber-reinforced polymer (FRP) has low density, high strength, good corrosion resistance, and many other advantages. FRP bars were first proposed in 1941 by Jackson [2], and were used in some bridge structures in the United States, Germany, and other countries [3]. More recently, there has been growing interest in their use in a number of civil engineering [4–8]. The application of FRP bars to the repair of corroded beam-slabs in high-pile wharfs can effectively reduce or even prevent the effects of reinforcement corrosion without affecting the bearing capacity of the structure.

In this paper, we present a new method for evaluating the actual bearing capacity of corroded beam-slabs in a high-pile wharf. By accurately determining the decrease of in bearing capacity as a result of corrosion, it can provide the basis for developing a wharf maintenance program [9]. Taking Zhanjiang port as an example, and evaluating the bearing capacity of the beam and slab, we propose a scheme in which steel bars are replaced with FRP bars to repair corroded beam-slabs.

2. RESISTANCE CALCULATION OF CORRODED REINFORCEMENT BEAM-SLAB

2.1. Beam-slab Calculation Items

As inputs, the parameters governing wharf structural security and usability are required, including the capacities of the panel, track beam, stringer, and beam [10]. The quantities to be determined include flexural capacity, shear capacity, crack width, and deflection.

2.2. Factors Influencing Member Resistance

The factors influencing the ultimate capacity of

---

*Author to whom correspondence should be addressed.
E-mail: xhsnac@163.com; xieyf@seu.edu.cn

1544-8053/16/02 S141-06

doi:10.12783/issn.1544-8053/13/4/S18

reinforced concrete members are principally the deterioration in concrete strength, the decrease in steel cross- sectional area due to corrosion [11], the decrease in steel yield strength, and the reduced bond strength between the concrete and the steel.

Steel corrosion, spalling, and cracking damage appear in parts of the panels and beams of structures in Zhanjiang Port that have been subject to long-term erosion by seawater. Steel corrosion causes thinning of the protective layer of concrete and a decrease in the steel's bearing capacity, which raises the question of whether the structures in the port can satisfy their original design loadings [12].

2.3. Resistance Calculation Methods

According to the regulations [13], the resistance of corroded reinforced concrete elements is calculated as follows.

1. The design strength of the corroded steel reinforcement is given by

$$f_{yc} = \frac{1-1.077\eta_s}{1-\eta_s} f_y \tag{1}$$

where f_y is the original design strength of the reinforcement under tension and η_s is the section loss rate of the corroded steel reinforcement.

2. The index of the corroded reinforcement is given by

$$q_0 = \frac{A_{sc} f_{yc}}{f_c b h_0} \tag{2}$$

here f_c is the original design strength of the concrete under compression, b and h_0 are respectively the width and height of the corroded section of the steel reinforcement, and

$$A_{sc} = \mu A_s \tag{3}$$

A_{sc} is the cross-sectional area of the corroded section in the tension zone, where A_s is the original cross-sectional area and μ is the loss rate due to corrosion; f_c is the original compressed concrete design strength; b is the corroded member section width; h_0 is the corroded member section height. The resistance of the corroded reinforcement in the tension zone is

$$P_{yc} = \alpha_s f_{yc} A_{sc} \tag{4}$$

and the resistance in the compression zone is

$$P'_{yc} = \alpha_s f'_{yc} A'_{sc} \tag{5}$$

where α_s is the sectional coefficient of resistance, f'_y is the original design strength of the reinforcement under compression, and A'_{sc} is the cross-sectional area of the corroded reinforcement in the compression zone.

3. CALCULATION AND ASSESSMENT OF THE ACTUAL BEARING CAPACITY OF THE WHARF

3.1. The Wharf Situation

Zhanjiang port is located in the Xiashan harbor district and was completed in 1993. The wharf has a high piled beam-slab structure whose main body consists of 13 standard structural segments, each of length 51 m, with the terminal having a total length 761.0 m, a width of 33.0 m, and a row spacing of 6 m. The main components include steel piles, stringers, beams, plates, berthing members, and rubber fenders and bollards, etc.

From ship classifications, flow conditions, and wind rose diagram data, the ship mooring force is calculated to be $N = 488$ kN, based on a 550 kN bollard is selected for the evaluation. The fender meets the maximum impact energy absorption requirements.

3.2. Determination of the Most Adversely Affected Member

3.2.1. The Beam

Figure 1 shows a typical picture of the bottom spall-

Figure 1. *Beam damage.*

Table 1. Dimensions of Beam ZLs2.

Width (mm)	Height (mm)	Upper Protective Layer Depth (mm)	Bottom Protective Layer Depth (mm)	Steel Area Under Tension (mm^2)	Steel Area Under Compression (mm^2)	Original Design Strength of Steel f_y (N/mm^2)	Original Design Strength of Concrete Under Axial Compression f_c (N/mm$_2$)
400	1500	50	50	5803	3088	300	14.3

ing concrete of the beam, for which the steel corrosion rate is in accordance with a rate of loss of cross-sectional area of less than 5% and a corrosion depth of less than 0.3 mm.

The calculation is carried out for the most seriously corroded beam, ZLs2, the dimensions of which are shown in Table 1.

The sectional loss rate of the beam is small and is taken as 5% in the calculation. The actual area of reinforcement in the original tension zone is 5803 mm^2, and so

$$A_{sc} = 0.95 \times 5803 = 5513 \text{ mm}^2$$

The actual area of reinforcement in the original compression zone is 3088 mm^2, and so

$$A_{sc} = 0.95 \times 3088 = 2934 \text{ mm}^2$$

The resistance of the corroded reinforcement in the tension zone is

$$P_{yc} = \alpha_2 f_{yc} A_{sc} = 1.58 \times 106 = 167.48 \text{ kN}$$

and that in the compression zone is

$$P'_{yc} = \alpha_2 f'_{yc} A'_{sc} = 88 \times 106 = 93.28 \text{ kN}$$

In the calculation of the bearing capacity of the beam structure, the following values are assumed: f_c = 14.3 N/mm^2, f_{yc} = 300 N/mm^2, α = 80 mm, h_0 =1500 – 80 = 1420 mm, and α' = 60 mm. Then the condition $\xi < 0.85\xi_b$ is satisfied, since

$$\xi = \frac{f_y A_s - f'_y A'_s}{f_c b h_0} = 0.095 < 0.85\xi_b = 0.468$$

Also, the condition $x \geq 2a'$ is satisfied, since $x = \xi h_0$ = 135 mm > $2a'$ = 120 mm.

Therefore,

$$\alpha_s = \xi(1 - 0.5\xi) = 0.090$$

$$M_u = \alpha_s f_c b h_0 + f'_y A'_s (h_0 - \alpha') = 1197.80 \text{ kN} \cdot \text{m}$$

The ultimate bending moment capacity of the beam M = 1385.56 kN·m, and so, because $M_u/M = 0.864 < 1.35$, the bearing requirement is not satisfied.

3.2.2. The Panel

Panel BS2 is selected for evaluation since it is the most seriously corroded plate. The corroded condition of the panel is shown in Figure 2. Such damage appears in two panels, with about 20% steel corrosion.

The strength utilization coefficient of the corroded tensile reinforcement can be selected according to the following requirements.

In the calculation of the bearing capacity of the panel structure, the following values are assumed: f_c = 14.3 N/mm^2, f_{yc} = 300 N/mm^2, and a = 65 mm, and h_0 = 400 – 65 = 335 mm. Then the conditionis $\xi < \xi_b$ satisfied, since

$$\xi = \frac{f_y A_s}{f_c b h_0} = 0.061 < \xi_b = 0.55$$

Then

$$\alpha_s = \xi(1 - 0.5\xi) = 0.399$$

$$M_u = \alpha_s f_c b h_0^2 = 80.74 \text{ kN} \cdot \text{m}$$

The ultimate bending moment capacity at the center of the span is calculated to be M = 90.5 kN·m, so $M_u < M$, and therefore the bearing requirement is not satisfied.

Figure 2. *Panel corrosion condition.*

3.3. Evaluation of Usability Under Normal Service Conditions

Under normal service conditions, the loadings are taken as the original design values, and the actual bearing capacities of the panels and beams are used. The final results indicate whether the wharf can satisfy bearing requirements under the original loadings.

3.3.1. Crack Width Calculation

The maximum crack width is given by

$$\omega_{\max} = \alpha \frac{\sigma_{sk}}{E_s}\left(30 + c + 0.07\frac{d}{\rho_{te}}\right) \tag{6}$$

here α is the comprehensive effect coefficient, the value of which is 2.1 for flexural members, σ_{sk} is the stress on the tensile steel bars calculated from the characteristic value of the load, c is the distance between the edge of the lateral tensile steel bars and the edge of the tension zone, d is the diameter of each steel bars, and $\rho_{te} = A_{te}/A_s$ is the effective reinforcement ratio of the tensile bars, where A_{te} is the effective area of the tension zone of the concrete, and A_s is the cross-sectional area of the longitudinal steel bars in the tension zone.

The results of this calculation are shown in Table 2.

3.3.2. Deflection Calculation

The deflection is given by

$$f = S\frac{Ml_0^2}{EI} \tag{7}$$

where S is a coefficient related to the load and the support conditions, M is the bending moment of the flexural members, l_0 is the calculated span, and EI is the flexural rigidity of the section.

The results of this calculation are shown in Table 3.

A comparison between the calculated results and the original deformation is shown in Table 4, from which it can be seen that the decreases in bearing capacity of the panel, the track beam, and the beam are significant, while that of the stringer is not.

Table 2. Results of Crack Width Calculation.

Member Name	Crack Location	Crack Width S_d (mm)	Allowable Value R_d (mm)	R_d/S_d
Panel	Bottom	0.10	0.3	3.00
	Top	0.12	0.3	2.50
Track beam	Span Center	0.08	0.3	3.75
	Support	0.11	0.3	2.73
Stringer	Span Center	0.09	0.25	2.78
	Support	0.12	0.25	2.08
Beam	Span Center	0.11	0.3	2.73
	Support	0.09	0.3	3.33

Table 3. Results of Deflection Calculation.

Member	Calculated Deflection, fs/l_0	Allowable Value, fs/l_0	Satisfied?
Panel	1/658	1/300	Yes
Track beam	1/1581	1/800	Yes
Stringer	1/2102	1/600	Yes
Beam	1/4968	1/600	Yes

3.4. Main Impact Index of Corroded Reinforcement Wharf Member

The calculation results suggest that corrosion causes a decrease in strength. Deformation of panels and beams increase the deflection of structural members. Therefore, in the future, limits should be imposed on loadings on panels, although beams can be used under their original design loadings.

4. APPLICATION OF FRP TO THE REPAIR OF CORRODED COMPONENTS

FRP bars can be used instead of steel bars in wharf repair. Most damage to wharf structure is due to reinforcement corrosion. FRP bars are not subject to corrosion and have high strength, and can therefore replace steel bars. In addition, FRP reinforcement is very light, is non-magnetic, and has very good fatigue resistance, a study at the University of West Virginia using glass fiber-reinforced polymer (GFRP) bars has shown that FRP-reinforced concrete beams can have better bending strength than steel reinforced beams.

Table 4. Deflection Comparison.

Member	Calculated Deflection, fs/l_0	Original Deflection, fs/l_0	Rate of Increase (%)
Panel	1/658	1/937	42
Track beam	1/1581	1/3286	108
Stringer	1/2102	1/4127	96
Beam	1/4968	1/4975	0.1

However, FRP is a brittle material, with a low elastic modulus. Therefore in order to prevent brittle failure of the beam-slab, which can occur suddenly, steel bars should be only partly replaced so that steel bars can maintain the ductility of the beam-slab. To make full use of the high tensile strength of FRP bars, they are usually placed in the tension zone of the beam-slab.

The calculation of the flexural bearing capacity of components with mixed reinforcement is similar to that for general concrete components, and is based on the following assumptions:

1. The plane cross-section assumption is satisfied.
2. It is assumed that the concrete tension zone is not in a cracking state;
3. An idealized stress-strain relationship is adopted for the concrete in the compression zone.
4. The stress-strain relationship of the steel bars is simplified as an ideal elastic-plastic one, and that of the FRP bars as a linear elastic one.

Based on these assumptions and the stress-strain relationship for the FRP reinforcement, a formula for calculating the flexural bearing capacity of mixed-reinforcement beams has been derived [14]. Considering realistic engineering situations, in this paper, the failure mode of beams is taken to be fit-reinforced failure. The calculation proceeds as follows:

$$f_c bx = f_y A_s + E_f A_f \varepsilon_f \tag{8}$$

$$\varepsilon_f = 0.0033\left(\frac{0.8}{\xi} - 1\right) \tag{9}$$

$$M_u = f_c b h_0^2 \xi\left(1 - \frac{\xi}{2}\right) \tag{10}$$

where f_c is the design compressive strength of the concrete, b is the width of the section, x is the compression height of the rectangular stress graph, f_y is the yield strength of the tensional steel bars, A_s is the cross-sectional area of the longitudinal steel bars in the tension zone, E_f is the elastic modulus of the FRP bars, A_f is the cross-sectional area of the longitudinal FRP bars in the tension zone, ε_f is the tensional strain of the FRP bars, $\xi = x/h_0$, is the relative compression height, h_0 is the effective height of the section, and M_u is the ultimate flexural moment of the section.

The following formula for calculating the sectional effective moment of inertia of mixed-reinforcement beams has been derived by Bischoff [15],

$$I_e = \frac{I_{cr}}{1 - \eta\left(\frac{M_{cr}}{M_a}\right)^2} \tag{11}$$

with

$$\eta = 1 - \frac{I_{cr}}{I_g} \tag{12}$$

where I_{cr} is the cracking moment of inertia of the section, I_g is the elastic moment of inertia of the section, M_{cr} is the cracking moment of the beam, and M_a is the corresponding bending moment from the calculation of the effective moment of inertia.

When the component is under stress, the steel bars will enter into a yield state earlier than the FRP bars, and therefore, the component's bearing capacity is determined by the bearing capacity limit of the FRP bars. As an example, we take the beam ZLs2 of the Zhanjiang wharf, in which steel bars in the tension zone have been partly replaced by FRP bars ,as shown in Figure 3.

The performance parameters of the FRP bars are shown in Table 5.

The calculation gives a value of 3586.45 kN·m for the flexural capacity of the steel-FRP reinforced concrete beams, which increase by 85% compared with that of the original beams (1938.62 kN·m). The deflection of the steel-FRP reinforced beams is 1/1362, which is within the allowed range of values. This result

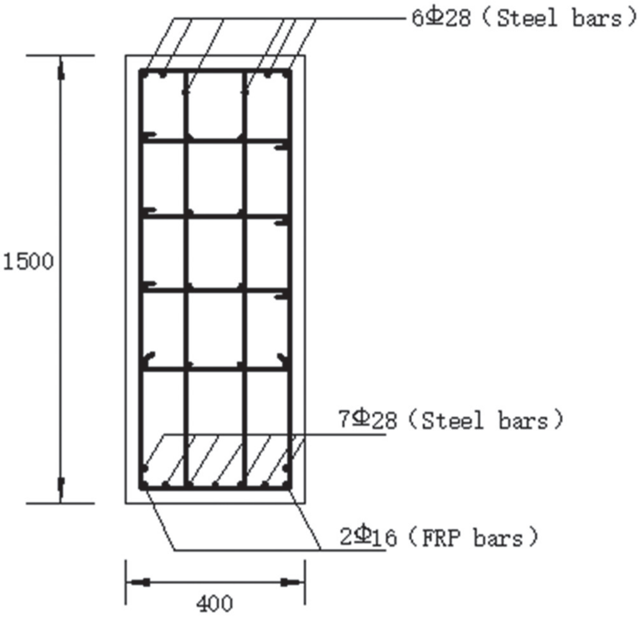

Figure 3. *Reinforcement of beam ZLs2.*

Table 5. Performance Parameters of FRP Bars.

Parameter	f_f (N/mm^2)	E_f (N/mm^2)	A_f (mm^2)
Value	1000	1.1×10^5	1232

shows that the mixed-reinforcement beams possess better strength and usability, making them suitable for application to wharf repair.

The calculation method for panels is similar to that for beams.

5. CONCLUSION

1. The wharf in Zhanjiang Port is subject to long-term erosion by seawater, leading to spalling and other structural damage. This results in decreased of bearing capacity of panels, beams, and the whole wharf.
2. The new method proposed here can determine the actual capacity of a wharf and provide the rate of decrease of bearing capacity, allowing a comparison of the results of the evaluation and those calculated in the original design.
3. The new method can be used for further evaluations of high-pile wharfs and is an efficient approach to measuring the actual bearing capacity of old wharfs.
4. The evaluation method proposed here can be used in engineering practice. It allows a decision to be made about whether to strengthen a wharf structure to limit service loads to meet engineering requirements.
5. A method has been proposed for repairing corroded wharf structure, by replacing some of the corroded steel bars with FRP bars, to solve the problem of decreased bearing capacity due to steel corrosion. The basic assumptions and calculation methods for the mixed-reinforcement components have been discussed.

6. REFERENCES

1. Y. Wang, S. Gao. Probability Distribution of Ultimate Bearing Capacity of Beam and Slab High-pile Wharf. *Waterway and Harbor*, 2012(6): 515–522.
2. ACI committee 440, State of the art report on reinforced plastic for concrete structures. Detroit, MI: American Concrete Institute, February, 1996.
3. L. Ye, P. Feng. Applications and development of fiber-reinforced polymer in engineering structures. *China Civil Engineering Journal*, 2006, 39(3):24–36.
4. C. Apostolopoulos, V. Kappatos. Tensile Properties of Corroded Embedded Steel Bars B500c in Concrete. *International Journal of Structural Integrity*, 2013, 4(2). https://doi.org/10.1108/17579861311321744
5. G. Diamantogiannis, C. Apostolopoulos, P. Nikolakopoulos. Mechanical behavior of B500c steel with aluminum layer coating in marine environment. *Journal of Materials in Civil Engineering (ASCE)*, 27(4), 2014, 27(4): 04014155. https://doi.org/10.1061/(ASCE)MT.1943-5533.0001094
6. C. Apostolopoulos, S. Demis, V. Papadakis. Chloride-Induced Corrosion of Steel Reinforcement-Mechanical Performance and Pit Depth Analysis. *Journal Construction and Building Materials*, 2013, 38: 139–146. https://doi.org/10.1016/j.conbuildmat.2012.07.087
7. W. Salvatore, S. Caprili, A. Braconi, *et al.* Final Report of European Commission, Effects of Corrosion on Low Cycle Fatigue (seismic) behavior of High Strength Steel reinforcing bars. RFSR-CT-2009-00023 project, Brussels, 2014.
8. C. Apostolopoulos, G Diamantogiannis, A. Apostolopoulos. Assessment of the Mechanical Behavior in Dual-Phase Steel B400C, B450C and B500B in a Marine Environment. *Journal of Materials in Civil Engineering*, 2015, 28(2): 04015097. https://doi.org/10.1061/(ASCE)MT.1943-5533.0001271
9. C. Q. Li. Initiation of Chloride-induced Reinforcement Corrosion in Concrete Structural Members-Prediction. *ACI Structure Journal*, 2002, 99(2): 133–141. https://doi.org/10.1016/S0022-2860(01)00882-1
10. C. Q. Li. Reliability Based Service Life Prediction of Corrosion Affected Concrete Structures. *ASCE Journal of Structural Engineering*, 2004, 130(10): 1570–1577. https://doi.org/10.1061/(ASCE)0733-9445(2004)130:10(1570)
11. Y. Wang, Y. Sun, C. Huang. Time-dependent Resistance Model for Reinforced Concrete Members of Open High Piles Wharf. APAC2005, September 4–8, 2005, Jeju, Korea
12. A. Kim, G. Mark. Structural Reliability of Concrete Bridges Including Improved Chloride induced Corrosion Models. *Structural safety*, 2000(22): 313–333.
13. JTJ 302—2006, Detection and assessment technical specification of the port structure.
14. W. Qu, D. Chen, H. Huang. Bending Moment Resistance Calculation of Steel-GFRP Reinforced Concrete Beam. *Building Structure*, 2006, 36(12): 22–24.
15. P.H. Bischoff. Deflection calculation of FRP reinforced concrete beams based on modifications to the existing branson equation. *Journal of Composites for Construction*, 2007, 11(1): 4–14. https://doi.org/10.1061/(ASCE)1090-0268(2007)11:1(4)

A Case Study on Utilization of 50-year-old Concrete in Recycled Aggregate

ZONGPING CHEN[1,3], JINJUN XU[2,*], YULIANG CHEN[1] and CHENGGUI JING[1]
[1]*College of Civil Engineering and Architecture, Guangxi University, Nanning 530004, China*
[2]*College of Civil Engineering, Nanjing Technology University, Nanjing 211816, China*
[3]*Key Laboratory of Disaster Prevention and Structural Safety of China Ministry of Education, Nanning 530004, China*

ABSTRACT: This paper investigates some mechanical properties of recycled aggregate concrete (RAC) with 50-year-old recycled coarse aggregate (RCA), and theoretically analyzes the corresponding RAC stress-strain curves relative to those of normal aggregate concrete. Concrete prism specimens, including 66 standard prisms and 33 nonstandard ones, were fabricated and tested through 11 groups of RCA replacement ratios from 0% to 100% with an interval of 10%. On this basis, the standard prism compressive strength at ages of 28 days and two years, the flexural strength of the nonstandard prism, the cube strength after flexural test and the strain at the maximum standard prism compressive stress for 28 days, as well as Poisson's ratio of the standard prisms for two years was investigated. Finally, analytical expressions were proposed for predicting the peak strain, the stress-strain curves of RAC and the strength conversion relationships.

1. INTRODUCTION

SUSTAINABLE development involves many interlinked aspects including nature, environment, society, economy, technology and politics, and it is an embodiment of an integrated performance index. In developing countries, due to great efforts in infrastructure constructions, the urbanization process is surely accelerated at a high-speed rate. However, along with the rapid development of construction, construction waste has been produced continuously, which exerts a side effect on environmental quality. The term "construction and demolition waste (CDW)" has been widely used for referring to the solid waste produced during new construction, renovation, and demolition of buildings [1]. To a large extent, CDW has caused a series of terrible environmental problems, and produced a bad effect on economic construction and social development. Around the world, CDW frequently accounts for 10%–30% of the solid waste at many landfill sites [1]. Worse still, it accounts for 30%–40% of the total municipal solid waste in China. It is noticed that waste concrete is the main ingredient of CDW, and its content accounts for more than 40% of the total amount [2].

In order to effectively utilize the waste concrete, it is necessary to employ it as recycled aggregate of new concrete, which can be named as recycled aggregate concrete (RAC). In view of this, mechanical properties of RAC need to be deeply investigated so as to expand the application scope of RAC, especially in building structures. In China, RAC has attracted much attention from construction departments as a structural concrete [2]. So far, some research has been carried out on its material properties. For example, Zhu *et al.* [3] carried out some experimental investigations on the thermal properties of concrete blocks prepared with low grade recycled aggregates; Akash *et al.* [4] studied the behavior of RAC under drop weight impact load; Belen *et al.* [5] analyzed the concrete with 100% recycled coarse aggregate (RCA) content for the structural RAC; Xiao *et al.* [6] conducted a series of tests on shear transfer across a crack in RAC. Besides, some studies on the durability properties of RAC have been launched by some researchers, such as Salomon *et al.* [7], Abbas *et al.* [8], and Patrícia *et al.* [9]. Notably, the above strength indexes of RAC were all tested after a standard curing age (28 days).

2. RESEARCH SIGNIFICANCE

It seems that the research on time-based mechanical properties of RAC under uniaxial compression and

---

*Author to whom correspondence should be addressed.
E-mail: jjxu_concrete@163.com
Postal address: College of Civil Engineering, Nanjing Technology University, Nanjing 211816, China

1544-8053/16/02 S147-06

doi:10.12783/issn.1544-8053/13/4/S19

flexural condition is still limited for using the original RCA, and the experimental data based on the long-age concrete are in a state of blank. Meanwhile, previous studies just selected rough and large interval of RCA replacement ratio, which might lose some special performances of RAC under certain kinds of RCA replacement ratio. Further, the constitutive relationship between stress and strain also needs to be clarified for RAC with micromesh increasing ratio when it is applied to structural members. This paper just attempt to address the above listed issues so as to fill the lack of knowledge in this filed.

3. EXPERIMENTAL INVESTIGATION

The design consisted of two batches of concrete: one was tested after maintained for the standard age (28 days), and the other was tested after a long age (two years) of maintenance. 11 groups of concrete with RCA replacement ratios of δ = 10%, 20%, 30%, 40%, 50%, 60%, 70%, 80%, 90% and 100% were fabricated, and three specimens were prepared under the given replacement ratio in each group. The RAC specimens included 66 standard prisms (5.91 in. × 5.91 in. × 11.81 in. [150 mm × 150 mm × 300 mm]) and 33 nonstandard prisms (5.91 in. × 5.91 in. × 21.64 in. [150 mm × 150 mm × 550 mm]). Standard tests were carried out to determine their basic mechanical properties: the prism compressive strength cured under the standard age and the long age, the flexural strength using the nonstandard prism specimens under the standard age and the long age, and the Poisson's ratio.

3.1. Materials

River sand was used as the fine aggregate (FA) in this study. The RCA was obtained from the artificial broken concrete poles, which started to serve at the year of 1958 and were dismantled and transported to the laboratory because of the ice disaster at the year of 2008 in P.R China. The particle size of RCA was 0.552–1.103 in. (14–28 mm), and the bulk density was 1385 kg/m^3. The natural coarse aggregate (NCA) was continuously graded gravel with particle size of 0.394–1.103 in. (10-28 mm), and its bulk density was 1437 kg/m^3. The RCA and NCA were washed for several times and dried out naturally before concrete mixing.

3.2. Concrete Mixtures

In fact, the most distinctive feature of RCA compared to NCA is its higher water absorption capacity, which is mainly due to the adhered mortar (also called as old cement mortar substrate) [10]. In other words, additional absorbed moisture of RCA can reduce the actual water-cement ratio (W/C) in concrete, which means a curing effect on concrete strength. Based on the above considerations, in this study, the designed W/C was kept constant for each concrete type in order to focus only on the influences of RCA water absorption capacity on the mechanical performances of RAC. The mix proportions of concrete are shown in Table 1.

3.3. Preparation of Specimens

The fabrication and curing of all mixtures were conducted in the Chinese Education Ministry Key Laboratory of Disaster Prevention and Structural Safety at Guangxi University, P.R. China. The cement, sand and coarse aggregate were placed and dry-mixed for about 3 min before water addition. After another three-minute mixing with water, a slump test was carried out to determine the workability. For the standard prism

Table 1. Mix Proportions of Concrete.

No.	δ (%)	W/C	Sand Ratio	C (kg/m^3)	W (kg/m^3)	FA (kg/m^3)	NCA (kg/m^3)	RCA (kg/m^3)
RAC-0	0	0.41	0.32	524	215	532	1129	0
RAC-10	10	0.41	0.32	524	215	532	1016	113
RAC-20	20	0.41	0.32	524	215	532	903	226
RAC-30	30	0.41	0.32	524	215	532	790	339
RAC-40	40	0.41	0.32	524	215	532	677	452
RAC-50	50	0.41	0.32	524	215	532	564	565
RAC-60	60	0.41	0.32	524	215	532	452	667
RAC-70	70	0.41	0.32	524	215	532	339	790
RAC-80	80	0.41	0.32	524	215	532	226	903
RAC-90	90	0.41	0.32	524	215	532	113	1016
RAC-100	100	0.41	0.32	524	215	532	0	1129

specimens, the mixture in each group was cast in 5.91 in. × 5.91 in. × 11.81 in. (150 mm × 150 mm × 300 mm) prisms in six wood moulds. In contrast, for the nonstandard prism specimens, the same type mixture in each group was tossed in 5.91 in. × 5.91 in. × 21.64 in. (150 mm × 150 mm × 550 mm) prisms in three wood moulds. One day after casting, the prisms were demoded and then cured in a fog room (20 ± 2°C, 95% relative humidity) for 28 days (the standard age). After that, the first batch of specimens, including 33 standard prisms and 33 nonstandard prisms, were taken to test the uniaxial compressive strength, the stress-strain curves and the flexural strength, respectively. As for the rest specimens, they were cured under the same laboratory conditions for two years, and then used to test the axial compressive strength and the Poisson's ratio at a long-term age.

3.4. Test Settings and Methods

For the axial compression test, the loading setup was an RMT-201 rock and concrete mechanics test system. In order to get complete stress-strain curves, the displacement-controlled loading method was adopted and the loading rate was kept constant as 1.97 × 10^{-4} in./s (0.005 mm/s). Each specimen was preloaded before actual loading in order to lessen the impacts due to the loose of specimen end. For the flexural strength test, the loading setup was a flexural testing device, and the span of testing segment was 17.73 in. (450 mm).

4. EXPERIMENTAL RESULTS AND DISCUSSION

4.1. Compressive Stress-strain Relationships

Figure 1 shows the typical stress-strain curves of RAC with different RCA contents at the standard age. It can be seen that there is basically no deviation from the stress-strain theory of elasticity-plasticity in the structural design process.

4.2. Peak Strain

Peak strain is the strain corresponding to peak stress in the stress-strain curve. In this study, three peak strain values of each group of RAC specimens with different RCA contents are got averaged as the final peak strain. It can be seen that the value of peak strain presents an increasing trend as the RCA content increases. The main reason for the increase of the peak strain can be attributed to the brittleness of RCA containing old

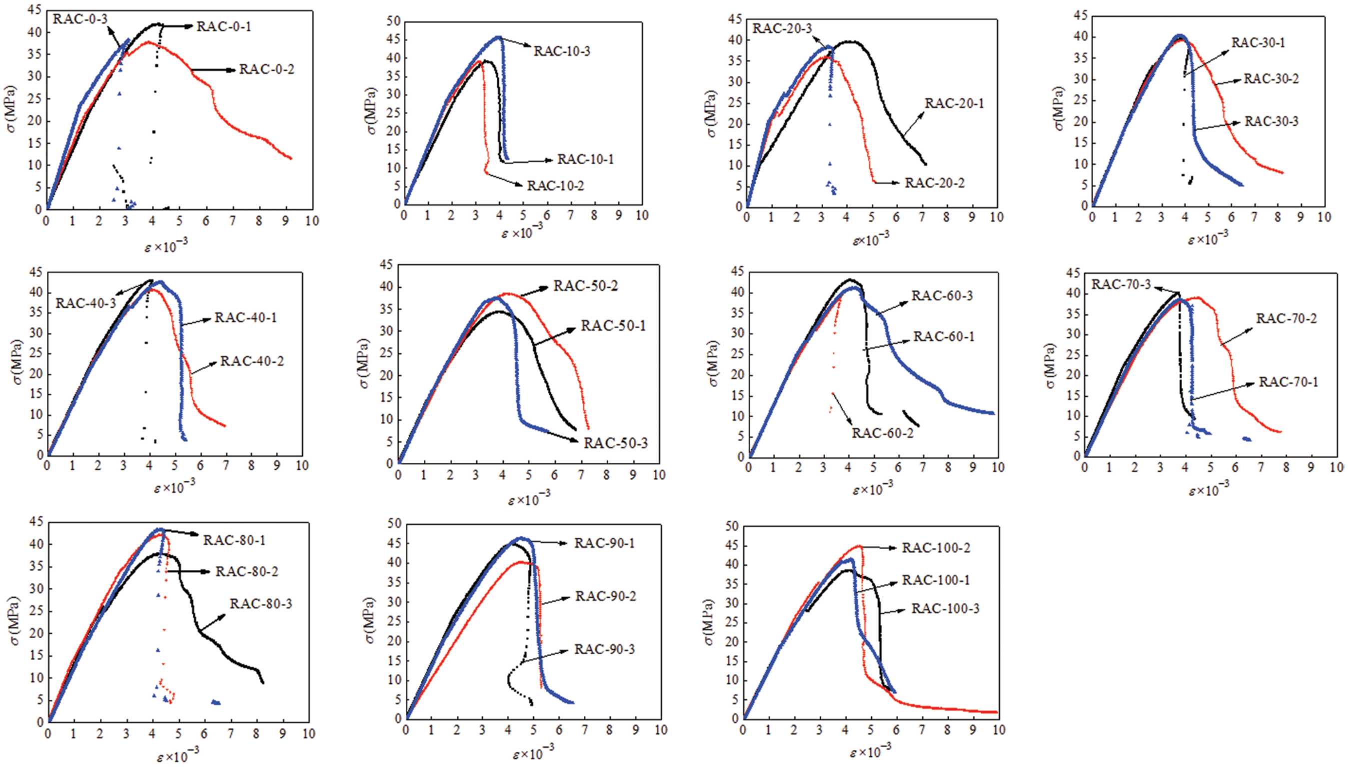

Figure 1. *Stress-strain curves of RAC standard prisms at the age of 28 days.*

cement-mortar substrate, which can lead to a larger deformation. In this study, the following fitting expression is suggested for calculating the peak strain:

$$\varepsilon_0^r = \varepsilon_0^n \times (-7\times10^{-7}\delta^3 + 9\times10^{-5}\delta^2 + 4\times10^{-3}\delta + 1.642) \tag{1}$$

where ε_0^n is the peak strain of NAC, and ε_0^r is the peak strain of RAC.

4.3. Compressive Strength

Compressive strength is the peak stress of the test specimen under uniaxial compression. Table 2 gives the prism compressive strength at the standard age (f_c^s) and at two years (f_c^1) with different RCA replacement ratios. As can be seen, the prism compressive strength of RAC is generally higher than that of NAC except that of RAC-10, RAC-50, RAC-60 and RAC-80 at the standard age and that of RAC-20, RAC-50 and RAC-70 at two years. Overall, the prism compressive strength of RAC at the long age on average is 16.8% higher than that of NAC at the standard age. As for a certain replacement ratio, the former is also higher than that of the latter. That is to say, as the curing time goes on, the hydration extent of internal cement colloid develops deeply so that the strength of RAC is improved.

According to the test results of strength waving phenomenon, it can be concluded that there is a close relationship between the concrete compressive strength and RCA properties. The water absorbing capacity of RCA, the micro-crack in RAC and the content of old adhered mortar attaching to the original coarse aggregate can significantly affect the strength of concrete. Because of the stronger water absorbing capacity of RCA, the actual water-cement ratio in concrete mixture will be lower compared to the designed water-cement ratio, so that the concrete strength will be improved to some extent. In this study, the designed water-cement ratio is controlled at the same level ($W/C = 0.41$). Thus, with increasing the replacement ratio of RAC, its prism compressive strength will be enhanced naturally, which means that the better water absorbing capacity of RCA plays a positive role in improving the concrete strength. On the other hand, the concrete strength may be undermined due to the micro-crack in RAC and the content of old adhered mortar attaching to the original coarse aggregate. The micro-crack is formed in the process of crushing the RCA, and its existence will increase the brittleness of the coarse aggregate. As a result, the RAC strength will become worse with the increase of the replacement ratio of RAC. At the same time, the old adhered mortar attaching to the original coarse aggregate will change the interfacial bonding conditions between the original natural coarse aggregate in RCA and the new formed adhered mortar. Because of the lower compressive strength of old adhered mortar and its brittleness compared to NCA, it is obvious that the RAC prism compressive strength will be reduced. Comprehensively speaking, if the positive effect is stronger than the negative one, the RAC strength will be improved; otherwise, the strength will be worsened.

4.4. Flexural Strength

The flexural strength $f_t (f_t = F_t\, l/bh^2)$ of RAC is determined by the Chinese Code [JTG E30–2005] 'Test method of cement and concrete for highway engineering'. Here, F_t is the failure flexural load, l is the length of prism specimen, b is the breadth of the cross-section, and h is the height of cross-section. In this test, l is set to 17.73 in. (450 mm), b is 5.91 in. (150 mm), and h is 5.91 in. (150 mm). The flexural strength of RAC is also shown in Table 2. It can be seen that RCA content has significant influences on the flexural strength of RAC.

Table 2. Test Results of RAC Strength.

No.	RAC –0	RAC –10	RAC –20	RAC –30	RAC –40	RAC –50	RAC –60	RAC –70	RAC –80	RAC –90	RAC –100
f_t (MPa)	5.50	5.70	5.90	6.00	6.10	5.10	5.70	5.50	5.30	5.40	5.90
f_c^s (MPa)	39.33	41.35	38.03	39.75	42.06	36.77	41.3	39.32	41.06	43.83	41.63
f_c^1 (MPa)	46.67	44.27	50.57	46.67	46.71	46.15	43.60	49.76	46.03	46.86	50.67
f_{cu} (MPa)	45.30	46.50	44.70	47.20	46.80	43.40	49.20	44.60	48.40	47.40	48.40
f_t/f_{cu}	0.12	0.12	0.13	0.13	0.13	0.12	0.12	0.12	0.11	0.11	0.12
f_c^s/f_{cu}	0.87	0.89	0.85	0.84	0.90	0.85	0.84	0.88	0.85	0.92	0.86
f_t/f_c	0.14	0.14	0.16	0.15	0.15	0.14	0.14	0.14	0.13	0.12	0.14
f_c^1/f_c^s	1.19	1.07	1.33	1.17	1.11	1.26	1.06	1.27	1.12	1.07	1.22

Generally, there are two tendencies for different levels of replacement ratio of RAC: when the replacement ratio is lower than 50%, the flexural strength of RAC increases with the increase of RCA content, whereas when the replacement ratio is over 50%, the flexural strength decreases with the increase of RCA content. Besides, it is well worth mentioning that the average ft of RAC is 5.66 MPa, which is 2.91% higher than that of NAC.

4.5. Poisson's Ratio

Poisson's ratio υ_c is an important index of the lateral deformation of concrete. Although this ratio at the standard age has been researched already, it is not the real value when the RAC is applied to structural concrete for long-time use. In this test, the longitudinal strain ε' and lateral strain ε of all prism specimens were acquired in the stable stress stage. Thus, the value of Poisson's ratio can be easily calculated by the equation of $\upsilon_c = \varepsilon'/\varepsilon$.

Figure 2 shows the influence of the RAC replacement ratio on Poisson's ratio. Based on the test results, an empirical formula can be given as follows:

$$\upsilon_c = 0.21 - 0.0003\delta \tag{2}$$

4.6. Approximation of the Stress-strain Relation

Nondimensionalization is an unexceptionable way to probe the variation rules at different stress stages in the constitutive relationship curves. For structural analysis and design in practical engineering applications, an analytical expression for the stress-strain curves of RAC is desirable. In this study, the analytical expression of normalized stress-strain relation of RAC is approximated by the following equation:

$$\bar{\sigma} = \begin{cases} a\bar{\varepsilon} + (3-2a)\bar{\varepsilon}^3 + (a-2)\bar{\varepsilon}^3, & 0 < \bar{\varepsilon} < 1 \\ \bar{\varepsilon} \big/ [b(\bar{\varepsilon}-1)^2 + \bar{\varepsilon}], & \bar{\varepsilon} \geq 1 \end{cases} \tag{3}$$

where a is the slope of the initial tangent of the dimensionless stress-strain curves, which reflects the initial elastic modulus of RAC; b is related to the area under the descending portion of the dimensionless stress-strain curves. Based on 11 groups of the acquired curves of RAC, the parameters a and b can be obtained by data fitting analysis, as shown in Table 3. Here, the curves of specimens with δ = 0%, 10%, 20%, 30%, 40%, 50%, 60%, 70%, 80%, 90% and 100% are selected for data fitting, and their rendezvous graph is shown in Figure 3. It can be seen that the curves at the ascent stage are basically coincident, and their discreteness is relatively large once the curves exceed the peak stress. Compared to NAC, with the increase of the RAC replacement ratio, the declining curve is much steeper, which means that the variation tendency of RAC replacement ratio at the stress nonlinear stage of each curve plays a vital role in the concrete ductility.

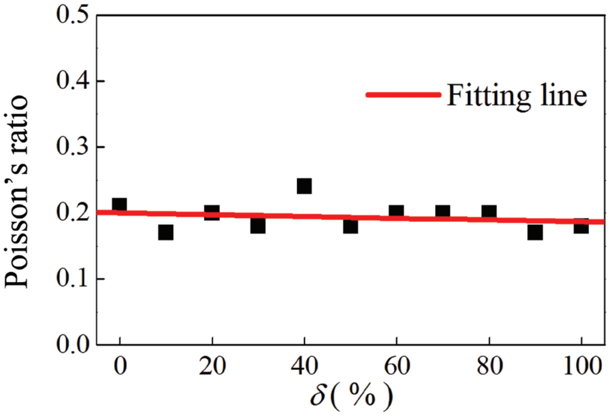

Figure 2. *Poisson's ratio of RAC.*

5. CONCLUSIONS

Based on the results of this experimental investigation, the following conclusions are drawn:

1. The peak strain value of RAC generally increases with the increase of the RCA content. For the RCA replacement ratios of 80%, 90% and 100%, the peak strain values increase by about 15% compared to that of the NAC.
2. The compressive strength of RAC including the prism compressive strength at the standard age and at two years, the flexural strength and the cube compressive strength generally increase with the increase of RCA content.

Table 3. Fitting Results of Parameters a and b Under Different RCA Replacement Ratios.

Parameter	0%	10%	20%	30%	40%	50%	60%	70%	80%	90%	100%	Average
a	0.80	0.80	1.20	1.20	0.98	1.20	1.20	1.40	1.30	1.10	0.95	1.10
b	5.0	10.0	3.0	4.5	8.0	2.3	5.0	13.0	6.0	18.0	38.0	10.3

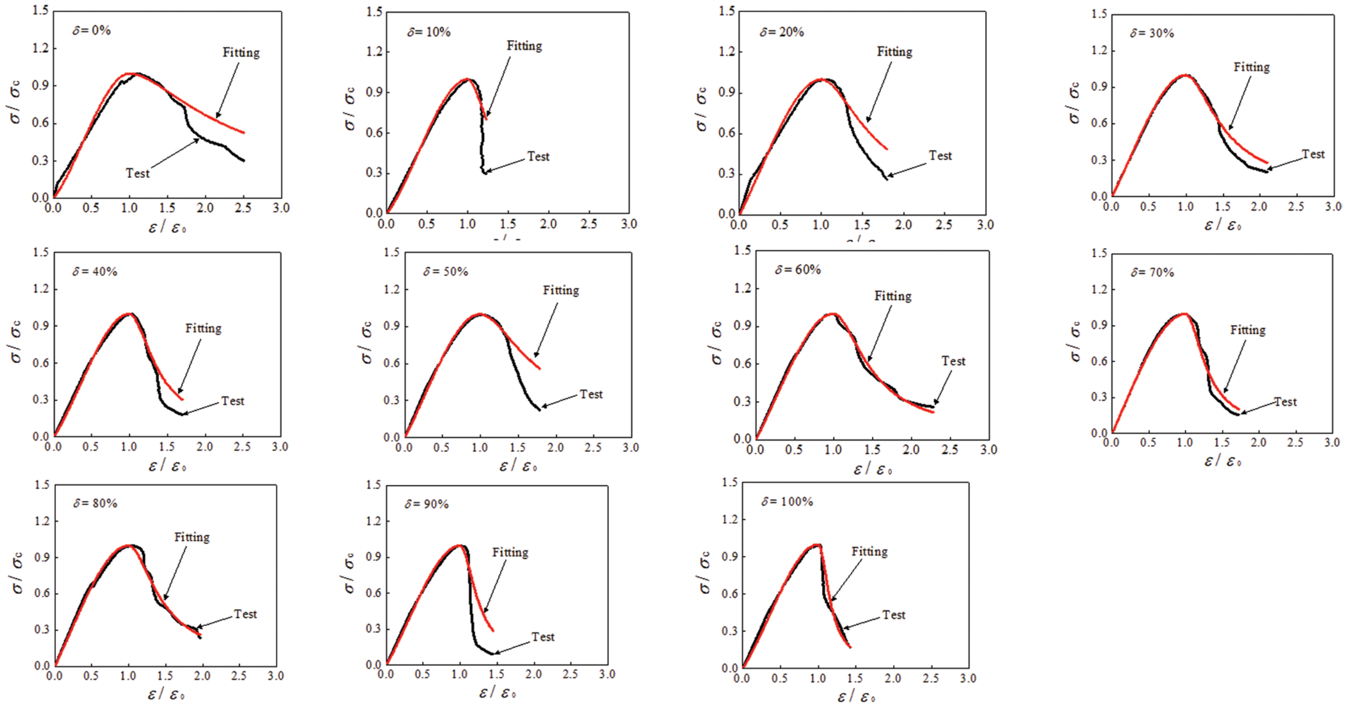

Figure 3. *Normalized stress-strain curves.*

3. The prism compressive strength of RAC at two years is higher than that of the specimens at the standard age.
4. Poisson's ratio of RAC ranges from 0.17 to 0.24.
5. The strength in RAC structures can be predicted by our proposed analytical expression of normalized stress-strain relation of RAC.

6. ACKNOWLEDGMENTS

The research reported in this paper was supported by the National Natural Science Foundation of China (Project No: 51578163) and Key Project of Natural Science Foundation of Guangxi Province (Project No: 2016GXNSFDA380032).

7. REFERENCES

1. Wang, J. Y., Yuan, H. P., Kang X. P., and Lu, W. S., "Critical success factors for on-site sorting of construction waste: A china study," *Resources Conservation and Recycling*, V. 54, No. 11, 2010, pp. 931–936. https://doi.org/10.1016/j.resconrec.2010.01.012
2. Xiao, Z. J., Ling, T. C., Kou, S.C., Wang, Q. Y., and Poon, C. S., "Use of wastes derived from earthquakes for the production of concrete masonry partition wall blocks," *Waste Management,* V. 31, No. 8, 2011, pp. 1859–1866. https://doi.org/10.1016/j.wasman.2011.04.010
3. Zhu, L. H., Dai, J., Bai, G. L., and Zhang, F.J., "Study on thermal properties of recycled aggregate concrete and recycled concrete blocks," *Construction and Building Materials*, V. 94, 2015, pp. 620–628. https://doi.org/10.1016/j.conbuildmat.2015.07.058
4. Akash, R., Kumar, N. J., and Sudhir, M., "Use of aggregates from recycled construction and demolition waste in concrete," *Resources Conservation and Recycling*, V. 50, No. 1, 2007, pp. 71–81. https://doi.org/10.1016/j.resconrec.2006.05.010
5. Belen, G. F., Fernando, M. A., Manuel, F. H., and Sindy, S. P., "Structural recycled concrete: Behaviour under low loading rate," *Construction and Building Materials*, V. 28, No. 1, 2012, pp. 111–116. https://doi.org/10.1016/j.conbuildmat.2011.08.010
6. Xiao, J. Z., He, X., and Yang, Z. J., "Shear transfer across a crack in recycled aggregate concrete," *Cement and Concrete Research*, V. 42, No. 5, 2012, pp. 700–709. https://doi.org/10.1016/j.cemconres.2012.02.006
7. Salomon, M. L., and Paulo, H., "Durability of recycled aggregates concrete: a safe way to sustainable development," *Cement and Concrete Research*, V. 34, No. 11, 2004, pp. 1975–1980. https://doi.org/10.1016/j.cemconres.2004.02.009
8. Abbas, A., Fathifazl, G., Isgor, O. B., Razaqpur, A. G., Fournier, B., and Foo, S., "Durability of recycled aggregate concrete designed with equivalent mortar volume method," *Cement and Concrete Composites*, V. 31, No. 8, 2009, pp. 555–563. https://doi.org/10.1016/j.cemconcomp.2009.02.012
9. Patrícia, S. L., Edna, P., Denise, C. C. D. M., Ângela, B. M., and José, L. D. R., "Modeling of mechanical properties and durability of recycled aggregate concretes," *Construction and Building Materials*, V. 26, No. 1, 2012, pp. 437–447. https://doi.org/10.1016/j.conbuildmat.2011.06.043
10. Chen, Z. P., Xu, J. J., Xue, J. Y., and Su Y. S., "Performance and calculations of recycled aggregate concrete-filled steel tubular (RACFST) short columns under axial compression," *International Journal of Steel Structures*, V. 14, No. 1, 2014, pp. 31–42. https://doi.org/10.1007/s13296-014-1005-5

Composite Performance of FRP—Concrete Composite Slabs

WEICHEN XUE*, SHIQIAN ZHANG and CHANG GE

Department of Structural Engineering, College of Civil Engineering, Tongji University, Shanghai, 200092, China

ABSTRACT: In this paper, four FRP-concrete composite slabs and one FRP profile without concrete slabs were tested through two types of shear connectors including FRP perfobond shear connectors and epoxy adhesive under positive and negative loads. For composite specimens under negative loads, flexural buckling failure was observed on the top flanges of FRP profiles; while shear buckling failure occurred on the webs of FRP profiles for those under positive loads. At the ultimate state, the measured mid-span deflection was more than 1/90 of the span for all specimens. Besides, it was noticed that relative slip at the interface between FRP profiles and concrete slabs for composite specimens with epoxy adhesive was lower than that for specimens with FRP perfobond shear connectors. Based on the Tsai-Wu criterion, the Tsai-Wu index of the two failure modes was calculated for composite slabs when buckling failure occurred.

INTRODUCTION

FRP-CONCRETE composite slabs consist of FRP profiles and concrete slabs that are connected by shear connectors to work together. Compared with steel-concrete composite slabs, FRP-concrete composite slabs present several advantages, such as lightweight, high specific strength, resistance to corrosion, easy installation and low maintenance requirements. In 1981, Fardis and Khalili [1] proposed a new FRP concrete composite beam (one of the first published studies) containing a rectangular FRP box section with one open side to be filled with concrete. Available investigations revealed that shear connectors were important components of composite slabs, which could ensure the materials work together. In engineering applications, epoxy adhesive and steel bolts are two kinds of commonly used shear connectors.

In order to guarantee the composite action between FRP profiles and concrete slabs, some shear tests have been investigated since the 1990s. Neto and Rovere [2] conducted double shear test to study the bond strength at the interface of GFRP profile and concrete based on the shear connector of epoxy adhesive, and the results showed that epoxy adhesive had a good bonding behavior. Nguyen *et al.* [3] performed 14 push-out tests for shear connection between UHPFRC slab and FRP beam to evaluate the effects of straight/inclined bolt shear connectors and embedment depth-to-bolt diameter ratio, and proposed an empirical equation to predict the shear capacity of bolt shear connectors. However, to the best of our knowledge, few researches have been reported for FRP perfobond shear connectors. Based on previous work of Nam *et al.* [4], FRP perfobond shear connectors exhibited the advantages of high shear capacity and convenient construction. In 2012, Xue [5] performed an experimental study on shear behavior of epoxy adhesive and FRP perfobond connectors, and the results showed that shear capacity of FRP perfobond connectors increased slightly relative to the epoxy adhesive while relative slip at the interface increased rapidly as the applied load increased, indicating the lower shear stiffness of FRP perfobond connectors.

In 1995, Deskovic *et al.* [6] proposed a novel composite beam that consisted of a GFRP box beam with a CFRP laminate bonded to its tension side and a concrete layer cast on its compression side. In 1998, Hall and Mottram [7] proposed a new composite beam with a concrete slab cast on a GFRP pultruded walkway panel, which comprised T-upstands acting as shear studs. In their test, concrete was either directly cast onto the FRP panel or onto an intermediate epoxy adhesive layer to increase the shear behavior at the interface, and the results proved that epoxy adhesive at the interface could enhance the performance of composite beams. Other investigations on the FRP-concrete composite slab systems, including commonly used shear connectors, were also conducted by Neto [2], Keller

---

*Author to whom correspondence should be addressed.
E-mail: xuewc@tongji.edu.cn; Tel/ Fax: +86-21- 65981216;
Postal address : No.1239,SiPing road, Shanghai, China,200092

1544-8053/16/02 S153-09

doi:10.12783/issn.1544-8053/13/4/S20

Table 1. Specimen Design.

Specimen Code	**S–1**	**CS–1**	**CS–2**	**CS–3**	**CS–4**
Type	FRP box deck	FRP–concrete composite slab	FRP–concrete composite slab	FRP–concrete composite slab	FRP–concrete composite slab
Depth of concrete slab (mm)	—	60	60	60	60
Type of shear connection	—	epoxy adhesive	epoxy adhesive	FRP perfobond shear connectors	FRP perfobond shear connectors
Clear span, (mm)	1600	1600	1600	1600	1600
Loading setup	—	Positive load test	Negative load test	Positive load test	Negative load test

and Gurtler [8], Alnahhal *et al.* [9], Julio *et al.* [10] and Gonilha and Correia *et al.* [11], and the results demonstrated that the bonded interface improved the performance of composite slabs, showing the composite slabs were viable and very promising. Moreover, Nguyen *et al.* [12,13] conducted five flexural tests for composite beam systems, in which flexural behavior of the HFRP-UHPFRC composite beams with varying UHPFRC slab geometries and different shear connection types (epoxy adhesive and/or bolt shear connectors) was examined.

Overall, there are still many deficiencies in the research on FRP-concrete composites as follows: (1) current studies mainly focus on feasibility and structural behavior of FRP-concrete composite beams/decks under positive loads, but ignore the research on the composite slabs subjected to negative loads; (2) shear connectors such as epoxy adhesive and steel bolts have been widely investigated, but FRP-concrete composite slabs with FRP perfobond shear connectors are seldom reported; (3) calculation and analysis of composite slabs subjected to buckling failure are rarely reported.

In this paper, the pilot experimental study on four FRP-concrete composite slabs and one FRP profile was carried out, and the test variables involved two types of shear connectors (epoxy adhesive and FRP perfobond shear connectors) and two loading patterns (positive loading and negative loading). Then, the failure mode, bearing capacity and deflection of all specimens were discussed.

EXPERIMENTAL

Specimen Design

Five specimens, coded as S-1 and CS-1 to CS-4, were designed with a geometrical scale of 1:2. Details of each specimen are listed in Table 1. Among these specimens, S-1 was the FRP profile without concrete slabs as a control specimen, while others were FRP-concrete composite slabs. Details of reinforcements and dimensions of specimens are shown as Figure 1. For CS-1 and CS-2, the FRP profiles and concrete slabs were connected by epoxy adhesive (E-51), while for CS-3 and CS-4, the two kinds of materials were connected by FRP perfobond connectors [5]. FRP profiles and FRP perfobond connectors were both produced through pultrusion process.

Test Setup

The simply supported composite slabs were loaded monotonically to failure. Figure 2 shows the digital photos of loading configuration, including positive loads for CS-1/CS-3, negative loads for CS-2/CS-4 and loads for S-1. Since the behavior of S-1 under negative loads was identical with that under positive loads, the loading direction was no longer considered.

During the test, deflection at the mid-span and relative slip at the interface between FRP profiles and concrete slabs were measured with displacement trans-

Table 2. Mechanical Properties from Test Results.

		Mechanical Properties						
Direction		**Tensile Strength f_{ft} (MPa)**	**Compressive Strength f_{fc} (MPa)**	**Shear Strength f_{fv} (MPa)**	**Tensile Modulus E_{ft} (GPa)**	**Compressive Modulus E_{fc} (GPa)**	**Shear Modulus G_{12} (GPa)**	**Poisson's Ratio**
Longitudinal	Flanges	227	258	32	21.2	19.2	4.6	0.28
	Webs	208	228	38	21.0	19.2	5.0	0.36
Transverse	Flanges	40	56	32	10	72	4.6	0.28
	Webs	38	45	38	10	7.2	5.0	0.36

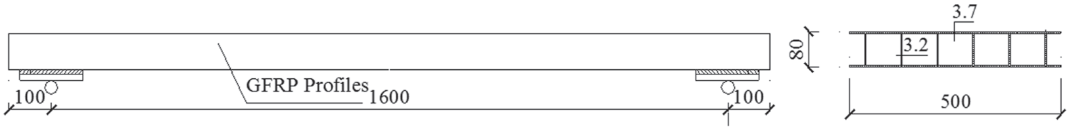

FRP profiles (S-1)

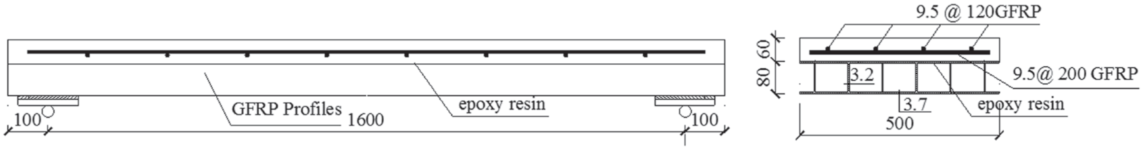

FRP–concrete composite deck with epoxy adhesive (CS-1, CS-2)

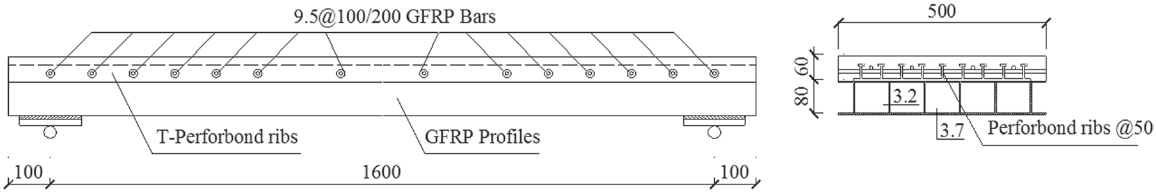

FRP–concrete composite deck with FRP perfobond shear connectors (CS-3, CS-4)

Figure 1. *Details of the specimens (Unit: mm).*

ducers. Strain distribution along the mid-span section depth and the strain on the top and bottom of specimens at the mid-span was measured by strain gauges. In addition, strain in shear span sections of FRP profile webs was monitored throughout the test.

Material Properties

The pultruded FRP profile, produced by Nanjing Spare composites Co., Ltd., was made of a polyester matrix reinforced with E-glass fibers. The tensile, compressive and shear properties were determined through extensive mechanical characterization based on the coupons cut from the original profile, as shown in Table 2.

The ultimate tensile strength (f_{fu}) and the Young's modulus (E_f) of GFRP bars are 664 MPa and 4.23 × 10^4 MPa, respectively. The concrete cube compressive strength is 51.01 MPa, and the Young's modulus is 3.54 × 10^4 MPa.

RESULTS AND DISCUSSION

Failure Pattern

Two kinds of failure patterns were observed in the test: buckling failure on the flanges of FRP profiles along the constant moment region under negative loads, and shear buckling failure on the webs of FRP profiles near the loading point under positive loads.

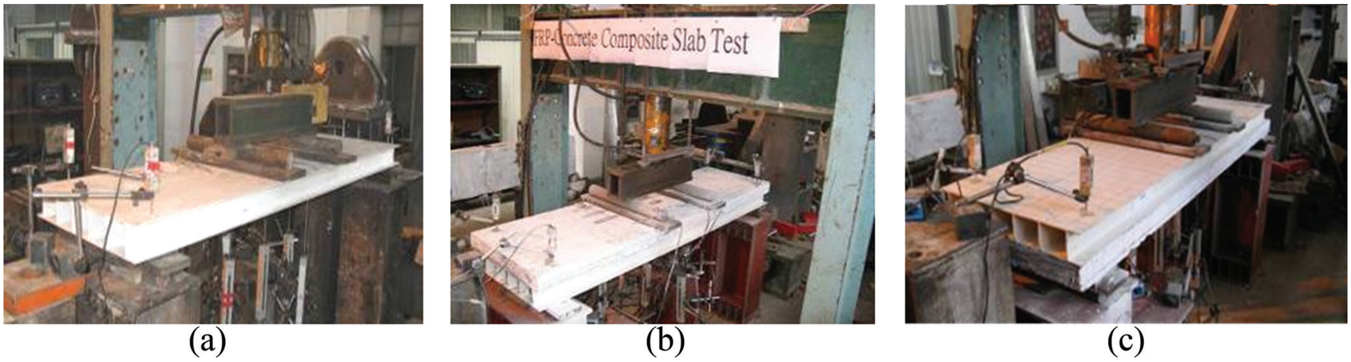

(a) (b) (c)

Figure 2. *Test setup. (a) S-1, (b) positive loads for CS-1/CS-3, and (c) negative loads for CS-2/CS-4.*

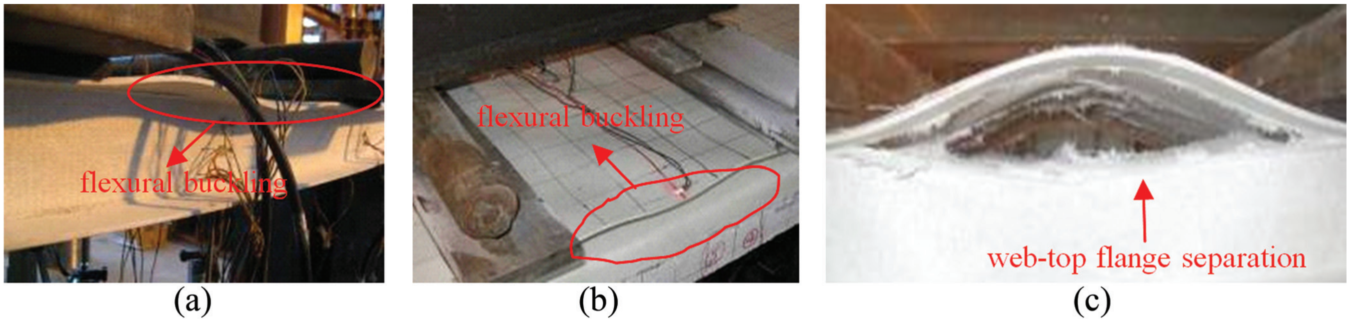

Figure 3. *Failure patterns of the specimens. (a) Fanges buckling for S-1, (b) Flanges buckling for CS-2 and CS-4, and (c) Details of web-top flange separation.*

Flexural Buckling Failure on the Flanges of FRP Profiles

Flexural buckling failure of the top flanges occurred for S-1, CS-2 and CS-4 under negative loads, followed by web-top flange separation along the constant moment region. For CS-2 and CS-4, as the applied load increased, relative slip began to increase slowly, and several cracks appeared on the bottom of concrete slabs and further developed upward on the profiles of concrete slabs. When the applied load increased to 0.9 P_u, the flanges of FRP profiles buckled [see Figures 3(a) and 3(b)] in a wavy way, with the snap of fibers in FRP profiles. At the ultimate state, separation of web-top flanges occurred for the three specimens, and the composite structure was failed, as shown in Figure 3(c).

Shear Buckling Failure on the Webs of FRP Profiles

CS-1 and CS-3 were tested under positive loads. Shear buckling failure and longitudinal interlaminar shear failure occurred successively on the webs of FRP profiles near the loading point. As the applied load increased, several cracks appeared and developed within the constant moment region, and relative slip at the interface between FRP profiles and concrete slabs occurred. When the applied load increased to 0.9 P_u, shear buckling occurred on the webs of FRP profiles near the loading point [see Figure 4(a)]. Meanwhile, a color change of the webs of FRP profiles was observed, which might be attributed to local failure of the fibers and resin. As the applied load approached the ultimate load, longitudinal interlaminar shear failure occurred on the webs of FRP profiles near the top flange around loading point, as can be seen in Figure 4(b).

Axial Strain Distribution Along the Mid-span Section Depth

Figure 5 shows the mid-span strain distribution through the section depth of specimens at different loads (20%, 40%, 60%, 80% and 100% P_u). As can be seen, the strain through the cross-section of slab CS-1 with epoxy adhesive followed a linear distribution under positive loads, indicating that CS-1 showed almost a full interaction up to final failure [Figure 5 (a)]; the strain of CS-2 with epoxy adhesive under negative loads approximately exhibited a linear distribution

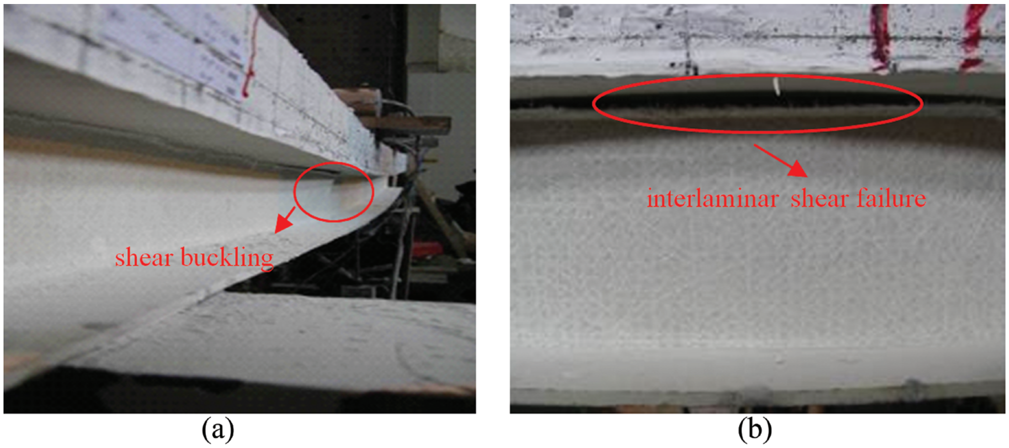

Figure 4. *Shear failure of FRP deck webs. (a) Shear buckling and (b) Interlaminar shear failure.*

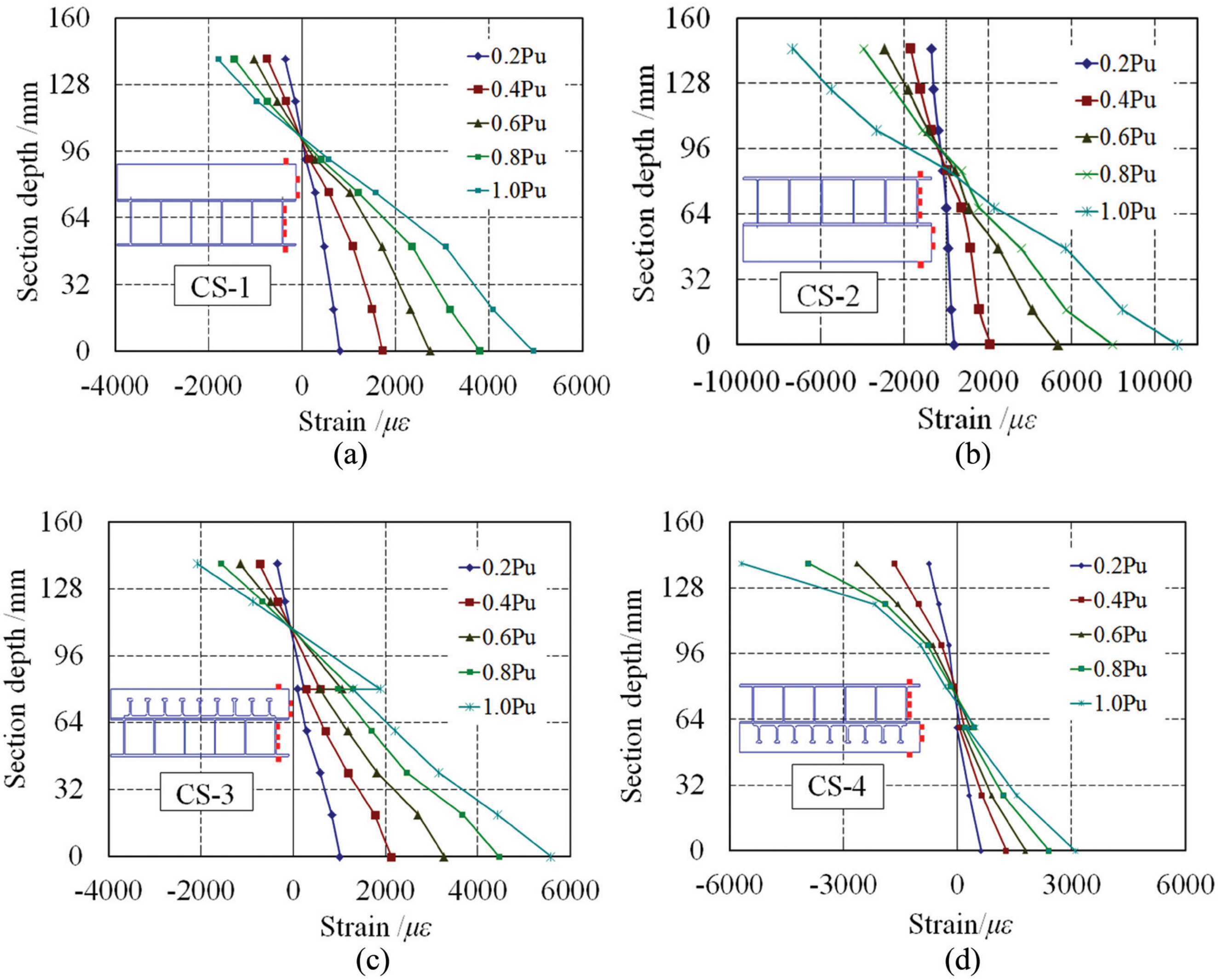

Figure 5. *Strain distribution along slab depth. (a) CS-1, (b) CS-2, (c) CS-3, and (d) CS-4.*

along the depth of section in 0.2 P_u–0.6 P_u load phase [Figure 5 (b)]. Besides, the neutral axis height for CS-2 in the FRP profiles decreased towards its middle height in 0.8 P_u–1.0 P_u load phase due to concrete cracking in tension, and there was a slight slip at the concrete slab/FRP profile interface at a load of 0.8 P_u. In contrast, large slip was observed at the concrete slab/FRP profile interface of CS-3 and CS-4 with FRP perfobond connectors, as shown in Figures 5(c) and 5(d). This phenomenon might be attributed to the fact that FRP perfobond connectors were not sufficient to resist the horizontal shear force applied at the concrete slab/FRP profile interface, so that the composite section could not remain plane.

Load-deflection Curves

Figure 6 shows the load versus mid-span deflection curves of all tested slabs. The control slab presented an almost linear curve up to the failure load (63.8 kN), whereas the FRP-concrete composite slabs exhibited higher stiffness and bearing capacity than those of the control slab. The load–deflection curve of slab CS-2 with epoxy adhesive under negative loads could be divided into five stages. In the first stage, the curve was almost linear and there was no slip between the slabs and the FRP profiles in the load range from 0 to 15 kN. The second stage showed a stiffness reduction as the load increased from approximately 15 to 30 kN due to cracking on concrete slabs in flexural slab and slipping at the interface. When the load increased from 30 to 35 kN, the stiffness continuously reduced because of crack flooding. Further, with the increase of applied load, the fourth stage showed an almost linear behavior, and the displacement increased from 12 to 30 mm. Finally, the fifth stage showed buckled compression

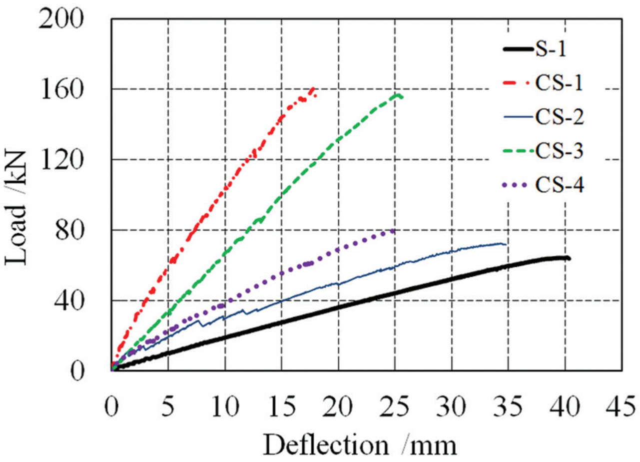

Figure 6. *Load-deflection curves of the specimens.*

flanges of FRP profiles and then a sudden failure of the slab at the ultimate load. The load-deflection curve of slab CS-4 with FRP perfobond connectors under negative loads was similar to that of slab CS-2, but an obvious stiffness reduction was observed as the load increased to approximately 60 kN due to large slip between the slabs and the FRP profiles.

The load–deflection curve of slab CS-1 with epoxy adhesive under positive loads could be divided into three stages. In the first stage, the curve was almost linear in the load range from 0 to 30 kN, which represented the slip resistance of epoxy adhesive. The second stage exhibited a gradual development of shear buckling failure on the webs of FRP profiles with slipping between FRP profiles and concrete slabs and concrete cracking. The final stage showed a sudden interlaminar shear failure of the slabs at an ultimate load without epoxy bonding. The load-deflection curve of slab CS-3 with FRP perfobond connectors under positive loads was similar to that of slab CS-3.

Table 3. ***Test Results of the Maximum Load and Deflection.***

		Positive Loading		Negative Loading	
	S–1	**CS–1**	**CS–2**	**CS–3**	**CS–4**
Ultimate load P (kN)	63.8	159.2	156.8	72.0	79.5
S-1 (%)	100	250	246	113	125
Ultimate deflection Δ_{max} (mm)	40.4	17.8	25.4	34.7	24.7
Δ_{max}/L	1/40	1/90	1/63	1/46	1/65

Note: *L* is the distance between the supports.

Compared with S-1, stiffness of CS-2 and CS-4 under negative loads increased slightly due to the slight contribution of concrete in tension zone, while that of CS-1 and CS-3 subjected to positive loads increased significantly due to the significant effect of concrete in compression zone. Under negative loads, stiffness of CS-2 with epoxy adhesive was close to that of CS-4 with FRP perfobond connectors up to cracking. After full development of cracks on concrete slabs, stiffness of CS-2 suffered a large loss due to the significant influence of concrete cracking in tension zone. In contrast, stiffness of CS-4 remained approximately constant because of the contribution of FRP perfobond ribs although concrete cracked. When the specimens were subjected to positive loads, stiffness of CS-3 with FRP perfobond connectors was lower than that of CS-1 with epoxy adhesive due to the relatively larger slip of CS-3 at the interface.

Characteristic Value of Bearing Capacity and Deflection

Table 3 shows the maximum load and deflection measured in the test. Compared with S-1, the ultimate

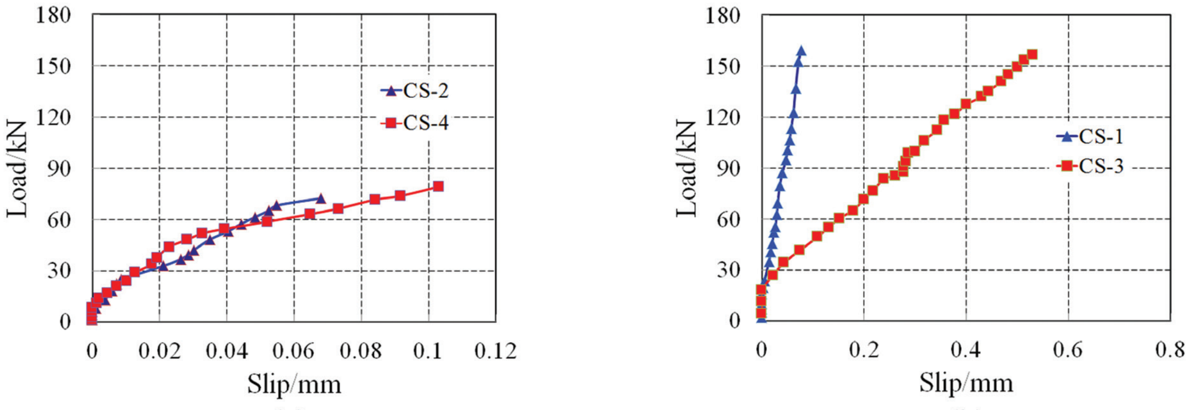

(a) (b)

Figure 7. *Load-slip curves. (a) CS-2 and CS-4, (b) CS-1 and CS-3.*

$$\frac{X_c - X_t}{X_c X_t}\sigma_1 + \frac{Y_c - Y_t}{Y_c Y_t}\sigma_2 + \frac{1}{X_c X_t}\sigma_1^2 + \frac{1}{Y_c Y_t}\sigma_2^2 + \frac{1}{S^2}\sigma_6^2 - \frac{1}{\sqrt{X_c X_t Y_c Y_t}}\sigma_1\sigma_2 \geq 1 \qquad (1)$$

load increased by about 150% and 146% for CS-1 and CS-3 respectively under positive loads because concrete slabs in compression zone had a significant effect on the ultimate load, and by about 13% and 25% for CS-2 and CS-4 respectively under negative loads due to the slight contribution of concrete in tension zone. At the ultimate state, the measured mid-span deflection of CS-1 was 1/90~1/40 of the simply supported span, which reflected the large deformability of FRP-concrete composite slabs; that of CS-3 was 25.4 mm, which was 1.43 times that of CS-1 due to the relatively large slip of CS-3 at the interface. In contrast, under negative loads, the ultimate mid-span deflections of CS-2 with epoxy adhesive was 1.4 times that of CS-4, which might be attributed to the increase of stiffness for CS-4 due to FRP perfobond connectors in tension.

Load-slip Curves

Under positive and negative loads, relative slip occurred at the interface between FRP profiles and concrete slabs for FRP-concrete composite slabs. Figure 7 shows the measured load-slip curves of composite slabs. For CS-2 and CS-4 subjected to negative loads, no slip occurred up to cracking load. Then, relative slip began to develop with the increase of applied load. At the ultimate state, the maximum relative slip reached 0.068 mm and 0.103 mm for CS-2 and CS-4, respectively. Stiffness of load-slip curve of CS-2 and CS-4 at the interface was similar to each other during the whole process due to the small shear force at the interface and the cracking on concrete slabs in tension. Under positive loads, no slip was observed under the applied load of $0.1P_u$ for CS-1 and CS-3, and relative slip between the two materials began to develop after $0.1P_u$ (cracking on the concrete slabs). It was noticed that the slip developed rapidly for CS-3 as the applied load increased, and stiffness of load-slip curve was lower than that of CS-1 because shear stiffness at the interface between the two materials for CS-3 with FRP perfobond connectors was lower than that for CS-1 with epoxy adhesive. At the ultimate state, the maximum relative slip reached 0.53 mm and 0.08 mm for the CS-3 and CS-1, respectively. The load-slip responses exhibited an approximate linear relationship up to P_u, due to shear connectors in elastic state.

Tsai-Wu index of Buckling Failure in FRP-concrete Composite Slabs

From the failure patterns of the test, it could be seen that, under the load of $0.9P_u$, flexural buckling failure and shear buckling failure occurred on the specimens under negative and positive loads, as shown in Section 2.1. Here, strength index of the bucking failure was calculated by a failure criterion developed for FRP composite materials, i.e., the Tsai-Wu failure criterion [14], which considers the difference between tension performance and compression performance of composite materials. The Tsai–Wu failure criterion can be expressed by Equation (1). Where X_c, X_t, Y_c, Y_t and S are longitudinal compression, longitudinal tension, transverse compression, transverse tension and in-plane shear strength of the unidirectional lamina, respectively; σ_1 and σ_2 are the stresses in longitudinal and transverse directions, respectively; and σ_6 is the shear stress in the plane defined by those directions(longitudinal and transverse directions).

According to the characteristics of strain distribution in the FRP profiles, the critical section on the flanges and webs of FRP profiles was analyzed based on the Tsai-Wu failure criterion, and the results are shown in Table 4.

For CS-2 and CS-4 subjected to negative loads and S-1, flexural buckling failure occurred on the constant moment region under the applied load of $0.9P_u$, and the Tsai-Wu index was 0.59, 0.55 and 0.65, respectively. It could be concluded that the failure of specimens oc-

Table 4. Tsai-Wu Index.

Specimens		**S–1**		**CS–1**		**CS–2**		**CS–3**		**CS–4**	
Loads		$0.9\ P_u$	$1.0\ P_u$	$0.9\ P_u$	$1.0\ P_u$	$0.9\ P_u$	$1.0\ P_u$	$0.9\ P_u$	$1.0\ P_u$	$0.9\ P_u$	$1.0\ P_u$
Tsai-Hill Index	Webs	0.52	0.60	0.90	1.50	0.65	0.91	0.88	1.83	0.69	0.80
	Flanges	0.65	1.04	0.50	0.56	0.59	1.03	0.53	0.60	0.55	1.01

Note: Flanges of S-1, CS-2 and CS-4 refer to the top flanges in FRP profiles, and flanges of CS-1 and CS-3.

Table 5. Shear Carried by FRP Profile Webs (%).

	0.2 P_u	0.4 P_u	0.6 P_u	0.8 P_u	1.0 P_u
CS-1	24.6	37.9	45.0	54.2	72.8
CS-2	40.2	45.3	66.1	69.3	74.8
CS-3	47.1	60.4	67.2	68.6	78.7
CS-4	52.9	55.8	64.6	67.7	73.4

curred due to flexural buckling when the index exceeded 0.60 for FRP-concrete composite slabs. However, shear buckling failure did not happen on the webs, and the Tsai-Wu indexes on the webs were 0.65, 0.69 and 0.52 under the applied load of $0.9P_u$, respectively.

For CS-1 and CS-3 subjected to positive loads, under the applied load of $0.9P_u$, shear buckling failure on the webs of FRP profile occurred, and the Tsai-Wu index on the webs of FRP profiles were 0.90 and 0.88, respectively. Thus, it could be concluded that shear buckling failure occurred on the webs when the index exceeded 0.90 for FRP-concrete composite slabs. The Tsai-Wu index at the bottom flanges of FRP profiles were 0.5 and 0.53 for CS-1 and CS-3 respectively, so that the failure at bottom flanges of FRP profiles should not happen under positive loads, just as verified by experimental observation.

Under the applied load of P_u, for S-1, CS-2 and CS-4, the Tsai-Wu index on the top flanges within the constant moment region all exceeded 1.0 and strength failure occurred at the web-flange junction due to flexural buckling; the index on the webs of FRP profiles was less than 1.0. For CS-1 and CS-3, under the applied load of P_u, the index on the webs of FRP profiles was 1.5 and 1.83 and strength failure occurred on the webs of FRP profiles near the top flanges around loading point due to shear buckling; the index on the bottom flanges for CS-1 and CS-3 was less than 1.0.

Shear Capacity of FRP Profile Webs in FRP-concrete Composite Slabs

Assume that shear stress distribution across the web depth was approximately uniform in FRP profiles [15], and then results from strain gauges were used to estimate the shear carried by the webs in FRP profiles. Table 5 shows the percentage of shear carried by FRP profile webs under different loads (20%, 40%, 60%, 80% and 100% P_u) in FRP-concrete composite slabs. With the increase of applied load, shear carried by FRP profile webs increased rapidly. Prior to failure, due to non-linear behavior of concrete, these values were almost 70%~80% of the total shear, indicating that shear force should be carried by FRP profile webs as a conservative consideration.

CONCLUSIONS

This paper presented the experimental study on four FRP-concrete composite slabs and one FRP profile that were subjected to positive and negative loads. Some conclusions can be drawn as follows:

1. Under negative loads, flexural buckling failure of top flanges and web-top flange separation along the region of pure flexure occurred successively for FRP profile and FRP-concrete composite slabs. Under positive loads, shear buckling failure followed by longitudinal interlaminar shear failure occurred on the webs of FRP profiles near the cross-section loading point for composite slabs.
2. At the ultimate state, the measured mid-span deflection was 1/90~1/40 of the span, which demonstrated the large deformability of composite slabs. Relative slip at the interface for composite specimens with epoxy adhesive was lower than that for slabs with FRP perfobond shear connectors.
3. Based on the characteristics of strain distribution in the composite deck and the Tsai–Wu criterion, FRP profiles could absorb almost 70%~80% of the total shear at the ultimate prior to failure, which indicated that shear force should be carried by FRP profile webs as a conservative consideration.

ACKNOWLEDGEMENTS

The authors gratefully acknowledged the financial support of the National Key Basic Research Program of China (Project No. 2012CB026200), and the Fund of National Natural Science Foundation of China (No. 50978193).

REFERENCES

1. Fardis, M. N., and Khalili, H., “Concrete Encased in Fiberglass-Reinforced Plastic,” *ACI Journal, Proceedings*, V. 78, No. 2, 1981, pp. 440–446.
2. Almir Barros da S. Santos Neto, Henriette Lebre La Rovere, “Composite concrete/GFRP slabs for footbridge deck systems,” *Composite Structures*, V. 92, No. 10, 2010, pp. 2554–2564. https://doi.org/10.1016/j.compstruct.2010.02.005
3. Hai, Nguyen, H. Mutsuyoshi, and W. Zatar., “Push-out tests for shear connections between UHPFRC slabs and FRP girder,” *Composite Structures*, V. 118, 2014, pp. 528–547. https://doi.org/10.1016/j.compstruct.2014.08.003

4. Nam, J.H., Yoon, S.J., Ok, D.M. & Cho, S.K., "Perfobond FRP Shear Connector for the FRP-Concrete Composite Bridge Deck," *Key Engineering Materials*, 334–335 I, 2007, pp. 281–284.
5. XUE Weichen, "Research on FRP Perfobond Shear Connector," Report, Tongji University, China, 2012, 35pp.
6. Deskovic, N., Triantafillou, T.C. & Meier, U., "Innovative design of FRP combined with concrete short-term behavior," *Journal of Structural Engineering*, V. 121, No. 7, 1995, pp. 1069–1078. https://doi.org/10.1061/(ASCE)0733-9445(1995)121:7(1069)
7. Hall, J.E. & Mottram, J.T. "Combined FRP reinforcement and permanent framework for concrete members," *Journal of Composites for Construction*, V. 2, No. 2, 1998, pp. 78–86. https://doi.org/10.1061/(ASCE)1090-0268(1998)2:2(78)
8. Keller, T., Gurtler, H., "Composite action and adhesive bond between FRP bridge decks and main girders," *Journal of Composites for Construction*, V. 9, No. 4, 2005, pp. 360–368. https://doi.org/10.1061/(ASCE)1090-0268(2005)9:4(360)
9. Wael Alnahhal, Amjad Aref, Sreenivas Alampalli, "Composite behavior of hybrid FRP-concrete bridge decks on steel girders," *Composite Structures*, V. 84, No. 1, 2008, pp. 29–43. https://doi.org/10.1016/j.compstruct.2007.06.005
10. Julio F. Davalos, An Chen, Bin Zou, "Performance of a scaled FRP deck-on-steel girder bridge model with partial degree of composite action," *Engineering Structures*, V. 40, No. 7, 2012, pp. 51–63. https://doi.org/10.1016/j.engstruct.2012.02.020
11. José A. Gonilha, João R. Correia, Fernando A. Branco, "Structural behaviour of a GFRP-concrete hybrid footbridge prototype: Experimental tests and numerical and analytical simulations," *Engineering Structures*, V. 60, No. 2, 2014, pp. 11–22. https://doi.org/10.1016/j.engstruct.2013.12.018
12. Hai, Nguyen, H. Mutsuyoshi, and W. Zatar., "Hybrid FRP-UHPFRC composite girders: Part 1–Experimental and numerical approach," *Composite Structures*, V. 125, 2015, pp. 631–652. https://doi.org/10.1016/j.compstruct.2014.10.038
13. Hai, Nguyen, W. Zatar, and H. Mutsuyoshi, "Hybrid FRP–UHPFRC composite girders: Part 2–Analytical approach," *Composite Structures*, V. 125, 2015, pp. 653–671. https://doi.org/10.1016/j.compstruct.2014.12.001
14. Tsai, S. W. and Hahn, H. T., 1980, *Introduction to Composite Materials*, Technomic Publishing Co., Inc., Lancaster, Basel.
15. João Ramôa Correia, Fernando A. Branco, João Ferreira, "GFRP-concrete hybrid cross-sections for floors of buildings," *Engineering Structures*, V. 31, No. 6, 2009, 1331–1343. https://doi.org/10.1016/j.engstruct.2008.04.021

Survey of Chloramphenicol in Honeys from China

HAOAN ZHAO, NI CHENG*, HUI GAO and WEI CAO*

Department of Food Science and Engineering, School of Chemical Engineering,
Northwest University, 229 North TaiBai Road, Xi'an City, China 710069

ABSTRACT: Chloramphenicol (CAP) is a broad-spectrum antibiotic and a potential carcinogen that has been banned for use in apiculture in China and other countries. The aim of this study was to investigate the occurrence of CAP residues in various Chinese honeys. In total, 219 raw honeys and 149 commercial honeys from China produced during four consecutive years (2011–2014) were analyzed by ELISA for the detection of CAP residues. The results showed the percentage of positive samples of CAP of 12.33% in the 219 raw honeys, withan obvious decreasefrom 2012 (20.97%) to 2014 (7.27%), the incidence of CAP showed a significant decrease. The CAP residues in all raw honeys ranged from ND (not detected) to 1.34 μg/kg, with a mean value of 0.08 μg/kg. The mean incidence of CAP in 149 commercial honeys was 6.04%. From 2012 (8.82%) to 2014 (2.78%), the incidence of CAP in commercial honeys showed an obvious decrease.

1. INTRODUCTION

CHLORAMPHENICOL (CAP), which is also called chloromycetin, was first isolated from *Streptomyces venezuelae* in 1947 and later synthesized and introduced into clinical treatment in 1949. CAP is an effective antibiotic for treating gram-positive bacteria-related diseases and, therefore, has wide clinical applications in humans and animals [1] (Lovett, 1996). However, certain studies have reported that CAP can cause fatal bone marrow depression and aplastic anemia [2,3,4] (Wiholm *et al.*, 1998; El-Mofty, Abdelmeguid, Sadek, Essawy and Abdel Aleem, 2000; Saba, Awe, Akinloye and Oladele, 2002). Therefore, a maximum residue level (MRL) of 0.30 μg/kg CAP in animal-derived food was established by the European Union (EU) in 2003 [5] (European Commission, 2003).

Honey, is natural, and functional food, has been considered a favorite bee product, though the possible hazard caused by antibiotic residues has risen increasing attention in recent years [6,7,8] (Cheng *et al.*, 2012; Bargańska, Ślebioda, Namieśnik, 2014; Mahmoudi, Norian and Pajohi-Alamoti, 2014). China is a country where history of bee keeping is more than 2,000 years long, and the use of antibiotics for the prevention and treatment of diseases was legal in apiculture in certain periods of time. However, due to emerged awareness of antibiotic hazards from animal-derived foods, four highly poisonous antibiotics (CAP, streptomycin, oxytetracycline and tetracycline) were prohibited from use in animal feed in 2000 by the Chinese Ministry of Agriculture [9]. Nevertheless, because of its efficiency and low cost, CAP continues to be used secretly and illegally by some beekeepers. In 2002, low levels of CAP were found in honeys from China in the EU, and all honeys from China were removed from this market, resulting in large economic and reputational losses to China. Subsequently, the MRL of CAP in honeys imported from China was reduced to 0.10 μg/kg by the EU. Since then, the Chinese Ministry of Agriculture has regulated the beekeeping practice strictly, particularly with regard to the use of CAP. In an effort to define the present situation of CAP residues in Chinese honeys, we surveyed and analyzed the occurrence of CAP in raw and commercial honeys produced in China during four consecutive years. This report presents the results of first long-term survey of CAP residues in Chinese honeys.

2. MATERIALS AND METHODS

2.1. Chemicals

Ethyl acetate (analytical grade) was purchased from Tianjin Kermel Chemical Reagent Co., Ltd (Tianjin, China). An ELISA kit (batch number: HE09001) for

---

*Authors to whom correspondence should be addressed.
chengni@nwu.edu.cn (N. Cheng), caowei@nwu.edu.cn (W. Cao);
Tel./fax: +86 29 88302213

1544-8053/16/02 S163-05

doi:10.12783/issn.1544-8053/13/4/S21

the quantitative detection of CAP residues was purchased from Huaan Magnech Bio-Tech Co., Ltd (Beijing, China); this kit has been widely used for detection of antibiotics in food in China.

2.2. Sample Preparation

Information regarding the 219 raw honey samples is provided in Table 1. Of the 149 commercial honey samples, 36 were collected in 2014, 41 in 2013, 34 in 2012, and 38 in 2011. All samples were pretreated prior to CAP residue detection by ELISA. Briefly, 3.00 g of honey was mixed with 6.00 mL of distilled water for 3 min. Ethyl acetate (6.00 mL) was added to the mixture, which was mixed well for 5 min. Then, 4 mL of supernatant was extracted for centrifugation at 1130 g for 10 min and evaporated under a nitrogen stream at 60°C. The residue was redissolved in 1 mL of sample dilution (isooctane: chloroform (2:3/v: v) mixture) and stored at 4°C for CAP residue detection[10].

2.3. Enzyme-linked Immunosorbent Assay

To investigate the presence of CAP residues in Chinese honeys, 219 raw honey samples from 70 districts in China and 149 commercial honey samples from 27 Chinese bee product companies were collected during four consecutive years. The CAP residues in the honey samples were quantified by ELISA [11].

All sample solutions (obtained from Section 2.2) and reagents for ELISA were allowed to equilibrate at 25°C for 30 min. The sample solution (70 μL) was added to well sprecoated with CAP antigens, and 50 μL of secondary antibody was added. The reaction was allowed to proceed at 25°C for 30 min. The reaction solution was discarded, and the wells were washed five times with a washing solution provided by the ELSIA kit. Before termination of the reaction, the color reaction was allowed to proceed at 25°C for 15 min in the dark [12]. The absorbance was determined at 450/630 nm using a multifunctional plate reader (TECAN Infinite M200Pro, Switzerland). The CAP content in all samples was expressed as μg/kg. The limit of detection of the CAP test was 0.05 μg/kg, and the recovery rate was tested in this study by spiking blank honey with three different concentrations of a CAP standard.

2.4. Statistical Analysis

All samples were analyzed in triplicate. The standard deviation calculations for the three repetitions were performed using SAS software (SAS Institute, Cary, NC, USA).

3. RESULTS

Residue recoveries of CAP in raw honey and commercial honey samples were determined by spiking blank honey samples with a CAP standard in concentrations of 0.10, 1.00 and 10.00 μg/kg prior to extraction. The results are shown in Table 2. The average recoveries of CAP in the raw honey samples ranged from 86.00% to 101.00% and from 93.00% to 106.00% in the commercial honey samples. The relative standard deviation (% RSD) ranged from 2.00% to 6.00%, indicating that ELISA was appropriately precise in the determination of CAP in all the honey samples.

The CAP residues in the honey samples were quantified by ELISA, and the results are shown in Table 3. Of the 219 raw honey samples, 27 were positive for CAP. The mean frequency of detection of CAP was 12.33%. From 2012 to 2014, the frequency of detection of CAP ranged from 20.97% in 2012 to 7.27% in 2014 possibly, exhibiting an obvious decrease. The concentrations of CAP residues in all raw honeys ranged from ND to 1.34 μg/kg, with a mean concentration of 0.08 μg/kg. In 2012, the mean CAP concentration was 0.13 μg/kg, which is just above the MRL. A positive rate of detection of only 6.90% was found for the 29 raw honey samples from 2011. Of the 149 commercial honey samples, 9 were positive for CAP residues. The mean frequency of detection of CAP residues was 6.04%, which was one half of those detected in the raw honeys. From 2012 to 2014, the percentage of positive samples of CAP in commercial honeys ranged from 8.82% to 2.78%, which was lower than the same year of the raw honeys.

To further understand the origins of CAP residue, all raw honey samples were classified according to their botanical origin. Thirteen botanical origins were designated in this study, 6 were positive for CAP residues; vitex; jujube; black locust; rape; buckwheat; and longan honey (Figure 1). Vitex honey had the greatest positive identification in 34.48%, of all samples which was higher than those of the other honeys. The mean CAP content in the 10 positive vitex honeys was 0.61 μg/kg, which is six fold greater than the MRL; this greater mean CAP content is attributed to the three vitex honey samples that have been collected from Liaoning Anshan in 2013 (1.31 μg/kg and 1.17 μg/kg) and 2012 (1.34 μg/kg). Three positive locust honeys were detected among the 38 locust honey samples analyzed,

Table 1. Information of All Raw Honey Samples.

Year	Botanical Origin	Geographical Origin	No.
2014 (55)	Rape (*Brassica campestris L.*)	Shaanxi Ankang	1
		Sichuan Neijiang	1
		Shaanxi Hanzhong	9
	Jujube (*Ziziphus jujube Mill.*)	Shaanxi Yulin	1
		Shaanxi Weinan	1
	Sunflower (*Helianthus annuus L.*)	Xinjiang Yili	1
	Sour jujube (*Ziziphus jujuba var. spinosa*)	Gansu Ningxian	3
	Locust (*Robinia pseudoacacia L.*)	Shaanxi Yanchang	2
		Gansu Ningxian	2
		Shaanxi Luochuan	2
		Shaanxi Xunyi	1
		Shaanxi Chunhua	2
		Gansu Tianshui	3
		Shaanxi Huangling	1
		Shaanxi Fuxian	1
		Shaanxi Hancheng	1
		Henan Lushi	12
		Shaanxi Fuping	5
		Shaanxi Yichuan	2
	Lime (*Tilia amurensis Rupr.*.)	Jilin Changchun	1
		Heilongjiang Raohe	1
		Heilongjiang Harbin	1
		Jilin Yanji	1
2012 (43)	Buckwheat (*Fagopyrum esculentum Moenc*h)	Shaanxi Jianxian	2
	Lyciumbarbarum (*Lycium chinense Mill.*)	Ningxia Zhongning	1
		Ningxia Guyuan	6
	Jujube (*Ziziphus jujube Mill.*)	Shaanxi Dali	5
		Shaanxi Wubao	1
		Shaanxi Jiaxian	3
		Hebei Zhaoxian	2
		Hebei Shijiazhuang	1
		Shandong Linyi	1
		Henan Lingbao	2
		Shanxi Linxian	1
	Rape (*Brassica campestris L.*)	Shaanxi Ankang	1
		Sichuan Jiangyou	2
		Zhejiang Ningbo	2
		Shaanxi Yangxian	1
		Hubei Hanjiang	2
	Vitex (*Vitexagnus-castue L.*)	Liaoning Anshan	
		Hebei Zhaoxian	
		Shanxi Yangquan	
		Shanxi Pingding	
	Locust (*Robinia pseudoacacia L.*)	Henan Lingbao	2
		Shanxi Linxian	1
2013 (73)	Vitex (*Vitex agnus castue L.*)	Shanxi Pingding	5
		Hebei Zanhuang	6
		Henan Huixian	6
		Liaoning Anshan	4
	Rape (*Brassica campestris L.*)	Sichuan Zigong	2
		Hubei Jingzhou	3
		Sichuan Meishan	2
		Shaanxi Ankang	1
		Sichuan Mianyang	5
		Hubei Dangyang	2
		Shaanxi Hanzhong	3
		Shaanxi Yangxian	1
		Sichuan Neijiang	2
		Sichuan Jianyang	2
	Medlar (*Lycium chinense Mill.*)	Ningxia Guyuan	2
	Jujube (*Ziziphus jujube Mill.*)	Shaanxi Yanchuan	2
		Shaanxi Jiaxian	6
		Shanxi Linxian	3
		Hebei Zhaoxian	1
		Henan Lingbao	7
		Hebei Zanhuang	3
	Locust (*Robinia pseudoacacia L.*)	Liaoning Anshan	2
	Buckwheat (*Fagopyrum esculentum Moench*)	Gansu Longnan	1
		Ningxia Guyuan	1
		Shaanxi Yulin	1
2012 (19)	Longan (*Dimocarpus longan Lour.*)	Guangxi Guiping	2
		Guangxi Nanning	2
		Jiangsu Lingshan	2
		Guangxi Maoming	3
		Guangxi Pingnan	5
		Guangxi Daxin	1
		Heilongjiang Mudanjiang	2
		Guangxi Wuzhou	2
		Guangdong Heyuan	1
2011 (29)	Jujube (*Ziziphus jujube Mill.*)	Shanxi Lvliang	3
		Shaanxi Fuping	2
		Shaanxi Jiaxian	3
		Shaanxi Dali	2
	Sunflower (*Helianthus annuus L.*)	Neimeng Hetao	3
	Leechee (*Litchi chinensis Sonn.*)	Guangxi Yulin	2
		Fujian Zhangzhou	2
	Buckwheat (*Fagopyrum esculentum Moench*)	Jilin Tonghua	1
		Gansu Dingxi	2
		Shaanxi Yan'an	3
	Apocynum (*Apocynumvenetum L.*)	Xinjiang Kashi	2
	Longan (*Dimocarpus longan Lour.*)	Hainan Wenchang	4

Table 2. Recovery of CAP (n = 3).

Honey Sample	Added (μg/kg)	Found (μg/kg)	% Recovery	% RSD
Raw honey	0.10	0.09	91.00	5.00
	1.00	0.86	86.00	3.00
	10.00	10.13	101.00	6.00
Commercial honey	0.10	0.09	93.00	6.00
	1.00	1.06	106.00	2.00
	10.00	9.86	99.00	5.00

with a positive rate of 7.89%; the mean CAP residue concentration of the three positive locust honey was 0.58 μg/kg. The mean concentration of CAP residues of the honeys of the six botanical origins ranged from 0.33 to 0.61 μg/kg.

4. DISCUSSION

CAP is a broad-spectrum antibiotic and a potential carcinogen that has been banned from use in food-producing animals, including honey bees, in China and in other countries. However, in this study 12.33% of analysed raw honey samples were positive for CAP residues (Table 3). In general, CAP residues are present in raw honey for two reasons. First and most crucial, CAP is illegal usage of CAP in bee keeping because of its low cost and efficiency in prevention and control of some bee diseases, although it has been banned for these purposes for several years; high doses of CAP residues typically occur in such cases. Thus, the finding that the concentrations of CAP residues in three vitex honeys (1.17, 1.31 and 1.34 μg/kg) in more greater 10 times higher levels than the MRL could be a result of such action. The raw honey samples collected in 2012 exhibited a high positive rate (20.97%), which may be related to a high drug-feeding rate. In Switzerland, 13 honey samples, 17% of them were contaminatedwith CAP residues, ranging from 0.40 to 6.00 μg/kg; two samples contained approximately 5.0 μg/kg, which is 50 times higher than the EU MRL [10] (Ortelli *et al.* 2004). Such high residues must be due to the administration of large doses of CAP to honey bees. In a survey of antibiotic residues in Iranian honeys [11] (Mahmoudi *et al.* 2014), 7.40% of autumn honey samples were contaminated with CAP, most likely because of the application of CAP in an effort to resist the high incidence of disease in autumn. In that investigation, it confirmed that water pollution is another factor attributable to the detection of CAP residues in honey samples. Indeed, polluted water from farms or pharmaceutical factories near bee pastures was taken up by the plants and thus present in bee products. Nonetheless, the level of CAP residues presents in honeys due to water contamination is low.

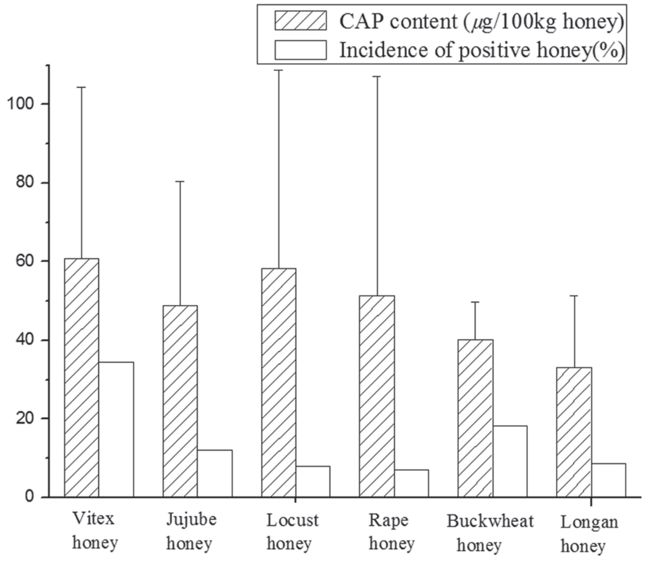

Figure 1. *The mean CAP content in honeys and positive incidence.*

Notably, current study revealed 9 of the 149 commercial honeys from 27 Chinese bee product companies contaminated with CAP residues. This positive incidence was significantly lower than in raw honeys.

Table 3. CAP Contents in Analysed Honey Samples.

	Raw Honey				Commercial Honey		
Years	Positive Samples (> 0.1 μg/kg) Over Total Samples	Incidence (%)	Range (μg/kg)	Mean CAP Residue (μg/kg)	Positive Samples (>0.1 μg/kg) Over Total Samples	Incidence (%)	Range (μg/kg)
2014	4/55	7.27%	ND –1.27	0.07	1/36	2.78%	ND –0.34
2013	8/73	10.96%	ND –1.31	0.07	3/41	7.31%	ND –0.51
2012	13/62	20.97%	ND –1.34	0.13	3/34	8.82%	ND –0.26
2011	2/29	6.90%	ND –0.47	0.07	2/38	5.26%	ND –0.29
Total	27/219	12.33%	ND –1.34	0.08	9/149	6.04%	ND –0.51

ND: not detected

The most important reason is that the honey processing manufacturers in China consider that testing for pesticides and veterinary drug residues in raw honey is of great importance during the acquisition process (GB14963 in China); in particular, testing for CAP residues is performed because the use of CAP in beekeeping has been prohibited by the Chinese government. Another reason worth considering is the effect of raw honey processing. In general, four steps, i.e., preheating, filtration, vacuum concentration, and pasteurization, are included in raw honey processing in China. In our previous study, a 13.70% decrease in the presence of CAP residues was achieved after these four steps of raw honey processing [6] (Cheng *et al.*, 2012). Specifically, vacuum concentration contributed to a 9.90% decrease in CAP residues, and the primary reason for this decrease is that CAP easily volatilizes from hydrophilic liquid honey under low vapor pressure and low pH.

5. CONCLUSION

In summary, our survey of CAP residues in Chinese honeys during four consecutive years revealed CAP residues in 12.33% and 6.04% raw and commercial honeys, respectively. Additionally, CAP residues in honey samples from 2012 and 2014 showed a decreasing trend, illustrating that beekeepers in China are adapting to new regulations however continuous monitoring of CAP and other residues is needed over a longer period to ensure the decreasing trend identified is true.

6. ACKNOWLEDGMENT

This work is financially supported by Agricultural Science and Technology Innovation Program of Shaanxi Province (2012NKC01-21), Agricultural Science and Technology Project of Shaanxi Province (2013K01-47-01) and Social development of Science and Technology Project (2016SF-425).

7. DISCLOSURE STATEMENT

No potential conflict of interest was reported by the authors.

8. REFERENCES

1. Lovett PS. 1996. Translation attenuation regulation of chloramphenicol resistance in bacteria-a review. *Gene*, 179: 157–162. https://doi.org/10.1016/S0378-1119(96)00420-9
2. Wiholm BE, Kelly JP, Kaufman D, Issaragrisil S, Levy M, Anderson T, Shapiro S. 1998. Relation of aplastic anaemia to use of chloramphenicol eye drops in two international case-control studies. *Brit Med J* 316: 666. https://doi.org/10.1136/bmj.316.7132.666
3. El-Mofty MM, Abdelmeguid NE, Sadek IA, Essawy AE, Abdel Aleem EA. 2000. Induction of leukaemia in chloramphenicol-treated toads. *East Mediterr Health J* 6: 1026–1034.
4. Saba AB, Awe OE, Akinloye AK, Oladele GM. 2002. Haematological changes accompanying prolonged ocular chloramphenicol administration in laboratory rabbits. *Afr J Biomed Res* 5: 131–135.
5. European Commision. 2003. Amending decision 2002/657/EC as regards the setting of minimum required performance limits (MRPLs) for certain residues in food of animal origin. *Offical Journal of European Commun*, 71: 17–18.
6. Cheng, N., Gao, H., Deng, J. J., Wang, B. N., Xu, R. H. & Cao, W. 2012. Removal of chloramphenicol by macroporous adsorption resins in honey: a novel approach on reutilization of antibioticscontaminated honey. *Journal of Food Science 77*(9): 169–172. https://doi.org/10.1111/j.1750-3841.2012.02868.x
7. Barganska, ?., ?lebioda, M., & Namie?nik, J. 2014. Determination of Pesticide Residues in Honeybees using Modified QUEChERS Sample Work-Up and Liquid Chromatography-Tandem Mass Spectrometry. *Molecules, 19*(3), 2911–2924. https://doi.org/10.3390/molecules19032911
8. Mahmoudi, R., Norian, R., Pajohialamoti, M. R., & Aliakbarlu, J. 2014. Effect of season on microbial and chemical characteristics of milk and yoghurt from sheep. *Animal Production Science, 54*(8), 1091–1094. https://doi.org/10.1071/AN13217
9. Bargańska Ż, Namieśnik J, Ślebioda M. 2011. Determination of antibiotic residues in honey. *TrAC- trend Anal Chem 30*: 1035–1041.
10. Ortelli D, Edder P, Corvi C. 2004. Analysis of chloramphenicol residues in honey by liquid chromatography-tandem mass spectrometry. *Chromatographia 59*: 61–64.
11. Mahmoudi R, Norian R, Pajohi-Alamoti M. 2014. Antibiotic residues in Iranian honey by ELISA. *Int J Food Prop 17*: 2367–2373. https://doi.org/10.1080/10942912.2013.809539
12. Hamamoto, S., Kanda, Y., Shimoda, M., Tatsumi, F., Kohara, K., Tawaramoto, K., ... & Kaku, K. 2013. Vildagliptin preserves the mass and function of pancreatic β cells via the developmental regulation and suppression of oxidative and endoplasmic reticulum stress in a mouse model of diabetes. *Diabetes, Obesity and Metabolism, 15*(2), 153–163. https://doi.org/10.1111/dom.12005

Experiment on Whole Section Stress Under Compressive Failure of CFST Column

KAIZHONG XIE, GUANGQIANG CHEN*, XIAOLIANG ZHAO and SHENGPING CHEN
Dept. of Civil & Architecture Engineering of Guangxi University, Daxue Road 100, Nanning, 530004, China

ABSTRACT: Concrete filled steel tube composite structure, known as CFST composite structure, has many merits and is widely used in some realms such as building and bridge. However, theoretical research on mechanical behaviors of CFST members lags far behind engineering applications. Based on the compressive and eccentricity tests of nine CFST columns, this paper mainly focuses on the stress variation in the section of steel tubes and core concrete during failure process, especially in the mechanical behaviors impacted by three experimental factors of eccentricity ratio, concrete strength and slenderness ratio that can affect the capacity and durability of CFST columns. The results demonstrate the process of stress development as well as the failure mechanism of compression member in testing section, and meanwhile show that the stress of concrete in eccentricity compression member grows along with the load.

1. INTRODUCTION

CONCRETE filled steel tube composite structure is one of the most popular shapes in architectural engineering and bridge engineering because of its irreplaceable advantages such as superior mechanical properties, aesthetic outlook and convenient construction. A set of experimental researches around the world had been carried out to explore the mechanism behavior of CFST since 1960s. For example, Kloppel and Goder (1957) [1], and Jiang [2] conducted a simplistic bearing capacity formula by axial compression test; O'shea (2000) [3], Bridge [4–5] (2003, 2007) and Cai [6] fitted the bearing capacity calculation formula based on axial and eccentric compression tests; Gardner and Jacobson [7] (1967), and Bridge [8] (1976) carried out axial experimental studies respectively on two factors of diameter to thickness ratio and bidirectional eccentric angle; Campione and Scibilia [9], and Prion H. G. L (1994) [10] simplified the calculation mode by a series of bending test; Han [11–12] proposed a simplified bending capacity formula and studied the confining factors by bending test; Zhang [13] and Chen [14] studied CFST bearing capacity influenced by length to tube diameter and eccentricity ratio; Zhang [15–16] explored different mechanisms about shear-shaped and drum-shaped failure based on the testing results of eight steel reinforced concrete member; S. Abdalla and F. Abed [17–18] carried out experiments of thirty-five CFST and CCFST specimens to investigate the effects of different parameters on their behaviors, and the results showed that the dominant failure mode of CCFST specimens was the explosive rupture of the GFRP wrapping at the specimen's mid-height region, in which the effect of (D/t) ratio on the compressive behavior of the CFST specimens was greater than that of other factors.

Although numerous aspects of theoretical and experimental studies have been made on mechanical behavior of CFST members, theoretical research is far lagged behind engineering applications, especially in some areas such as the progress from elasticity to losing the bearing capacity, the stress state of steel tube and its core concrete, and the failure process of CFST members. According to mechanical characteristics of arch ribs in CFST arch bridge, three sets of CFST members are designed with different design parameters to determine the destruction test. In this study, eccentricity ratio, concrete strength and slenderness ratio are selected as experimental factors to determine their effects on the mechanical behavior in CFST members. After measuring the stress in steel tube and core concrete during failure, the process of stress development and failure mechanism of compression member in test section are confirmed. Meanwhile, the results show

---

*Authors to whom correspondence should be addressed.
E-mail: gqchen@gxu.edu.cn 13507709332

1544-8053/16/02 S169-09

doi:10.12783/issn.1544-8053/13/4/S22

Table 1. Specimens and Main Parameters of Specimens.

Specimens	$D \times t \times L$	Concrete	ξ	λ	e_0	$2e_0/D$
A1	273 × 6 × 1200	C50	0.957	17.582	0	0
A2			0.957	17.582	40	0.3065
A3			0.957	17.582	80	0.6130
B1	273 × 6 × 850	C50	0.957	12.454	0	0
B2			0.957	12.454	40	0.3065
B3			0.957	12.454	80	0.6130
C1	273 × 6 × 850	C30	1.546	12.454	0	0
C2			1.546	12.454	40	0.3065
C3			1.546	12.454	80	0.6130

that the stress of concrete in eccentricity compression member grows along with the load.

2. MODEL TEST

2.1. Experimental Design

The factors of this experiment are concrete strength, slenderness ratio and eccentricity ratio. Cross section dimension of steel tube is ∅273 mm × 6 mm, and material grade is Q235B. Concrete is produced using commercially available materials, and its design strength is 30 or 50 MPa. Parameters of this experiment are in Table 1.

2.2. Specimen Preparation

2.2.1. Support Design

Plate hinge support is adopted for axial compression members. In contrast, rolling hinged support is adopted as simply-supported boundary condition for eccentric compression members.

2.2.2. Stress Test Method

Numbers of measuring points are illustrated as Figure 1. area ① is close to the eccentric load and area ③ is the opposite side, whereas area ② and area ④ are the rest of the two areas. For axial compression members, there is no difference among the four areas, so that each measuring point test data of average strain values can be taken as the research object. The numbering method of measuring points is as below: outer-wall of steel tube are numbered from 1H to 4H or from 1Z to 4Z (the number represents the area of strain gauge, H is the horizontal strain and Z is the vertical strain of outer-wall), and internal concrete longitudinal measuring points are numbered from 1 to 12, as shown in Figure 1.

2.2.3. Measuring Equipment

The type of measuring equipment is YAW-10000J, which is a micro-computer controlled servo pressure testing machine. Experiment of the CFST specimens are shown as Figure 2.

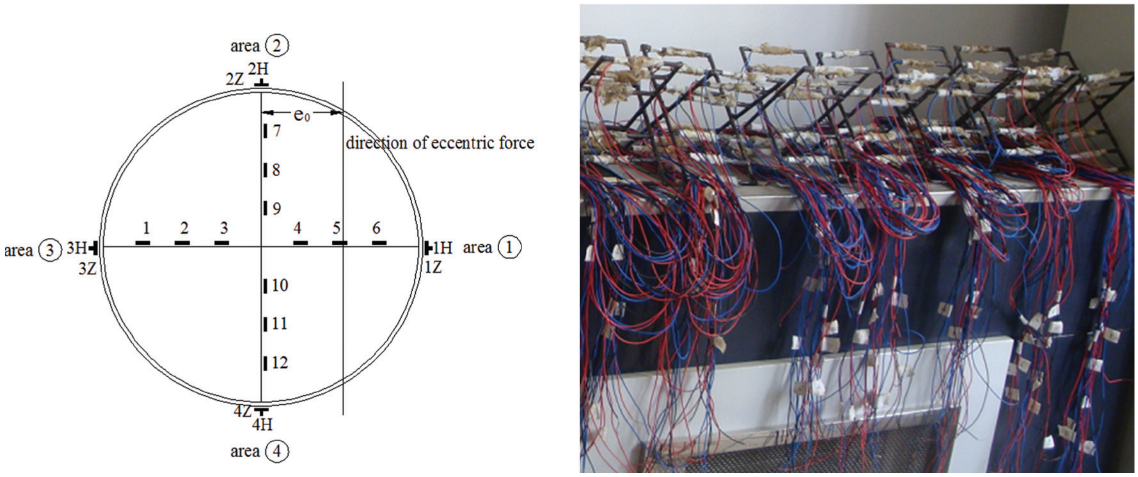

***Figure 1.** Strain gage distribution of the section.*

Figure 2. *Experiment of the CFST specimens.*

3. EXPERIMENTAL ANALYSIS

3.1. Failure Mode

The experimental results show that all the members have a similar failure mode and a good ductility. Members in the elastic stage have no obvious change by comparison with the time. When the peak load is about 80%, cross oblique cracks and oblique shear slip line appear on the outer wall of steel tube. Then, the oblique crack expands and the corrosion layer drops off, which means that the steel tube reaches its yield strength. Along with the increase of load, the hoop strain of steel tube also increases, finally leading to a well-developed confining effect. As shown in Figure 3, diagonal shear slips and tube protrudes obviously from the central part.

During the loading preliminary stage, members under eccentric compression have no obvious deformation. However, when vertical load reaches the ultimate value, the stress and deflection grow faster, and the displacement in middle section increases faster, which is larger than that in quartile section. As a result, bending deformation in the central part of specimen is rather obvious. With the decrease of load, the wall of steel tube is distinctly protruded. In this stage, the compression zones including column base and cap are buckling, the lateral deformation curve presents a approximate half-wave sin curve, the maximum lateral displacement occurs in the central column specimens,

Figure 3. *Failure Patterns of Specimens.*

Table 2. Test Results of the Specimens.

Specimen	Concrete	L (mm)/λ	e_0 (mm)	Ultimate Bearing Capacity (kN)	Displacement (mm)	Bending Moment (kN·m)
A1	C50	1200/17.6	0	5020	10.3	—
A2			40	2614	2.7	111.6
A3			80	2296	4.1	193.1
B1	C50	850/12.4	0	5110	6.7	—
B2			40	2980	4.3	132.0
B3			80	2492	5.5	213.1
C1	C30	850/12.4	0	4589	7.8	—
C2			40	2504	4.0	110.2
C3			80	2161	8.0	190.2

area ③ protrusions and area ① has small depression. When the failure occurs, the steel tube bursts out and the concrete cracks.

3.2. Ultimate Bearing Capacity

Table 2 shows the ultimate bearing capacity of all members measured during the experiment.

It can be known from Table 2 and Figure 3 that, eccentricity distance, concrete strength, and slenderness ratio are the main factors influencing the bearing capacity of CFST.

3.2.1. Impact of Eccentricity Distance

From Figure 3, it can be seen that eccentricity distance plays a significant role in the ultimate bearing capacity of CFST. When eccentricity distance is 40 mm, the ultimate bearing capacity of A2 is 47.9% lower than A1, that of B2 is 41.7% lower than B1, and that of C2 is 45.4% lower than C1. When the distance extends to 80mm, the ultimate bearing capacity of A3 is 54.3% lower than A1, that of B3 is 51.2% lower than B1, and that of C3 is 52.9% lower than C1.

3.2.2. Impact of Concrete Strength

From Table 2, it can be seen that with the increase of eccentricity distance, there is a positive relationship between concrete strength and concrete ultimate bearing capacity. The ultimate bearing capacity of B1 is 11.3% higher than C1, that of B2 is 15.3% higher than C2, and that of B3 is 19.1% higher than C3.

3.2.3. Impact of Slenderness Ratio

The ultimate bearing capacity of A1 is 1.8% lower than B1, that of A2 is 12.3% lower than B2, and that of A3 is 7.9% lower than B3. It can be summarized that for different slenderness ratios (12.4 and 17.6), the ultimate bearing capacity is influenced by eccentricity ratio.

3.3. Load-longitudinal Strain Curve

In this experiment, there are four points employed to measure the longitudinal strain of the tube. Figure 4 shows all types of load-longitudinal strain curve, in which the value depends on each type of member. For axial compression members, the value is the average of four longitudinal strains, while the value close to area ① is the maximum of four measure points.

The above load-longitudinal strain curves can be distinctively divided into three stages: linear growth phase (linear elastic stage), non-linear growth phase (yielding stage) and gradual development phase or descent stage (failure stage).

At the first stage of loading, member of longitudinal strain presents a linear increase along with loading. At the non-linear growth stage, longitudinal strain increases dramatically, and the yield load is approximately 70% to 80% of the ultimate load, with a strain value of about 2000 $\mu\varepsilon$. According to experimental data from references, uniaxial tensile yield strain of the steel tube is about 1578 $\mu\varepsilon$. That is to say, the stress between steel tube and concrete is redistributed on account of the decrease of elastic modulus at the elastic-plastic stage. Consequently, when the members are at the elastic-plastic stage, load-longitudinal strain curve deviates from straight line slowly and gradually presents a curve shape.

3.4. Longitudinal Stress of Axial Compression Members

Figure 4(a) shows the relationship between load

N (kN) and longitudinal strain ε ($\mu\varepsilon$) of A1 specimen, and Table 3 gives the longitudinal stress distribution and its corresponding core concrete and steel tube. As can be seen, the longitudinal stress of point A reaches the proportional elastic limit (namely the longitudinal strain of steel tube reaches $0.8 f_y/E_s$, where f_y is the test yield strength of steel tube and E_s is the elastic modulus of steel tube); that of point B begins to step at the yield stage (the longitudinal strain of steel tube reaches the yield strain of 1578 $\mu\varepsilon$); that of point C is at somewhere near the ultimate bearing capacity.

Figure 4(b) shows the relationship between load N (kN) and longitudinal strain ε ($\mu\varepsilon$) of B1 specimen, and Table 4 gives the longitudinal stress distribution of the middle cross section for the four characteristic points in the curve. The characteristic points are confirmed through the following methods: the longitudinal strain of steel tube is 1000 $\mu\varepsilon$ at point A by which the stress distribution of cross section can be observed when the steel tube is at the elastic stage; the longitudinal stress of steel tube reaches the elastic proportional limit at point B; the steel tube begins to step at the yield stage at point C; the CFST member is close to the ultimate bearing capacity at point D.

Figure 4(c) shows the relationship between load N (kN) and longitudinal strain ε ($\mu\varepsilon$) of C1 specimens, and Table 5 gives the longitudinal stress distribution of the middle cross section for the four characteristic points in the curve. The characteristic points are confirmed through the following methods: the longitudinal stress of steel tube reaches the elastic proportional limit at point A; the steel tube begins to step at the yield stage at point B; the longitudinal strain of steel tube is 2000 $\mu\varepsilon$ at point C; the CFST member is close to the ultimate bearing capacity at point D.

Based on the stress development rules of axial compression members A1, B1 and C1, some conclusions can be drawn:

1. Before the steel tube reaches the elastic proportional limit, the bearing capacity sum of steel tube and concrete is close to the measured value. The concrete and steel tube basically bears the longitudinal load independently and the longitudinal stress distribution of concrete along the radial direction is uniform.
2. When the steel tube enters into the elastic-plastic stage, it produces an obvious confinement effect on the concrete, and the longitudinal stress distribution of concrete along the radial direction becomes different, i.e., the increment speed of longitudinal

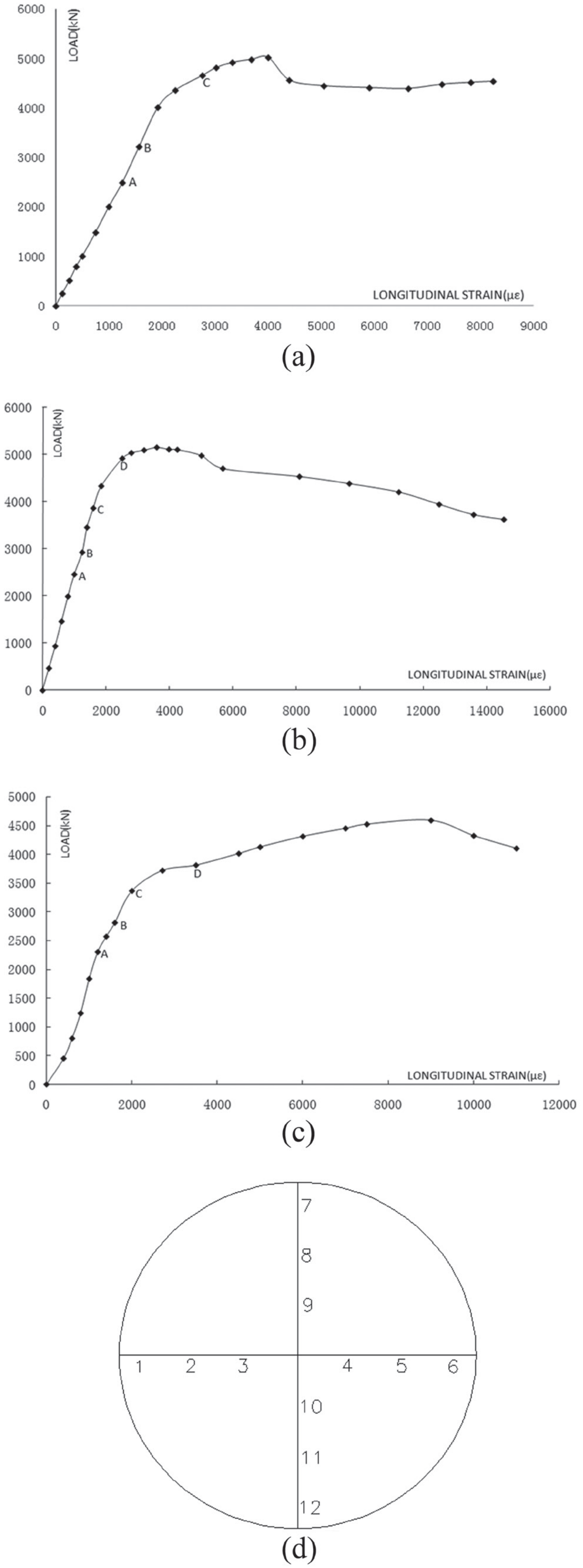

(a)

(b)

(c)

(d)

__Figure 4.__ Load-strain curve. (a) A1 specimen, (b) B1 specimen, (c) C1 specimen and (d) Numbering of concrete stress measuring point.

Table 3. Stress Distribution of Cross Section at the Load Characteristic Points of A1 Specimen.

	Concrete												Tube	
	Outer Circle Stress (MPa)				Middle Circle Stress (MPa)				Inner Circle Stress (MPa)				Longitudinal Strain (MPa)	Load (kN)
Point	**1**	**6**	**7**	**12**	**2**	**5**	**8**	**11**	**3**	**4**	**9**	**10**		
A	20.1	19.1	19.8	21	20.6	19.0	23.3	18.5	20.5	18.6	21.1	19.6	258	2492
B	25	24.4	23.8	24.3	29	28.4	28.1	29.5	33	30.2	32.1	28.6	325	3218
C	50.9	46.1	51.1	69	54.6	51.2	48.6	50.6	58	65	51.0	60.3	325	4656

Table 4. Stress Distribution of Cross Section at the Load Characteristic Points of B1 Specimen.

	Concrete												Tube	
	Outer Circle Stress (MPa)				Middle Circle Stress (MPa)				Inner Circle Stress (MPa)				Longitudinal Strain (MPa)	Load (kN)
Point	**1**	**6**	**7**	**12**	**2**	**5**	**8**	**11**	**3**	**4**	**9**	**10**		
A	19.5	18.6	18.4	19.3	21.2	20.1	19.3	18.4	19.1	14.8	18.6	19	205	2457
B	21	24.5	23.6	25.3	25.1	22.6	24.6	23.8	24.1	18.8	21	22	260	2925
C	32.6	31.2	28.6	36.1	37	32.9	32.5	33.6	35.2	36.3	39.6	38	325	3861
D	72.2	62.1	53.2	66.1	54	46.0	52.1	55.3	59.3	54.2	56	61	325	4914

Table 5. Stress Distribution of Cross Section at the Load Characteristic Points of C1 Specimen.

	Concrete												Tube	
	Outer Circle Stress (MPa)				Middle Circle Stress (MPa)				Inner Circle Stress (MPa)				Longitudinal Strain (MPa)	Load (kN)
Point	**1**	**6**	**7**	**12**	**2**	**5**	**8**	**11**	**3**	**4**	**9**	**10**		
A	22.1	18.6	19.3	17.9	24.8	21	19.3	17.8	21.4	19.4	16	25.3	247	2302
B	26	23	26.3	24.1	26.4	28.6	31	25	31.3	28	33.1	31	325	2810
C	33.9	30	31.2	37	31.6	34.2	35.8	31	38.4	33.9	39.6	41	325	3364
D	45.2	46	43	47	46.3	38.1	39.2	41	42.3	52	48.6	42.6	325	3810

stress in the core concrete is greater than that in the outside concrete;

3. When the steel tube reaches the yield stage, the concrete does not reach the ultimate bearing capacity, the longitudinal stress presents a decreasing trend, and the concrete yields from its core part.

3.5. Concrete Strain of Eccentric Compression Members

Figure 5 shows the section position of strain test points, and Figure 6 presents the longitudinal strain distribution of eccentric compression members for different test points. Depending on various bearing capacity of different members, different sTab. strain values are adopted from the preliminary elastic stage to the peak value stage.

As can be seen from Figure 6, for eccentric compression members, the section agrees well with "plane section" assumption, and strain line distribution obvious along with the increase of load; when the steel tube is under yielding condition, its section does not agree "plane section" assumption any more, especially for No. 5 and No. 6 test points whose strain suddenly rises and then descends. This means that the area of concrete has been destroyed. According to the Saint-Venant's Principle, when the members are under eccentric force, the closer the point to axial line, the larger the value of concentrated force. From the longitudinal strain distribution of test member section, No. 1 test point experiences a process from compression to tension, and the concrete is under whole cross-section compression condition when the eccentricity ratio is 0.306. When the eccentricity distance is 80 mm, the distance between neutral axis and center of circle is about 6 cm. With the increase of eccentricity, neutral axis section gradually moves towards the pressure side.

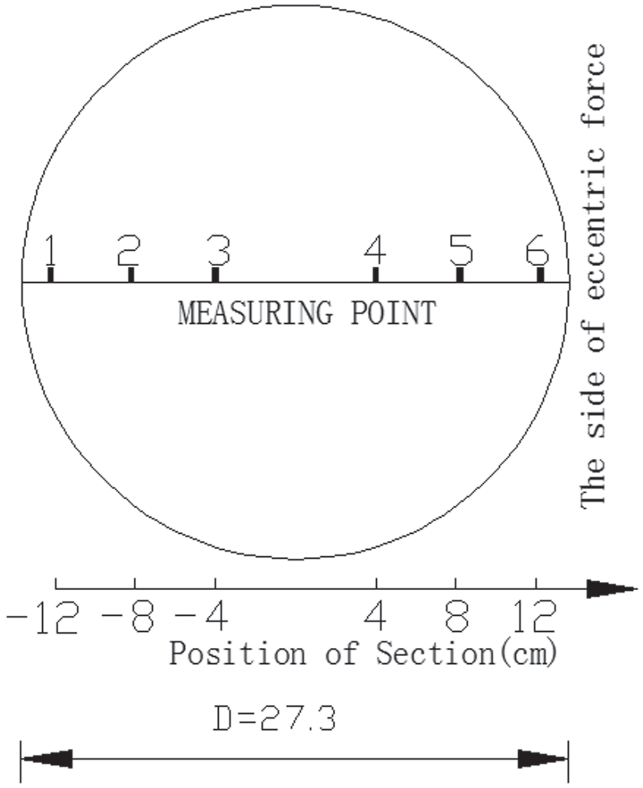

Figure 5. Strain test points in the section.

4. CONCLUSIONS

This paper mainly focuses on the stress variation in the section of steel tube and core concrete during failure process, especially in the mechanical behaviors impacted by eccentricity ratio, concrete strength, and slenderness ratio. Through experimental studies on a set of typical members (different eccentricity rate), it is revealed that eccentricity rate is an important factor influencing the confinement effect. By analyzing the process of stress development in axial and eccentric compression member, stress development from elastic stage to elastoplastic stage is confirmed, and the failure mechanism is clearly deduced.

The results show that compression bearing strength of the core concrete can be enhanced because of the confinement effect of steel tube. Before the confinement effect acts, the cross section stress of core concrete is uniform, while after the confinement effect works, the longitudinal strain of core concrete presents a significantly different distribution. For small eccentric compressive members, the section agrees well with "plane section" assumption in the elastic stage. When the steel tube enters into the yield stage, the core concrete does not agree with "plane section" assumption any more, but the whole cross section can bear load yet. With the increase of load and side deflection, the concrete beyond eccentricity gradually bears tensile stress, and the crush of the core concrete close to eccentricity deteriorates for the increase of steel tube's yield deformation.

SYMBOLS

D = outer diameter (Unit: mm)
t = wall thickness (Unit: mm)
L = length of specimen (Unit: mm)
ξ = confinement index, $\xi = A_s f_y/(A_c f_c)$

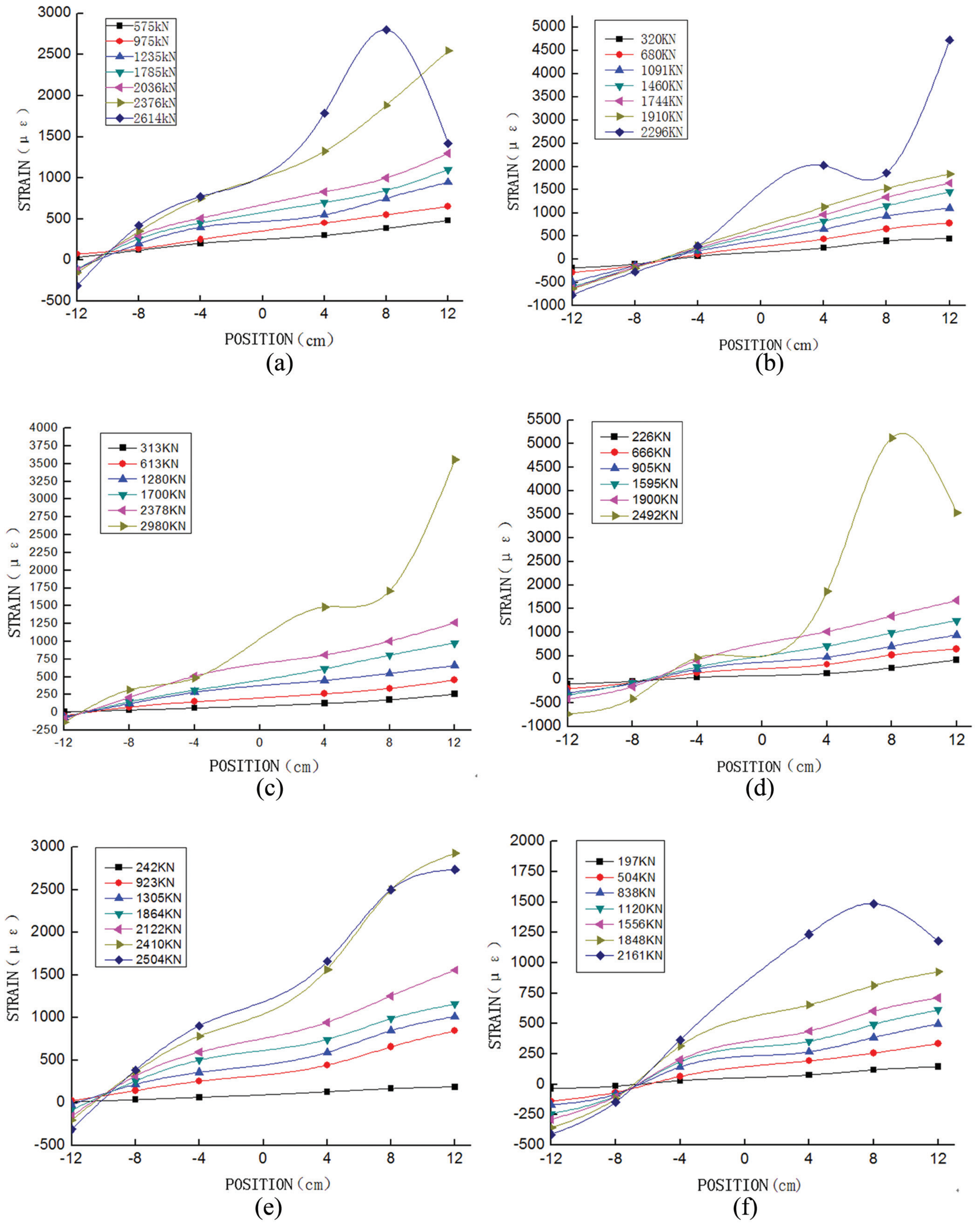

(a) (b) (c) (d) (e) (f)

Figure 6. *Load-strain curve of sections for different specimens. (a) Load-strain curve of sections of A2 specimen, (b) Load-strain curve of sections of A3 specimen, (c) Load-strain curve of sections of B2 specimen, (d) Load-strain curve of sections of B3 specimen, (e) Load-strain curve of sections of C2 specimen and (f) Load-strain curve of sections of C3 specimen.*

λ = length-diameter ratio, $\lambda = L/i$
i = radius of gyration, $i = D/4$
e_0 = eccentricity (Unit: mm)
$2e_0/D$ = eccentricity ratio
A_s = cross sectional area of steel tube
A_c = cross sectional area of concrete
f_y = yield strength of steel tube
f_c = axial compression strength of core concrete

ACKNOWLEDGEMENTS

XIE was grateful for the financial support from the National Natural Science Foundation of China (Nos.51068001 and 51368005), the Technology Development Key Project of Guangxi (No.12426001), the Systematic Project of Guangxi Key Laboratory of Disaster Prevention and Structural Safety the Scientific Research (No.2012ZDX04) and the Scientific Research Foundation of GuangXi University (No. XBZ100762).

REFERENCES

1. Kloppel VK, Goder W. An investigation of the load carrying capacity of concrete-filled steel tubes and development of design formula[J]. *Der Stahlbau*, 1957, 26(2):44–50.
2. Jiang Zao, Qian jiaru, Study on Compressive Strength And Steel Tube Functions of Centrally Loaded Short Concrete Filled-Steel Tube Columns[J], *Journal of Building Structures*, 2010, 40(8): 94–98.
3. O'shea M, Bridge R Q. Design of circular thin-walled concrete filled steel tubes[J]. *Journal of Structural Engineering*, 2000, 126(11), 1295–1303. https://doi.org/10.1061/(ASCE)0733-9445(2000)126:11(1295)
4. Martin D. O'Shea. Russell. Q. Bridge. Design of Circular Thin-walled Concrete Filled Steel Tubes[J]. *Journal of Structural Engineering*. 2003, 126(11):1295–1303.
5. P.K.Gupta, S.M.Sarda and M.S.Kumar. Experimental and computational study of concrete filled steel tubular columns under axial loads. *Journal of constructional Steel Research*[J], 2007, 63(2):182–193.
6. Cai Shaohuai, Gu Wanli, The Basic Properties of The Concrete Filled Steel Tube Long Column and Strength Calculation[J], *Journal of Building Structures*, 1986, 6(1):32–40.
7. Gardner J, Jacobson R. Structural behavior of concrete filled steel tubes [J]. *ACI Journal of Structural Division*, 1967(64-38):404–413.
8. Bridge R Q. Concrete filled steel tubular columns. Report No. R283, School of Civil Engineering. University of Sydney, Sydney, Australia, 1976.
9. Campione G,Scibilia N.Beam-column behavior of concrete filled steel tubes. *Steel and Composite Structures*, 2002, 2(4):259–276. https://doi.org/10.12989/scs.2002.2.4.259
10. Prion H.G.L, Boehme J. Beam-column behavior of steel tubes filled with high strength concrete[J]. *Canadian Journal of Civil Engineering*, 1994, 21(2):207–218. https://doi.org/10.1139/l94-024
11. Han L H, Zhao X L, Tao Z. Tests and mechanics model for concrete-filled SHS stub columns, columns and beam-columns. *Steel and Composite Structures–An International Journal*, 2001, 1(1):51–74. https://doi.org/10.12989/scs.2001.1.1.051
12. Han Linhai, *Concrete Filled Steel Tube Structure–Theory and Application* [M], Beijing: Science Press, 2007.
13. Zhang Lei, Experiment Analysis of Different Slenderness Ratios of Concrete Filled Steel Tubular Column Under Eccentric Load [J], *Mechanics in Engineering*, 2011, 33(4):38–41.
14. Chen Baochun, Experimental Study of Stress-Strain Relation of Eccentrically-Loaded concrete-Filled Steel Tubular Columns [J], *Engineering Mechanics*, 2003, 20(6):154–159.
15. Zhang sumei, Guo lanhui, Wang yuyin etc. Experimental Research and Theoretical Analysis of High Strength Concrete-Filled Square Hollow Section Steel Tubes Subjected to Eccentric Loading [J], *Journal of Building Structures*, 2004, 25(1):17-24
16. Zhang sumei, Wang yuyin, Failure Mode of Short Columns of High-Strength Concrete –Filled Steel Tubes[J], *China Civil Engineering Journal*, 2004, 37(9):1–10.
17. Suliman Abdalla, Farid Abed, Mohammad AlHamaydeh. Behavior of CFSTs and CCFSTs under quasi-static axial compression. *Journal of Constructional Steel Research*, 2013, 90:235–244. https://doi.org/10.1016/j.jcsr.2013.08.007
18. F. Abed, M. Al Hamaydeh, S. Abdalla Experimental and numerical investigations of the compressive behavior of concrete filled steel tubes (CFSTs). *Journal of Constructional Steel Research*. 2013,80:429–439. https://doi.org/10.1016/j.jcsr.2012.10.005

Analysis on the Post-construction Settlement and Influencing Factors for Preloaded Soft Subgrade Based on Parameter Inversion

F. YU*, S.X. CHEN, J. LI and X.J. CHU

State Key Laboratory of Geomechanics and Geotechnical Engineering, Institute of Rock and Soil Mechanics,
Chinese Academy of Sciences, Wuhan 430071, China

ABSTRACT: Aiming at the problem that along a special passenger railway line, the soft soil foundation is widely distributed and the thickness is generally quite deep, leading to diverse foundation reinforcement methods, and in order to ensure required stability and post-construction settlement of soft subgrade, field tests of surcharge pre-loading were carried out in concurrence with field observations. The generalized Kelvin rheological model was employed for foundation parameter inversion and numerical simulation on track-laying construction as well as post-construction settlement prediction were also performed. Results of numerical inversion showed that the foundation parameters were reasonable and reliable and the post-construction settlement was significantly reduced after three months of pre-loading. Several influential factors related to post-construction settlement are highlighted including standing time after roadbed completion, pre-loading height and pre-loading time. It shows that the longer the standing time, the smaller the settlement, and an increase in pre-loading height and time may accelerate the foundation consolidation, thus reducing post-construction settlement.

1. INTRODUCTION

THE design speed of Han-Yi passenger railway is approximately 200 km/h [1], and it adopted ballasted track. This railway line passes through the Jianghan Plain, and the wide distribution of deep soft soil represents a potentially critical adverse geological problem in terms of roadbed construction tenders. In order to meet the high-speed railway subgrade requirements pertaining to load bearing capacity and deformation control, a variety of measures have been employed to contend with foundation reinforcement, such as high-pressure jet grouting piles [2,3], cement mixed piles and multi-directional mixed piles [4,5].

The control standards of subgrade settlement are strict in order to meet the requirements for the 'smoothness' of high-speed railway. So, the accurate observation, prediction and evaluation of subgrade settlement during the construction period are of primary importance [6–8].

Long-term creep deformation of soft soil foundation under varying roadbed pressures, track and train loadings may occur gradually over extended time [9,10]. Accordingly, it is not possible to accurately reflect this deformation via settlement observations during the construction period, i.e., the majority of long-term creep deformation occurs during the railway operational period.

In addition, subgrade settlement is significantly affected by soft foundation treatments, and the level and type of construction technology, as well as the roadbed filler and compaction quality [11,12]. The most direct and reliable method for stability testing and evaluation on subgrade post-construction settlement is the simulation on the load in operational period via pre-loading [13–15].

Accordingly, the current study aims to analyze the late creep deformation of the soft subgrade through pre-loading techniques coupled with a numerical inversion method. The study results may have important significance for the assessment of railway embankment track-laying conditions, and the optimization of design and construction schemes, which is an important safety guarantee for the railway line running operations [16,17].

---

*Authors to whom correspondence should be addressed.
E-mail: yufei8720@163.com; Tel: (+86)13667287425

1544-8053/16/02 S179-07

doi:10.12783/issn.1544-8053/13/4/S23

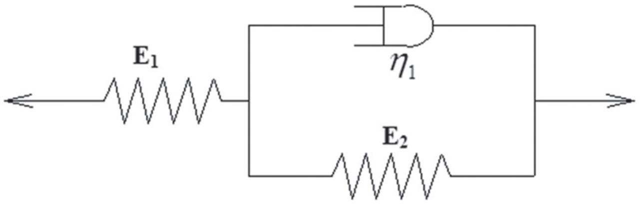

***Figure 1.** Generalized Kelvin rheological model.*

2. GEOLOGY AND ENGINEERING OVERVIEW OF PRE-LOADING TEST SECTION

2.1. Regional Geology

Quaternary soft soils were widely distributed within the study region; the upper strata were primarily comprised of alluvial lacustrine clays, silty clays and mucky soils, with the thickness in the range 3.0~36.5m. The lower strata were characterized by silty sands, hard plastic clays and silty clays. Subgrades within the study region need reinforcement due to poor geological conditions in terms of engineering design specifications.

2.2. Engineering Conditions of Pre-loading Section

According to the design survey data, three sections were selected for the pre-loading tests. Associated soft soil thickness, ground reinforcement method and thickness and other project design information are presented in Table 1.

3. PARAMETER INVERSION PROCEDURE

3.1. Constitutive Model

The filler embankments and ground composition are primarily characterized by unsaturated soils and therefore subject to initial instantaneous elastic deformation [18], with cumulated subgrade settlement tending towards a constant value over time. The finite difference software FLAC3D was used to establish the numerical analysis model of subgrade, and generalized Kelvin model was employed to effectively represent the instantaneous elastic deformation and stabilized creep deformation [19].This model may be used to reflect the deformation rules of both embankments and associated subgrades. The physical components of the generalized Kelvin rheological model are outlined in Figure 1 [20], and the constitutive equation is listed in Equation (1):

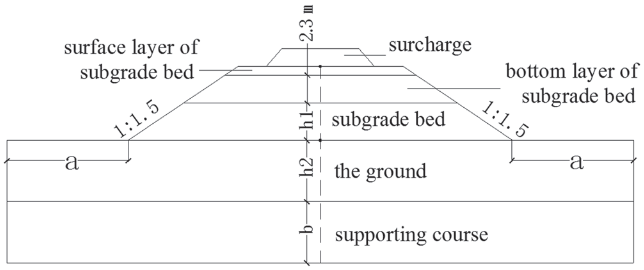

***Figure 2.** Schematic diagram of computational model.*

$$\varepsilon(t) = \frac{\sigma_0}{E_1} + \frac{\sigma_0}{E_2}(1 - e^{(E_2/\eta)t}) \tag{1}$$

where $\varepsilon(t)$ is total strain; σ_0 is total stress; E_1 is the modulus of elasticity; and E_2 is viscoelastic modulus; η_1 is the coefficient of viscosity.

3.2. Computational Model

The computational model employed was based on the design presented in Figure 2. Within this design schema, the subgrade is composed of bed surface, bed bottom and subgrade body, and the subgrade height of testing section is listed in Table 1. The thickness of subgrade bed surface is 0.4m, and that of bed bottom is 2.3m. The thickness of subgrade body (h_1) and reinforcement ground (h_2) are presented in Table 1; these parameters are changed for different testing subgrades and a is the border width of the model and b represents the thickness of the supporting course. In each model, a is equal to 45m, b is 6m.

The top surface of the computational model is a free

Table 1. Engineering Information on Study Area.

Mileage of Testing Subgrade	Height of Subgrade (m)	Height of Surcharge (m)	Thickness of Subgrade Body h_1 (m)	Reinforcement Thickness of Ground h_2 (m)	Reinforcement Method of Ground
DK84+400~DK84+500*	3.5	1.67	0.8	10.5	Multi-directional mixing pile
DK98+400~DK98+500	4.5	2.63	1.8	13.3	Cement mixing pile
DK102+700~DK102+800	5.7	2.25	3.0	30.2	High-pressure jet grouting pile

*DK mean the kilometer from starting point of the railway to the testing subgrade.

Table 2. Calculation Parameters.

		Model Parameters		
Roadbed Structure	**Constitutive Model**	**Modulus (kPa)**	**Poisson Ratio**	**Density (kg/m^3)**
Bed surface	Elastic model	230×10^3	0.20	2.35×10^3
Bed bottom, Subgrade body	Elastic model	160×10^3	0.25	2.19×10^3
Ground	Rheological model	*80×10^3	0.25	2.14×10^3
Supporting course	Rheological model	*30×10^3	0.25	2.05×10^3

*The initial modulus parameter E_1 in rheological model.

boundary layer, with the bottom being wholly constrained; there is a fixed horizontal displacement on both the left and right borders. A two-step calculation process is applied: firstly, an initial stress field analysis of the roadbed structure is conducted, comprising all afore-mentioned components, then followed by rheological calculations for the filling process; track-laying is simulated with applying equal loads.

3.3. Calculation Parameters

Calculation parameters were obtained via a combination of prior engineering experience and inversion of on-site monitoring data. According to the compacting degree, the E_{vd} values of subgrade bed surface, bed bottom and subgrade body, as well as the material parameters are given in Table 2 and elasticity constitutive model was used for these filling layers. For reinforced ground and supporting course, rheological constitutive model was adopted and the material parameters were obtained via inversion analyses, and the initial trial material parameters are listed in Table 2.

4. RESULTS AND DISCUSSION 1 (PARAMETER INVERSION)

In numerical calculations, parameter inversion is a critical task [21] due to its direct effect on the analytical results. Firstly, the determination of the approximate range of elastic modulus and viscosity was made based on prior engineering experience; subsequently, parameters are finely adjusted for result calculation via extracting the displacement value of the surface center point of the test section. The displacements shown in Figure 4 were produced based on per-loading, and simulation results were compared with observation results, as shown in Figure 4. Curve-fitting demonstrates that inversion parameters are within reasonable ranges. The inversion analysis results of roadbed rheological parameters are presented in Table 3, with calculated and actual results compared in Figure 4.

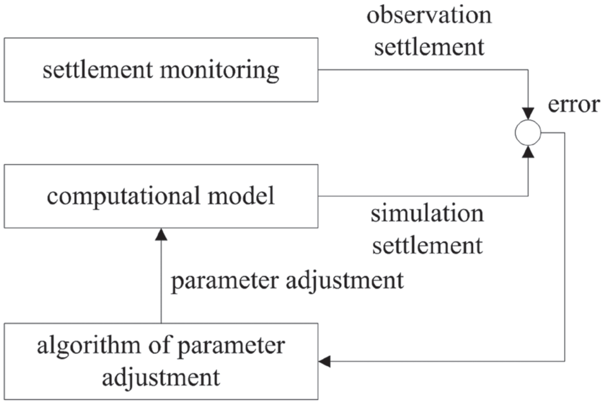

Figure 3. Flow chart of foundation parameter inversion.

As shown in Figure 4, the calculated curve is irregular, primarily due to the effects of unbalanced force and time steps associated with the initial model. Although the calculated curve displays significant variation, it appears to represent an appropriate rheological pattern, particularly over an extended time of period. Using current parameters, the simulated subsidence curve is consistent with the measured curve (Correlation Coefficient: 0.95–0.99, parametric correlation [22]), thus indicating the reasonableness of the foundation rheological parameters obtained by numerical inversion.

5. RESULTS AND DISCUSSION 2 (POST-CONSTRUCTION SETTLEMENT AFTER TRACK-LAYING)

5.1. Analysis of Post-construction Settlement in Normal Condition

The post-construction settlement refers to the settlement of subgrade following track-laying, including incremental settlement due to the train load and creep deformation of the subgrade. According to relevant requirements [1], for the ballasted track design speed of 200 km/h, the subgrade post-construction settlement

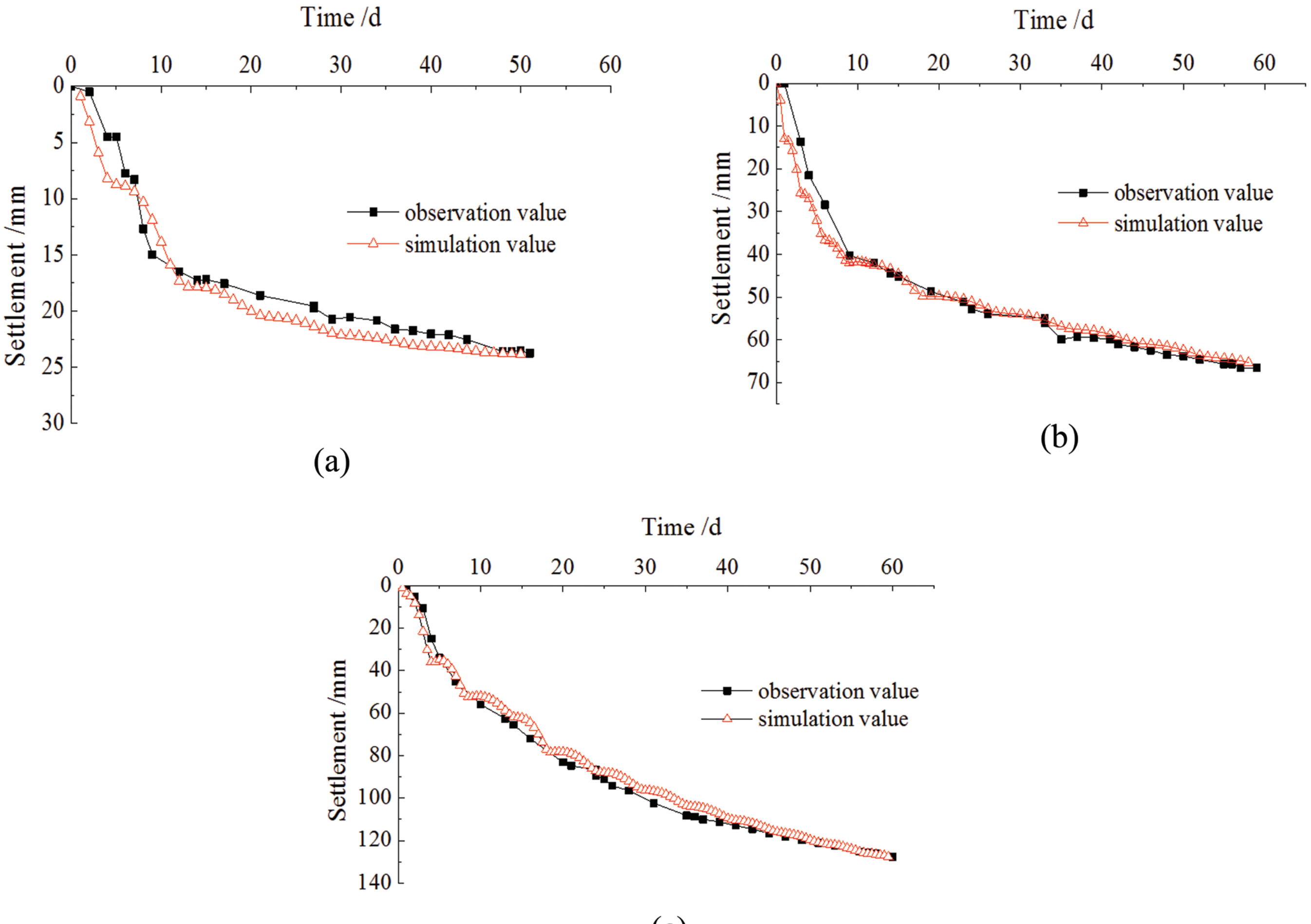

(a)

(b)

(c)

Figure 4. *Numerical simulation and observed values of settlement. (a) DK84+415, (b) DK98+420 and (c) DK102+750.*

should not exceed 150 mm of the initial value and 40 mm/year.

In normal conditions without pre-loading treatment, let the subgrade stew six months after roadbed construction, and then track-laying load is applied. From this time on, the deformation increment of subgrade is referred to as post-construction settlement. The calculated results are shown in Table 4, which indicates that the post-construction settlements of the three test sections meet the aforementioned settlement requirements. However, the maximum annual settlement rate did not meet the requirements. Accordingly, it suggests a high roadbed settlement rate after six months of stewing period.

5.2. Analysis of Post-construction Settlement in Pre-loading Condition

The calculations presented here are the subgrade post-construction settlement and deformation development trend under pre-loading condition, and a comparison was made with similar sections without pre-loading treatment. The time of pre-loading treatment was three months, then unloading the surcharge. The track-laying was constructed 15 days later after the unloading. From this time on, the deformation increment of subgrade is referred to as post-construction settlement, and the calculated results are presented in Table 4. It can be shown that the post-construction settle-

Table 3. Foundation Parameter Inversion Results.

Test Sections	**E_1 (kPa)**	**E_2 (kPa)**	**η_1 (MPa·d)**	**Density (kg/m^3)**	**Poisson's Ratio**
DK84	25×10^3	17×10^3	1.0×10^8	2.05×10^3	0.35
DK98	18.5×10^3	6.1×10^3	4.5×10^8	2.05×10^3	0.35
DK102	10×10^3	1.8×10^3	3.5×10^7	2.05×10^3	0.35

Table 4. Post-construction Settlement Results in Normal Conditions and Preloading Conditions.

	Post-construction Settlement (mm)		Maximum Annual Settlement Rate (mm)	
Test Sections	No Pre-loading	Pre-loading	No Pre-loading	Pre-loading
DK84	18.2	5.3	17.2	3.5
DK98	94.8	21.8	85.6	18.76
DK102	116.3	32.3	115.1	31.2

Table 6. Subgrade Settlements Under Different Track-laying Time Conditions.

Stewing Time After the Roadbed Construction is Completed (month)	Post-construction Settlement (mm)	Maximum Annual Settlement Rate (mm)
3	165.5	150.9
6	116.3	110.1
9	76.1	71.4
12	61.0	58.4
24	42.1	41.6

ment of the subgrade was significantly reduced in three months after pre-loading, while both settlement values and maximum annual settlement rates could meet the specified requirements.

6. RESULTS AND DISCUSSION OF INFLUENTIAL FACTORS ON SETTLEMENT

6.1. Numerical Simulation of Track-laying Construction

Thirteen varying numerical simulation conditions were supposed with respect to section DK102 which has the largest settlement among three test sections (Table 5), in order to analyze the effects of track-laying time, pre-loading height and time on the subgrade post-construction settlement.

6.2. Effects of Track-laying Time

In consideration of the effects of track-laying time (i.e. stewing time after completion of roadbed construction) on settlement, five periods of 3, 6, 9, 12 and 24 months were adopted for numerical simulations. Simulation results and associated curves of subgrade settlement under different stewing time conditions are presented in Table 6 and Figure 5.

Table 5. Numerical Simulation Conditions of Post-construction Settlement.

Condition No.	Stewing Time After the Roadbed Construction is Completed (month)	Pre-loading Height (m)	Pre-loading Time (month)
1	3	0	0
2	6		
3	9		
4	12		
5	24		
6	1	1.5	3
7		2.0	
8		2.5	
9		3.0	
10	1	2.25	3
11			4
12			5
13			6

As shown in Figure 5, the stewing time exerted a significant effect on calculated settlement, and longer stewing time may reduce the post-construction settlement after track-laying. An obviously increased level of subgrade settlement was observed in association with a stewing time less than 12 months as compared with the stewing time longer than 12 months. Thus, the settlement within one year after track-laying is supposed to be a safety guarantee for the railway line running operations.

6.3. Effects of Pre-loading Height

In consideration of the effects of pre-loading height, the height increments of 1.5m, 2.0m, 2.5m, and 3.0m were employed for numerical simulations, with results presented in Table 7. Associated subgrade settlement curves representing the settlement process under different pre-loading height conditions are shown in Figure 6.

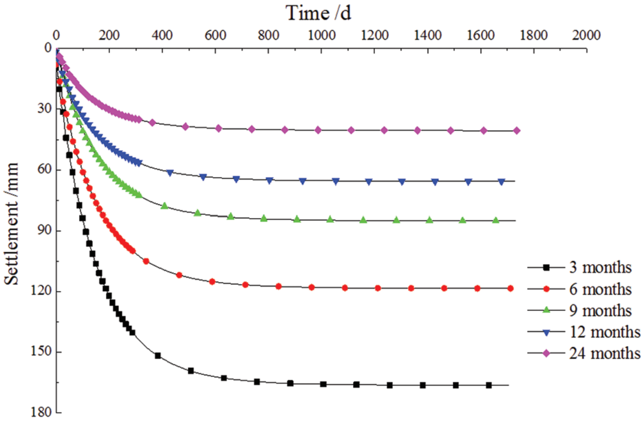

Figure 5. Post-construction settlements under different track-laying time conditions.

Table 7. Subgrade Settlements Under Different Pre-loading Height Conditions.

	Unloading 3 Months After Pre-loading	
Pre-loading Height (m)	Post-construction Settlement (mm)	Maximum Annual Settlement Rate (mm)
1.5	48.5	46.8
2.0	36.3	35.1
2.5	29.1	28.1
3.0	24.2	23.4

It can be shown that increasing pre-loading height can accelerate the consolidation settlement of ground in a relatively short time, thus effectively reducing post-construction settlement after track-laying and shortening the overall construction period.

6.4. The Influence Rules of Pre-loading Time

Pre-loading time was analyzed via numerical simulation using 3, 4, 5, and 6 month pre-loading increments (Table 8). Associated subgrade settlement curves are presented in Figure 7.

Increased pre-loading time was shown to accelerate settlement, thus serving to reduce post-construction settlement after track-laying (Figure 7). In order to achieve similar effects, an increased pre-loading time exerts less effect than an increased stewing time. Accordingly, based on the results presented in the study, embankment construction period may be shortened considerably through pre-loading treatments.

7. CONCLUSIONS

Main conclusions can be drawn as follows:

1. High correlation between simulation curves and on-site data indicates the appropriateness of selected rheological parameters of subgrades
2. For soft foundations, the settlement rate was found to remain relatively high six months later after the completion of roadbed construction. Thus, post-construction settlement may be significantly reduced by three months of pre-loading, leading to a considerably shorter construction period. This is considered highly beneficial in terms of long-term stable and safety railway line running operations.

Table 8. Subgrade Settlements Under Different Pre-loading Time Conditions.

Pre-loading Height (m)	Post-construction Settlement (mm)	Maximum Annual Settlement rate (mm)
3	32.3	31.2
4	26.2	25.5
5	21.3	20.6
6	17.2	16.7

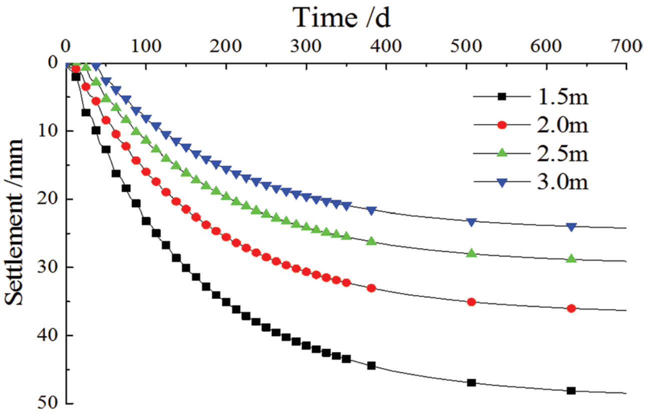

Figure 6. Post-construction settlements under different pre-loading height conditions.

3. Through the analysis on the effects of stewing time, pre-loading height and time on post-construction settlement, results suggest that all the three factors are significantly influential.
4. For soft foundations, consolidation settlement may be accelerated through increasing pre-loading height and pre-loading time, so as to reduce the post-construction settlement and shorten the construction period. For a 20m-thick soft soil roadbed, the post-construction settlement can be effectively reduced through three months of 3m pre-loading.

8. REFERENCES

1. Ministry of Railways: “New speed of 200 to 250 km/h of railway pas-

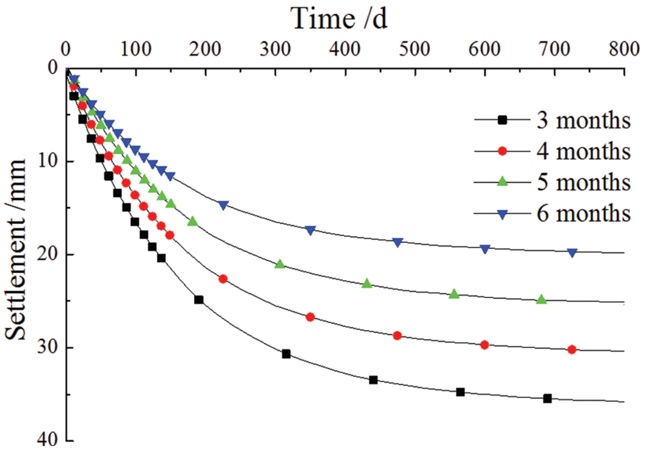

Figure 7. Post-construction settlements under different pre-loading time conditions.

senger line design interim provisions (Railway Construction [2005] No. 140)", Railway industry standard of China, 2005.

2. Z.S. Zheng and G.L. Dai: "Application of high-pressure chemical churning pile to high-speed railway subgrade", *Chinese and Overseas Architecture*, 2009, 01, pp. 161–163.
3. J.J. Hou: "Construction technology of high-pressure rotary jet grouting pile in soft soil foundation treatment of railway", *Shanxi Architecture*, 2010, 09, pp. 261–262.
4. J.J. Hou: "Construction technology of cement mixing pile in soft soil foundation treatment of railway", *Shanxi Architecture*, 2010, 08, pp. 265–266.
5. B. Zhao: "Piling and its inspection of cement mixing pile of railway at Yingkou coastal industrial base", *Railway Standard Design*, 2013, 02, pp. 44–47.
6. J.G. Shang and X.Z. Zhang: "Study on subgrade settlement observation and evaluation method of high-speed railway", *Subgrade Engineering,* 2011, 03, pp. 26–28, 32.
7. X.F. Yang: "Observation and evaluation of subgrade settlement and deformation on Beijing-Shanghai high-speed railway", *High Speed Railway Technology*, 2012, 02, pp. 79–81.
8. M.L. Li: "Deformation monitoring and assessment technology for substructure of unballasted track on railway passenger dedicated line", *Engineering Sciences*, 2009, 01, pp. 48–59.
9. S.S. Zhou: "The Analysis of Subgrade Settlement after Construction Considering Rheology in Soft Soil Area", Unpublished Master Thesis, Tianjin University, Tianjin, China, 2010.
10. Z.L. Wang, J.Z. Huang, X.H. Yang: "Study on settlement prediction model considering rheological properties of soft soils", *Rock and Soil Mechanics*, 2006, 09, pp. 1567–1570.
11. B.L. Wang, S.H. Zhou and L.C. Yang: "Experimental study on soft soil settlement of high-speed railway subgrade after construction", *Journal of Tongji University (Natural Science)*, 2003, 10, pp. 1163–1167.
12. J.C. Xu: "Settlement Control of Soft Soil and Dynamic Analysis of High-Speed", Unpublished Master Thesis, Tianjin University, Tianjin, China, 2010.
13. Y.B. Wang: "Appraisal of Improvement Effect of Soft Soil and Analysis on Dynamic Response of Subgrade of High-Speed Railway", Unpublished Master Thesis, Xi'an University of Architecture and Technology, Xi'an, China, 2010.
14. Y.H. Liao: "Research on Observation and Analysis of Settlement for Soft Soil Ground of a Dedicated Passenger Line", Unpublished Master Thesis, Huazhong University of Science and Technology, Wuhan, China, 2011.
15. F.Q. Qiu: "Influential factors in observation for settlement of Beijing-Shanghai high speed railway", Railway Investigation and Surveying, 2010, 04, pp. 14–20.
16. L. Dong, Y.S. Ye, D.G. Cai, B. Wu and N.H. Yang: "Contrast test on soft ground improvement of high-speed rails", *Rock and Soil Mechanics*, 2006, 10, pp. 1856–1860.
17. D.Y. Wu, Y.P. Yang and X.JJ. Hu: "Analysis of high-speed railway settlement observation data processing", *Journal of Railway Science and Engineering*, 2010, 02, pp. 89–92.
18. L.J. Wu: "Study on Compressibility and Consolidation of Unsaturated Soil and Reinforced Technique on High-speed Railway", Unpublished PhD Thesis, Southwest Jiaotong University, Chengdu, China, 2011.
19. Y.H. Yang and C.H. Wang: "Elastic-visco displacement back analysis in tunnel engineering considering temporal-spatial effects", *Chinese Journal of Underground Space and Engineering*, 2009, 03, pp. 468–472, 629.
20. M.L. Zhu, Z.D. Zhu, G. Li: "Experimental study of dynamic characteristics of granite under cyclic loading", *Chinese Journal of Rock Mechanics and Engineering*, 2009, 28, pp 2520–2526.
21. S.J. Liu, W.Y Xu and J.F. Shao: "Identification of rock viscoelastic model and back analysis of mechanical parameters", *Journal of Hydraulic Engineering*, 2002, 06, pp 101–105.
22. S.J. Li, Y.X. Liu and W. Sun: "Intelligent Computing and Parameter Inversion", Monograph, Science Press, Beijing, China, 2008.

Effects of Powder Additives on Thermal Shrinkage of Nanoporous Silica Insulation

JINPENG FENG[1,*], YOULAN WANG[2] and XIA FENG[2]
[1]College of Resource and Metallurgy & College of Chemistry and Chemical Engineering, Guangxi University, Nanning, China
[2]College of Resource and Metallurgy, Guangxi University, Nanning, China

ABSTRACT: In this study, four powder additives were introduced as high-temperature shrinkage inhibitors to make high performance nanoporous silica insulation. The introduction of fumed alumina could greatly improve the thermal stability of the composites at higher temperatures, and the maximum service temperature could be increased to about 1000°C. When 5% fumed alumina was added, the volume shrinkage decreased from 18.49% to 3.47%. Moreover, better results could be achieved with the increase in mass ratio. In addition, fumed titania also improved the thermal stability of the composites to some extent, while boron carbide and boron nitride led to poor performance.

1. INTRODUCTION

NANOPOROUS silica thermal insulation is a new high-efficiency material with excellent performance at intermediate temperature. It plays an important role in the fields of energy savings, aerospace, architecture, etc. [1]. The typical material is silica aerogel insulation, which has been studied for many years [2]. Several studies show that the use of silica aerogel insulation may be limited due to some disadvantages including complicated preparation method, low mechanical strength, poor thermal insulation and stability at high temperatures. Therefore, a more promising nanoporous silica thermal insulating composite has been proposed and studied, in which fumed silica is adopted as a basic material, and fiber as enforced material. Fumed silica, a high-purity non-crystalline silica, is produced by fusing naturally occurring quartz crystals of high purity at approximately 2000°C. It has many excellent properties, and especially its thermal insulating property is superior to other types of thermal insulations due to the nano-scale particle size (about 20 nm) [3–5]. Low thermal conductivity makes it a useful and basic material for thermal insulation [6]. The thermal conductivity of nanoporous silica thermal insulation is only 0.033 W/(m·K) under ambient conditions (25°C and atmospheric pressure). However, with increasing service temperature, the volume shrinkage of this material becomes critical. As a result, the value of volume shrinkage ranges from 1.18–8.49%, corresponding to the calcining temperature from 800–1000°C. The results indicate that most fumed silica particles could retain original shapes and the structure of composites has not been completely destroyed at temperatures below 1000°C. But serious sintering phenomenon is observed when the composites are treated at temperatures above 1000°C. The deformation in appearance directly affects its mechanical property and thermal insulating performance [7–9]. In order to decrease the thermal shrinkage of the composites, fumed titania, fumed alumina, boron carbide and boron nitride were selected as additives to integrate with fumed silica and fibers to study the effects on thermal shrinkage. In this way, a desirable inhibitor could be found to resolve the problem of thermal shrinkage of the composites at high temperatures.

2. MATERIALS AND EXPERIMENTAL PROCEDURE

2.1. Materials

In this work, fumed silica, reinforced fiber, and powder additives were used as the basic components [10–12]. Fumed silica was AEROSIL 200 from Degussa with specific surface area of 200 m^2/g and average primary particle size of 12 nm [13]. Reinforced fiber was alkali-free ultrafine glass fiber with average diameter of about 7 μm and length of 5 mm. The first pow-

---

*Authors to whom correspondence should be addressed.
E-mail: goldminer@sina.com

1544-8053/16/02 S187-05

doi:10.12783/issn.1544-8053/13/4/S24

der additive was fumed titania, which has excellent thermal stability and the weight loss percentage was below 2% when it was calcined at 1000°C for 2h [14]. Its particle size ranged between 20 and 50 nm with a weight loss percentage of 1.5%. The second powder additive was fumed alumina from Degussa with specific surface area of 130 m^2/g and the weight loss percentage was below 3% when it was calcined at 1000°C for 2h and the particle size is 30 nm. Boron carbide was the third powder additive with a diameter of 1.69 μm. It is one of the hardest known materials with melting point of 2450°C. The last powder additive was boron nitride with average particle size of 1.372 μm with excellent chemical stability and its melting point was up to 3000°C in inert gas.

2.2. Preparation and Characterization Method

A range of composite samples were prepared by mechanically mixing fumed silica, reinforced fiber and additives together in different mass ratios. A high-speed multifunctional disintegrator was used as the mixing equipment and the mixing time was limited for 30 mins. Although good homogeneity of the mixture could be achieved after a long time of mixing, excessive mixing may possibly break up the fibers, resulting in a loss in mechanical strength. Then, powder samples were uniaxially compacted in a circular cross-section die at an applied pressure of 2 MPa at room temperature to make the samples of size φ50 mm × 15 ± 1 mm. Various samples could be prepared by adjusting the size and shape of the die. After maintaining pressures for ten minutes, fumed silica based thermal insulating composites were obtained.

In this study, different mass ratios of samples were placed into a muffle furnace to be heated to a temperature of 1000°C in order to simulate the service environment. The volume shrinkage (φ) was introduced to characterize the change in sample size to evaluate the thermal stability at a certain temperature, and it could be written as in Equation (1), in which V_0 and V represent the volumes of the samples before and after treatment, respectively.

$$\varphi = \frac{V_0 - V}{V_0} \times 100\% \qquad (1)$$

For ensuring the accuracy of the results, three samples were treated under the same conditions and the average volume shrinkage of three samples was the final result. In addition, the morphology of the composites was characterized by using FESEM (Field Emission Scanning Electron Microscopy).

Thermal conductivity of nanoporous silica thermal insulation was measured by a small guarded hot plate apparatus, at the National quality center for refractory material, designed for small samples of low thermal conductivity values. Thermal conductivity was measured over an area of 200 mm × 200 mm at a mean sample temperature of 25°C. The measuring zone was located on the warm upper side of the sample under measurement.

3. RESULTS AND DISCUSSION

3.1. Effects of Fumed Titania on Thermal Shrinkage of Nanoporous Silica Insulation

Effects of mass ratio of fumed titania on volume shrinkage of nanoporous silica insulation at 1000°C were investigated and the result is shown in Figure 1. It could be clearly seen that, with increasing mass ratio of fumed titania, the value of volume shrinkage was nearly constant in the range of 5–20%. When the mass ratio of fumed titania was more than 20%, the thermal shrinkage began to decrease to a certain degree. At this moment, slight sintering phenomenon was found while most particles could retain original shapes and there were many nano-scale pores in the interior of the material, as shown in Figure 2. Therefore, the addition of fumed titania was able to restrain thermal shrinkage, but the volume stability was not significantly improved. When the service temperature became higher, fumed titania was unsuitable to be adopted as an inhibitor to reduce thermal shrinkage.

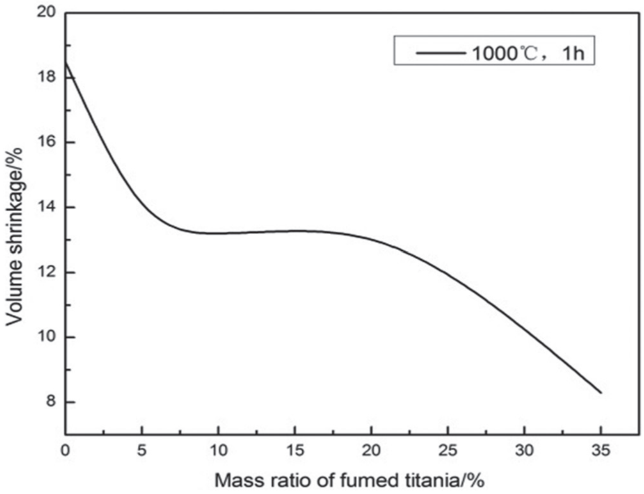

Figure 1. Effects of mass ratio of fumed titania on volume shrinkage.

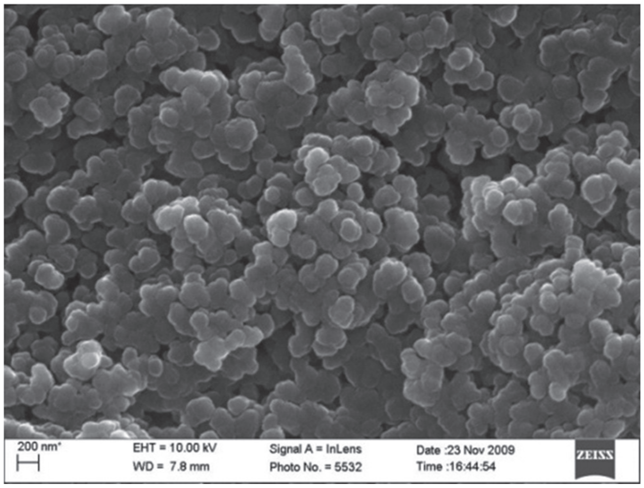

Figure 2. *FESEM image of nanoporous silica insulation with 20% fumed titania treated at 1000°C for 1h.*

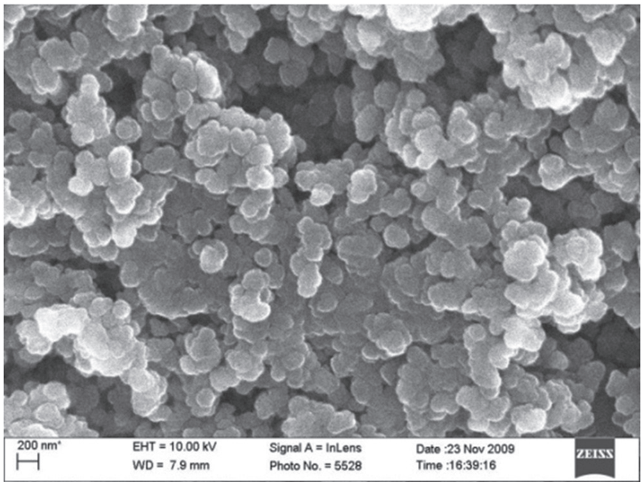

Figure 4. *FESEM image of nanoporous silica insulation with 20% fumed alumina treated at 1000°C for 1h.*

3.2. Effects of Fumed Alumina on Thermal Shrinkage of Nanoporous Silica Insulation

From Figure 3, it was clear that the utilization of fumed alumina could improve the thermal stability of the composites. The volume shrinkage decreased from 18.49% to 3.47% at 1000°C with the addition of 5% fumed alumina. Moreover, there was no significant influence of mass ratio of fumed alumina on volume shrinkage. When the calcining temperature is 1000°C, the volume shrinkage ranged from 3.47% to 1.45% with the increase in mass ratio of fumed alumina. FESEM image of the composites, with 20% fumed alumina, calcined at 1000°C for 1h is presented in Figure 4. It could be seen that most particles retained their original shapes; only few particles appeared to be lightly sintered and rich nano-scale pore structures were found in the material interior. In summary, the suitable amount of fumed alumina was about 5–10% for the composites used at 1000°C. Fumed alumina, as an inhibitor, could remarkably restrain thermal shrinkage at high service temperatures. The reason for this behavior may be attributed to the following property: fumed alumina has certain inertia at high temperature, and the introduction of fumed alumina can change the diffusion mechanism and reduce thermal shrinkage of fumed silica particles at high temperatures.

3.3. Effects of Boron Carbide on Thermal Shrinkage of Nanoporous Silica Insulation

Boron carbide was selected as an additive to integrate with nanoporous silica insulation due to its excellent properties including high melting point, high temperature resistance, high hardness, high chemical stability and low density. The results in Figure 5 show

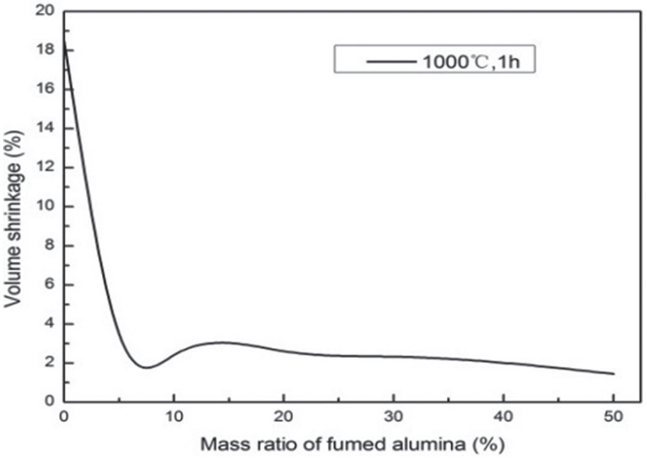

Figure 3. *Effects of mass ratio of fumed alumina on volume shrinkage.*

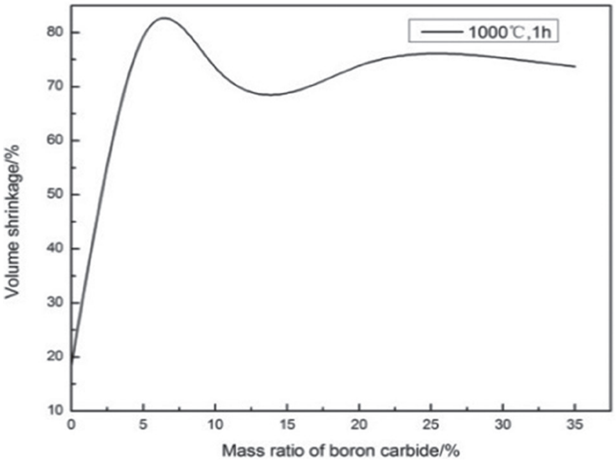

Figure 5. *Effects of mass ratio of boron carbide on volume shrinkage.*

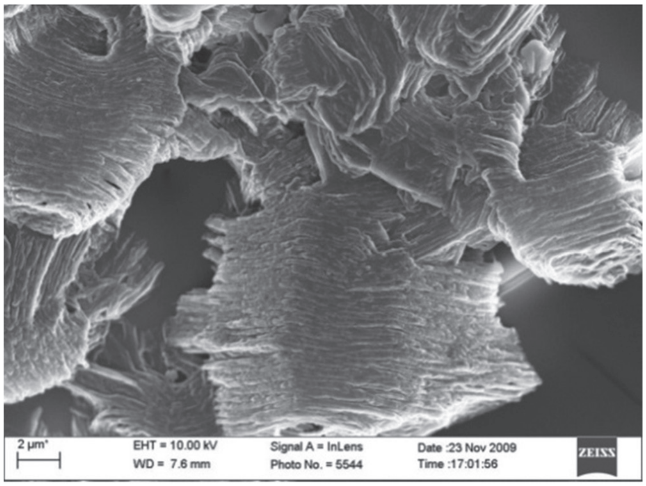

Figure 6. *FESEM image of nanoporous silica insulation with 20% boron carbide treated at 1000°C for 1h.*

that the introduction of boron carbide has a negligible effect on the thermal stability of the composites at calcining temperature of 1000°C; even the value of volume shrinkage increased significantly. Moreover, when 20% boron carbide was added, serious sintering was found as shown in Figure 6. The experimental results show that boron carbide is not suitable to be adopted to reduce thermal shrinkage. Reasons could be explained as follows: Boron carbide, used in this study, is an ultra-fine powder with characteristics of large specific surface area, higher surface activity, more internal defects in atoms and bigger crystal lattice distortion. Therefore, the sintering process is accelerated, which causes the length of diffusion of atoms to shorten and the diffusion velocity of the particles in the solid state is improved. Additionally, because of the presence of the transition element oxides in SiO_2, the sintering temperature of boron carbide decreases and the sintering speed is accelerated, which lowers the thermal stability of the composites at higher temperatures.

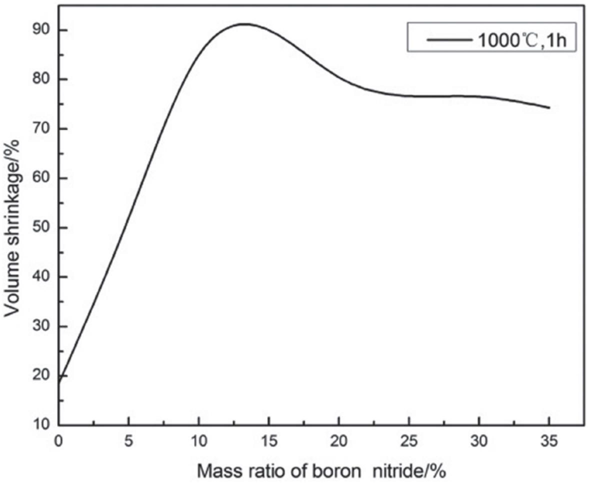

Figure 7. *Effects of mass ratio of boron nitride on volume shrinkage.*

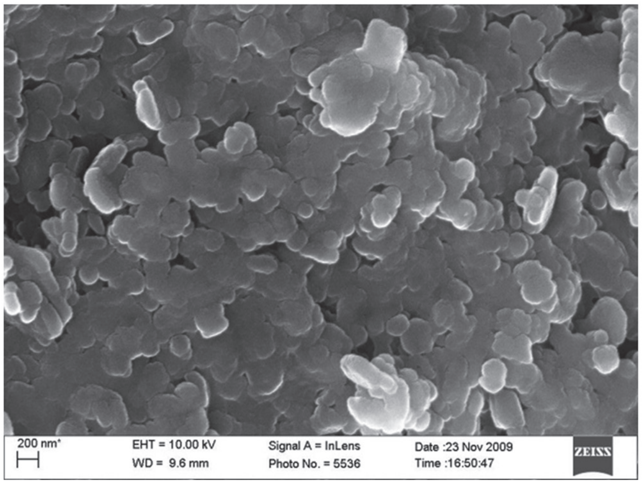

Figure 8. *FESEM image of nanoporous silica insulation with 20% boron nitride treated at 1000°C for 1h.*

3.4. Effects of Boron Nitride on Thermal Shrinkage of Nanoporous Silica Insulation

Boron nitride was selected as an additive because of its low thermal expansion coefficient. The relationship between volume shrinkage and mass ratio of boron nitride is shown in Figure 7. The volume shrinkage is proportional to mass ratio of boron nitride when a small amount of boron nitride is added. When the mass ratio of boron nitride is more than 10%, the volume shrinkage shows a negative correlation with mass ratio of boron nitride, but not significantly. Moreover, serious sintering phenomenon is observed and the porosity decreases significantly when 20% boron nitride is added, as shown in Figure 8. Boron nitride is easy to be oxidized in an oxygen atmosphere, which is the reason for the decrease in thermal stability.

3.5. Thermal Conductivity of Nanoporous Silica Composites Containing Fumed Alumina

The volume shrinkage of nanoporous silica insulation decreased gradually with increasing fumed titania, but not significantly. When 5% fumed alumina was added, the volume shrinkage decreased from 18.49% to 3.47% at 1000°C. The thermal shrinkage of nanoporous silica insulation was accelerated when boron carbide and boron nitride were introduced. Referring to the four groups of the experiments above, fumed alumina could be used as a desirable inhibitor to resolve

Table 1. Thermal Conductivity of Nanoporous Silica Insulation in Different Cases.

Materials	200°C	800°C	1000°C
5% fumed alumina added	0.022 W/(m·K)	0.028 W/(m·K)	0.032 W/(m·K)
Fumed alumina not added	0.019 W/(m·K)	0.024 W/(m·K)	material defected

the problem of thermal shrinkage of the composites at high temperatures.

Therefore, the thermal conductivity of nanoporous silica insulation with 5% fumed alumina was tested to determine whether fumed alumina had a negative impact on the insulation performance of nanoporous silica. Experimentally measured values of thermal conductivity are shown in Table 1. Nanoporous silica insulation containing fumed alumina mass ratio of 5% had a low thermal conductivity of 0.022W/(m·K) and with increasing temperature from 200–800°C, the thermal conductivity of the composites increased from 0.022 to 0.028 W/(m·K). The measurements indicated that the addition of fumed alumina led to a very small increase compared with nanoporous silica insulation without fumed alumina added. Moreover, when the testing temperature was increased to 1000°C, the nanoporous silica insulation, without fumed alumina added, did not perform well. However, the thermal conductivity of nanoporous silica insulation with 5% fumed alumina added was only 0.032W/(m·K).

4. CONCLUSIONS

Higher thermal stability of nanoporous silica insulation, consisting of fumed silica, fiber and powder additives has been developed and tested for its thermal shrinkage. FESEM has been employed to characterize the microstructure. The volume shrinkage of nanoporous silica insulation could be restrained with fumed titania added, but not significantly. The utilization of fumed alumina could significantly improve the thermal stability of the composites. When 5% fumed alumina is added, the volume shrinkage decreases from 18.49% to 3.47% at 1000°C. The higher service temperature requires more addition of fumed alumina. In addition, the thermal shrinkage of nanoporous silica insulation is accelerated when boron carbide and boron nitride are introduced. Thus, fumed alumina could be adopted as an ideal powder additive to nanoporous silica insulation to decrease the thermal shrinkage.

5. ACKNOWLEDGEMENTS

This work was financially supported by National Natural Science Foundation of China (No. 51264002) and Foundation of Guangxi Key Laboratory of Petrochemical Resource Processing and Process Intensification Technology (No.2012K12).

6. REFERENCES

1. P.S. Liu. 2004. Review of Porous Materials, Beijing, Tsinghua University Press,Inc.
2. Ya-Ling He and Tao Xie. "Advances of thermal conductivity models of nanoscale silica aerogel insulation material", *Applied Thermal Engineering*, Vol.81, 2015, pp.28–50. https://doi.org/10.1016/j.applthermaleng.2015.02.013
3. J.P. Feng; D.P.Chen; and W.Ni. "Study of IR absorption properties of fumed silica-opacifier composites", *J. Non-Cryst Solids*, 2010, 356,480–483. https://doi.org/10.1016/j.jnoncrysol.2009.12.015
4. Abe, K.Sato and H.Abe. "Formation of Porous Fumed Silica Coating on the Surface of Glass Fibers by a Dry Mechanical Processing Technique", *Adv. Powder Technol.*, Vol.17, 2008, pp.311–320. https://doi.org/10.1163/156855208X314976
5. J.T.Saavedra and J.L.Beceiro, "Effect of silica content on thermal stability of fumed silica/epoxy composites", *Polym Degrad Stabil*, Vol. 93, 2008, pp. 2133–2137. https://doi.org/10.1016/j.polymdegradstab.2008.08.006
6. J.P.Feng and Y.Y.Yan. "Study of thermal stability of fumed silica based thermal insulating composites at high temperatures", *Compos. Part B-Eng.*, Vol. 42, 2011, pp. 1821–1825. https://doi.org/10.1016/j.compositesb.2011.06.023
7. N.Al-Yassir and R.Le Van Mao. "Thermal stability of alumina aerogel doped with yttrium oxide, used as a catalyst support for the thermo catalytic cracking (TCC) process: An investigation of its textural and structural properties", *Appl. Catal. A-Gen.*, Vol. 317, No. 2, 2007, pp.275–283. https://doi.org/10.1016/j.apcata.2006.10.030
8. D.Z.Chen and Y.Liu. "Synergistic effect between POSS and fumed silica on thermal stabilities andmechanical properties of room temperature vulcanized (RTV) silicone rubbers", *Polym Degrad Stabil,* Vol. 97, 2012, pp. 308–315. https://doi.org/10.1016/j.polymdegradstab.2011.12.016
9. V.M.Gunko and I.F. Mironyuk. "Morphology and surface properties of fumed silicas", *J. Colloid Interface. Sci.*, Vol. 289, 2005, pp. 427–445. https://doi.org/10.1016/j.jcis.2005.05.051
10. J.Kuhn and T.Gleissner. "Arduini-Schuster. Integration of mineral powders into SiO_2 aerogels", *J. Non-Cryst Solids*, Vol. 186, 1995, pp. 291–295. https://doi.org/10.1016/0022-3093(95)00067-4
11. J.M. Kim and T.H.Song. "Vacuum insulation properties of glass wool and opacified fumed silica under variable pressing load and vacuum level", *Int. J. Heat Mass Tran.*, Vol. 64, 2013, pp. 783–791. https://doi.org/10.1016/j.ijheatmasstransfer.2013.05.012
12. J.Wang and J.Kuhn. "Monolithic silica aerogel insulation doped with TiO2 powder and ceramic fibers", *J. Non-Cryst Solids*, Vol. 86, 1995, pp. 296–300. https://doi.org/10.1016/0022-3093(95)00068-2
13. V.M.Gunko and J.P.Blitz. "Surface structure and properties of mixed fumed oxides", *J.Colloid Interface Sci.*, Vol. 314, No. 1, 2007, pp. 119–130. https://doi.org/10.1016/j.jcis.2007.05.025
14. V.I.Zarko and V.M.Gunko. "Study of surfaces properties of fumed alumina/silica materials", *Colloids and Surfaces A: Physicochemical and Engineering Aspects*, Vol. 127, No. (1–3), 1997, pp.11–18.

Anti-rutting Performances of Coarse Aggregate Porous Asphalt Mixtures

BIN YANG[1,2,3,*], XINKUN WEN[1], KAI ZHONG[1], and YUNPENG LIU[1]
[1]*College of Civil Engineering and Architecture, Guangxi University, P.R. China, 530004*
[2]*Key Laboratory of Disaster Prevention and Structural Safety of Ministry of Education, Nanning, P.R. China*
[3]*Key Laboratory of Disaster Prevention and Engineering Safety of Guangxi, P.R. China*

ABSTRACT: The anti-crack performances of coarse aggregate porous asphalt mixtures were better than those of the common fine aggregate or medium aggregate asphalt mixtures. High temperature and the vehicle loading usually lead to early rutting of porous asphalt mixtures. In this paper, the rutting tester was used to study the anti-rutting effects of the asphalt content, the porosity, the temperature on the asphalt mixture AM-40 (Maximum aggregate size is 40 mm).The rutting depth of coarse aggregate porous asphalt mixtures increased with porosity growth and temperature growth. The anti-rutting performances of three different coarse aggregate porous asphalt mixtures was compared, with the decreasing performance order of the semi-flexible asphalt mixtures, the rubber asphalt mixtures, and the pure asphalt mixtures.

1. INTRODUCTION

THE anti-crack performances of coarse aggregate porous asphalt mixtures were better than those of the general fine aggregate or medium aggregate asphalt mixtures. The spreading rate of the reflection crack in coarse aggregate porous asphalt mixtures was obviously smaller than the one in general asphalt mixture. Coarse aggregate porous asphalt mixtures used for preventing the reflection crack from the asphalt overlay referred to the mixture with the maximum aggregate size of 25–63 mm and the porosity larger than 15% [1–3]. Coarse aggregate porous asphalt mixtures are placed between the old cement concrete pavement and the asphalt overlay, which effectively blocks the spreading route of the refection crack, weaken the stress intensity factor of the crack tip. With the increase of porosity, the intensity and modulus decreased. High temperature and the vehicle loading usually lead to early rutting, which decreases the performance of the pavement, endangers the traffic safety, shorten the service life of the asphalt pavement. Nowadays, worldwide scholars have studied the rutting performance of the asphalt mixture effectually.

In 2003, the American Association of State Highway and Transportation Officials (AASHTO) and the Transportation Research Board (TRB) put forward several new and reconstructed rutting prediction models for asphalt pavement, where rutting was considered in the pavement design and the rutting depth was used as an index for the rutting control. In 2008, Charles W. Schwartz and Regis L. Carvalho [5] studied the permanent deformation and distribution law of the structural rutting in the hot mix asphalt mixture. In 2008, Hui Wang [6] studied the structure and the material of the structure of the asphalt pavement under heave-loading and high temperature. Combined with the research and the rutting test method the relationship between the rutting and the material was studied by variance analysis, correlation analysis, and regression analysis, leading to the relevant design standards. In 2009, Xingwei Chen and Zhihong Xu [7] studied the influence of the temperature and the loading on the anti-rutting of Stone Mastic Asphalt SMA-13 (Maximum aggregate size is 13mm) and super pavement SUP-19 (Maximum aggregate size is 19 mm). In 2009, Hui Wang, Luexian Li, Qiseng Zhang concluded that the rutting deformation mainly detected on the super layer, according to the rutting data, section ship, and the factor analysis of the deformations at driveway. And the deformation was different among the upper (25% or so), middle (60% or so), and lower (15% or so) layer. Nowadays, rutting of general fine size and medium size asphalt mixture were studied. And the study on anti-rutting performance of coarse aggregate porous asphalt mixtures were few. In

---

*Authors to whom correspondence should be addressed.
E-mail: yangbin5612@163.com

1544-8053/16/02 S193-06

doi:10.12783/issn.1544-8053/13/4/S25

this study, the effect of the asphalt content, the porosity, the temperature, and different types of asphalt mixtures on the anti-rutting of coarse aggregate porous asphalt mixtures AM-40 were studied.

2. THE DETERMINATION OF THEOPTIMUM ASPHALT CONTENT OF COARSE AGGREGATE POROUS ASPHALT MIXTURES AM-40

All the asphalt was heavy traffic asphalt AH-70, the penertration degree is 60–80 (0.01 mm), the softening point was 48.4°C and the ductility was 1401 mm (25°C). Coarse and fine aggregates chose limestone and mineral powder chose slaked lime, respectively. All raw materials met the requirements of Chinese road design and construction specifications. The coarse aggregate porous asphalt mixtures were AM-40.

According to Technical Specification for Construction and Acceptance of Highway Asphalt Pavement (JTG F40-2004) [9] and Standard Test Methods of Bitumen and Bituminous mixtures for Highway engineering (J052-2000) [10] as well as Marshall Test, the gradation and the optimum asphalt content of AM-40 was determined as 3.2% with 6% mineral powder with the highest stability (7.36 kN). Other parameters of Marshall Test were: maximum theoretical relative density of 2.563 g/cm^3, porosity of 15.642%, voids in mineral aggregate of 20.893%, and flow vale of 12.2 mm.

3. RUTTING TEST METHODS

Rutting tester (Figures 1 and 2) made in Changsha of China (LHC-2) was used in the test following Standard Test Methods of Bitumen and Bituminous mixtures for Highway engineering (J052-2000). The test specimen was made with the asphalt content of 3.2% and 6.0% mineral powder. The asphalt mixture and the test mold were put in the thermostatic chamber under the test temperature for at least 5 hours and not exceeding 24 hours. They were placed on the test bench of the rutting tester later. The center of the test specimen was pressed by the test wheel and the forward direction was kept same with the rolling one. Either a hour walking of the test wheels or the deformation of 25 mm reached, the test stopped and the deformation curves obtained automatically by the tester.

The deformation depth at 45 min (d_1) and 60 min (d_2) were recorded, which were accurate to 0.01 mm. If the 25 mm deformation depth reached within 60 min, the time at which the 25 mm reached was referred to t_2 and the time of 15 min before was referred to t_1 with the instaneous deformation of d_1.

$$DS = \frac{(t_2 - t_1) \times N}{d_2 - d_1} \times C_1 \times C_2 \tag{1}$$

where,

DS = the dynamic stability (time/mm)
d_1 = the instantaeous deformation at t_1 (mm)
d_2 = the instantaeous deformation at t_2 (mm), respectively
C_1 = the correction factor of the tester, with the value of 1.0 for variable walking mode of the crank connecting rod specimen and the value of 1.5 for constant mode of chain driven test wheel
C_2 = an influencing factor of the tester, with the 1.0 value for the 300 mm × 300 mm specimen prepared in lab and 0.8 for the 300 mm × 150 mm specimen cut from the road.
N = the rolling frequency with a generally value of 42 ± 1 (time/min)

Figure 1. *Rutting tester.*

Figure 2. *Operation system of rutting test.*

Table 1. Asphalt Content Effects on the Anti-rutting Performances of Coarse Aggregate Porous Asphalt Mixtures.

Asphalt Content/%	d_1/mm	d_2/mm	N/time/min	t_1/min	t_2/min	C_1	C_2	DS/time/mm
2.8	5.69	6.78	42	45	60	1.0	1.0	577.98
3.1	4.27	4.69	42	45	60	1.0	1.0	1500.00
3.4	4.15	5.36	42	45	60	1.0	1.0	520.66
3.7	8.33	9.40	42	45	60	1.0	1.0	588.79
4.0	12.53	13.45	42	45	60	1.0	1.0	677.42

4. ANTI-RUTTING TEST FOR THE COARSE AGGREGATE POROUS ASPHALT MIXTURES AM-40

4.1. The Effects of Asphalt Content on Rutting

The effects of asphalt content on the anti-rutting and stable performance at a high temperature of coarse aggregate porous asphalt mixtures AM-40 were studied by changing the content of asphalt in the asphalt mixture. The each specimen size was 300 mm (length) × 300 mm (width) × 50 mm (height). The test results were shown in Table 1 and Figures 3–5.

It was figured out in Table 1 and Figure 3 that the rutting depth of coarse aggregate porous asphalt mixtures AM-40 increased upon testing time and grow fast in the 0–5 min and then flatten. Moreover, it was shown in Figure 4 and Figure 5 that the relationship between the asphalt content and rutting depth of mixture performs a "U" style curve. When the asphalt content was 2.8%, the rutting depth was 6.78 mm, and then it changed to 4.69 mm when content increased to 3.1%, meanwhile, the rutting deformation decreased 30.83% and the dynamic stability *DS* arrived the maximum value of 1500/min. However, the rutting depths increased with the growth of asphalt content and arrived 13.45 mm when the content of asphalt was 4.0% with an increment of 187%.

4.2. The Effects of Porosity on the Anti-rutting Performances of Coarse Aggregate Porous Asphalt Mixtures

The effects of porosity on the anti-rutting performance of coarse aggregate porous asphalt mixtures AM-40 were studied by the rutting test of three group specimen with porosity of 10%, 15%, 20%, respectively. The each specimen size was 300 mm (length) × 300 mm (width) × 50 mm (height). The results of which were shown in Figures 6–8.

It was shown in Figure 6 that the rutting depth of coarse aggregate porous asphalt mixtures AM-40 grow rapidly in the first 5 minutes of loading test, and then the deformation curve became flatten and the rutting grow slowly for the asphalt mixture became more dense and less porosity. It also was figured out in Figures 6–8 that the rutting depth of coarse aggregate porous asphalt mixtures AM-40 grow with the increase of porosity. The rutting depth was 3.36 mm when the porosity was 10% and arrived 4.68 mm when the porosity increased to 20%, with a increment of 39.3% while

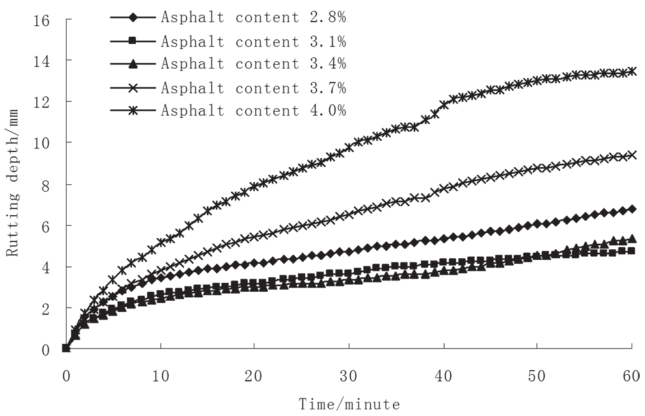

***Figure 3.** The rutting depth-time curves of asphalt mixtures with different asphalt contents.*

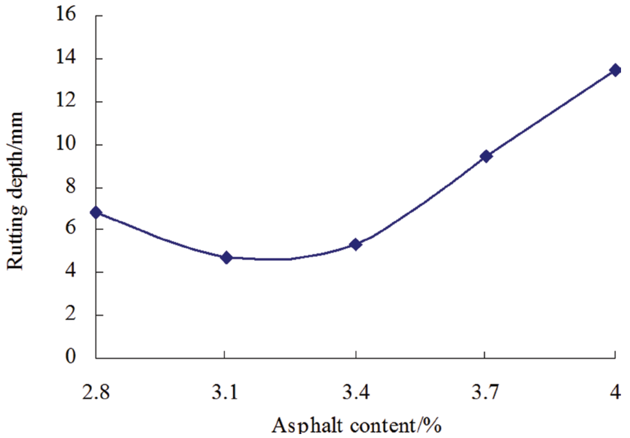

***Figure 4.** The curve of asphalt content effect on the anti-rutting performance of asphalt mixture.*

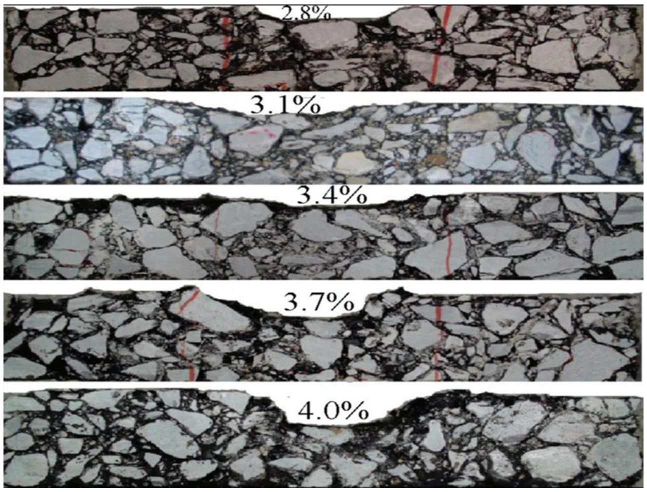

Figure 5. *The cross-section graph of rutting depth with different asphalt content.*

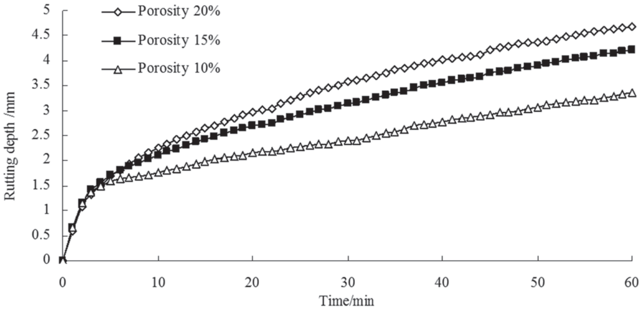

Figure 6. *The rutting depth-time curves of coarse aggregate porous asphalt mixtures with different porosity.*

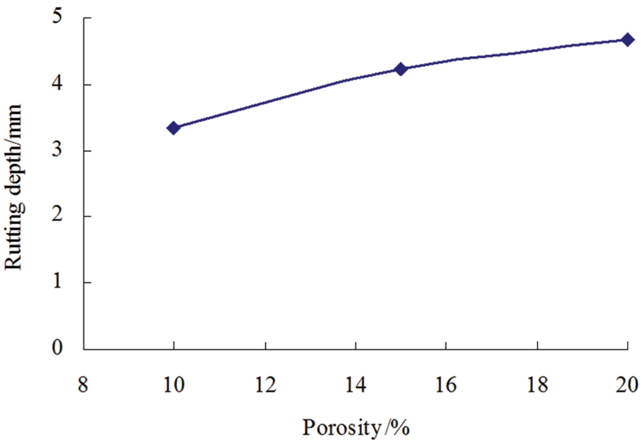

Figure 7. *The rutting depth-porosity curve.*

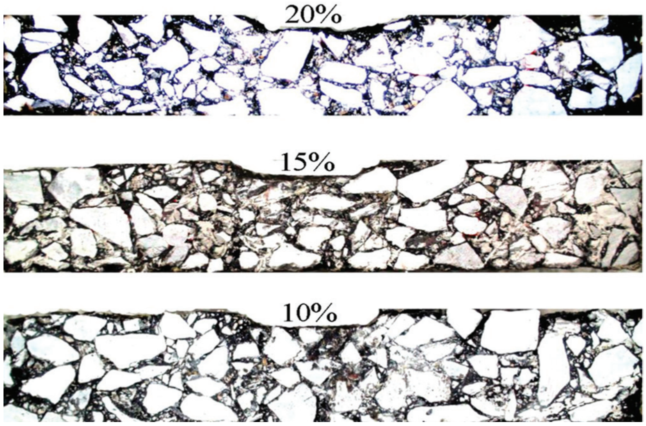

Figure 8. *The cross-section graph of specimen rutting with different porosity.*

the dynamic stability decreased from 1400 time/mm to 1382 time/mm.

4.3. Anti-rutting Performances of Different Asphalt Mixture

The test specimens were made with asphalt content of 3.25% and percent air void of 14.43%. The loading test applied temperature of 20°C, 40°C, 60°C to determine the effect of temperature on the rutting depth of coarse aggregate porous asphalt mixtures AM-40, the results of which were shown in Figures 9–11.

It was figured out that the rutting depths of specimen at temperature of 20°C, 40°C, 60°C in 60 min were 1.14 mm, 2.01 mm and 4.45 mm, respectively, which means the depth grow with the temperature. The rutting depth at 60°C increased 290.4% compared with the rutting depth at 20°C and increased 121.4% compared with that at 40°C. The dynamic stability *DS* of each temperature was 3000.00/min, 3937.50/min, 1125.00/min, respectively.

4.4. Test of Addition Effect on the Anti-rutting Performances

The anti-rutting performance of pure asphalt mixture AM-40, semi-flexible asphalt mixture SFAM-40 and rubber asphalt mixture RAM-40 were tested and compared. The semi-flexible asphalt mixture used the cement mortar to fix the surface gap of coarse aggregate porous asphalt mixtures, and the formula of cement mortar was cement: water: fine sand: mineral powder: coal ash = 1:0.75:0.25:0.2:0.06. The rubber asphalt mixture mixed 20% rubber powder to replace the mineral powder in the general AM-40.

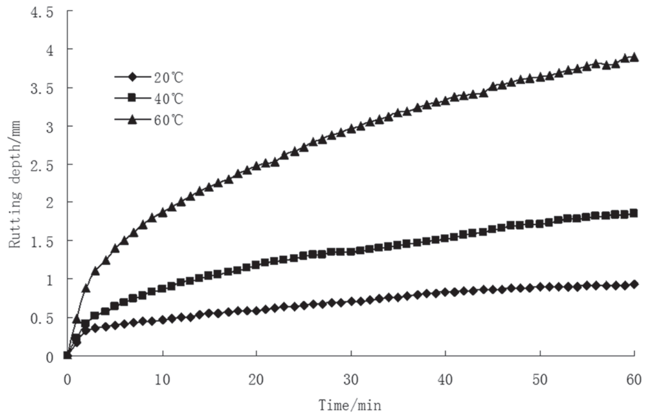

Figure 9. *The rutting depth-time curve of coarse aggregate porous asphalt mixtures AM-40 at different temperature.*

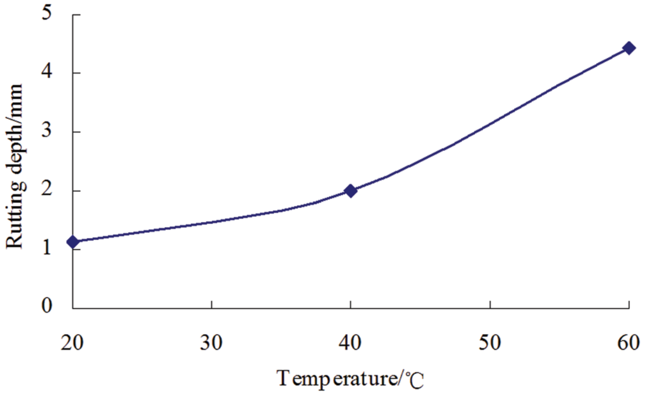

Figure 10. *The rutting depth-temperature curve.*

Figure 11. *The cross-section graph of rutting at different temperature (AM-40).*

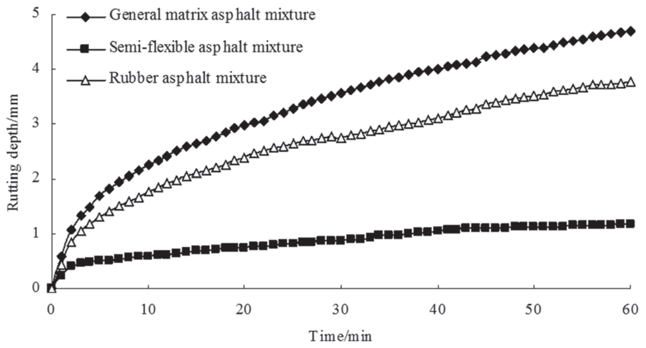

Figure 12. *The rutting depth-time curves of three different kinds of asphalt mixture.*

It was figured out in Figure 12 and Figure 13 that the rutting depth of pure asphalt mixture, semi-flexible asphalt mixture and rubber asphalt mixture in 60min was 4.68 mm, 1.17 mm and 3.78 mm respectively, which revealed that the rutting of pure asphalt mixture was deepest, which was 5.5 times of semi-flexible asphalt mixture and 23.8% deeper than rubber asphalt mixture. As a result, the mixture performs the best anti-rutting performance of coarse aggregate porous asphalt mixtures was semi-flexible asphalt mixture, and then rubber asphalt mixture, while the general asphalt mixture was worst.

5. CONCLUSIONS

1. The relationship between the asphalt content and rutting depth of coarse aggregate porous asphalt mixtures performs like a "U" style curve, which shown the rutting depth reached the lowest value and the dynamic stability DS arrived the maximum

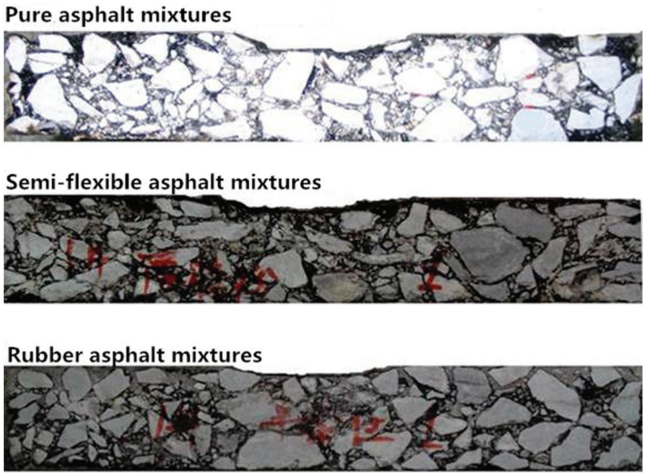

Figure 13. *The cross-section graph of rutting of three different kinds of asphalt mixture.*

value of 1500 time/min when the asphalt content was 3.1%.

2. The rutting depth of coarse aggregate porous asphalt mixtures increased with the porosity growth. The deformation curve of rutting became flatten when the asphalt mixture became more dense and less porosity.
3. The rutting depth of coarse aggregate porous asphalt mixtures increased with the temperature. The rutting depth at 60°C was 5.5 times of it at 20°C, which means the higher temperature, the more serious rutting came.
4. The anti-rutting performances of the pure asphalt mixtures were worst among the three compared asphalt mixtures.

6. ACKNOWLEDGMENTS

The material is based upon the work supported by the National Science Foundation of China (grant No. 51168005 and 51268003), the Foundation Project of Key Laboratory of Disaster Prevention and Engineering Safety of Guangxi (2012ZDX08).

7. REFERENCES

1. Zhang Dengliang: "Asphalt pavement", Beijing: People's Communication press, 1999. 76–90.
2. Sha Qingling: "Asphalt Pavement on Semi-rigid Base of High-grade Highway", Beijing: People's Communication press, 1999.168–173.
3. Shen Jinan: "Pavement Performance of Asphalt and Asphalt Mixture", Beijing: People's Communication press, 2001.231–250.
4. Wang Xudong: "Report of Overloading Asphalt Pavement Design Specification", Highway Research Institute, 2002.06.
5. Charles W. Schwartz and Regis L. Carvalho: "Distribution of Permanent Deformations within HMA Layers", Department of Civil and Environmental Engineering, University of Maryland, College Park, 2008. https://doi.org/10.1061/41005(329)8
6. Wang Hui: "Study of Asphalt Pavement Structure and Material in Overloading and high temperature Area", Central South University, 2008.
7. Xingwei Chen and Zhihong Xu: "Effects of Load and Temperature on Permanent Deformation Properties of HMA", Louisiana Transportation Research Center, 4101 Gourrier Ave., Baton Rouge, LA, USA, 2009. https://doi.org/10.1061/41043(350)7
8. Wang Hui, Li Xue lian, Zhang Qisen: "Rutting in asphalt pavement under heavy load and high temperature", China civil engineering journal, 42(5), 2009.
9. Technical Specification for Construction of Highway Asphalt Pavements (JTG F40-2004)(S), Beijing: People's Communication press, 2004.
10. Standard Test Methods of Bitumen and Bituminous Mixtures for Highway Engineering (JTJ 052-2000) [S]. Beijing: People's Communication press, 2000.

A Cobalt (II) Complex $[Co(VIM)_4](NCS)_2$ Based on 1-vinylimidazole (VIM) and SCN^-

Y. M. TANG[1,*], S.Y. GAO, L. HAN and Y. ZHANG
School of Pharmacy, Xi an Medical University, Xi'an 710021, PR China

ABSTRACT: A cobalt complex of $[Co(VIM)_4](NCS)_2$ (VIM = 1-vinylimidazole) was synthesized by 1-vinylimidazolium with $CoCl_2$ and KSCN in acetone. The structure was determined by X-ray crystallography, infrared spectrum, and elemental analysis. The coordination environment of the Co atom was basically octahedron, comprising four nitrogen atoms from 1-vinylimidazole ring and two nitrogen atoms from NCS^- anion. The 3D supramolecular structure is constructed with the hydrogen bond intermolecular interactions. The melting temperature of complex $[Co(VIM)_4]$ $(NCS)_2$ is 153.6°C, the solidification temperature is 119.9°C. The title complex is easily soluble in acetone, slightly soluble in methanol, alcohol, chloroform and ethyl acetate, insoluble in petroleum ether, water, and benzene.

1. INTRODUCTION

METAL-ORGANIC COMPLEXES (MOCS) contain metal ions and organic molecules. Metal ions may be of different geometries, thereby providing more variations for the molecular geometry, and in general, extending the properties of traditional metal inorganic-complexes. Thus, MOCs are widely used in electronics [1], optics [2–4], magnetism [5], selective catalysis [6–8], and molecular recognition [9]. Moreover, as core units, heterocycles play an important role in the molecular shape of MOCs. The introduced heteroatoms (S, O and N) [10–12] cause a considerable change of corresponding physical properties of MOCs. Therefore, MOCs with benzimidazole and imidazole ligands (N atoms ligand on heterocycles) including silver with 1-alkylimidazoles ligand [13], gold with benzimidazole and imidazole ligands [14], and silver and gold derived from 3-(4-dodecyloxybenzyl)-1-methyl-1H-imidazolium ligand [15], have been reported by several recent studies. As well known, although MOCs of cobalt with imidazole or SCN^- ligand have recently been reported [16–18], few reports, especially that providing examples of crystal data, focus on MOCs such as cobalt with 1-vinylimidazole (VIM) and SCN^- ligand. In this paper, the synthesis of a novel cobalt MOCs of $[Co(VIM)_4](NCS)_2$ and its crystal structure data are reported. In addition, the title complex used as the raw material for the preparation of molecularly imprinted microspheres can be foreseen in the future.

2. EXPERIMENTAL

2.1. Materials

KSCN was recrystallized from ethanol. Red $CoCl_2 \cdot 6H_2O$ crystal was dried in a muffle furnace until the crystal water was removed. Other chemicals were of analytical grade.

2.2. Measures

The crystal structure at 296(2) K was determined by using a Brucker Smart Apex II CCD diffractometer. Thermogravimetric (TG) analysis was performed in nitrogen atmosphere (Flow rate: 100 $mL \cdot min^{-1}$) on Q1000DSC + LNCS + FACEQ600 SDT (FA, USA). The differential scanning calorimetry (DSC) analysis was carried out in nitrogen atmosphere (Flow rate: 50 $mL \cdot min^{-1}$) on Q1000 DSC. Infrared spectrum of the complex was recorded on a fourier transform infrared spectrometer (FTIR WQF-310, SHIMADZU) at a wave number range of 400 cm^{-1} to 4000 cm^{-1}. The contents of C, H and N for the complex were determined on PE2400CHN C/H/N Analyzer (PE, USA).

---

*Authors to whom correspondence should be addressed.
E-mail: tangymhkf@163.com, Telephone: 13488136413.

1544-8053/16/02 S199-05

doi:10.12783/issn.1544-8053/13/4/S26

2.3. Synthesis and crystallization of [Co(VIM)$_4$](NCS)$_2$

A mixture of acetone solution of VIM (4.156 g, 44.16 mmol) and $CoCl_2$ (1.435 g, 11.04 mmol) with KSCN (2.146 g, 22.08 mmol) was stirred vigorously in a one-port flask. After reaction at 313.15 K for 12 h, the deep blue liquid was collected with filtration (KCl). The red crystalline powder was further collected by reduced pressure distillation and dried in vacuum at 333.15 K for 48 h, and then naturally cooled to room temperature, with a yield of > 95%.

A single crystal was obtained from ethyl acetate solution at T = 293.15 K for 5 d. The large crystal had a regular trapezoidal body.

2.4. Single-crystal Structure Determination

Suitable single crystals with compounds of [Co(VIM)$_4$](NCS)$_2$ were carefully selected with an optical microscope and glued to thin glass fibers. Empirical absorption corrections were applied using the SADABS program [19]. Crystal data and structural refinement parameters for [Co(VIM)$_4$](NCS)$_2$ are listed in Table 1.

3. RESULTS AND DISCUSSION

3.1. Infrared Spectrum and Elemental Analysis of [Co(VIM)$_4$](NCS)$_2$

The bands at *ca*. 2065 cm^{-1} are assigned to the υ(CN) on the NCS$^-$. The band at ca. 831 cm^{-1} is attributed to the υ(CS). A very sharp peak at *ca*. 480 cm^{-1} is δ(NSC) [21–22]. Calcd (%) for [Co(VIM)$_4$](NCS)$_2$: C, 47.90; H, 4.39; N,25.40; Found: C, 48.24; H, 4.40; N, 25.37.

3.2. Crystal Structure Analysis of [Co(VIM)$_4$](NCS)$_2$

As shown in Figure 1(a), Co1 center is coordinated to two nitrogen atoms (N9, N9A) from two different NSC$^-$ anions, and to four nitrogen atoms (N1, N1A, N3, N3A) from four different VIM ligands, respectively. The coordination geometry of Co1 can be described as a distorted octahedral. The bond distances of Co(1)–N(1, 1A) [2.155(3) Å], Co(1)–N(3, 3A) [2.162(3) Å], Co(1)–N(9, 9A) [2.114(3) Å] can be comparable with those reported for $\{[Co(NCS)_2(C_8H_{12}N_6)_2]\cdot 2H_2O\}n$ [2.151(2) Å][23] complexes. The bond angles of N(1)–Co(1)–N(3)[87.12(3)°], N(1)–Co(1)–N(9)[89.52(10)°] and N(3)–Co(1)–N(9) [89.46(11)°] can be close to the corresponding values in a similar complex [23]. Molecules of the complex are packed in an interdigitated bilayer fashion with the layer thickness of 10.3 Å. Every molecule is associated with neighboring molecules through six C-S…H-C (the H atom to carbon atom of imidazole ring) hydrogen bonds. Each bilayer is further linked to the neighboring bilayer through C-H…S hydrogen bonds, which form a lamellar structure by the bilayers [Figure 1(b)]. There is a weak C–H...S intermolecular hydrogen bond with the distance between donor and acceptor of 3.591~3.636 Å for C...S, which further confirms the whole backbone.

3.3. Thermal Analysis of [Co(VIM)$_4$](NCS)$_2$

The DSC curve [Figure 3(a)] for the complex [Co(VIM)$_4$](NCS)$_2$ proves an endothermic effect at 153.6°C, which is considered as the melting point of the sample. The solidification temperature is 119.9°C, which is obviously lower than the melting point. This temperature is attributed to the super cooling due to the existence of 1-vinylimidazole molecule. As shown in Figure 3(b), the weight loss is 67.4% from 23.6°C to 453.2°C. Theoretically, based on the molecular structure of [Co(VIM)$_4$](NCS)$_2$, the weight percentage of 1-vinylimidazole molecule that links to Co(II) is 68.3%, which is very close to that (67.5%) obtained by TG analysis. The result indicates that the title complex decomposes quickly at 453.2°C, with only Co(NCS)$_2$ debris remaining. In addition, the DTGA curve has a sharp peak at 192.7°C, which is attributed to the first decomposition process of [Co(VIM)$_4$](NCS)$_2$. After the first process of weight loss, the second decomposition process occurs at the temperature range of 256.4°C to 453.2°C.

3.4. Solubility of [Co(VIM)$_4$](NCS)$_2$

The complex [Co(VIM)$_4$](NCS)$_2$, with the special structure of four vinyl, has the potential to be the crosslinking agent, thus, the solubility (S) of [Co(VIM)$_4$](NCS)$_2$ is remarkable in general solvents. As seen in Table 2, it is easily soluble in acetone, slightly soluble in methanol, alcohol, chloroform and ethyl acetate, i.e., $S_{\mathrm{acetone}} > S_{\mathrm{chloroform}} > S_{\mathrm{ethyl\ acetate}} > S_{\mathrm{ethanol}} > S_{\mathrm{methanol}}$, while insoluble in petroleum ether, water, and benzene.

Owing to the existing three interactions between acetone and the title complex, the solubility for the title complex in acetone is higher than that in other solvents. Firstly, acetone is polar protophobic solvent, and

Table 1. *Crystal Data and Structural Refinement Parameters for [Co(VIM)$_4$](NCS)$_2$.*

Crystal Data	
Chemical formula	$C_{22}H_{24}CoN_{10}S_2$
M_r	551.56
Crystal system, space group	Triclinic, *P*-1
Temperature (K)	296(2)
a, *b*, *c* (Å)	9.704 (3), 10.284 (3), 14.747 (4)
α, β, γ (°)	109.388 (4), 90.063 (4), 100.138 (4)
V (Å^3)	1363.8 (6)
Z	2
Radiation type	Mo *Kα* (λ = 0.71073 Å)
μ (mm^{-1})	0.81
Crystal size (mm)	0.30 mm × 0.22 mm × 0.15 mm
Data Collection	
Diffractometer	Bruker *APEX-II* CCD diffractometer
Absorption correction	—
No. of measured, independent and observed [$I > 2\sigma(I)$] reflections	6878, 4776, 3786
R_{int}	0.0243
$(\sin \theta/\lambda)_{\max}$ (Å^{-1})	0.596
Refinement [20]	
$R[F^2 > 2\sigma(F^2)]$, $wR(F^2)$, *S*	0.048, 0.137, 1.03
No. of reflections	4776
No. of parameters	339
No. of restraints	2
Final *R* indices [$I > 2\sigma(I)$]	R_1 = 0.0434, wR_2 = 0.1102
R indices (all data)	R_1 = 0.0572, wR_2 = 0.1204
H-atom treatment	H atoms treated by a mixture of independent and constrained refinement
Symmetry transformations used to generate equivalent atoms	#1: $-x + 1, -y + 2, -z + 1$ #2: $-x + 2, -y + 2, -z + 2$
$\Delta\rho_{\max}$, $\Delta\rho_{\min}$ (*e* Å^{-3})	0.369, –0.351

Table 2. *Selected Bond Lengths Å) and Angles (°).*

Co(1)-N(9A)	2.1133(11)	Co(1)-N(9)	2.1133(11)
Co(1)-N(1A)	2.1534(10)	Co(1)-N(1)	2.1534(10)
Co(1)-N(3)	2.1609(10)	Co(1)-N(3A)	2.1609(11)
S(1)-C(21)	1.6252(12)	S(2)-C(22)	1.6147(13)
N(1)-C(1)	1.3098(15)	N(1)-C(2)	1.3732(17)
N(2)-C(1)	1.3520(16)	N(2)-C(3)	1.3634(19)
N(2)-C(4)	1.4240(17)	N(3)-C(6)	1.3005(16)
N(3)-C(7)	1.3649(19)	N(4)-C(8)	1.349(2)
N(4)-C(6)	1.358(2)	N(4)-C(9)	1.417(2)
N(9)-C(21)	1.1491(14)	N(9A)-Co(1)-N(9)	180.0
N(9A)-Co(1)-N(1A)	89.48(4)	N(9)-Co(1)-N(1A)	90.52(4)
N(9A)-Co(1)-N(1)	90.52(4)	N(9)-Co(1)-N(1)	89.48(4)
N(1A)-Co(1)-N(1)	180.0	N(9A) -Co(1)-N(3)	90.54(4)
N(9)-Co(1)-N(3)	89.46(4)	N(1A) -Co(1)-N(3)	92.80(3)
N(1)-Co(1)-N(3)	87.20(4)	N(9A)-Co(1)-N(3A)	89.46(4)
N(9)-Co(1)-N(3A)	90.54(4)	N(1A) -Co(1)-N(3A)	87.20(4)
N(1)-Co(1)-N(3A)	92.80(4)	N(3)-Co(1)-N(3A)	180.000(1)
C(1)-N(1)-C(2)	105.22(10)	C(1)-N(1)-Co(1)	127.57(9)
C(2)-N(1)-Co(1)	127.21(8)	C(1)-N(2)-C(3)	106.35(11)
C(1)-N(2)-C(4)	128.26(12)	C(3)-N(2)-C(4)	125.36(12)
C(6)-N(3)-C(7)	104.69(11)	C(6)-N(3)-Co(1)	125.86(10)
C(7)-N(3)-Co(1)	129.00(7)	C(8)-N(4)-C(6)	106.83(11)
C(8)-N(4)-C(9)	117.06(16)	C(6)-N(4)-C(9)	136.07(17)
C(21)-N(9)-Co(1)	161.76(10)		

the interaction force between the carbonyl oxygen of acetone and VIM (C-H…O) is similar to that of hydrogen bond. The carbon atom on the imidazolium ring is between two nitrogen atoms, which makes the carbon atom have part of positive charge ($^{+\delta}$C—H), thus, the interaction between the carbon atom and the carbonyl oxygen (C=O$^{\delta-}$) becomes easier [24–25]. Secondly, due to the active hydrogen on the $^{-}CH_3$ of acetone and the presence of abundant acetone in the solution, the hydrogen bond interaction (S…H) between NCS^{-} and the active hydrogen on the imidazolium ring can exist. Thirdly, the carbonyl oxygen (C=O$^{\delta-}$) of acetone can generate the interaction with Co^{II}. The three reasons can cause the increase of the solubility of the title complex in acetone. In the three reasons, the first one has been verified [24–25]. By the comparison with the solubility of [RVIM][FeX_4] magnetic ionic liquids (under review) and [RVIM]X ionic liquids [25], the latter reasons can be indirectly confirmed.

As seen in Table 3, the solubility of the complex in chloroform is higher than that in ethyl acetate. The reason is that the size of the chloroform molecule is smaller, which makes the steric hindrance less obvious, leading to the formation of more hydrogen bond easier with VIM [25]. As for ethyl acetate, the hydrogen interaction (C–H…O) between the carbonyl oxygen (C=O$^{\delta-}$) and the active hydrogen on the VIM and the interaction between the carbonyl oxygen (C=O$^{\delta-}$) and Co^{II} can lead to a higher solubility.

Table 3. *Solubility(S) of Magnetic Complex [Co(VIM)$_4$](NCS)$_2$ in Common Solvents at 293.15 K.*

Solvents (100 g)	[Co(VIM)$_4$](NCS)$_2$-S (g)	Phenomenon
Water	0.0000	—
Methanol	0.1551	light pink solution
Ethanol	0.2224	sky blue
Acetone	7.6323	deep blue
Ethyl acetate	0.2826	blue
Chloroform	0.6075	light pink-light purple
Benzene	0.0012	—
Petroleum ether[a]	0.0000	—

[a] Theoretically, the value of solubility is not 0.000 g. The result shows the solubility of the title complex is very low and insoluble without phenomenon under the experiment.

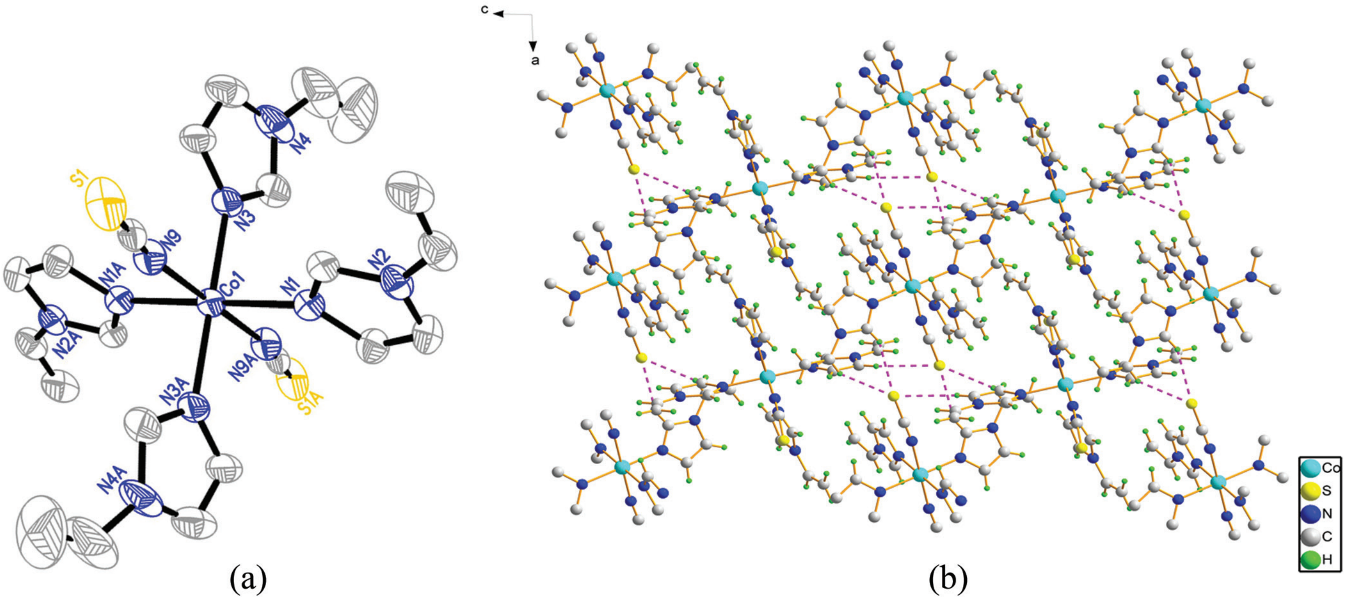

Figure 1. (a) ORTEP drawing of complex $[Co(VIM)_4](NCS)_2$, with partial atomic numberings. (b) Craystal packing view along the b-axis.

4. CONCLUSION

In this paper, complex $[Co(VIM)_4](NCS)_2$ was successfully synthesized and characterized. For complex $[Co(VIM)_4](NCS)_2$, we successfully grew a large single crystal, which was crystallized in the triclinic *P*-1 space group, and the crystal structure was determined by using single crystal X-ray diffraction. The 3D supramolecular structure was constructed through hydrogen bond intermolecular interactions. The special structure of the title complex ensured that the title complex could be used to prepare molecularly imprinted microspheres in the future. The thermodynamic parameters suggested that the melting temperature was higher than that of Co^{II} analogues.

5. SUPPLEMENTARY MATERIAL

Crystallographic data for the structural analysis have been deposited with the Cambridge Crystallographic Data Centre, CCDC reference number 948495. Copies of this information may be obtained free of charge from The Director, 12 Union Road, Cambridge, CB21EZ, UK (fax: +44-1223–336033; e-mail: deposit@ccdc.cam.ac.uk or http://www.ccdc.cam.ac.uk).

6. ACKNOWLEDGEMENTS

This work is supported by the Special Funds of the Natural Science Foundation from the Education Department of Shaanxi Provincial Government (Grant

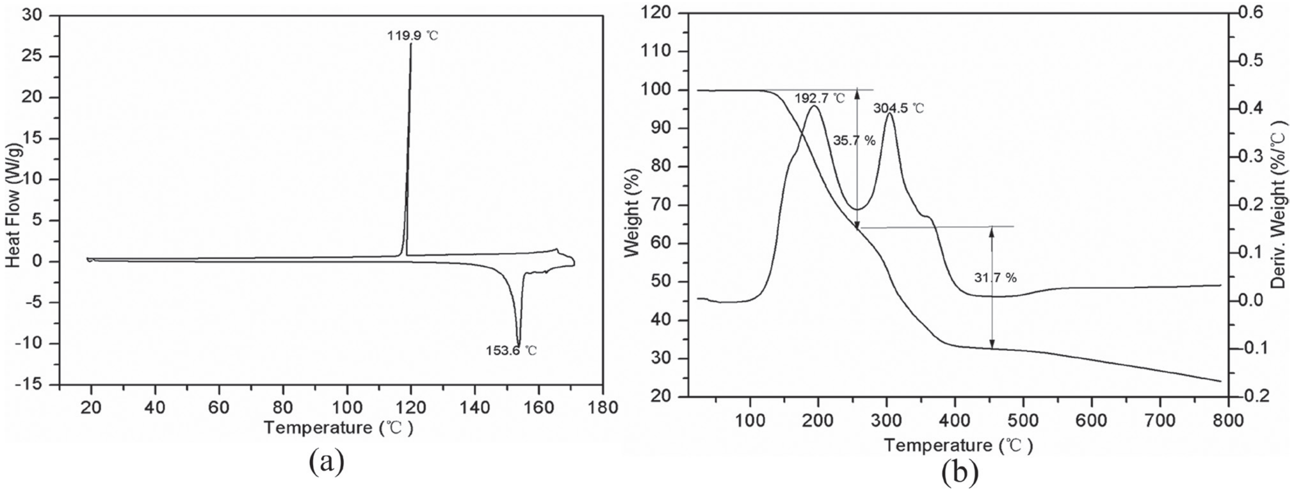

Figure 2. (a) DSC heating curve (2°C·min^{-1}) of complex $[Co(VIM)_4](NCS)_2$. (b) TG curve (10°C·min^{-1}) of complex $[Co(VIM)_4](NCS)_2$.

No. 16JK1653) and Xi'an Medical University (Grant No. 2015DOC14).

7. REFERENCES

1. Kikoin, K., Kiselev, M. N., Wegewijs M. R., "Vibration-induced Kondo tunneling through metal-organic complexes with even electron occupation number", *Phys. Rev. Lett.*, Vol. 96, No. 17, 2006, pp. 176801–176804. https://doi.org/10.1103/PhysRevLett.96.176801
2. Yuster, P., Weissman S. I., "Effects of perturbations on phosphorescence: luminescence of metal organic complexes", *J. Phys. Chem. A*, Vol. 17, No. 12, 1949, pp. 1182–1188. https://doi.org/10.1063/1.1747140
3. Paquette, M. M., Patrick, B. O., Frank, N. L., "Determining the magnitude and direction of photoinduced ligand field switching in photochromic metal–organic complexes: molybdenum–tetracarbonyl spirooxazine complexes", *J. Am. Chem. Soc.*, Vol. 133, No. 26, 2011, pp. 10081–10093. https://doi.org/10.1021/ja109776z
4. Che, G. B., Liu, C. B., Liu, B., Wang, Q. W., Xu, Z. L., "A one-dimensional chain structure based on unusual tetranuclear manganese(II) clusters", *Acta Cryst. C*, Vol. 64, No. 11, 2008, pp. 184–191. https://doi.org/10.1107/S0108270108031272
5. Bellitto, C., Righini, G., Gomez-Garcia, C. J., Caminiti, R., Carbone, M., Matassa, R., Bauer, E. M., Matassa R., "Nickel(II) 3,4;9,10-perylenediimide bis- phosphonate pentahydrate: a metal–organic ferromagnetic dye", *Inorg. Chem.*, Vol. 51, No. 12, 2012, pp. 7332–7339. https://doi.org/10.1021/ic300706h
6. Lagutschenkov, A., Lorenz, U. J., Dopfer, O., "IR spectroscopy of isolated metal-organic complexs of biocatalytic interest evidence for number four for Zn^{2+} (imidazole)^{4}", *Int. J. Mass Spectrom.*, Vol. 308, No. 2–3, 2011, pp. 316–329. https://doi.org/10.1016/j.ijms.2011.08.019
7. Carrettin, S., Corma, A., Iglesias, M., Sanchez, F., "Stabilization of Au(III) on heterogeneous catalysts and their catalytic similarities with homogeneous Au(III) metal organic complexes", *Appl. Catal. A-gen.*, Vol. 291, No. S1-2, 2005, pp. 247–252.
8. Bauer E. B., "Chiral-at-metal complexs and their catalytic applications in organic synthesis", *Chem. Soc. Rev.*, Vol. 41, No. 8, 2012, pp. 3153–3167. https://doi.org/10.1039/c2cs15234g
9. Vandegoor, G., Freyhardt, C. C., Behrens P., "The cobalticinium cation $[Co(\eta 5\text{-}C_5H_5)_2]+$: A metal organic complex as a novel template for the synthesis of clathrasils", *Zeitschrift Fur Anorganische Und Allgemeine Chemie*, Vol. 621, No. 5, 1995, pp. 311–322. https://doi.org/10.1002/zaac.19956210218
10. Matharu A. S., Chambers-Asman D., "Structure-property investigation of 2- and 3-thienyl- acrylates bearing laterally fluorinated azobenzene moieties", *Liq. Cryst.*, Vol. 34, No. 11, 2007, pp. 1317–1336. https://doi.org/10.1080/02678290701697447
11. Gallardo, H., Zucco, C., Da Silva L., "Synthesis and characterization of a new series of liquid crystal compounds derived from isoxazoles", *Mol. Cryst. Liq. Cryst.*, Vol. 373, No. 1, 2002, pp. 181–190. https://doi.org/10.1080/10587250210533
12. Gallardo, H., Magnago, R., Bortoluzzi A. J., "Synthesis, characterization and mesomorphic properties of Ag(I) and Pd(II) complexes containing the pyridyl and tetrazoyl rings:crystal structure of [$C_{30}H_{46}N_{10}AgClO_4$]", *Liq. Cryst.*, Vol. 28, 2001, pp. 1343–1352. https://doi.org/10.1080/02678290110066813
13. Lee, C. K., Hsu, K. M., Tsai, C. H., Lai, C. K., Lin I. J. B., "Liquid crystals of silver complexes derived from simple1-alkylimidazoles", *Dalton T.*, Vol. 8, No. 8, 2004, pp. 1120–1126. https://doi.org/10.1039/b314367h
14. Hsu, S. J., Hsu, K. M., Leong, M. K., Lin, I. J. B., "Au(I)-benzimidazole/imidazole complexes: liquid crystals and nanomaterials", *Dalton T.*, Vol. 14, No. 14, 2008, pp. 1924–1931. https://doi.org/10.1039/b717787a
15. Dobbs, W., Suisse, J. M., Douce, L., Welter, R., "Electrodeposition of silver particles and gold nanoparticles from ionic liquid-crystal precursors", Angew. Chem. Int. Ed., Vol. 45, 2006, pp. 4179–4182. https://doi.org/10.1002/anie.200600929
16. Jian, F. F., Wang, K. F., "Liquid crystal of cobalt complex from 1-dodecyl-1H-benzo[d] imidazole", *Liq. Cryst.*, Vol. 35, No. 12, 2008, pp. 1415–1421. https://doi.org/10.1080/02678290802626949
17. Pang, S. J., Su, J., Lin, Q., "Bis(thiocyanato-κN)tetrakis(1-vinyl-1H-imidazole-κN3) nickel (II)", *Acta Cryst. E*, Vol. 363, No. 9, 2007, pp. m2369–m2369. https://doi.org/10.1107/S1600536807039888
18. Sheldrick G. M., SADABS., Program for Area Detector Adsorption Correction, University of Gottingen, Gottingen, Germany, 1996.
19. Sheldrick, G. M., SHELXL-97. Program for Solution of Crystal Structures, University of Gottingen, Gottingen, Germany, 1997.
20. Nakamoto, K., Infrared and Raman Spectra of Inorganic and Coordination Compounds (Third ed.), John Wiley: New York, 1978.
21. Bailey, R. A., Kozak, S. L., Michelse, T. W., Mills, W. N., "Infrared spectra of complexes of the thiocyanate and related ions", *Coordin. Chem. Rev.*, Vol. 6, No. 4, 1971, pp. 407–445. https://doi.org/10.1016/S0010-8545(00)80015-6
22. Tao, J. Q., Mao, D., Wang, J., "Magnetic investigations of a two-dimensional coordination polymer with a three-dimensional supra¬molecular framework: poly[[bis¬[2-1,4-bis¬(1,2,4-triazol- 1-yl) butane]¬bis¬(thio¬cyanato- N)cobalt(II)] dihydrate]", *Acta Cryst. C*, Vol. 69, No. 6, 2013, pp. m597–600. https://doi.org/10.1107/S0108270113011153
23. Zhai, C. P., Wang, J. J., Xuan, X. P., Wang, H. Q., "NMR Study on the Interactions of Ionic Liquids with Acetone", *Acta Phys.-Chim. Sin.*, Vol. 22, No. 4, 2006, pp. 456–459.
24. Tang, Y. M., Hu, X. L., Guan, P., Tian, T., Wang, S. J. I., "Ivestigation of surface properties and solubility of 1-vinyl-3-alkyl/esterimidazolium halide ionic liquids by density functional methods", *J. Chem. Eng. Data*, Vol. 59, No. 8, 2014, pp. 2464–2471. https://doi.org/10.1021/je500205z

Analysis of Slurry Diffusion Mechanism of the Splitting Grouted in Dam Reinforcement

KE WU[1], ZHEN SUN[2], SHUCHEN LI[1,*], HAOTIAN WU[3], WEN ZHANG[3], YAJUN WANG[3], YALIN YU[1]
and JINLONG LIU[4]
[1]School of Civil Engineering; Shandong University; Jinan; Shandong 250061, China
[2]Shandong Sanjian Engineering Detection CO., LTD., Jinan Shandong 250100, China
[3]Research Center of Geotechnical and Structural Engineering; Shandong University; Jinan; Shandong 250061, China
[4]Department of Civil Engineering, Hefei University, Hefei 230022, China

ABSTRACT: The reinforcement of disease dam in China is one urgent problem to be solved. Because the rivers and lakes in south of China are quite a lot, and many dams have been built in these rivers and lakes for power station and farmland irrigation in the 1960s or 1970s. Those dams are being "ill" because the building technology at that time is under-developed which causes those dams mostly to be being "ill". With the increase of dam operation time, the majority of disease dams have been becoming seriously and have to be reinforced to extend the operation time. As one techology of dam reinforcement methods for environmental protection and save material, the splitting grouted has been created firstly and used in many dam reinforcements in China. With this technology, a certain amount of grouting pressure is applied at the dam axis to control the split dam body at first; after that, an appropriate amount of seriflux is injected into the dam body to fill the holes and crannies in the dam body, and form an effective anti-seepage solid bodies, thus improving the stress state of dam body and achieving the consolidating the dam structure. In the reinforcement technology, the slurry has been filled inside dam body, the slurry diffusion mechanism is the important for studying the working principle of splitting grouted. So, based on the numerical simulation, the slurry diffusion law has been simulated to investigate the mechanism of slurry diffusion. At the same time, the deformation of dam during the splitting grouted has been comparative demonstration. Through those numerical calculation, it can be founded that the strength of dam is improved and cracks are filled which because the splitting slurry has been diffusing from grouting port to dam body, and the dam has been moving to both sides of dam body. Those would lead to fill the fractures in dam body and form the impervious wall along the grouted ports.

1. INTRODUCTION AND BACKGROUND

The reinforcement of disease dam in China is one urgent problem to be solved. Because the rivers and lakes in south of China are quite a lot, and many dams have been built in these rivers and lakes for power station and farmland irrigation in the 1960s or 1970s. Those dams are being "ill" because the building technology at that time is under-developed which causes those dams mostly to be being "ill". With the increase of dam operation time, the majority of disease dams have been becoming seriously and have to be reinforced to extend the operation time. As one technology of dam reinforcement methods for environmental protection and save material, the splitting grouted has been used in many dam anti-seepage and reinforcement, and also used in foundation treatment and tunnel strengthening, but the theory of technology has been less and in the discovery-stage. As one inexpensive and uncomplicated dam reinforcement technology, the splitting grouted technology was the first obtained and applied in engineering in China and less applied in foreign country. With this technology, a certain amount of grouting pressure is applied at the dam axis to control the split dam body at first; after that, an appropriate amount of seriflux is injected into the dam body to fill the holes and crannies in the dam body, and form an effective anti-seepage solid bodies, thus improving the stress state of dam body and achieving the consolidating the dam structure [1–3].

However, the mechanism of dam reinforcement by

---

*Author to whom correspondence should be addressed.
E-mail: wk4223@163.com; Tel.: t86 0531 88399712

1544-8053/16/02 S205-05

doi:10.12783/issn.1544-8053/13/4/S27

splitting grouted technology has many aspects. Firstly, the distribution of internal stresses of dam and theory of hydraulic fracturing provide the possibility for using the splitting grouted. Secondly, the slurry of splitting grouted also do the effects of split filling, interaction pressures between slurry and dam, dam collapse and consolidation, internal stresses adjustment of dam body, and so on [4]. In order to reveal the mechanism and effect of splitting grouted in dam reinforcement, many researchers and their theories are reported to investigate the deformation of dam and effect of splitting grouted in dam reinforcement based on numerical simulation and theoretical deduction. Based on the theoretical research, S. Feng [5] deduced the deformation of grouting zone and forecasted the effect of seepage control. As the same method, L. Fuchen [6] studied the defect of split-grouting on earth-rack dam stress, strain and stability. However, those researches were based on the numerical simulation or theory and less model test or site test. Based on the wetting deformation mechanism, the causes of wetting deformation of the dam after split grouting are analyzed here systematically and comprehensively and all sorts of phenomenon during split grouting are explained rationall [7]. W. Ke [8,9] was used model test to investigate the change regulation of seepage line before and after splitting grouted for dam reinforcement. However, the important factor for investigating the mechanism is the slurry diffusion in the dam body, which is less perfect. If the constructors could not understand the theory of slurry diffusion in the dam body, the effect of dam reinforcement by splitting grouted is not improved which not meets the demand of design.

So, in order to investigate the mechanism of slurry diffusion in dam body during splitting grouted, the numerical simulation is used to study the slurry diffusion tendency in dam body and the deformation of dam during splitting grouted.

2. NUMERICAL SIMULATION METHOD

Although the dam body during splitting grouted is splitted, the slurry is quickly filling the cracks and dam body to become one coherent body. For simple and clear researching, the dam body is assumed as one coherent body and the slurry is assumed as liquid. So, based on the Plaxis 2D finite element method, one finite element model of dam reinforcement by splitting grouted is found [10]. The slurry diffusion tendency in dam body during splitting grouted is simulated considering grouting times and port position, and the stress and strain of dam body are researching to find the regulation and range of slurry. Those research results will be used to obtain the mechanism of splitting grouted in dam reinforcement.

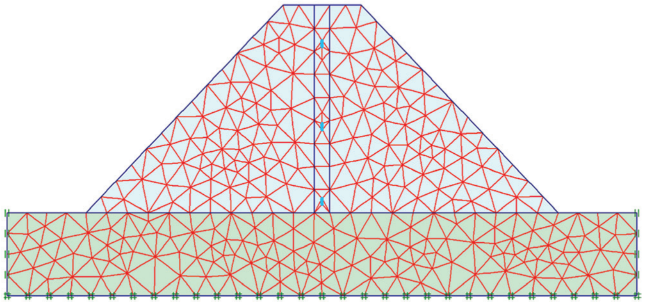

Figure 1. *Finite element model.*

2.1. Finite Element Model

One finite element model of earth dam is built by using finite element software. The finite element model is combining dam body with foundation. The length of dam foundation is 80.0 m and height is 10.0 m which is using the Hardening Soil model. As one advanced model for the simulation of soil behaviour, the Hardening Soil model describes the limiting states of stress not only by means of the friction angle, φ, the cohesion, c, and the dilatancy angle, ψ, but also describes much more accurately by using three different input stiffnesses: the triaxial loading stiffness, E_{50}, the triaxial unloading stiffness, E_{ur}, and the odometer loading stiffness, E_{oed}. As average values for various soil types, we have $E_{ur} \approx 3E_{50}$ and $E_{oed} \approx E_{50}$, but both very soft and very stiff soils tend to give other ratios of E_{oed}/E_{50}.

Then, the height of dam body is 25.0 m, the length of dam's top is 10.0 m and the length of dam's bottom is 60.0 m, which rate of slope for both edges is 1:1. The dam body is using the Hardening Soil model. And the grouted port lies the bottom of dam axis. All finite element models have 8932 nodes and 12498 elements. The finite element model is shown in Figure 1.

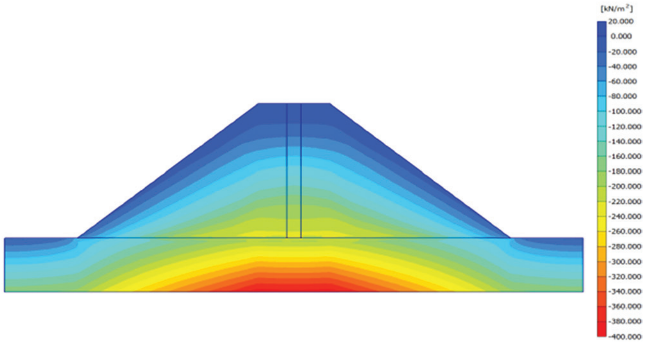

Figure 2. *Initial geostress equilibrium.*

Table 1. Parameters of Physico-mechanical Properties of Dam.

Project	***r*** **(kN/m^3)**	***c*** **(kPa)**	**ø (°)**	**ψ (°)**	**E_{50}^{ref} (kN/m^2)**	**E_{oed}^{ref} (kN/m^2)**	**E_{ur}^{ref} (kN/m^2)**	***m***
Grouting influence zone	22.00	40.00	25.00	0.0	1.8×10^4	1.8×10^4	5.4×10^4	0.25
Dam body	17.50	28.00	18.00	0.0	0.9×10^4	0.9×10^4	2.7×10^4	0.25
Dam foundation	24.00	43.00	32.00		5.0×10^6			

The parameters of physico-mechanical properties of dam is shown in Table 1.

2.2. Simulation Method

In the numerical simulation process, it can be assumed that the grouting port in the middle of the grouting core region is applied grouting pressure 0.5 MPa. In order to simulate the practical grouting pressure, the numerical simulation of grouting process is divided into 4 times irrigation. Once per cycle is including filling stage and reperfusion stage, and the stopping irrigation is removing the grouting pressure 0.5 MPa. Considering initial geostress equilibrium calculation in Figure 2, the dam foundation is set as the impervious boundary.

3. RESULTS AND DISCUSSSION

3.1. Seepage Vector

The Figure 3 gives the seepage vector in different grouting times. It can be observed that: (1) the grouting slurry will be diffusing from grouted port to any places in dam body and the speed of diffusion is slowing with the development of slurry diffusion. It is because that the slurry will fill the cracks of dam body and permeate into dam body along these cracks. But the speed of slurry permeation is affected by grouted pressure which is gradually reducing from grouted ports to dam body. (2) With the increasing of grouted times, the slurry diffusion point is moving from bottom to top of dam because slurry is grouted from the bottom of grouting pipe and spreading or filling the cracks in the dam. When the bottom of dam body is filled by lots of slurry, it's cracks are plugged and strength is improved effectively and slurry is not able to permeate into any place. So, the slurry diffusion is upward movement in order to improve the strength of dam body elsewhere. However, during the slurry spreading and filling the cracks in the dam, the dam body will be squeezed to produce the deformation which deformations are not unfavorable factor for dam body if these exceeded the value of design.

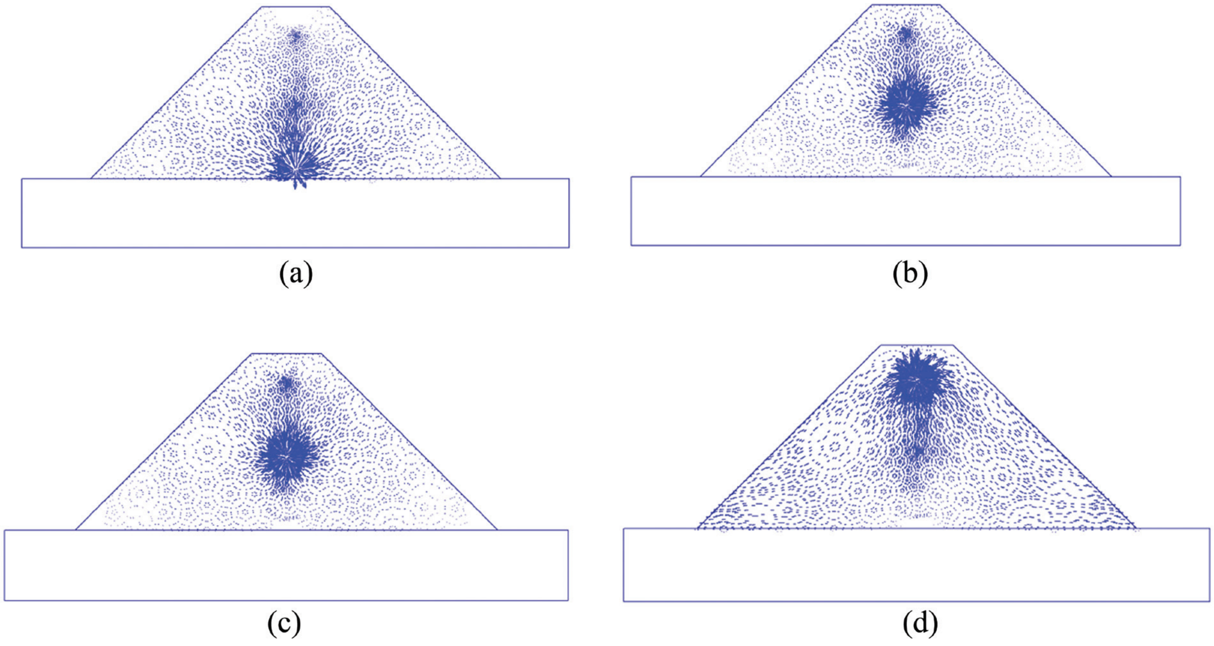
(a) (b) (c) (d)

Figure 3. *Seepage vector in different grouted times. (a) First grouted time, (b) Second grouted time, (c) Third grouted time and (d) Fourth grouted time.*

3.2. Strain and Stress

Firstly, the deforamtion of dam body during the splitting gourted is shown in figrure 4. It can be founded that: (1) with the development of slurry diffusion, the vertical deformation is produced from the top to bottom of dam body and the horizontal deforamtion is from the axis of dam to both sides. Because the grouted slurry is squeezing into the dam body and the bottom of dam is not permeable, the slurry is only moving into both sides of grouted port. The extrusion pressures will cause dam to deformate along the horizontal. And, the slurry will be consolidated with the slurry moving from bottom to top along the grouted port. (2) The deformation quantity is decreasing with the increase of grouted times. On the other hand, those results are proving that the slurry diffusion is spreading from bottom to top and both sides of dam, which is togethering with results of seepage vector in agreement.

Secondly, Figure 5 is giving the effective stress in the dam during the splitting grouted. It can be obtained that: (1) the effective stress in the grouted zone is improved significantly. (2) With the increase of the effective stresss in the grouted zone, one dam body zone along the axis of dam will be created which the strength is improved and the effect of seepage is control.

3.3. Protective Measures

The splitting grouted will lead the dam to produce the horizontal deformation, which causes the dam body to crack and grout. And, the dam body along the splitting grouted will crack because the grouted pressures will split the dam along the minimum principal stress which is along the axis of dam. Those phenomenons during the splitting grouted are not unfavorable factors for dam reinforcement, the constuctors need to monitor the deformation of dam and grout place. At the same time, the grouted time and grouted pressure are two key factors for splitting grouted, the constructors should strictly control during the splitting grouted.

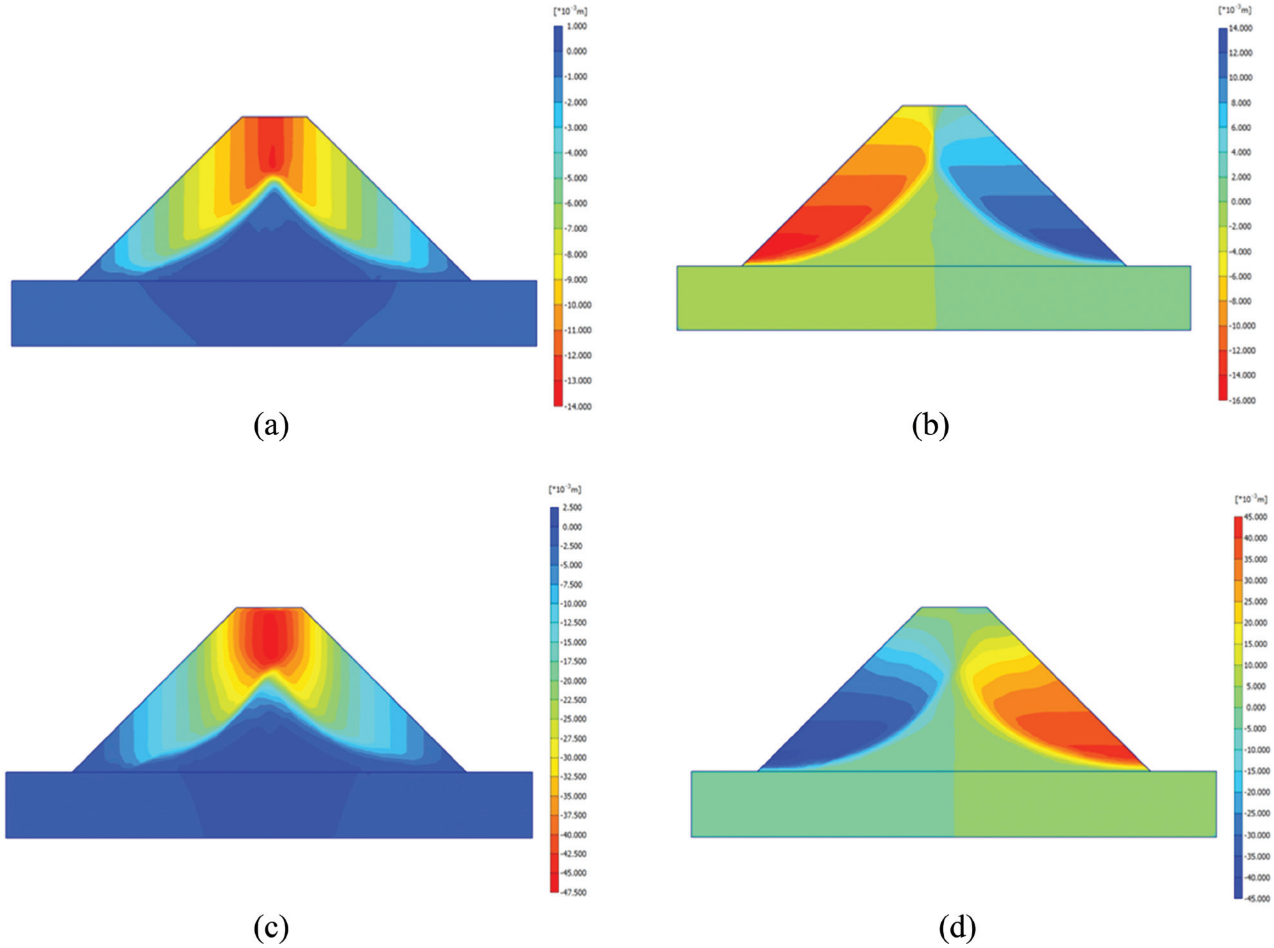

Figure 4. *Deforamtion of dam body during the splitting gourted. (a) Vertical deformation in the first grouting, (b) Horizontal deformation in the first grouting, (c) Vertical deformation in the third grouting, and (d) Horizontal deformation in the third grouting.*

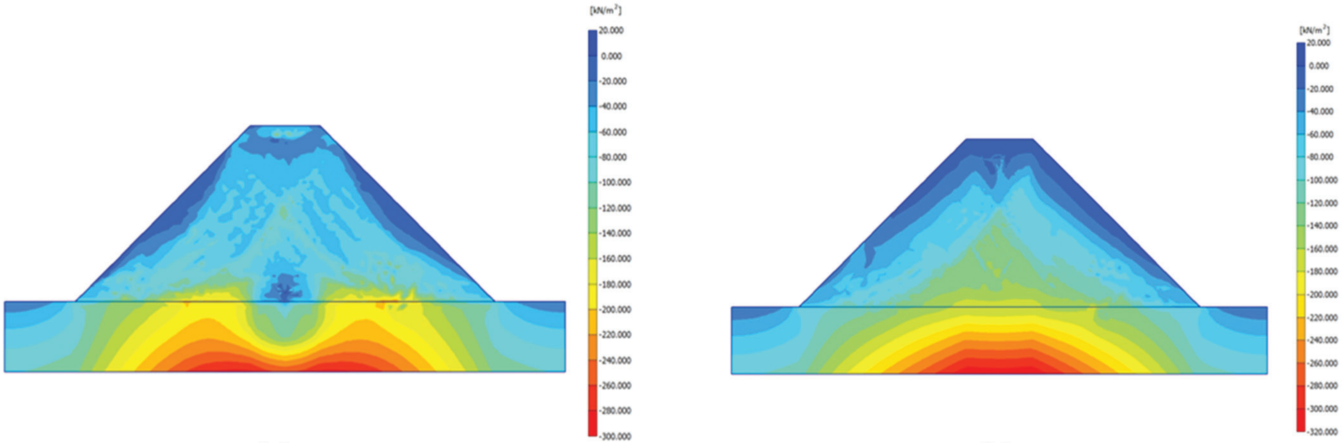

(a) (b)

Figure 5. *Effective stress of dam body during the splitting gourted. (a) First grouting and (b) Third grouting.*

4. CONCLUSIONS

In order to investigate the slurry diffusion mechanism of splitting grouted in dam reinforcement, the numerical simulation is using to calculate the change of strain and stress during the splitting grouted. The research results are shown as following,

1. The grouting slurry will be spreading from grouted port to any places alony the cracks in dam body and the speed of diffusion is slowing with the development of slurry diffusion.
2. With the development of slurry diffusion, the vertical deformation is produced from the top to bottom of dam body and the horizontal deformation is from the axis of dam to both sides.
3. The effective stress in the grouted zone is improved significantly.

Based on the comprehensive analysis, the splitting grouted in dam reinforcement is effective. And, the slurry diffusion is mostly filling the cracks in dam body which is availability for improving the strength of dam.

5. ACKNOWLEDGMENTS

This work was financially supported by Open Fund of Research Center of Dam safety and Disease Control in Ministry of Water Resources (2014008) and National Natural Science Fund (51308323).

6. REFERENCES

1. Bai Yongnian, Wu Shining, Wang Hongeng, etc. Reinforcement of Earth-rock Dam. Beijing: Water Conservancy and Hydropower Press, 1992.
2. Bai Yongnian. The Outline on the Splitting Grouting Technology. *Construction and Management Water Conservancy Project*, 2000, 5:52–53.
3. Sun Jianzheng. On the Design and Application of Splitting Grouting in the Anti-seepage of Earth Dam. *Guangdong Building Materials*, 2008, (7):12–13.
4. Wu Ke. Research and analysis of dam reinforcement test and numerical simulation by splitting grouted. ShanDong University Master Degree Thesis, 2004.
5. S. Feng, Zh. Dingli, Y. Haibo: "Study of effects of split grouting for reinforcing bottom of embankment". *Rock and Soil Mechanics*, 2010, 31(4):1187–1192.
6. L. Fuchen, Ch. Xingqi: "Effect of split-grouting on earth-rack dam stress, strain and stability", *Rock and Soil Mechanics*, 2009, 30(8):2452–2456.
7. Zhao Lizi, Shi Zitang: "Analysis on wetting deformation of split grouting", *Journal of Water Resources and Architectural Engineering*, 2011, 9(5):125–128.
8. W. Ke: "Change regulation of seepage line before and after splitting grouted for dam reinforcement based on model test", *Electronic Journal of Geotechnical Engineering*, 2015, 20(6):1425–1429.
9. Wu Ke, Ma Mingyue, Hao Dongxue, Chen Rong. Numerical Analysis on Mechanics of Interaction Between Slurry and Soil in Earth Dam by Splitting Grouted. 2012 International conference on modern hydaulic engineering, 2012, 351–355.
10. Itasca Consulting Group Inc. FLAC3D User Service Manual. USA: [s.n.], 1997.

Neural Net Expansion Model for Fissured Strong Expansive Soil

ZHANG-JUN DAI*, OJEKUNLE V. O. and SHAN-XIONG CHEN
State Key Laboratory of Geomechanics and Geotechnical Engineering, Institute of Rock and Soil Mechanics,
Chinese Academy of Sciences, Wuhan 430071, China

ABSTRACT: Fissured strong expansive soil swelling behavior is complicated. In this paper, considering the typical filling fissures of strong expansive soils, fissure rate K_r was given as a fissure content quantitative indicator. A prediction model was developed for the prediction of swelling effect on a fissured strong expansive soil using BP neural network approach, the gradient descent and the conjugate gradient algorithm methods were adopted. The actual test and predicted results of the two algorithms network showed high degree of similarity. The BP neural network model described by fissure rate, dry density, initial moisture content and overlying load can meet the precision requirements. The conjugate gradient method when compared with the gradient descent method, has a significantly improved calculation efficiency, the convergence rate is about 30 times lesser than the latter, therefore, conjugate gradient algorithm BP network prediction model for swelling in the actual engineering calculation has obvious advantages.

1. INTRODUCTION

DUE to the unique mineral composition and structural characteristics of expansive soil, it shows mutual soil-water relationship, with the penetration of moisture, soil moisture increase, and water molecules gradually enter between clay sheets within the structure, leading to the release of large amount of stress, prompting soil volume to expands, i.e. swelling of expansive soil.

Expansive soil swelling effect give rise to the main factors of expansive soil causing geologic disasters, it is affected by the influence of soil fissure, compactness, moisture content, and various environmental factors caused by changed hydrological conditions [1–3]. Based on the South-to-North Water Transfer Project geological survey work, on strong expansive soil macro-structure, the most characteristic feature is extremely developed fissure, and its large amounts of filling material, swelling effect is very significant [4–7]. There was not a good quantitative description method for fissure development. Fissured strong expansive soil has significant impact during channel design and construction. In order to research on expansive soil swelling and contraction effect, established expansive soil multiple factors swelling model for disaster prevention and engineering construction, which has significant importance.

Artificial neutral network tool have a strong non-linear massive parallel processing capabilities, it become an effective way to solve many complex non-determined problems [8]. Recently, this theory and technology has been applied in geotechnical engineering for rock deformation and damage [9–12], rock seepage characteristics [13], soil strength characteristics [14–15] and rock subtle concept structure [16–17].

In this paper, based on field research, the method to quantify filling fissure of strong expansive soil will be determine, fissure quantitative indicator will be established, by developing remodeling strong expansive soil expansion test, to obtain the expansion law for fissured expansive soil. The use of BP neural network is employed to carry out intelligent prediction of the non-linear relationship between strong expansive soil swelling rate and fissure rate, dry density, the initial moisture content and the overlying load through established fissured strong expansive soil BP network swelling model.

2. FISSURE CHARACTERISTICS AND QUANTITATIVE GENERALIZATION PATTERN

Fissures of strong expansive soil are basically filled (see Figure 1). Due to the occurrence of strong expan-

---

*Authors to whom correspondence should be addressed.
E-mail: daizj0078@163.com

1544-8053/16/02 S211-08

doi:10.12783/issn.1544-8053/13/4/S28

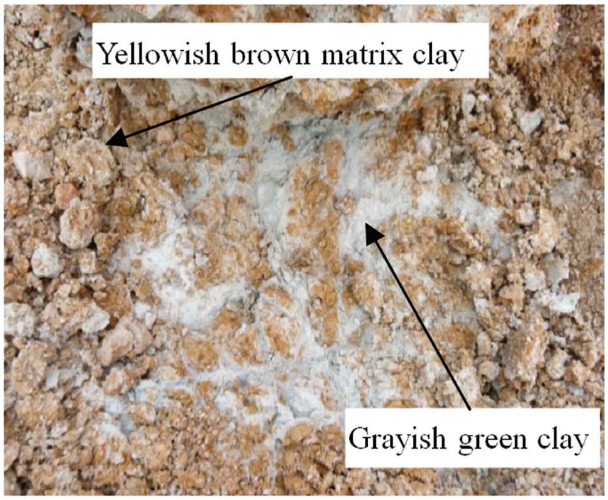

Figure 1. *Strong expansive soil filling fissure.*

sive soil at depth generally up to 15 m or more, in such a high overburden stress conditions, fissure often do not exist in the normal form of having gaps between matrix, instead of being filled with gray-grayish green cohesive soil, which has high content of clay particles and hydrophilic mineral. These filling materials form in the process of migration of groundwater in cracks, during which ion exchange effects or mineral deposition effects happen with clay minerals such as montmorillonite and illite in strong expansive soil. The filling clay soil is very fine, and the natural moisture content is generally high.

Filling material network form irregular morphology, vertical and horizontal alternating distribution in the soil, filling thickness is 2~5 mm, film-like or lenticular, partially, the thickness is 2 mm or less and more than 10 mm.

As a result of the frequent activities of the Nanyang expansive soil slope soil groundwater, most of the fissures are filled with grayish green clay soil, the rest fissure filling material are Calcium and Ferromanganese matter, etc. with very few non filled fissure.

Research shows that, weak expansive soil grayish green clay filling fissures accounted for fissure total amount of 64.3%~83.9%. In middle expansive soil region, grayish green clay filling fissure has vertical zonation characteristics, at depth within 6 m accounted for about 80%, and strong expansive soil depths are relatively high, grayish green filling fissure development is more significant, accounting for total amount of fissure for more than 90%.

As a result, considering the strong expansive soil typical filling fissures, proposed filling material content to determine the extent of fissure growth, according to statistical results made the assumption of strong expansive soil fissures are completely filled with grayish green clay. Fissure rate K_r, i.e. the ratio of fissure volume and soils volume, can be indirect described as the ratio of the content of grayish green clay and the content of yellowish brown matrix clay, in order to establish strong expansive soil fissure content quantitative indicators.

3. FISSURED EXPANSIVE SOIL EXPANSION TEST

Using quantitative indicator fissure rate, the fissure can be seen as one of the key factors included in the strong expansive soil swelling deformation model. Fissured expansive soil expansion test is carried out (see Figure 2), gray filling clay in fissure surfaces were scraped from Nanyang segment, canal section TS95, TS105, TS109, as a fissure matrix, soil matrix using Nanyang segment TS106, TS95 canal slope and canal bottom yellowish brown soil, both physical property are shown in Table 1.

Based on ratio of gray and brown clay content, configured gray clay content of 35%, 50%, 65% remolded expansive soil samples respectively for indoor test, simulated fissure were respectively 35%, 50%, 65%, different fissure rate expansive soil moisture absorption swell deformation research were conducted using no load and load swelling test, for three kinds of fissure rate of soil samples, respectively conducted three dry density value (1.45, 1.50, 1.55 g/cm^3), three initial water content amount (20%, 25%, 30%), three load (0, 25, 50 kPa) conditions swelling test, analysis of strong expansive soil hygroscopic expansion deformation law and influencing factors.

Table 1. Physical Properties Index of Fissured Expansive Soil.

Type	Moisture Content, %	Density, g/cm^3	Particles (mm) Composition, %			Liquid Limit, %	Plastic Limit, %	Free Expansion, %
			< 0.05	< 0.005	< 0.002			
Fissure matrix	29.54	1.92	92	41	15	93.51	32.76	112
Soil matrix	24.87	1.93	87	30	12	55.42	27.45	68

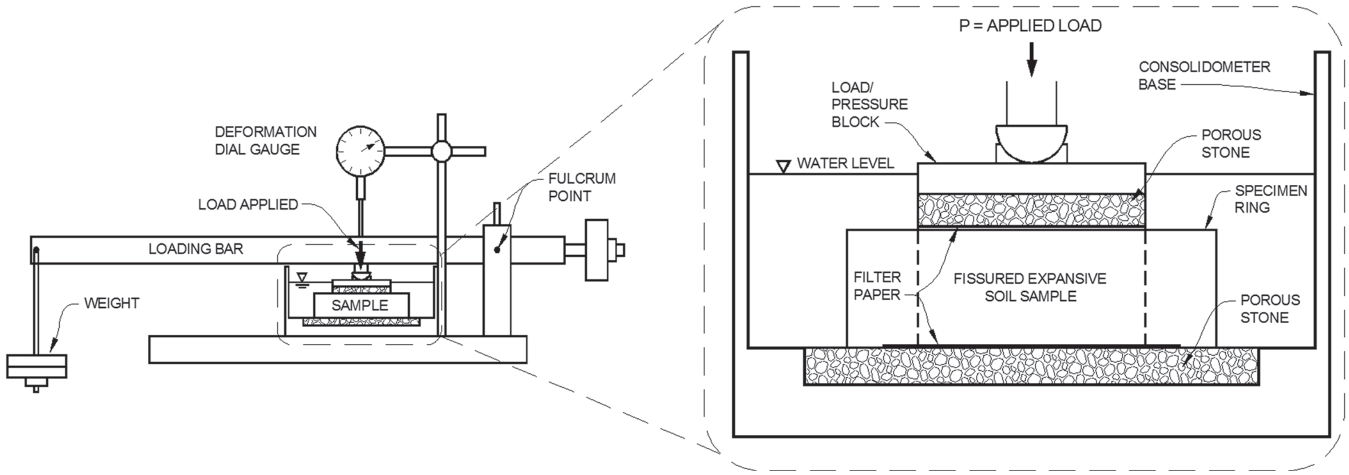

Figure 2. *Fissured expansive soil expansion test.*

4. BP NEURAL NETWORK ALGORITHMS

BP neural network is a kind of neural network model that can achieve nonlinear mapping multilayer feed-forward. Multilayered networks are capable of computing a wider range of Boolean functions than networks with a single layer of computing units. The basic three feed-forward BP neural network consists of an input layer, an output layer and a hidden layer, the topological structure is shown in Figure 3.

Through the learning samples, mapping from input layer *n*-dimensional Euclidean space to the output layer *m*-dimensional Euclidean space can be completed, which can be used for pattern recognition and interpolation, and it can approximate any nonlinear function in arbitrary precision. One hidden layer structure is generally used, for hidden layer quantity increase have no direct effect to improve precision of the network as well as enhance the network ability to express.

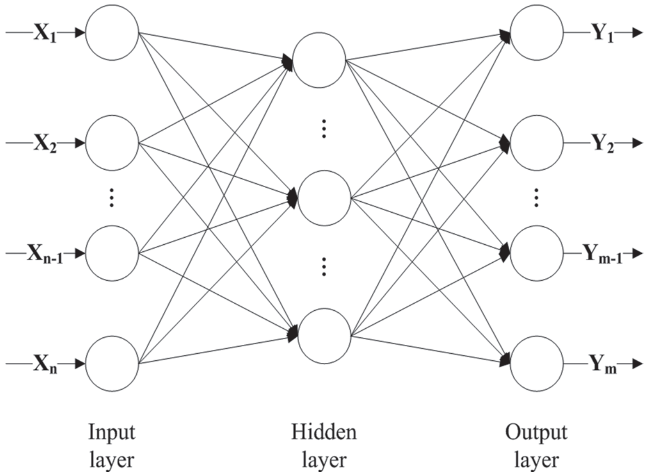

Figure 3. *BP neural network topology diagram.*

BP network study process is the process of error back propagation algorithm, through the forward calculation and the error back-propagation, gradually adjusting the connection weights, until the network error $E(k)$ reduce to the desired value, or reach the intended learning frequency.

Neurons function is normally the derivable *S* (sigmoid) type function [18]:

$$f(x) = \frac{1}{1+e^{-x}} \tag{1}$$

$$f'(x) = f(x)[1 - f(x)] \tag{2}$$

Error function *R* is:

$$R = \frac{\Sigma(Y_{mj} - Y_j)^2}{2} \quad (j = 1, 2, \ldots, n) \tag{3}$$

Where, Y_j is the desired output; Y_{mj} is the actual output; n is the sample length.

The most widely used standard BP algorithm is gradient descent algorithm, Let k be the iteration frequency, from any given point $\vec{z}(k)$, along the negative gradient direction $\vec{s}(k)$ in which the function declines the fastest to conduct 1-dimensional search:

$$\vec{s}(k) = -\nabla f[\vec{z}(k)] \tag{4}$$

Where, $\nabla f[\vec{z}(k)]$ is the gradient vector iterative point $\vec{z}(k)$. Then the next iteration point is

$$\vec{z}(k+1) = \vec{z}(k) + \vec{a}(k)\vec{s}(k) \tag{5}$$

Where, $\vec{a}(k)$ is the optimal step size. Terminal condition of the iteration is:

$$\left\|\Delta\vec{z}(k)\right\| < \varepsilon \tag{6}$$

Conjugate gradient algorithm, by improving the search direction, using a linear combination of the gradient of the previous iteration points and the gradient of the present iteration points, obtained a new search direction, Fletcher-Reeves algorithm (Traincgf) as follows:

$$\vec{z}(k+1) = \vec{z}(k) + \vec{a}(k)\vec{s}(k) \tag{7}$$

$$\vec{s}(k+1) = -\vec{g}(k) + \beta(k)\vec{s}(k) \tag{8}$$

$$\beta(k) = \frac{[\vec{g}(k+1)]^{\mathrm{T}}\vec{g}(k+1)}{[\vec{g}(k)]^{\mathrm{T}}\vec{g}(k)} \tag{9}$$

$$\vec{g}(k) = -\nabla f[\vec{z}(k)] \tag{10}$$

Where, $\vec{s}(k)$ is the search direction, which is a set of conjugate vectors; $\vec{a}(k)$ is rep increments.

5. STRONG EXPANSIVE SOIL BP NETWORK SWELLING PREDICTION MODEL

5.1. Network Model Structure

For fissured strong expansive soil neural network swelling prediction model, using basic three feed-forward BP network, i.e. network model consists of an input layer, an output layer and a hidden layer, which guarantees high prediction accuracy. According to the network accuracy requirements and strong expansive soil swelling rate change controlled factors, the input layer includes fissure rate, dry density, the initial moisture content and the overlying load, obtained a network model input layer consisting of 4-dimensional vector components:

$$X = [K_r, \rho_d, w_0, \sigma] \tag{11}$$

i.e. fissure rate K_r (%), dry density ρ_d (g/cm^3), the initial moisture content w_0 (%), the overlying load σ (kPa) respectively are for the four input neurons. Output layer is 1-dimensional vector:

$$Y = [\delta_{ep}] \tag{12}$$

Swelling rate of expansive soils δ_{ep} (%) is the output neuron, thereby established strong expansive soil swelling prediction network model. Figure 4 is the schematic model.

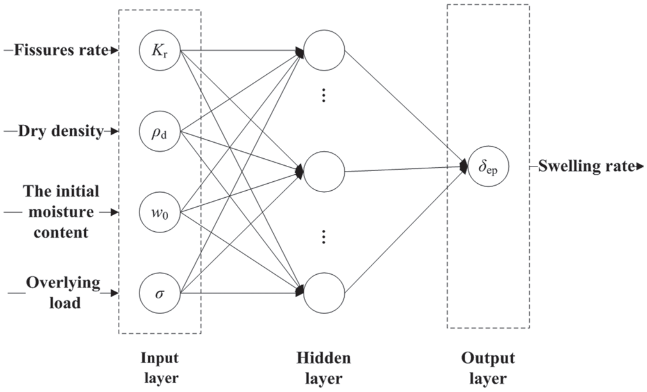

Figure 4. Strong expansive soil prediction BP network structure diagram.

5.2. Samples Data Analysis and Processing

The total number of train samples for BP neural network is 81, sample sources are laboratory test data, soil characteristics include three fissure rate (35%, 50%, 65%), three dry density (1.45, 1.50, 1.55 g/cm^3), three initial water content (20%, 25%, 30%), three load (0, 25, 50 kPa). Table 2 gives an example of train samples.

Singular sample data refer to the significant large or small sample data relative to other input sample. It can be seen from Table 2, expansive soil dry density is between 1.45~1.55 g/cm^3, its value is significantly small compared to the fissure rate, moisture content, and load expressed in percentage. Dry density, which is the singular sample data, may reduce the computational efficiency, and cause the results inability to converge during calculation. So, before the network computing, there is need to conduct normalization process for train data. An adequate normalization, not only for the network output variables but also for the input ones, previous to the training process is very important to obtain good results and to significantly reduce calculation time.

Data normalization is a process whereby target data will be limited within the specific range with the calculation requirement after the treatment through some algorithm, and transform variables to dimensionless scalars. On the one hand it can ensure the convenience

Table 1. Train Sample Illustration.

Input Layer				
K_r (%)	ρ_d (g/cm^3)	w_0 (%)	σ (kPa)	Output Layer δ_{ep} (%)
35	1.45	20	0	13.05
35	1.55	30	50	0.84
65	1.55	30	0	10.81

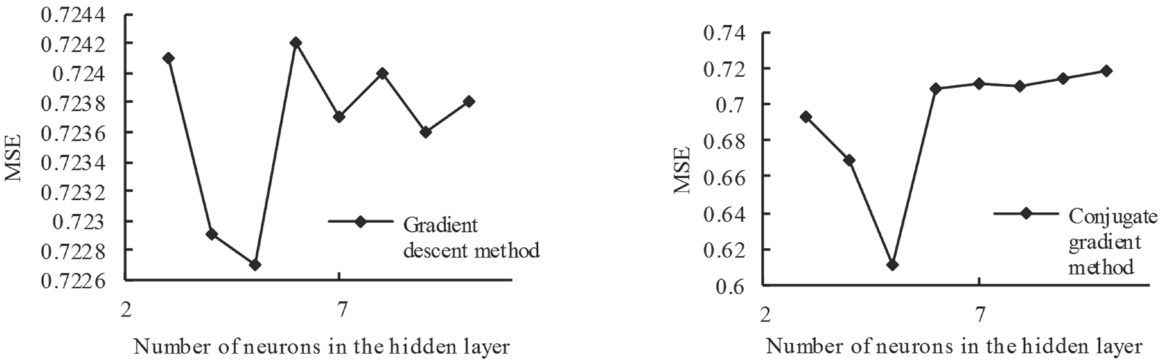

Figure 5. *MSE of predicted results for different hidden layer neurons.*

of subsequent data processing, the other is to speed up the convergence rate. Using premnmx function, network input data and output data were normalized, the normalized data is distributed within [–1,1], eliminating the singular sample data.

Assuming that data $d = \{d_i\}$ is normalized $d' = \{d'_i\}$, it can be calculated through the formula below:

$$d'_{\mathrm{i}} = (y_{\max} - y_{\min}) \frac{d_{\mathrm{i}} - d_{\min}}{d_{\max} - d_{\min}} + y_{\min} \tag{13}$$

Where, $y_{\max} = 1$, $y_{\min} = -1$, $d_{\max}$ and $d_{\min}$ are the maximum and minimum formula data in the samples, $y_{\min} \le d'_{\mathrm{i}} \le y_{\max}$.

5.3. Network Model Parameters

Model training functions are traingdm function and traincgf function respectively, for gradient descent algorithm and conjugate gradient algorithm, hidden layer activation function is tansig function, the output layer activation function is purelin function, the maximum number of iterations is epochs = 6000, the minimum expected error setting value is goal = 0.01, learning efficiency correction weights is lr = 0.05.

The number of hidden layer nodes complies with the accuracy and reasonableness of the entire network, generally uses spreadsheet optimization method to find the optimal solution.

Adopt MSE as an index, for predicting data and raw data corresponding point error squares and mean value:

$$\mathrm{MSE} = \mathrm{SSE}/n = \frac{1}{n}\sum_{i=1}^{n}(w_i \ \ y_i - \hat{y}_i)^2 \tag{14}$$

The closer the MSE to 0, the better the data prediction possibility and the fitting model.

Number of neurons in the hidden layer takes 3 to

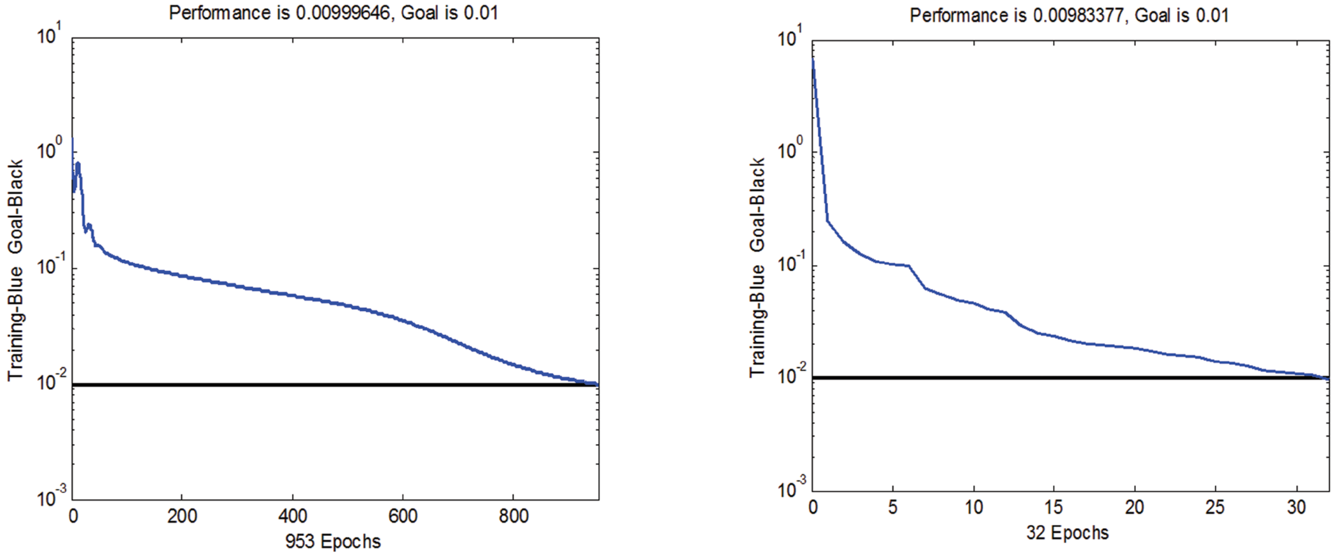

(a) (b)

Figure 6. *Operating results for different algorithm program. (a) Gradient descent algorithm, and (b) Conjugate gradient algorithm.*

Table 3. Gradient Descent Algorithm BP Neural Network Structure Parameters.

	Hidden Layer					Output Layer		
Number of Neurons in the Hidden Layer	**Weights w_1**				**Threshold b_1**	**Hidden Layer Node Number**	**Weights w_2**	**Threshold b_2**
5	–-0.4091	–0.0078	0.8350	1.9573	1.6289	1	–0.7429	–0.0264
	1.7492	–0.4154	0.7599	0.4727	–1.1377	2	0.0491	
	0.2801	1.0547	0.6010	–1.5505	0.0275	3	0.0610	
	1.1448	–1.0334	1.2182	–0.8692	0.7488	4	0.0072	
	–1.0582	–0.8798	0.5686	1.3874	–2.1083	5	–0.1891	

10 respectively, adopted gradient descent and conjugate gradient algorithm, MSE of predicted results are shown in Figure 5.

For the gradient descent algorithm and conjugate gradient algorithm, when hidden layer contains 5 neurons, MSE reached its minimum at 0.7227 and 0.6117 respectively, so the network hidden layer number of neurons is set to 5.

6. NETWORK MODEL PREDICTED RESULTS ANALYSIS

Strong expansive soil network model gradient descent algorithm and conjugate gradient algorithm program operation results are shown in Figure 6.

Comparison of the two algorithms operation results, shows after 953 iterations for gradient descent algorithm, the network error is 0.00999646, less than the expected error of 0.01, while the conjugate gradient algorithm is only requires 32 iterations to achieve the desired error, thus conjugate gradient algorithm convergence rate is far higher than the gradient descent algorithm, network model structural parameters of the two algorithms are shown in Table 3 and Table 4.

Figure 7 shows the comparison of fitted values and measured values of expansive soil swelling rate calculated from the trained data. As can be seen, expansion deformation fitted values and measured values of the gradient descent algorithm and conjugate gradient algorithm were consistent, error can be controlled within a narrow range, indicating that the network model has a high fitting precision.

After the network is fully trained, to verify the accuracy of the model, a set of measured data different from training samples is selected, the results calculated through the model are shown in Figure 8.

As can be seen, for fissured strong expansive soil deformation prediction, the measured results and the prediction results are similar for the two networks of the gradient descent algorithm and the conjugate gradient algorithm, and the network model can meet the accuracy requirements. Through fissure rate, dry density, the initial moisture content and the overlying load, BP neural network can be used intelligently to predict the expansion effect of strong expansive soil. By comparing different algorithms, found that the conjugate gradient algorithm relatively gradient descent, significantly improve computational efficiency, the convergence rate of about 30 times the latter, therefore, conjugate gradient algorithm of BP network predicted model for expansion in the actual engineering calculation has obvious advantages.

7. CONCLUSION

Considering the strong expansive soil typical filling fissures, proposed filling material content to determine the extent of fissure growth, fissure rate K_r is given as

Table 4. Conjugate Gradient Algorithm BP Neural Network Model Structure Parameters.

	Hidden Layer					Output Layer		
Number of Neurons in the Hidden Layer	**Weights w_1**				**Threshold b_1**	**Hidden Layer Node Number**	**Weights w_2**	**Threshold b_2**
5	–0.5157	–1.0865	1.3420	–1.0923	2.0438	1	–0.0476	0.4107
	1.5204	0.8745	–0.8515	0.0430	–0.7941	2	0.1455	
	0.1425	0.0548	–0.3567	–1.8996	–1.8809	3	0.9882	
	–0.3334	1.1245	0.6279	1.7224	–0.4459	4	–0.0539	
	0.7652	0.4226	0.6090	1.6750	2.2501	5	–0.0092	

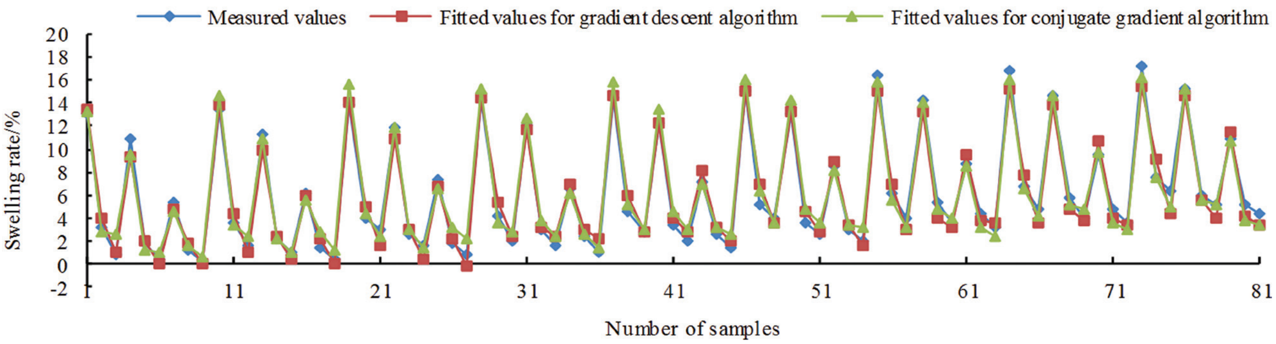

Figure 7. *BP model fitted and measured values comparison.*

a strong expansive soil fissure content quantitative indicator, which can be indirect described as the ratio of the content of grayish green clay and the content of yellowish brown matrix clay of strong expansive soil.

The back-propagation training algorithm is explained. Partial derivatives of the objective function with respect to the weight and threshold coefficients are derived.

These derivatives are valuable for an adaptation process of the considered neural network. Training and generalization of multi-layer feed-forward neural networks are discussed. Improvements of the standard back-propagation algorithm are reviewed.

For fissure expansive soil deformation prediction adopt gradient descent and the conjugate gradient algorithms, the actual test results and predicted results of the two algorithms network shows high degree of similarity. The network model described by fissure rate, dry density, initial moisture content and the overlying load, which using BP neural network intelligence for predicting strong expansive soil swelling effect, can meet the precision requirements. It is found that the conjugate gradient method when compared with the gradient descent method, has a significantly improved calculation efficiency, the convergence rate is about 30 times lesser than the latter, therefore, conjugate gradient algorithm BP network prediction model for swelling in the actual engineering calculation has obvious advantages.

8. ACKNOWLEDGEMENTS

The research was supported by Key Projects in the National Science & Technology Pillar Program during the Twelfth Five-year Plan Period (No. 2011BAB10B02).

9. REFERENCES

1. Meisina, C., 2004. Swelling-shrinking properties of weathered clayey soils associated with shallow landslides. *Quarterly Journal of Engineering Geology & Hydrogeology*. 37 (2), 77–94. https://doi.org/10.1144/1470-9236/03-044
2. Gadre A D, Chandrasekaran V S, 1994. Swelling of black cotton soil

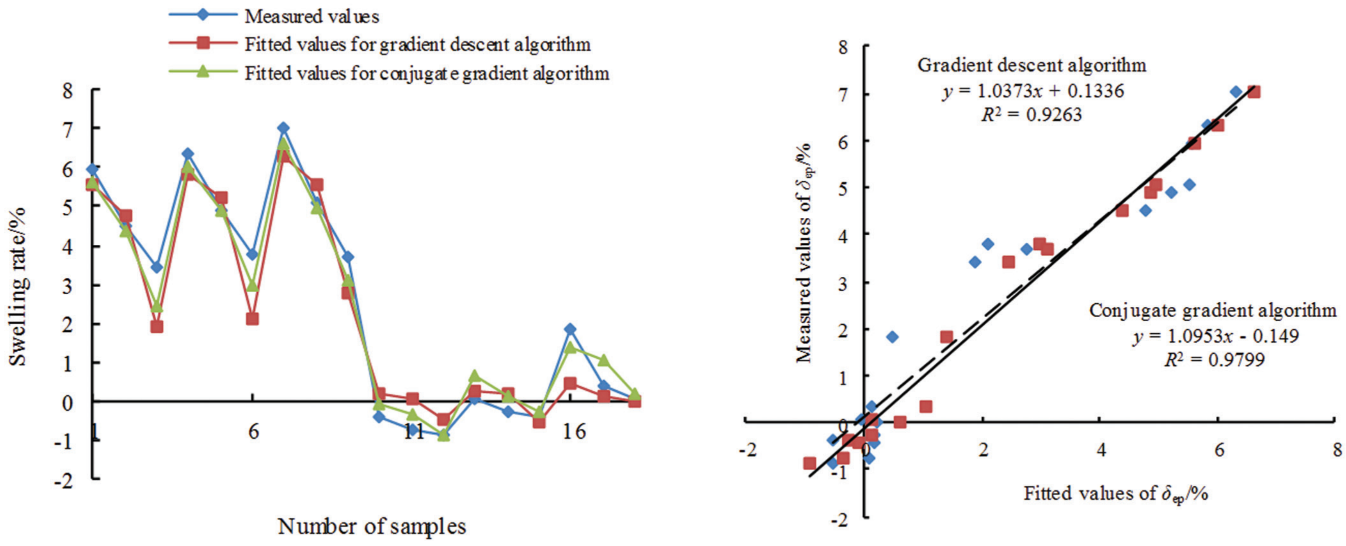

Figure 8. *Expansion model prediction results.*

using centrifuge modeling. *Journal of Geotechnical Engineering*. 120, 914–919. https://doi.org/10.1061/(ASCE)0733-9410(1994)120:5(914)

3. Basma Adnan A, Azm S A1-Homoud, Abdallah I Husein Malkawi, *et al.* 1996. Swelling-shrinkage behavior of natural expansive clays. *Applied Clay Science*. 11, 211–227. https://doi.org/10.1016/S0169-1317(96)00009-9
4. Chen, Sheng-shui, Zheng, Cheng-feng, Wang, Guo-li, 2007. Researches on long-term strength deformation characteristics and stability of expansive soil slopes. *Chinese Journal of Geotechnical Engineering*. 29 (6), 795–799.
5. Bao, Cheng-gang, 2004. Behavior of unsaturated soil and stability of expansive soil slope. *Chinese Journal of Geotechnical Engineering*. 26 (1), 1–15.
6. Huang, Run-qiu, Wu, Li-zhou, 2007. Stability analysis of unsaturated expansive soil slope. *Earth Science Frontiers*. 14 (6), 129–133.
7. Yin Zong-Ze, Xu Bin, 2011. Slope stability of expansive soil under fissure influence. *Chinese Journal of Geotechnical Engineering*. 33 (3), 454–459.
8. Wang Cheng-hua, Zhang Wei, 2002. Application of artificial neural networks to pile foundation engineering. *Rock and Soil Mechanics*. 23(2), 173–178.
9. Abbas Majdi, Morteza Beiki, 2010. Evolving neural network using a genetic algorithm for predicting the deformation modulus of rock masses. *International Journal of Rock Mechanics and Mining Sciences*, 47(2), 246–253. https://doi.org/10.1016/j.ijrmms.2009.09.011
10. Morteza Beiki, Ali Bashari, Abbas Majdi, 2010. Genetic programming approach for estimating the deformation modulus of rock mass using sensitivity analysis by neural network. *International Journal of Rock Mechanics and Mining Sciences*. 47(7), 1091–1103. https://doi.org/10.1016/j.ijrmms.2010.07.007
11. Hosein Rafiai, Ahmad Jafari, 2011. Artificial neural networks as a basis for new generation of rock failure criteria. *International Journal of Rock Mechanics and Mining Sciences*. 48(7), 1153–1159. https://doi.org/10.1016/j.ijrmms.2011.06.001
12. Zhang Meng-xi, Li Gang, Feng Jian-long, *et al.* 2008. Coupling analysis of surrounding rocks in double-arch tunnel by FE and BP neural networks. *Rock and Soil Mechanics*. 29(5), 1243–1248.
13. Jianping Sun, Zhiye Zhao, Yun Zhang, 2011. Determination of three dimensional hydraulic conductivities using a combined analytical/neural network model. *Tunnelling and Underground Space Technology*, 26(2), 310–319. https://doi.org/10.1016/j.tust.2010.11.002
14. G.R. Khanlari, M. Heidari, A.A. Momeni, *et al.* 2012. Prediction of shear strength parameters of soils using artificial neural networks and multivariate regression methods. *Engineering Geology*, 131, 11–18. https://doi.org/10.1016/j.enggeo.2011.12.006
15. Besalatpour, A., Hajabbasi, M. A., Ayoubi, S. *et al.* 2012. Soil shear strength prediction using intelligent systems: artificial neural networks and an adaptive neuro-fuzzy inference system. Soil Science and Plant Nutrition. 58(2), 149–160. https://doi.org/10.1080/00380768.2012.661078
16. P.H.S.W. Kulatilake, Wu Qiong, T. Hudaverdi, *et al.* 2010. Mean particle size prediction in rock blast fragmentation using neural networks. *Engineering Geology*, 114(3-4), 298–311. https://doi.org/10.1016/j.enggeo.2010.05.008
17. Zhou Yu, Wu Shun-chuan, Jiao Jian-jin, *et al.* 2011. Research on mesomechanical parameters of rock and soil mass based on BP neural network. *Rock and Soil Mechanics,* 32(12), 3821–3826.
18. Jiang Jian-ping, Zhang Yang-song, Yan Chang-hong, *et al.* 2010. Application of BP neural network in prediction of compression index of soil. *Journal of Central South University (Science and Technology)*. 41(2), 722–727.

Design Strategies for Developing Sustainable Consumer Electronics

ZHENWEI YOU[1,*], WENJUN HOU[1], XIAOCHUN WANG[1], JINSHENG MA[2] and JIAN LIU[3]
[1]*School of Digital Media and Design Arts, Beijing University of Posts and Telecommunications, Beijing, 100876, China*
[2]*Department of Industrial Design, Beijing University of Aeronautics and Astronautics, Beijing, 100191, China*
[3]*College of Architecture and Urban Planning, Beijing University of Technology, Beijing, 100124, China*

ABSTRACT: Consumer electronics produce a huge amount of waste and harmful residuals every year. This study investigated how to avoid or reduce environmental pollution through the design of consumer electronic products. Through a literature review, analyses, discussions, and case studies, we defined design strategies for developing sustainable consumer electronics. First, material selection should be considered from the perspectives of users, usages, and use environment in accordance with environmental protection requirements. The application of recyclable and remanufacture-able materials is the inexorable trend. Second, electronic products should be designed with simply disassembled structures that employ as many recyclable functional components as possible. Third, the information on the packaging or labels of consumer electronic products should be designed with graphics that are as easy to understand as possible and within an appropriate amount. Moreover, ingenious design solutions that can motivate users positively and actively to alter their environmental protection behaviors are expected.

INTRODUCTION

With technological innovations, our daily lives benefit from increasingly functional electronic products. Seizing the opportunities, manufacturers and retailers have shortened the circle of developing new products. New electronic devices are continually entering the market. According to statistics from the Consumer Electronics Association, each American household on average owns more than twenty electronic products [1]. As a result, waste from consumer electronics such as cell phones, computers, televisions, fridges, and washing machines has already become the fastest-growing waste stream all over the world [1–4]. In 2011, less than 40 percent of the electronic waste was recycled in the European Union. The rest was landfilled or incinerated as waste residuals [2].

To reverse the environmental problem, the European Union is aggressively controlling electronic waste and continuously increasing initiatives such as environmental policy and law toward electronic products [2]. More and more developing countries have realized the severity of the problem and are beginning to emulate the European Union [4]. Manufacturers and retailers are facing increasing legal, market, and financial pressures on manufacturing sustainable products. To help industry to achieve the aim, many concepts, approaches, and tools have been developed in management and manufacturing [3,5,6]. However, the waste of consumer electronics is usually a complex mixture of multiple materials and components. Some of them have hazardous content that can cause major environmental and health problems if not properly dealt with. Moreover, the manufacturing of consumer electronics requires scarce and expensive resources, which are precious to the earth [3]. Alleviating the environmental pollution from electronic waste, contributing to a circular economy, and enhancing resource efficiency are the core tasks. Most existing investigations focus on late collecting, treating, managing, and recycling and ignore the work before manufacturing electronic products.

The work before manufacturing is mainly design and development, which is collaboratively completed by designers and engineers. The designer is responsible for the initial work, and the engineer takes charge of the later implementation (see Figure 1). The investment cost gradually increases over time. Good material decisions and structural design in the initial phases

---

[*] Author to whom correspondence should be addressed.

1544-8053/16/02 S219-08

doi:10.12783/issn.1544-8053/13/4/S29

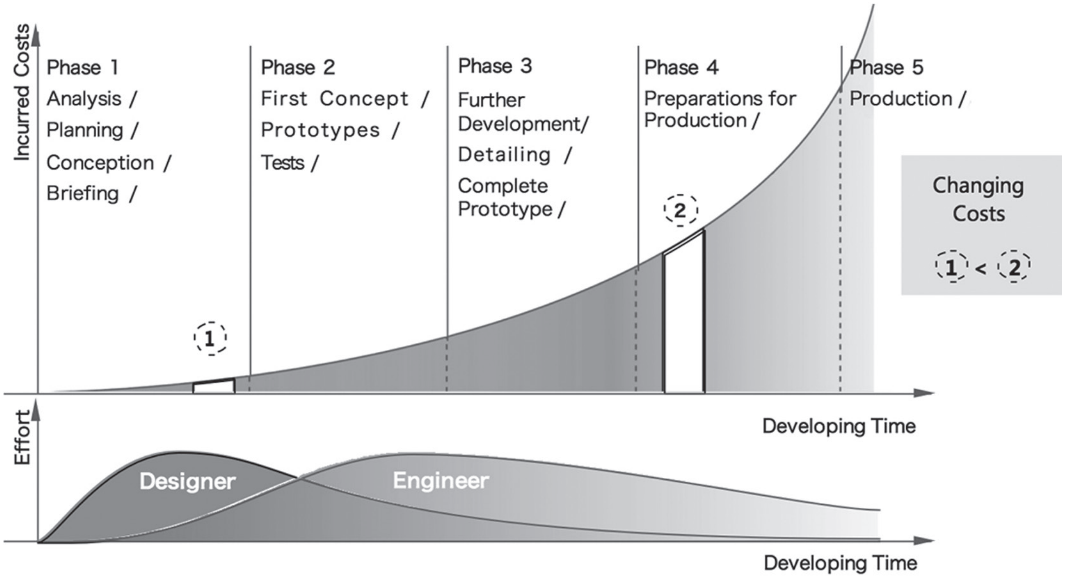

Figure 1. Product Design Process and Costs.

define the production costs. Changes in later phases cost money and time [7]. The waste of incinerated consumer electronics generates a large number of harmful or non-degradable residuals because the selected materials themselves are harmful or the components using multiple materials are assembled with chemical processing or complicated structures, that cannot be dismantled and can only be incinerated. An opportunity exists for designers to solve such environmental problems of electronic waste in the design phase.

In the design field, eco design and sustainable design have been well discussed regarding strategy, method, management, and evaluation [8–12]. However, until now, there was little in the way of guidance for designers indicating how to concretely implement the design of stainable consumer electronics. The goal of this paper is therefore to discuss and explore basic design strategies to enhance the materials' recycling possibilities and avoid or reduce hazardous residuals from the waste of consumer electronics.

FRAMEWORK OF DESIGN STRATEGIES

As shown in Figure 2, the lifecycle of a consumer electronic product starts with the conception design. After manufacture, the product will be distributed, purchased, and put into use. Then, after consumption, the product will end its life and be dismantled and disposed into raw materials or waste residuals [13].

Material selection and structure (assembly) design

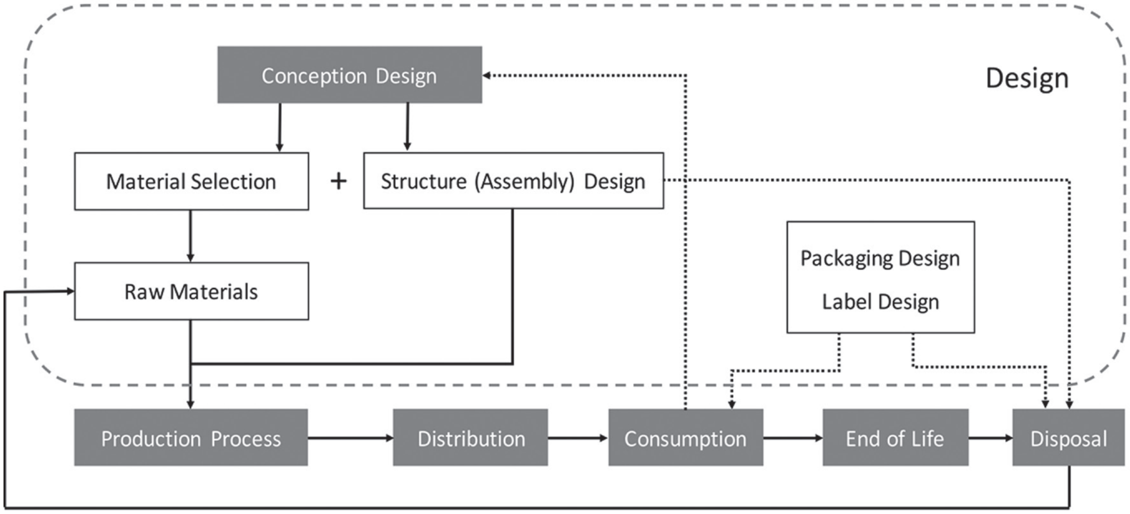

Figure 2. Design and Consumer Electronic Product Life Cycle.

are the essential links in the design phase because they are directly related to the waste of consumer electronics. Material selection determines what types of raw materials will be employed: harmful or harmless; recyclable or non-recyclable; and degradable and non-degradable. Structure (assembly) design defines how the components are assembled together: dismantle or non-dismantle and simple or complex. In the waste disposal phase, the structure of electronic products determines the costs and disposal means. Usually, to control costs, the components with complex structures are directly incinerated and produce harmful residuals.

Packaging design and label design are two potential elements that can influence the waste disposal of consumer electronics. The impacts of packaging and label design on purchase intention have been deeply investigated by marketing and design experts [14–17]. An individual must have either an emotional or a rational reason to buy a product (Stafford, 1993). From Stafford's point of view, rational appeals involve the basic facts of a product [18]. The informational appeals on packaging presume that consumers make decisions logically and rationally [19]. Eco-labels and the information that shows what materials are applied in the product packaging or body attract consumers' attention to environmental protection and affect their purchase behavior. If consumers refuse to purchase products with harmful or non-eco-friendly materials, the manufacturers have to adjust the material selections in the design phase. Gradually, it evolves into a virtuous cycle of supply and demand.

DESIGN IMPLEMENTATION STRATEGIES

Material Selection

The first principle of material selection in the design of consumer electronics is to employ non-toxic and non-polluting materials as much as possible. RoHS is a mandatory standard developed by the European Union legislation; its full name is "Restrictions on the Use of Certain Electrical and Electronic Equipment in the Instructions" (Restriction of Hazardous Substances). This standard was implemented mainly for the specification of electrical and electronic products, materials, and process standards, making it more conducive to human health and environmental protection [20]. The European Union legislation promotes the collection and recycling of such products [21]. The purpose is to eliminate lead, mercury, cadmium, and hexavalent chromium and flame retardants such as polybrominated biphenyls (PBB) or polybrominated diphenyl ethers (PBDE) in electrical and electronic products, requiring them to be substituted with safer alternatives [20]. These six hazardous materials are applied widely in consumer electronic products. Because of cost issues and industry tradition, many common components or processing technologies still employ these materials [20]. Lead is usually used as solder, as a glass additive, and a PVC stabilizer. Mercury is an important raw material for thermostats, sensors, switches, and lamps. Cadmium is commonly applied to produce switches, springs, housings, batteries, and so on. Hexavalent is mainly used as a metal anti-corrosion coating. Polybrominated biphenyls (PBB) and polybrominated diphenyl ethers (PBDE) have similar applications: in flame-retardant PCBs, connectors, and plastic housings. Through a literature review, possible substitutes for these materials have been identified to meet the same functional demands [21–30] (see Table 1). In relative design practice, designers can select substitutes according to their functions and costs.

Second, material selection should consider the use of the product, who the user is, and in which environment the product will be used. All consumer electronic products related to diet must employ food-grade mate-

Table 1. Hazardous Materials, Uses, and Substitutes.

Material	Use in Electronic Products	Possible Substitute
Lead	Solder, Glass, PVC Stabilizer	Sn-Ag-Cu, Copper, Conducting Resin, Hydrotalcite
Mercury	Thermostat, Sensor, Switch and Relay, Lamp	Alcohol, Superlattice in Semiconductor, Xenon
Cadmium	Switch, Spring, Connector, Housing and PCB, Contact, Battery	Steel, Sn-Zn Alloy
Hexavalent Chromium	Metal Anti-Corrosion Coating	Nanoplate Cobalt Alloy, Tungsten-nickel-boron (TNB)
Polybrominated Biphenyls (PBB)	Flame Retardant PCB, Connector, Plastic Housing	Aluminum hydroxide, PS,ABS
Polybrominated diphenyl ethers (PBDE)	Flame Retardant PCB, Connector, Plastic Housing	Aluminum hydroxide, PS, ABS

rials; examples include kettles, toasters, rice cookers, and so on. Consumer electronic products designed for children should use food-grade materials as well, as children often like to put toys or other items into their mouths. Low-density polyethylene (LDPE), polypropylene (PP), polystyrene (PS), polyvinylidene chloride (PVDC), and polycarbonate (PC) are the most commonly used food-grade plastics [30]. Actually, some material is non-toxic but changes under high temperature and produces harmful substances, such as polyvinyl chloride (PVC). Above 100°C or after long sun exposure, PVC will decompose and produce hydrogen chloride. Now, the use of PVC film bags is prohibited. Designers should anticipate the environment in which the product will be used and choose eco-friendly materials that are able to adapt to environmental change.

Third, many plastic materials themselves are non-toxic and possess stable properties; however, they cannot degrade. At the end of their lives, they have to be incinerated or landfilled. As substitutes for normal plastic, biodegradable materials have been a hot topic in recent years. Currently, two types are popular on the market: starch-based thermoplastic and aliphatic polyester plastic [31,32]. There is a line of cups and plates for sale in the market that are made of natural wheat straw (see Figure 3). Compared with plastic ones, they are easily recycled, remanufactured, and degraded without pollution. After this material is used, it could be indirectly converted into livestock feed or fertilizer.

Fourth, the material application of consumer electronic products should be simple, minimize the types of materials used, and avoid the use of a mixture of materials. In this way, the disposal difficulty of electronic waste will be dramatically reduced.

Figure 3. *Natural Wheat Straw-Made Cups or Plates [33].*

Table 2. Structure (Assembly) Design.

Bolt Connection	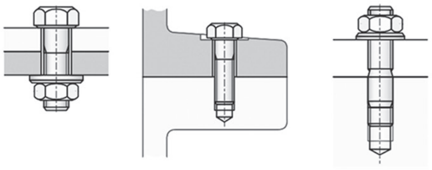	Easy to be dismantled
Snap Connection	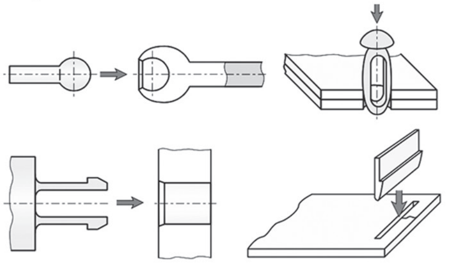	Fairly difficult to be dismantled
Glue Connection		Fairly difficult to be dismantled
Rivet Connection	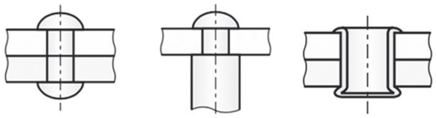	Extremely Difficult to be dismantled
Welding Connection	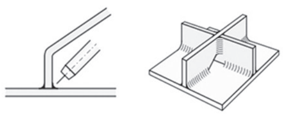	Unable to be dismantled

Consumer electronic products should be designed to be easily dismantled, reassembled, and reused to avoid the waste of resources and environmental pollution. The basic assembly modes of consumer electronic products are snap connections, rivet connections, bolt connections, welding connections, and glue connections [20]. As shown in Table 2, among these assembly modes, the bolt connection is easiest to dismantle; snap connections and glue connections can be dismantled, but it is fairly difficult; while rivet connections and welding connections mostly cannot be dismantled. Based on their similar structure and function, rivet connections could be substituted with bolt connections. If the two parts to be connected are of the same material and will be assembled into a non-closed body, welding and snap connections are good choices. In contrast, if the two parts are of different metals, welding connections should be avoided and substituted with snap connections using plastic to achieve the same structural requirements. To dismantle a glue connection, heating is the main means. Many adhesives release toxins under heating. Therefore, glue connections are not recommended. Considering the late waste disposal, bolt and snap connections should be mainly applied as assembly modes during design. Moreover, when designing bolt connections, the fewer screw types and amounts used, the higher the efficiency of dismantling is.

Welding connections are often applied to produce circuit boards, which are the most common and essential components of consumer electronic products (see Figure 4). Because of the technical limitations and costs, currently, no better substitutes for such components have been produced on a mass scale. Electronic components should be developed and designed with flexible assembly structures. After dismantling, these components can be reassembled as parts of new products. The more frequently the general components are reused, the lower the rate of waste production is.

Packaging Design and Label Design

Packaging normally shows important information such as the features, functions, or benefits of a product. It can substantially influence consumers' purchase choice and product experience [34].

The Amount and Form of Information

Previous studies have demonstrated how the information on the packaging of products affects consumers' purchase intentions. Wansink *et al.* and Feunekes *et al.* discovered that, compared with longer descriptions, shorter descriptions on a product packaging lead to a more positive impression and image [35,36]. Feunekes found that too much information (information overload) might cause confusion for consumers at the actual consumption point. At the choosing point, consumers normally have only a limited amount of time to read information on packaging. Therefore, they may pass over more information in detail [36]. Kimura and his colleagues claimed that a great amount of information caused higher valuation of a food product only when consumers actively searched for and read the information, whereas an appropriate amount of information had the best effect when the consumers were only required to read the information (not actively) [37]. These investigations illustrate two facts: first, the amount of information on the packaging should be moderate; second, environmental consciousness may influence the effects of the information on the packaging of consumer products. People who have a sense of environmental protection may read the information on the package more carefully.

To examine the information's effects, we asked 36 Chinese university students to view and evaluate one original information sheet in the package of a Logitech keyboard (see Figure 5). This sheet contains information on the hazardous substances, recycling, and environmental protection of the Logitech keyboard in Chinese. The results of eye tracking equipment showed that almost all the participants viewed the recycling mark for seconds, but they claimed that they did not know what the mark means; about 77.8% of the par-

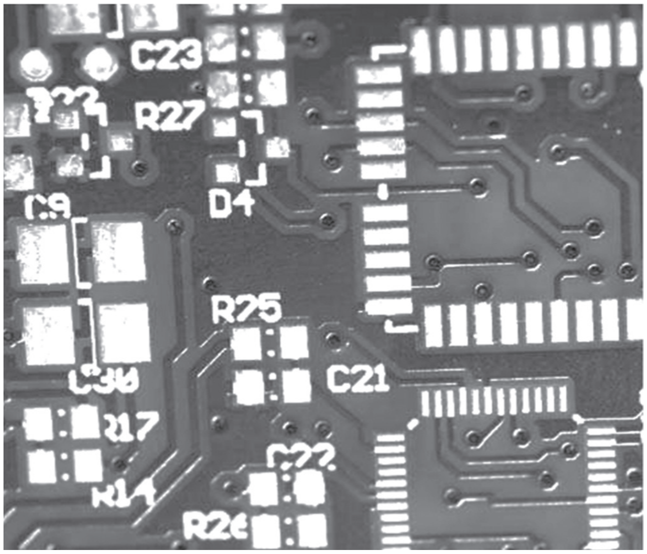

Figure 4. *Welding Joints on a Circuit Board.*

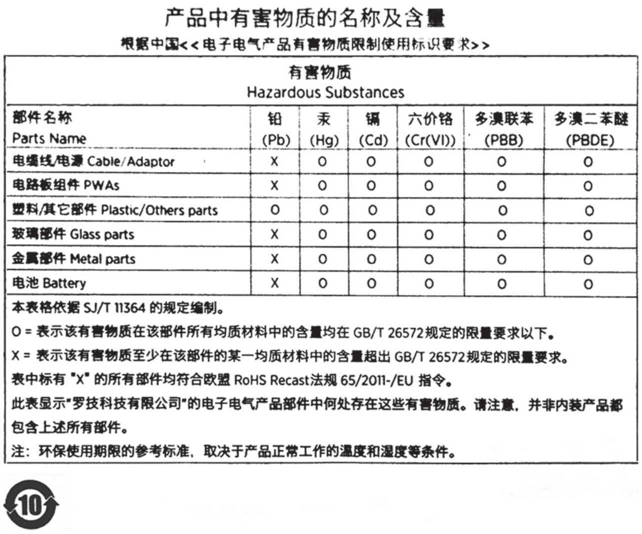

产品中有害物质的名称及含量

根据中国<<电子电气产品有害物质限制使用标识要求>>

部件名称 Parts Name	有害物质 Hazardous Substances					
	铅 (Pb)	汞 (Hg)	镉 (Cd)	六价铬 (Cr(VI))	多溴联苯 (PBB)	多溴二苯醚 (PBDE)
电缆线/电源 Cable/Adaptor	X	O	O	O	O	O
电路板组件 PWAs	X	O	O	O	O	O
塑料/其它部件 Plastic/Others parts	O	O	O	O	O	O
玻璃部件 Glass parts	X	O	O	O	O	O
金属部件 Metal parts	X	O	O	O	O	O
电池 Battery	X	O	O	O	O	O

本表格依据 SJ/T 11364 的规定编制。

O = 表示该有害物质在该部件所有均质材料中的含量均在 GB/T 26572规定的限量要求以下。

X = 表示该有害物质至少在该部件的某一均质材料中的含量超出 GB/T 26572规定的限量要求。

表中标有 "X" 的所有部件均符合欧盟 RoHS Recast法规 65/2011-/EU 指令。

此表显示"罗技科技有限公司"的电子电气产品部件中何处存在这些有害物质。请注意，并非内装产品都包含上述所有部件。

注：环保使用期限的参考标准，取决于产品正常工作的温度和湿度等条件。

Figure 5. *Hazardous substance description of Logitech Keyboard.*

ticipants did not view all the information on the sheet, but they looked at the table listing the six hazardous substances (Pb, Hg, Cd, Cr VI, PBB, and PBDE) for an average of 4.73 seconds. Compared with words, the graphic information drew more attention, but the existing recycling mark seems to lack efficiency. Moreover, this experiment proved the conclusion of previous studies that too much information on a sheet causes participants not to read the information carefully.

To enhance the efficiency of the environmental protection information on packaging and labels, the information should be designed in the form of graphics that can be easily understood, and the amount of information should be moderate, not too much.

Combining Motivations with the Packaging Design and Label Design

Motivation is not only a person's aspiration to accomplish a goal but also the energy that the person puts toward achieving that goal. Many people have motivation within themselves, and this motivation can push them to try to accomplish many things [38]. Happiness, interest, and benefits are three very important motivations of human behavior. Through combining it with motivations, design can promote people to alter their behavior actively and influence their awareness [39].

An example of label design application confirms the point of view above. In August 2004, China's government promulgated and implemented the labelling program "Measures for Administration of Energy Efficiency Labels" [40]. Now almost all consumer electronics in China are given China's energy label. Figure 6 contains the energy label of a Haier air conditioner. On this label are the manufacturer's name, a serial number, energy consumption levels, the energy efficiency ratio, and the standard the label was based on. Chinese consumers are concerned about this label when purchasing consumer electronics; sometimes, they even consider this label a standard in selecting consumer electronics because the energy consumption is related to the final issue. They may not think about saving energy and environmental protection, but they are concerned about saving money. Purchasing behavior is influenced by which product can benefit the consumers, not only from the functional aspects but also final aspects. The China energy label changes consumers' purchase behavior and promotes eco life. Designers should explore cleverer design solutions that can take advantage of motivations to lead people to alter their behavior positively and actively.

Labelling Material Types and Disassembly Methods

Each component of a consumer electronic product should be labelled with the material's name and whether it can be recycled or not. For normal consumers, it is impossible to determine the types of materials exactly. Labelling the material can help consumers learn about materials and judge which are environmentally friendly products. In the late waste disposal phase, this measure can save time for material cataloging.

Some electronic products show the assembly methods in product manuals, e.g., a vacuum cleaner, and multi-functional juicing machine. They are used to to illustrate different functional combinations and exchanges between parts. Correspondingly, we should provide the user with the dismantling methods. In this way, users can disassemble electronic products, classify the materials, and complete the most important job of electronic waste disposal.

Figure 7 shows the carton design of Kirin's (Japanese drink company) mineral water. On one side of the carton is a disassembly illustration that shows the detailed steps for opening and folding the carton. Japan is one of the countries doing best in waste disposal. This carton design shows us the Japanese designer's elaborate efforts to ensure the recycling of this packaging. In fact, all Japanese are educated to have consciousness of garbage classification from an early age. Their environmental behavior is worth learning and promoting all over the world.

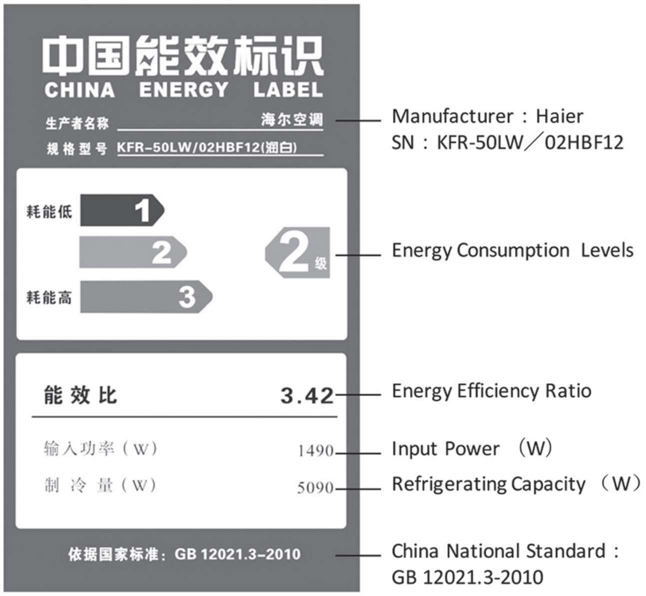

Figure 6. *China Energy Label.*

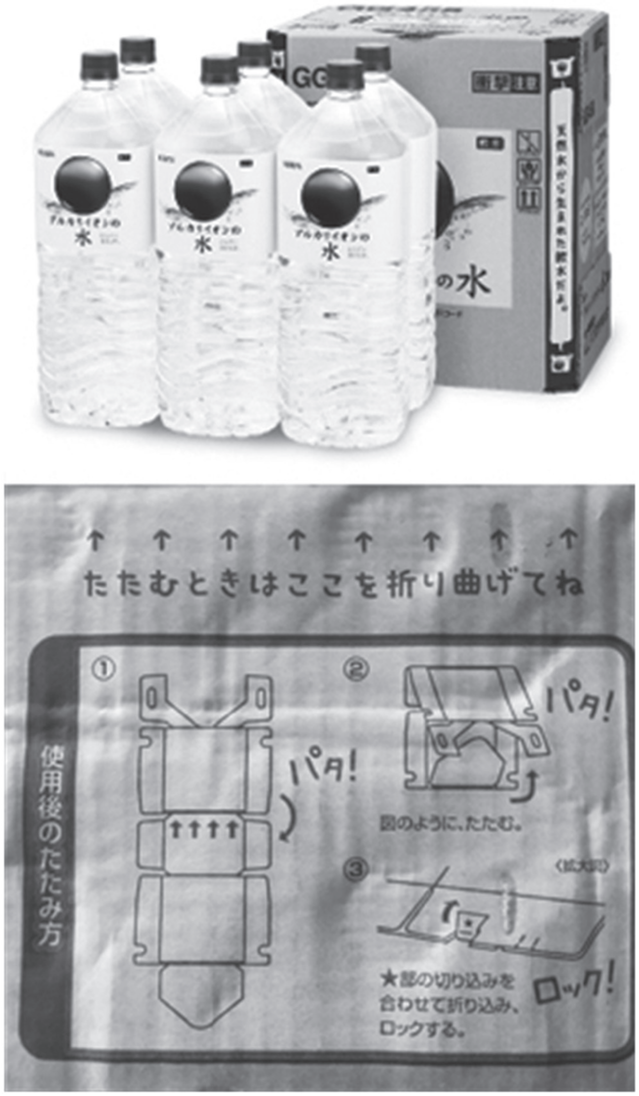

Figure 7. *Carton of Kirin Mineral Water.*

CONCLUSION

In this study, through an analysis of the designer's role and tasks in designing and developing consumer electronic products, we found that designers had the opportunity to avoid or reduce the environmental pollution problems caused by consumer electronics through correct material decision-making and rational structure design. Furthermore, after the analysis and discussion about the lifecycle of a consumer electronic product, two more potential design elements that can influence the environmental pollution of electronic waste were discovered: packaging design and label design. Eco-labels and information on what materials are applied in the product on the packaging or product body attract consumers' attention to environmental protection and affect their purchase behavior.

Based on the relevant laws and regulations, previous studies, and investigations on successful cases, we defined design strategies for developing sustainable consumer electronic products. First, the materials should be not only non-toxic and non-polluting but also well considered from the aspects of users, usages, and the use environment. The application of recyclable and remanufacture-able materials is the inexorable trend. Second, consumer electronic products should be designed with simply disassembled structures using bolt connections and snap connections and employ recyclable functional components as much as possible. Third, the information on the packaging or labels of consumer electronic products should be designed with graphics that are easy to understand and with an appropriate amount. We also need to explore clever design solutions that can motivate people positively and actively to alter their environmental protection behaviors.

These conclusions are only summarized design strategies. In further studies, we will verify their feasibilities and effectiveness in actual design implementations. Moreover, we would like to recommend that those who major in consumer electronic product design should consider the impacts on users and society as the most important design element. Designers have the opportunity to improve the world. In addition to achieving our goals and accessing benefits through design, we should also take responsibility for human and social development and create a better living environment in the future.

REFERENCES

1. Consumer Electronics Association, "Market Research Report: Trends in CE Reuse, Recycle and Removal", April 2008.
2. European Commission, "Proposal for a directive of the European parliament and of the council", 2014, Brussels.
3. Widmer, R., Oswald-Krapf, H., Shinha-Khetriwal, D., Schnellmann, M., and Böni, H., "Global perspectives on e-waste", *Environmental Impact Assessment Review*, Vol.25, Issue 5, 2005, pp.436–458. https://doi.org/10.1016/j.eiar.2005.04.001
4. Nnorom, I.C. and Osibanjo, O., "Overview of electronic waste management practices and legislations, and their poor aplications in the developing countries", *Resources, Conservation and Recycling*, Vol.52, Issue 6, 2008, pp. 843–858. https://doi.org/10.1016/j.resconrec.2008.01.004
5. Cui, J. and Forssberg, E., "Mechanical recycling of waste electronic and electronic equipment: A review", *Journal of Hazardous Materials*, Vol.99, Issue 3, 2003, pp. 243–263. https://doi.org/10.1016/S0304-3894(03)00061-X
6. Kahhat, R., Kim J., Xu, M., Allenby, B., Williams, E., and Zhang, P., "Exploring e-waste management systems in the United States", *Resources, Conservation and Recycling*, Vol.52, Issue 7, 2008, pp. 955–964. https://doi.org/10.1016/j.resconrec.2008.03.002
7. Kalweit, A., "Konstruktionstechnik", workshop at University Wuppertal, 2008.
8. Luke, A.F. 2002. *The eco-design handbook*, Thames & Hudson.

9. Cramer, J. “Towards innovative, more eco-efficient product design strategies”, *The Journal of Sustainable Product Design*, Vol. 1, No. 1, 1997, pp.7–16. https://doi.org/10.9774/gleaf.978-1-909493-05-6_21
10. Bhamra, T.A. “Eco-design: The search for new strategies in product development”, *Proceedings of the Institution of Mechanical Engineers, Part B: Journal of Engineering Manufacture*, Vol. 218, Issue 5, 2004, pp. 557–569. https://doi.org/10.1177/095440540421800509
11. Lu, L.Y., Wu, C.H., and Kuo, T., “Environmental principles applicable to green supplier evaluation by using multi-objective decision analysis”, *International Journal of Production Research*, Vol. 45, 2007, pp.4317–4331. https://doi.org/10.1080/00207540701472694
12. Pigosso, D.C., Zanette, E.T., Filho, A.G., Ometto, A.R., and Rozenfeld, H., “Eco-design methods focused on remanufacturing”, *Journal of Cleaner Production*, Vol. 18, Issue 1, 2010, pp. 21–31. https://doi.org/10.1016/j.jclepro.2009.09.005
13. Maxwell, D. and Vorst, R., “Developing sustainable products and service”, *Journal of Cleaner Production*, Vol.11, 2003, pp. 883–895. https://doi.org/10.1016/S0959-6526(02)00164-6
14. Mueller, S. and Szolnoki, G., “The relative influence of packaging, labelling, branding and sensory attributes on liking and purchase intent: Consumers differ in their responsiveness”, *Food Quality and Preference*, Vol.21, Issue 7, 2010, pp.447–783. https://doi.org/10.1016/j.foodqual.2010.07.011
15. Silayoi, P. and Speece, M., “Packaging and purchase decisions: An exploratory study on the impact of involvement level and time pressure”, *British Food Journal*, Vol.106, Issue 8, 2004, pp.607–628. https://doi.org/10.1108/00070700410553602
16. Clement, J., “Visual influence on in-store buying decisions: An eye-track experiment on the visual influence of packaging design”, *Journal of marketing management*, Vol.23, No.9-10, 2007, pp.917–928. https://doi.org/10.1362/026725707X250395
17. Wells, L.E., Farley, H., and Armstrong., G.A., “The importance of packaging design for own-label food brands”, *International Journal of Retail & Distribution Management*. Vol. 35, No. 9, 2007, pp. 677–690. https://doi.org/10.1108/09590550710773237
18. Stafford, M.R., “An evaluation of the effectiveness of the appeal and the medium within a classification of services”, Unpublished doctoral dissertation, University of Georgia, 1993.
19. Holbrook, M.B. and O Shaughnessy, J., “The Role of Emotion in Advertising”, *Psychology and Marketing*, Vol. 1, 1984, pp.45–64. https://doi.org/10.1002/mar.4220010206
20. Kalweit, A., Paul, C., Peters, S., and Wallbaum, R., 2006, *Handbuch für Technisches Produktdesign*, Springer. https://doi.org/10.1007/978-3-540-45919-4
21. Miller, C.M., Anderson, I.E., and Smith, J.F. “A viable tin-lead solder substitute: Sn-Ag-Cu”, *Journal of Electronic Materials*, Vol. 23, No. 7, 1994, pp. 595–601. https://doi.org/10.1007/BF02653344
22. Lin,Y.,Wang, J., Evans, D.G., and Li, D., “Layered and intercalated hydrotalcite-like materials as thermal stabilizers in PVC resin”, *Journal of Physics and Chemistry of Solids*, Vol. 67, No. 5, 2006, pp. 998–1001. https://doi.org/10.1016/j.jpcs.2006.01.016
23. Bissot, T.C., Parrym, R.W., and Campbell, D.H., “The physical and chemical properties of the methylhydroxylamines1”, *Journal of the American Chemical Society*, Vol. 79, No. 4, 1957, pp. 796–800. https://doi.org/10.1021/ja01561a005
24. Schulman, J. N. and Chang, Y., “Band mixing in semiconductor superlattices”, *Physical Review B*, Vol. 31, No. 4, 1985, p. 2056. https://doi.org/10.1103/PhysRevB.31.2056
25. Joux, F. and Lebaron, P., “Use of fluorescent probes to assess physiological functions of bacteriaat single-cell level”, *Microbes and infection*, Vol. 2, No. 12, 2000, pp. 1523–1535. https://doi.org/10.1016/S1286-4579(00)01307-1
26. Arici, M., Nazir, H., and Aksu, M.L., “Investigation of Sn–Zn electrodeposition from acidic bath on EQCM”, *Journal of Alloys and Compounds*, Vol. 509, No. 5, 2011, pp. 1534–1537. https://doi.org/10.1016/j.jallcom.2010.10.161
27. Heard, R., Erb, U., and Palumbo, G., “Exploiting hall-petch strengthening for sustainability”, Environmental Issues and Waste Management Technologies in the Materials and Nuclear Industries XII: Ceramic Transactions, Vol. 86, 2009, p. 177. https://doi.org/10.1002/9780470538371.ch17
28. Steffani, C., and Meltzer, M., “Electrodeposited Tungsten-Nickel-Boron: A Replacement for Hexavalent Chromium”, Lawrence Livermore National Lab, CA, 1995. https://doi.org/10.2172/72974
29. Pecht, M. and Deng, Y., "Electronic device encapsulation using red phosphorus flame retardants", Microelectronics Reliability, Vol. 46, No. 1, 2006, pp. 53–62. https://doi.org/10.1016/j.microrel.2005.09.001
30. Nikkei Design. 2012. Sozai to design no kyokasho dai 2 han, Nikkei Business Publications, Inc.
31. Lörcks, J., “Properties and applications of compostable starch-based plastic material”, *Polymer Degradation and Stability*, Vol.59, No.1, 1998, pp.245-249. https://doi.org/10.1016/S0141-3910(97)00168-7
32. Tokiwa, Y., Calabia, B.P., Ugwu, C.U., and Aiba, S., “Biodegradability of plastics”, *International Journal of Molecular Sciences*, Vol. 10, No. 9, 2009, pp. 3722–3742. https://doi.org/10.3390/ijms10093722
33. JuzDeals, Commodity Photo: “Natural wheat straw-made cups or plates”, Retrieved September 13, 2016, from http://www.juzdeals.com/hk/d/5584/a-set-natural-wheat-straw-made.
34. The power of packaging design has been widely recognized by the marketers. Packaging can substantially influence consumers’ purchase choice and product experience (Slavin, 2012).
35. Wansink, B., Sonka, S.T., and Halser, C.M., “Front label Health Claims: When Less Is More”, *Food Policy*, Vol. 29, 2004, pp.695-667. https://doi.org/10.1016/j.foodpol.2004.10.004
36. Feunekes, G.I., Gortemaker, I.A., Willems, A.A., Lion, R., and van den Kommer, M., “Front of Pack Nutrition Labeling: Testing Effectiveness of Different Nutrition Labeling Formats Front of pack in Four European Countries”, *Appetite*, Vol. 50, 2008, pp. 57–70. https://doi.org/10.1016/j.appet.2007.05.009
37. Kimura, A., Mukawa, N., Yamamoto, M., Masuda, T., Yuasa, M., Goto, S., Oka, T., and Wada, Y., “The Influence of Reputational Concerns on Purchase Intention of Fair trade Foods Among Young Japanese Adults”, *Food Quality and Preference*, Vol.26, 2012, pp.204-210. https://doi.org/10.1016/j.foodqual.2012.05.002
38. Maslow, A.H.1987. *Motivation and personality*. New York: Harper & Row.
39. You, Z., Hibino, H., and Koyama, S., “Changing human behavior through the options and feedback design of service systems”, *IEEE Tsinghua International Design Management Symposium*, 2013, pp. 331–337. https://doi.org/10.1109/tidms.2013.6981255
40. China National Institute of Standardization, “Label Development History”, Retrieved September 20, 2016, from http://www.energylabel.

Effects of L-cysteine and Giant Panda Excrement on Hydrogen Production from Cassava Residues

LUYAN ZHANG, JIE DING*, YAN LI, XIANSHU LIU, JINYU JIANG and NANQI REN
State Key Laboratory of Urban Water Resource and Environment, School of Municipal and Environmental Engineering,
Harbin Institute of Technology, Harbin 150090, China

ABSTRACT: This study investigated the anaerobic hydrogen production from cassava residues using the mixed culture from giant panda (*Ailuropoda melanoleuca*) excrement. The FTIR and XRD results demonstrated that cassava residues could be degraded by the anaerobic mixed culture from grand panda excrement, and that maximum H_2 production rate (R_{max}) and the maximum cumulative H_2 production (H_{max}) and were 152.86 $mL \cdot L^{-1} \cdot h^{-1}$ and 688.36 $mL \cdot L^{-1}$ respectively in the dark fermentation. The effects of L-cysteine on H_2 production, substrate utilization, metabolites distribution and biomass were studied in batch-mode tests. The results showed that the cassava residues were degraded by 31.6% through H_2 production. After adding L-cysteine (0.5–2.0 $g \cdot L^{-1}$) to the nutrient solution, the biomass concentration reached to 1.53 $g \cdot L^{-1}$, about 1.36 times higher than that of the control group without L-cysteine addition, and the dark fermentative H_2 production was 1.6–2.0 times higher than that of the control group. Our results demonstrated that by using the anaerobic mixed culture from giant panda excrement, cassava residues could be converted into H_2 efficiently with the addition of L-cysteine during the dark fermentation.

INTRODUCTION

WORLDWIDE use of renewable energies has been concerned by reason of energy shortages and environmental pollution [1,2]. Among various renewable energy resources, because of the advantage of cleanness, recyclability and gravimetric energy density (122 kJ/g), H_2 has upgraded interest around the world [3]. Compared with conventional chemical H_2 production, such as gasification of coal and steam reforming of natural gas, biological H_2 production processes from biomass have become a more desirable alternative, for their potential and capability to deal with agricultural and industrial organic wastes and meanwhile generate valuable H_2 fuel [4–7]. In addition, H_2 can play a considerable role in reducing greenhouse gases emissions. Among the wastes from agriculture and industry, feedstock such as lignocellulosic materials can be economically feasible for biological H_2 production processes [8,9].

Cassava residues are generated during the cassava-based starch production, and their yield in China has reached to 0.3 million tons per year [10–12]. These residues contain a large amount of lignocellulosic components, and their direct discharge to the environment will cause huge waste of the lignocellulosic resources and serious environmental pollution problems [13,14]. Instead, the application of cassava residues as fermentable substrates to produce H_2 is a feasible and desirable choice. However, due to the structural complexity of lignocellulose, direct digestion of these residues faces with the problems of low hydrolysis efficiency and consequent H_2 yield reduction. Hence, a promising microbial consortium with the ability of cellulose degradation and H_2 production, such as the bacteria from the excrement of herbivores [15], must be introduced to treat these materials for effective utilization of residues and obtainment of maximum H_2 yield.

It is well known that the giant panda with bamboo as the main food source which is indigenous to China belongs to the order Carnivora phylogenetically, but is characterized as herbivory physiologically. Therefore, it has been pointed out that the giant panda must possess special microbial communities capable of metabolizing cellulose, which are different from those in other herbivores. The intestinal microbial communities in the giant panda has been reported by several previous studies [15–18]. Zhu [19] found that 7 of 13 operational taxonomic units which contain taxa known to digest

---

*Author to whom correspondence should be addressed.
E-mail: dingjie123@hit.edu.cn; Telephone:+86-451-86289113(office)
Fax: +86-451-86289113

1544-8053/16/02 S227-08

doi:10.12783/issn.1544-8053/13/4/S30

cellulose were unique to the giant panda. Therefore, giant panda excrement can be used as ideal microbial consortium to produce biological H_2 from lignocellulosic resources.

In addition to raw materials and inoculum, H_2 production by anaerobic fermentation is also influenced by some other factors, such as metal ions, temperature, pH and reducing agents. Biohydrogen production is associated with the activities of hydrogenase and NAD^+/NADH, both of which favor low oxidation-reduction potential (ORP) environment [20]. As a unique natural amino acid, L-cysteine contains a thiol group that can form disulfide bond. Due to the existence of thiol group, L-cysteine is commonly used as a reducing agent to create an anaerobic environment so as to maintain the oxidation reduction potential at an optimal level for H_2 production [21]. Besides, L-cysteine has ever been reported as a mediator between substrate and bacteria. As a result, it can be used for increasing the bacteria growth, the fermentation extent, and the utilization rate of the substrate as playing a role of bioactive agent. Obviously, these factors are of great importance for improving H_2 productivity [22,23].

This study aims to investigate H_2 production from cassava residues using the anaerobic mixed culture in giant panda excrement, and the effects of L-cysteine on H_2 production, substrate utilization and metabolites distribution are determined in batch-mode tests.

MATERIALS AND METHODS

Materials

Cassava residues were collected from Nanning, Guangxi Province, China. The residues were dried at 60°C and sieved through a 40-mesh screen. The determination procedure of the chemical composition was according to the National Renewable Energy Laboratory [24]. The major physical characteristics and components of cassava residues were as follows: total solid (TS), 95.58 ± 0.31 wt%; volatile solid (VS), 89.53 ± 0.62 wt%; cellulose, 29.27 ± 0.45 wt%; hemicellulose, 10.00 ± 0.90 wt%; lignin, 12.07 ± 0.38 wt%; ash, 3.36 ± 0.41 wt%.

Microorganisms and Culture Conditions

Giant panda excrement sample was collected from Chengdu, Sichuan Province, China. To eliminate methanogenic bacteria and select spores from the hydrogen producing bacteria, the giant panda excrement sample was pretreated at 70°C for 50 min. The anaerobic mixed culture from giant panda excrement was cultured anaerobically at 37°C for 24 h. Dark fermentation was performed in 500 mL serum bottle with a working volume of 350 mL in batch experiments. Per liter of the medium for fermentation consisted of 20.0 g cassava residues, 1.0 g NH_4SO_4, 1.5 g K_2HPO_4, 0.75 g KH_2PO_4, 0.2 g $MgCl_2\cdot 6H_2O$, 1.0 g NaCl, 0.2 g KCl, 2.0 g yeast extract, 1 mL vitamin solution and 1 mL trace element solution [25]. L-cysteine concentrations ranged from 0 to 2 $g\cdot L^{-1}$. The initial pH of the medium was adjusted to 7.0 and the operation temperature of the serum bottles was controlled at 37°C. The serum bottles were shaken at 120 rpm for 24 h. Inoculum of 2% (v/v) was added to each reactor and nitrogen was pumped in to maintain the anaerobic condition. Each experiment was triplicate and the average values were calculated for further analysis.

Hydrogen Production and Cell Growth Kinetics

Modified Gompertz equation as shown in Equation (1) was used to describe the cumulative H_2 production progress in batch cultures. Time–course data of the cumulative H_2 production were simulated by the equation to determine the kinetic parameters in the dark fermentation.

$$H = H_{\max} \exp\left\{-\exp\left[\frac{R_{\max} e}{H_{\max}}(\lambda - t) + 1\right]\right\} \qquad (1)$$

where H denotes the cumulative H_2 production (mL H_2 per liter of culture), $H_{\max}$ denotes the maximum cumulative H_2 production (mL H_2 per liter of culture), $R_{\max}$ denotes the maximum H_2 production rate ($mL\cdot L^{-1}\cdot h^{-1}$), t denotes the culture time (h), λ denotes the duration time of the lag-phase (h), and $e = 2.71828$.

Logistic equation as shown in Equation (2) was used to interpret the relationship between the anaerobic mixed culture from giant panda excrement growth and cell concentration.

$$X = \frac{X_0 - X_{\max}}{1 + \left(\dfrac{t}{t_{\max}}\right)^P} + X_{\max} \qquad (2)$$

where X denotes the cell concentration ($g\cdot L^{-1}$) of the anaerobic mixed culture from giant panda excrement at time t (h); X_0 denotes the initial cell concentration ($g\cdot L^{-1}$); $X_{\max}$ denotes the maximum cell concentration

($g\cdot L^{-1}$); t denotes the culture time (h); t_{max} denotes the time when the maximum specific growth rate occurs (h).

Analytical Methods

The gas products were collected with gas collecting bags for gas analysis. Two Gas chromatographs which equipped with a thermal conductivity detector and a flame ionization detector, respectively, were used to measure the H_2 content and residual volatile fatty acids (VFAs) in dark fermentation. [26] The biomass concentration in dry weight (DW) was determined by filtering the samples through gauze to separate the biomass and cassava residues. Afterwards, the samples were dried at 105°C until constant weight was obtained.

Characterization of Cassava Residues

XRD Analysis

Cassava residues before and after fermentation were analyzed by a D8-ADVANCE X-ray diffractometer (BRUKER, Germany), at a working current of 10 mA and working voltage of 30 kV. The radiation source was Cu-K_α (1.54 Å) and the angle grade ranged between 10°–90° with a step size of 0.02°. Crystallinity index (CrI) of cellulose was calculated according to the peak intensity method as shown in Equation (3).

$$\mathrm{CrI}(\%) = \left[\frac{(I_{002} - I_{am})}{I_{002}}\right] \times 100 \qquad (3)$$

where CrI denotes the crystallinity index, I_{002} denotes the maximum intensity at $2\theta = 22.5°$, and Iam denotes the minimum intensity corresponding to the amorphous content at $2\theta = 18.0°$.

FTIR Analysis

The FTIR spectra were used to detect the changes of functional groups occurring in cassava residues during bioremediation. FTIR spectra of 32 scans were recorded by the FTIR spectrometer (PerkinElmer, Spectrum One, USA) in the absorption band mode within the range of 400–4000 cm^{-1} with a resolution of 4 cm^{-1}. IR absorption ratios between the absorbance intensities of 1372–2900 cm^{-1}, 1429–897 cm^{-1} and 1375–1512 cm^{-1} were used to evaluate the IR crystallinity of cellulose in cassava residues.

RESULTS AND DISCUSSION

Hydrogen Production in the Dark Fermentation

Giant panda excrement contains sufficient anaerobic mixed cultures to degrade cellulose and hemicellulose in cassava residues and produce H_2 in the dark fermentation. The anaerobic mixed culture from giant panda excrement grew well in the dark fermentation [Figure 1(a)]. It firstly took a lag phase about one hour, then grew exponentially during 2–8 h, and finally reached the stationary phase during 9–14 h. The final cell concentration reached to 1.11 $g\cdot L^{-1}$, which was comparable with the maximum anaerobic mixed culture cell concentration obtained from the Logistic model (1.18 $g\cdot L^{-1}$). The cumulative curve of dark fermentative H_2 production fitted the modified Gompertz equation [Figure 1(a)] ($R^2 > 0.99$). The maximum cumulative H_2 production (H_{max}) and the maximum H_2 production rate (R_{max}) were 688.36 $mL\cdot L^{-1}$ and 152.86 $mL\cdot L^{-1}\cdot h^{-1}$ respectively, which were close to the experimental data of 634.43 $mL\cdot L^{-1}$ and 142.17 $mL\cdot L^{-1}\cdot h^{-1}$. The degradation efficiency of cassava residues in the dark fermentation was 31.6%, decreasing from 20 $g\cdot L^{-1}$ at 0 h to 13.68 $g\cdot L^{-1}$ at 14 h. This result was close to the components (cellulose, 29.27 ± 0.45 wt%; hemicellulose, 10.00 ± 0.90 wt %) for H_2 production from cassava residues. Thus, it can be concluded that a high cassava utilization ability of the anaerobic mixed culture was achieved during the fermentation process. The H_2 yield obtained in this work was compared with those obtained from different anaerobic fermentation systems as reported in some selected literature (Table 1). As can be seen, without any pretreatment, the H_2 yield was as high as 688.36 $mL\cdot L^{-1}$, which was comparable to those achieved by using easily-utilized substrates. These results indicated that H_2 production from cassava residues by the anaerobic mixed culture from giant panda excrement during the dark fermentation had a high application potential. The main end-products of the dark fermentation were acetate and butyrate [Figure 1(b)], which were 871.19 and 733.96 $mg\cdot L^{-1}$ respectively in the effluent after fermentation for 14 h. Besides, low amounts of ethanol, propionate and valerate were also detected during the fermentation (data were shown here).

Variation of Cassava Residues in the Dark Fermentation

Structural changes in lignocellulosic biomass dur-

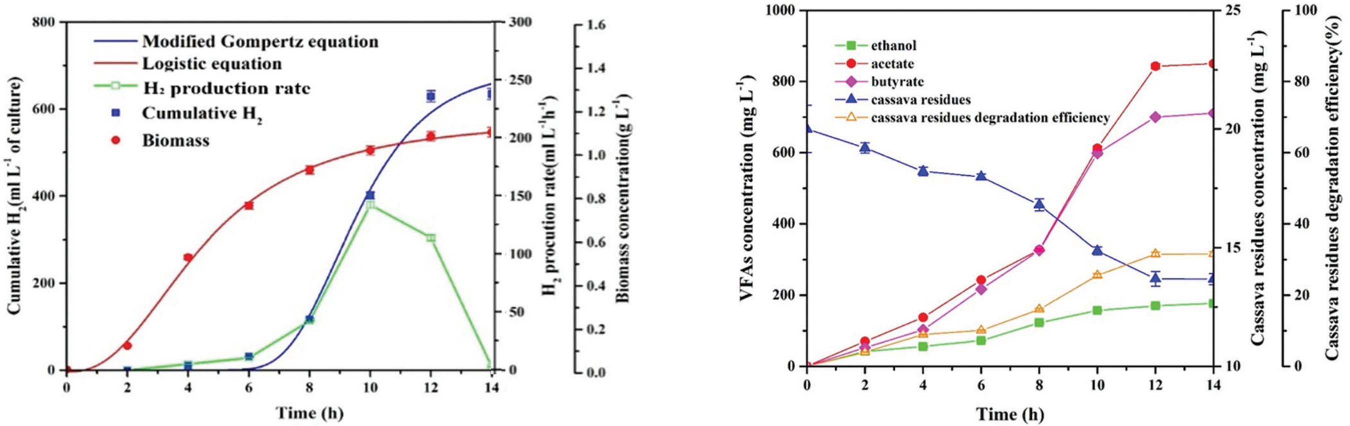

(a) (b)

Figure 1. *(a) Hydrogen production and growth characterization of giant panda excrement with cassava residues as the substrate; (b) accumulation profile of cassava residues degradation in the dark fermentation.*

ing the dark fermentation were determined using FTIR spectroscopy. The frequencies corresponding to the assignments in lignocellulosic biomass were listed in Table 2. Three FTIR absorbance ratios (A_{1375}/A_{1512}, A_{1372}/A_{2900}, and A_{1427}/A_{895}) were used in this study, i.e., the ratios of the peak heights (1375–1512 cm^{-1}, 1372–2900 cm^{-1}, and1429–897 cm^{-1}) before and after the fermentation of cassava residues (Table 3). The ratio of A_{1375}/A_{1512} was used for the determination of IR crystallinity of lignocellulosic biomass, in which the peak height at 1375 cm^{-1} represented the characteristic of cellulose and that at 1512 cm^{-1} represented the characteristic of lignin. Accordingly, for the FTIR absorbance ratios, A_{1427}/A_{895} and A_{1372}/A_{2900}, the peaks at 895 cm^{-1} and 1372 cm^{-1} represented the characteristic of cellulose and those at 1427 cm^{-1} and 2900 cm^{-1} represented the characteristic of lignin [37]. After fermentation, A_{1375}/A_{1512} and A_{1372}/A_{2900} decreased (0.978 and 0.967) while A1427/A895 increased (0.980) relative to those in raw cassava residues (A_{1375}/A_{1512}, A_{1372}/A_{2900} and A_{1427}/A_{895} were 0.985, 1.001 and 0.893 respectively). It might be attributed to the amorphous cellulose removal in the dark fermentation. Thus, it can be deduced that the anaerobic mixed culture from grand panda excrement can degrade the cellulose in cassava residues.

The crystallinity index (CrI) measurement by XRD analysis is a semi-quantitative and qualitative approach to evaluate the component of crystalline and amorphous cellulosic in lignocellulosic biomass. CrI % of cellulose has been used to determine the efficiency to hydrolysis [41,42]. Cellulose structure consists of two regions, i.e., amorphous and crystalline region, of which amorphous region is easier to be digested by enzymes than crystalline region [42]. In this study, amorphous and crystalline components in lignocellulosic biomass were quantitatively determined by XRD analysis. CrI measurement of cassava residues before and after fermentation showed that the crystallinity index after fermentation (63.21%) was lower than that of raw cassava residues (71.06%) (Table 4) due to the degradation of crystalline cellulose in the dark fermentation for producing H_2. These results were consistent with the FTIR results (Table 3). The biology mechanism of this degradation may be attributed to the enzyme action on easily degradable amorphous cellulose.

Effect of L-cysteine on Biomass Growth and Hydrogen Production

L-cysteine concentration (0.5–2.0 $g \cdot L^{-1}$) had a

Table 1. Comparison of the Reported Hydrogen Yields from Different Fermentation Systems.

Microorganism	Substrate	Maximum H_2 Yield	Reference
Anaerobic digester sludge	Rice slurry	346 mL g^{-1} starch	[27]
Anaerobic digester sludge	Food waste	101 mL g^{-1} COD	[28]
Meal of fermented soybean	Bean curd manufacturing waste	130 mL h^{-1} L^{-1} culture	[29]
Sewage sludge	Cassava starch	9.47 mmol H_2 g^{-1} starch	[30]
Granule sludge	Cassava pulp hydrolysate	342 mL H_2 g^{-1} COD reduced	[31]
Anaerobic mixed culture from giant panda excrement	Cassava residues	688 mL H_2 L^{-1} culture	This study

Table 2. Assignments of Frequencies in Lignocellulosic Biomass.

Frequency (cm^{-1})	Assignment	References
3300	H–bonded OH groups stretching	[32–33]
2900	C–H stretching	[34–35]
1710	carbonyl stretching (C=O) for acetyl groups of hemicelluloses	[36]
1620	aldehydic group of lignin	[37]
1512	stretching (C=C) of the aromatic ring of lignin	[37]
1430	symmetric CH_2 bending	[35,38]
1373	C–H bending	[35,39]
1320	symmetric CH_2 wagging	[36,39]
1237	O-H bending	[40]
1160	stretching (C–O–C) at the β (1–4) glycoside linkages	[38]
1033	stretching (C–O) at C-6	[38]
901	stretching (C–O–C)at the β (1–4) glycoside linkages	[38]

great effect on the biomass production of the anaerobic mixed culture from giant panda excrement [Figure 2(a)]. The biomass concentration of the control group was 1.11 g·L^{-1}, while it increased to the maximum biomass concentration of 1.53 g·L^{-1} at the L-cysteine concentration of 0.5 g·L^{-1}. However, further increase of L-cysteine concentration to 2 g·L^{-1} repressed the growth of the anaerobic mixed culture, and the final biomass concentration decreased to 1.22–1.40 g·L^{-1}. It has been reported that L-cysteine has a similar function as the growth factor and can promote the cell growth as its concentration increases. However, our study revealed that when its concentration was over 0.5 g·L^{-1}, the promoting effect on bacterial growth would be weakened. L-cysteine can affect the growth of bacteria because of its unique structure and ability to interact with some bacterial proteins. On the other hand, L-cysteine can facilitate H_2 production by reducing the ORP of the culture system. When L-cysteine concentration was less than 0.5 g·L^{-1}, the ORP of the culture system was the most desirable for cell growth. However, as the fermentation continued, the ORP gradually increased, thus decreasing the cell growth rate. When the L-cysteine concentration was over 0.5 g·L^{-1}, the biomass did not increase as quickly as expected. Hence, excessive L-cysteine was noxious to the microorganisms [43].

Under various L-cysteine concentrations, the cumulative H_2 volume experienced the lag phase, exponential phase, and stationary phase over time (data were shown here), and the modified Gompertz equation fitted well with the experimental data (Table 5) ($R^2 > 0.99$). This indicated that the modified Gompertz equation could accurately predict the cumulative H_2 production ($H_{\max}$) and the H_2 production rate ($R_{\max}$). When L-cysteine (0.5–2.0 g·L^{-1}) was added into the reactors, the lag time decreased substantially to 5.96–6.32 h, which was shorter than that of the control group (7.21 h). Meanwhile, the maximum H_2 production rate increased to 245.37–307.54 mL·h^{-1}, which was 1.6–2.0 times that of the control group (152.86 mL·h^{-1}). Besides, the end time of biohydrogen production decreased to about 10 h compared to that of the control group (about 12 h). The results indicated that L-cysteine increased the hydrogen-producing activity of the anaerobic mixed culture. The total H_2 volume with the addition of L-cysteine (725.93 mL·L^{-1}) was higher than that of the control group (688.36 mL·L^{-1}) (Table 4), since L-cysteine reduced the ORP in the fermentation systems to the level at which the growth of hydrogen-producing biomass could be accelerated [Figure 2(a)]. Previous studies also reported similar results [37]. Thus, the L-cysteine addition could promote the growth of hydrogen-producing biomass and finally increased the maximum H_2 production rate, which shortened the lag and end time.

Table 3. IR Crystallinity Ratios of Cassava Residues Before and After Fermentation.

Samples	IR Crystallinity Ratio		
	A_{1375}/A_{1512}	A_{1427}/A_{895}	A_{1372}/A_{2900}
Cassava residues	0.985	0.893	1.001
Cassava residues after fermentation	0.978	0.980	0.967

Table 4. Crystallinity Index (CrI %) of Cassava Residues Before and After Fermentation.

Samples	Peak Height		CrI %
	18°	22.5°	
Cassava residues	303	1047	71.06
Cassava residues after fermentation	280	761	63.21

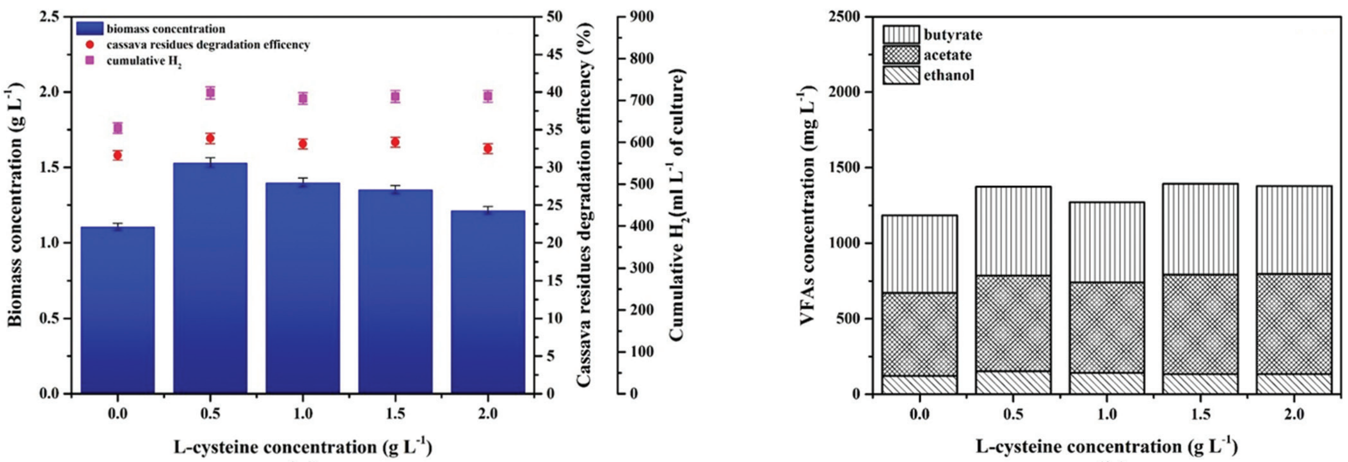

(a) (b)

Figure 2. *Effects of L-cysteine concentration on (a) biomass concentration, cassava residues degradation efficiency and cumulative H_2; (b) metabolite distributions of the anaerobic mixed culture.*

Effects of L-cysteine on Substrate Utilization Efficiency and Metabolites Distribution

The cassava residues degradation efficiency and metabolites distribution of the anaerobic mixed culture under varied L-cysteine concentrations were analyzed as Figure 2 shows. The substrate degradation efficiency ranged within 31% to 34%, which was close to the component (cellulose, 29.27 ± 0.45 wt%; hemicellulose, 10.00 ± 0.90 wt%) for H_2 production of cassava residues [Figure 2(a)], exhibiting that the anaerobic mixed culture can utilize substrate efficiently. Meanwhile, the major metabolites (e.g., ethanol, acetate and butyrate) in the control group were less than those produced by the culture with the addition of L-cysteine [Figure 2(b)]. Combined with the variation of cumulative H_2 volume [Figure 2(a)], the metabolites distribution indicated that the addition of L-cysteine increased the activity of hydrogen-producing bacteria to transform the substrate to H_2. In future studies, the relationship between the microbial communities in giant panda excrement and the H_2 production at different L-cysteine concentrations should be determined.

Table 5. Hydrogen Production of the Anaerobic Mixed Culture at Different L-cysteine Concentrations.

L-cysteine (g L^{-1})	R^2	H_{max} (mL L^{-1})	R_{max} (mL L^{-1} h^{-1})	λ (h)
0.0	0.991	688.36	152.86	7.21
0.5	0.997	725.93	307.54	6.21
1.0	0.997	715.47	257.79	5.96
1.5	0.995	723.60	245.37	6.22
2.0	0.995	723.57	253.15	6.32

CONCLUSIONS

In summary, dark fermentative H_2 production from cassava residues using the anaerobic mixed culture from grand panda excrement was studied in batch-mode tests. Along with the degradation of cassava residues by the anaerobic mixed culture, the maximum H_2 production rate and maximum cumulative H_2 production could reach to 152.86 mL·L^{-1}·h^{-1} and 688.36 mL·L^{-1} respectively in the dark fermentation. The effects of L-cysteine on H_2 production, cassava utilization and metabolites distribution were investigated. The results demonstrated that the anaerobic mixed culture from giant panda excrement could effectively degrade the organic compounds in cassava residues along with H_2 production. The lag time was shortened significantly by adding low concentration of L-cysteine (0.5–2.0 g·L^{-1}), thus improving the maximum H_2 production rate. Compared with the blank sample, the highest volume increment of total H_2 production (5.46%) could be achieved at the L-cysteine concentration of 0.5 g L^{-1}. This work implies that cassava residues can be used as a good substrate for H_2 production. Meanwhile, with the addition of L-cysteine during the dark fermentation, cassava residues can be converted into H_2 efficiently by using the anaerobic mixed culture from giant panda excrement.

ACKNOWLEDGMENTS

This research was supported by National High Technology Research and Development Program of China (863 Program) (No. 2011AA060905), State Key Laboratory of Urban Water Resource and Environment (Harbin Institute of Technology) (No.2012DX04).

REFERENCES

1. Masset J., Calusinska M., Hamilton C., Hiligsmann S., Joris B., Wilmotte A., Thonart P., "Fermentative hydrogen production from glucose and starch using pure strains and artificial co-cultures of *Clostridium* spp.", *Biotechnology for Biofuels*, Vol. 5, No. 1,2012, pp. 1–15. https://doi.org/10.1186/1754-6834-5-35
2. Abreu A.A., Karakashev D., Angelidaki I., Sousa D.Z., Madalena A.M., "Biohydrogen production from arabinose and glucose using extreme thermophilic anaerobic mixed cultures", *Biotechnology for Biofuels*, Vol. 5, No. 1,2012, pp. 1–12. https://doi.org/10.1186/1754-6834-5-6
3. Li J.Z., Ren N.Q., Li B.K., Qin Z., He J.G., "Anaerobic biohydrogen production from monosaccharides by a mixed microbial community culture", *Bioresour. Technol.*, Vol. 99, No. 14, 2008, pp. 6528–6537. https://doi.org/10.1016/j.biortech.2007.11.072
4. Li D., Yuan Z.H., Sun Y.M., Kong X.Y., Zhang Y., "Hydrogen production characteristics of the organic fraction of municipal solid wastes by anaerobic mixed culture fermentation", *Int J Hydrogen Energy*, Vol. 34, No. 2, 2009, pp. 812–820. https://doi.org/10.1016/j.ijhydene.2008.11.031
5. Ren N.Q., Guo W.Q., Liu B.F., Cao G.L., Ding J., "Biological hydrogen production by dark fermentation: challenges and prospects towards scaled-up production", *Curr Opin Biotechnol*, Vol. 22, No. 3, 2011, pp. 365–370. https://doi.org/10.1016/j.copbio.2011.04.022
6. Ozkan L., Erguder T.H., Demirer G.N., "Effects of pretreatment methods on solubilization of beet-pulp and bio-hydrogen production yield". *Int J Hydrogen Energy*, Vol. 36, No. 1, 2011, pp. 382–389. https://doi.org/10.1016/j.ijhydene.2010.10.006
7. Rai P.K., Singh S.P., Asthana P.K., Singh S., "Biohydrogen production from sugarcane bagasse by integrating dark- and photo-fermentation", *Bioresour. Technol*, Vol. 152, No. 1, 2014, pp. 140–146. https://doi.org/10.1016/j.biortech.2013.10.117
8. Ren N.Q., Wang A.J., Cao G.L., Xu J.F., Gao L.F., "Bioconversion of lignocellulosic biomass to hydrogen: potential and challenges", *Biotechnol Adv*, Vol. 27, No. 27, 2009, pp. 1051–1060. https://doi.org/10.1016/j.biotechadv.2009.05.007
9. Cheng C.L., Lo, Y.C., Lee K.S., Lee D.J., Lin C.Y., Chang J.S., "Biohydrogen production from lignocellulosic feedstock", *Bioresour Technol*, Vol. 102, No. 18, 2009, pp. 8514–8523. https://doi.org/10.1016/j.biortech.2011.04.059
10. Ray R.C., Ward O.P. 2008. *Microbial Biotechnology in Horticulture*, Vol. II. New Hampshire, USA: Science Publishers, Inc.
11. Su H.B., Cheng J., Zhou J.H., Song W.L., Cen K.F., "Improving hydrogen production from cassava starch by combination of dark and photo fermentation", *Int J Hydrogen Energy*, Vol. 34, No. 4, 2009, pp. 1780–1786. https://doi.org/10.1016/j.ijhydene.2008.12.045
12. Zhang J., Xu J.Y., Wang D.Q., Ren N.Q., "Anaerobic digestion of cassava pulp with sewage sludge inocula", *Bioresources*, Vol. 11, No. 1, 2016, pp. 451–465.
13. Zhang Q.H., Tang L., Zhang J.H., Mao G., Jiang L., "Optimization of thermal-dilute sulfuric acid pretreatment for enhancement of methane production from cassava residues", *Bioresour Technol,* Vol. 102, No. 4, 2011, pp. 3958–3965. https://doi.org/10.1016/j.biortech.2010.12.031
14. Zhang Q.H., He J., Tian M., Mao Z.G., Tang L., Zhang J.H., Zhang H.J., "Enhancement of methane production from cassava residues by biological pretreatment using a constructed microbial consortium", *Bioresour Technol*, Vol. 102, No. 19, 2011, pp. 8899–8906. https://doi.org/10.1016/j.biortech.2011.06.061
15. Hirayama K., Kawamura S., Mitsuoka T., Tashiro K., "The faecal flora of the giant panda (*Ailuropoda melanoleuca*)", *J Appl Bacteriol*, Vol. 67, No. 4, 1989, pp. 411–415. https://doi.org/10.1111/j.1365-2672.1989.tb02511.x
16. Schloss P.D., Handelsman J., "Introducing DOTUR, a computer program for defining operational taxonomic units and estimating species richness", *Appl Environ Microbiol*, Vol. 71, No. 3, 2005, pp. 1501–1506. https://doi.org/10.1128/AEM.71.3.1501-1506.2005
17. Wei G., Lu H.F., Zhou Z.H., Xie H.B., Wang A.S., Nelson K., Zhao L.P., "The microbial community in the feces of the giant panda (Ailuropoda melanoleuca) as determined by PCR-TGGE profiling and clone library analysis", *Microb Ecol*, Vol. 54, No. 1, 2007, pp. 194–202. https://doi.org/10.1007/s00248-007-9225-2
18. Li R.Q., *et al.*, "The sequence and de novo assembly of the giant panda genome", *Nature*, Vol. 463, No. 7279, 2010, pp. 311–317. https://doi.org/10.1038/nature08696
19. Zhu L.F., Wu Q., Dai J.Y., Zhang S.N., Wei F.W., "Evidence of cellulose metabolism by the giant panda gut microbiome", *PNAS*, Vol. 108, No. 43, 2011, pp. 17714–17719. https://doi.org/10.1073/pnas.1017956108
20. Valdez-Vazquez I., Poggi-Varaldo H.M., "Hydrogen production by fermentative consortia", *Renew Sust Energ Rew*, Vol. 13, No. 5, 2011, pp. 1000–1013. https://doi.org/10.1016/j.rser.2008.03.003
21. Song Y., Logan B.E., "Effect of O_2 exposure on perchlorate reduction by Dechlorosoma sp. KJ", *Water Res*, Vol. 38, No. 6, 2004, pp. 1626–1632. https://doi.org/10.1016/j.watres.2003.11.033
22. Doong R.A., Schink B., "Cysteine-mediated reductive dissolution of poorly crystalline iron (III) oxides by Geobacter sulfurreducens", *Environ Sci Technol*, Vol. 36, No. 13, 2002, pp. 2939–2945. https://doi.org/10.1021/es0102235
23. Bao M.D., Su H.J., Tan T.W., "Dark fermentative bio-hydrogen production: Effects of substrate pre-treatment and addition of metal ions or L-cysteine", *Fuel*, Vol. 112, No. 10, 2013, pp. 38–44. https://doi.org/10.1016/j.fuel.2013.04.063
24. Sluiter A. 2006. Determination of Structural Carbohydrates and Lignin in Biomass. USA: National Renewable Energy Laboratory, Golden, CO.
25. Wolin E.A., Wolin M.J., Wolfe R.S., "Formation of methane by bacterial extracts", *J Biol Chem*, Vol. 238, No. 8, 1963, pp. 2882–2886.
26. Ren H.Y., Liu B.F., Kong F.Y., Zhao L., Ren N.Q., "Hydrogen and lipid production from starch wastewater by co-culture of anaerobic sludge and oleaginous microalgae with simultaneous COD, nitrogen and phosphorus removal", *Water Research*, Vol. 85, 2015, pp. 404–412. https://doi.org/10.1016/j.watres.2015.08.057
27. Fang H.H.P., Li C.L., Zhang T., "Acidophilic biohydrogen production from rice slurry", *Int J Hydrog Energy*, Vol. 31, No. 6, 1963, pp. 683–692. https://doi.org/10.1016/j.ijhydene.2005.07.005
28. Chen W.H., Chen S.Y., Khanal S.K., Sung S., "Kinetic study of biological hydrogen production by anaerobic fermentation", *Int J Hydrog Energy*, Vol. 31, No. 15, 2006, pp. 2170–2178. https://doi.org/10.1016/j.ijhydene.2006.02.020
29. Mizuno O., Ohara T., Shinya M., Noike T., "Characteristics of hydrogen production from bean curd manufacturing waste by anaerobic microflora", *Water Sci Technol*, Vol. 42, 2000, pp. 345–350.
30. Lee K.S., Hsu Y.F., Lo Y.C., Lin P.J., Lin C.Y., Chang J.S., "Exploring optimal environmental factors for fermentative hydrogen production from starch using mixed anaerobic microflora", *Int J Hydrog Energy*, Vol. 33, No. 5, 2008, pp. 1565–1572. https://doi.org/10.1016/j.ijhydene.2007.10.019
31. Pantipa P., Paiboon D., "Hydrogen production from cassava pulp hydrolysate by mixed seed cultures: Effects of initial pH, substrate and biomass concentrations", *Biomass & Bioenergy*, Vol. 64, No. 3, 2014, pp. 1–10.
32. Blackwell J., Vasko P.D., Koenig J.L., "Infrared and Raman spectra of the cellulose from the cell wall of *Valonia ventricosa*", *J Appl Phys*, Vol. 41, No. 11, 1970, pp. 4375–4379. https://doi.org/10.1063/1.1658470
33. Wang L., Han G., Zhang Y., "Comparative study of composition, structure and properties of *Apocynum venetum* fbers under different pretreatments", *Carbohyd. Polym*, Vol. 69, No. 2, 2007, pp. 391–397. https://doi.org/10.1016/j.carbpol.2006.12.028
34. Pandey K.K., "Study of the effect of photo-irradiation on the surface chemistry of wood", *Polym Degrad Stabil*, Vol. 90, No. 1, 2005, pp. 9–20. https://doi.org/10.1016/j.polymdegradstab.2005.02.009
35. Binod P., Sindhu R., Singhania R.R., Vikram S., Devi L., Nagalakshmi S., Kurien N., Sukumaran R.K., Pandey A., "Bioethanol production

from rice straw: an overview", *Bioresour Technol*, Vol. 101, No. 13, 2010, pp. 4767–4774. https://doi.org/10.1016/j.biortech.2009.10.079

36. Sitti Fatimah M., Sulaiman O., Hashim R., Arai T., Kosugi A., Abe H., Murata Y., Mori Y., "Characterization of parenchyma and vascular bundle of oil palm trunk as function of storage time", *Lignocellulose*, Vol. 1, No. 1, 2012, pp. 33–44.
37. Lionetto F., Sole R.D., Cannoletta D., Vasapollo G., Maffezzoli A., "Monitoring wood degradation during weathering by cellulose crystallinity". Materials, Vol. 5, No. 10, 2012, pp. 1910–1922. https://doi.org/10.3390/ma5101910
38. Cao Y., Tan H., "Structural characterization of cellulose with enzymatic treatment", J Mol Struct. Vol. 705, No. 1-3, 2004, pp. 189–193. https://doi.org/10.1016/j.molstruc.2004.07.010
39. Colom X., Carrillo F., "Crystallinity changes in lyocell and viscose-type fibers by caustic treatment", *Eur Polym J*, Vol. 38, No. 11, 2002, pp. 2225–2230. https://doi.org/10.1016/S0014-3057(02)00132-5
40. Oh S.Y., Yoo D.I., Shin Y., Seo G., "FTIR analysis of cellulose treated with sodium hydroxide and carbon dioxide", *Carbohyd Res*, Vol. 340, No. 3, 2005, pp. 417–428. https://doi.org/10.1016/j.carres.2004.11.027
41. Fan L.T., Lee Y.H., Beardmore D.H., "Mechanism of the enzymatic hydrolysis of cellulose: Effect of major structural features of cellulose on enzymatic hydrolysis", *Biotechnol Bioeng*, Vol. 22, No. 1, 1980, pp. 177–199. https://doi.org/10.1002/bit.260220113
42. Park S., Baker J.O., Himmel M.E., Parilla P.A., Johnson D.K., "Cellulose crystallinity index: Measurement techniques and their impact on interpreting cellulase performance", *Biotechnol Biofuels*, Vol. 3, No. 1, 2010, pp. 103–111. https://doi.org/10.1186/1754-6834-3-10
43. Chen H.Q., Ma X.X., Fan D.D., Luo Y.E., Gao P.F., Yang C.Y., "Influence of L-Cysteine Concentration on Oxidation-reduction Potential and Biohydrogen Production", *Chinese Journal of Chemical Engineering*, Vol. 18, No. 4, 2010, pp. 681–686. https://doi.org/10.1016/S1004-9541(10)60275-3

Application of Deep Pyrosequencing to the Analysis of Soil Microbial Communities in Different Lotus Fields

RUQIANG CUI*, HEGUI WANG, YAJING ZENG and XIAOTANG SUN*

College of Agronomy/Key Laboratory of Crop Physiology, Ecology and Genetic Breeding, Ministry of Education,
Jiangxi Agricultural University, Nanchang, Jiangxi 330045, China

ABSTRACT: *Fusarium oxyporum* f. sp. *nelumbicola* is a very important plant pathogen that can cause lotus *Fusarium* wilt and lead to vast economic loss in Jiangxi Province, China. Sequencing data of 16S ribosomal RNA genes and internal transcribed spacer regions revealed that different bacterial and fungal communities were present in soil samples from healthy or *Fusarium* wilt-infected lotus fields with different years of continuous cropping, indicating that the long-term continuous cropping of lotus significantly altered the soil microbial communities. Fungal diversity indexes in the healthy soil samples increased with the years of monoculture, but decreased in the *Fusarium* wilt-infected soil samples, whereas bacterial community diversity in all the soil samples was relatively stable. A cluster analysis revealed that consecutive cropping time was a key factor for determining fungal community structure, but not for bacterial community structure. The relative abundances of *Proteobacteria*, *Acidobacterial*, *Ascomycota*, and *Basidiomycota* phyla decreased with the years of lotus monoculture. Compared with the healthy soil samples, the abundances of beneficial bacteria in the *Fusarium* wilt-infected soil samples significantly decreased with time. These observations indicate that soil weakness and lotus *Fusarium* wilt disease may be attributed to structural changes of soil microbial communities after long-term continuous cropping, and the changes include reduction of beneficial microorganisms and accumulation of fungal pathogens.

INTRODUCTION

LOTUS (*Nelumbo nucifera* Gaertn) is an important economic aquatic crop widely cultivated in India, Australia, Japan and China (Cai *et al.*, 2014). Lotus wilts caused by soil-borne fungi have infected most of long-term continuous cropping lotus fields, resulting in vast economic loss in China (Hu *et al.*, 2014). Particularly, the number of lotus suffering from rhizome rot has rapidly increased in recent years and it is difficult to be managed by agronomic and chemical controls (Cai *et al.*, 2014). This disease has been a major limiting factor in lotus production, which can cause almost a 100% loss. From 2012 to 2015, rhizome rot of lotus was found in Guangchang County of Jiangxi Province, China. Isolates from diseased lotus roots were obtained and their pathogenicity was confirmed by in vitro inoculation. A pathogen was identified to be *Fusarium oxyporum* f. sp. *nelumbicola* based on its morphological and molecular characteristics (Hu *et al.*, 2014).

Continuous mono-cropping means growing a same crop year after year on a same land and likely induces different types of microflora (Shipton, 1977). Continuous mono-cropping often results in problems such as yield and quality decline (Zhang *et al.*, 2013), which is considered a continuous cropping obstacle (Li *et al.*, 2013). Replanted perennial crops usually grow slowly and undergo continuous cropping obstacles (Mazzola *et al.*, 2012; Lake *et al.*, 1993).

Soil microorganisms are extremely important components of sustainable agro-ecosystems (Lupwayi *et al.*, 1998), and play a key role in crop production in agricultural systems (Zhao *et al.* 2013). Bacterial diversity is very high in soils (Gans *et al.*, 2005), where up to 6,000-50,000 bacterial species were estimated to be present in one gram of soil samples (Claire *et al.*, 2003). Bacteria play important roles in biogeochemical cycles, supplying nutrients to crops and keeping soil health in agricultural ecosystems (Kennedy *et al.*, 1995; Nacke *et al.*, 2011). Additionally, fungal pathogens can easily accumulate in continuous cropping systems (Chen *et al.*, 2012; Zhou *et al.*, 2012).

Previous studies have shown that soil microbial communities were affected by miscellaneous factors, including soil types (Girvan *et al.*, 2003), plant spe-

---

*Authors to whom correspondence should be addressed.
E-mail: cuiruqiang@jxau.edu.cn (Ruqiang Cui); xtsun80@163.com (Xiaotang Sun)

1544-8053/16/02 S235-07

doi:10.12783/issn.1544-8053/13/4/S31

cies (Garbeva *et al.*, 2006), temperature (Norris *et al.*, 2002), organ amendments (Stark *et al.*, 2007), nitrogen levels (Fierer *et al.*, 2012), soil pH (Lauber *et al.*, 2009; Nacke *et al.*, 2011) and contaminations (Lee *et al.*, 2011). Recently, an increasing number of studies have revealed that continuous cropping cause destruction of soil microbial community size and structure (Lu *et al.*, 2013; Li *et al.*, 2014). In this study, we revealed bacterial and fungal diversity and community structure in soils from different lotus fields in China by conducting a pyrosequencing-based analysis of the V3-V4 hypervariable regions of 16S ribosomal RNA (16S rRNA) and the internal transcribed spacer ITS1 (ITS5-ITS2). We aimed to compare soil microbial community composition and structure among different lotus fields and to explore relationships between microbial communities and lotus wilt disease.

MATERIALS AND METHODS

Soil Sampling and Treatment

Soil samples were collected from lotus fields in Lotus Research Institute of Guangchang, Jiangxi Province (26°79´N, 116°30´E). The fields are in a sub-tropical monsoon climate, and the annual mean temperature and precipitation are 16.3–19.5°C and 1,340–1,940 mm, respectively. The cultivar of lotus (*Nelumbo nucifera* Gaertn), agronomic management and fertilization regime were the same for the different fields. Soil samples were collected from healthy and *Fusarium* wilt-infected lotus fields with a continuous cropping history of 1, 2, 3, or 4 years and labeled as J1, J2, J3, J4, B1, B2, B3, B4, respectively. In each field, random sampling was conducted at 20 circular sites (each site with a depth of 0–25 cm and a diameter of 2 cm) in June 2015 and the samples were mixed to form a composite sample, which was stored in a sterile polyethylene bag under cold storage condition (0°C to 4°C) and brought to the laboratory where the composite samples from different fields were all stored at –70°C prior to soil microbial DNA extraction.

DNA Extraction and PCR Amplification

Total genomic DNA from each soil sample was extracted with TIANamp Soil DNA Kit (TIANGEN BIOTECH Inc., Beijing, China) following the manufacturer's instructions. DNA concentration and purity was monitored on 1% agarose gels. Universal bacterial primers 341F (5′-CCATYGGGRBGCSCAG-3′) and 806R (5′-GGACTACNNGGGTATCTAAT-3′) were used to amplify the V3 to V4 hypervariable regions in the bacterial 16S rRNA gene. ITS5 (5′-GGAAGTAAAAGTCGTAACAAGG-3′) and ITS2 (5′-GCTGCGTTCTTCATCGATGC) of fungi-specific primers were employed to amplify the fungal internal transcribed spacer (ITS1) region. These primer pairs were all barcoded. For 16S rRNA gene and ITS region PCR amplification, the PCR reactions were carried out in 30-μL reaction mixtures consisting of 15 μL of Phusion Master Mix (2×) (New England Biolabs), 2 μM of each primer, approximately 10 ng of template DNA and 2 μL of H_2O. The PCR steps were: (1) an initial denaturation at 98°C for 1 min, followed by 30 cycles of denaturation at 98°C for 10 s, annealing at 50°C for 30 s, polymerization at 72°C for 60 s, and a final elongation at 72°C for 5 min for the 16S V3+V4 rRNA gene; (2) an initial denaturation at 95°C for 10 min, followed by 15 cycles of denaturation at 95°C for 30 s, annealing starting at 65°C for 1 min with 1°C lower in each subsequent cycle, elongation at 72°C for 90 s, 20 cycles of denaturation at 95°C for 30 s, annealing at 50°C for 1 min, elongation at 72°C for 90 s, and a final extension at 72°C for 10 min for ITS gene.

PCR Products Mixing and Purification

The PCR products from each pair of barcoded primers were pooled and purified with 2% agarose gel electrophoresis. The final PCR products were purified by a gel extraction kit (Thermo Scientific Inc., MA, USA), and amplicons were pooled based on a Nanodrop 2000 machine (Thermo Fisher Scientific Inc., Wilmington, DE) at equimolar concentrations in a single tube, and the single strand PCR productions were amplified by emulsion PCR for Miseq sequencing.

Library Construction and Sequencing

Following the instructions for NEBNext Ultra DNA Library Prep Kit, sequencing libraries were generated and index codes were added to the libraries. Library quality was assessed on an Agilent Bioanalyzer 2100 system and a Qubit@ 2.0 Fluorometer (Thermo Scientific). At last, the libraries were sequenced on an Illumina MiSeq platform, producing 250 bp/300 bp paired-end DNA sequencing reads.

Data Analyses

Paired-end DNA sequencing reads were merged using the FLASH analysis (Magŏc & Salzberg, 2011), which is a tool able to merge paired-end reads rapidly and accurately while extending the reads' length by finding the overlap between paired-end reads from the other end of the same DNA sequence. Paired-end reads for each sample were allocated based on the unique barcodes.

Bacterial and fungal sequence analyses were performed in the software package UPARSE (Edgar, 2013). UPARSE was a method for generating clusters from next-generation sequencing reads of marker genes. Sequence reads were grouped into the same operational taxonomic units (OTUs) if they had more than 97% similarity. The representative sequence for each OUT was selected and taxonomically annotated based on the Ribosomal Database Project (RDP) classifier. For alpha diversity, we rarefied the OTU table and calculated three metrics: Chao 1 (an estimate of species abundance), ACE (an estimator of abundance-based coverage) and Shannon index. The percentage of the total species in each sequenced sample was calculated by ACE. Principal component analysis (PCA) was used to analyze these feature parameters in the QIIME software package in order to obtain parameters with lower dimension before cluster analysis (Kuczynski, 2012). By using QIIME to calculate both weighted and unweighted UniFrac, we estimated beta diversity. Principal coordinate analysis (PCoA) and UPGMA (Unweighted Pair Group Method with Arithmetic Mean) clustering were applied to unweighted UniFrac distance for soil protistan communities. PCoA is a distance-based ordination method that performs metric multidimensional scaling. UPGMA is a simple agglomerative hierarchical clustering method and can be used to show the distance matrix. Metastats software was used to analyze differences in the abundances of individual taxonomy between two groups. Biomarkers within different groups were quantitatively analyzed based on linear discriminant analysis (LDA) effect size (LEfSe).

RESULTS

Compositions of Bacterial and Fungal Communities

As shown in Table 1, the coverage of the bacterial and fungal samples was all above 95%, meaning that the deep sequencing could completely satisfy the experimental needs. In total, 360,815 tags comprising a total of 8,613 bacterial OTUs were acquired from 8 soil samples, and the number of high quality sequences in each sample changed from 27,784 to 62,827, and the number of OTUs varied from 911 to 1,216. A total of 371,813 tags comprising 5,000 fungal OTUs were acquired from 8 samples, and the number of high quality sequences in each sample changed from 34,413 to 58,554, and the number of OTUs varied from 318 to 964.

Table 1. Bacterial and Fungal α-diversity Indexes of Soil Samples from Different Lotus Fields.

Microbial Community	Lotus Fields	Coverage (%)	Chao 1	Shannon	ACE
Bacterial	J1 (1 year)	97.13 ± 0.52a	871.12 ± 67.12a	7.98 ± 0.05a	824.8 ± 63.14a
	J2 (2 years)	97.72 ± 0.64a	999.72 ± 84.06b	8.53 ± 0.07b	946.8 ± 80.27b
	J3 (3 years)	98.05 ± 0.33a	1274.79 ± 104.06c	8.85 ± 0.14b	1117.6 ± 74.23c
	J4 (4 years)	98.06 ± 0.50a	1271.12 ± 63.23c	8.85 ± 0.23b	1141.7 ± 103.58c
	B1 (1 year)	96.84 ± 0.55a	1143.86 ± 55.45b	8.33 ± 0.08b	989.8 ± 54.36b
	B2 (2 years)	97.62 ± 0.43a	890.91 ± 64.74a	8.04 ± 0.05a	822.9 ± 34.93a
	B3 (3 years)	97.27 ± 0.67a	1142.31 ± 18.09b	8.90 ± 0.06b	1090.8 ± 67.62c
	B4 (4 years)	97.71 ± 0.54a	1153.79 ± 33.87b	9.03 ± 0.13b	1122.9 ± 55.54c
Fungal	J1 (1 year)	97.72 ± 0.52a	807.41 ± 78.34a	3.98 ± 0.03a	630.0 ± 28.72a
	J2 (2 years)	98.99 ± 0.55a	854.19 ± 73.60ab	4.12 ± 0.04ab	663.0 ± 63.00a
	J3 (3 years)	98.63 ± 0.23a	868.72 ± 48.73b	4.48 ± 0.08b	732.0 ± 13.75b
	J4 (4 years)	98.22 ± 0.57a	985.34 ± 76.52c	4.70 ± 0.32b	862.0 ± 54.41c
	B1 (1 year)	98.39 ± 0.28a	765.36 ± 50.24a	5.56 ± 0.14a	693.0 ± 30.74a
	B2 (2 years)	98.27 ± 0.62a	605.47 ± 30.60b	4.13 ± 0.06b	520.0 ± 43.36b
	B3 (3 years)	97.11 ± 0.64a	507.02 ± 47.28c	2.78 ± 0.05c	392.9 ± 53.62c
	B4 (4 years)	97.46 ± 0.58a	361.58 ± 54.61d	2.10 ± 0.36d	250.0 ± 18.39d

Values are presented as the mean ± standard deviation (*n* = 3). Means followed by the same letter are not significantly different as detected by Turkey's HSD test at $P < 0.05$.
The soil samples were collected from healthy and *Fusarium* wilt infected lotus fields with 1, 2, 3, or 4 years of continuous cropping history and marked as J1, J2, J3, J4, B1, B2, B3, B4, respectively.

Under the classified sequences across all the samples, we selected the top 10 most abundant bacterial and fungal phyla (Figure 1). As shown in Figure 1, the top 10 bacterial phyla across all the samples were *Proteobacteria* (50.68%), *Acidobacterial* (13.33%), *Chlorobi* (6.65%), *Nitrospirae* (7.12%), *Chloroflexi* (5.43%), *Bacteroidetes* (3.28%), *Crenarchaeota* (2.35%), *Euryarchaeota* (1.43%), *Spirochaetes* (1.46%) and *Actinobacteria* (1.34%). The top 10 fungal phyla through all the samples were *Ascomycota* (48.34%), *Basidiomycota* (17.96%), *Un-s-Fungi* sp (9.29%), *Zygomycota* (3.20%), *Chytrtidiomycota* (1.10%), *Un-s-fungal sp WEF9* (1.03%), *Un-s-fungal endophyte* (0.24%), *IS-s-Sclerotium hydrophilum* (0.03%), *Un-s-fungal sp ARIZ L136* (0.02%) and *Un-s-fungal sp ARIZ L471* (0.02%).

Bacterial and Fungal *α*-Diversity

Bacterial and fungal richness and diversity are shown with Chao1, Shannon and ACE indexes in Table 1. Generally, Chao1 and ACE indexes of bacterial community richness in the healthy and *Fusarium* wilt-infected soil samples were significantly higher for the lotus fields with longer continuous cropping history than for the fields with shorter continuous cropping history. The Shannon index of bacterial community di-

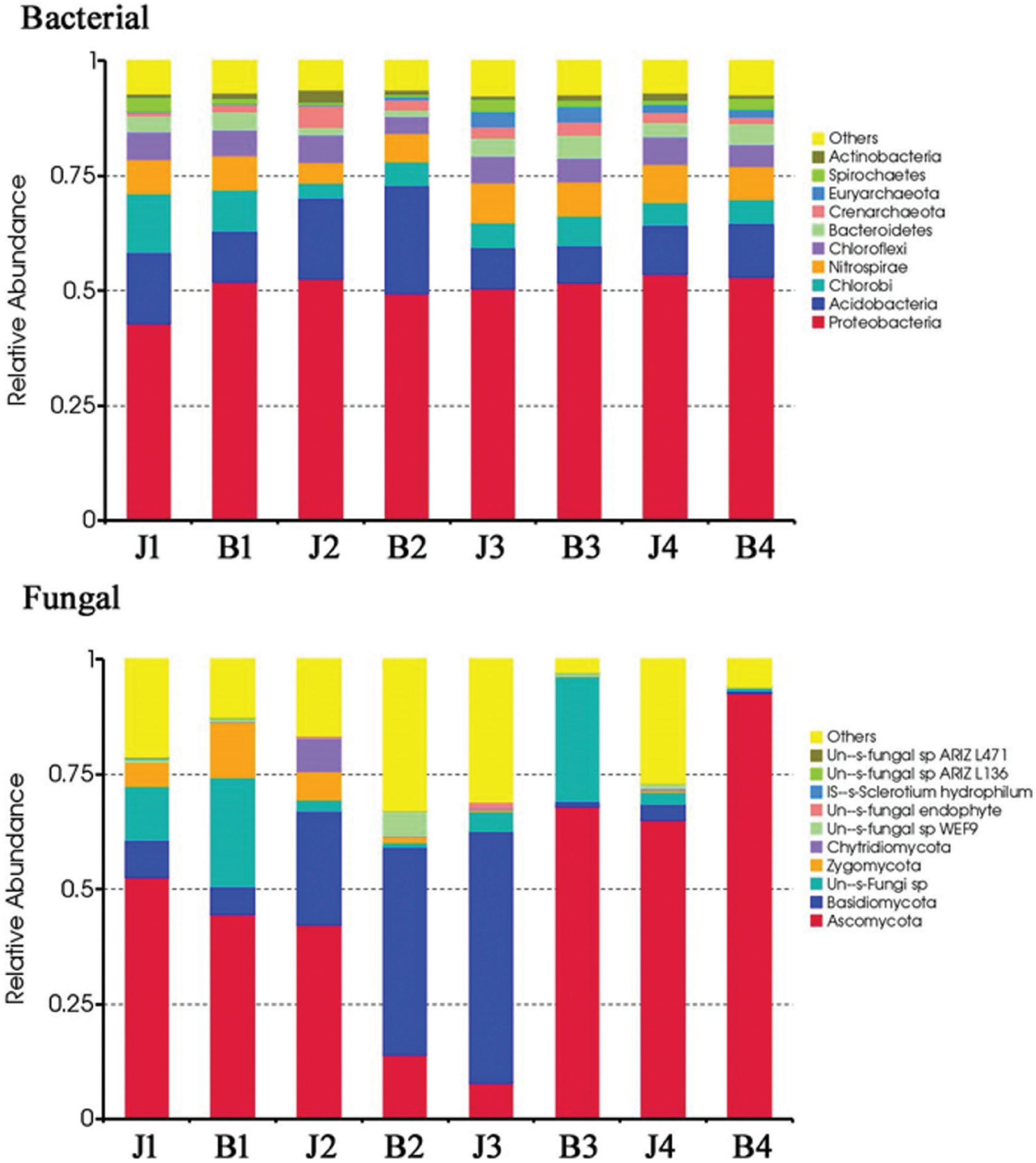

Figure 1. *Relative abundances of bacterial and fungal phyla. J1, J2, J3, J4 or B1, B2, B3 and B4 represent soil samples from healthy or Fusarium wilt-infected with 1, 2, 3, or 4 years of continuous cropping history, respectively.*

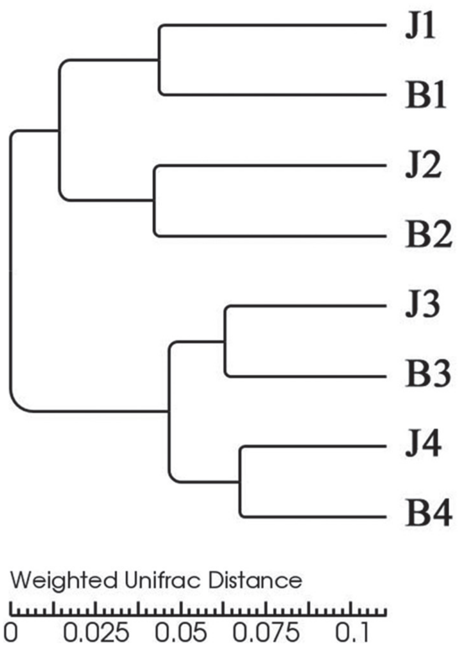

Figure 2. *UPGMA clustering of bacterial communities in soil samples from different lotus fields based on weighted Unifrac and unweighted Unifrac distance. J1, J2, J3, J4 or B1, B2, B3 and B4 represent soil samples from healthy or Fusarium wilt-infected fields with 1, 2, 3, or 4 years of continuous cropping history, respectively.*

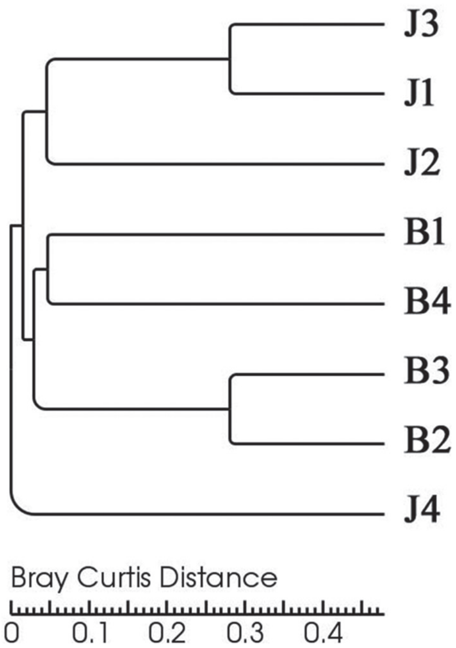

Figure 3. *Bray Curtis distance-based UPGMA clustering of fungal communities in soil samples from different lotus fields. J1, J2, J3, J4 or B1, B2, B3 and B4 represent soil samples from healthy or Fusarium wilt infected fields with 1, 2, 3, or 4 years of continuous cropping history, respectively.*

versity in healthy soil samples from the lotus field YJ1 and *Fusarium* wilt-infected soil samples from the lotus field YB2 was lower than in other soil samples. The richness and diversity of bacterial community did not show statistically significant difference between *Fusarium* wilt-infected and healthy soil samples (Table 1). As shown by the data of the four time-series lotus fields (Table 1), the Chao1 and ACE indexes of fungal community richness as well as the Shannon index of fungal community diversity increased with the years of continuous cropping history in healthy soil samples, while a trend of decrease for those indexes were observed in *Fusarium* wilt-infected infected soil samples.

Bacterial and Fungal *β*-Diversity

The heatmap of beta-diversity indexes based on Bray-Curtis distance showed that the soil bacterial communities identified in the lotus fields YJ1 and YB1, YJ2 and YB2, YJ3 and YB3, YJ4 and YB4 had similar species diversity (Figure 1). In contrast, the fungal species diversity increased with the years of continuous cropping history (Figure 1).

The UPGMA clustering analysis based on the weighted Unifrac distance showed that the soil bacterial communities identified in the lotus fields with 1–4 years of continuous cropping history. The four similar samples were grouped together (Figure 2). The Bray Curtis distance-based clustering analysis, when applied to the soil fungal communities identified in the different lotus fields, showed that J4 was separated from the other seven samples (Figure 3). For the fungal community compositions, healthy soil samples with different years of continuous cropping history (J1, J2 and J3) were grouped together, while *Fusarium* wilt-infected soil samples (B1, B2, B3 and B4) were grouped together (Figure 3). Figure 3 reveals that the soil microbial species diversity was similar among the same type of soil samples (healthy soil samples versus *Fusarium* wilt-infected soil samples) collected from the continuously cropped fields.

Discussion

The relative species abundance of bacterial and fungal phylum reported in this study generally agreed with previously reported pyrosequencing analysis results of soil microcommunities. The top two abundant phyla of bacteria were *Acidobacteria* and *Proteobacteria* through all the samples (Figure 2), and the abundance ranks of the two phyla agreed with those of 88 soil samples in North and South America (Lauber *et al.*, 2009) as well as with those of forest and grassland soil samples in Germany (Nacke *et al.*, 2011). The top two abundant phyla were *Actinobacteria* and *Bacteriodetes* identified in the soil samples of Texas (USA) where different agronomic and chemical management had been implemented (Girvan *et al.*, 2003). The top two abundant phyla of fungi were *Ascomycota* and *Basidiomycota*, and this result was consistent with the previously reported experimental data in peanut and soybean soils under continuous cropping (Li *et al.*, 2014; Li *et al.*, 2010). The same results have been observed in different types of soil (Buée *et al.*, 2009; Lauber *et al.*, 2008). However, this study showed that *Basidiomycota* accounted for 17.96% of the microbial abundance in our samples, in contrast to only 0.6% in the soil samples investigated by Liu *et al.* (2014). The difference may be attributed to the difference of soil type; moreover, the use of different amplified fragments and different sequence databases for the phylogenetic assignment may also affect the experimental results about the contribution of *Basidiomycota*.

In our study, the fungal diversity and bacterial communities in healthy soil samples increased with the number of cultivation years, but the fungal diversity in infected soil samples decreased in lotus fields with the years of continuous cropping history. There were some differences in our results and other reported results. For example, it was reported that soil fungal diversity increased during continuous cropping with peanut (Liu *et al.*, 2014) and during long-term monoculture of vanilla, while no obvious distinctions were observed among the bacteria (Xiong *et al.*, 2014). Therefore, the change of soil fungal diversity may be different between aquatic plant environment and terrestrial plant environment.

Soil microbial-ecological balance was broken by crops continuous cropping. The deep pyrosequencing technology has advantages such as high-throughput and high-sensitivity, and it may reflect true circumstances of microbiological quantities and compositions (Acosta-Martínez *et al.*, 2008). The deep pyrosequencing technology can be used to study and characterize soil microbes unable to be cultured, and to get more and complete information about soil microbial communities. With pyrosequencing and bioinformatics, soil microorganisms may be more accurately determined based on classification techniques (Sun *et al.*, 2009). Application of microbiological fertilizers to soil may improve beneficial microflora in the soil, thereby gradually enhancing the soil fertility, and therefore this method may help overcome continuous cropping obstacles.

In conclusion, the findings in this study demonstrated that long-term monoculture of lotus significantly altered soil microbial communities. Soil fungal diversity indexes increased with the years of consecutive cropping, whereas soil bacterial diversity was relatively stable. Soil bacterial diversity showed no obvious distinction in the *Fusarium* wilt-infected soil samples that had been subjected to different years of lotus monoculture, but showed statistically significant increase in the healthy soil samples. Soil fungal diversity showed statistically significant increase in the healthy soil samples, but decreased in the *Fusarium* wilt-infected soil samples during continuous cropping with lotus. Therefore, soil weakness and lotus *Fusarium* wilt disease may be attributed to structural changes of soil microbial communities after long-term continuous cropping, and the changes include reduction of beneficial microorganisms and accumulation of fungal pathogens.

ACKNOWLEDGEMENTS

This work was supported by the National Natural Science Foundation of China (31260423) and the National Natural Science Foundation of Jiangxi Province (20151BAB204027).

REFERENCES

Acosta-Martínez V., Dowd S., Sun Y., Allen V., "Tag-encoded pyrosequencing analysis of bacterial diversity in a single soil type as affected by management and land use", *Soil Biology and Biochemistry*, Vol. 41, No. 11, 2008, pp. 2762–2770. https://doi.org/10.1016/j.soilbio.2008.07.022

Buée, M., Reich, M., Murat, C., Morin, E., Nilsson, R. H., Uroz S., *et al.*, "454 Pyrosequencing analyses of forest soils reveal an unexpectedly high fungal diversity", *New Phytol*, Vol. 184, No. 2, 2009, pp. 449–456. https://doi.org/10.1111/j.1469-8137.2009.03003.x

Cai, C., Cai, J., Man, J., Yang, Y., Wang. Z., Wei. C., "Allomorph distribution and granule structure of lotus rihizome C-type starch during gelatinization", *Food Chemistry*, Vol. 142, No. 3, 2014, pp. 408–415. https://doi.org/10.1016/j.foodchem.2013.07.091

Chen, M., Li, X., Yang, Q., Chi, X., Pan, L., Chen, N., *et al.*, "Soil eukaryotic microorganism succession as affected by continuous cropping of peanut-pathogenic and beneficial fungi were selected", *PLoS ONE*, Vol. 7, No. 7, 2012, e40659. https://doi.org/10.1371/journal.pone.0040659

Claire, H. M., Leibold, M. A., Smith, V. H., Bohannan, B. J. M., "Bacterial diversity patterns along a gradient of primary productivity", *Ecol Lett*, Vol. 6, No. 7, 2003, pp. 613–622. https://doi.org/10.1046/j.1461-0248.2003.00472.x

Edgar, R. C., "UPARSE: highly accurate OTU sequences from microbial amplicon reads", *Nature methods*, Vol. 10, No. 10, 2013, pp. 996–998. https://doi.org/10.1038/nmeth.2604

Fierer, N., Lauber, C. L., Ramirez, K. S., Zaneveld, J., Bradford, M. A., Knight, R., "Comparative metagenomic, phylogenetic and physiological analyses of microbial communities across nitrogen gradients", *ISME J*, Vol. 6, No. 5, 2012, pp. 1007–1017. https://doi.org/10.1038/ismej.2011.159

Gans, J., Wolinsky, M., Dunbar, J., "Computational improvements reveal great bacterial diversity and high metal toxicity in soil", *Science*, Vol. 309, No. 5739, 2005, pp. 1387–1390. https://doi.org/10.1126/science.1112665

Garbeva, P., Postma, J., van Veen, J.A., van Elsas, J.D., "Effect of above-ground plant species on soil microbial community structure and its impact on suppression of Rhizoctonia solani AG3", *Environ Microbial*, Vol. 8, No. 2, 2006, pp. 233–246. https://doi.org/10.1111/j.1462-2920.2005.00888.x

Girvan, M.S., Bullimore, J., Pretty, J.N., Osborn, A.M., Ball, A.S., "Soil type is the primary determinant of the composition of the total and active bacterial communities in arable soils", *Appl Environ Microbial*, Vol. 69, No. 3, 2003, pp. 1800–1809. https://doi.org/10.1128/AEM.69.3.1800-1809.2003

Hu, C., Sun, X., Xie, K., Jiang, J., Zheng, X., Cui, R., "Isolation and identification of pathogens causing rhizome rot of lotus", *Journal of Changjiang Vegetables*, Vol. 18, No. 344, 2013, pp. 92–94.

Kennedy, A., Smith, K., "Soil microbial diversity and the sustainability of agricultural soils", *Plant Soil*, Vol. 171, No. 1, 1995, pp. 75–86. https://doi.org/10.1007/BF02183056

Kuczynski, J., Stombaugh, J., Walters, W. A., González, A., Caporaso, J. G., Knight, R., "Using QIIME to analyze 16S rRNA gene sequences from microbial communities", *Curr Protoc Bioinformatics*, 2012, DOI:10.1002/9780471729259.mc01e05s27. https://doi.org/10.1002/9780471729259.mc01e05s27

Lake. R. J., Falloon, P. G., Cook, D. W. M., "Replant problem and chemical components of asparagus roots", *NZJ Crop Hortic Sci*, Vol. 21, No. 1, 1993, pp. 53–58. https://doi.org/10.1080/01140671.1993.9513746

Lauber, C. L., Hamady, M., Knight, R., Fierer, N., "Pyrosequencing-based assessment of soil pH as a predictor of soil bacterial community structure at the continental scale", *Appl Environ Microbiol*, Vol. 75, No. 15, 2009, pp. 5111–5120. https://doi.org/10.1128/AEM.00335-09

Lauber, C. L., Strickland, M. S., Bradford, M. A., Fierer, N., "The influence of soil properties on the structure of bacterial and fungal communities across land-use types". *Soil Biol Biochem*, Vol. 40, No. 9, 2008, pp. 2407–2415. https://doi.org/10.1016/j.soilbio.2008.05.021

Lee, J., Lee, T. K., Löffler, F. E., Park, J., "Characterization of microbial community structure and population dynamics of tetrachloroethene-dechlorinating tidal mudflat communities". *Biodegradation*, Vol. 22, No. 4, 2011, pp. 687–698. https://doi.org/10.1007/s10532-010-9429-x

Li, C., Li, X., Kong, W., Wu, Y., Wang, J., "Effect of monoculture soybean on soil microbial community in the Northest China", *Plant Soil*, Vol. 330, No. 1, 2010, pp. 423–433. https://doi.org/10.1007/s11104-009-0216-6

Li, N., Deng, K., Song, Y., Wu, Y., Zhao, J., Raza, W., *et al.*, "Variation of rhizosphere bacterial community in watermelon continuous mono-cropping soil by long-term application of a novel bioorganic fertilizer", *Microbiological Research*, Vol. 169, No. 7–8, 2014, pp. 570–578. https://doi.org/10.1016/j.micres.2013.10.004

Li, X., Ding, C., Zhang, T., Wang, X., "Fungal pathogen accumulation at the expense of plant-beneficial fungi as a consequence of consecutive peanut monoculturing", *Soil Biol Biochem*, Vol. 72, 2014, pp. 11–18. https://doi.org/10.1016/j.soilbio.2014.01.019

Liu, X., Zhang, J., Gu, T., Zhng, W., Shen, Q., Yin, S., *et al.*, "Microbial community diversities and taxa abundances in soils along a seven-year gradient of potato monoculture using high throughput pyrosequencing approach", *PLoS ONE*, Vol. 9, No. 1, 2014, pp. e86610. https://doi.org/10.1371/journal.pone.0086610

Lu, L., Yin, S., Liu, X., Zhang, W., Gu, T., Shen, Q., *et al.*, "Fungal networks in yield-invigorating and debilitating soils induced by prolonged potato monoculture", *Soil Biol Biochem*, Vol. 65, 2013, pp. 186–194. https://doi.org/10.1016/j.soilbio.2013.05.025

Lupwayi, N. Z., Rice, W. A., Clayton, G. W., "Soil microbial diversity and community structure under wheat as influenced by tillage and crop rotation", *Soil Biol Biochem*, Vol. 30, No. 13, 1998, pp. 1733–1741. https://doi.org/10.1016/S0038-0717(98)00025-X

Magŏc, T., and Salzberg, S. L., "FLASH: fast length adjustment of short reads to improve genome assemblies", *Bioinformatics*, Vol. 27, No. 21, 2011, pp. 2957–2963. https://doi.org/10.1093/bioinformatics/btr507

Mazzola, M., and Manici, L. M., "Apple replant disease: role of microbial ecology in cause and control", *Annue Rev Phytopathol*, Vol. 50, No. 1, 2012, pp. 45–65. https://doi.org/10.1146/annurev-phyto-081211-173005

Nacke, H., Thurmer, A., Wollherr, A., Will, C., Hodac, L., Herold, N., *et al.*, "Pyrosequencing-based assessment of bacterial community structure along different management types in German forest and grassland soils", *PLos ONE*, Vol. 6, No. 2, 2011, pp. e17000.

Shipton, P. J., "Monoculture and soilbome plant pathogens", *Annu Rev Phytopathol*, Vol. 15, No. 1, 2003, pp. 387—407. https://doi.org/10.1146/annurev.py.15.090177.002131

Stark C., Condron L. M., Stewart A., O'Callaghand M., "Influence of organic and mineral amendments on microbial soil properties and processes", *Appl Soil Ecol*, Vol. 35, No. 1, 2007, pp. 79–93. https://doi.org/10.1016/j.apsoil.2006.05.001

Sun Y., Cai Y., Liu L., Farmerie W., "ESPRIT: estimating species richness using large collections of 16S rRNA pyrosequences", *Nucleic Acids Research*, Vol. 37, No. 10, 2009, pp. e76. https://doi.org/10.1093/nar/gkp285

Xiong, W., Zhao, Q., Zhao, J., Xun, W., Li, R., Zhang, R., *et al.*, "Different continuous cropping spans significantly affect microbial community membership and structurein a vanilla-grown soil as revealed by deep pyrosequencing", *Microb Ecol*, Vol. 70, No. 1, 2015, pp. 209–218. https://doi.org/10.1007/s00248-014-0516-0

Zhang, X., Lang, D., Zhang, E., Bai, C., Wang, H., "Diurnal changes in photosynthesis and antioxidants of Angelica sinensis as influenced by cropping systems", *Photosynthetica*, Vol. 51, No. 2, 2013, pp. 252–258. https://doi.org/10.1007/s11099-013-0013-6

Zhao, J., Zhang, R., Xue, C., Xun, W., Sun, L., Xu, Y., *et al.*, "Pyrosequencing reveals contrasting soil bacterial diversity and community structure of two main winter wheat cropping systems in China", *Micro Ecol*, Vol. 67, No. 2, 2014, pp. 443–453. https://doi.org/10.1007/s00248-013-0322-0

Zhou, X., and Xu, F., "Dynamics of the diversity of fungal and Fusarium communities during continuous cropping of cucumber in the greenhouse", *FEMS Microbiol Ecol*, Vol. 80, No. 2, 2012, pp. 469–478. https://doi.org/10.1111/j.1574-6941.2012.01312.x